به نام خدا

مرکز دانلود رایگان
مهندسی متالورژی و مواد

---

www.Iran-mavad.com

Arc welding control

Arc welding control

Pan Jiluan

CRC Press
Boca Raton Boston New York Washington, DC

WOODHEAD PUBLISHING LIMITED
Cambridge England

Published by Woodhead Publishing Limited, Abington Hall, Abington
Cambridge CB1 6AH, England
www.woodhead-publishing.com

Published in North America by CRC Press LLC, 2000 Corporate Blvd, NW
Boca Raton FL 33431, USA

First published 2003, Woodhead Publishing Limited and CRC Press LLC

British Library Cataloguing in Publication Data
A catalogue record for this book is available from the British Library.

Library of Congress Cataloging in Publication Data
A catalog record for this book is available from the Library of Congress.

Woodhead Publishing ISBN 1 85573 687 X
CRC Press ISBN 0-8493-1772-X
CRC Press order number: WP1772

Typeset by SNP Best-set Typesetter Ltd., Hong Kong
Printed by TJ International, Cornwall, England

Contents

Preface

Welding is a relatively new manufacturing process that has only existed for about a hundred years. However, it is an extremely important technology because, without it, many modern industries would never have developed. One such is the nuclear power plant industry. Nuclear power plants are large complex structures that place incredible demands on structural integrity. Without welding technology, such structures could never be built. Industrial products need to be both robust and structurally sound.

Before liberation in China, welding technology did not exist. It was only during the first five-year plan of economic construction, in the 1950s, that an urgent need for welding technology was first recognised. Welding technology became of prime importance in many universities and major research institutes. During these first stages of development and implementation of welding technology in China, the USSR supported over 156 new construction projects. However, the welding technology and materials industries could not meet this increased demand and it was because of this that the author focused his key research on welding metallurgy (for example, the hot crack problem) and other technologies which were used for the welding of industrial products at that time.

By the 1970s, the welding materials and technology industries were more or less fully developed. The prime focus moved then to welding automation. Due to the complexity of this process, welding automation was incredibly difficult to develop and implement. For example: in order to seal-weld the root side of a pressure vessel made of low-alloy steel, the worker would have to enter the vessel at a preheated temperature of 100–200°C. Even when the worker wore a wet asbestos suit, the working time could be only 20 minutes. This situation seriously affected the quality of the product and the health of the worker. For mass production such as the welding of pipelines, where the conditions were significantly better, a mechanised welding process could be used. But with a low level of automation, incomplete penetration often occurred due to the misalignment of the arc in the weld-groove. This, in turn, caused many rejects and significant economic loss.

With the economic development in his country, the author has devoted much of his time to research into welding automation. The train of thought in this particular field can be divided into two specific types. The first is to use modern science to analyse the welding process through quantitative methods. The second is to develop and perfect welding automation through the application of modern technology. These two fields of research both complement and promote one another. The focus of this research is to grasp and solve the key individual problems of automation and then to try to synthesis results so they can be implemented. In this monograph the theory and developments made by the author are systematically described.

It is the author's intention that this book will not only promote welding automation but will also play a significant role in guiding further development in this important area of technology.

The book is divided into five parts, with fifteen chapters. Part I, 'The dynamic process of arc welding', quantitatively describes the dynamic behaviour of arc welding, the power sources that are used and their effect on welding technology through the basis of control theory. Part II, 'Welding arc control', describes new ways of controlling the welding arc through using modern electronics. The methods of arc control that are introduced are unique, original and demonstrate outstanding performance. The author demonstrates significant systematic achievements in this field that have never before been published. These methods provide important means for developing new welding processes and power sources.

Arc sensors are a type of sensor that have significant potential for automatic seam tracking in arc welding. In Part III, 'Arc sensors and seam tracking', the author establishes the first mathematical model of the sensor on the basis of control theory, giving a clear picture of the essence and phenomena of the sensor. Subsequently, the author has also analysed the output signals of the sensors and proposed a space transformation method that can improve the reliability and accuracy of the weld-groove recognition. Finally, a rotating-arc sensor and two typical seam-tracking welding machines have been developed by the author using the sensor described. Part IV, 'Real-time measurement of welding temperature fields and its application', describes a new method developed by the author for measuring weldment temperature fields using a colorimetric-image method. Experimental studies demonstrate that the method is simple and convenient, the data is reliable, and the speed fast. The method can be used in practice for real-time control. This development is original and has not been published before.

Part V, 'Automatic path programming of welding robots', describes the idea of recognising weld grooves with a three-dimensional vision system and automatic programming of the welding path. It discusses the method

for recognising three-dimensional weld grooves. An arc-welding robot using hardware and software based on this method has already been designed and built. Practical welding has been performed with this robot in the laboratory. In this part, the idea of using robots for arc welding large structures on site, or under extreme conditions such as underwater, are proposed.

The five parts of the book present subjects that can be treated independently of each other, but they all relate to arc-welding automation. Therefore, the theme of the book can be regarded as one subject of technology as a whole. The contents of this monograph are at the frontier of arc-welding technology and they are, in fact, the author's achievements over the last 20 years. However, in writing this monograph, the author stresses the systematic relationship between all parts of the book. Therefore, it may be regarded as a systematic treatise.

All of the author's research was accomplished in the Welding Department of Tsinghua University, with the assistance of the author's colleagues and doctoral students. They have not only co-operated extensively in accomplishing both governmental and industrial projects but have also been instrumental in performing both creative and innovative work. The material in this book was obtained from the papers and reports of both the author and his colleagues, from published and unpublished work, in addition to the doctoral dissertations of the author's students. The author wishes to acknowledge the contribution of these colleagues and doctoral students.

As this monograph is very long and the academic and administrative responsibilities of the author very heavy, the author's wife, Miss Li Shiyu, Professor at Beijing University, has helped greatly in writing this book by collecting and collating the many references. The author could not have written this monograph without her assistance, encouragement and support. For this he is eternally grateful.

Colleagues at Nanchang University have assisted in many important ways in the preparation of this book. Ms Xie Danping and Ms Hu Xinlu typed the text, and Ms Gu Lijing produced the many drawings and charts. The author wishes to express his sincere thanks to all of them for their hard work. A special note of thanks is also due to Dr Daniel Hauser of EWI, USA, who edited and revised the manuscript, making it legible to English-speaking readers.

Pan Jiluan
Nanchang University

Symbols

Numbers in round brackets refer to the chapters to which the symbols apply. Some symbols can take on meanings different from those given in the list. Such meanings are defined locally in the text.

a	[cm^2/s]	Heat-diffusion coefficient (14)
a_T	[A]	Amplitude of characteristic harmonic (9)
A_1	[A]	Constant (2)
A_2	[A]	Constant (2)
b		Heat-dissipation coefficient of plate (14)
B	[mm]	Weld width (6)
c	[J/g·°C]	Specific heat capacity (14)
C	[m/s]	Light velocity (11–12)
C	[mm]	3D co-ordinates of focus (15)
C_1	[V]	Constant for voltage across wire extension (linearised) (8)
C_1	[W·m^2]	First radiation constant (Planck radiation formula) (11–12)
C_2	[m.K]	Second radiation constant (Planck radiation formula) (11–12)
C_2	[mm/s]	Constant for wire-melting rate (linearised) (8)
C_m	[mm/s]	Constant for wire-melting rate (8)
DFT		Discrete Fourier transform (9)
e	[mm]	Deviation of torch centre (9)
E	[V]	Electromotive force, emf (2)
E	[W/m^2]	Irradiance (11–12)
E_a	[V]	Armature voltage (1)
E_λ	[W/m^2]	Spectrum irradiance (11–12)
EH	[mm]	Arc sensor, output signal to fuzzy controller (10)
EH_F	[mm]	Arc sensor, filtered output signal to fuzzy controller (10)

f	[(N·m)/(°/s)]	Coefficient of viscosity (1)
f	[Hz]	Frequency (2)
f	[Hz]	Pulse frequency (5)
f'	[mm]	Focal length (13)
f_f		Coefficient of power distribution in front part of weld pool (14)
f_r		Coefficient of power distribution in rear part of weld pool (14)
F		Geometric factor of optical system (11–12)
F		Aperture coefficient of lens (13)
g_m	[mA/V]	Transconductance of transistor (2)
$h(n)$	[mm]	Instantaneous torch height (9)
$h(t)$	[mm]	Discrete value of instantaneous torch height (9)
H		Vignetting coefficient (13)
H	[mm]	Welding-torch height (3)
H	[mm]	Reinforcement (6)
i_a	[A]	Instantaneous dropping current after short-circuiting (3)
i_a	[A]	Armature current (1)
$i(n)$	[A]	Discrete value of instantaneous welding current (9)
i_s	[A]	Instantaneous rising current at short-circuiting (3)
$i(t)$	[A]	Instantaneous welding current (9)
I	[A]	Current (2)
I	[A]	Welding current (1)
I	[W/m^2]	Radiation intensity (11–12)
I_0	[A]	Static arc operating point (8)
I_1	[A]	Current in magnetic exciting circuit (2)
I_a	[A]	Arc current (6)
I_b	[A]	Background current (2) (5) (6)
I_c	[A]	Critical short-circuiting current (2)
I_f	[A]	Welding current (2)
I_{fd}	[A]	Short-circuiting current due to droplet transfer (2)
I_{fd1}	[A]	Short-circuiting current (2)
I_{fd2}	[A]	Short-circuiting current (2)
I_m	[A]	Imaginary part of amplitude of characteristics harmonic (9)
I_m	[A]	Steady current during arc burning (3)
I_M	[A]	Steady current during short-circuiting (3)
I_{min}	[A]	Minimum falling-down current (2)

I_p	[A]	Pulse current (A) (5)
I_s	[A]	Short-circuiting current (6)
I_{sc}	[A]	Current output (4)
I_{sd}	[A]	Instantaneous peak current while starting arc (2)
I_{SM}	[A]	Short-circuiting peak current (3)
I_{sr}	[A]	Current input (4)
I_{wd}	[A]	Stable short-circuiting current (2)
I_λ	[W/m^2]	Spectrum radiation intensity (11–12)
J	[N·m/(°/s)]	Moment of inertia (1)
k	[V/A]	Constant ($k = k_0k_1$) (1)
k_0		Gain of power source (1)
k_1	[V/A]	Current feedback gain (1)
k_2		Open-loop gain of the motor circuit (1)
k_3	[N·m/A]	Constant of motor (1)
k_4	[V/(°/s)]	Constant of motor (1)
k_a	[V/mm]	Potential gradient of arc column (1) (8)
k_c	[mm/A.s]	Melting-rate coefficient (due to arc heat) (8)
k_d	[V/A]	Dropping slope of output characteristics of power source (8)
k_d	[V/A]	Slope of output characteristics (5)
k_i	[V/mm]	Coefficient of voltage drop on wire extension (linearised) (8)
k_l	[V/A]	Coefficient of voltage drop on wire extension (linearised) (k_sL_{so}) (8)
k_m	[mm/A·s]	Wire melting-rate coefficient (1) (5)
k_N		Compound constant (8)
k_P	[V/A]	Arc constant (1)
k_P	[V/A]	Equivalent resistance of arc spot (8)
k_q		Compound constant, k_ik_c-k_rk_N-$k_ak_Nk_m$ (8)
k_r	[1/s]	Coefficient for melting rate due to wire extension (linearised) ($k_\eta \cdot I_0$) (8)
k_s	[V/mm.A]	Voltage-drop coefficient on wire extension (8)
k_η	[1/A^2.s]	Coefficient for melting rate due to resistance on wire extension (8)
K		Conversion coefficient of heat to electricity (for CCD) (11–12)
K	[V]	Constant of generator (2)
K_1	[V/A]	Constant of generator $\left(\frac{kN_1}{R_m}\right)$ (2)
K_c	[V/A]	Constant of generator $\left(\frac{kN_c}{R_m}\right)$ (2)

K_f	[mV]	Feedback coefficient (8)
K_g		Amplification coefficient of reference input of transistorised power source (2)
K_i	[V/A]	Amplification coefficient of feedback current of transistorised power source (2)
K_m		Gain of wire-feed motor (1)
K_u		Amplification coefficient of feedback voltage of transistorised power source (2)
l	[mm]	Object distance (13)
l'	[mm]	Image distance (13)
L	[mH]	Inductance of winding loop (1) (2)
L	[W/m^2·sr]	Radiance (11–12)
L_1	[mH]	Inductance in magnetising winding (2)
L_a	[mm]	Arc length (1) (3) (8)
L_a	[mH]	Armature inductance (1)
L_{ao}	[mm]	Arc length when it reaches DE segment (5)
L_{ap}	[mm]	Arc length during pulse duration (5)
L_c	[mH]	Equivalent inductance in the loop inside transistorised power source (2)
L_s	[mm]	Wire extension (3)
L_{so}	[mm]	Arc length at static arc-operating point (8)
L_λ	[W/m^2·sr]	Spectrum radiance (11–12)
M	[mH]	Mutual inductance (2)
M	[W/m^2]	Radiant exitance (11–12)
M_λ	[W/m^2]	Spectrum radiant exitance (11–12)
N	[mm]	Arc-length disturbance, magnitude of step change (1)
N	[s^{-1}]	Number of samples per revolution of torch (9)
N	[mV]	Output signal of CCD pixel (11–12)
N_1		Number of coils of excitation winding (2)
N_c		Number of coils of series winding (2)
p	[mm/(°)]	Motor constant (1)
p_1		Root of characteristic polynomial of differential equation (2)
p_2		Root of characteristic polynomial of differential equation (2)
q	[W]	Effective power of heat source (14)
Q	[C]	Electric charge (13)
r	[mm]	Radius of welding-torch rotation (9)
r	[°]	Turning angle of welding tractor (10)
r_{be}	[Ω]	Equivalent resistance between base and emitter (4)

$\bar{r}$	[mm]	Polar co-ordinates of observed point (13)
R		Colorimetric ratio
R	[mΩ]	Resistance or resistance of welding loop (1) (2)
R_1	[Ω]	Resistance in magnetising winding (2)
R_a	[Ω]	Armature resistance (1)
R_b	[Ω]	Resistance connected in series with base of transistor (4)
R_c	[Ω]	Equivalent resistance in the loop outside transistorised power source (2)
Re	[A]	Real part of amplitude of characteristic harmonic (9)
R_e	[Ω]	Equivalent resistance in the loop outside transistorised power source (2)
R_e	[Ω]	Resistance of feedback loop (4)
R_F	[Ω]	Resistance of feedback loop (4)
R_L	[Ω]	Resistance of load (4)
R_m	[Ω]	Reluctance of magnetic circuit (2)
R_u	[V]	Reference input of power source (1)
S		Sensitivity of the colorimetric ratio (13)
t	[s]	Time (2)
t_b	[s]	Background-current duration (2)
t_{br}	[ms]	Background-current duration at DCRP (6)
t_{bs}	[ms]	Background-current duration at DCSP (6)
t_p	[ms]	Pulsed-current duration (2)
t_{pr}	[ms]	Pulsed-current duration at DCRP (6)
t_{ps}	[ms]	Pulsed-current duration at DCSP (6)
T_b	[ms]	Background-current duration (5)
T_m	[s]	Time constant for wire-feed motor (1)
T_p	[K]	Apparent temperature (13)
T_p	[ms]	Pulsed-current duration (5)
U	[V]	Voltage-drop across load (2)
U_o	[V]	Open-circuit voltage of power source (5) (6) (8)
U_1	[V]	Voltage across excitation winding (2)
U_a	[V]	Potential at point A of transistorised power source (2)
U_a	[V]	Arc voltage (1) (5) (8)
U_{ap}	[V]	Arc voltage during pulsed current (5)
U_b	[V]	Potential at point B of transistorised power source (2)
U_c	[V]	Potential at point C of transistorised power source (2)
U_c	[mV]	Constant for arc-voltage drop (8)

U_c	[V]	Constant for arc voltage (8)
U_d	[V]	Short-circuiting voltage (2)
U_f	[V]	Arc voltage (2)
U_g	[mV]	Reference potential (5)
U_{min}	[V]	Minimum value of restored voltage (2)
U_p	[V]	Output voltage of power source (1) (5) (8)
U_s	[V]	Voltage-drop across wire extension (8)
U_{sc}	[V]	Voltage output (4)
U_{sr}	[V]	Voltage input (4)
U_x	[V]	Lower threshold of arc voltage (6)
U_y	[V]	Upper threshold of arc voltage (6)
U_z	[V]	Voltage drop across Zener diode (3)
V	[cm/s]	Welding speed (14)
V_f	[mm/s]	Wire-feed rate (1) (3)
V_m	[mm/s]	Wire-melting rate (1) (3) (5) (8)
V_w	[mm/min]	Welding speed (9) (10)
w	[mm]	Parameter of Gaussian distribution (14)
w	[cm]	Gap of I-butt joint (9)
w_{x1}	[cm]	Distributive coefficient of bi-elliptic heat source (14)
w_{x2}	[cm]	Distributive coefficient of bi-elliptic heat source (14)
w_y	[cm]	Distributive coefficient of bi-elliptic heat source (14)
x_D	[mm]	Nut position signal of cross-slide (10)
X_z		Average number of arc breakdowns for 10 times of starting arc (2)
X_{zi}		Number of arc breakdowns for a certain number of arc starts (2)
Z	[Ω]	AC impedance of circuit (2)
β		Current amplification factor of transistor (2) (4)
γ(λ)		Transmissivity of filter (11–12)
ζ		Damping factor (1)
η(λ)		Relative spectrum sensitivity of receiving element (11–12)
$\eta(\lambda_m)$		Maximum spectrum sensitivity of receiving element (11–12)
θ	[°]	Phase angle (9)
θ	[°]	Angular displacement of motor shaft (1)
λ	[μm]	Spectrum wavelength (11–12)
λ	[mm]	Distance from camera focus to 3D point P (15)
λ	[J/cm·s·°C]	Heat transmission coefficient (14)

λ_m	[μm]	Wavelength corresponding to maximum radiant exitance (11–12)
ζ		Emission coefficient (11–12)
ζ		Stray-light coefficient of lens (13)
ρ	[g/cm^3]	Material density (14)
σ		Attenuating factor (1)
σ	[W.m^{-2}.K^{-4}]	Stefan-Boltzmann constant (11–12)
τ	[ms]	Exposure time (13)
τ	[ms]	Pulsed-current duration (9)
τ	[s]	Cooling time (14)
Φ	[W]	Total radiation flux (11–12)
Φ_λ	[W]	Spectrum radiation power (11–12)
φ		Form factor of weld (6)
φ(λ)		Transmissivity of optical element (11–12)
ω	[°]	Angle between principal light-ray and optical axis (13)
ω_d	[Hz]	Damped oscillation frequency (1)
ω_n	[Hz]	Undamped natural frequency (1)
ω_q	[Hz]	Frequency at singular point of amplitude-frequency characteristics (2)

Part I

Dynamic behaviour of arc welding

1
Theoretical analysis

1.1 Introduction

Although arc welding was invented approximately 100 years ago, many aspects lack systematic theoretical analysis. In modern publications, there is only a limited qualitative description of its static process and no scientific analysis of its dynamic process. On the basis of control theory, the arc welding process is viewed by the author as a control unit. The steps are to define the mathematical expression of each element of the control unit, and then take Laplace transform of the equations. By synthesising these Laplace equations to obtain the interconnections of all the elements and the full picture of the control unit, the mathematical representation of the dynamic behaviour of the control unit can be easily derived.[1,2] Applying this theory, a deeper understanding of the physical essence of the arc welding process can be obtained; both the static and dynamic arc-length response due to load disturbance can be analysed, and the direction and method for improvement of the welding process can be established.[3–5]

To simplify the discussion of the problem in the following paragraphs, three assumptions are made. First, that the melting rate of the welding wire is constant during the whole process; second, that the torch-to-workpiece distance is constant; and third, that the effect of wire extension on the load-voltage drop and wire-melting rate is neglected. These assumptions do not affect the objects of discussion in this chapter but, in discussing other subjects, these assumptions must not be applied arbitrarily. For example, in discussing the characteristics of the arc sensor, the factors in the last two assumptions become the main parameter of consideration, so that these assumptions should not be used. More details regarding this matter will be discussed in Chapter 8.

Conventional arc welding can be divided into two categories.[382] The first category is where the wire-feed rate is constant, which implies automatic regulation of the arc length. The second category is where the wire-feed rate is controlled by the arc voltage. In the text that follows, these two

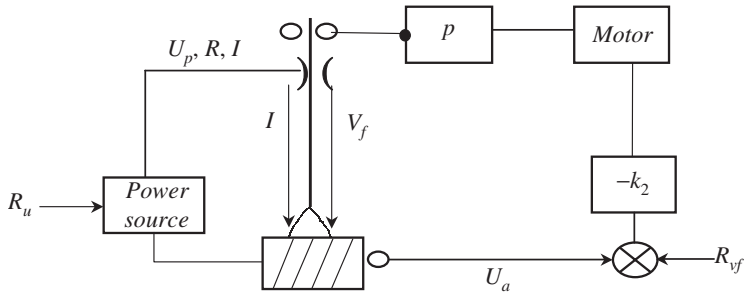

1.1 Physical representation of arc welding

categories will be discussed separately. For simplicity, the first category will be called the constant-rate wire feed or constant-rate type; the second category will be called regulated-rate wire feed or regulated-rate type. The control unit that represents the arc welding process should include all of the mechanical or electrical devices that affect the welding arc. Figure 1.1 shows its physical configuration.

1.2 Welding with constant wire-feed rate

In this category of welding the wire-feed rate remains unchanged and the arc length is regulated by the change of arc current induced by the change of the arc length itself. In accordance with the assumption that the melting rate is continuous and neglecting the effect of wire extension, the dynamic equations of all the elements of the control unit may be established as follows:

For the electrical circuit of the welding process,

$$U_p = L\frac{di}{dt} + Ri + U_a \qquad [1.1]$$

where U_p is output voltage of power source
L is inductance of welding loop
R is resistance of welding loop
i is instantaneous welding current
U_a is arc voltage.

For the arc voltage,

$$U_a = k_a L_a + k_p I + U_c \qquad [1.2]$$

where L_a is arc length,
I is effective value of arc current,
k_a, k_p, U_c are parameters of arc characteristics.

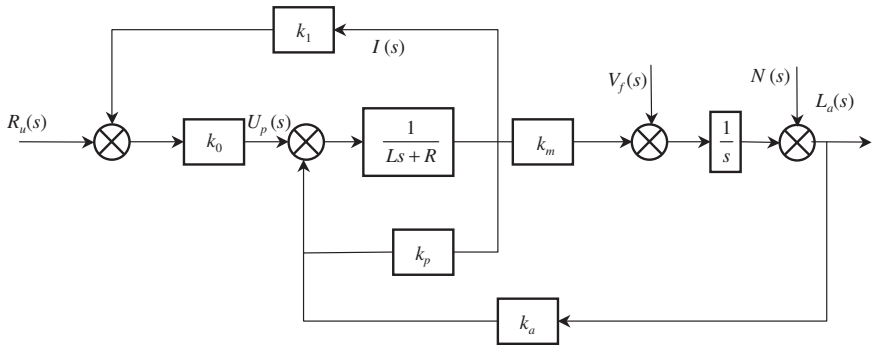

1.2 Block diagram of an arc-control unit for a constant wire feed-rate system

For the wire-melting rate,

$$V_m = k_m I \qquad [1.3]$$

where V_m is wire melting rate,
k_m is coefficient of wire melting rate.

For the arc length,

$$V_m - V_f = \frac{dL_a}{dt} \qquad [1.4]$$

where V_f is wire feed rate.

For the power source,

$$U_p = (R_u + k_1 I)k_0 \qquad [1.5]$$

where R_u is control input of power source,
k_0 is gain of power source,
k_1 is feedback gain.

Taking the Laplace transform of above equations and connecting them according to their physical relationship, one can obtain the configuration of the control unit as shown in the block diagram of Fig. 1.2.

According to Fig. 1.2, the transfer function of the control unit can be derived and obtained finally as follows:

$$\frac{L_a(s)}{R_u(s)} = \frac{k_0 k_m}{Ls^2 + (R + k_p - k_1 k_0)s + k_a k_m} \qquad [1.6]$$

From Eq. [1.5] it can be seen that $k_1 k_0$ represents the slope of the power source. When $k_1 < 0$, the output of the power source has a drooping characteristic; when $k_1 = 0$, it has a flat characteristic; when $k_1 > 0$, it has a rising

characteristic. The slope of the characteristic can be adjusted by changing k_1. Assuming that $k_1k_0 = k$, then

$$\frac{L_a(s)}{R_u(s)} = \frac{k_0k_m}{Ls^2 + (R + k_p - k)s + k_ak_m} \quad [1.7]$$

When $k > R + k_p$, the control unit is unstable; obviously there is no stable arc current and arc length. When $k = R + k_p$, the unit is in a critical stable state. When $k < R + k_p$, the unit is stable.

Normally, in a conventional constant-rate system, the output characteristic, $k \leq 0$, is in the range $k < R + k_p$, therefore it is stable. Physically, R represents the degree of drooping of the power source characteristic; the greater R, the greater the degree of drooping k_p represents the degree of rising of the arc characteristic; the greater k_p, the steeper it rises. k represents degree of positive feedback of the power source, i.e. the rising slope of its characteristic. $k = R + k_p$ means that the degree of positive feedback of the power source has not only compensated for the drooping effect induced by R, but has made the rising slope as large as the slope of the arc characteristic. In other words, the output characteristic of the power source runs parallel to the characteristic of the arc; therefore the arc is unstable and the control unit is in a critical stable state. For the same reason, $k > R + k_p$ means that the rising rate of the power source characteristic is larger than the rising rate of the arc characteristic. Therefore, the arc is not stable; the arc operating point will move according to a certain rule, which will be discussed in Chapter 5.

When $k < R + k_p$, the slope of the power source output characteristic is smaller than the slope of arc characteristic; therefore the arc is stable.

According to Eq. [1.7], the dynamic characteristics of the control unit are:

- Damping factor

$$\zeta = \frac{R + k_p - k}{2\sqrt{Lk_ak_m}} \quad [1.8]$$

- Undamped natural frequency

$$\omega_n = \sqrt{\frac{k_ak_m}{L}} \quad [1.9]$$

- Damped oscillation frequency

$$\omega_d = \frac{\sqrt{4Lk_ak_m - (R + k_p - k)^2}}{2L} \quad [1.10]$$

- Attenuating factor

$$\sigma = \zeta\omega_n = \frac{R + k_p - k}{2L} \quad [1.11]$$

Table 1.1 Dynamic response parameters for arc welding of the first category

No.	Material	Wire diameter (mm)	k_m*	ζ	σ	ω_n	$\sqrt{\zeta^2-1}$
1	Aluminum	1.2	0.68	1.16	115	99	0.59
2	Aluminum	1.6	0.366	1.58	115	72.7	1.22
3	Aluminum	2.4	0.165	2.35	115	48.8	2.13
4	Steel	1.6	0.25	1.85	115	62.1	1.56
5	Stainless steel	1.2	0.49	1.36	115	83.3	0.92

* Data obtained by experiment

Therefore, when $k < R + k_p - 2\sqrt{Lk_ak_m}$, $\zeta > 1$, the system is in an overdamped state; when $k = R + k_p - 2\sqrt{Lk_ak_m}$, $\zeta = 1$, the system is in a critically damped state; and when $R + k_p - 2\sqrt{Lk_ak_m} < k < R + k_p, 0 < \zeta < 1$, the system is in an underdamped state.

For arc-welding processes applied in industry, the control system is in an overdamped state. Table 1.1 shows the dynamic response parameters for conventional arc welding processes.

1.2.1 Self-regulation ability

During arc welding, there are many factors that disturb the arc length. How does the system respond to these disturbances? How does the rate at which the arc length is restored to its normal value determine the stability and quality of the welding process? Three causes of disturbance to the arc length are fluctuation of the line voltage, uneven wire-feed rate and fluctuation of the torch-to-plate distance. The influence of the first cause can be easily eliminated by proper design of the power source. Therefore, in the following text, the response of the arc length to the latter two causes of disturbance are discussed.

According to Fig. 1.2, the response of the arc length due to wire-feed rate disturbance may be expressed as:

$$\frac{L_a(s)}{V_f(s)} = \frac{-(Ls + R + k_p - k)}{Ls^2 + (R + k_p - k)s + k_ak_m} \qquad [1.12]$$

If the wire feed-rate disturbance is a step change, ΔV_f, since

$$V_f(s) = \frac{\Delta V_f}{s} \qquad [1.13]$$

the arc length change will be

$$L_a(s) = -\frac{(Ls + R + k_p - k)\Delta V_f}{[Ls^2 + (R + k_p - k)s + k_a k_m]s} \quad [1.14]$$

According to the terminal-value theorem, the steady-state error of the arc length is

$$\lim_{t\to\infty} L_a(t) = \lim_{s\to 0} sL_a(s) = -\frac{R + k_p - k}{k_a k_m}\Delta V_f \quad [1.15]$$

It can be seen from Eq. [1.15] that the steady-state error is not zero due to a step change of wire-feed rate. This means that the arc length will not restore itself to its original value. The negative sign in the equation means that the larger the feed rate, the shorter the arc length will be. It also can be seen that, under the same step change of wire-feed rate, the flatter the output characteristic of the power source, the smaller the arc-length change will be. Furthermore, the arc-length change depends on the wire material, wire diameter, and some parameters of the electrical circuit of the welding system such as resistance. In the case of a flat output characteristic of the power source (k = 0), a wire diameter of 1.2 mm (k_m = 0.43, k_a = 0.716, k_p = 0.0245), and a resistance of the welding loop of 15 mΩ, the steady-state error of arc length can be derived from Eq. [1.15] as

$$\lim_{t\to\infty} L_a(t) = -0.128\Delta V_f \quad [1.16]$$

The arc length will be shortened by 0.128 mm due to a 1 mm/s (0.06 m/min) change of wire-feed rate. Because the arc length cannot be restored due to a wire-feed disturbance, the welding process will be very difficult to control if the disturbance of wire-feed rate is large.

From Fig. 1.2, the effect of arc-length disturbance also can be derived:

$$\frac{L_a(s)}{N(s)} = \frac{(Ls + R + k_p - k)s}{Ls^2 + (R + k_p - k)s + k_a k_m} \quad [1.17]$$

Assume that the arc length has a step disturbance N, or $N(s) = \frac{N}{s}$, then the response of the arc will be

$$L_a(s) = \frac{(Ls + R + k_p - k)N}{Ls^2 + (R + k_p - k)s + k_a k_m} \quad [1.18]$$

The steady-state error of the arc length will be

$$L_a(t)_{t\to\infty} = \lim_{s\to 0} sL_a(s) = \lim_{s\to 0} \frac{(Ls + R + k_p - k)Ns}{Ls^2 + (R + k_p - k)s + k_a k_m} = 0 \quad [1.19]$$

From Eq. [1.19] it can be seen that the steady-state error of the arc length is 0, i.e. the arc length can be restored.

In order to analyse the instantaneous change of arc length due to such a disturbance, take the inverse Laplace transform of Eq. [1.18] to obtain

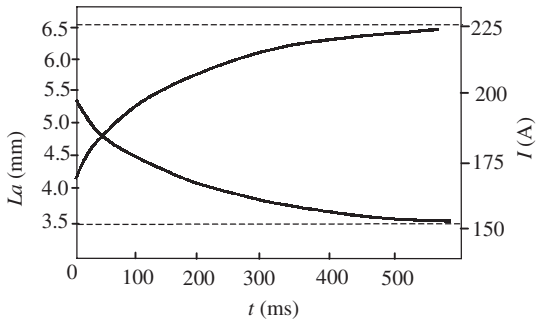

1.3 Response to arc-length disturbance

$$L_a(t) = \frac{s_2 N}{s_2 - s_1} e^{-s_1 t} + \frac{s_1 N}{s_1 - s_2} e^{-s_2 t} \qquad [1.20]$$

where

$$s_1 = \frac{(R + k_p - k) + \sqrt{(R + k_p - k)^2 - 4Lk_a k_m}}{2L}$$

$$s_2 = \frac{(R + k_p - k) - \sqrt{(R + k_p - k)^2 - 4Lk_a k_m}}{2L}$$

In the case where $\zeta >> 1$ or $(R + k_p - k)^2 >> 4Lk_a k_m$, s_1 has a large numerical value, i.e. $s_1 >> s_2$, so the first term of Eq. [1.20] may be neglected; then Eq. [1.20] may be simplified as

$$L_a(t) = Ne^{-s_2 t} \qquad [1.21]$$

The instantaneous transient value of the arc length after a disturbance can be calculated on the basis of Eq. [1.20] by computer. Assume that the parameters of the power source and arc are

$$k = 0, \quad R = 23.5\,\text{m}\Omega, \quad L = 10\,\mu\text{H}, \quad k_a = 0.716\,\text{V/mm},$$

$$k_P = 0.0245\,\text{V/A}, \quad N = -3\,\text{mm}, \quad k_m = 0.43\,\text{mm/As},$$

and that before the disturbance, $L_a = 6.5\,\text{mm}$, and $I = 153\,\text{A}$. The results of the calculated value may be depicted as shown in Fig. 1.3.

From Fig. 1.3, it is obvious that, initially, the instantaneous current is large and restoration of the arc length is rapid; after some time, the instantaneous current decreases and the arc-length restoration rate becomes slower. The specific values of transient current and arc length are shown in Table 1.2. From this table, it can be seen that the current rises to 198 A when the step change of arc length is 3 mm and the transient time for restoration of the arc length to 95% of its original value is 485 ms.

Table 1.2 Instantaneous current and arc length during a transient process

L_a (mm)	3.5	4.00	4.47	5.01	5.55	6.09	6.36	6.5
$\frac{L-L_0}{N}$	0	16.7%	32.3%	50.3%	68.3%	86.3%	95.3%	100%
I (A)	198	189	183	175	167	159	155	153
t (ms)	0	32.5	60.9	109.4	180.5	313	485	∞
ΔL_a (mm)	–3	–2.44	–2.03	–1.49	–0.95	–0.41	–0.14	0

Table 1.3 Damping factor for different slopes of the output characteristic

k	–0.1	–0.01	0	0.019	0.03	0.04
ζ	7.74	2.78	2.26	1.27	0.70	0.18

From this analysis, it can be concluded that the dynamic characteristics of the system depend on the parameters k, R, L and k_p, k_a, k_m. In the following section, the effects of major parameters on the dynamic characteristics of the system and situations where this analysis can be applied are discussed.

1.2.2 Effects of major parameters

(i) Slope of the output characteristic of the power source.
From Eq. [1.8] it can be seen that the slope of the output characteristic will influence the damping factor. In the case of 1.2 mm wire diameter, $k_a = 0.716$, $k_p = 0.0245$, $R = 19\,\text{m}\Omega$, and $L = 0.3\,\text{mH}$, the effect may be shown as in Table 1.3. It can be seen that the larger the slope, the smaller the damping factor will be. It is known that too small a value of ζ will result in overshoot during a transient process. According to control theory, the optimum value of ζ is 0.7 and thus the slope of the output characteristic can be derived as

$$k = R + k_p - 2\zeta\sqrt{Lk_ak_m} = R + k_p - 1.4\sqrt{Lk_ak_m} \qquad [1.22]$$

From Table 1.3, it can be seen that the optimum output characteristic is $k = 0.03\,\text{V/A}$; using a slightly rising output characteristic could change the control unit from an overdamped state to an underdamped state, and expedite the dynamic response.

(ii) Effect of welding-loop parameters
The inductance of the welding loop includes both external inductance and internal inductance due to leakage flux. Large inductance makes the control

unit become underdamped and increases the overshoot. If ζ and the overshoot are kept unchanged, then ω_n will decrease and the transient time will increase. From Eq. [1.11], it is seen that the attenuation factor is inversely proportional to L; therefore an increase of inductance is detrimental to the dynamic characteristics of the system. According to Eq. [1.8], a decrease of L makes it possible to increase the slope of the output characteristic of the power source while keeping ζ unchanged, which can increase the attenuation factor and shorten the transient time. Furthermore, according to Eq. [1.15], the effect of a disturbance to the arc length can be reduced by increasing the slope of the output characteristic. It can be seen that an increase of inductance is detrimental to the improvement of the control characteristics of the welding system. In the case of short-circuiting metal transfer, however, appropriate inductance is necessary to limit the rate of the rising short-circuit current to reduce the degree of spatter generation.

Although the resistance of the welding loop also affects the static and dynamic characteristics of the system, due to the fact that the magnitude of the welding current is usually very large, the resistance in the loop is normally kept as small as possible in order to avoid large energy losses.

(iii) Wire diameter and arc parameters

As the slope of the output characteristic for a conventional constant feed-rate system $k \leq 0$, the system is normally overdamped. For smaller gauge wires, the values of k_a, k_m (particularly the melting rate coefficient k_m) are larger; therefore they have smaller values of ζ and larger values of ω_n and consequently better dynamic response to arc-length disturbances. According to Eq. [1.15], the smaller gauge wire also has better response to wire-feed rate disturbances. It may be concluded, therefore, that a constant wire-feed rate system is more suitable for smaller-gauge wire rather than large-gauge wire. Of course, it may be used for large-gauge wire if the dynamic characteristics of the system are improved by increasing the output characteristics of the power source or by using a new control method, as described in Chapters 4 and 5.

Obviously, the main shortcoming of the constant wire-feed system is the contradiction between the stability of the welding current and the self-regulation ability of the arc length. The self-regulation ability of the arc length is, in fact, obtained by variation of the instantaneous welding current. Better self-regulating ability of the arc length is associated with larger fluctuations of the welding current. The latter is obviously detrimental to the metal transfer and stability of the arc. This contradiction is particularly notable in GMA welding.

1.3 Welding with regulated wire-feed rate

In this system, changing the wire-feed rate regulates the arc length; the wire-feed motor used is generally a DC servomotor. The mathematical equation describing its dynamic function may be expressed as

$$E_a = L_a \frac{di_a}{dt} + R_a i_a + k_4 \frac{d\theta}{dt} \quad [1.23]$$

$$J \frac{d^2\theta}{dt^2} + f \frac{d\theta}{dt} = k_3 i_a \quad [1.24]$$

$$V_f = p \frac{d\theta}{dt} \quad [1.25]$$

Where E_a is armature voltage,
L_a is armature inductance,
R_a is armature resistance,
i_a is armature current,
J is moment of inertia of the motor and mechanical load converted to the motor shaft,
f is coefficient of viscosity of the motor and mechanical load converted to the motor shaft,
θ is angular displacement of the motor shaft,
V_f is wire-feed rate,
k_3, k_4, p are constants.

Taking the Laplace transform of these equations, the configuration of the control unit of the motor can be shown as the block diagram in Fig. 1.4.

According to Fig. 1.4, the transfer function can be derived as

$$\frac{\theta(s)}{E_a(s)} = \frac{k_3}{s[L_a J s^2 + (L_a f + R_a J)s + R_a f + k_3 k_4]} \quad [1.26]$$

If the motor inductance, L_a, is neglected, then

$$\frac{\theta(s)}{E_a(s)} = \frac{k_3}{s(R_a J s + R_a f + k_3 k_4)} = \frac{K_m}{s(T_m s + 1)} \quad [1.27]$$

The gain of the wire-feed mechanism is

$$K_m = \frac{k_3}{R_a f + k_3 k_4} \quad [1.28]$$

The time constant of the wire-feed mechanism is

$$T_m = \frac{R_a J}{R_a f + k_3 k_4} \quad [1.29]$$

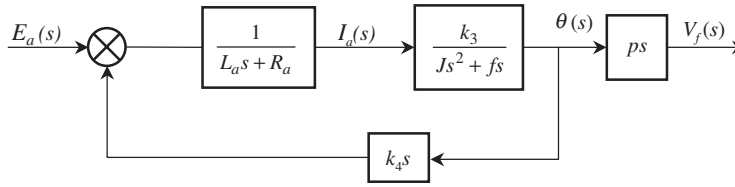

1.4 Block diagram of wire-feed motor

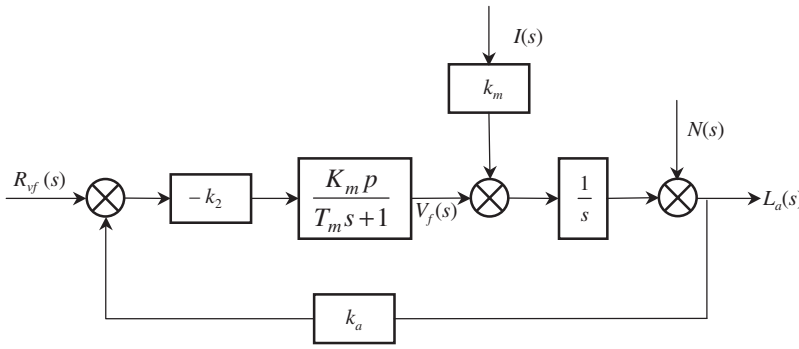

1.5 Block diagram of regulated wire feed-rate system

Therefore, the transfer function of the wire-feed mechanism may be simplified as

$$\frac{V_f(s)}{E_a(s)} = \frac{K_m p}{T_m s + 1} \qquad [1.30]$$

Assuming that the power source has a constant-current characteristic and neglecting the influence of wire extension on melting rate, the control-block diagram of the regulated wire-feed rate system may be simplified as shown in Fig. 1.5.

In Fig. 1.5, $R_{vf}(s)$ represents the control input to the wire-feed motor and k_2 is the open-loop gain of the motor circuit. According to Fig. 1.5, the transfer function of the system and its dynamic characteristics can be derived as

$$\frac{L_a(s)}{R_{vf}(s)} = \frac{k_2 K_m p}{T_m s^2 + s + k_2 K_m p k_a} \qquad [1.31]$$

$$\zeta = \frac{1}{2\sqrt{k_2 K_m p k_a T_m}} \qquad [1.32]$$

$$\omega_n = \sqrt{\frac{k_2 K_m p k_a}{T_m}} \qquad [1.33]$$

$$\omega_d = \frac{\sqrt{4k_2K_m pk_a T_m - 1}}{2T_m} \approx \frac{\sqrt{k_2K_m pk_a}}{T_m} \quad [1.34]$$

$$\sigma = \zeta\omega_n = \frac{1}{2T_m} \quad [1.35]$$

In most instances, $k_2K_m pk_a T_m > 1$ and $0 < \zeta < 1$; therefore the system is in an underdamped state.

In the following sections, the effects of the major parameters on the control characteristics are discussed.

1.3.1 Effect of wire-feed mechanism

The dynamic-characteristics parameters ζ, ω_n, ω_d, and σ depend on the time constant of the wire-feed mechanism, T_m. The greater the value of T_m, the smaller the damping factor ζ will be, and the greater the overshoot; the system is likely to oscillate. Additional increase of T_m makes ω_n, ω_d and σ smaller and the transient time longer, and thus worsens the dynamic characteristics. Decreasing the value of T_m improves the dynamic characteristics of the system, or increases the control accuracy by increasing the open-loop gain while the dynamic characteristics remain unchanged. According to Eq. [1.29], in order to decrease time constant, T_m, a motor having a small time constant, or rational design of the mechanical parts are effective. Decreasing the moment of inertia, J, and increasing the viscosity coefficient, f, also can decrease T_m. In addition, by using a negative feedback-control loop for the wire-feed motor, plus appropriate compensation elements and a brake mechanism, the time constant of the wire-feed mechanism may be greatly reduced.

1.3.2 Effect of wire diameter

When the wire diameter is decreased, the diameter of the arc column decreases, k_a increases, the damping factor ζ decreases, overshoot increases, and oscillation may occur. In conventional systems having a regulated wire-feed rate, the time constant is usually large; therefore, they can be used only for large gauge wire. It can be seen, however, that if T_m is reduced significantly, k_a may be increased greatly, keeping ζ unchanged, so that the wire diameter can be considerably decreased. ω_n, ω_d and σ will increase and the dynamic characteristics of the system will be greatly improved. Therefore, the traditional idea that a regulated wire-feed system can be used solely with large-gauge wire is correct only under certain conditions. In situations where the time constant of the wire-feed mechanism can be reduced, the system can be quite suitable for small-gauge wire. This can be realised easily with the application of modern control techniques.

1.4 Welding with both regulated wire-feed rate and self-regulation

In practice, a power source having a regulated wire feed-rate system does not have a completely perpendicular drooping characteristic (constant current). Simultaneous with regulation by feedback-control functions, self-regulation also plays a role in arc-length change. Therefore, analysing the cross-coupling interrelationship between two regulation actions is meaningful. Of course, in practical applications only one regulation action normally is dominant. In this section, the interrelationships of these two regulation actions and the possibility for using both actions in one system are discussed.

Integrating Sections 1.2 and 1.3, a block diagram of a cross-coupled control system can be depicted as in Fig. 1.6.

From Fig. 1.6 it can be seen that the system is a multi-loop, interactive, feedback control. Its signal-flow diagram is shown in Fig. 1.7.

Using Mason's gain formula, the closed-loop transfer function of the system can be derived as

$$\frac{L_a(s)}{R_{vf}(s)} = \frac{k_2 K_m p(Ls + R + k_p - k)}{LT_m s^3 + [(R + k_p - k)T_m + L]s^2 + (R + k_p - k + k_a k_m T_m + k_2 K_m p k_a L)s + k_2 K_m p k_a (R - k) + k_a k_m} \quad [1.36]$$

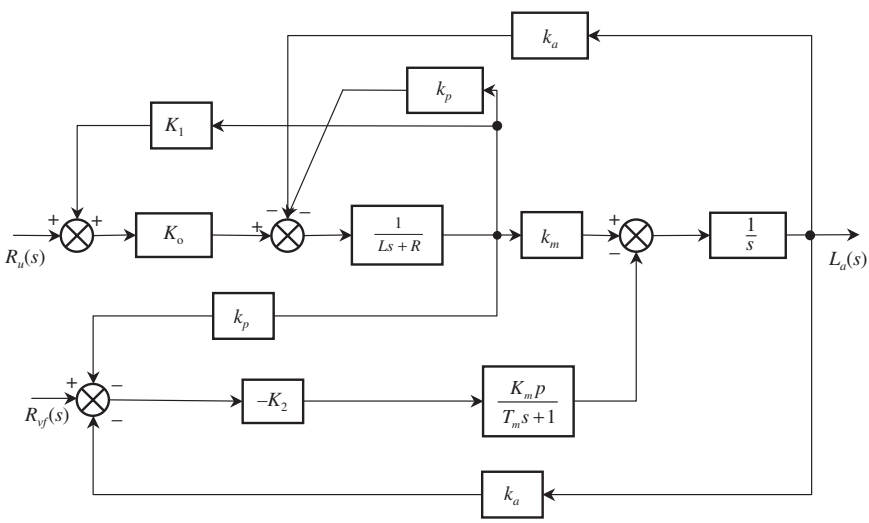

1.6 Block diagram of a cross-coupled wire-regulation system

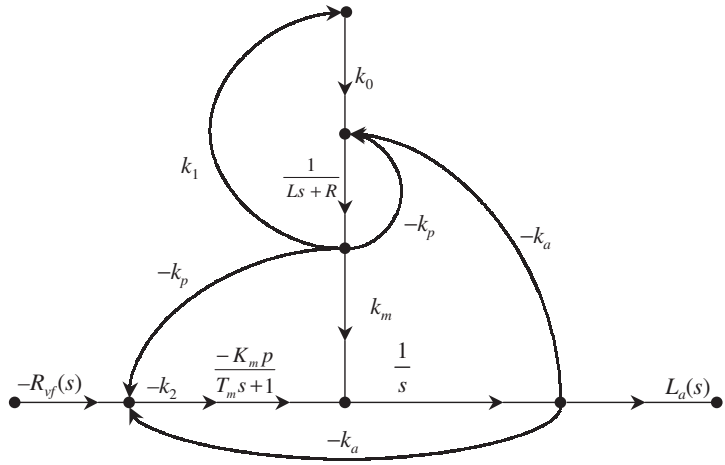

1.7 Signal-flow diagram of an interactive wire-regulation control system

If the inductance in the welding loop is neglected, the transfer function can be simplified as

$$\frac{L_a(s)}{R_{vf}(s)} = \frac{k_2 K_m p(R + k_p - k)}{(R + k_p - k)T_m s^2 + (R + k_p - k + k_a k_m T_m)s + k_2 K_m p k_a (R - k) + k_a k_m} \quad [1.37]$$

The Routh array of the system is

s^2	$(R + k_p - k)T_m$	$k_2 K_m p k_a (R - k) + k_a k_m$
s^1	$R + k_p - k + k_a k_m T_m$	0
s^0	$k_2 K_m p k_a (R - k) + k_a k_m$	

According to the Routh stability criterion, the conditions for stability are

$$\begin{cases} k < R + k_p \text{ ---------- (1)} \\ k_2 K_m p k_a (R - k) + k_a k_m > 0 \text{ -------- (2)} \end{cases} \quad [1.38]$$

The stability criterion Eq. [1.38] has an explicit physical meaning; Condition (1) is required for stability of self-regulation. The output characteristic of the power source should intersect the arc characteristic such that the point of arc operation is stable. In addition, the system must satisfy Condition (2).

When $k \le R$, the system satisfies both Conditions (1) and (2) and it is stable.

When $R < k < R + k_p$, Condition (2) can be written as

$$k_2 K_m p k_a < \frac{k_a k_m}{k - R} \quad [1.39]$$

The right side of the equation represents the change of melting rate per unit change of arc length; the left side represents the change of wire-feed rate due to a unit change of arc length. Therefore, the physical meaning of Condition (2) can be expressed as follows: If the output characteristic of the power source is $R < k < R + k_p$, the system could be stable only when the change of melting rate due to the change of arc length is larger than the change of wire feed rate. The reason for this statement is that when $R < k < R + k_p$, the increase of arc length makes the gain of negative feedback smaller. In other words it is, in fact, a positive feedback loop. As the self-regulation action maintains negative feedback, the system then can be kept stable if the self-regulation action is stronger than the wire-feed regulation. This condition can be satisfied if the slope of the output characteristic of the power source satisfies the following equation:

$$k < R + \frac{k_m}{k_2 K_m p} \quad [1.40]$$

From the above analysis, it can be seen that the change of the output characteristic of the power source not only changes the dynamic characteristics of the self-regulated system but also changes the dynamic characteristics of the wire-feed regulated system; it can change even the polarity of the feedback loop. In the following text, the interaction of two regulation systems is analysed assuming the system is stable.

If $k < R$, both regulation systems provide negative feedback. According to Eq. [1.37], the dynamic characteristics can be obtained as

$$\zeta = \frac{R + k_p - k + k_a k_m T_m}{2\sqrt{(R + k_p - k) T_m [k_2 K_m p k_a (R - k) + k_a k_m]}} \quad [1.41]$$

$$\begin{aligned} \omega_n &= \sqrt{\frac{k_2 K_m p k_a (R - k) + k_a k_m}{(R + k_p - k) T_m}} \\ &= \sqrt{\frac{k_2 K_m p k_a}{T_m} + \frac{k_a k_m - k_2 K_m p k_a k_p}{(k_p + R - k) T_m}} \end{aligned} \quad [1.42]$$

Normally, ζ is determined by the allowable overshoot and the response time is determined by the undamped oscillation frequency ω_n. According to Eq. [1.42], if the wire-feed regulation is weak, or $k_2 K_m p k_a k_p < k_a k_m$ and the self-regulation function is stronger, ω_n will increase due to the greater slope of the output characteristic of the power source. The response time will be smaller and the dynamic characteristics will be greater. In contrast, if the wire-feed regulation function is stronger than the self-regulation function, i.e. if $k_2 K_m p k_a k_p > k_a k_m$, ω_n will decrease due to the increase of the slope

of the output characteristic of the power source; the response time will increase and the dynamic characteristics of the system will be worsened. Therefore, it is hard to select a suitable slope of the output characteristic of a power source to fully use both regulation functions. In fact, only one of the regulation functions is applied in major practical applications. Consequently, in available publications, the following qualitative statement is made: In constant wire-feed systems, a flatter output characteristic of the power source effectively provides self-regulation, but in regulated wire-feed systems, it is reasonable to use steep output characteristics in order to obtain stronger arc-length regulation. This statement is explained explicitly by the theoretical analysis given in this chapter.

2

Dynamic characteristics of power sources

2.1 Status of research

The power source is one element in the control of a welding process; its characteristics have been studied since welding was first introduced. Different welding processes require different power-source characteristics because they determine both the ability to carry out the welding process and weld quality. Although power sources are commonly described by their static output characteristics, the static output characteristics are an incomplete description. Power sources having the same static output characteristics may perform differently because their dynamic characteristics are different. Therefore, a power source should be described by both its static and dynamic characteristics. Describing the dynamic characteristics of a power source is much more difficult than describing its static characteristics. There is no unified way or standard method for describing the dynamic characteristics of a power source anywhere in the world at this time. In Chapter 1, the power source was assumed to be a constant-voltage output electrical machine with internal resistance, R, and inductance, L. This assumption greatly simplified the analysis of the problem. In traditional welding, an AC transformer or DC generator is used for the power source. In such cases, it is convenient to describe the dynamic properties by mathematical expressions. But with the development of modern welding technology, new power sources and new processes appear continuously. As the dynamic characteristics of power sources become more complicated, the understanding of these characteristics becomes more necessary. For example, in order to study the phenomena associated with short-circuiting metal transfer, the dynamic properties of the power source must be understood because of their important effects on the process. Different dynamic properties of the power source will produce considerably different metal-transfer behaviour. Another example is the arc sensor. In order to study and develop an arc sensor, its frequency-response characteristics must be known (see Chapter 8).

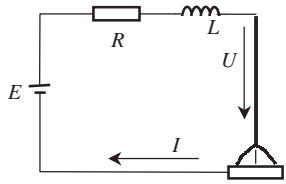

2.1 Equivalent electrical circuit for a power source with a drooping characteristic

A lot of research regarding static and dynamic properties of power sources has been carried out previously.[6–26] In the following section, the results of previous investigators are introduced first, then the theory and method proposed by Bojin Qi and the author will be described.[29,133,381]

2.1.1 Analytical methods

Several decades ago, scientists studied dynamic characteristics using analytical methods. They analysed the dynamic properties of motor-generators and simple DC machines with drooping characteristic, and derived the rule about the dynamic response of the welding current. For a simple DC machine, the current change due to a step change of output voltage can be expressed as:

$$\Delta I = \frac{\Delta U}{R}(1 - e^{-Rt/L}) \qquad [2.1]$$

where ΔU is the step change of the output voltage and ΔI is the current response.

The equivalent electrical circuit of a power source with a drooping characteristic can be illustrated as in Fig. 2.1, where R is the internal resistance and L is the internal inductance. The derivation is omitted.

A theoretical analysis of a motor-generator type of power source is given in references.[7,8] The generator has a series demagnetising winding and a magnetising winding excited by an external magnetising power source, as shown in Fig. 2.2. In this figure, L_1 and R_1 denote the inductance and resistance of the magnetising winding, respectively, M denotes the mutual inductance between the series winding and the excitation winding, R and L denote the resistance and inductance of the welding circuit, respectively, and U_1 denotes the voltage of the power-source excitation winding.

If K is the generator constant, R_m is the reluctance of the magnetic circuit, and N_1 and N_C are the numbers of coils of the excitation winding and series winding, respectively, then the emf of the generator, E, is given by

$$E = \frac{KN_1}{R_m} I_1 - \frac{KN_c}{R_m} I$$

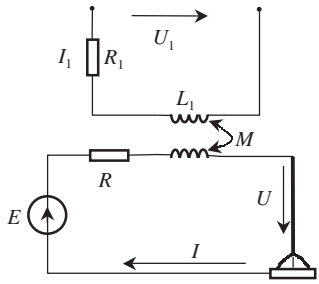

2.2 Equivalent circuit for a welding DC generator

According to the principles of electrical circuits, the dynamic relationship of the magnetic exciting circuit can be expressed as:

$$U_1 = I_1 R_1 + L_1 \frac{dI_1}{dt} - M \frac{dI}{dt} \qquad [2.2]$$

The equation for the welding loop is:

$$K_1 I_1 - K_c I = IR + L \frac{dI}{dt} - M \frac{dI_1}{dt} + U \qquad [2.3]$$

where $$K_1 = \frac{KN_1}{R_m} \quad \text{and} \quad K_C = \frac{KN_C}{R_m}$$

If a stable operating point (I_{10}, I_0, U_0) is taken as the origin, and assuming that

$$I = I_0 + i, \quad I_1 = I_{10} + i_1, \quad U = U_0 + u,$$

the following differential equation can be obtained based on Equations [2.2] and [2.3]:

$$(L_1 L - M^2)\frac{d^2 i}{dt} + [(R + K_c)L_1 + R_1 L - K_1 M]\frac{di}{dt} + (R + K_c)R_1 i = -Ru - L\frac{du}{dt} \qquad [2.4]$$

Assuming that a step change U is the input to the system, the current response can be obtained by solving the differential equation as:

$$i = A_1 e^{p_1 t} + A_2 e^{p_2 t} \qquad [2.5]$$

where p_1, p_2 are the roots of the characteristic polynomial of the differential equation. A_1, A_2 are determined by the initial conditions.

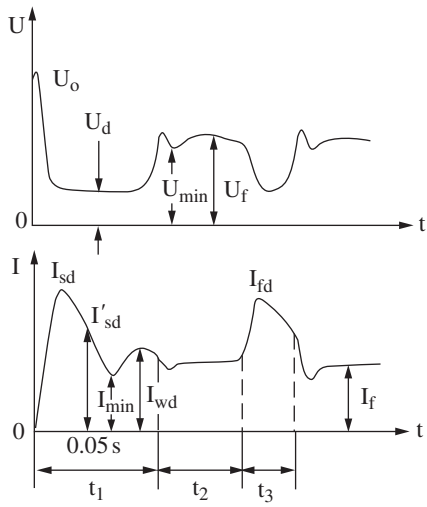

2.3 Voltage and current waveforms for manual arc welding

In references[7,8] some special cases were discussed. If $M \approx 0$, the current response from an open circuit to a short circuit can be obtained as:

$$I = I_{wd}\left(1 - e^{-(K_c+R)t/L}\right) \qquad [2.6]$$

where $I_{wd} = \dfrac{U_0}{K_c + R}$ is the stable short-circuit current (U_0 is the open-circuit voltage).

2.1.2 Direct-measurement methods

In the previous section, the analytical method was shown to be feasible, but it has limitations. Using analytical methods, the properties can be determined only qualitatively. The process of calculating the equation and obtaining quantitative results is complicated. In particular, the configurations of power sources have become very complicated with advances in electronics; analytical characterisations cannot be made. Therefore, experimental methods have been developed in many countries. Generally speaking, the experimental methods are based on measurements of current responses to step changes of input. For example, from an open circuit to a short circuit, a load to a short circuit, etc. and taking some index in time domain as the description of the dynamic characteristic of the power source. In reference,[6] some of the indices used to describe dynamic characteristics are introduced: see Fig. 2.3.

I_{sd}: Instantaneous peak current while starting arc
I_{wd}: Stable short-circuit current
I_f: Welding current
I'_{sd}: Instantaneous short-circuit current after 0.05 s
U_d: Short-circuit voltage
U_f: Arc voltage
U_{min}: Min. value of restored voltage
I_{min}: Min. falling-down current
I_{fd}: Short-circuit current due to droplet transfer

Examples of indices are:

- I_{sd}/I_{wd} I'_{sd}/I_{wd} I_{fd}/I_f, used as indices to describe the dynamic characteristics of the power source.
- Under conditions that the short-circuit duration is $t_3 = 10\,\text{ms} \pm 10\,\text{ms} \times 30\%$ and the arc duration is $t_2 = 300\,\text{ms} \pm 300\,\text{ms} \times 30\%$, I_{fd} is used as an index to describe the dynamic characteristics of the power source.
- The ratio of dynamic parameters $Sd_1 = \dfrac{U_{min}}{I_{wd}}$, $Sd_2 = \dfrac{U_0}{I_{sd}}$.
- The ratio of dynamic parameters I_{min}/I_f and W_{min}/W_f, where $W_{min} = I_{min} \times U_f$, W_f is arc power.
- For a CO_2-welding power source, the index for its overall characteristic is $X_z = \dfrac{1}{N}\sum_{i=1}^{N} X_{zi} (N = 10)$, where X_{zi} is the number of arc breakdowns for a specific arc-initiation event and X_z is the average number of arc breakdowns for 10 arc initiations.
- The time required for the voltage to rise from a short-circuit condition to an arc operating voltage of 25 V.

On the basis of experiments, different criteria and standard values have been drawn up, but there is no unified, worldwide standard.

In China, the following standards were established:

- The dynamic characteristics of a power source for coated-electrode welding, see Table 2.1.

  In Table 2.1, I_{sd} is peak short-circuit current from an open circuit to a short-circuit and I_{fd} is peak short-circuit current for a load to a short-circuit.
- Dynamic characteristics for a MIG/MAG welding power source.
  a. Average time for starting an arc 10 times in a time period less than or equal to 0.1 s.
  b. Spatter loss coefficient: see Table 2.2.

In Germany, a criterion was established as follows:[10]

$$I_{fd} \le I_c$$

Table 2.1 Criteria of dynamic characteristics for rectifier-type welding power sources[9]

No.	Item	Specification		Standard
1	From open-circuit to short-circuit	Rated	Peak current I_{sd}/I_f	≤3
			Sustained time	0.03~0.1 s
		20% of rated	Peak current I_{sd}/I_f	≤5.5
			Sustained time	0.03~0.1 s
2	From load to short-circuit	Rated	Peak current I_{fd}/I_f	≤2.5
			Sustained time	0.01~0.04 s
		20% of rated	Peak current I_{fd}/I_f	≤3
			Sustained time	0.01~0.04 s

Table 2.2 Spatter-loss coefficients

Welding current (A)	Wire diameter (mm)	Spatter-loss coefficient (%)
100	0.8	3.5
150	1.0	4
180	1.2	5
300	1.6	8

Table 2.3 I_c for different wire diameters

Wire diameter (mm)	2	2.5	3.25	4	5	6
I_c (A)	145	175	215	300	400	600

where I_{fd} is defined as indicated in Fig. 2.3 and I_c is the critical short-circuit current, which depends on the wire diameter and is also given in Table 2.3.

From the introduction given above, it is seen that, until now, the descriptions and measuring methods for the dynamic characteristics of power sources have been simple and not rigorous. For example, in China, I_{fd}/I_f is taken as the index of the dynamic characteristics, where I_{fd} is the peak current from the load to a short-circuit, which is measured by an instrument

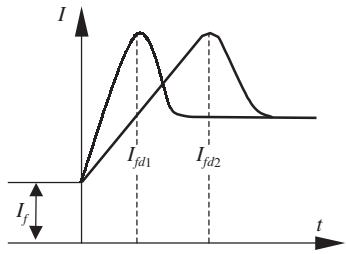

2.4 Schematic drawing of current waveform

consisting of a resistance and an electro-magnetic switch. I_f is the load current.

It obviously is not exact. Figure 2.4 shows the current wave-form for two different power sources. Both have the same index I_{fd}/I_f, but, in fact, they have quite different dynamic behaviours.

In a more detailed discussion in the literature,[11–13] it was pointed out that the index i_{fd}/I_f is not reasonable. $i_{fd}/I_f(t_0)$ during the short-circuit period, the duration of which is t_0, was proposed as the criterion where t_0 is the maximum probable time of short-circuiting, but due to different wire diameters and materials, the index $i_{fd}/I_f(t_0)$ can vary for the same power source. In the literature,[11] it was pointed out that SCR and magnetic-amplifier power sources have been tested and assessed; it was found that the dynamic characteristics were different even for power sources having the same $i_{fd}/I_f(t_0)$.

The problem is that it is not sufficient to use some characteristic point on the short-circuit waveform as the index; the whole short-circuit event should represent the dynamic behaviour of the power source.

It can be concluded that the existing criteria and measuring methods are not complete and rigorous; they have no strict physical meaning. For power sources developed using modern electronics, the existing criteria, in fact, do not reflect their dynamic properties. The purpose of this chapter is to find a scientific way for describing and evaluating the dynamic characteristics of all types of power sources.

2.2 Description of dynamic characteristics

In reference,[24] three different ways to experimentally study power-source characteristics have been introduced:

(i) Subjective direct measurement; the assessment is made by the worker in the practical welding application;
(ii) Objective direct measurement; during or after welding, some feature is measured as the characteristic of the power source;

(iii) Objective indirect measurement; actual welding is not carried out but, rather, the load of the power source is simulated and some feature is measured and designated as the dynamic characteristic.

The first method is based on personal judgment; it is subjective and therefore is not appropriate as a scientific method. The second method is a better characterisation method but its results depend on many factors such as welding parameters, operating experience, etc. Therefore, the repeatability of the results is poor. The third method is the best approach to the problem. The power source is treated as an independent unit so that a good understanding of the power source can be obtained. Most modern measuring methods use this approach. Some years ago, Budai, Pan, and Qi proposed[29,30,133,259] use of the transfer function for describing the characteristics of power sources. This technique is even more scientific than the methods described above. In control theory, the transfer function is used to describe the characteristics of a unit. The relationship between an output and an input represents the static and dynamic characteristics of the unit. For welding power sources, the output voltage can be viewed as the input of the unit and the current may be viewed as the output of the unit. The transfer function between the input and output, together with the static output characteristic can be used as the representation of the static and dynamic characteristics of the power source.

2.3 Transfer functions of power sources

2.3.1 Power source with a simple drooping characteristic

(i) The transfer function of a simple power source having a drooping characteristic will be derived first. Assume that the equivalent electric circuit is shown as in Fig. 2.5. Set up the differential equation of the circuit, take the Laplace transform of it, and the transfer function can be easily obtained.

According to the principles of electric circuits, the differential equation of the circuit can be written as

$$E = Ri + L\frac{\mathrm{d}i}{\mathrm{d}t} + U$$

Obtain the Laplace transform of the equation and rearrange it; the transfer function can be derived as

$$0 = RI(s) + LsI(s) + U(s) \qquad G(s) = \frac{I(s)}{U(s)} = \frac{-1}{Ls + R} = \frac{-1/R}{(L/R)s + 1}$$

For simplicity, the transfer function and the frequency-response characteristics can be derived more easily using an equivalent AC circuit. The

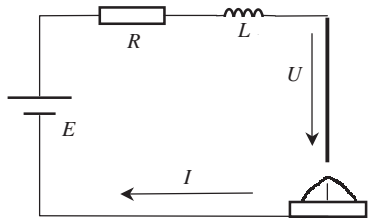

2.5 Equivalent circuit of a simple drooping-characteristic power source (A)

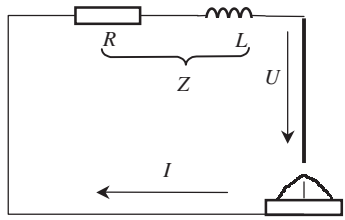

2.6 Equivalent AC circuit of simple drooping-characteristic power source (A)

equivalent electrical circuit is illustrated in Fig. 2.6. According to the principles of electric circuits, the following equation can be established:

$$IZ + U = 0 \qquad [2.7]$$

where $Z = R + j\omega L$, which is the AC impedance of the circuit.

Therefore, the transfer function of the power source is:

$$G(j\omega) = \frac{I}{U} = -\frac{1}{Z} = \frac{-1}{R + j\omega L} = \frac{-1/R}{j\omega L/R + 1} \qquad [2.8]$$

From the derivation above, an important conclusion can be made; the negative reciprocal function of impedance is the transfer function of the power source. This conclusion will be applied in the following discussion.

From Eq. [2.8], it can be seen that the amplification coefficient is $-1/R$ and the time constant is L/R. The amplitude frequency characteristics of the unit for different values of R and L are depicted in Fig. 2.7.

From Fig. 2.7 and the transfer function, the following conclusions can be drawn:

- In the case where L = Const., the larger the value of R, the smaller the amplitude-frequency characteristic. This means that the amplification coefficient decreases or the characteristic curve moves down.

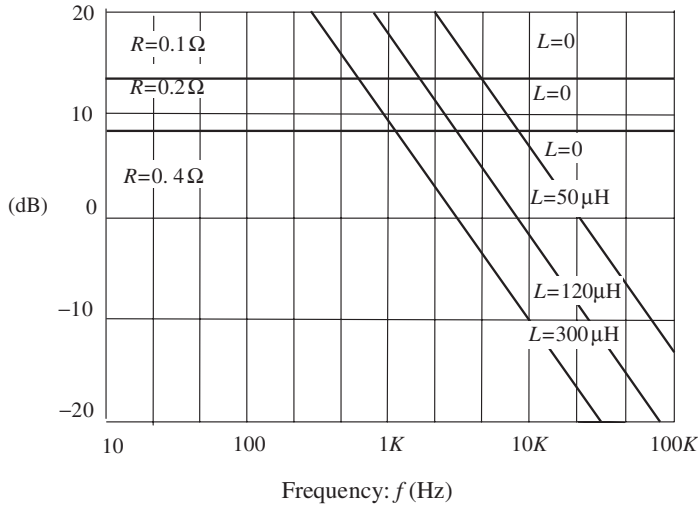

2.7 Amplitude-frequency characteristics of power source (A) (Asymptote)

- In the case where R = Const., the larger the value of L, the narrower the frequency response range. This means that the characteristic curve moves to the left but the static amplification coefficient remains unchanged.
- In the case where $L = 0$, the characteristic curve becomes a horizontal line and the dB remains unchanged.

From the analysis above, it is obvious that the amplitude-frequency characteristic has a clear and definite physical meaning. Therefore, the transfer function explicitly represents the characteristics of power sources. To explore the relationship of the transfer function, configuration, and dynamic characteristics of power sources, more types of arc-welding power sources and their transfer functions are discussed in the (ii)–(iv) below and Sections 2.3.2 and 2.3.3.

(ii) Suppose that the configuration of a power source is as shown in Fig. 2.8: then, following the derivation procedure described above, the transfer function can be obtained as

$$G(j\omega) = -\frac{1}{Z} = \frac{-1}{R + j\omega L \,//\, \dfrac{1}{j\omega C}} = \frac{-\dfrac{1}{R}\left[LC(j\omega)^2 + 1\right]}{LC(j\omega)^2 + \dfrac{L}{R} j\omega + 1} \qquad [2.9]$$

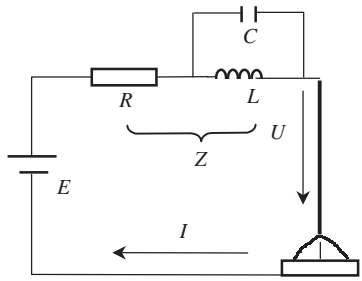

2.8 Equivalent electric circuit of a simple drooping-characteristic power source (B)

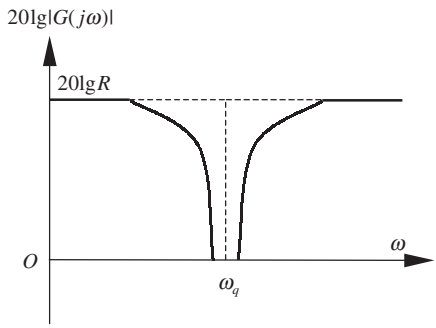

2.9 Ampltiude-frequency characteristics of power source (B) (Asymptote)

From this equation, it can be seen that the amplification coefficient is $-1/R$, and the capacitance does not effect the static characteristics but does change the dynamic characteristics. The amplitude-frequency characteristics can be depicted as in Fig. 2.9.

From Fig. 2.9, it can be found that there is a singular point $\omega_q = 1/\sqrt{LC}$ that depends on L and C; the high and low frequency parts far away from ω_q are horizontal lines.

(iii) If a power source has the configuration that is shown in Fig. 2.10, then the equivalent impedance can be expressed as Eq. [2.10] and the transfer function as Eq. [2.11].

$$Z = R // \frac{1}{j\omega C} + j\omega L = \frac{(j\omega)^2 RCL + j\omega L + R}{j\omega RC + 1} \qquad [2.10]$$

$$G(j\omega) = -\frac{1}{Z} = \frac{-(j\omega RC + 1)/R}{(j\omega)^2 LC + j\omega L/R + 1} \qquad [2.11]$$

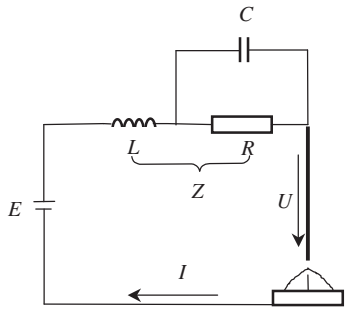

2.10 Equivalent electrical circuit of a simple drooping-characteristic power source (C)

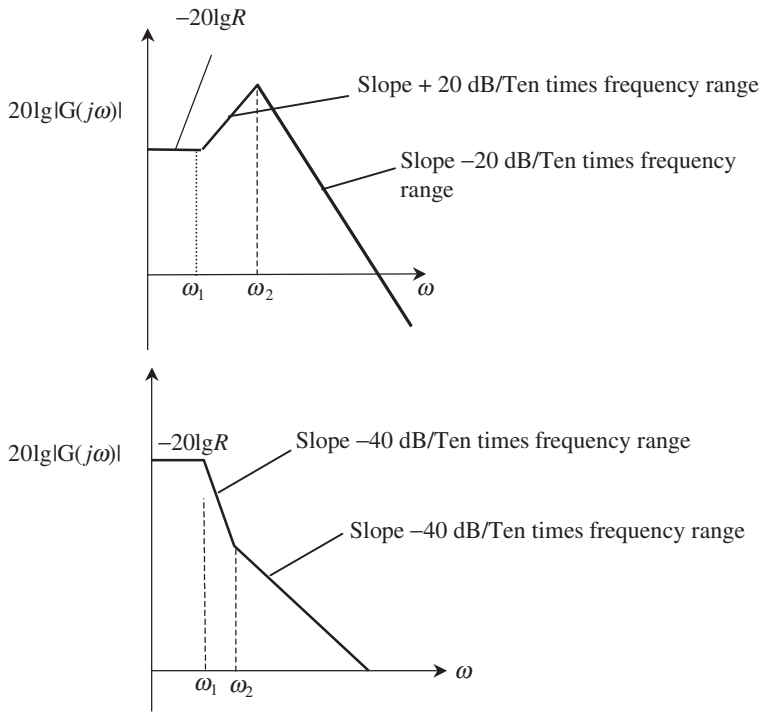

2.11 Amplitude-frequency characteristics of power source (C) (Asymptote)

The amplification coefficient is still $-1/R$. Let $\omega_1 = 1/RC$, $\omega_2 = 1/\sqrt{LC}$, then its amplitude-frequency characteristics can be depicted as shown in Fig. 2.11.

From the figure, it can be seen that the characteristic curve takes a different form if ω_1 and ω_2 are assumed to have different values.

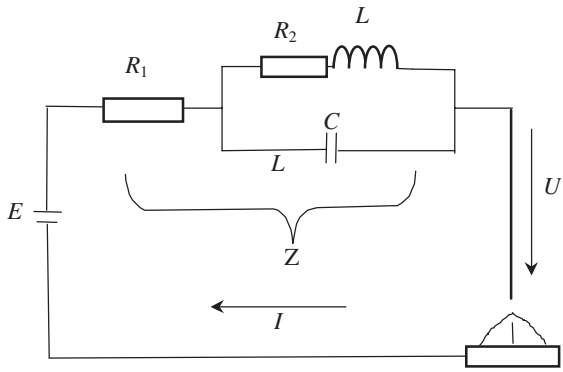

2.12 Equivalent electric circuit of power source (D)

(iv) If the power source has a configuration as shown in Fig. 2.12, then its impedance and transfer function can be expressed as Eq. [2.12] and Eq. [2.13].

$$Z = R_1 + (R_2 + j\omega L) // \frac{1}{j\omega C}$$
$$= \frac{(j\omega)^2 R_1 LC + j\omega(R_1 R_2 C + L) + R_1 + R_2}{(j\omega)^2 LC + j\omega R_2 C + 1} \qquad [2.12]$$

$$G(j\omega) = -\frac{1}{Z} = -\frac{1}{R_1 + R_2} \frac{(j\omega)^2 LC + j\omega R_2 C + 1}{(j\omega)^2 \frac{R_1 LC}{R_1 + R_2} + j\omega \frac{R_1 R_2 C + L}{R_1 + R_2} + 1} \qquad [2.13]$$

The static-amplification coefficient is $-1/(R_1 + R_2)$ In the case where $R = R_1 + R_2$, the amplification coefficient of the power source D is the same as that of power sources A,B,C.

Assuming $\omega_1 = 1/\sqrt{LC}$ and $\omega_2 = 1/\sqrt{LCR_1/(R_1 + R_2)}$, which implies that $\omega_1 \le \omega_2$; then the amplitude-frequency characteristics can be illustrated as shown in Fig. 2.13.

Summarising the descriptions (i)–(iv), it can be concluded that although four types of power sources, A, B, C, and D, have the same static characteristics, they have quite different dynamic characteristics due to different configurations. The differences can be explicitly illustrated by the amplitude-frequency characteristic curves shown in Fig. 2.14.

From the discussions of this section, it can be concluded that the transfer function can explicitly describe the overall characteristics, particularly dynamic characteristics, of a power source. Therefore, it can be regarded as a more scientific and rigorous method for evaluation of power-source characteristics.

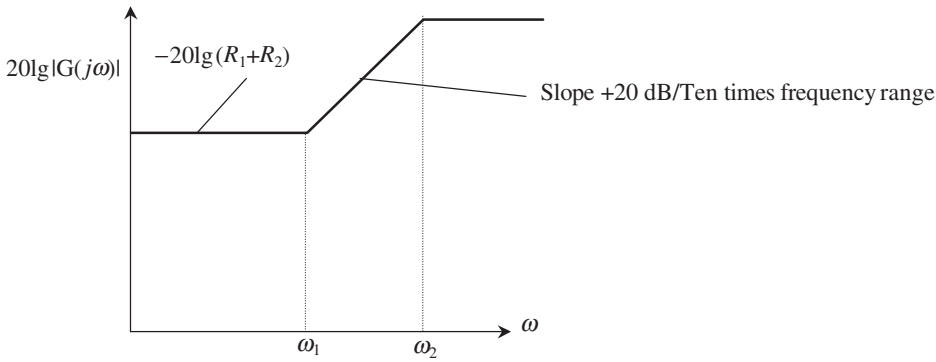

2.13 Amplitude-frequency characteristics of power source (D) (Asymptote)

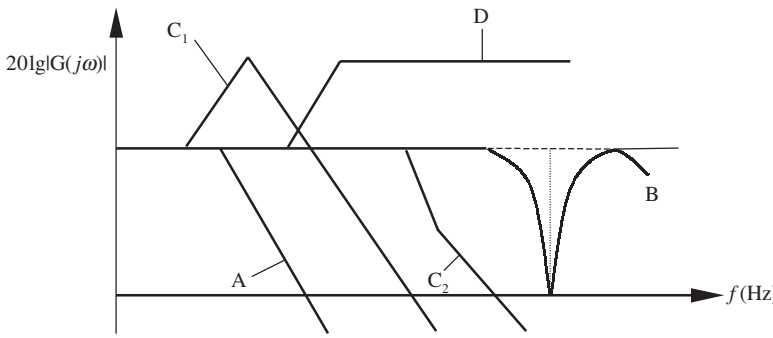

2.14 Amplitude-frequency characteristics of four different power sources

2.3.2 Generator-type power sources

Among generator-type DC welding power sources, generators with series demagnetising windings are the most typical. The transfer function of this type of power source is discussed in this section.

The equivalent electrical circuit of the generator has been shown in Fig. 2.2 in Section 2.1.1. According to electrical circuit principles, the following equations may be used.

$$U_1 = I_1 R_1 + L_1 \frac{dI_1}{dt} - M \frac{dI}{dt} \qquad [2.14]$$

$$E = IR + L \frac{dI}{dt} - M \frac{dI_1}{dt} + U \qquad [2.15]$$

$$E = \frac{K}{R_m}(I_1 N_1 - I N_C) \qquad [2.16]$$

For further derivation, the small deviation method is applied for analysis. Assume that the static stable working point is (I_{10}, I_0, E_0, U_0) and let $\Delta I_1 = I_1 - I_{10}$, $\Delta I = I - I_0$, $\Delta E = E - E_0$, $\Delta U = U - U_0$. Then the following equations are obtained:

$$0 = \Delta I_1 R_1 + L_1 \frac{d\Delta I_1}{dt} - M \frac{d\Delta I}{dt} \quad [2.17]$$

$$\Delta E = \Delta I R + L \frac{d\Delta I}{dt} - M \frac{d\Delta I_1}{dt} + \Delta U \quad [2.18]$$

$$\Delta E = K_1 \Delta I_1 - K_c \Delta I \quad [2.19]$$

where $$K_1 = \frac{KN_1}{R_m}, \quad K_c = \frac{KN_c}{R_m}$$

Applying the Laplace transform to the above equations, and letting

$$I_1(s) = \Delta I_1(s), \quad I(s) = \Delta I(s), \quad E(s) = \Delta E(s), \quad U(s) = \Delta U(s), \quad [2.20]$$

one can obtain

$$I_1(s) R_1 + L_1 s I_1(s) - M s I(s) = 0 \quad [2.21]$$

$$E(s) = I(s) R + L s I(s) - M s I_1(s) + U(s) \quad [2.22]$$

$$E(s) = K_1 I_1(s) - K_c I(s) \quad [2.23]$$

Eq. [2.21] can be written as $$I_1(s) = \frac{M s I(s)}{R_1 + L_1 s} \quad [2.24]$$

Substituting Eq. [2.23] into Eq. [2.22], we obtain

$$K_1 I_1(s) - K_c I(s) = I(s)(R + Ls) - M s I_1(s) + U(s) \quad [2.25]$$

Substituting Eq. [2.24] into the above equation, we obtain

$$U(s) = -\frac{\begin{array}{c}(LL_1 - M_2)s^2 + (RL_1 + R_1 L + K_c L_1 - K_1 M)s \\ + R_1(R + K_c)\end{array}}{R_1 + L_1 s} I(s) \quad [2.26]$$

$$\begin{aligned} G(s) &= \frac{I(s)}{U(s)} \\ &= -\frac{R_1 + L_1 s}{(LL_1 - M^2)s^2 + [(R + K_c)L_1 + R_1 L - K_1 M]s + R_1(R + K_c)} \\ &= \frac{-\frac{1}{R + K_c}\left(\frac{L_1}{R_1} s + 1\right)}{\frac{LL_1 - M^2}{R_1(R + K_c)} s^2 + \frac{(R + K_c)L_1 + R_1 L - K_1 M}{R_1(R + K_c)} s + 1} \end{aligned} \quad [2.27]$$

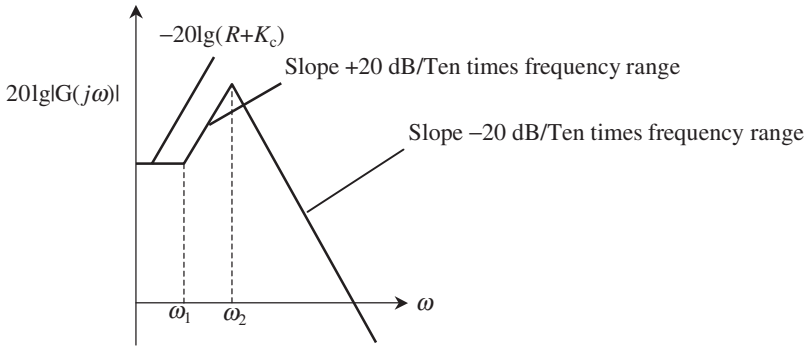

2.15 Amplitude-frequency characteristics of a welding generator (Asymptote)

From the derived equation, it can be seen that the transfer function of a generator-type power source is a Type 2 control system with one zero. The static-amplification coefficient is $-1/(K_c + R)$ and the time constant depends on the configuration. Assume that

$$\omega_1 = \frac{R_1}{L_1}, \qquad \omega_2 = \sqrt{\frac{R_1(R+K_c)}{LL_1 - M^2}} \qquad [2.28]$$

As in most cases, the external excitation circuit for welding generators has a larger time constant, *i.e.* $\omega_1 < \omega_2$. Therefore, the amplitude-frequency characteristics can be depicted as shown in Fig. 2.15.

In the following paragraphs, the transfer function of the welding generator under two special conditions is discussed.

(i) In the case $M = 0$, there is a very small mutual inductance and Eq. [2.27] can be written as

$$G(s) = \frac{-1/(R+K_c)}{Ls/(R+K_c)+1} \qquad [2.29]$$

The transfer function becomes a Type 1 control system, the external excitation winding has no effect on the dynamic characteristics of the power source, and the time constant depends only on the parameters of the major circuit. The dynamic-response speed can be increased by decreasing the value of $L/(R + K_c)$. Letting $\omega_n = (R + K_c)/L$, then the amplitude-frequency characteristics can be depicted as shown in Fig. 2.16.

(ii) In the case $M = \sqrt{LL_1}$, the mutual inductance of the generator has the maximum value. From Eq. [2.27], the transfer function can be derived as

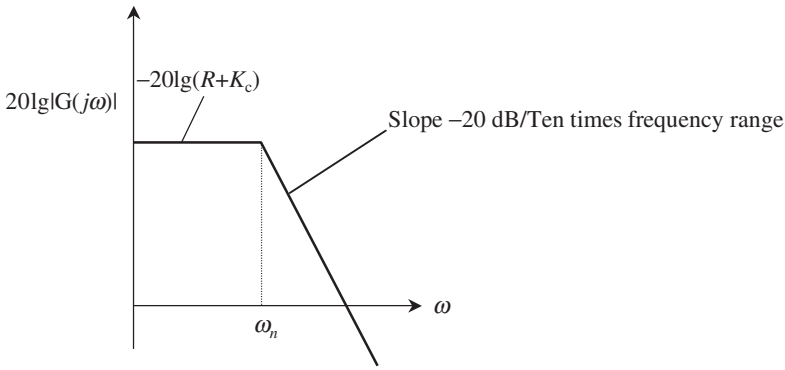

2.16 Amplitude-frequency characteristics of a welding generator where M = 0

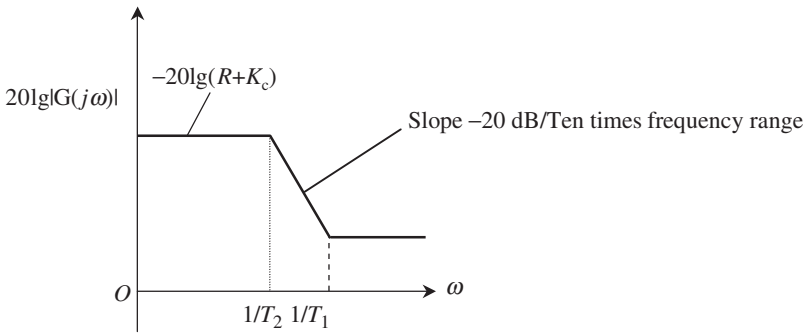

2.17 Amplitude-frequency characteristics of a welding generator where $M = \sqrt{LL_1}$

$$G(s) = \frac{-\frac{1}{R+K_c}\left(\frac{L_1}{R_1}s+1\right)}{\left(\frac{L_1}{R_1}+\frac{L}{R+K_c}-\frac{K_1M}{R_1(R+K_c)}\right)s+1} \qquad [2.30]$$

From this equation, it can be seen that the transfer function of the generator is a Type 1 control system with one zero. Let

$$T_1 = \frac{L_1}{R_1} \qquad T_2 = \frac{L_1}{R_1}+\frac{L}{R+K_c}-\frac{K_1M}{R_1(R+K_c)}$$

Then, the amplitude-frequency characteristics can be drawn as shown in Fig. 2.17.

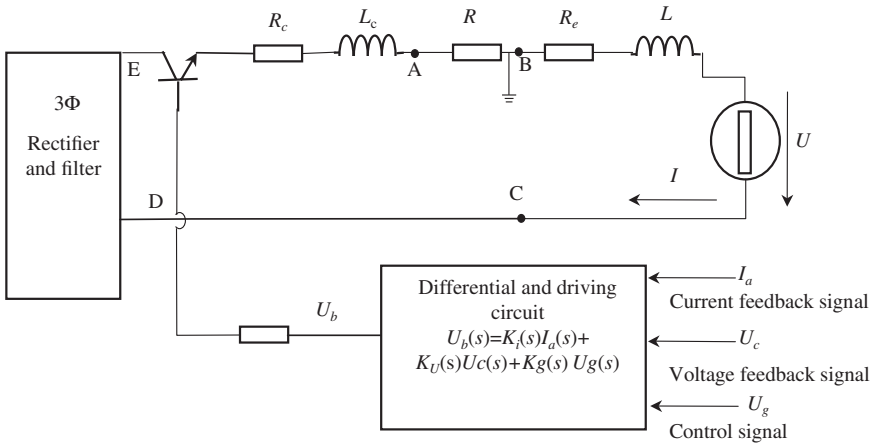

2.18 Equivalent circuit of analogue-type transistorised power sources

From the analysis above, it can be seen that the transfer function can express the overall characteristics of the generator, i.e. both the static and dynamic properties of the power source.

2.3.3 Transistorised power sources

The equivalent electrical circuit of a transistorised power source can be constructed as shown in Fig. 2.18. In this figure, R represents the sampling resistance, R_c,L_c are the equivalent resistance and inductance in the loop AEDC (loop inside the power source), and R_e and L are the equivalent resistance and inductance in the loop BC (loop outside the power source). All of the distributed parameters are expressed by equivalent lumped parameters. The current signal is sampled at point A where $U_a = IR$. The voltage signal is sampled at C, which is the voltage U_c across BC. In most cases, the values of R_e,R_c,L_c are much smaller than other parameters in the circuit; therefore they may be neglected.

Applying the principle of equivalent circuits based on small deviations for transistors[27] and taking the above-mentioned factors into consideration, the equivalent circuit of the power source can be configured as shown in Fig. 2.19, where g_m is the transconductance of the transistor.

According to electrical circuit principles and the diagram of Fig. 2.19, the following equations can be written.

$$U_a = IR \qquad [2.31]$$

for circuit CA,

$$I = g_m V_{r2} + C_2 \frac{dV_{ca}}{dt} + \frac{V_{ca}}{R_3} \qquad [2.32]$$

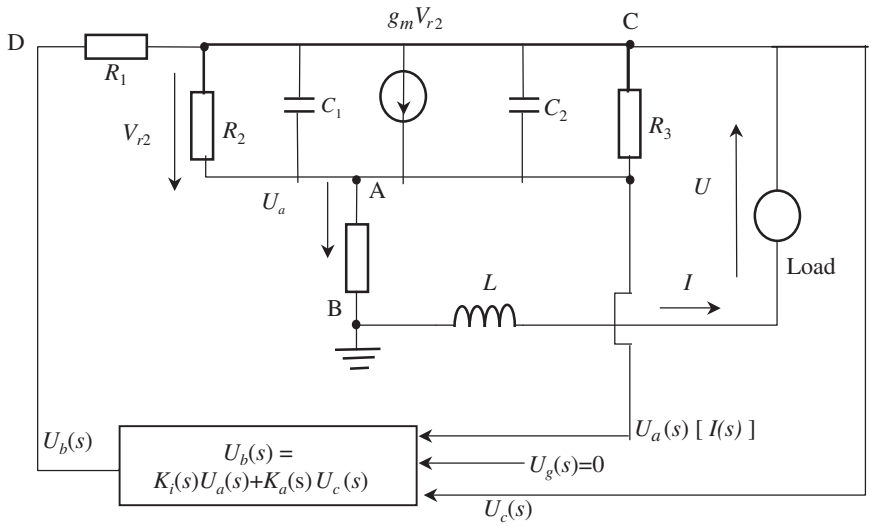

2.19 Equivalent circuit based on a small deviation for transistorised power sources

for circuit ABC,
$$V_{ca} = -U - L\frac{\mathrm{d}I}{\mathrm{d}t} - U_a \qquad [2.33]$$

for circuit DAB,
$$\frac{U_b - U_a - V_{r2}}{R_1} = \frac{V_{r2}}{R_2} + C_1\frac{\mathrm{d}V_{r2}}{\mathrm{d}t} \qquad [2.34]$$

for circuit CB,
$$U_c = -U - L\frac{\mathrm{d}I}{\mathrm{d}t} \qquad [2.35]$$

Applying the Laplace transform to the above equations, we obtain

$$U_a = I(s)R \qquad [2.36]$$

$$I(s) = g_m V_{r2}(s) + C_2 s V_{ca}(s) + V_{ca}(s)/R_3 \qquad [2.37]$$

$$V_{ca}(s) = -U(s) - LsI(s) - U_a(s) \qquad [2.38]$$

$$\frac{U_b(s) - U_a(s) - V_{r2}(s)}{R_1} = \frac{V_{r2}(s)}{R_2} + C_1 s V_{r2}(s) \qquad [2.39]$$

$$U_c(s) = -U(s) - LsI(s) \qquad [2.40]$$

The control rule is

$$U_b(s) = K_i(s)I(s) + K_u(s)U_c(s) \qquad [2.41]$$

Substituting Eq. [2.36] into Eq. [2.38] and then into Eq. [2.37], we obtain

$$I(s) = g_m V_{r2}(s) - (C_2 s + 1/R_3)U(s) - (R + Ls)(C_2 s + 1/R_3)I(s) \quad [2.42]$$

Substituting Eq. [2.36] into Eq. [2.39], we find that

$$\frac{U_b(s) - RI(s)}{R_1} = \left(\frac{1}{R_1} + \frac{1}{R_2} + C_1 s\right)V_{r2}(s) \quad [2.43]$$

Substituting Eq. [2.40] into Eq. [2.41], we obtain

$$\begin{aligned} U_b(s) &= K_i(s)I(s) + K_u(s)[-U(s) - LsI(s)] \\ &= [K_i(s) - K_u(s)Ls]I(s) - K_u(s)U(s) \end{aligned} \quad [2.44]$$

Substituting Eq. [2.44] into Eq. [2.43] and then into Eq. [2.42], we find

$$\begin{aligned} I(s) = g_m &\frac{[K_i(s) + K_u(s)Ls]I(s) - K_u(s)U(s) - RI(s)}{(1/R_1 + 1/R_2 + C_1 s)R_1} \\ &-(C_2 s + 1/R_3)U(s) - (R + Ls)(C_2 s + 1/R_3)I(s) \end{aligned} \quad [2.45]$$

As $g_m \approx \beta/R_2$ (β-current-amplification factor of the transistor), substituting it into above equation, we obtain

$$\begin{aligned} I(s) = &\frac{\beta[K_i(s) - K_u(s)Ls - R]I(s) - \beta K_u(s)U(s)}{R_1 + R_2 + R_1 R_2 C s} \\ &-(C_2 s + 1/R_3)U(s) - (R + Ls)(C_2 s + 1/R_3)I(s) \end{aligned} \quad [2.46]$$

$$\therefore\ G(s) = \frac{I(s)}{U(s)}$$

$$= \frac{\dfrac{-\beta K_u(s)}{R_1 + R_2 + R_1 R_2 C_1 s} - C_2 s - \dfrac{1}{R_3}}{1 - \dfrac{\beta[K_i(s) - K_u(s)Ls - R]}{R_1 + R_2 + R_1 R_2 C_1 s} + (R + Ls)\left(C_2 s + \dfrac{1}{R_3}\right)} \quad [2.47]$$

Letting $T_b = R_1 R_2 C_1/(R_1 + R_2)$, $T_c = R_3 C_2$, $T = L/R$ and substituting these into the above equation, we obtain

$$\begin{aligned} G(s) = &\frac{-\beta K_u(s) - (T_c s + 1)(T_b s + 1)\dfrac{R_1 + R_2}{R_3}}{(R_1 + R_2)(T_b s + 1) - \beta[K_i(s) - RK_u(s)Ts - R]} \\ &+ (Ts + 1)(T_b s + 1)(T_c s + 1)R\frac{R_1 + R_2}{R_3} \end{aligned} \quad [2.48]$$

This equation is the expression of the transfer function of an analogue-type transistorised arc-welding power source. The power source would have

different static characteristics when $K_i(s)$ and $K_u(s)$ take different values in combination.

- If $K_u(s) = K_u$, $K_i(s) = 0$ ($K_u > 0$), which means there is only negative voltage feedback; the power source will have a flat output characteristic.
- If $K_u(s) = 0$, $K_i(s) = -K_i$ ($K_i > 0$), which means there is only negative current feedback; the power source will have a constant-current output characteristic.
- $K_u(s) = K_u$, $K_i(s) = -K_i$ ($K_i > 0$, $K_u > 0$), which means there are both negative voltage and current feedback; the power source will have a drooping characteristic.
- If $K_u(s) = K_u$, $K_i(s) = K_i$ or $K_u(s) = -K_u$, $K_i(s) = -K_i$ ($K_i > 0, K_u > 0$), which means the system provides negative voltage feedback plus positive current feedback or positive voltage feedback plus negative current feedback; the power source will have a rising output characteristic. If $K_u(s)$ and $K_i(s)$ are substituted into the transfer function of Eq. [2.48], it can be seen that the pole or zero can locate on the right half of s-plan. This means that the system includes an unstable element and is a minimum-phase system.

In the following paragraph, the transfer function of constant-voltage and constant-current power sources are discussed further.

(i) Constant-voltage power source. Substituting $K_i(s) = 0$, $K_u(s) = K$ into Eq. [2.48], the transfer function of the power source can be obtained as follows:

$$G(s) = \frac{-\beta K - (T_c s + 1)(T_b s + 1)(R_1 + R_2)/R_3}{(R_1 + R_2)(T_b s + 1) + \beta R(KTs + 1) + (Ts + 1)(T_c s + 1)(T_b s + 1)R(R_1 + R_2)/R_3} \quad [2.49]$$

From this equation, it is seen that the power source is a third-order system with two zeros. In order to simplify the equation, some minor factors can be neglected. Generally, for analogue-type transistorised power sources, K and β are larger and R is smaller Neglecting some high-order terms, the equation above can be written as

$$G(s) = \frac{-\beta K - \dfrac{R_1 + R_2}{R_3}(T_c + T_b)s}{[(R_1 + R_2)T_b + \beta KRT]s + \beta R + R_1 + R_2} = \frac{-\dfrac{\beta K}{\beta R + R_1 + R_2}\left[\dfrac{R_1 + R_2}{\beta R R_3}(T_c + T_b)s + 1\right]}{\dfrac{(R_1 + R_2)T_b + \beta KRT}{\beta R + R_1 + R_2}s + 1} \quad [2.50]$$

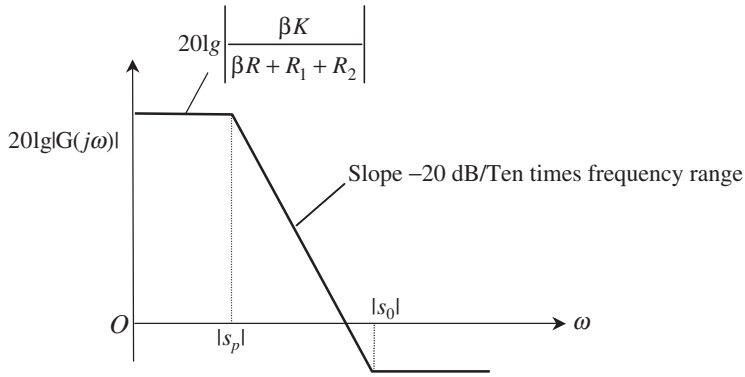

2.20 Schematic diagram of amplitude-frequency characteristics for a transistorised power source with a flat power-source characteristic

From the simplified equation, it can be seen that the power source is equivalent to a first-order system with one zero; the amplification coefficient is $-\beta K/(\beta R + R_1 + R_2)$, the value of zero is $s_0 = -\beta K R_3/[(R_1 + R_2)(T_c + T_b)]$ and the value of the pole is $s_p = -(\beta R + R_1 + R_2)/[(R_1 + R_2)T_b + \beta K R T]$. The factors that affect the dynamic characteristics are the characteristic parameters of the transistor, R and L of the main circuit, and the amplification coefficient of the feedback loop. For conventional transistorised power sources having flat output characteristics, the value of zero and the pole are $|s_0| > |s_P|$; therefore, the amplitude-frequency characteristics can be depicted as shown in Fig. 2.20.

(ii) Constant-current power source. Substituting $K_i(s) = -K$, $K > 0$, $K_u(s) = 0$ into Eq. [2.48], we obtain

$$G(s) = \frac{-(T_c s + 1)(T_b s + 1)(R_1 + R_2)/R_3}{(R_1 + R_2)(T_b s + 1) + (Ts + 1)(T_b s + 1)(T_c s + 1)R(R_1 + R_2)/R_3 + \beta K + \beta R} \quad [2.51]$$

From this equation, it is seen that the power source is a third-order control system with two zeros. The characteristics of the transistors, parameters of the main circuit, and the amplification coefficient of the feedback loop determine concretely the character of the transfer function. From this equation, the amplification coefficient of the system can be derived as

$$-(R_1 + R_2)/[(R_1 + R_2)(R + R_3) + \beta R_3(R + K)].$$

In summarising the descriptions above, it can be concluded that the transfer function can be used as a means for describing the characteristics of power sources. However, due to the complicated configuration of the power

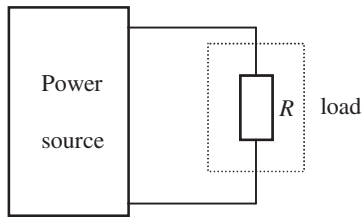

2.21 Schematic diagram for the measurement of power-source characteristics

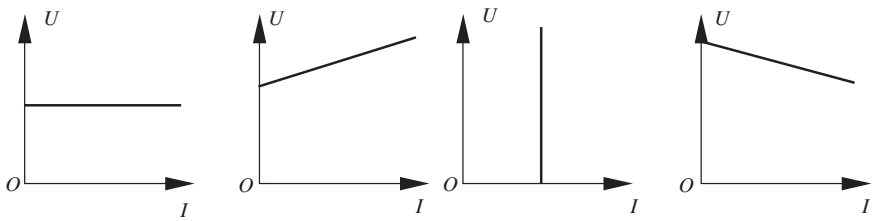

2.22 Different characteristics of load

source, the concrete determination of the transfer function has to be made using experimental methods. In Section 2.4, the experimental method proposed by the author and his colleague, together with the results that were obtained, are introduced.

2.4 Measurement of the transfer function[381]

2.4.1 Apparatus

The measurement apparatus is shown schematically as Fig. 2.21. The current and voltage are measured across the load. It is easy to obtain the static characteristics by slowly sweeping the load resistance from $0 \rightarrow \infty\Omega$. The transfer function can be obtained by measuring the current response while the voltage across the load is varied according to a sinusoidal signal. In order make these measurements, the load should be controllable. The voltage across the load or the current passing through the load should be controlled by some signals. This kind of load can be realised by using transistors. Because the current can be very large, many transistors, up to several hundred, should be connected in parallel for the measurements. Using current feedback, voltage feedback, or both, different types of load, constant current, constant voltage rising or drooping characteristic load can be obtained, as shown in Fig. 2.22.

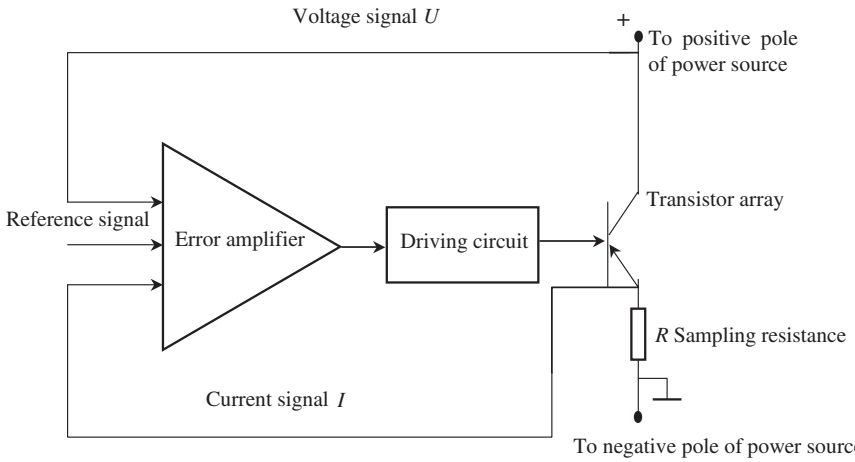

2.23 Diagram showing the principle of a controllable load

As the constant-voltage load is not affected basically by external factors, the frequency-response range can be up to 200 kHz, which is sufficient for the study of the power-source characteristics. For this reason, the constant voltage load characteristic is used for measurement except for those power sources that have a rising output characteristic and cannot be detected by this kind of load. The principle of the controllable load is shown in the diagram of Fig. 2.23, in which 200 15 A/150 W power transistors are connected in parallel as the load.

2.4.2 Measuring method

To study the characteristics in frequency domain, in fact, is to measure the amplitude-frequency characteristics and the phase–frequency characteristics. The measuring method is as follows.

(i) Set the load current and voltage of the power source at a stable point.
(ii) Vary the voltage across the controllable load according to a sine wave at a certain frequency. Both the voltage and current across the load are measured.
(iii) Change the frequency of the sinusoidal signal from $0 \rightarrow \infty$ Hz and repeat the measurement.

The block diagram of the measuring method is shown in Fig. 2.24. Of course, it is possible also to use a random signal and detect its response. In this case,

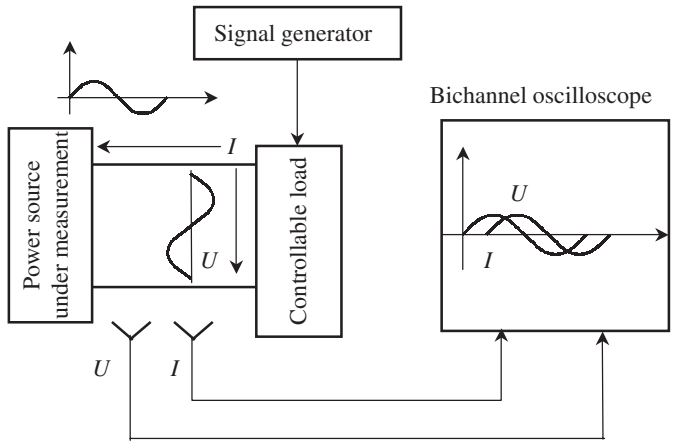

2.24 Block diagram of the measuring method

special signal-processing apparatus should be used to find the amplitude-frequency and phase-frequency characteristics.

2.4.3 Experimental results and analysis

Different types of power sources have been tested and characterised by the author and his colleague using the method described in the previous section. Some of the results are shown in Fig. 2.25. From these results, it can be seen that power sources having different configurations have different amplitude-frequency and phase-frequency characteristics. Some of them are minimum-phase systems. For example, an analogue-type transistorised power source with rising output characteristics has an unstable element in its transfer function. The amplitude- and phase-frequency characteristics in the low-frequency range represent the static characteristics of the system; those in the medium- and high-frequency ranges represent the dynamic characteristics of the system. From the amplitude-frequency characteristics, the static-amplification coefficient of the system, which represents the reciprocal of the slope of the output characteristic of the power source at the working point where the measurement is conducted, can be obtained. Therefore, the larger the amplification coefficient, the flatter the output characteristic will be, and vice versa, or, the smaller the amplification coefficient, the steeper the output characteristic will be (or closer to a constant-current output characteristic). In normal cases, the power source can be considered to have a flat output characteristic if the amplitude at the low-frequency end is over 30 dB and can be considered to have a constant-current output characteristic if the amplitude is less than –5 dB. The power

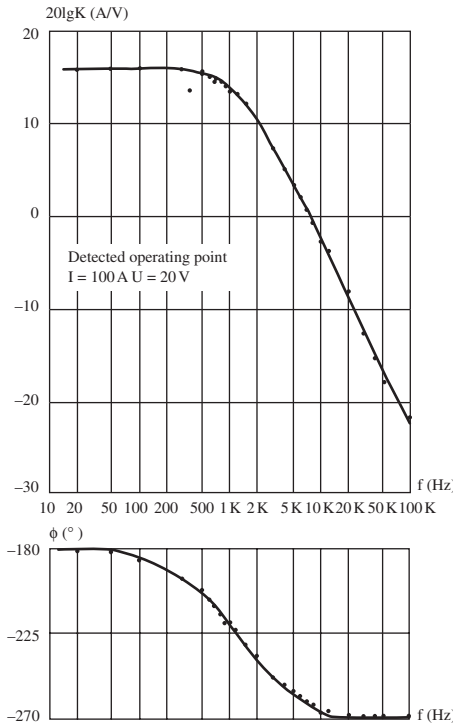

(a) Power source of simple droop characteristics
(Made in TH University)

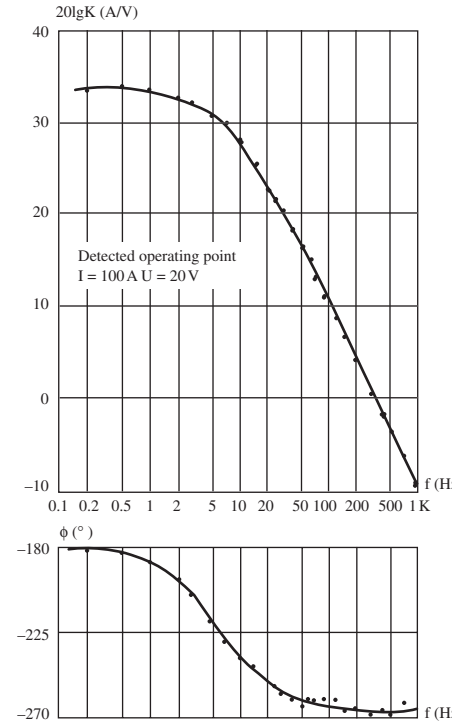

(b) Analogue type transistorized power source
with flat output characteristics (A)
(Made in TH University, Modified QHT–80)

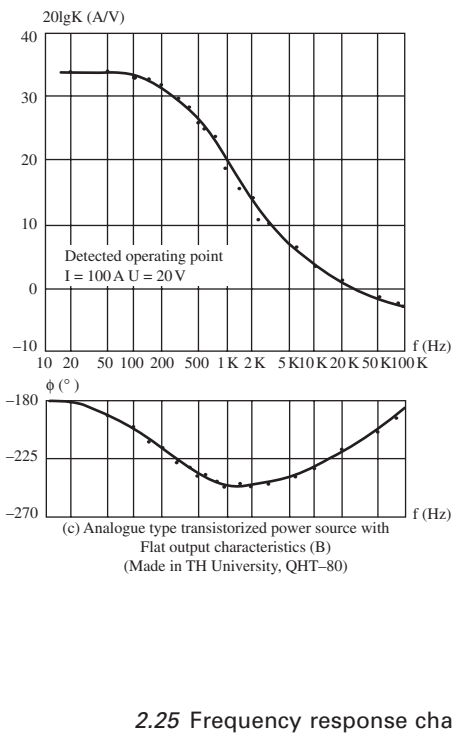

(c) Analogue type transistorized power source with
Flat output characteristics (B)
(Made in TH University, QHT–80)

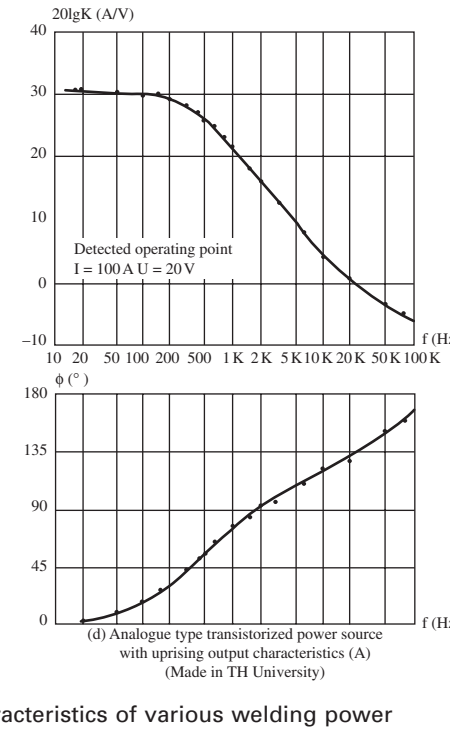

(d) Analogue type transistorized power source
with uprising output characteristics (A)
(Made in TH University)

2.25 Frequency response characteristics of various welding power sources (a–i)

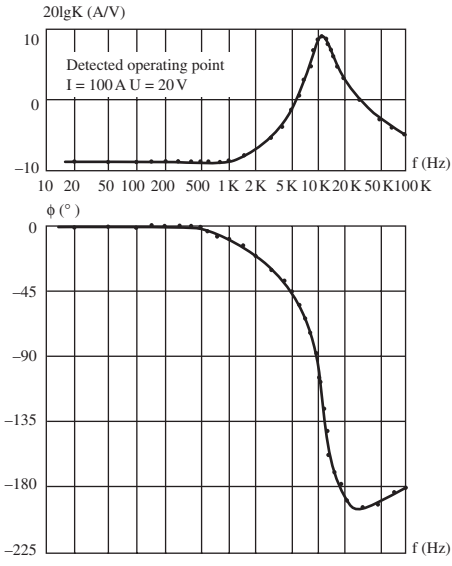

(e) Analogue type transistorized power source with uprising output characteristics (B) (Made in TH University)

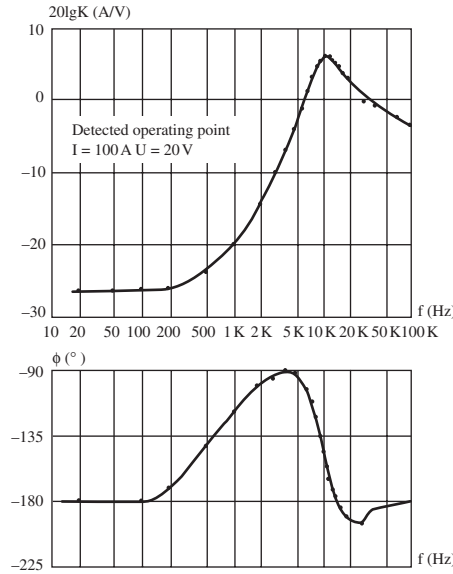

(f) Analogue type transistorized power source with constant current characteristics (A) (Made in TH University, QHT–80)

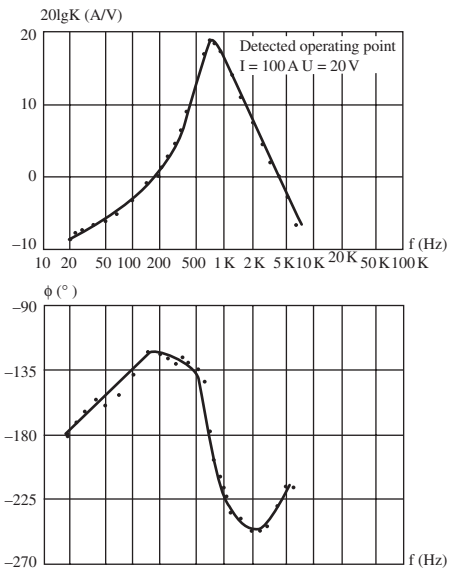

(g) Switching type transistorized power source with constant current output characteristics (Developed by TH University, ZX4–400)

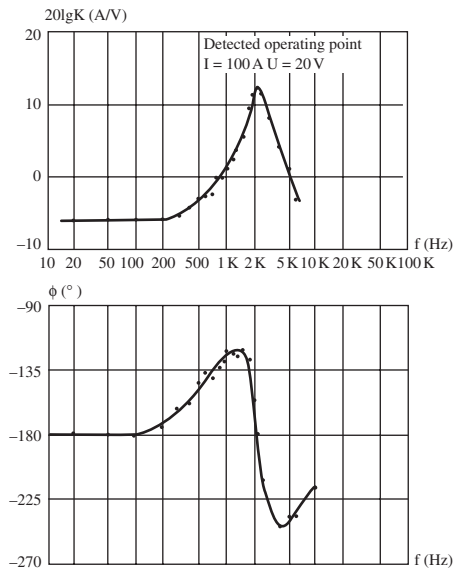

(h) Analogue type transistorized power source with constant current output characteristics (B) (Made in TH University, Modified QHT–80)

2.25 Continued

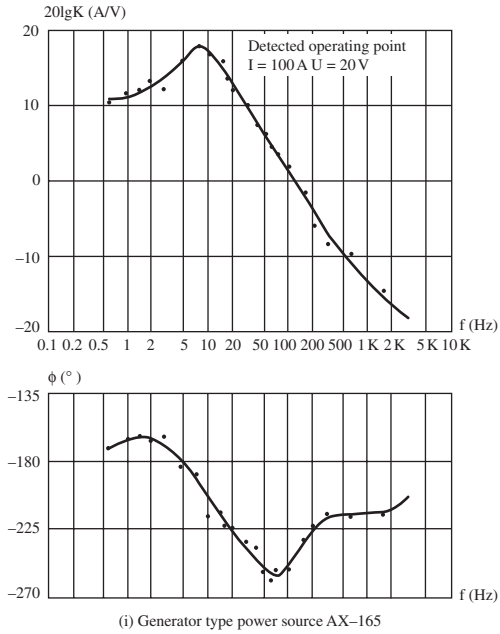

(i) Generator type power source AX–165

2.25 Continued

source will have a drooping characteristic if the amplitude is in between these amplitudes. The phase-frequency characteristics at the low-frequency end can be used to determine whether the output characteristic is rising or drooping. If the magnitude of the phase at the low-frequency end is zero, the power source has a rising output characteristic. To envision these better, the amplitude-frequency diagrams of all of the power sources that were characterised are plotted together in Fig. 2.26.

It can be seen that there are large differences between these characteristics, particularly the dynamic characteristics of the power sources.

On the basis of control theory,[28] the transfer function of a power source can be obtained by fitting the experimental curves of the frequency-response characteristics. The method is to determine the values of zeros and poles and then establish the mathematical expression of the transfer function. Some practical examples are introduced as follows:

(i) For a simple drooping characteristic, the frequency-response characteristic is shown in Fig. 2.25a. The transfer function can be obtained by fitting the following equation:

$$G(s) = \frac{-K}{Ts+1} \qquad [2.52]$$

where $K = 6\,\text{A/V}$, $T = 0.127\,\text{ms}$

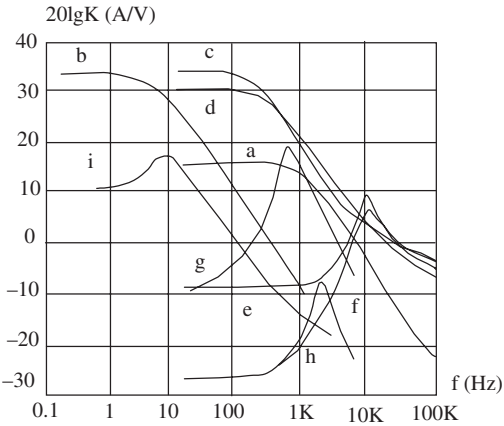

2.26 Amplitude-frequency characteristics of various welding power sources

(ii) For an analogue-type transistorised power source with a series inductance and a flat output characteristic, the frequency-response characteristic is shown in Fig. 2.25b. The transfer function can be obtained by fitting the following equation:

$$G(s) = \frac{-K}{Ts+1}, \qquad [2.53]$$

where $K = 47.5\,\text{A/V}$, $T = 24\,\text{ms}$

(iii) For an analogue-type transistorised power source with a flat output characteristic, the frequency-response characteristic is shown in Fig. 2.25c. The transfer function can be obtained by fitting the following equation:

$$G(s) = \frac{-K(T_2 s+1)}{T_1 s+1} \qquad [2.54]$$

where $K = 47.5\,\text{A/V}$, $T_1 = 0.65\,\text{ms}$, $T_2 = 12\,\mu\text{s}$

(iv) For a generator-type welding power source, the frequency-response characteristic is shown in Fig. 2.25i. The transfer function can be obtained by fitting the following equation:

$$G(s) = \frac{-K(T_1 s+1)(T_2 s+1)\omega_n^2}{s^2 + 2\xi\omega_n s + \omega_n^2} \qquad [2.55]$$

where $K = 1.72\,\text{A/V}$, $T_1 = 0.05\,\text{s}$, $T_2 = 0.11\,\text{ms}$, $\omega_n = 51.5\,\text{Hz}$, $\xi = 0.65$

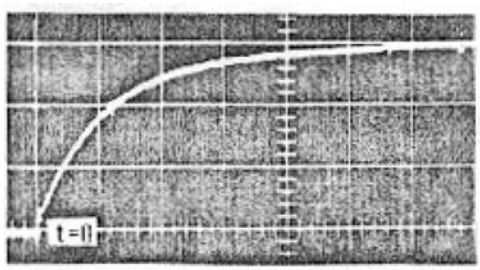

x: 0.5 ms/Div
y: 15 A/Div

a) Data by direct measurement

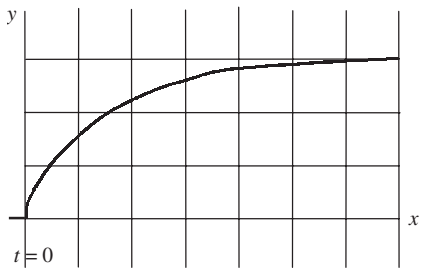

x: 0.5 ms/Div
y: 15 A/Div

a) Data by calculation of the transfer function

2.27 Step response of current

As T_2 is relatively small compared with the other constants, its effect can be neglected. The transfer function above can be simplified as:

$$G(s) = \frac{-K(T_1 s + 1)\omega_n^2}{s^2 + 2\xi\omega_n s + \omega_n^2} \qquad [2.56]$$

Comparing the experimental results to the fitted transfer function with the theoretical analyses described previously, it can be concluded that the theoretical analyses coincide with the experimental results. On the basis of the transfer function obtained by fitting, the characteristics of the power source in time domain can be derived and compared with the experimental results measured by a step response. For example, Fig. 2.27b shows the step response of an analogue-type transistorised power source calculated on the basis of the transfer function obtained by fitting, and Fig. 2.27a is the step response of the power source measured directly by experiment. Obviously, they are nearly the same, which demonstrates that the transfer function is correct and is able to describe the overall characteristics of the power source.

2.5 Influence of the transfer function on technological properties

The transfer function describes the characteristics of the power source and the power source affects the technological behaviour; consequently, the

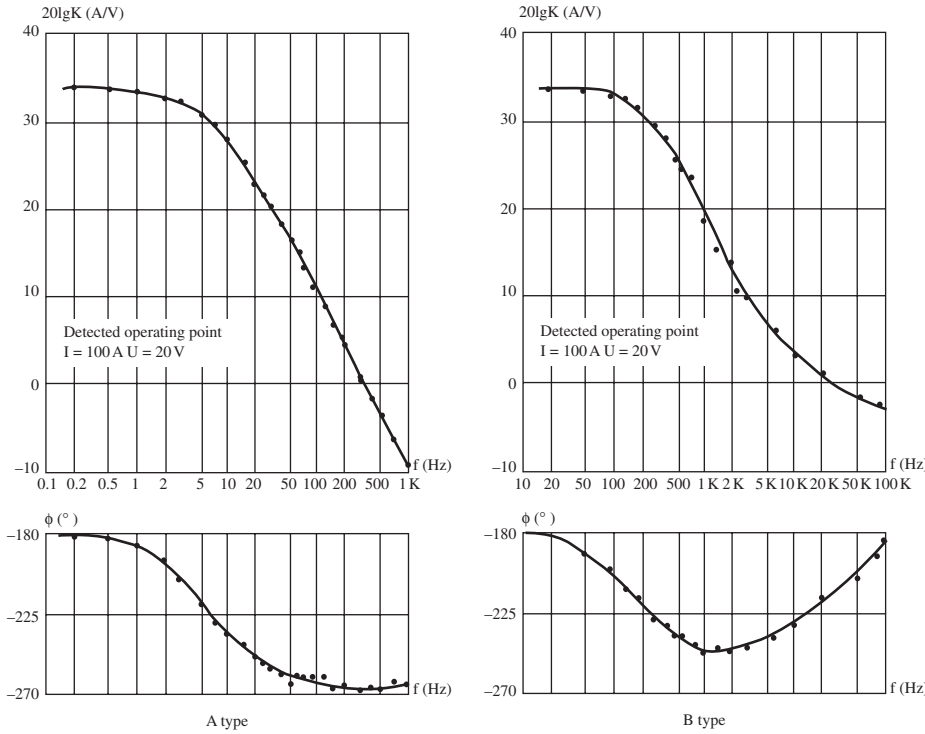

2.28 Frequency-response characteristics of power sources A and B

transfer function should have certain relationships with the technological properties. This should be an important project for study in the future. In the following paragraph, the evaluation of a power source and its technological properties that was carried out by the author is introduced.

It is well known that, for CO_2 welding using small-gauge wire, a power source with a flat output characteristics and short-circuiting droplet transfer is used. In this case, the dynamic properties of the power source are of great importance to the behaviour of the welding arc and production of satisfactory technological properties. For example, low spatter and good bead formation could not be obtained with an improper power source. Figure 2.28 shows the frequency-response characteristics of two power sources for CO_2 welding. Both of them have the same static characteristics but different dynamic characteristics (compare the curves at medium- and high-frequencies). Technological experiments show clearly that power-source A behaves better than power-source B. It produces less spatter and has a more stable arc.

The discussion above demonstrates that it is possible to evaluate the technological behaviour of a power source via its transfer function. In other words, the power source can be evaluated by its transfer-function parameters.

2.6 Summary

(i) The transfer function, which represents both static and dynamic characteristics, can be used to describe the characteristics of a power source. It is a more scientific and comprehensive evaluation method than the existing method based on time domain.

(ii) The transfer function of a power source can be established by direct measurement using the frequency-domain method. From experiments conducted by the author, the following conclusions can be drawn:

- A power source with a simple drooping characteristic is a first-order control system and its transfer function can be written as

$$G(s) = \frac{-K}{Ts+1}$$

- An analogue-type transistorised power source with a flat output characteristic is a first-order control system with one zero and the transfer function can be written as:

$$G(s) = \frac{-K(T_2 s+1)}{T_1 s+1}$$

- A generator-type power source is a second-order control system and the transfer function can be written as

$$G(s) = \frac{-K(Ts+1)\omega_n^2}{s^2+2\xi\omega_n s+\omega_n^2}$$

The specific parameters of the transfer function can be obtained from the frequency-response characteristics. For the power sources mentioned above, they are

a. $K = 6\,\mathrm{A/V}, \quad T = 0.127\,\mathrm{ms}$
b. $K = 47.5\,\mathrm{A/V}, \quad T_1 = 0.65\,\mathrm{ms}, \quad T_2 = 12\,\mu\mathrm{s}$
c. $K = 1.72\,\mathrm{A/V}, \quad T = 0.05s, \quad \omega_n = 51.5\ \mathrm{Hz}, \quad \xi = 0.65$

(iii) From the results measured in frequency domain, we can determine the transfer function. In turn, from the transfer function, we can derive the

step response in time domain, so as to relate the transfer function with the experimental method in time domain existing up to the present time. Study of the correlation of the power-source transfer function with the technological properties of the welding process will be an important future endeavour.

3
Experimental study

3.1 Introduction

In Chapter 1, theoretical principles were presented that explain arc-length regulation, but the discussion was based on two assumptions: the first assumed that wire melting is continuous and the second assumed a constant-voltage power source with a simple circuit consisting of L and R. These assumptions, in fact, are different from practical welding processes. To obtain the actual dynamic behaviour of the process using a theoretical method is rather difficult because first, the wire melting is not even, and second, the transfer function of the power source is variable, which is not easily expressed by mathematical functions and solved by calculations. Therefore, experimental methods must be employed. The experimental difficulties include:

- Measurement of arc length, particularly during a dynamic process. High-speed photography often is used but the facilities are complicated and expensive.
- The realization of step changes of either the torch-to-plate distance or the wire-feed rate.
- There are various sources of random interference due to technological factors such as surface condition, shielding-gas composition, etc., which effect the accuracy of the experimental results.

To solve the problem, Pan, Rehfeldt, and Qi proposed two approaches.[29,33,37] The first was to use an arc simulator that has the same characteristics as the real arc, connect it into the welding loop, and measure the welding parameters directly to obtain the dynamic behaviour of the simulated arc. The second was to measure the welding parameters repeatedly during the welding process to obtain a large number of data. The data then were analysed using statistical methods to obtain the dynamic behaviour of the real arc. Statistical methods can eliminate the effect of the random interferences so that objective laws of the arc behavior can be obtained.

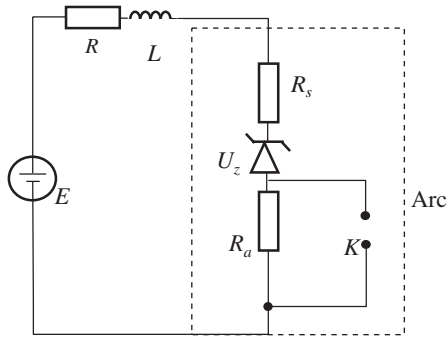

3.1 The electrical circuit for CO_2 welding

The principle of the method and some of the experimental data obtained using these two approaches are described in this chapter.

3.2 CO_2 welding

Because CO_2 welding is performed in the short-circuiting mode, studying the dynamic behaviour of this process is, in fact, the study of the short-circuiting process.[30,31]

3.2.1 Welding arc simulator[32,33]

The electrical circuit of the arc simulator for CO_2 welding can be constructed as shown in Fig. 3.1.

In this figure, the dashed rectangular frame represents the arc, R_s represents the resistance of the wire extension, R_a represents the rising part of the arc characteristic, U_z represents the constant-voltage part of the arc, and K is the switch that shorts and opens the circuit during welding.

Assume that the power source is a constant-voltage type with R, L connected in the welding loop. The transient process of welding with the arc simulator shown above may be analysed as follows:

The steady current before short circuiting is

$$I_m = \frac{E - U_z}{R + R_s + R_a} \qquad [3.1]$$

The steady current after short circuiting is

$$I_M = \frac{E}{R + R_s} \qquad [3.2]$$

The transient process while switching on can be expressed by the differential equation

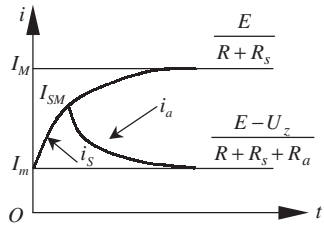

3.2 Welding current during short-circuiting arc welding

$$L\frac{di}{dt}+i(R+R_s)=E \qquad [3.3]$$

The transient process during switching off can be expressed by the differential equation

$$L\frac{di}{dt}+i(R+R_s+R_a)=E-U_z \qquad [3.4]$$

The instantaneous short-circuit current can be obtained by solving Eq. [3.3]

$$i_s=I_M-(I_M-I_m)e^{-\frac{R+R_s}{L}t} \qquad [3.5]$$

and the instantaneous current after the short circuit by Eq. [3.4]

$$i_a=(I_{SM}-I_m)e^{-\frac{R+R_s+R_a}{L}t}+I_m \qquad [3.6]$$

in which I_{SM} is the short-circuit peak current.

The current rise rate during short circuiting is

$$\frac{\mathrm{d}i_s}{\mathrm{d}t}=(I_M-I_m)\left(\frac{R+R_s}{L}\right)e^{-\frac{R+R_s}{L}t} \qquad [3.7]$$

The current drop rate after short circuiting is

$$\frac{\mathrm{d}i_a}{\mathrm{d}t}=-(I_{SM}-I_m)\left(\frac{R+R_s+R_a}{L}\right)e^{-\frac{R+R_s+R_a}{L}t} \qquad [3.8]$$

The current rise rate at the first moment of short circuiting $t = 0$ is

$$\left(\frac{\mathrm{d}i_s}{\mathrm{d}t}\right)_{t=0}=(I_M-I_m)\left(\frac{R+R_s}{L}\right) \qquad [3.9]$$

Eq. [3.5] and Eq. [3.6] can be expressed explicitly by Fig. 3.2.

The discussion above can be summarised as follows:

- The current rise rate during short circuiting depends on two factors, viz. $\frac{R+R_s}{L}$ and $(I_M - I_m)$. The former is the reciprocal of the time constant, $1/\tau$, and the latter is the difference between the steady current before and after short circuiting, which depends on the output characteristics of the power source.
- The change of L results in a change of the time constant of the power source but not of the value $(I_M - I_m)$.
- The change of R results in a change of both the time constant of the power source and the value $(I_M - I_m)$.
- In the case of MIG – MAG welding, the dynamic characteristics are regulated by L and the output characteristics are regulated by R. But regulation of R changes the transient process, i.e. the current-rise rate and drop rate of the short circuit, simultaneously.
- Regulation of R can be carried out by two means. The first is to keep E unchanged and change R to regulate I_m. I_m is the arc current and can be regarded as the welding current. In this case, Eq. [3.9] can be rewritten as

$$\left(\frac{\mathrm{d}i_s}{\mathrm{d}t}\right)_{t=0} = \frac{E}{L} - \left(\frac{E-U_z}{L}\right)\frac{R+R_S}{R+R_s+R_a} \qquad [3.10]$$

Obviously, $\left(\frac{\mathrm{d}i_s}{\mathrm{d}t}\right)_{t=0}$ decreases while R increases. Normally, E = 25 to 40 V, U_z = 10 to 20 V, L = 0.1 to 0.5 mH, R_a = 0.1 to 0.02 Ω, R_s = 0.1 to 0.02 Ω, and R is a quantity of the same order. Substituting these data into Eq. [3.10] shows that the change of R produces only a slight change of $\left(\frac{\mathrm{d}i_s}{\mathrm{d}t}\right)_{t=0}$. Another means of changing R is to keep I_m constant and consequently increase the open-circuit voltage of the power source E. In this case, Eq. [3.9] can be rewritten as

$$\left(\frac{\mathrm{d}i_s}{\mathrm{d}t}\right)_{t=0} = \frac{I_m R_a + U_z}{L}. \qquad [3.11]$$

Obviously $\left(\frac{\mathrm{d}i_s}{\mathrm{d}t}\right)_{t=0}$ does not change while R is regulated. Regulation of R results in a change only of I_M and time constants.

- From the discussions above, it is clear that the current-change rate at the moment of short circuiting, $\left(\frac{\mathrm{d}i_s}{\mathrm{d}t}\right)$, and after it, $\left(\frac{\mathrm{d}i_a}{\mathrm{d}t}\right)$, can be flexibly regulated by changing R, L and E. The waveform of the rising

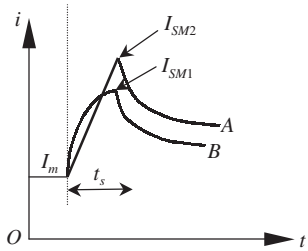

3.3 Short-circuiting current

current can be different, as shown in Fig. 3.3, for a different combination of R, L and E. Practical experience shows that optimum welding results can be obtained using an appropriate combination of drooping characteristics of the power source and inductance in the welding loop. The current waveform during short circuiting is an important characteristic. Comparing the waveforms of A and B in Fig. 3.3, it is seen that, in case A, $\left(\frac{\Delta I_s}{\Delta t}\right)$ is larger, but $\left(\frac{\mathrm{d}i_s}{\mathrm{d}t}\right)_{t=0}$ is smaller than in case B. Therefore, in order to study the dynamic behaviour of the power source, measuring the parameters both during short circuiting and after the short circuiting event is necessary.

- The dynamic behaviour of the welding loop depends not only on the parameters of the power source, but also on the parameters of the arc, R_a, R_s, U_z.

  The parameters R_a, R_s, U_z and the on-off frequency of the switch K in the apparatus shown in Fig. 3.3 can be changed steplessly. The advantages of the measuring method are a) the dynamic behaviour of the welding process with different loads can be measured directly, and b) as the short-circuiting frequency can be kept stable, an oscillograph can record the waveform of the short-circuit current, from which $\frac{\mathrm{d}i}{\mathrm{d}t}$ and other related parameters can be calculated.

3.2.2 Detecting dynamic characteristics using an arc simulator[37]

From the previous discussion, it is known that the dynamic behaviour measured by an arc simulator includes the characteristics of both the power source and the arc. Should the arc simulator be kept unchanged and the measurement be carried out with different power sources, the results then can be used for analysing the characteristics of the power sources.

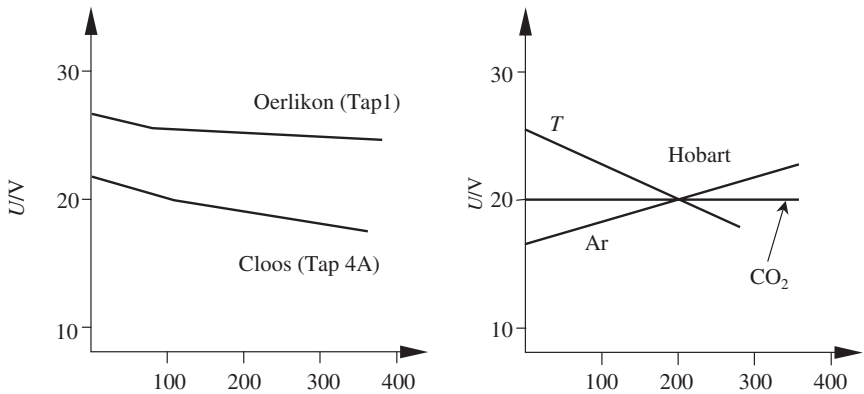

3.4 Output characteristics of power sources

The author characterised three different power sources. The power sources used were

(i) a full-wave rectifier type made by the Cloos Company,
(ii) a full-wave rectifier made by the Oerlikon Company and having an external inductance with taps, and
(iii) a Hobart motor-generator type with a series (positive) excitation coil giving rising output characteristics. This power supply also had a resistance included in its welding loop so that the slope of the output characteristics could be regulated. Changing the resistance could change the output characteristics from a rising to a drooping state.

Before the welding tests were started, the output characteristics of the machines were measured. Namely, the characteristics were measured using tap No.4A of the Cloos machine, tap No. 1 of the Oerlikon machine, which has three different taps of inductance 1.2, 1.6, 2.4, and the Hobart machine with three resistance settings for obtaining rising, flat and drooping output characteristics. The results of the measurements are shown schematically in Fig. 3.4.

After the arc simulator was connected to the power source, the waveforms of the welding voltage and current were recorded using an oscillograph.

Figure 3.5 shows the results for the Oerlikon power source when the arc simulator with the conditions of 230 A, 23 V, short-circuiting frequency of 90 Hz, and short-circuiting time of 3 ms was connected to it. Figure 3.5a, b, and c show the results for three different inductance values. Figure 3.6 shows the results for the Hobart machine when the arc simulator was set with the conditions of 210 A 20.5 V, short-circuiting frequency of 90 Hz, and a short-circuiting time of 3 ms. Figure 3.6a, b and c are the results

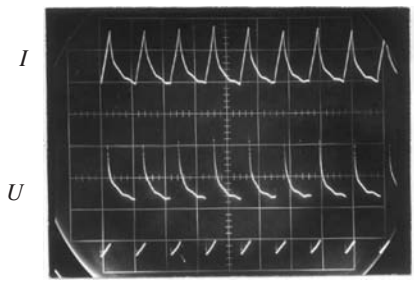

a) $L = 1.2$

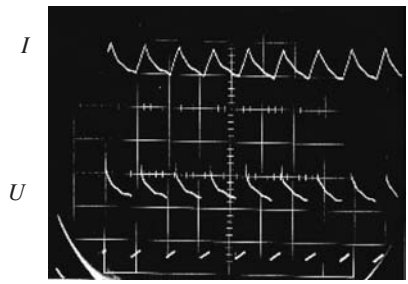

b) $L = 1.6$

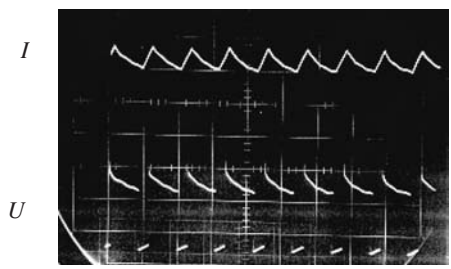

c) $L = 2.4$

3.5 Current and voltage waveforms of the Oerlikon machine

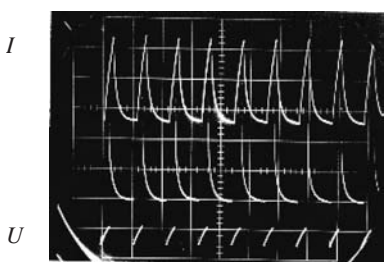

a) Ar

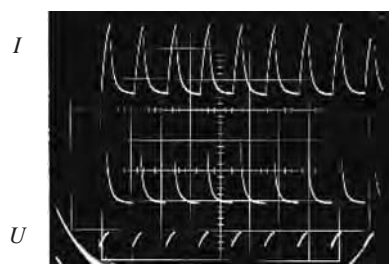

b) CO_2

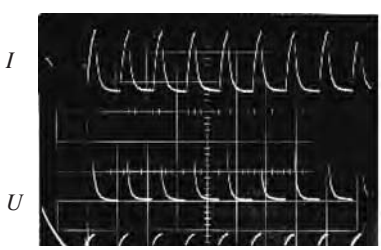

c) T

3.6 Current and voltage waveforms of the Hobart machine

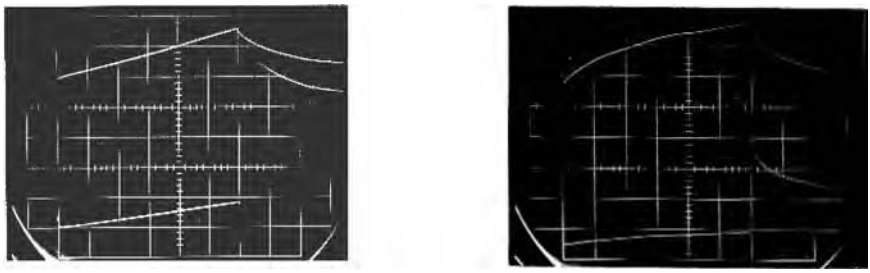

a) *Oerlikon*, L = 1.2 b) *Hobart*, T

X = 0.5ms/Div I = 100*A*/Div U = 5*V*/Div

3.7 Comparison of current and voltage waveforms of Oerlikon and Hobart machines

when R was increased. In the experiment, in order to keep the static working point of the arc unchanged, the open-circuit voltage of the machine was increased accordingly: see the Ar, CO_2 and T curves of Fig. 3.4b. It was found that the Oerlikon and Hobart machines had different current-rise rates when the circuit was shorted. The current waveforms were more distinct when the scanning speed of the oscillograph was increased: see Fig. 3.7.

By measuring the waveforms, the dynamic characteristics of the various power sources can be calculated. Table 3.1 shows the values of $\left(\frac{\Delta I_s}{\Delta t}\right)$ and $\left(\frac{\mathrm{d}i_s}{\mathrm{d}t}\right)_{t=0}$ for seven tests. Obviously, the data for $\left(\frac{\Delta I_s}{\Delta t}\right)$ and $\left(\frac{\mathrm{d}i_s}{\mathrm{d}t}\right)_{t=0}$ are greatly different for the Hobart machine at a short-circuit time of 3 ms. This feature is different from the other two types of machines, which would certainly affect the technological properties of the welding process.

3.2.3 Direct measurement

As mentioned previously, the direct measurement of the dynamic behaviour of the arc is difficult because of various random interferences that occur during welding. Taking advantage of the Hanover Arc Analyser invented by Rehfledt,[32,33] the author measured the dynamic behaviour of CO_2 welding. Then, statistical methods were used to process and analyse the large quantity of data that were obtained.[37]

Table 3.1 Dynamic parameters of short-circuiting welding

No.	Machine	Tap setting	$\frac{\Delta I_s}{\Delta t}\left(\frac{\text{kA}}{\text{sec}}\right)$	$\left(\frac{\text{d}i_s}{\text{d}t}\right)_{t=0}\left(\frac{\text{kA}}{\text{sec}}\right)$
1	Cloos, GLS303 PA/3	No.4A	61.7	61.7
2	Oerlikon, CP-GL 500	$L = 1.2$ (Low inductance)	55.0	55.0
3	Oerlikon, CP-GL 500	$L = 1.6$ (Medium inductance)	29.2	29.2
4	Oerlikon, CP-GL 500	$L = 2.4$ (High Inductance)	22.3	22.3
5	Hobart, Multiwire MC-500	Ar (Rising-output characteristic)	93.3	210
6	Hobart, Multiwire MC-500	CO_2 (Flat-output characteristic)	76.7	210
7	Hobart, Multiwire MC-500	T (Drooping-output characteristic)	66.7	210

The functions of the Hanover Analyser are

- high-speed measurement of arc current and voltage (20000 times/s), automatic sorting of the data, and sending them to a printer
- recording the number and time duration of the short circuits, sorting them according to their time duration, and sending them to a printer, and
- recording the current and voltage waveforms.

The aims of the measurements were to observe

- the effect of inductance,
- the effect of output characteristics, and
- the effect of arc voltage.

Experiments were carried out with the parameters shown in Table 3.2. The welding parameters were established using normal optimum short-circuiting conditions.

For each set of welding parameters, five pieces of 400 mm long specimens were welded. During welding of each specimen, the Hanover Arc Analyser was operated for 30 s; therefore, 150 s of parameters were measured. That means that 3 million values of welding current and voltage and 15000 short-circuits were recorded. The data then were statistically analysed. The results

Table 3.2 Welding parameters

No.	Machine	Regulation tap	Current (A)	Voltage (V)	Welding travel speed (cm/min)	Shielding gas flow-rate (L/min)
1	Cloos	4A	195–210	17	37.5	15
2	Oerlikon	$L = 1.2$	210	22	37.5	15
3	Oerlikon	$L = 1.6$	210	22	37.5	15
4	Oerlikon	$L = 2.4$	207	21	37.5	15
5	Hobart	Ar	190	18.5	37.5	15
6	Hobart	CO_2	195	17.5	37.5	15
7	Hobart	T	200	18.5	37.5	15

Wire dia Φ1.2 mm, Gas: Ar-rich mixture Coxogen

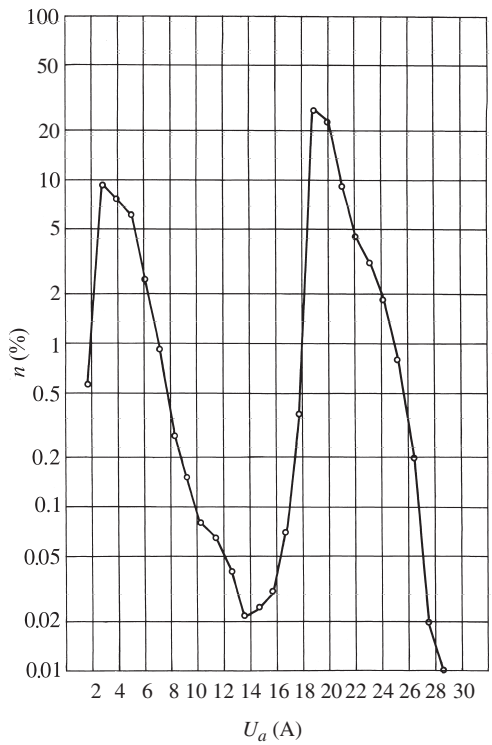

3.8 Probability of arc-voltage samples (Cloos machine)

are shown in Figures 3.8 to 3.13. Figures 3.8 to 3.10 present probability distributions of the arc voltage; the abscissae represent the voltage and the ordinates represent the probability of the sampled data expressed in percentage on a logarithmic scale. From these figures, it can be seen that

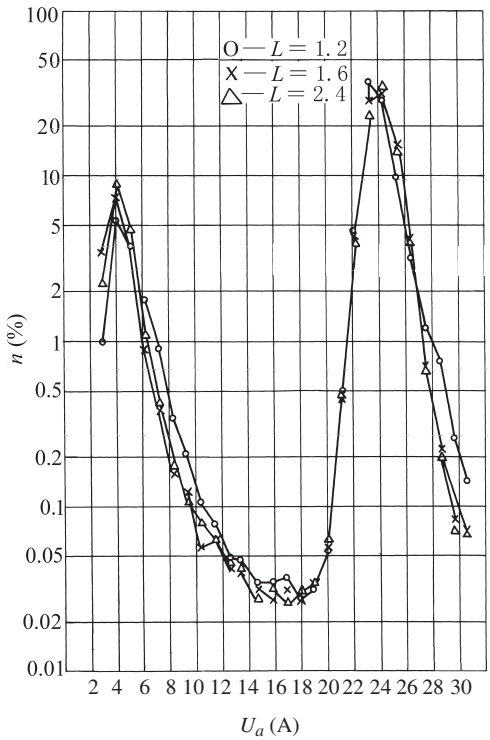

3.9 Probability of arc-voltage samples (Oerlikon machine)

all the sets of welding parameters for the three types of power sources represented typical short-circuiting behaviour.

The arc-voltage probability curves have two peaks. The left-hand peak represents the probability of short circuits and the right-hand peak represents the magnitude of the actual arc voltage. The Cloos machine showed the lowest value, 19–20 V; the Hobart machine was at 20–21 V; and the Oerlikon power supply showed the highest value at 23–24 V. The voltage values of these three peaks were coincident with the static working point of the arc. Furthermore, the three curves in Figures 3.9 and 3.10 almost coincided, which means the static arc working point remained unchanged while their dynamic characteristics were regulated.

Figures 3.11 to 3.13 show the durations of the short circuits and the probability of their appearance. The abscissae represent the duration of the short circuit and the ordinates represent the probability of occurrence of the short-circuit expressed as a percentage. These curves will be denoted 'short-

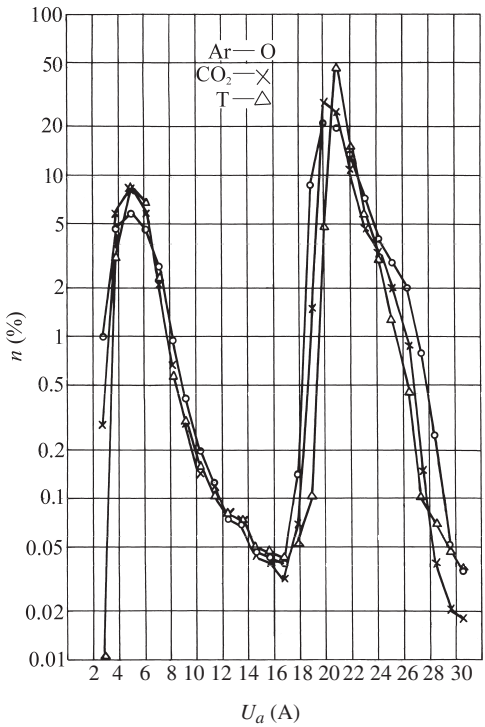

3.10 Probability of arc-voltage samples (Hobart machine)

circuit probability curves'. It can be seen from these figures that the probability curves are quite different for the seven sets of welding parameters. In summary:

(i) Although the seven short-circuit probability curves are different, there is a common configuration, i.e. all of them have two peaks. One is near $t_s \cong 0$, the other is at $t_s > 2$ ms.

(ii) From the three curves for the Oerlikon machine, it can be seen that when the inductance is increased, the position of the first peak does not change but the position of second peak shifts to the right. Therefore, the short circuits can be classified into two categories: the first is $t_s < 2$ ms and the second is $t_s > 2$ ms. The duration of first category is short and is not affected by inductance, which is manifested by the droplet transfer not being related to the electromagnetic force and current. The duration of the second category is longer, is closely

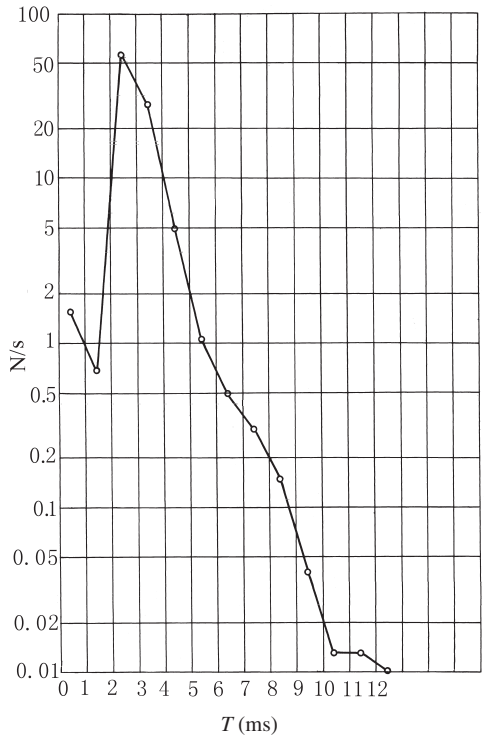

3.11 Probability of short-circuits (Cloos machine)

related to the inductance (the larger the inductance the longer the duration) and is manifested by the droplet transfer being affected considerably by the electromagnetic force and current.

The oscillograph recording shown in Fig. 3.14 presents the current and voltage waveforms for small and large inductances. From these figures, it can be seen that the peak of the short-circuit current is obviously decreased and the duration of short circuit is increased when the inductance is increased.

In order to obtain quantitative data, the author statistically analysed the results recorded by the Hanover Analyser. Table 3.3 summarises the average short-circuit frequency (N_A/s), the total duration of short circuits per second (t_{ss}), the short-circuit frequency of the first category (N_1/s), the short-circuit frequency of the second category (N_2/s), the average duration of the short circuit of the second category (t_{s2}), the maximum short-circuit current (I_{SM}), average $\int i_s^2 dt$, and average $\int i_s dt$, etc.

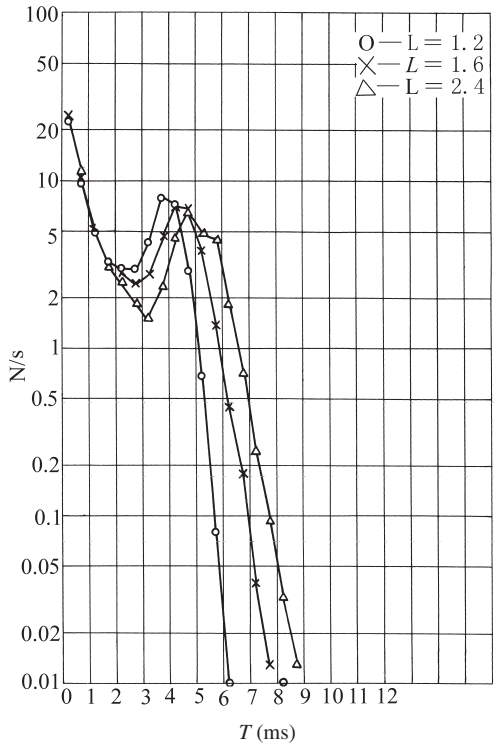

3.12 Probability of short-circuits (Oerlikon machine)

(iii) From the three probability curves of the Hobart machine shown in Fig. 3.13 and Table 3.3, it can be seen that when R is increased, the total duration of short-circuits per second (t_{ss}) and the average duration of short-circuits of the second category (t_{s2}) are increased, and the right part of the probability curve shifts to the right. These phenomena are the same as the effect of increasing L. However, in the present case, when R is increased, the short-circuits of the first category are also affected; their number is greatly increased.

Figure 3.15 shows the waveforms of the Hobart machine with rising and drooping characteristics. Comparing these two wave forms, the following phenomena can be observed:

a. For the Hobart machine using Ar, the major short circuits are of the second category; there are very few of the first category. For the Hobart machine using T, some of the short circuits of the second category convert to the first category.

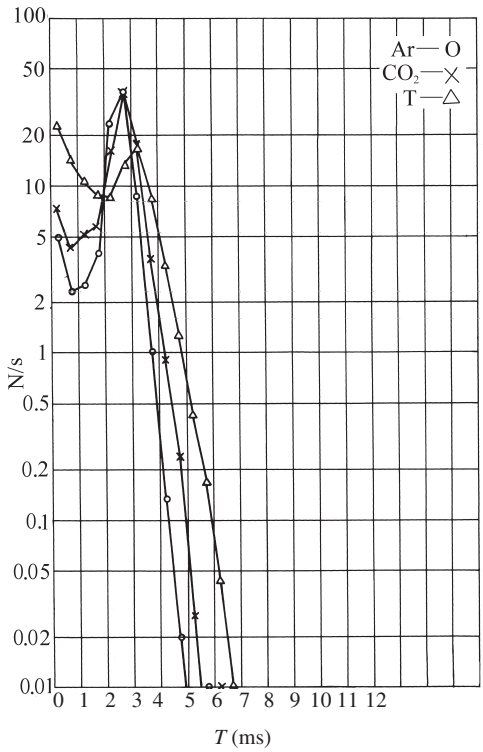

3.13 Probability of short-circuits (Hobart machine)

b. The duration of the second category short circuits for the Hobart T arrangement is obviously longer than that for the Hobart Ar arrangement.

c. The current-rise curves, $\left(\frac{di_s}{dt}\right)$, for these two arrangements are quite different and the value of $(I_M - I_m)$ is smaller for the Hobart T arrangement.

d. The current-drop rate, $\left(\frac{di_a}{dt}\right)$, after short-circuits is different as well. The Hobart T has a much smaller time constant.

e. The arc current for the Hobart T has a much higher value.

All of these phenomena, particularly e., make the short-circuit transfer from the second category to the first category.

(iv) The Cloos machine has a short-circuit probability curve that is different from all of those described above; it has a very small amount of short-circuits of the first category; the majority are of the second category, as shown in Fig. 3.16. This results from lower arc voltage.

Table 3.3 Statistic data of short-circuits

No.	Welding machine	Average voltage during arc burning U_a (V)	Average short-circuit frequency (N_A/s)	Total duration of short-circuit per sec t_{ss} (ms)	Short-circuit frequency of 1st category (N_1/s)	Short-circuit frequency of 2nd category (N_2/s)	Average duration of short-circuit of 2nd category t_{s2} (ms)	Maximum short-circuit current I_{SM} (A)	Average $\int i_s dt$ (A.s)	Average $\int i_s^2 dt$ (A^2.s)
1	Cloos	19–20	91.5	271	2.2	89.3	2.99	304	0.635	143
2	Oerlikon $L = 1.2$	23–24	69.4	131	40.2	29.2	3.85	372	1.025	287
3	Oerlikon $L = 1.6$	23–24	76.0	159	43.5	32.5	4.32	286	0.965	221
4	Oerlikon $L = 2.4$	23–24	76.1	174	43.9	31.7	4.80	267	1.026	224
5	Hobart Ar	20–21	84.0	199	13.7	70.3	2.59	354	0.603	164
6	Hobart CO_2	20–21	96.1	229	22.7	73.4	2.66	324	0.590	140
7	Hobart T	20–21	108.9	210	56.7	52.2	2.71	340	0.679	170

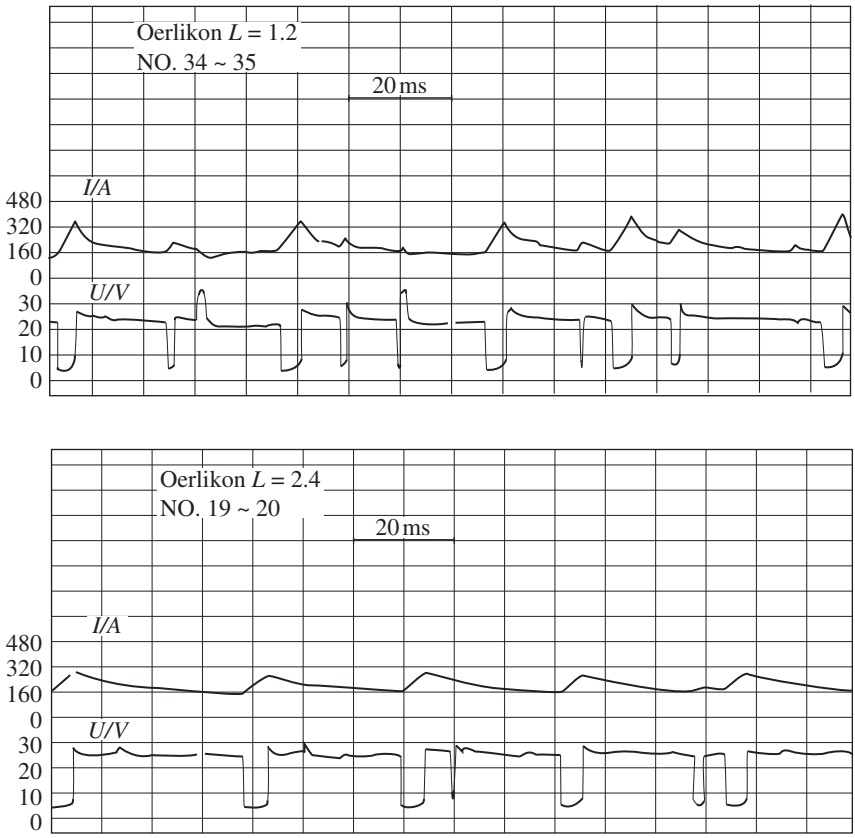

3.14 Current and voltage waveforms for the Oerlikon machine

The arc simulator provides a means for measuring the dynamic behavior of welding arcs. The Hanover Analyser can record large quantities of arc parameters for statistical analysis of the arc characteristics. It may be a promising approach to establish an ideal and accurate index of the dynamic characteristics of the arc that could be used as the norm for evaluation of the power source or welding process. This would allow a more detailed comparison between the technological properties of welds (e.g. spattering and bead formation) and the statistical results of the arc characteristics.

3.3 DC MIG welding

Because CO_2 welding is a short-circuiting process, it is a transient process for each short circuit. The characteristics of the transient process determine the quality of the welding arc and the weldment. For this reason, the arc

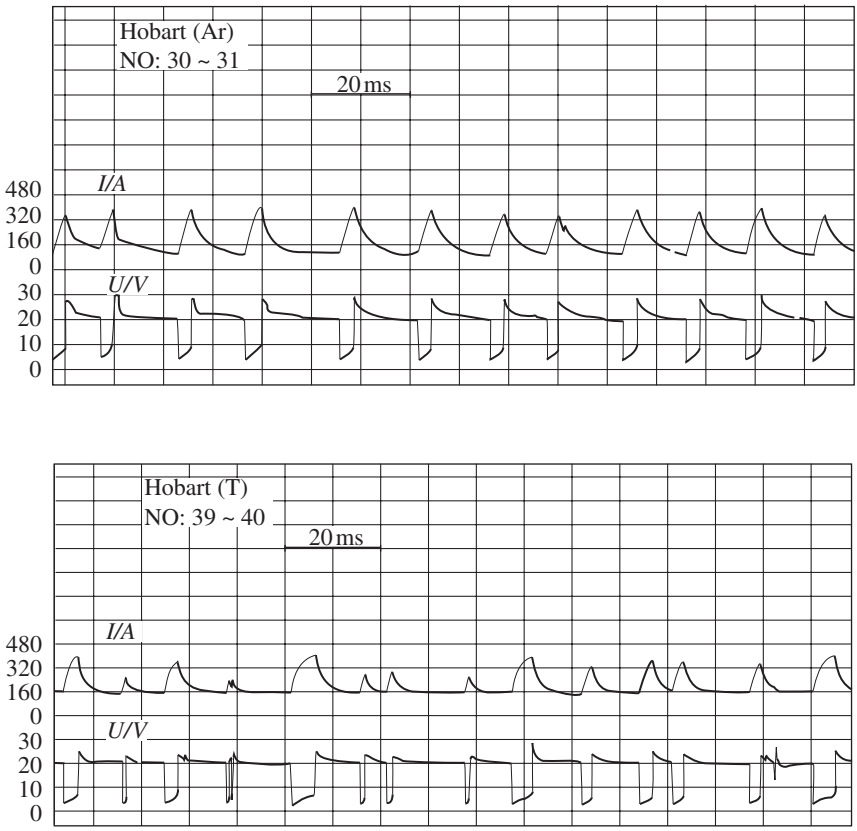

3.15 Current and voltage waveforms for the Hobart machine

simulator described in Section 3.2.1 was designed to characterise the transient process of the short circuit. It can be used for characterising CO_2 welding and other welding processes that produce short circuits. In DC MIG welding on the other hand, short-circuiting occurs only occasionally. Therefore, research for such a process is focused on the steady-state arc behaviour. For example, the effect of changes to the torch-to-plate distance, incoming-voltage, and the wire-feed rate on the technological properties and the quality of the weldments are of interest. From the introduction to the CO_2 arc-simulator design in Section 3.2.1, it is seen that it is based on the assumption that the arc length, torch-to-plate distance, and wire-feed rate are stable and the short circuit is simulated by an artificial constant-frequency switching action. This design does not affect the simulation and measurement of the CO_2 welding process but it would not work for DC

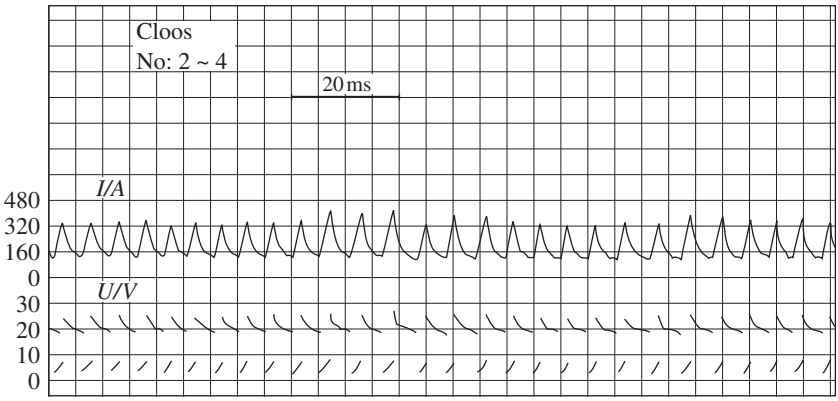

3.16 Current and voltage waveforms for the Cloos machine

MIG welding. A different design for a DC MIG welding arc simulator is necessary.

3.3.1 MIG welding arc simulator[29]

For MIG welding, four dynamic equations that incorporate process parameters can be written as:

$$H = L_s + L_a \qquad [3.12]$$

$$U = k_i L_s + k_q I + k_a L_a + C_1 \qquad [3.13]$$

$$V_f - V_m = dL_s / dt \qquad [3.14]$$

$$V_m = k_r L_s + k_c I + C_2 \qquad [3.15]$$

where H is torch–to plate distance, L_s is wire extension, L_a is arc length, I is welding current, V_m is wire-melting rate, U_a is voltage drop across arc column, U is arc voltage including the voltage drop of the wire extension, and V_f is wire-feed rate.

Although Eq. [3.12] and Eq. [3.14] are accurate expressions, Eq. [3.13] and Eq. [3.15] are derived from more accurate expressions that are nonlinear equations. Linear expressions are derived using the Taylor-expansion formula. For more details, see Reference[29], Sections 8.1.2 and 8.2.2, and Equations [8.26], [8.27], [8.28], and [8.29].

Taking Laplace transforms of the above equations, a block diagram can be constructed according to their interactions, as shown in Fig. 3.17, which is the configuration of the MIG arc simulator.

By performing a large number of experiments and applying linear regression analysis, the parameters of Equations [3.13] to [3.15] were obtained for

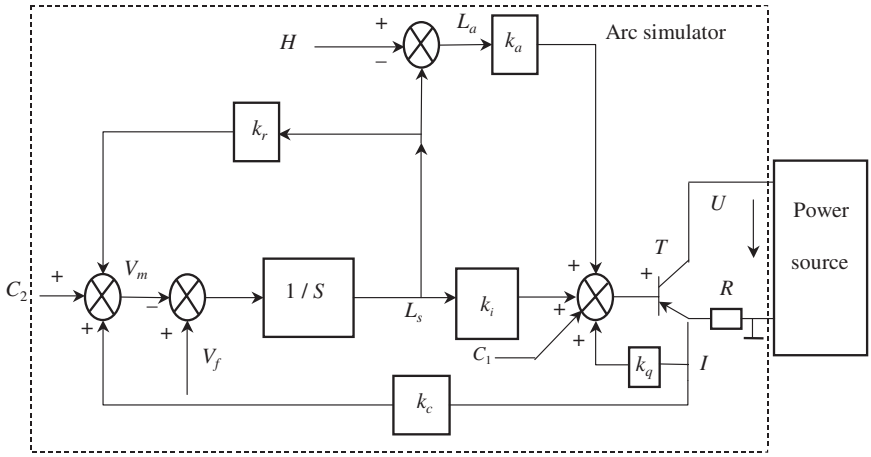

3.17 Configuration of MIG arc simulator

certain welding conditions, as shown in Equations [3.16] and [3.17]. The specific welding conditions were 1.0 mm wire diameter, H08Mn2Si wire material, Ar + 10% CO_2 shielding gas, 28 V arc voltage, and 200 A arc current.[29]

$$U = 14.3 + 0.944L_a + 0.0386I + 0.12L_s \qquad [3.16]$$

$$V_m = 0.0488I + 0.288L_s - 6.31 \qquad [3.17]$$

By substituting the welding parameters into the block diagram and designing the electrical circuit, the MIG arc simulator can be constructed.

From Fig. 3.17, it can be seen that the transistor T is the analogue element of the arc simulator; if the welding current is very large, an array of transistors can be applied. R is the resistance for the sampling current. The control circuit of transistors is configured according to the block diagram shown in the rectangular frame. Following the variation of torch-to-plate distance, H, wire-feed rate, V_f, and welding current, I, the voltage across the transistors varies according to Equations [3.12] to [3.15], thereby simulating the static and dynamic behaviour of the arc.

3.3.2 Experimental verification

In order to verify the validity of the arc simulator, an experimental method was designed by the author. An analogue-type transistorised power source with a constant-voltage output characteristic was applied. Its output voltage was controlled by the input signal, U_g. The parameters for the actual welding process and the design of the arc simulator in the experiment were: 1.0 mm

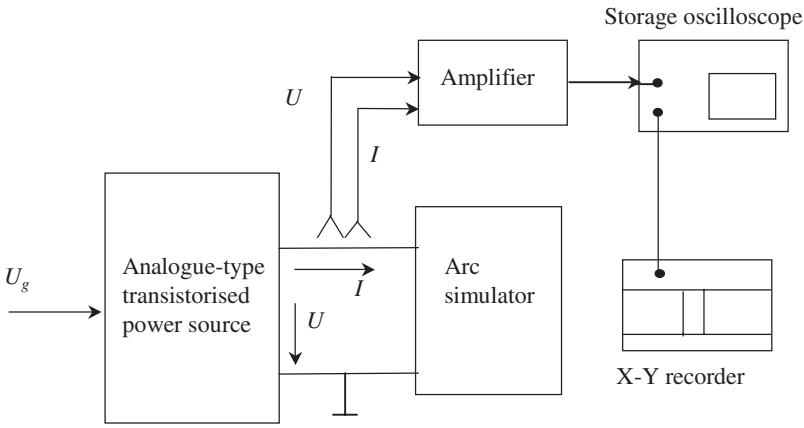

3.18 Block diagram for arc-simulator verification experiments

wire diameter, H08Mn2Si material, Ar + 10%CO_2 shielding gas, 28 V arc voltage, and 200 A welding current. The parameters for the design of the arc simulator were obtained from Equations [3.16] and [3.17]. The block diagram for the experiment is shown in Fig. 3.18.

The voltage and current signals were recorded in two ways: (i) by an X-Y recorder, and (ii) by photography directly from the screen of the oscilloscope. For convenience, most of the experimental results were obtained from the X-Y recorder.

For detecting the dynamic response of the process, a step-input signal was given to U_g of the power source. Then, the voltage and current changes were recorded, both for the actual welding process and for the arc simulator. The experimental results are shown in Fig. 3.19.

Comparing Figures 3.19a and 3.19b shows that the feedback gain, rise time, and settling time for both the actual arc and the simulated arc are very close to each other. When the experiments were repeated for different welding-arc voltages and currents, similar results were obtained. Because the power source used for both cases was the same, it can be concluded that the arc simulator represents the real welding arc and can be used for studying the dynamic process of real MIG welding.

3.3.3 Dynamic behaviour of MIG welding

As it has been shown that the arc simulator can be used instead of the real arc for studying the transient response of the welding process, the experiments were conducted as shown in the block diagram of Fig. 3.20.

3.3.3.1 Effect of the dynamic characteristics of the power source

The transfer function of a transistorised power source, which is the object of this investigation, is

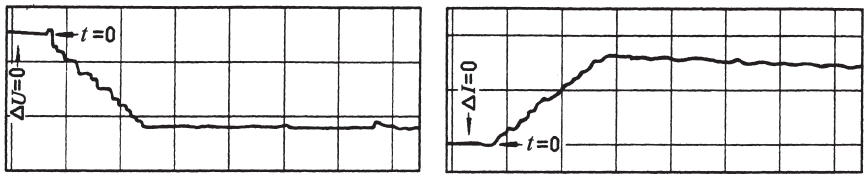

Voltage waveform Current waveform

a. Step response of the arc simulator

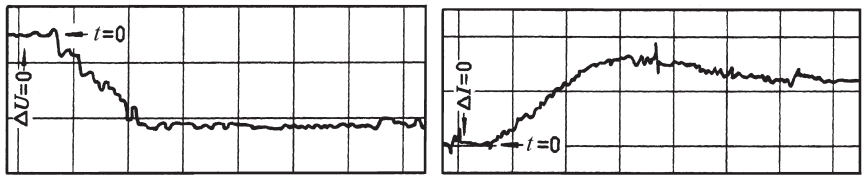

Voltage waveform Current waveform

Ordinate ΔU: 1.1*V*/Div, Abscissa: *t*: 1*ms*/Div Ordinate ΔI: 250*A*/Div, Abscissa: *t*: 1*ms*/Div

b. Step response of the actual welding arc

3.19 Step response of welding voltage and current

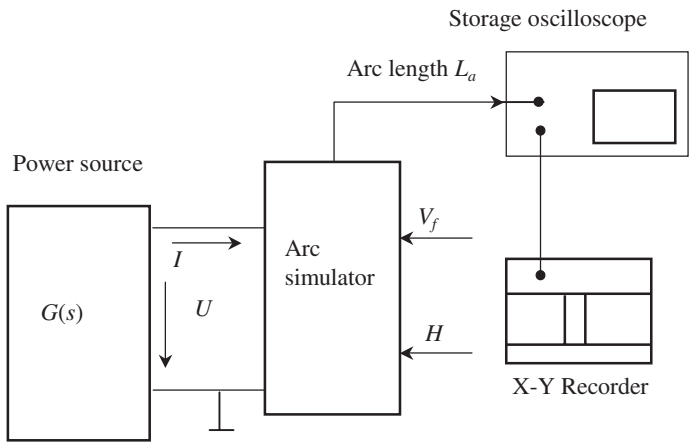

3.20 Block diagram for detecting the dynamic response of the MIG arc

$$G(s) = \frac{1}{K_p(T_s + 1)}$$

Power source A, $K_p = -1/47.5$, $T = 0.65$ ms
Power source B, $K_p = -1/47.5$, $T = 24$ ms

The dynamic response of the arc length is shown in Fig. 3.21. It can be seen that, for power sources A and B, the difference is not big so it can be

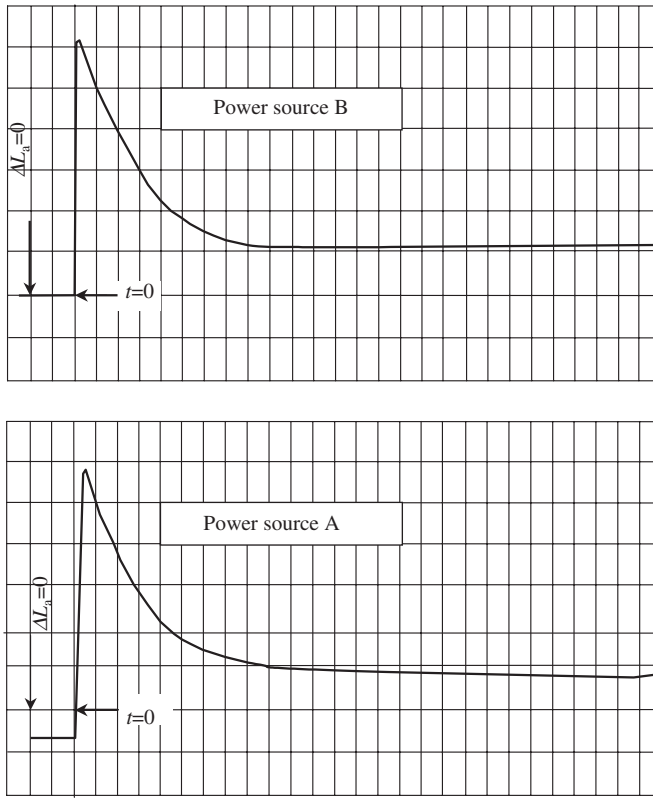

Step change of torch-to-plate distance
Abscissa t: 0.025 s/Div Ordinate ΔL_a: 0.2 mm/Div

3.21 Effects of power-source dynamic characteristics on arc-length self-regulation

concluded that the time constants of the power sources have small effects on the dynamic responses to arc-length changes if the difference of arc length is not large.

3.3.3.2 Effect of the static characteristics of the power source

The power sources that were studied were analogue, transistorised units that had the following static-output characteristics.

A Slope of static output characteristic $K_p = -1/21.1$
B Slope of static output characteristic $K_p = -1/44.8$

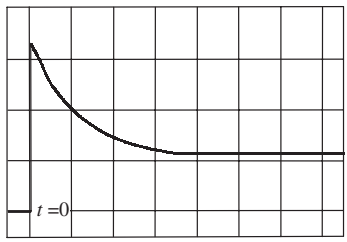

Abscissa $\triangle L_a$: 0.4 mm/ Div. Ordinate t: 0.1s/Div.

a) $K_P = -1/21.1$

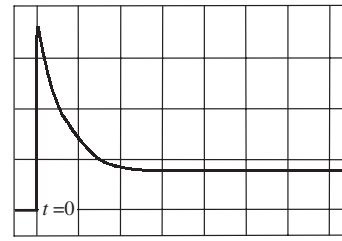

Abscissa $\triangle L_a$: 0.4 mm/ Div. Ordinate t: 0.1s/Div.

b) $K_P = -1/44.8$

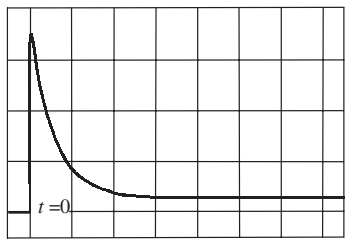

Abscissa $\triangle L_a$: 0.4mm/ Div. Ordinate t: 0.1s/Div.

c) $K_P = 1/120$

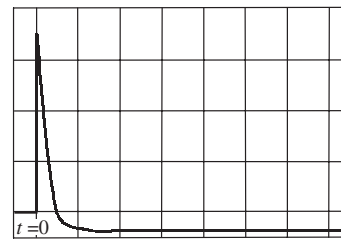

Abscissa $\triangle L_a$: 0.4mm/ Div. Ordinate t: 50μs/Div.

d) $K_P = 1/33.3$

3.22 Effect of power-source static characteristics on arc-length self-regulation

C Slope of static output characteristic $K_p = 1/120$
D Slope of static output characteristic $K_p = 1/33.3$

The experimental results are shown in Fig. 3.22. It can be seen that the arc-length self-regulation ability was strengthened when the slopes of the output characteristics were increased. First, the response speed was increased and second, the steady-state error was reduced. Both of these results agree with theoretical analysis. But when K_p exceeds a certain value, the steady-state error will be negative, which means that the arc length is decreased when the torch-to-plate distance is increased. In other words, the arc length self-regulation ability is not normal. Therefore, it cannot be said that the arc length self-regulation ability is the best when the slope of the power source static characteristic coincides with the slope of arc static characteristic. This conclusion can also be drawn from the theoretical analysis.

3.4 Pulsed MIG welding

Pulsed MIG welding is a new arc-welding process. The outstanding advantage of this process is that the droplet transfer is controlled such that the droplets are very small and uniform with little spatter. The face of the weld bead is smooth and cosmetically attractive. As a wide range of welding

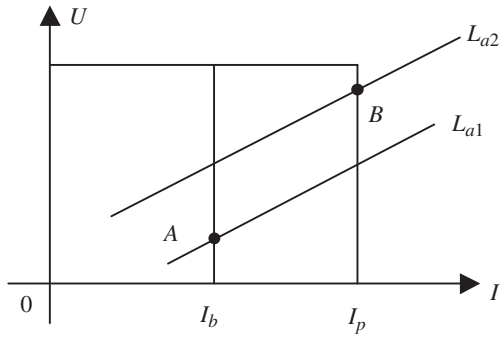

3.23 Static output characteristics of a power source

parameters can be achieved, it can be used for various plate thicknesses. However, there are several welding parameters that interact in a complex manner including pulse-current duration (t_p) and amplitude (I_p), background-current duration (t_b) and amplitude (I_b), and wire-feed speed (V_f). They must be co-ordinated properly to obtain a satisfactory arc. Even when this is accomplished, the arc can be disturbed by external perturbations that impair arc stability and weldment quality. For many years, welding experts have worked on control methods for pulsed MIG welding (see Chapters 4 and 5) to simplify the setting of welding parameters and ensure a stable arc even under disturbances. To achieve this goal, evaluation of existing pulsed MIG welding and testing of newly developed pulsed MIG processes are needed. Because the pulsed MIG process is complicated, theoretical analyses are difficult and the application of an arc simulator for study is useful.

The pulsed MIG process can be classified into the following categories (see Sections 4.1, 4.2, 5.2, and 5.3).

(i) Pulsed MIG using *Synergic* control. This control system was invented by TWI in the UK and is now widely applied in industry worldwide.[34] In this system, the power source has two constant-current output characteristics. Pulsed current is obtained by periodically switching these two output characteristics. The switching frequency is controlled by the wire-feed speed, which is designed on the basis of a mathematical model so that optimum and even droplet transfer can be obtained using a one-knob control.

(ii) Pulsed MIG controlled by instantaneous arc voltage. The principle of this control system can be described with the help of Fig. 3.23. The power source has two constant-current output characteristics. For

control purposes, two arc voltages are set; see A and B in the figure. When the arc is on the background-current characteristic, the wire-feed rate is higher than the melting rate; therefore, the arc is shortened and the operating point moves down along the output characteristic of the power source. As the arc operating point reaches point A, the control circuit triggers the power device and transfers the arc to a pulsed-current characteristic. At this stage, the wire-feed rate becomes less than the wire-melting rate; therefore, the arc operating point moves upward along the pulsed-current output characteristic. As it reaches point B, the control circuit triggers the power device and transfers the arc to the background output characteristic. The action repeats itself continuously and the arc length varies between L_{a1} and L_{a2}. If A and B are properly chosen, a stable arc will be realized. Because transfer of one droplet during each pulse is required, the control circuit should be modified so that t_p is not too short and one droplet could not be transferred during this time period. This control system provides very strong arc length self-regulation. The arc length can be maintained even when the torch or wire feed shakes.

(iii) Pulsed MIG controlled by an arc-length feedback circuit. Many research projects have been conducted, both in China and abroad, on arc-length feedback control. One of the developments was made by the Mitsubishi Company of Japan.[35] In this system, an open loop and a feedback loop are used simultaneously to control pulsed MIG welding. A wire-feed rate signal is used according to a mathematical model for control of the pulse frequency, which makes the melting rate equal to the wire-feed rate. In addition, an average arc-voltage signal is used for a feedback loop to adjust the pulse parameters and compensate for random disturbances. The disadvantage of this system is that the time required to take the average arc-voltage signal degrades the dynamic characteristics of the control. Furthermore, the average arc voltage does not represent the arc length when there is arc blow. In another feedback control method that was proposed,[36] the arc voltage at some instant during each pulse period was taken as the arc length (for instance, the arc voltage 1 ms after the leading edge of the pulse current) and used as the feedback-circuit signal. Normally the feedback loop controls the duration of the background current and thus provides the control of the pulsed MIG process.

3.4.1 Pulsed MIG welding arc simulator

One of the difference between MIG and pulsed MIG welding is associated with the melting rate. In DC MIG welding, melting is basically continuous,

but in pulsed MIG welding, melting is intermittent. The wire does not melt during the background-current period. Melting during welding is due to two factors; one is the pulse current, just like normal MIG welding, and the other is the previous background current, which depends on I_b and t_b. If I_b remains constant, then melting is proportional to t_b. For simplicity, assume that the contribution is offered evenly during the pulse period; then the melting rate during pulsing can be expressed as follows:

$$V_{mp} = k_r L_s + k_c I_p - k_u U_a + C_2 + k_b t_b (n-1)/t_p(n)$$

where k_b is the factor of influence, $t_b(n-1)$ is the previous background current duration and $t_p(n)$ is the pulse current duration.

In the case of steel wire and an arc that is not too short, the effect of k_u can be neglected; then

$$V_{mp} = k_r L_s + k_c I_p + C_2 + k_b t_b (n-1)/t_p(n) \quad (n = 0, 1, 2, \ldots)$$

For most pulsed MIG machines, the range of t_p is not wide, so that k_b/t_p can be approximately taken as a constant k_g. The equation for V_{mp} can be simplified as:

$$V_{mp} = k_r L_s + k_i I_p + C_2 + k_g t_b (n-1) \qquad [3.18]$$

Other dynamic functions for pulsed MIG are the same as those for the DC MIG process, which can be rewritten as follows:

$$H = L_s + L_a, \quad V_f - V_m = dL_s/dt, \quad U = k_i L_s + k_g I + k_a L_a + C_1$$

Using the same method as described in previous paragraphs, the Laplace transforms of the four equations above are taken and the block diagram drawn according to their interactions. The configuration of the pulsed MIG arc simulator can be obtained as shown in Fig. 3.24. Similarly, the coefficients of Eq. [3.18] can be obtained from a large number of experiments and linear-regression analysis of the data by the multi-parametric method of least squares. Then Eq. [3.18] can be written as[29]

$$V_{mp} = 4.49 L_s + 0.705 I_P - 148.1 + 8.37 t_b/t_p$$

The parameters are substituted into the block diagram and the electrical circuit designed according to the diagram. The pulsed MIG arc simulator can thus be obtained.

3.4.2 Experimental verification

The validity of the arc simulator needs to be experimentally verified. For this purpose, an experimental method was designed by the author. The power source used for the experiments is shown in Fig. 3.25. It consists of

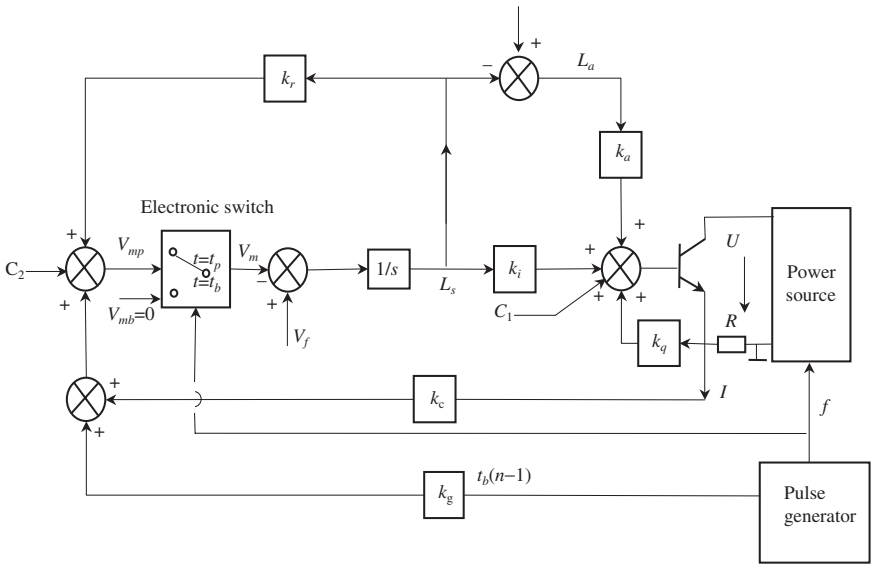

3.24 Block diagram of the pulsed MIG arc simulator

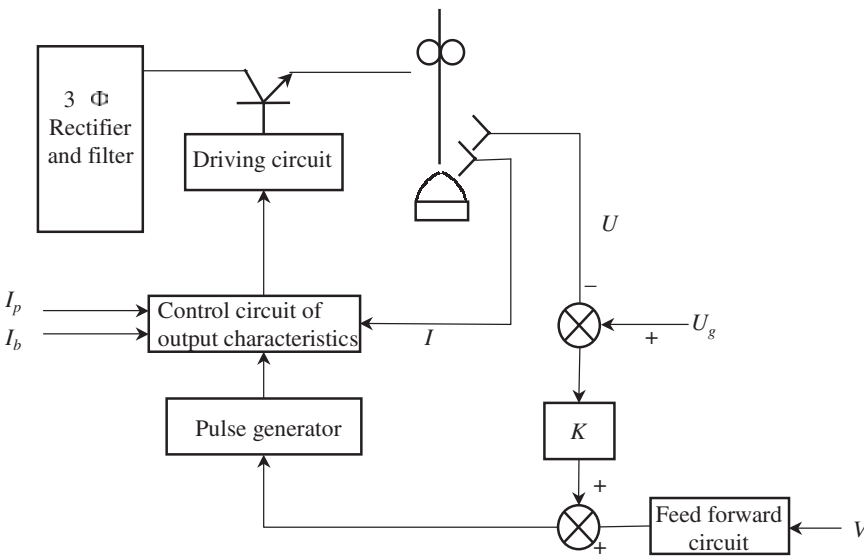

3.25 Pulsed MIG machine with an arc-length feedback control

one feed-forward path controlled by the wire-feed rate signal and one feedback loop controlled by the arc voltage during the current pulse.

In this system, signal U is sampled and held during the current-pulse. According to Eq. [3.13], when I_p is constant and the voltage drop on the

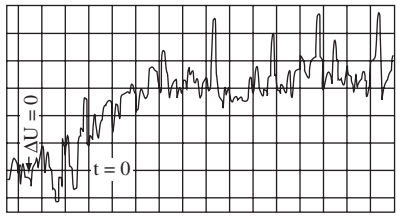

Abscissa *t*: 0.1 s/Div., Ordinate Δ*U*: 0.46 V/Div.

a) Real welding arc

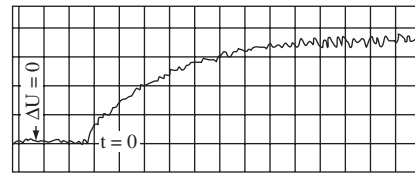

Abscissa t: 0.1 s/Div., Ordinate DU: 0.46 V/Div

b) Arc simulator

3.26 Voltage response for pulsed MIG welding

wire extension is small, then U can be regarded as the arc-length signal. For verification of the validity of the arc simulator, the dynamic response of both the actual welding arc and the arc simulator are recorded while a step change is given to input U_g. The welding conditions were: H08Mn2Si wire material, 1.0 mm wire diameter, Ar + 10% CO_2 shielding gas, 100 A average welding current, 22 V average welding voltage, and 20 mm torch-to-plate distance.

The arc simulator was designed on the basis of parameters obtained by experiments. The average welding current was 100 A and the average welding voltage was 22 V. The experimental results are shown in Fig. 3.26. From this figure, it can be seen that the arc-voltage response for both the actual arc and the arc simulator were almost the same, although, for the real arc, the process gain was smaller and the settling time was shorter. The experiments have been repeated using different welding currents and voltages. The same conclusion was drawn from all of these experiments. All of these results verified that the arc simulator adequately represents the real arc and can be used for further study of pulsed MIG welding.

3.4.3 The dynamic behaviour of pulsed MIG welding

The arc simulator can be used for measuring the dynamic behaviour of the arc with different pulsed MIG welding machines. It can also be used for developing new types of pulsed MIG machines. Various existing pulsed MIG welding machines have been tested by the author. The block diagram for testing was the same as that shown in Fig. 3.20. The results are shown in Fig. 3.27.

From the experimental results, it can be seen that the machine controlled by instantaneous arc voltage has the fastest response to changes of arc-

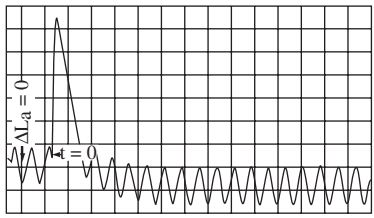

Abscissa t: 10 ms/Div.,
Ordinate ΔL_a: 0.2 mm/Div.

a) Pulsed *MIG* controlled by arc-voltage threshold

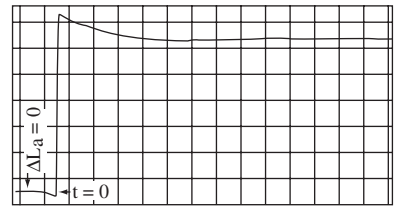

Abscissa t: 10 ms/Div.,
Ordinate ΔL_a: 0.2 mm/Div.

b) *Synergic* pulsed *MIG*

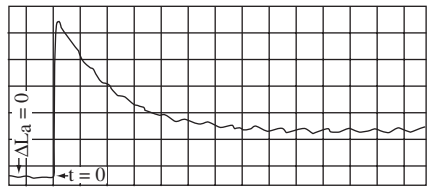

Abscissa t: 0.1 ms/Div.,
Ordinate ΔL_a: 0.2 mm/Div.

c) Pulsed *MIG* controlled by arc-length feedback

3.27 Dynamic response of arc length for various pulsed MIG welding MIG welding processes

length. The arc-length error could be corrected in one pulse period when a disturbance occurred. Moreover, it had the least static error. The settling time for the *Synergic* machine was the longest; there was almost no self-regulation of arc length. Arc-length correction using a closed-loop controlled machine had dynamic properties between them.

3.5 Summary

Welding current and voltage can be sampled and recorded at very high speed using the Hannover Arc Analyser. Certain rules of arc behaviour can be obtained by statistically analysing the data and relating it to the technological behaviour of the welding arc. This can be recommended as a good approach for the study of the dynamic behaviour of the arc.

An arc simulator can be used for detecting the dynamic characteristics of a power source, as well as their effects on the welding process. The most important feature of the arc simulator is that it can avoid random disturbances and represent the dynamic behavior of a real arc. The procedures for designing an arc simulator are as follows:

(i) Set up the dynamic functions of the welding process.
(ii) Determine the coefficients of the dynamic functions by experiments.
(iii) Set up the block diagram of the arc simulator.
(iv) Design the electrical circuit according to the block diagram.

The arc simulator provides a good means for studying and developing power sources and their controls.

Part II

Welding arc control

4
Control method QH-ARC 101

4.1 Status of research on welding arc control

An important area in the development of arc welding is the control of the arc. The most basic control is to maintain the arc, or, in other words, keep the output characteristic of the power source steeply drooping. To accomplish this is rather simple; leakage flux in the transformer or a separate inductor is used with an AC power source, or split magnetic-pole or negative-feedback magnetic pole excitation is used with a generator-type DC power source. Each of these measures can produce a drooping characteristic, but they do not control dynamic characteristics, which have important effects on weldment quality. New arc controls were developed when automatic welding processes were invented, mainly the automatic regulation of arc length. For manual arc welding, the arc is controlled by the welder so there is no necessity to control the arc length. For automatic welding, however, in order to maintain a continuous arc there must be automatic arc-length regulation. Two approaches have been developed for this purpose: the constant wire feed-rate system and the arc voltage feedback-controlled wire feed-rate system, which were described in Chapter1. However, the dynamic characteristics of both of these systems cannot be controlled up to the present, and their theoretical analyses have not been presented.

Since the 1960s, welding arc controls have been developed simultaneously with the rapidly developing electronics industry. For manual arc welding, a high open-circuit voltage and a steeply drooping power-source characteristic are connected in parallel with the main power source in order to improve the stability of the arc and decrease the capacity of the main power source. A combination of a constant-current characteristic at high arc voltage and a drooping characteristic at low voltage is used to improve arc ignition.[38]

For TIG welding, because the electrode is not melted, the arc-length control is much easier and more effective.[39–41] A magnetic field is applied

to control the deflection of the arc.[42] Much research has been done on the correlation between welding current-pulse parameters, and bead formation and penetration.[43,44] A lot of work also has been done on arc-length and weld-penetration control for plasma-arc welding; photo-electronic sensors have been developed for keyhole and penetration control.[45–49]

For CO_2 welding, the traditional way is to control spatter formation, arc energy and penetration is by controlling the dynamic characteristics of the power source.[37,50] The drooping output characteristic also affects the dynamic properties of the arc and the amount of spatter produced.[51] In recent years, step-output characteristics have been used to prevent arc breakdown, decrease spatter formation, and improve bead formation.[52–54,111] Current pulsing,[55–59] mechanical wire-feed pulsing[60–63] and a combination of both[64] also have been developed in recent years for controlling the short-circuiting process, decreasing spatter, and improving bead formation. Magnetic fields also are applied for controlling the CO_2 arc to reduce the bead penetration.[65] As the parameters of CO_2 welding are simpler than those of other processes, one-knob control can be achieved using an appropriate combination of wire-feed rate and output voltage of the power source.[55]

Pulsed MIG is one of the most widely used processes among the MIG welding methods. It can achieve spray transfer over a very wide range of welding currents and provide excellent weld quality. Its arc characteristics,[66–69] arc shape and droplet transfer[70–81] have been studied thoroughly. Square-wave TIG welding[82] and quasi spray-transfer MIG welding[83–86] were successfully developed for Al welding. In the 1970s, a high-power transistorised power source was developed for investigating and realising welding-arc control. Since the invention of the power source, a great deal of attention has been devoted by industrial scientists and engineers, and research and development work has been carried out by many institutions.[87–104]

The traditional method of pulsed MIG control is based on control of the arc length and metal transfer by setting the current and pulse parameters.[105–109] There are many parameters; for example, the pulsing parameters (I_b, I_p, T_b, T_pf), which should be set manually in order to match the wire-feed rate and obtain a satisfactory arc length and metal transfer. The problem with this method is that the parameters must be reset when any welding circumstance is changed. Moreover, the robustness of the system to random disturbances is poor. During practical welding, disturbances due to arc-length, wire-extension and wire-feed change are inevitable. In such cases, the arc length, metal-transfer mode and arc stability will change, which will impair weld quality.

In order to improve arc-length self-regulation, researchers outside China have investigated the effect of output characteristic slope on self-regulation

ability.[112–114] Non-linear output characteristics were used to improve the arc stability and its resistance to disturbances.[115,116] In 1981, Ohshima in Japan applied two slowly rising output characteristics ($0 < K < k_a$) and alternated between them to achieve arc stability.[117] In this control method, as the arc length was regulated by the arc current, the metal-transfer mode was disrupted due to the change of current; therefore, there was a contradiction between the improvement of arc-length self-regulation ability and maintenance of optimum metal transfer. Obviously, alternating the output characteristics would not significantly improve the resistance of the arc to disturbances, no matter how complicated the output characteristics were. Moreover, there were too many parameters to be controlled, which complicated the regulation.

In order to simplify the regulation of parameters, a control method called *Synergic* was invented by TWI in the UK.[34] The wire-feed rate was taken as the input signal and a mathematical model determined the welding parameters so that the arc length and metal-transfer mode could be obtained using an arbitrary wire-feed rate. Because this was an open-loop control, its resistance to arc-length disturbances was inadequate. If disturbance other than changes in the wire feed-rate happened, the arc length and metal-transfer mode were disrupted.

To improve the self-regulation ability of the MIG arc, a closed-loop control method for pulsed MIG has been studied. For example, one closed-loop and one open-loop control circuit was used simultaneously for pulsed MIG by the Mitsubishi Company of Japan. This method was patented in Europe.[35] In this system, the wire-feed rate is taken as the input signal to control the pulse frequency, so the melting rate is basically equal to the wire feed rate. The average arc voltage is then taken as a feedback signal for controlling the pulse parameters, which then can adapt to random disturbances. The drawbacks of the system are as follows:

(i) The average arc voltage is taken as the closed-loop input, but the average arc voltage does not represent the instantaneous arc length.
(ii) The average arc-voltage signal is obtained by an integral element that has a long time constant; thus, the arc-length regulation ability and dynamic response are inadequate.
(iii) As switching-type transistors and an inductor filter are used for the main power circuit, pulsation of the current is large and the dynamic characteristics are inferior.

Due to the nature of the welding process, the welding current always fluctuates and random disturbances occur repeatedly. Therefore, detecting the instantaneous arc-length signal is difficult. On the other hand, because the droplet-transfer arc length varies continuously during welding, it is impossible to keep the arc length constant. Attempts to keep the arc length constant

would result in resonance of the system. That is the reason the average arc length is used as the input control signal. As the welding-pulse frequency varies over a wide range, in order to ensure system stability at low frequency, the time constant of the integral element or filter for the arc-voltage signal must be sufficiently large. This is the primary reason why the dynamic characteristics of the closed-loop arc-length control system are deficient.

In order to improve the dynamic characteristics of the closed loop arc-length control system, a discrete closed-loop control system was developed by a scientist at Kyoto University, and others, in 1982.[118] It takes the arc voltage at a certain instance for each current pulse as a measure of the arc length and keeps the arc-length value unchanged using a closed-loop control. In this system, however, the background current is the controlled variable. Because too small a background current can break down the arc and too large a background current would result in globular metal transfer, this approach has a limited area of application. Moreover, the arc-voltage sampling frequency is fixed, but the pulsed current frequency can be regulated when welding parameters are changed; the sampling frequency of the arc voltage should be changed accordingly. Summarising above descriptions, the new control methods have the following features:

(i) On the basis of electronic technology, a high precision, high dynamic-performance power source has been developed that can furnish accurate static characteristics.
(ii) A closed-loop control system has been developed on the basis of control theory.
(iii) Pulsing technique has been applied to improve arc behaviour and bead formation.
(iv) Using an electronic circuit, a one-knob control has been developed to simplify setting welding parameters.

Since 1978, the author and his colleagues have proposed several original arc-control methods. They are quite different from all existing methods. Although they were developed for certain welding processes, they have universal applicability to newly-developed welding power supplies and their control systems.

4.2 Principle of control method QH-ARC 101[89,110]

An ideal arc-welding control system should have the following properties:

(i) Provide a stable and continuous arc.
(ii) Produce even and reliable droplet transfer without spatter.
(iii) Provide good arc-length self-regulation, good resistance to random disturbances, and good dynamic response.
(iv) Should be easy to operate with any set of welding parameters.

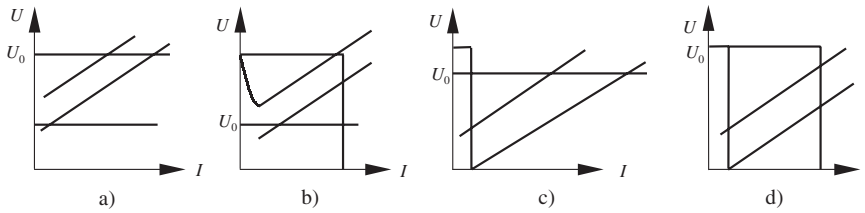

4.1 Control methods for pulsed MIG welding

The development of electronics technology is stimulating improved technology for welding power sources. The traditional AC power-source transformers and DC generators have been replaced rapidly by rectifiers, SCRs, transistorised power supplies, and recently, IGBT inverter-type power sources. Their static accuracy and dynamic characteristics have been improved significantly but the control method basically has not changed. The output characteristics of all types of machines can be classified into three categories, namely flat, vertical and drooping. For pulsed MIG welding, the characteristics are a combination of the three types given above: see Fig. 4.1. Although these output characteristics are simple, they cannot meet the arc-control requirements of modern machines. These are described below in more detail using the characteristics shown in Fig. 4.1 as examples.

The characteristic shown in Fig. 4.1a is the conventional method for pulsed MIG welding. Constant-voltage output characteristics are used for both the background current and the pulsing current. The method shown in Fig. 4.1b also applies a constant-voltage output characteristic for its background current. For both methods, the arc is easily extinguished during the background current when a random disturbance appears. In order to ensure arc stability, a high background current should be provided. In the method shown in Fig. 4.1c, a constant-current output characteristic is used for the background current. In this case, the arc is not easy to extinguish, but it can easily short circuit when a disturbance occurs. Furthermore, igniting the arc at a low welding current is difficult because the background-current duration is long. In the method shown in Fig. 4.1d, a constant-current output characteristic is applied to both the pulsed and background currents. In this case, the arc length has no self-regulation ability; the arc is difficult to maintain and restore when a disturbance occurs. It also is difficult to initiate the arc at a low welding current. Using the constant-voltage output characteristic shown in Fig. 4.1a for pulsed current, the pulsed current can fluctuate violently during a disturbance such that globular droplet transfer may be initiated. If this occurs, the arc is not stable. The method shown in Fig. 4.1b applies a constant-current output characteristic for the pulsed current. This pulsed current will not change due to a disturbance, spray transfer can be

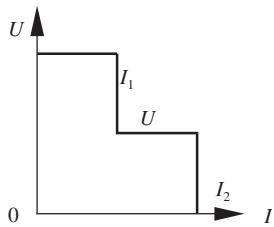

4.2 Double-step output characteristic

maintained, and the arc is elastic. However, the torch tip may be burned if a disturbance makes the arc length too long. It can be concluded, therefore, that all of these four methods cannot satisfy the requirements for a stable pulsed MIG arc. In order to solve this problem, the QH-ARC 101 method has been proposed by the author, the principle of which is described in detail in the following sections.

4.2.1 Double-step output characteristics

The double-step output characteristic is illustrated in Fig. 4.2, in which I_1, U, and I_2 can be regulated over a wide range: specifically, $I_1 = 0{\sim}790$ A $U = 0{\sim}39$ V and $I_2 = 0{\sim}890$ A. As analysed in the paragraph above for the background current in pulsed MIG welding, a constant-voltage output characteristic can result in extinguishing the arc and a constant-current output characteristic can result in a short circuit when the arc is disturbed. To overcome this drawback, a double-step output characteristic has been proposed by the author. The constant-current part I_1 maintains the arc without breakdown, the constant-voltage part U provides self-regulation of the arc to avoid short circuits, and the constant-current part I_2 provides sufficient current for arc ignition and limiting short-circuiting current to avoid spatter. Obviously, the double-step output characteristic can increase the resistance of the arc to random disturbances and maintain the arc at low currents. Thus, the range of welding parameters can be expanded.

This kind of output characteristic can be used not only for the background current of pulsed MIG welding, but also for other arc welding processes according to the special features of each welding process. The parameters of different parts of the output characteristic can be regulated independently and all of the segments of the characteristic can be used for the arc operating point. For example, in manual arc welding, I_1 can be used for controlling the arc and I_2 can be used for limiting short circuit current: see Fig. 4.3a. For MIG welding, the constant voltage part, U, is used for controlling the arc, I_1 for preventing arc breakdown, and I_2 for limiting short-circuit current: see Fig. 4.3b.

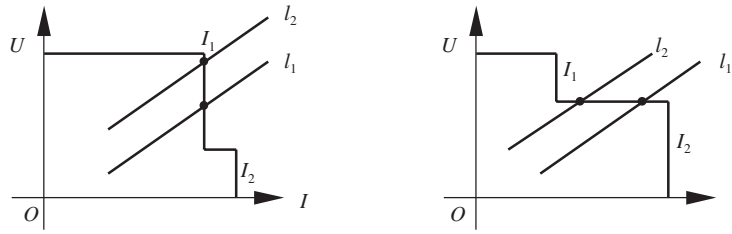

a) Manual arc welding b) *MIG* welding

4.3 Application of the double-step output characteristic

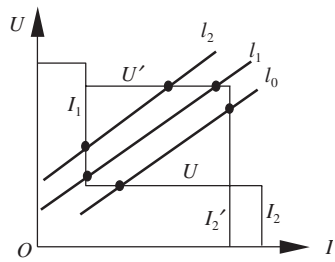

4.4 Rectangle-output characteristic

4.2.2 Combination of two double-step characteristics

For pulsed MIG welding, two double-step output characteristics can be applied. In this application, the arc operating point moves from one to another by alternating the two characteristics quickly so that the background arc and the pulsed arc can operate on different parts of the characteristics and achieve excellent results. When the two characteristics alternate quickly, a rectangle-output characteristic can be obtained, as shown in Fig. 4.4. Using this kind of output characteristic for pulsed MIG welding, the arc operating point can be confined in the frame of the rectangle that effectively improves the arc stability. During pulsing, the operating point is in the segment I_2', which ensures a stable and elastic arc. Droplets transfer continuously, independent of the arc length. Spray transfer can be obtained even when an arc-length disturbance occurs. The constant-voltage segment, U', limits the maximum arc length and prevents the torch tip from burning. During the background-current period, the operating point is on I_1, which eliminates the risk of arc breakdown. If a disturbance makes the arc length too short, the operating point transfers to the constant-voltage part U, which increases the current and arc length and thus avoids short-circuiting.

It can be concluded that the characteristic confines the arc-operating point within the frame of the rectangle; neither breakdown nor short-

circuiting can occur. Normally, the arc maintains spray transfer; the arc can automatically adjust itself in the frame and maintain itself when a large arc-length disturbance occurs.

4.3 Realisation of double-step characteristic

A completely different method than those used with traditional power sources is needed to produce a double-step characteristic. During welding, the current changes quickly between different parts of the characteristic; it also changes quickly between two double-step characteristics. The key point for realizing the QH-ARC 101 method depends on developing a power source that can meet the requirements given above. The Welding Department of Tsinghua University has conducted a lot of research on power transistors since 1978 and has successfully developed a power source designated the QHT-80, which can fully meet the expected requirements given above. Its features can be described as follows:

(i) Fast dynamic response and high static accuracy. The double-step output characteristic consists of three segments, I_1, U, and I_2. The arc-operating point transfers among these segments automatically, according to the state of the arc. The transfer duration needs to be very short in order to control the arc in a short time. Therefore, the power source needs to have fast dynamic response. In addition, the time to alternate between the two double-step characteristics also must be very short. The dynamic response of the transistorised power source that was developed is excellent; the closed-loop frequency response for constant-current control is 10 kHz and that for constant-voltage control is 20 kHz. The transient time for alternating between the two characteristics is less then 0.05 ms.

For accurate control of welding parameters, the static accuracy should be good, the constant-voltage segment should be as flat as possible, and the constant current segment should be as vertical as possible. The welding parameters should not be affected by fluctuation of the mains power, the arc length, and other random disturbances. For the constant-current part, the variation of current is less than 0.2% while the voltage across the load varies from 40 V to a short-circuit. The current change is less than 0.2% when the voltage fluctuation of the mains power is 10%. In the constant-voltage regime, the change of voltage is less than 0.2 V when the current variation is 100 A. The output voltage remains unchanged when the main power voltage fluctuates.

(ii) Reliable protection measures. The overload capacity for transistors is very low, the range of current and voltage fluctuation is normally wide

and short-circuiting occurs often. The power consumption in transistors is very large. Moreover, because the welding loop has inductive character, voltage spikes often occur across the transistors during the transient process. Therefore, there should be reliable overvoltage, overcurrent and overpower protection. On the other hand, the short-circuit time for arc ignition and metal transfer is usually short; therefore, if the method for protecting the transistors from overpower depends on the instantaneous power, the capacity of the transistors would not be used sufficiently and the output of the machine would be very small. For these reasons, special protection measures have been developed to ensure the safety and reliability of the transistors on the one hand and possibly greater power output of the power source on the other hand.

4.3.1 Possible methods of realisation

As described above, the double-step output characteristic of the power source consists of three segments: a constant-current segment, I_1; a constant-voltage segment, U; and a constant-current segment, I_2, as shown in Fig. 4.2. They might be realised by connecting three separate negative-feedback control loops. The key problem in realising this circuit is determining how to connect three loops together so that the arc-operating point can transfer among them rapidly without introducing resonance during the transient process or a dead zone. As analysed above, in the application of a rectangle-output characteristic, the arc-operating point is usually at the corner of the rectangle frame; it often jumps from one segment to another and vice versa. Therefore, the characteristic at the corner of the frame determines the possibility of successfully accomplishing the control method. Although there may be different ways to achieve the transfer between segments, an improper way will introduce serious problems. Two possible methods for designing the transfer circuit are described below. Experiments proved that the first method was not successful whereas the second method was successful. For a deeper understanding, both methods are described in detail.

4.3.2 Transfer between segments using a logic-strobe circuit

In this method, the load current and voltage are taken as signals and compared with a reference circuit. Taking advantage of a logic strobe, one of three closed-loop control circuits is connected and activated. Assume that the reference values of the three comparing elements, a, b, and c, are I_1' U' and I_2' (the comparing elements are composed of three operational amplifiers). Assume also that the output of the comparing element a will be

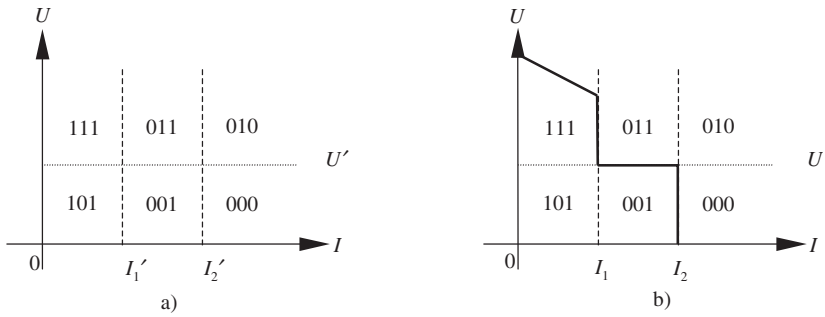

4.5 Logic-strobe circuit and ideal output characteristic

1 (high electric potential), when the load current is less than the reference I_1' and the output of a will be 0 (low electric potential) when the current is larger than the reference I_1'. The comparing element b is used for detecting the voltage; when the load voltage is higher than U', the b output is 1 and when the load voltage is lower than U', the b output 0. Similarly, the comparing element c detects I_2'. If a U-versus-I plane or graph is used to express the logic, then it can be seen that the three logic-strobe circuits divide it into 6 regions, as shown in Fig. 4.5a. The closed-loop circuit is then selected according to the state of the outputs a, b, and c. If the state is 011, 101, or 111, the closed-loop control circuit for I_1 is connected. If the state is 001 or 010, the closed-loop control circuit for U is connected. If the state is 000, the closed-loop control circuit for I_2 is connected. When the inputs of the comparing elements, I_1', U', and I_2', are exactly the same as the reference inputs of the closed loop circuit, I_1, U, and I_2, and there is no steady-state error of the closed-loop circuits, the ideal double-step output characteristic can be obtained, as shown in Fig. 4.5b. Due to inevitable steady-state error, the actual output characteristic is different from the inputs of the logic-strobe circuits and the logic division of the U-I plane. It is impossible for the logic circuit to follow the actual welding current and voltage, particularly at a corner of the characteristic. A resonance zone, dead zone or an overlapping zone may be generated.

Assume that the reference inputs of both the power-source control loop and the logic circuit are I_1', U', and I_2'. Due to steady-state error of the control loops, the actual output characteristics of the power source are I_1, U, and I_2. For a more explicit explanation, the steady-state error is exaggerated; the output characteristic, I_1, U, I_2, are shown in Fig. 4.6 by real lines. Assume that the closed-loop gain is unit value; then, the ideal (with no steady error) output characteristic of the power source are I_1', U', and I_2', as indicated in Fig. 4.6 by the dotted line. If the load R_L is between R_1 and R_2, then the resonance between the characteristic I_1 and U will develop. Supposing that the

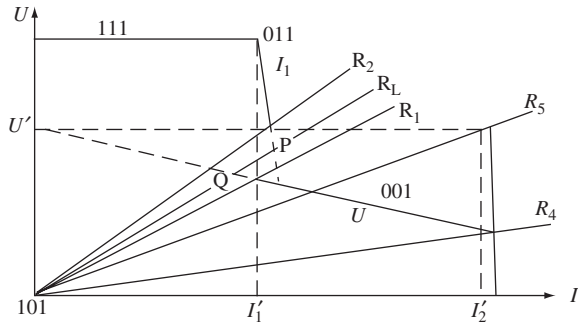

4.6 Resonance region and overlapping region

characteristic of the load R_L intersects with I_1 at P, the output state of the logic circuit is 001 and consequently the constant-voltage loop will be connected and the load characteristic R_L will intersect with the constant-voltage characteristics at Q. Once the arc-operating point reaches Q, the logic-circuit output state will change to 101 and consequently the constant-current loop, I_1, will be connected. Thus, resonance develops between P and Q. The resonance range of the load is $R_1 < R_L < R_2$, in which the arc-operating point has no stable state. Obviously, due to steady-state error, the larger the value of I_1, the larger the resonance range becomes. Consistent with the design of control method QH-ARC 101, the arc-operating point normally remains at the corner of the rectangle characteristic so the arc cannot be controlled when the resonance range is large.

In addition, at the corner of the constant-voltage segment, U and I_2, an overlapping region exists in Fig. 4.6, because the arc-operating point could be on a constant-current segment, I_2, or on a constant-voltage segment. If R_L is a load that rises from a low value up to R_4, the arc-operating point will be on segment I_2. It will transfer to a constant-voltage segment only when $R_L > R_5$ and the logic-strobe circuit output is 010. On the contrary, if R_L is a load that drops from a high value down to R_5, the arc-operating point would be on a constant-voltage segment. It will transfer to a constant current segment only when $R_L < R_4$. Therefore, there are two possible output characteristics for the power source when the load is between R_4 and R_5. That also interferes with arc control. It can be seen from Fig. 4.7, that if the reference input of comparing element a is decreased and becomes less than the reference input of the constant-current closed control loop, then I_1' will shift to the left of I_1 and the resonance between I_1 and U can be avoided. However, a dead region on I_1 will occur between R_1 and R_2 because the arc-operating point could appear only on a constant-voltage segment. Furthermore, an overlapping region will occur between R_2 and R_3.

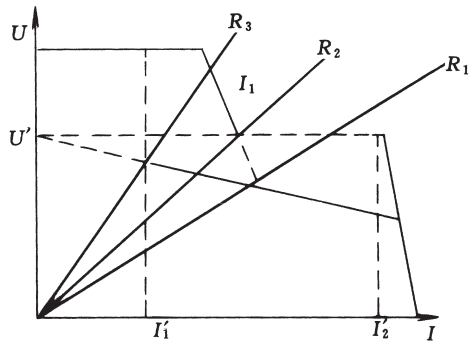

4.7 Dead region and overlapping region

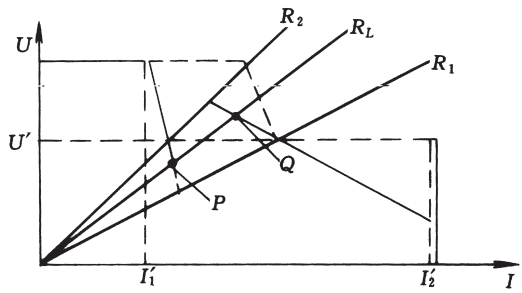

4.8 Effect of regulation of I_1

It also can be seen from Fig. 4.6 that, if the reference input, U', of the comparing element b is decreased so that it is less than the input of the control circuit, U, the resonance range and the overlapping range can be decreased. The resonance can be eliminated when U' equals the voltage at the corner of the output characteristics. For welding, however, it is normally necessary to regulate the value of I_1 over a large range. If I_1 is increased, the resonance range may again develop due to the drooping slope of the constant-voltage segment as shown in Fig. 4.6. If I_1 is decreased, a new resonance range can occur as shown in Fig. 4.8. If the load is R_L, it intersects I_1 at point P and, at this moment, the logic-circuit output would be 001. Therefore a constant-voltage loop will be connected and activated. Once the constant-voltage segment develops, the logic-circuit output would be 011. At this moment, a constant-current loop will be connected and activated and segment I_1 will appear again. The resonance range is $R_1 < R_L < R_2$.

From this analysis, it can be seen that in order to avoid resonance regions, dead regions, and overlapping regions at the corner of the rectangle-output

characteristic, the reference inputs of the logic circuit should be equal and exactly the same as the output current and voltage of the power source at the corner, i.e. I_1' and U' must be equal to the actual current and voltage of the intersecting point. However, due to the steady-state error of the control loop, the value of the output segment is different from the reference inputs of the control loops. Moreover, because the output segments should be regulated in practice to meet the needs of the welding process, the voltage at the intersecting point can be different even for a constant-voltage output and the current at the intersecting point can be different even for a constant-current output. Therefore, it can be concluded that it is impossible for the reference inputs of the logic circuit to follow the current and voltage of the intersecting points. The resonance, dead, and overlapping regions cannot be avoided by any means. Although a lot of study and improvements have been made by the author, no success has been achieved.

4.3.3 Transfer between segments using an automatic-feedback strobe circuit

To overcome the problems described above, a new transfer method, namely an automatic-feedback strobe circuit, was proposed by the author and successful results were obtained. The current and voltage at which transfer takes place always follow the actual current and voltage at the corner of the rectangle characteristic exactly. Therefore, resonance, dead, and overlapping regions no longer develop. The method is illustrated diagrammatically in Fig. 4.9. Three feedback-control loops were designed separately for I_1, U, and I_2 and they are connected by three diodes. The feedback signals automatically trigger one of the control loops and connect it into operation. The principle of its operation is described as follows:

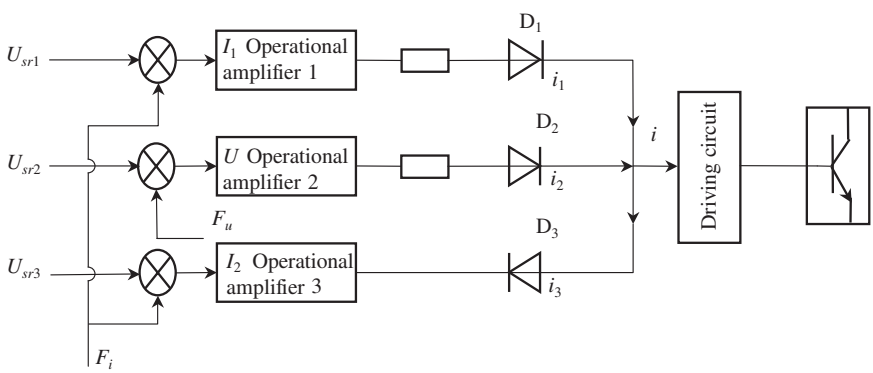

4.9 Automatic-transfer circuit

When the arc-operating point is on the constant-current segment I_1, the operational amplifier 2 is in negative saturation because the feedback voltage is greater than its reference input. Therefore diode D_2 is blocked and the control loop does not function. For operational-amplifier 3, the output is in positive saturation because $I_1 < I_2$ and the feedback signal is much smaller than its reference input. Therefore, diode D_3 is also blocked and $i_3 = 0$. Thus, the operational amplifier 1 is automatically connected for controlling the welding current I_1.

When the load resistance decreases and the voltage drops to the corner of the rectangle characteristic, the output of operational amplifier 2 will increase until the diode D_2 is biased open. At first, i_2 is small and the load current will be slightly greater than I_1 as $i > i_1$. Thus, the feedback signal of operational amplifier 1 increases and its output decreases as its reference input remains unchanged. It attempts to draw back the current i_1 to maintain a constant-current output, but at this moment, the voltage-feedback loop starts to play a role. The current i_2 increases while i_1 decreases; therefore, it maintains a constant-voltage output. The feedback-current signal results in a decrease of i_1 until it ceases to control the loop. In this way, the circuit automatically transfers to a constant-voltage segment and the control loop for I_1 and I_2 are closed. Actually, once D_2 is biased open, the negative current-feedback loop makes $i_1 = 0$ and the control current transfers immediately to i_2. Therefore, the transfer is sudden and the transfer location is a sharp corner.

This transfer action is reversible. Assuming that the arc-operating point is on a constant voltage segment, the current will decrease when the load increases. If the current is greater than the current at the corner, operational amplifier 1 is in negative saturation. Then, when the current reaches the value of the corner, the amplifier is still operating. Once the load increases slightly, the diode D_1 is biased open and the output is i_1 so that $i_1 > i_2$. The voltage across the load becomes slightly greater than the voltage at the corner. Then the negative voltage feedback makes i_2 decrease. Due to the operation of the constant-current segment at this time, i_1 increases to maintain the current output constant and finally $i_2 = 0$ so that the constant-current feedback loop is connected for I_1.

In this method, the current and voltage at the transferring point are always identical with the current and voltage at the corner of the characteristic. This is true even when the currents and voltages of the segments are regulated. For example, for the same constant-voltage segment, due to the steady-state error, the voltage and current at the corner will change when the I_1 segment is regulated. In this case, the current and voltage of the transferring point will change and follow the change of parameters at the corner. Suppose that the input current of the driving circuit at the corner is I_b. Following the decreasing load on the constant-current segment, i_1 will

decrease to maintain the current constant. When it reaches the corner, $i_1 = I_b$ and the load resistance is still decreasing. Then, the operating point transfers to constant voltage and the current i_1 is transferred to i_2. For the point on the constant-voltage segment, i_2 will decrease when the load is increased. Once it reaches the corner, $i_2 = I_b$ and the load is still increasing, then the operating point transfers to constant current I_1. Obviously, the input current to the driving circuit at the moment the operating point transfers is I_b. It is the minimum value of i_1 and i_2. Transfer occurs when I_b is less than this minimum current. The load current and voltage corresponding to I_b is exactly the current and voltage at the corner. If the segment I_1 is regulated to a larger value, then i_1 is increased. I_b for the transferring segments is also increased. As I_b is also the value for transfer, i_2, an increase of I_1 results in an increase of the transfer current of i_2. As the input resistance of the driving circuit is unchanged, its output voltage at the moment of transfer is also higher. As the output of amplifier 2 can be expressed as $U_{out} = K(U_r - FU_L)$, in which the reference voltage, U_r, and feedback coefficient, F, remain unchanged, the load voltage, U_L, at the time of transfer is lower. Consequently, when I_1 is increased, the load current is larger and voltage is lower at the transfer point, it always follows the current and voltage at the corner of the square characteristic. There is no resonance range, dead range, or overlapping range.

The transfer between the constant voltage segment, U, and the constant current segment, I_2, is somewhat different from what was described above, but it also applies the principle of transfer by the feedback strobe. Assume that the arc operating point is on a constant-voltage segment, the operational amplifier 1 is in negative saturation, and amplifier 3 is in positive saturation due to the negative feedback signals. Therefore, the diodes D_1 and D_3 are closed. When the current is increased, the feedback current of amplifier 3 increases but it still remains in saturation as long as the current is less than the value at the corner. If the current continues to increase and reaches the current value at the corner, the amplifier divorces from saturation, the output potential decreases, and a further decrease of the load resistance opens diode D_3. The output of amplifier 3 clamps the input of the driving circuit. At this time, amplifier 2 is in positive saturation due to the load voltage but the circuit is controlled by amplifier 3 because of its clamping function and the output is at segment I_2.

As the transfer between the constant-voltage and I_2 segments is realised by this clamping method, the output of amplifier 3 decreases when the load resistance decreases so that the current in diode D_3 is increased from 0. Due to the non-linear characteristics of the diode, the voltage drop across the diode varies during transfer and thus results in a small round corner. The round corner can be made very small (as low as 2 A, 3 V) by proper selection of the diode and negative feedback. In the QH-ARC 101 control

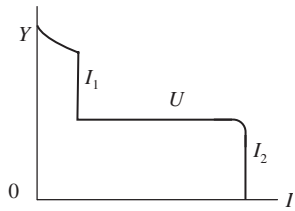

4.10 Measured double-step output characteristic

method, the arc-operating point is basically on the segment I_2; the constant-voltage segment is used only for preventing too long an arc and burning of the torch tip. Therefore, the small corner at the transfer does not affect the quality of arc control. In the new control method, the requirements for transfer between segment I_1 and segment U are strict Fortunately, from the analysis described above, it can be seen that diodes D_1 and D_2 are opened abruptly from their closed state during the transfer. They do not work in the nonlinear range and therefore, there is no round corner at the intersecting point of I_1 and U.

From the discussion given above, the advantage of transfer between segments using an automatic-feedback strobe circuit is that the operational amplifiers are used not only as elements in the closed-loop control circuit but also as detecting devices. For example, when the arc-operating point is on segment I_1, amplifier 1 is used as an amplifying element of the control loop and amplifiers 2 and 3 service as detecting devices. When the arc-operating point is on a constant voltage segment, amplifier 2 becomes the amplifying element and the amplifiers 1 and 3 become detecting devices. The other advantage of this control circuit is that it uses the feedback circuit and automatically connects one of the loops at a specific operating point; there is no forced action to transfer the segments. Therefore, there are neither resonance, dead, nor overlapping ranges; the continuity and performance of transfer are extremely good. Figure 4.10 shows the output characteristic actually measured in the laboratory. Three segments, I_1, U, and I_2 can be regulated separately; the regulation range is I_1 = 0~790 A U = 0~39 V and I_2 = 0~890 A. As all of the segments can be regulated, the normal constant-voltage or constant-current characteristics of conventional power sources can be regarded as special cases of the double-step characteristic.

4.4 Circuit for alternating between two double-step output characteristics

Pulsed MIG welding can be realised by rapidly switching between two output characteristics so that the arc operates on different characteristics

for the background and pulsed currents. Alternating between two double-step output characteristics forms a rectangle output characteristic, which is the basis of the QH-ARC 101 control method. This method has demonstrated great improvement in welding-process control.

Alternating between the characteristics can be accomplished in different ways; two possible means are described in the following section.

4.4.1 Control circuit with two alternating control circuits

The two feedback loops shown in Fig. 4.9 are used for welding control. One feedback loop is used to control the background current and the second is used to control the pulsed current. An electronic switch is connected between the two feedback loops and the driving circuit to produce switching between the sets of feedback loops so that two different output characteristics are obtained. The main drawback of this method is that a high voltage spike develops during the transfer from the background current to the pulsed current. The reason is that, in the background-current stage, the pulsed-current circuit is an open-loop. Because the feedback signals are much smaller than their reference inputs and the amplifier outputs are in positive saturation at the initiation of switching, this produces a high driving-circuit input so that the transistors of the primary circuit are out of control. The control loop starts to operate only after the feedback signals increase. At this moment, the current depends only on the voltage of the power source and the load resistance. The magnitude of the spike can be very high when the short circuit occurs during droplet transfer. This phenomenon not only increases spatter, but also can destroy the power transistors. It was concluded that this was not a suitable switching method.

4.4.2 Circuit with alternating reference inputs

In order to overcome the drawbacks related above, another method was proposed. One set of control loops is used but their reference inputs are alternated. As shown in Fig. 4.11, there are two sets of reference inputs, which are used separately for the background and the pulsed current. The input parameters can be regulated in advance according to the requirements of the welding process. By alternating between these two sets of references, the effect is to switch between two double-step characteristics that control the background and the pulsed current respectively. Alternating using an electronic switch guarantees high-speed and synchronous changes of all of the input references. Because the dynamic properties of both the constant-voltage and the constant-current control circuits are excellent, the switching time from one output characteristic to the other is very short. The time required to transfer from the background current to the pulsed current (the

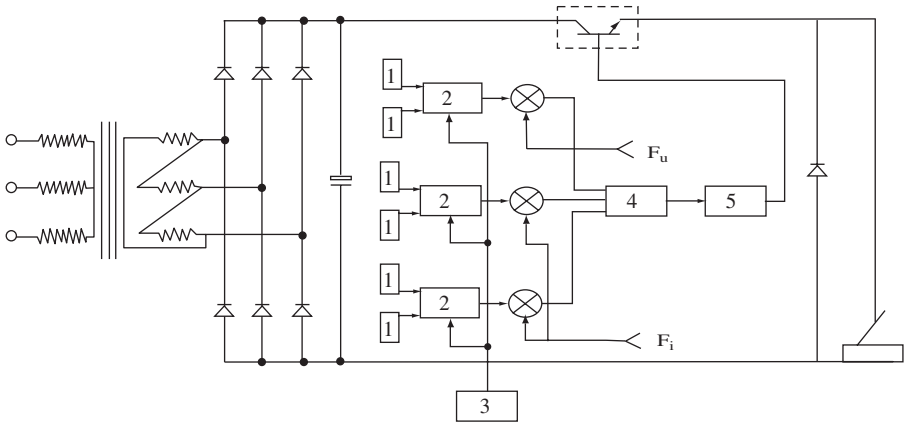

1—Reference input
2—High-speed electronic switch
3—Square wave generator
4—Circuit for switching of output characteristics
5—Driving circuit

4.11 Circuit showing alternation of reference

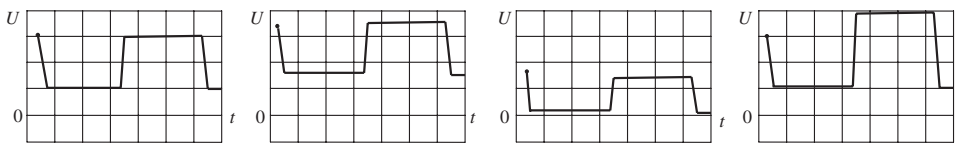

a) Background: constant voltage 15V
pulse: constant voltage 30V
b) Background: constant current 100A
pulse: constant voltage 30V
c) Background: constant voltage 15V
pulse: constant current 200A
d) Background: constant current 100A
pulse: constant current 300A

4.12 Voltage waveforms across load with alternating output characteristics

time for continuous current on inductance load) is less than 0.02 ms. The voltage waveforms across the load alternate, as shown in Fig. 4.12 in which both the pulsed-current and the background-current durations are 6 ms.

A square-wave generator produces the alternating of the reference signals. The generator is composed of two mono stable trigger-action circuits, which trigger each other. A dial regulates the duration of each circuit's signal separately, so that both the background-current width and pulsed-current width can be regulated easily and can be repeated accurately. There are two ranges for the pulsed-current and background-current width regulation, namely 1–99 ms and 10–990 ms. The first range is for intermediate-frequency pulsed-current welding and the second is for low-frequency pulsed-current welding.

4.5 Static accuracy and dynamic characteristics

For accurate control of welding parameters and to avoid interference due to fluctuation of the mains power and arc length, high static accuracy of the power source is required. The constant-voltage characteristics are required to be as horizontal as possible and the constant-current characteristics are required to be as vertical as possible. To control the arc, good power-source dynamic characteristics are required so that the arc-operating point can transfer rapidly from one segment of the output characteristic to another and switching between the two double-step output characteristics will be rapid. Should the dynamic characteristics be inferior, the double-step output characteristics and switching between them will be ineffective. Therefore, good static accuracy and dynamic characteristics are critical elements for realizing the QH-ARC 101 control method.

For conventional transistorised power sources in which there is no transfer between segments and no switching between characteristics, it is easy to obtain high static accuracy and good dynamic characteristics. But for power sources using the QH-ARC 101 control method, these requirements are hard to meet. The problem is due to the contradiction between the requirements for accurate constant-voltage and constant-current outputs, and the requirements for fast action of the arc operating-point transfer and output-characteristic switching.

4.5.1 Contradiction between static accuracy and switching speed

In order to increase static accuracy and reduce the influence of disturbances, increasing the open-loop gain of the feedback system is necessary. However, too large a gain would result in system oscillation and instability. Normally, the application of integral control will raise the gain of the system at low frequency, reduce the static error, and provide high static accuracy while the stability of the system will remain unaffected. But, for the QH-ARC 101 control method in which the output characteristics of the power source alternate between one-double step output characteristic and another, the existence of the integral element would affect the switching speed.

According to the analysis of the switching process described above (see Fig. 4.9), while the arc-operating point is on the constant-current part, I_1, the constant-voltage loop is in an open state; its amplifier 2 is negatively saturated due to negative feedback, and its output is –12 V. If amplifier 2 is a control element of integral compensation, then the capacitor of the integral element is charged to –12 V. The constant-voltage loop will not operate until the voltage of the amplifier rises from –12 V to the opening point for diode D_2. In other words, there is a time delay while the arc-operating point attempts to jump from A to B (see Fig. 4.13). During this delay, the arc-

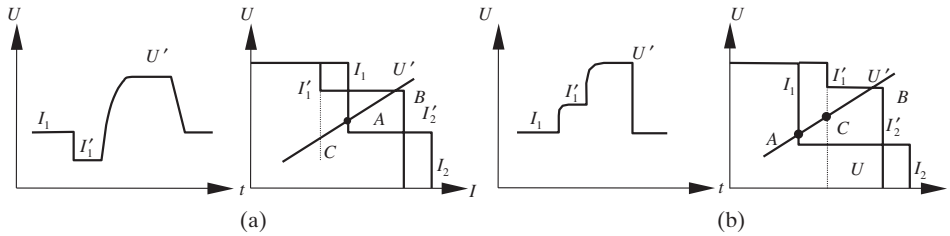

4.13 Problem during high-speed switching

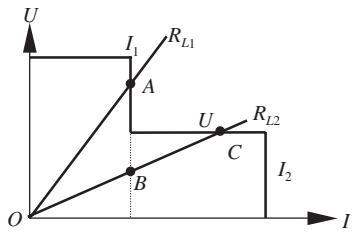

4.14 Problem while transferring between segments

operating point will stay on I_1', which means that the arc-operating point will jump first to C and then to B. If I_1' is not equal to I_1, then there will be either a breach or a step on the load-current waveform. The breach occurs when $I_1' < I_1$ (see Fig. 4.13a) and a step occurs when $I_1' > I_1$ (see Fig. 4.13b). After the time delay, the constant-voltage loop starts to operate and the load current rises to the pulsed-current value according to the time constant of the feedback-control loop.

If amplifier 1 is also an integration element, then there is a breach or a step on the waveform both before and after the pulse. This means there is also a delay while the pulsed current transfers to the background current. It can be concluded that the existence of an integration element is detrimental to both the switching of the output characteristics and the stability of the arc.

In the event that switching of the output characteristic is not necessary, transfer of the arc-operating point between the different segments within the double-step output characteristic is inevitable. If an integration element is present, it produces a time delay during transfering. For example, if the negative-voltage feedback control is an integration element (see Fig. 4.14), then the constant-voltage feedback loop does not act immediately when the load changes from R_{L1} to R_{L2} because there is a capacitor in the circuit. Therefore, the constant-current loop remains active and the arc-operating point jumps first from A to B. After the time delay, it transfers slowly from B to C; short circuiting and spatter may occur during this time interval. Similarly, if there is an integration element in the constant-current loop, short

circuiting and spatter may occur while the operating point transfers from the constant-voltage segment, U, to the constant-current segment, I_1. It can be concluded as well that the arc is not stable while transfering; therefore, high static accuracy has no significance.

4.5.2 Primary circuit

In the normal case for a constant-voltage power source, the transistor emitter is used for the output; for a constant-current power source, a transistor collector is used for the output. But for QHT-80 power sources, both constant-voltage and constant-current outputs are required. Furthermore, both high static accuracy and high dynamic characteristics are required. The most technically logical major circuit is discussed in the following paragraph using the QHT-80 power source as an example. Although using transistors as the power element of welding power sources is out of date, its analysis helps clarify the control method and the development of welding power sources relative to other kinds of power elements.

4.5.2.1 Emitter-output circuits

In emitter-output circuits, the output impedance is small and obtaining high static accuracy when a constant-voltage characteristic is required is easy. If it is used to provide a constant-current characteristic, the gain of the control circuit should be very high to give accurate welding-current values, because the variation of the current is large. The block diagram of the primary circuit is shown in Fig. 4.15a. Because the voltage across the load is much higher than the voltage across the transistor, the voltage-amplification factor of the primary circuit may be regarded as 1. When a negative current feedback loop is used, the control-block diagram is as illustrated in Fig 4.15b.

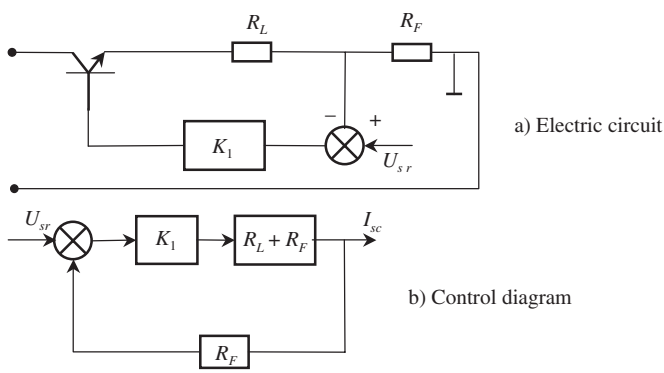

4.15 Emitter-output primary circuit

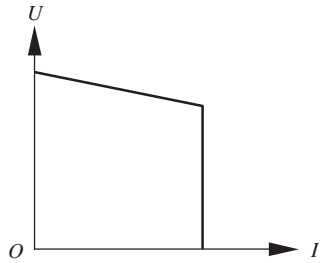

4.16 Characteristics for emitter output

From Fig. 4.15b, the relationship between the output current and the input voltage can be written as:

$$\frac{I_{sc}}{U_{sr}} = \frac{K_1 \dfrac{1}{R_L + R_F}}{1 + \dfrac{K_1 R_F}{R_L + R_F}} = \frac{K_1}{R_L + (1 + K_1) R_F} \approx \frac{K_1}{R_L + K_1 R_F}$$

$$\therefore I_{sc} = \frac{K_1 U_{sr}}{R_L + K_1 R_F} = \frac{K_1 U_{sr}}{\dfrac{U}{I_{sc}} + K_1 R_F}$$

$$\therefore U = K_1 U_{sr} - K_1 R_F I_{sc} \qquad [4.1]$$

$U \le U_0$ U_0 is the open circuit voltage

Equation. [4.1] expresses the function of the output-characteristic curve from which the slope of the output characteristic is $-K_1 R_F$ and the short-circuit current is $I_{sc} = U_{sr}/R_F$. The larger the value of $K_1 R_F$, the more constant the current value remains. But it is not appropriate to have too large a value of R_F because it results in too low an output voltage. When the output current is less than the preset constant-current value, the feedback current is small, the power transistor is working in a saturated state, and R_F is the only internal resistance of the power source. The voltage drop of the output before it reaches the constant-current value is large if R_F is large as shown in Fig. 4.16. For pulsed MIG welding, it requires not only a large constant current, but also a high voltage at the constant-current segment; therefore, too large a value of R_F does not meet the requirements of welding technology. For a given value of R_F, a different slope of the output characteristic can be obtained by regulating the gain, K_1, of the control loop, as shown in Fig. 4.17.

The gain of the control circuit is determined by the requirement of the output-characteristic slope. The relationship between the slope of the characteristic and the circuit gain in the case where R_F is 1 mΩ, 3 mΩ and 5 mΩ is shown diagrammatically in Fig. 4.18. The more rigorous the requirement for constant current, the larger the circuit gain should be. For example, if

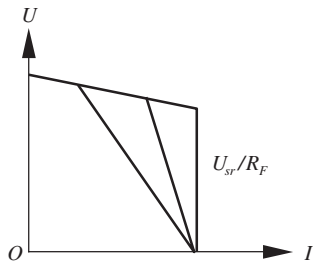

4.17 Role of control-circuit gain

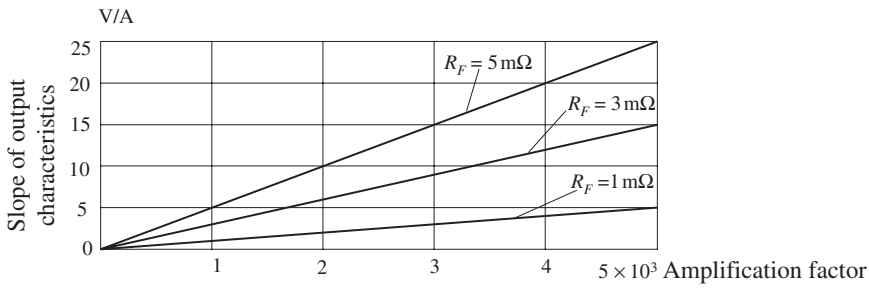

4.18 Relationship between control-circuit gain and output-slope characteristics

the current change is required to be less than 4 A when the voltage drops from 40 V to short-circuit at 200 A welding current, then the slope is 40 V/4 A = 10. Figure 4.18 shows that the control-circuit gain should be greater than 33 000 when $R_F = 3\,\text{m}\Omega$. Figure. 4.18 was generated on the basis of ideal characteristics of the transistor. In fact, a large change of the load voltage induces a large change of the voltage drop across the transistor and thus produces a large disturbance of the current. Therefore, a circuit gain greater than 33 000 is required to keep the characteristic slope of 10. In a conventional control system, a high open-loop gain can be obtained easily by integral compensation. But as described above, the integral element delays the transfer of the arc-operating point and causes arc instability. Therefore, using an integral element in the control circuit is not recommended. The problem with using proportional control is that too much amplification often causes system oscillation. Because droplet transfer causes large disturbances of the arc, the circuit parameters fluctuate violently. It is hard to design a proportional element that can eliminate oscillation in all cases. The capacitor in the element causes time delays as well. Therefore, this control circuit cannot be compensated as in a normal case.

One method to avoid oscillation at high open-loop gain, is to make the feedback loop a Type 1 system when designing the circuit. Such design ele-

ments include, for example, avoiding the use of inertial elements as much as possible, using distributed elements instead of integrated chips (for operational amplifiers), and using non-inductance resistors instead of winding resistors. Of course, using distributed elements instead of operational amplifiers also introduces some disadvantages, e.g. more complicated circuit structure, inconvenience of multi-input design, inconvenience of dial regulation of the output characteristics, and thus lower repeatability of the welding parameters.

4.5.2.2 Collector-output circuits

To achieve accurate control and avoid too much loop gain, two negative-current feedback loops can be used. The electrical circuit is shown in Fig. 4.19a where the resistance R_e (= R_{e1} + R_{e2}) is connected in series with the emitter, which naturally forms a negative-current feedback loop. For constant-current output, a signal is taken from R_{e2} to form the second negative-current feedback loop.

As the load is connected to the collector, the transistor has a constant-current output characteristic even in the open-loop state. But, due to variation of the load, the voltage drop on the transistor, power consumption, and temperature changes, the load current disturbance, $\Delta I''$, may happpen. The magnitude of $\Delta I''$ depends on the variation of the voltage drop on the transistor, characteristics of the transistor, and transistor cooling conditions. Introducing a negative feedback, R_e, will suppress the disturbance $\Delta I''$.

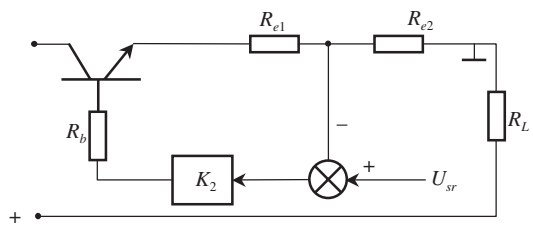

a) Electric circuit

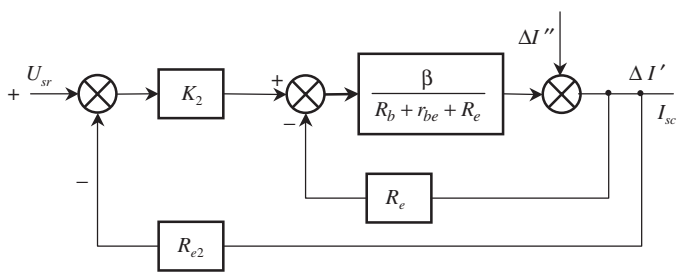

b) Control diagram

4.19 Collector-output circuit (for constant current)

Assuming the circuit is in an open-loop state, the disturbance $\Delta I''$ results in a change of output, $\Delta I'$. The relationship between $\Delta I''$ and $\Delta I'$ can be seen from Fig. 4.19b and can be expressed more explicitly as follows:

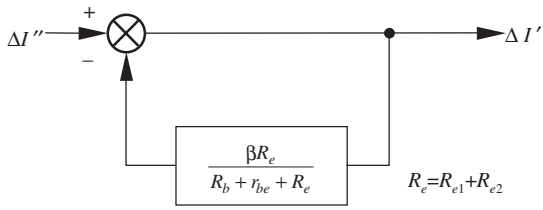

$$\therefore \frac{\Delta I'}{\Delta I''} = \frac{1}{1 + \dfrac{\beta R_e}{R_b + r_{be} + R_e}} = \frac{R_b + r_{be} + R_e}{R_b + r_{be} + R_e(1+\beta)} \qquad [4.2]$$

Obviously the negative-current feedback loop in the primary circuit decreases the influence of the disturbance, but due to the fact that R_e should not be too large, there is not enough suppression.

If a negative-current feedback loop is in the control loop, the disturbance can be suppressed further so that the accuracy of the constant-current control can be improved. It can be seen from Fig. 4.19b that the relationship between the output-current change, I_{sc}, and the current disturbance, $\Delta I'$, can be illustrated as follows:

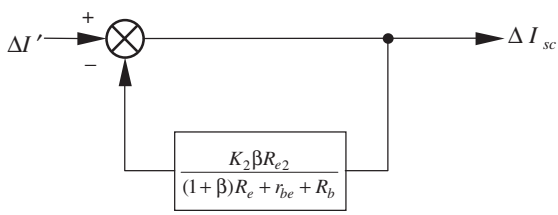

$$\frac{\Delta I_{sc}}{\Delta I'} = \frac{R_e + r_{be} + R_b}{\beta R_e + r_{be} + R_b + K_2 \beta R_{e2}} \qquad [4.3]$$

From Eq. [4.2] and Eq. [4.3], the change of the output current due to the current disturbance $\Delta I''$ can be written as

$$\Delta I_{sc} = \frac{R_e + r_{be} + R_b}{\beta R_e + r_{be} + R_b + K_2 \beta R_{e2}} \Delta I'' \qquad [4.4]$$

From this analysis, it can be seen that the load-current change due to a disturbance is decreased distinctly by two negative-feedback loops and thus high constant-current output accuracy can be obtained.

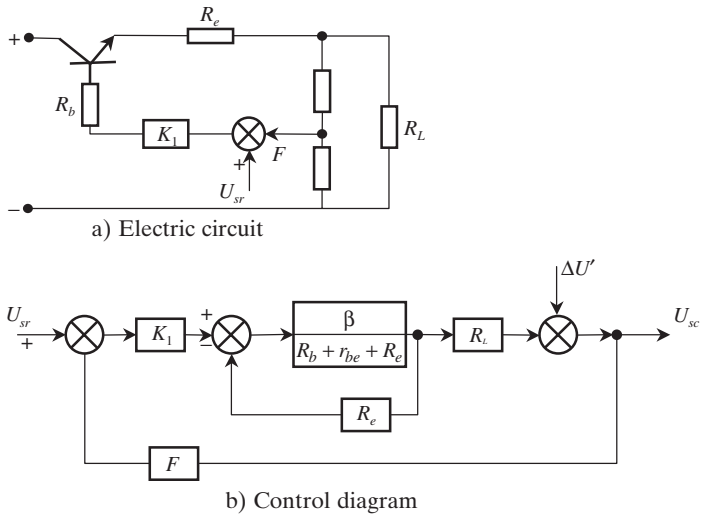

4.20 Collector-output circuit (for constant-voltage characteristics)

In the case of a constant-voltage output, a negative voltage feedback loop can be applied in the control loop as illustrated in Fig. 4.20.

From the diagram, the relationship between the change of output voltage and the voltage disturbance $\Delta U'$ can be illustrated as follows:

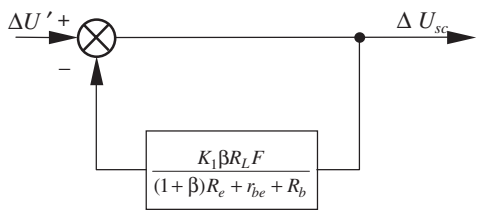

$$\therefore \frac{\Delta U_{sc}}{\Delta U'} \approx \frac{\beta R_e + r_{be} + R_b}{\beta R_e + r_{be} + R_b + K_1 \beta R_L F}$$

If $k_1 \beta R_L F >> \beta R_e + r_{be} + R_b$

$$\Delta U_{sc} \approx \frac{\beta R_e + r_{be} + R_b}{k_1 \beta R_L F} \Delta U'$$

Let $$M = \frac{\beta R_e + r_{be} + R_b}{\beta}$$

then $$\Delta U_{sc} = \frac{M}{k_1 R_L F} \Delta U' \qquad [4.5]$$

When the load changes, the internal resistance of the primary circuit causes the voltage disturbance $\Delta U'$. As the primary circuit has a constant-

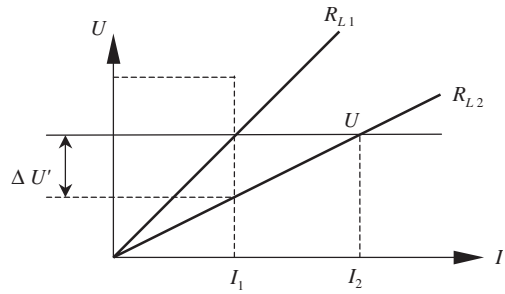

4.21 Diagram showing change of load

current characteristic, the change of the load resistance causes a large voltage disturbance. Assuming that the load resistance is ΔR_L, the disturbance $\Delta U' = I\Delta R_L$, as shown in Fig. 4.21. The effect of the voltage disturbance on the output voltage due to the change of internal resistance of the circuit is discussed below.

Supposing that the primary circuit is an ideal constant-current power source, the voltage disturbance due to the load change in the primary circuit is shown in Fig. 4.21.

For a load change from R_{L1} to R_{L2}

$$\Delta U' = I_1\Delta R_L = I_1(R_{L1} - R_{L2}) = I_1\left(\frac{U}{I_1} - \frac{U}{I_2}\right) = U\left(1 - \frac{I_1}{I_2}\right)$$
$$= \frac{U}{I_2}(I_2 - I_1) = R_{L2}(I_2 - I_1) \qquad [4.6]$$

According to Equations [4.5] and [4.6], the effect on output voltage of a voltage change produced by the internal resistance of the circuit is

$$\Delta U_{sc} = \frac{M}{k_1 R_L F}\Delta U' = \frac{M}{k_1 F}(I_2 - I_1) \qquad [4.7]$$

From this derivation, it can be seen that although the voltage disturbance is proportional to R_L at the same current change (see Eq. [4.6]), the open loop gain is also proportional to R_L (see Eq. [4.5] and Fig. 4.20b); therefore, the change of the output voltage, ΔU_{sc}, is proportional to the change of current. The slope of the voltage-output characteristic remains constant over its full range (see Eq. [4.7]).

From Eq. [4.7], it can be seen that, for a definite magnitude of load-current change, the change of the output voltage, ΔU_{sc}, is smaller when K_1F is larger, or the characteristic line is flatter. Assuming that $F = 1/5$, $R_e = 0.0048$, $r_{be} = 0.33$, $R_b = 2.1$, $\beta = \beta_1\beta_2 = 20 \times 50 = 1000$ (these data are taken from the actual QHT-80 power source), the relationship between ΔU_{sc} and

Table 4.1. Relationship between characteristic slope and amplification factor

Slope of constant voltage characteristic (V/100A)	0.3	0.2	0.1	0.05	0.01
Amplification factor K_1	12	18	36	72	360

the amplification factor, K_1, is as shown in Table 4.1 for a current-change range, $I_2 - I_1 = 100\,\text{A}$.

It can be found from Table 4.1 that the amplification factor is not very high for a reasonable requirement of the characteristic slope. For example, for the slope 0.2 V/100 A, the required circuit gain is equal to 18.

Obviously, both the constant-voltage and constant-current output characteristics are satisfactory if the collector-output circuit is used. Therefore, this kind of circuit is used for the QHT-80 power source. More concrete data are calculated for the power source below.

4.5.3 Slope of constant-voltage output characteristics

Following Eq. [4.7], the effect on the voltage output of a voltage disturbance induced by the internal resistance of the power amplifier is

$$\Delta U_{sc} = \frac{M}{k_1 F}(I_2 - I_1)$$

where $M = \dfrac{\beta R_e + r_{be} + R_b}{\beta}$

Assume that $\Delta I = I_2 - I_1 = 100\,\text{A}$ and

parameters of the circuit $R_e = R_{e2} + R_{e1} = \dfrac{0.2}{64} + \dfrac{0.34}{204} = 0.0048$

where R_{e2} is made of 64 resistors each of 0.2 Ω and R_{e1} are balance resistors connected in series with the transistor emitter. The average value of the balance resistors is 0.34 Ω and the total number of resistors is 204. $r_{be} = 4/12 = 0.33$ (the dynamic resistance of the transistor over the current range of 1 to 3 A is 4 Ω; 12 transistors are connected in parallel in each module). As the number of transistors is large, the working current is large and r_{be} can be neglected. $R_b = 25/12$ (the resistance of the input of each module is 25 Ω; 12 modules are connected in parallel). $\beta = \beta_1\beta_2 = 20 \times 50 = 1000$ (β_1 is the amplification factor of the driving transistor; its average value is 20: β_2 is the amplification factor of the power transistor; its average value is 50). The amplification factor of the control circuit is $K_1 = 100\,\text{k}\Omega / 4.7\,\text{k}\Omega$. The

Table 4.2 Slope of the experimentally-measured constant voltage output characteristic

Current (A)	20	100	205	305	400	500	600	700	760
Change of voltage ΔU (V)	0	0.2	0.4	0.61	0.79	0.98	1.16	1.35	1.45

negative feedback gain is $F = \dfrac{1\text{k}\Omega}{3.6\text{k}\Omega + 1\text{k}\Omega}$. Substituting all of these values into the equation, one obtains

$$\Delta U_{sc1} = 0.156\,\text{V}$$

which is the change of the output voltage over the current range of 100 A. The disturbance induced by the internal resistance of the amplifier is 0.156 V, which is less than 0.2 V. Practical measurements were conducted on the QHT-80 power source. The experimental data are shown in Table 4.2.

In the present design, an individual power supply with good voltage-stabilizing circuitry is used for the control circuit. Only the voltage drop across the transistor U_{ce} changes when the main power supply fluctuates. In the case where the volt-ampere characteristic of the transistor is flat, there is little influence on the voltage output when the main power supply fluctuates. Even when the volt-ampere characteristic of the transistor is not quite as good, the voltage output changes only slightly because the open-loop gain of the control circuit is sufficiently large. Thus, a constant-voltage output can be kept very stable when the main power fluctuates.

4.5.4 The slope of constant-current output characteristics

When a collector-output circuit is used for the power source, the current fluctuation due to the variation of load resistance is small. In this case, the current fluctuation depends on the voltage drop, power loss, and junction temperature of the transistor. Therefore, the current disturbance is greatly reduced by the two negative feedback loops and its accuracy is high. According to the analysis in Section 4.5.2.2, the effect of a disturbance on the output can be written as

$$\Delta I_{sc} = \frac{R_b + r_{be} + R_e}{\beta R_e + r_{be} + R_b + K_2 \beta R_{e2}} \Delta I''$$

where $K_2 = \dfrac{62}{4.7}$, $R_{e2} = 0.003125$

and the parameters of the circuit are the same as in the previous section, Substituting them into the equation gives

$$\Delta I_{sc} = 5\% \Delta I''$$

which means that the current disturbance can be reduced to 5% of its initial value using the two negative-feedback loops.

In order to make the current-output characteristic steeper, additional measures are taken in the QHT-80 power source. It is known that current disturbances result mainly from variations of the voltage drop across the transistor. Normally, composite transistors are used for the primary circuit in order to generate large currents. Thus, the voltage drops across all stages of the transistor vary due to the load resistance. That produces variations of current in all stages of the composite transistor. Naturally, the variation of current in a previous stage will be amplified by the next stage. It can be said that the current disturbance due to a voltage variation is caused mainly by the preceding transistor. In order to reduce the current disturbance, it is important to choose transistors with good volt-ampere characteristics. A particular effect can be achieved if the collectors of the preceding transistors are separated from the main transistor and connected to an individual, well-stabilized power supply so that the voltage across the preceding transistors is independent of the load voltage. Thus, the constant-current characteristics can be more nearly vertical. However, a second-stage transistor needs a large power supply that furnishes in the order of 10 A. It has to be connected to the collector of the main transistor. The circuit diagram for this is shown in Fig. 4.22.

This circuit has been analysed. The experimental data showed that the current change can be kept within 2% when the load varies from open circuit to short circuit, i.e. a change of 40 V.

The circuit also adapts to fluctuations of the mains power. Because the circuit uses a collector output, the effect of mains-power fluctuation is the same as a load-voltage change or, explicitly, the current change due to a

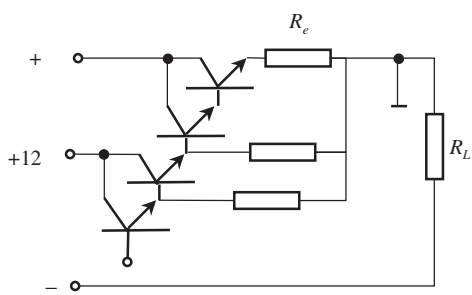

4.22 Driving circuit of a power transistor

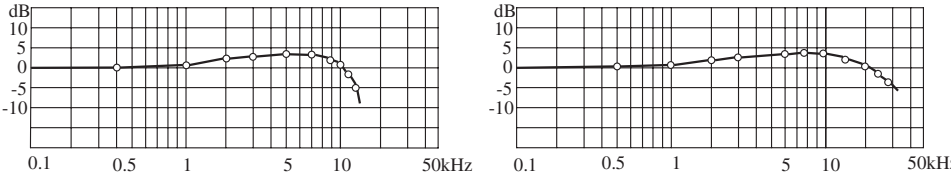

a) Constant current b) Constant voltage

4.23 Frequency-response characteristics

voltage drop across the transistor, U_{ce}. From the description in the paragraphs above, it is known that the current change is within 0.2% when the load varies from open circuit to short circuit or when the voltage drop across the transistor is 100% of the output voltage of the power source. Consequently, the current change should be within 0.2% when the main power fluctuates 10%.

4.5.5 Dynamic characteristics of the QHT-80 power source

The QHT-80 power source has very good dynamic properties. Practical measurements showed that the closed-loop response frequency was 12 kHz under constant-current control (see Fig. 4.23a) and the closed-loop response frequency was 20 kHz under constant-voltage control (see Fig. 4.23b). The transfer time needed to switch from the background-output characteristic to the pulsed-output characteristic was less than 0.05 ms (see Fig. 4.12). Due to its excellent dynamic proprerties, it has been demonstrated that it can be used for amplification of music without distortion. The machine can furnish real-time control of the welding arc without any problem.

4.6 Circuit diagram of the power source

The block diagram of the circuit is shown in Fig. 4.24 where 1–17 are control components and 18–29 are protection components. Reliable overvoltage and overcurrent protection circuits have been incorporated. In order to enhance the safety and reliability of the power supply and maximize the transistor's capacity, two special protection circuits also were incorporated. Devices 18–22 are used to control the circuit so that its maximum current does not exceed 850 A and continue for more than 0.5 s. In other words, the protection circuit does not act unless the current exceeds 850 A for 0.5 s. Devices 23–29 are average power-consumption protection circuits. These circuits measure the average voltage drop across the transistor and the average current passing through the transistor every second. The circuit switches off the main circuit when the voltage drop reaches 30 V and the current reaches 600 A. That means that the protection circuit does not cut

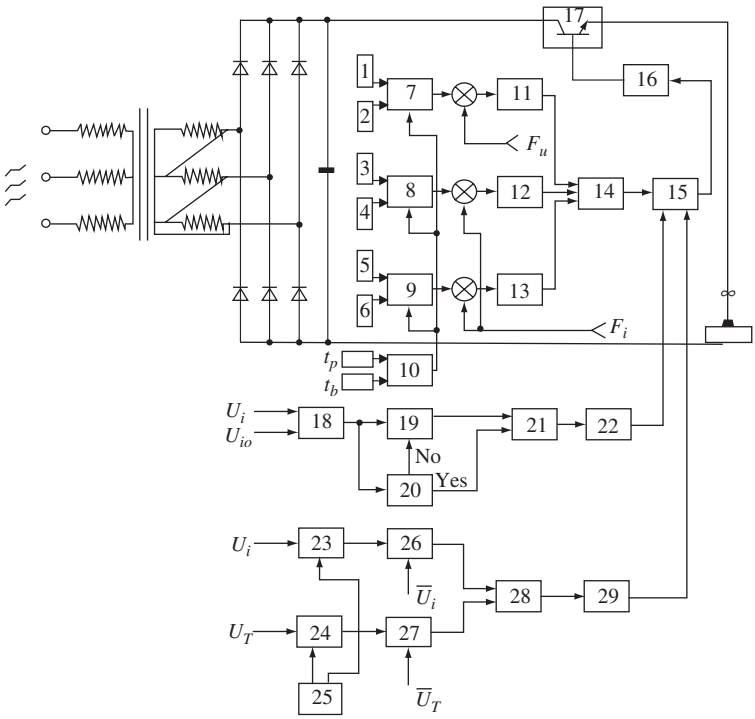

4.24 Circuit diagram of the QHT-80 power source

off the main circuit unless the voltage drop exceeds 30 V and the current exceeds 600 A simultaneously. Obviously these protection measures maximize the transistor's capacity on one hand and ensure its safety on the other hand.

1 3 5	Dial for references of background current-output characteristic.
2 4 6	Dial for references of pulse-current output characteristics.
7 8 9	High-speed electronic switch.
10	Square-wave generator.
t_p	Pulse-current width regulator.
t_b	Background-current width regulator.
11 12 13	Amplifier
14	Circuit for switching of output characteristics.
15	Electronic switch
16	Driving circuit.
17	Transistors, 204 pieces of 3DF20U.
18	Compare and shaping circuit.
19	Clock.

20	Over current detector.
21	AND gate.
22	Latch for over current state.
23	Integration element for current.
24	Integration element for voltage drop.
25	Timer
26 27	Comparing element.
28	AND gate
29	Latch for overpower consumption state.
F_i	Current-feedback signal.
F_u	Voltage-feedback signal.
U_i	Current signal
U_{io}	Preset over current value 850 A
U_T	Voltage drop across transistor
$\overline{U}_i$	Average integration value of curent 600 A
$\overline{U}_T$	Average integration value of voltage drop 30 V

4.7 Technological behaviour[383]

Technological experiments have been conducted with different wire diameters. The QH-ARC 101 control method and conventional pulsed MIG welding were compared. The results demonstrated that the QH-ARC 101 control provided a more stable arc having good resistance to disturbances. A wider range of welding parameters can be selected.

4.7.1 Experimental study of the effect of different control methods

In order to study the features and properties of the QH-ARC 101 control method, a set of experiments was designed using constant-current characteristics and constant-voltage characteristics in different combinations for pulsed MIG welding. The current and voltage waveforms, as well as the trajectory of the arc-operating point on the U-I plane, were recorded by an oscillograph. Ten combinations of the control method were included in the experimental design as shown in Table 4.3. The results are summarised in Table 4.4.

In Table 4.3, the first column identifies the control method. It is described by two characters. The first character represents the control method for the background current and, the second character represents the control method for the pulsed current. U represents a constant-voltage characteristic and I represents a constant-current characteristic. ⌞ and ¬ represent the double-step output characteristics; the former is used for the constant current-constant voltage segments of the background current, (constant

Table 4.3 Control method and parameters

No.	Control method	Parameters for background current		Parameters for pulse current		Duration of background current t_b (ms)	Duration of pulsed current t_p (ms)
		Constant current value (A)	Constant voltage value (V)	Constant current value (A)	Constant voltage value (V)		
1	*U–U*	—	24	—	34	9	3
2	└–*U*	60	24	—	33	9	3
3	*U–I*	—	23	420	—	9	3
4	└–*I*	40	23	420	—	9	3
5	*I–U*	40	—	—	36	9	3
6	└–*U*	40	10	—	36	9	3
7	*I–I*	70	—	420	—	9	3
8	└–*I*	70	10	420	—	9	3
9	└–*U*	60	20	—	36	9	3
10	└–┐	70	15	320	39	9	4

Wire dia. 1.2 mm; shield gas 85% Ar + 15% CO_2; wire-feed rate 139 m/h

Table 4.4 Experimental results

Control method No.	Experimental results				
	Average current (A)	Average voltage (V)	Arc-operating point on $U-I$ plane	$U-t$, $I-t$ oscillogram	Stability of arc and spatter
1	180	27	Fig. 4.25a	Fig. 4.27	Bad
2	180	27	Fig. 4.25b	Fig. 4.28	Excellent
3	160	30	Fig. 4.25c	–	Bad
4	170	27	Fig. 4.25d	–	Excellent
5	140	24	Fig. 4.25e	Fig. 4.29	Good
6	150	24	Fig. 4.25f	Fig. 4.30	Excellent
7	170	24	Fig. 4.25g	–	Good
8	170	26	Fig. 4.25h	Fig. 4.32	Excellent
9	160	25		Fig. 4.31	Excellent
10	–	–	Fig. 4.26	–	Excellent

current first followed by constant voltage). The latter is used for the constant voltage-constant current segments of the pulsed current, (constant voltage first followed by constant current).

Experiments No. 1–10 were designed to compare the effect of conventional constant-voltage, constant-current characteristics with double-step output characteristics ⌞, for the control of the arc. The results are shown in Figures 4.25 to 4.32, among which Figures 4.25 and 4.26 are the trajectory of the arc-operating point on U-I plane (oscillogram). Figures 4.27 to 4.32 are U-t and I-t waveforms of the arc recorded by the oscillograph.

From Figures 4.25a to h, it is obvious that the application of the ⌞ output characteristic can effectively prevent arc breakdown and short circuiting. For example, Figures 4.25a and 4.25b are the trajectories of the arc on the U-I plane for U-U and ⌞-U control. From the first picture, a lot of arc breakdown can be observed but none can be seen in the latter. The background arc was kept basically on the constant-voltage segment. Occasionally it jumped to the constant-current segment; that is the effective measure for preventing arc breakdown. Figures 4.25c and d are arc trajectories on the U-I plane for the U-I and ⌞-I control methods. Similiarly, a lot of breakdown can be seen in the former, but not in the latter.

Figures 4.25e and f are arc trajectories on the U-I plane for the I-U and ⌞-U control methods. Although no breakdown can be seen in the former, short circuiting often happens because there is no automatic regulation of arc length. Short circuiting can be eliminated completely in the latter control method.

Figures 4.25g and h represent the trajectories on the U-I plane for the control methods I-I and ⌞-I. Similiarly, as mentioned in the paragraph

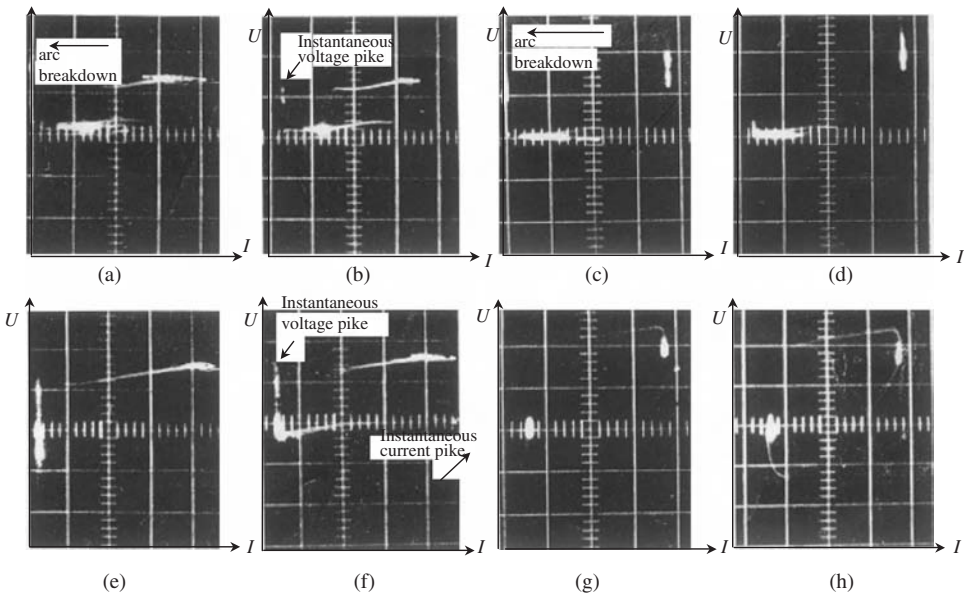

4.25 Trajectory of the arc-operating point on the *U-I* plane for different control methods

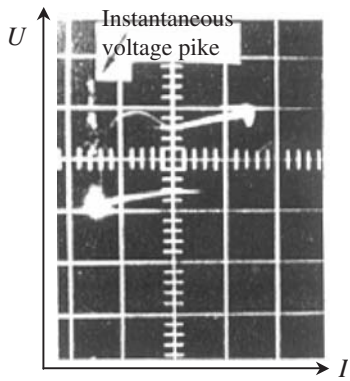

4.26 Trajectory of the arc-operating point on the *U-I* plane for the QH-ARC control

above, the ⌐ output characteristic completely eliminated the short-circuiting phenomenon.

The mechanism of the elimination of arc breakdown by the ⌐ output characteristic can be explained by Figures 4.27 and 4.28. The former is U-U control and the latter is ⌊-U, control. From Fig. 4.27, it can be seen that because the background current is low, a very small disturbance, such as a

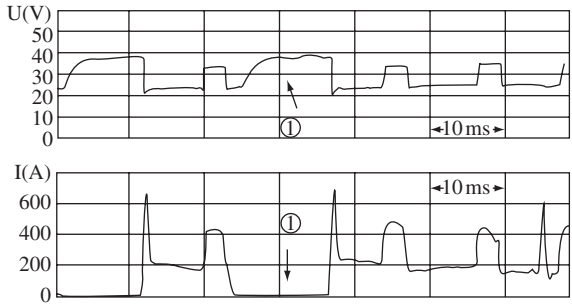

① Arc breakdown
Background: Constant voltage 24 V, 9 ms
Pulse: Constant voltage 34 V, 3 ms

4.27 U-U control

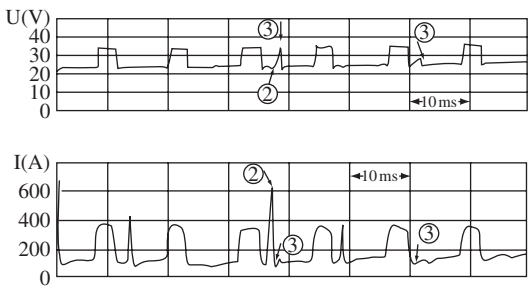

② Short-circuit ③ Voltage peak
Background: Double step characteristics
60 A, 24 V, 700 A, 9 ms
Pulse: Constant voltage 34 V, 3 ms

4.28 ⌞*-U* control

longer arc length momentarily, can break down the arc (see Fig. 4.27, point 1). From Fig. 4.28, it can be seen that if any tendency for short circuiting occurs, the ⌞ characteristic introduces a current peak that burns off the droplet (see Fig. 4.28, point 2) and maintains the arc. If the arc length increases and the arc current decreases , the ⌞ charactersitic produces a voltage peak that maintains the arc (see Fig. 4.28, point 3).

Figures 4.29 and 4.30 also demonstrate very clearly the role of the ⌞ characteristic in stabilising the arc. The former is the I-U control and the latter is the ⌞-U control. In I-U control, the background current does not change at all; if a short circuit occurs, there is no capability to resist the disturbance (see Fig. 4.29, point 2). In ⌞-U control, the ⌞ characteristic introduces a current peak and burns off the droplet while the short circuit occurs (see Fig. 4.30, point 4).

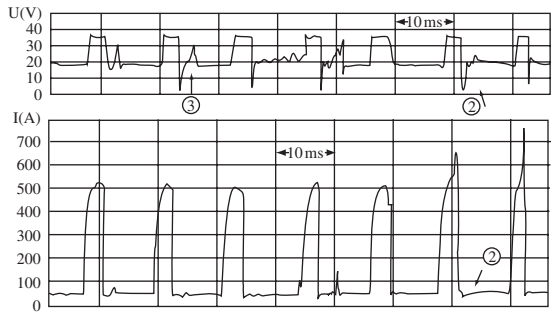

② Short-circuit ③ Voltage peak

Background: constant current 40 A, 9 ms
Pulse: constant voltage 36 V, 3 ms

4.29 I-U control

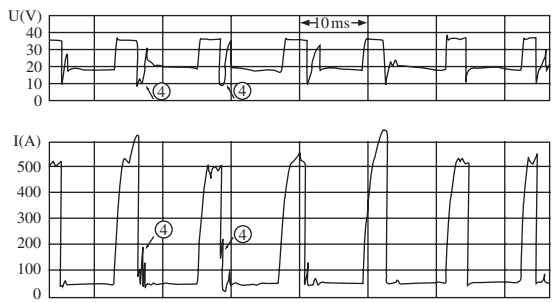

④ Current peak

Background: Double-step characteristics
40 A, 10 V, 9 ms
Pulse: Constant voltage 36 V, 3 ms

4.30 ⌊-*U* control

The background current varies adaptively according to the condition of the arc if the ⌊ characteristics are properly set. The arc-operation point sometimes is on a constant-voltage segment and sometimes on a constant-current segment in order to maintain a stable arc (see experiment No. 9 and Fig. 4.31). It is recommended that the parameters be set so that the arc-operating point is normally on the constant-voltage segment; the constant-current segment avoids arc breakdown, (see experiment No. 8 and Fig. 4.32).

Experiment No. 10 is ⌊–¬ control. The trajectory of the arc-operating point on the U-I plane can be confined securely in the frame of a rectangle. As shown in Fig. 4.26, experimental results show that it is better to set the background current on the constant-voltage segment and the pulsed current on the constant-current segment: see Fig. 4.33. The ⌊ characteristic

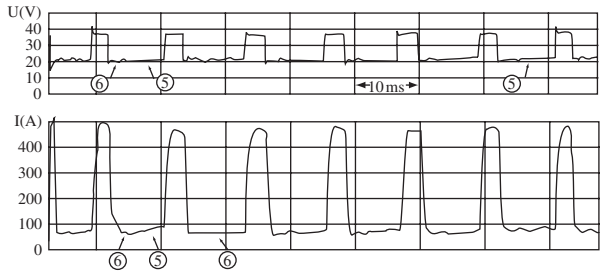

⑤ Constant voltage ⑥ Constant current

Background: Double-step output characteristics
60 A, 20 V, 9 ms
Pulse: constant voltage 36 V, 3 ms

4.31 ⌊-*U* control

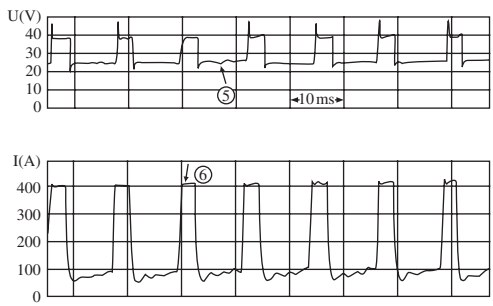

⑤ Constant voltage ⑥ Constant current

Background: Double-step characteristics
70 A, 10 V, 9 ms
Pulse: Constant current 420 A, 3 ms

4.32 ⌊-*I* control

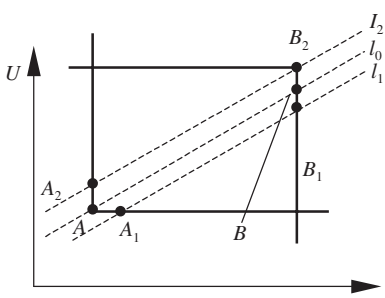

4.33 Optimum parameters for QH-ARC control

Table 4.5 Minimum welding parameters for wire Φ1.2 mm

	t (ms)	Output characteristics			Average voltage and current
		I_1	*U*	I_2	
Pulse	2	20	39	300	35A
Background	50	20	15	400	19V

Wire-feed rate 0.75 m/min

resists short circuiting and breakdown. The ¬ characteristic prevents excessive arc length and burning of welding-torch tip.

4.7.2 Range of welding parameters

As the QH-ARC 101 controlled arc has very good resistance to arc disturbances, the range of the welding parameters can be greatly expanded. The background current is controlled by the double-step characteristic; the arc can be kept stable without breakdown and short circuiting so the magnitude of the background current can be decreased to a very low value. Experiments demonstrated that 20 A can maintain a stable arc for a wire diameter of 1.2 mm, and 30 A for wire diameter of 2.5 mm. The pulsed current is always constant and therefore spray transfer can be maintained even during an arc disturbance. The average welding current can thus be set very low. Experiments have been conducted by the author with a wire-feed rate of 0.75 m/min for wire diameters of 1.2 mm, 1.6 mm, and 2.5 mm of alloy 0.8 Mn2Si. Spray transfer can be obtained readily. For a wire diameter of 1.2 mm, the average current was 35 A. A 1 mm thick sheet can be welded without difficulty. For a wire diameter of 1.6 mm, the average current was 65 A; it is used for welding 1.5 mm thick sheet. Good back-bead formation can be obtained using these conditions. For a wire diameter of 2.5 mm, the average welding current was 140 A. The minimum parameters that can be used for welding with wire diameters of 1.2 mm, 1.6 mm, and 2.5 mm are shown in Tables 4.5, 4.6 and 4.7.

Experiments have been conducted using the parameters given above but with conventional pulsed MIG control. They demonstrated once again that the process was uncontrolled; breakdown, spatter and explosions happened frequently. If a constant-voltage characteristic was used instead of the ⌞ characteristic, then a breach existed in the rectangular frame. The arc-operating point jumped to the open-circuit voltage point, and the arc extinguished. The arc could be reignited during the background-current or pulsed-current period but the process was not stable; serious spatter always

Table 4.6 Minimum welding parameters for wire Φ1.6 mm

	t (ms)	Output characteristics			Average voltage and current
		I_1	*U*	I_2	
Pulse	3	40	38	450	65A
Background	35	30	18	600	20.5V

Wire-feed rate 0.75 m/min

Table 4.7 Minimum welding parameters for wire Φ2.5 mm

	t (ms)	Output characteristics			Average voltage and current
		I_1	*U*	I_2	
Pulse	3	60	39	500	140A
Background	22	60	21	850	23V

Wire-feed rate 0.75 m/min

occurred. If a constant-current characteristic was used during the background period and a constant-voltage characteristic was used during the pulsed-current period, then short circuiting often happened during the background-current segment. When the pulsed-current period began, a very large current passed through the droplet, resulting in an explosion, and which subsequently extinguished the arc. The arc-operating point jumped to an open-circuit segment of the characteristic and a stable welding process could not be achieved.

From the analysis above, without the QH-ARC 101 control a stable welding process could not be achieved with low values of the welding parameters or a slow wire-feed rate. In order to get a stable arc with conventional control, the background current had to be greater than some minimum value. Experimental results demonstrated that, for a wire diameter of 1.2 mm using 0.8 Mn2Si steel, a satisfactory stable arc could be obtained with U-U control if the average current was greater than 180 A. Some information[67] indicates that the minimum average current for 1.2 mm wire is 90–110 A and for 1.6 mm wire is 110–120 A. Obviously the QH-ARC 101 control can ensure a stable arc at much lower currents. That means the range of welding parameters for QH-ARC 101 control is much wider than that for the conventional pulsed MIG process.

5

Control method QH-ARC 102 and 103

5.1 Introduction

In the previous chapter, the QH-ARC 101 control method was discussed in detail, including how to control the arc. Special output characteristics were described to confine the arc-operating point in a predefined area on the U-I plane. The design and implementation methods were also described. The discussion was applied to pulsed MIG welding but it is applicable to all arc-welding processes. The control of pulsed MIG welding is discussed further in this chapter.

Pulsed MIG welding is one of the most rapidly developing welding process. It can maintain stable spray metal transfer over a wide range of welding parameters. It can be used for both thin and thick plate. Welding can be conducted with large-diameter wire and low average current. However, there are several inadequacies.

First, setting the welding parameters is complicated. The melting rate of the wire using a normal wire extension can be written as

$$V_m = \frac{K}{T}\int_0^T i dt = f(I_p,\ I_b,\ T_p,\ T_b) \qquad [5.1]$$

This equation means that once the wire-feed rate is set, then four other parameters, namely I_P, I_b, T_P, T_b, also must be set to properly maintain the arc length, which makes the practical welding operation difficult.

Second, the resistance of the process to arc-length disturbances is poor. When the wire-feed rate is not stable, the welding torch wobbles, or the work piece surface is uneven, the balance between the melting rate and the wire-feed rate will be upset. This produces an unstable arc length. These deficiencies hinder the further development of pulsed MIG welding. The solution of these problems is an important research area in welding. Much research on this topic has been undertaken worldwide as outlined below.

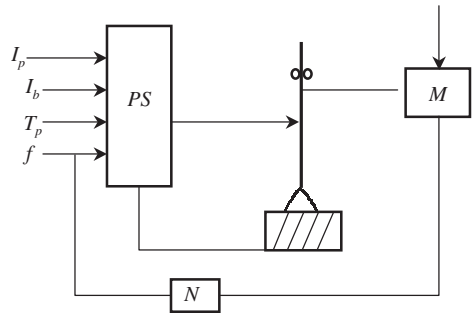

5.1 Open-loop cntrol for pulsed MIG welding

5.1.1 Open-loop control of pulsed MIG welding

The essence of this method is to link the wire-feed rate with the pulsed-arc parameters. The wire-feed rate is used as a signal so that the conditions of Eq. [5.1] will be satisfied. A schematic diagram of this control method is shown in Fig. 5.1. Obviously, the operator needs to choose only three parameters, viz. I_p, I_b and T_p. The frequency, f, need not be set as this is determined by the wire-feed rate over a certain range. However, there is then no response to disturbances produced by factors other than the wire-feed rate.

5.1.2 *Synergic* control

Amin published an article on *Synergic* control in 1981.[34] It links the wire-feed rate with four pulsing parameters. The relationship between these parameters is based on a mathematical model that was obtained experimentally. With this control, the wire-feed rate automatically controls the process over a wide range of welding parameters. But, because the control is of an open loop, there is no response to disturbances of the arc length itself. The control diagram is illustrated in Fig. 5.2.

5.1.3 Closed-loop control of pulsed MIG welding

Figure 5.3 shows the closed-loop control system developed by Ueguri.[35] In this system, both the wire-feed rate and arc voltage are linked to the pulsing parameters. The principle of operation can be described as follows:

- The welding current is supplied by transistors VT_1 and VT_2.
- The parameters I_P and I_b are preset.
- The wire feed-rate signal, V_f, is input to controller C_1, and C_1 outputs a pulse frequency f according to the following formula:

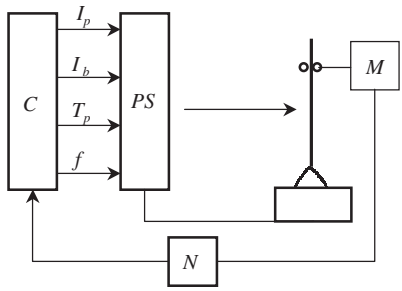

5.2 Synergic control

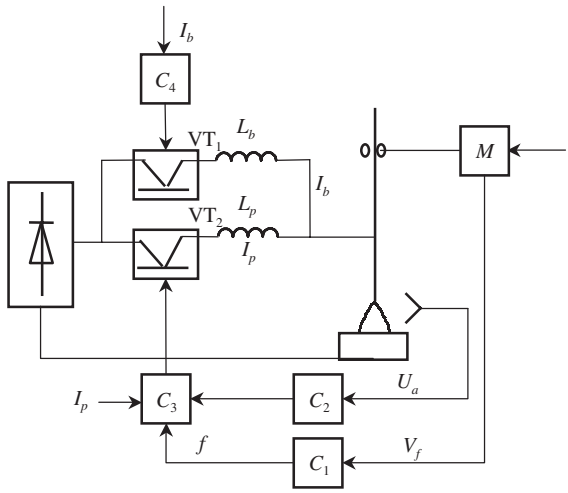

5.3 Closed-loop control of pulsed MIG welding

$$\frac{V_f}{f} = \frac{1}{15} \cdot \frac{a^3}{d^2} \qquad [5.2]$$

where a is the required droplet diameter and d is the wire diameter.

- The arc voltage, U_a, is taken as a signal to control the pulse width T_P.

The welding arc can respond to many kinds of disturbances and maintain stability. However, there are deficiencies in its electrical circuit as well:

(i) The transistor array works in an on–off mode; two inductances are connected to smooth the current waveform (see Fig. 5.4); therefore the dynamic properties of the system are poor.
(ii) An integration element is used to record the pulsed-current voltage, the output of which is taken as the arc voltage; that also is harmful to dynamic response.

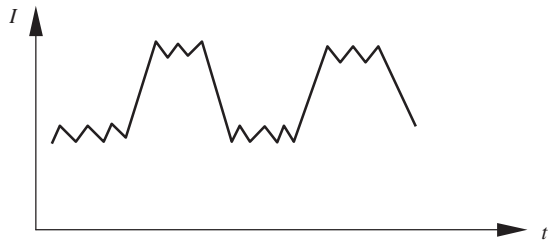

5.4 Current waveform of on–off mode transistorised power source

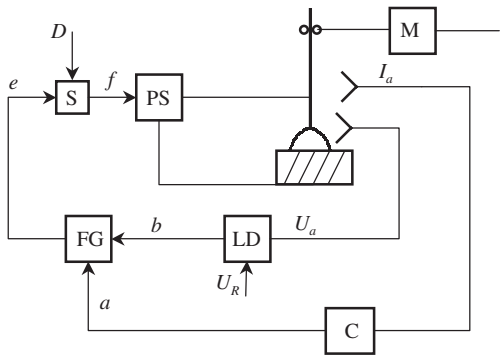

5.5 Schematic diagram of the QH-ARC102 control method

5.2 Control method QH-ARC102

A research group at Tsinghua University developed the QH-ARC 101 control method and the transistorised power source for its realisation. It opened up a new approach for control of pulsed MIG welding.[110] Subsequently another control method, designated QH-ARC 102,[2] was developed. It is a discrete sampling and closed-loop control system. The pulsing parameters vary automatically according to the wire-feed rate. The arc is stable, spray metal transfer is obtained, little spatter is produced, and a wide range of welding parameters can be used. It can be applied to pulsed or programmed wire-feed rate, which introduces a new welding technology.[120]

5.2.1 Block diagram

The schematic diagram in Fig. 5.5 illustrates the QH-ARC 102 control method.

- PS is a transistorised power source, which has double-step output characteristics. Under the control of signal *f*, it alternates between two

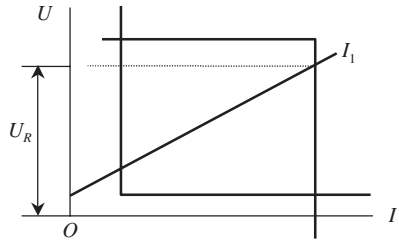

5.6 Output characteristics for the QH-ARC 102 control method

double-step output characteristics within 0.45 ms, so that a rectangle-like output characteristic is obtained, as shown in Fig. 5.6. The arc is on a constant-current segment both during the pulsed- and background-current periods. Therefore the metal transfer is even, the arc is stable, and the bead formation and penetration are uniform. The background current can be set quite low and the range of welding parameters is wide. The parameters of the double-step output characteristic D are input into the strobe element S to accommodate different wire diameters.

- The square-wave generator FG triggers the strobe element S according to the signal, a,b.
- The current signal I_a is input via C into FG to regulate the pulse width T_p. $T_p \nless 3$ ms to ensure that at least one droplet transfers during one pulse.
- The detected arc voltage signal U_a is compared with a preset reference U_R, then an output signal b is input to FG to control the background duration T_b. The arc voltage of each pulse is used to control the successive background-current duration so that the dynamic response is excellent.
- Not only is the background duration T_b controlled, but the pulse duration T_p also is regulated. Therefore the variation of pulse frequency is small, the arc noise is low, and the dynamic response is fast.

5.2.2 Sampling of the arc-length signal

A discrete sampling method is used for detecting the arc-length signal. The arc-voltage magnitude is integrated by a circuit during a certain portion of the pulsed current; the duration is from 0.2 ms to 1.8 ms after the leading edge of pulsed voltage. The features are as follows:

- The voltage is sampled during the pulse period, which is not affected by the variation of arc voltage.
- The instant of sampling is triggered by the leading edge of the pulse.

- During sampling, the disturbance of the arc is smallest. The sample is taken after 0.2 ms so it can avoid the circuit transients during switching of the output characteristic. Sampling ends after 1.8 ms to avoid disturbances caused by droplet transfer. The arc voltage is not measured during the background period because it is not stable.
- The arc voltage is integrated so that random disturbances of the arc voltage can be eliminated. The integration duration is short so that it will not affect the dynamic properties of the system.

5.2.3 Features of the control system

- The arc voltage and arc length vary periodically and violently in conventional pulsed MIG welding. Only its average value is controlled so the dynamic response is poor. In the QH-ARC 102 control method, the dynamic response is improved because the arc length during each pulse period is sampled for control.
- In the QH-ARC 102 control method, I_p and I_b are held constant. T_p and T_b are used to regulate the arc length; therefore, a stable arc length and optimum droplet transfer can be obtained simultaneously.
- Because the sampling frequency varies with the wire-feed rate, the system and the arc length can oscillate when the pulse frequency is low. To compensate for this, a time constant can be introduced into the control circuit of T_b. Because too large a constant affects the dynamic properties of the system, variable time constants are used for the system to maintain acceptable dynamic properties for different average welding currents (see $F_1(t)$ and $F_2(t)$ of Fig. 5.7).
- The voltage drop and temperature of the wire extension increase when the welding current increases; consequently, the arc length shortens. On the other hand, a larger arc length is desirable while the current is higher in order to achieve good bead formation. Therefore, a compensation circuit was designed in which the welding-current signal is supplied to automatically increase the arc length.

5.2.4 Principle of operation

The principle of operation of the QH-ARC 102 control can be illustrated by the block diagram Fig. 5.7.

When the pulsed current starts, the arc voltage is input to a mono-stable trigger-action circuit FF0 and the integration circuit composed of operational amplifier A_1. The front edge of U_a triggers FF0 and produces a pulse of 0.2 ms width; the back edge of this pulse (see point b) triggers mono-stable trigger-action circuit FF3, which produces a pulse of 2.0 ms. This back edge simultaneously triggers a mono-stable trigger-action circuit FF1, which

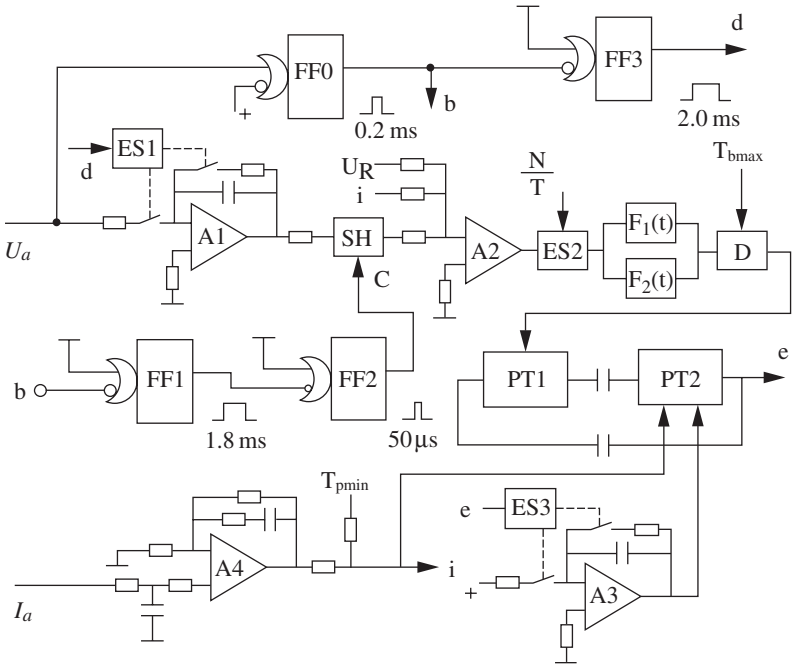

5.7 Block diagram of the QH-ARC102 control

produces a pulse of 1.8 ms. The output of FF3 controls the electronic switch ES1, which connects the U_a with the integration circuit A_1 and starts the integration operation for 2.0 ms. The back edge of the output FF1 triggers mono-stable trigger action circuit, FF2, which produces a pulse of 50 µs. This pulse, via point C, outputs to the sample-and-hold element, SH, so that the integrated value of the arc voltage is sampled and held. When the pulse at point d passes through ES1, the connection of U_a with A_1 is cut-off so that the integration element is reset and prepared for the next arc-voltage pulse. This process repeats itself and thereby produces the discrete sampling operation.

Operational amplifier, A_2, makes up the comparing element, which detects the difference of arc length, U_a, with the set value, U_R. Another signal, i, is input to it for compensation of the arc length according to the increase of welding current.

ES2 is another electronic switch that alters the time constants $F_1(t)$ and $F_2(t)$, according to the sampling frequency N/T. The IC circuits PT1 and PT2 form the square-wave generator. The delay time of PT1 determines the background duration T_b, which is controlled by the output value of the comparing element via D. Another signal $T_{b\,max}$ is used to limit the maximum background duration to improve the stability of the welding arc.

Table 5.1 Applicable welding parameters

Wire dia. (mm)	Range of welding current (A)
1.0	45~200
1.2	60~320
1.6	80~360

The welding-current signal is input into the integration element composed of A_4 to control PT2 or the pulse duration T_p. The signal $T_{p\,min}$ is used to limit the minimum pulse duration to ensure spray transfer.

Operational amplifier A_3 outputs a saw-tooth waveform synchronously with PT1 and PT2 to ensure that T_p is proportional to the average welding current.

5.2.5 Welding experiments

- Many welding experiments have been conducted using the welding machine described above. The results demonstrate that the system is stable, that the range of welding parameters is wide, and that spray transfer can always be obtained. The applicable range of welding current for different wire diameters is shown is Table 5.1.
- The regulation of welding parameters is simplified; the operator needs to regulate only the wire-feed rate. The wire-feed rate can be changed over a wide range, rapidly. Good bead formation and a stable arc can always be ensured without spatter and arc breakdown.
- The arc length has good resistance to disturbances, a stable arc can be maintained without spatter, and arc breakdown is avoided even under conditions where the work-piece surface is uneven and the welding torch wobbles.
- New welding technology, i.e. pulsed wire-feed rate welding can be realized and good bead formation can be obtained.

In summary, the QH-ARC 102 control provides closed-loop control of pulsed MIG welding with good properties. It can be applied in the following fields:

(i) One-knob control of pulsed MIG welding.
(ii) Pulsed wire-feed rate or programmed wire-feed rate.
(iii) Heat-input control.
(iv) All-position welding.
(v) Bead-formation control.
(vi) Open-loop or closed-loop bead-formation control.

(vii) One-side welding with back-bead formation.
(viii) Thin-gauge plate welding.
(ix) Robotic welding or adaptive control of the welding process.

5.3 Control method QH-ARC 103[3,121,127]

Closed-loop control of pulsed MIG welding has been realised with the QH-ARC102 control method. There is no doubt that this development is a big improvement in pulsed MIG control. However, the system is not a continuous-control process but a discrete process. The important point is that the sampling frequency changes with the change of wire-feed rate and disturbances to the arc length. The control-circuit parameters should be designed very carefully. If the control parameters are set improperly, the system may work very well under some conditions but may oscillate or provide slow response under other conditions. Such phenomena are unacceptable, of course, in practice. In order to avoid a complicated control-system design, an arc-length adaptive-control system, namely the QH-ARC 103 control, was developed by the author, Ou, Zhang, Wu, and others.[3,121,127]

5.3.1 Principle of control method QH-ARC 103

(i) *Multi-segment output characteristics.* Differing from all conventional welding processes, a multi-segment output characteristic was designed for this control, as shown in Fig. 5.8.

The function of each part of the output characteristic is as follows. A is the open-circuit voltage. BC is the segment for controlling the background current; from the figure it can be seen that this segment is not perpendicular but has a positive slope. This means that the longer the arc length, the

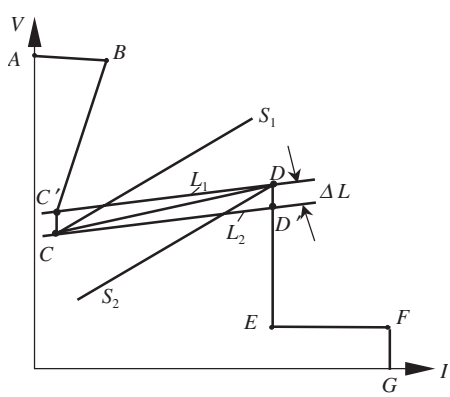

5.8 Multi-segment output characteristics

larger the background current will be, which is very helpful for stabilizing the arc in the background-current period. CD is the segment for controlling the movement of the arc-operating point and confining the range of arc-length variation. It can be seen from the figure that its slope is slightly greater than the slope of the volt-ampere characteristics of the arc, which means that it is impossible for the arc-operating point to stay on this segment. Any disturbance of the arc length will push the arc-operating point upward or downward. Therefore, the function of this segment is mainly to compel the arc-operating point to jump either from C to D or from D to C. Because the difference between the slope of this segment and the volt-ampere characteristics of the arc is not large, the movement of the arc-operating point is slow. Actually, this segment does not exist. It moves in a scanning manner all the time. The function of this segment will be discussed in more detail in the following paragraphs. DE is the segment for controlling the pulsed-current magnitude. The segments EF and FG control the short-circuiting current magnitude and time; their function is to facilitate arc ignition.

(ii) *Moving-output characteristics.* Moving-output characteristics or scanning-output characteristics (see Fig. 5.8) are used for driving the arc-operating point to jump from the background-current segment to the pulsed-current segment or vice versa. As described in previous paragraphs, when the slope of the power-source output characteristic is greater than the slope of the arc volt-ampere characteristic, the arc-operating point moves. The speed of movement depends on the difference in the slopes of these characteristics. The greater the difference, the faster the speed of movement is. In the present design, segment CD is able to scan. According to the real state of the arc, it may take C as the centre of rotation and scan counterclockwise (see S1 of Fig. 5.8) or take D as the centre of rotation and scan clockwise (see S2 of Fig. 5.8). After scanning, the difference between the slopes becomes larger and the speed of the movement of the arc-operating point increases. Also, after scanning, the segment returns to the position CD. Assuming that, at the moment, the arc-operating point is at C′, the arc is in the background period, the melting rate of the wire is very low, the arc length is decreasing and therefore C′ moves toward C. Once C′ reaches C, the scanning-action circuit is triggered. The segment scans counterclockwise around the axis at C, and drives the arc-operating point C to jump to D′ (the arc length at the moment is L_2). The welding current increases suddenly to its pulsed-current value and the melting rate and the arc length increase. The arc-operating point D′ moves upward. When it reaches the intersection of CD and ED at D (the arc length at the moment is L_1), a scanning circuit is again triggered and CD starts to scan clockwise around the axis at D. Thus, the arc-operating point is pushed from D to C′. The process repeats continuously so that the arc-operating point moves along

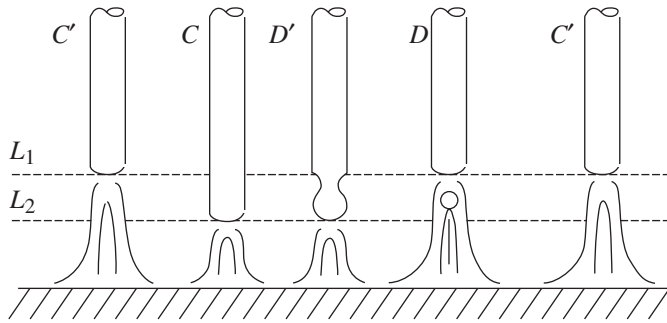

5.9 Automatic control of arc length

the frame of a quadrilateral figure (see Fig. 5.8). The scanning output characteristic accelerates the movement of the arc-operating point on the one hand and it also controls the duration of pulsed-current period on the other. Too short a pulse duration is unfavourable for droplet transfer. The function of the scanning-output characteristic will be discussed in detail in Sections 5.4.2 and 5.4.3.

(iii) *Automatic control of arc length.* From the description in the section above, it can be seen that the arc length is automatically controlled (see Fig. 5.9). Assuming that at point C′ the arc length is L_1, due to the fact that the melting rate is smaller than the wire-feed rate, the arc length is gradually shortened; C′ gradually approaches C and the arc length becomes L_2. When C jumps to D′, because the melting rate is greater than the wire-feed rate, the arc length gradually increases; the point D′ gradually approaches D. At this moment, the arc length again becomes L_1. The process repeats continuously in this way so that the arc length varies between L_1 and L_2. The magnitudes of L_1 and L_2 are defined by the output characteristic CD, which can be set in advance. The difference between L_1 and L_2 or ΔL, can be set as one diameter of a metal droplet; this difference, in fact, is the technological requirement of the welding process. It can be said that the arc length is virtually unchanged. The most important point is that the process proceeds automatically no matter how the wire-feed rate changes or how the arc length is disturbed; the arc-operating point remains between L_1 and L_2 (Note: In order to ensure reliable spray transfer, the segment CD scans all the time; therefore the value of L_1 automatically varies in a certain range. More details are given in Sections 5.4.2 and 5.4.3). Automatic control of arc length is realised by the automatic adjustment of the pulsed- and background-current durations. Because the dynamic properties of the power source and its control system are excellent, the arc-operating point moves and jumps without any delay. Figure 5.10 shows the trajectory of

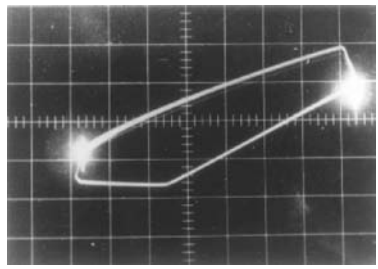

5.10 Trajectory of the arc-operating point on the *U-I* plane

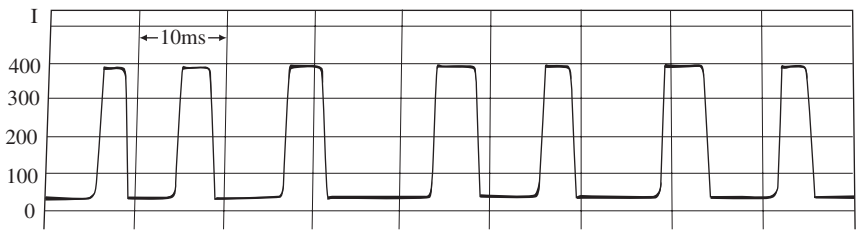

5.11 Current waveform for the QH-ARC 103 control in a normal case

the arc-operating point on the U-I plane, obtained using an oscillograph.

The highlights of the control method can be summarised as follows:

- The pulsed- and background-current durations are varied automatically according to the variation of arc length. The control system responds very quickly to the changes of wire-feed rate or arc length. The arc is stable and maintains spray transfer. Figure 5.11 shows the welding current waveform in a normal case. It can be seen that the durations of both the pulsed and background currents are not fixed; they vary in response to the variation of arc length. In the present control circuit, the pulsed-current duration is controlled by the scanning-output characteristics so that it is greater than 2.5 ms (see Section 5.4.3).
- The arc length is kept within a specific range; the range can be preset by setting the CD segment.
- The metal transfers during the pulsed-current period: the current in this period also can be preset so it is easy to guarantee optimum spray transfer, which provides a stable arc, minimum spatter, and good bead formation.

(iv) Many technological experiments have been conducted with different wire diameters such as 1.0, 1.2, 1.6 mm, Ar or mixed Ar shielding gas, and with different parent metals such as low-carbon steel, low-alloy steel,

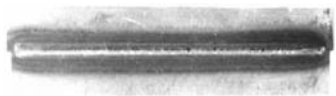

a) front side of weld

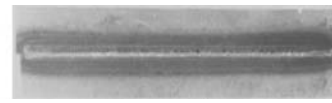

a) back side of weld

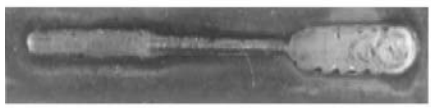

b)

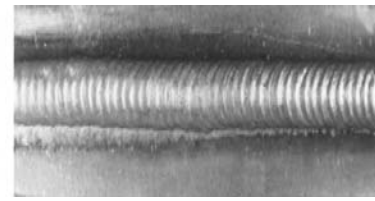

c)

5.12 Appearance of the weld made using the QH-ARC 103 control

stainless steel, Al and Al alloys, and Cu and Cu alloys. The results can be summarised as follows:

- Spray transfer can be obtained over a wide range of welding currents, namely for 1.0 mm diameter wire at 45–220 A, 1.2 mm diameter wire at 60–320 A, and 1.6 mm diameter wire at 80–360 A. It is impossible to use the lower limit of welding current indicated for the conventional pulsed-welding process. Because these lower limits are possible with the new process, very thin steel plate can welded without backing. Figure 5.12a shows a weld in a 1.0 mm thick steel plate made using 1.2 mm diameter wire at 45 A current. The two figures show the face and the root of the weld.
- Taking advantage of the peculiarity mentioned above, a pulsed wire-feed welding process was designed and evaluated (see Section 5.5) in order to control the heat input and penetration. Fig. 5.12b shows the weld made with abrupt changes of wire feed rate. Fig. 5.12c shows the weld made with pulsed wire feed rate.

5.3.2 Electrical circuit

For achieving control, the key problem is to design the electrical circuit. The circuit diagram is described in detail in this section.

5.3.2.1 Block diagram of the control system

Figure 5.13 illustrates the electrical configuration of the control system. It can be divided into two parts: the power source, 12, and the wire-feed mechanism, 13. The power source consists of four parts: the output-

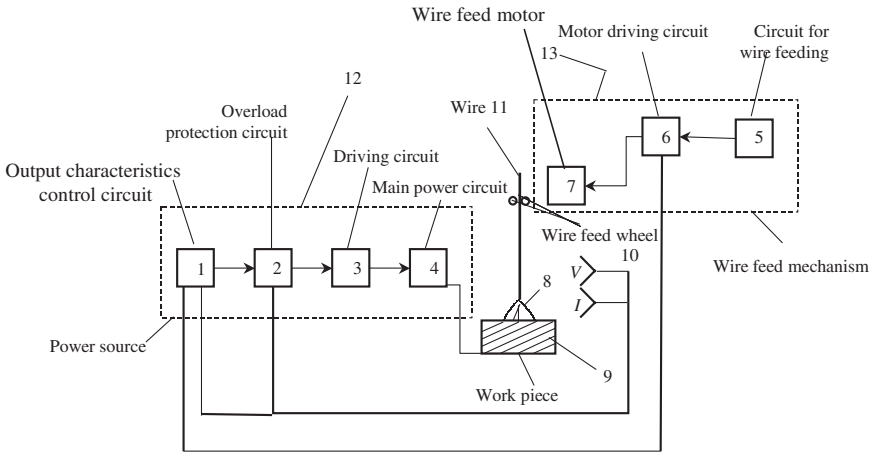

5.13 Electrical configuration of the QH-ARC 103 control

characteristic control circuit, 1, the overload-protection circuit, 2, the driving circuit, 3, and the main power circuit, 4. The terminals of the main circuit are connected to the wire, 11, and work-piece, 9, between which the arc and thus the current I and voltage V are produced. The wire-feed mechanism, 13, consists of three parts; the control circuit, 5, the driving circuit, 6, and the motor, 7. The parameters I and V of the arc, 8, negatively feed back to the output-characteristic circuit. These are the major control signals. The signal from the wire-motor driving circuit, 6, which represents the wire-feed rate, also is the feedback signal to the control circuit, 1, so that the output characteristic can adjust itself according to the wire-feed rate. The parameters I and V also feed the overload-protection circuit to protect the power source.

In this circuit, inductance is excluded, except that from the welding-cable loop, in order to reduce the time constant (L/R) and increase the response speed.

5.3.2.2 Welding power source

The power source consists of four parts; the detailed electrical circuit is shown in Fig. 5.14. Block 1 is the output-characteristic control circuit, Block 2 is the overload-protection circuit, Block 3 is the driving circuit, and Block 4 is the main power circuit. The main power circuit is a power-transistor array with two-cascade amplification; the maximum welding current is 800 A. The positive terminal is grounded and connected to the welding wire; the negative terminal is connected to the work piece. A small resistance is connected to the positive terminal to sample the current signal before it

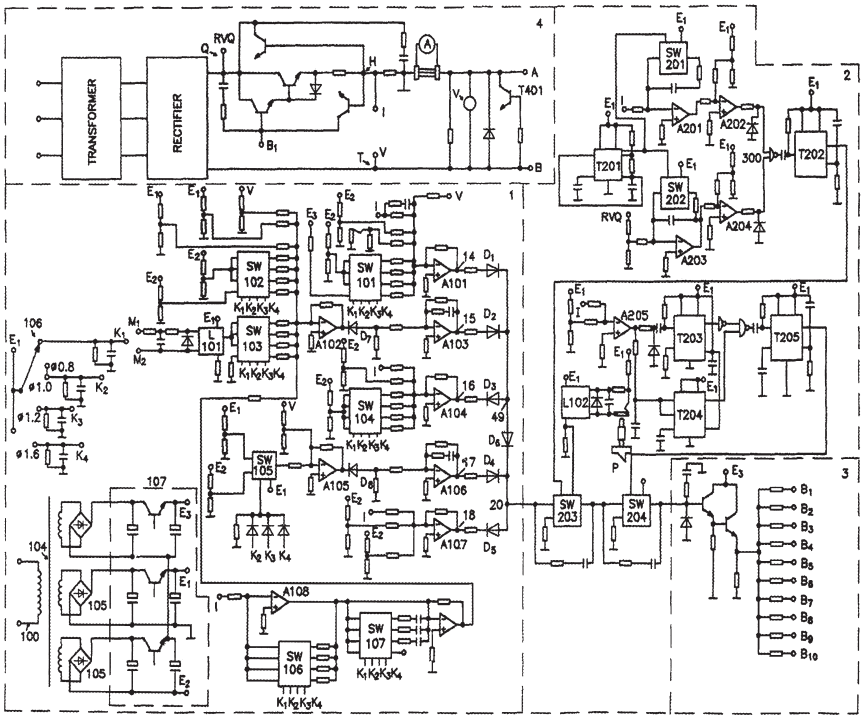

5.14 Electrical circuit of the QH-ARC 103 control system

goes to the ground; see point H of Fig. 5.14. The arc-voltage signal is sampled at the negative terminal; see point T. It is obvious that the current signal I is positive and the voltage signal V is negative. In the description of the circuit in the following paragraphs, these conditions are implied if not stated.

The driving circuit uses a two-cascade amplifier circuit. Because many power transistors are used for the main power circuit, the transistors are driven in groups in order to obtain an even distribution of current among the transistors. Transistors of similar characteristics are connected in parallel. The output of the driving circuit is shown in the figure as B_1–B_{10}. In Block 4, a main power transistor is shown together with its input, B_1, as an example. The circuit design of the main power transistors in Block 4 and their driving circuit in Block 3 are the same as those in a conventional welding power source.

The overload protection circuit in Block 2 consists of two parts. One part controls the electronic switch SW203 and the other part controls SW204. SW203 and SW204 are connected in series with the output of the characteristic control circuit 20 and the input of the driving circuit. Once an over-

load is detected by sampling the arc current and voltage, the protection circuit cuts off SW203 and SW204, which terminates the output of the driving circuit. There are two inputs for switch SW203. The first input is the output of the clock T202, which is an oscillator providing a logical high or low as a result of the logic network comprising clock T201, digital switches SW201 and SW202, amplifiers A201, A202, A203, and A204, and NAND gate 300 as shown in Fig. 5.14. The function of A201 and A203 is integration; A201 integrates the arc-current signal *I* and A203 integrates the voltage drop across the transistor RVQ. Both integrations are performed simultaneously and controlled by T201. The frequency and duration of integration are controlled by T201, SW201, and SW202. When both values of the integrations reach a critical magnitude, which indicates the current and voltage drop across the transistor is overloaded, they are fed to the NAND gate 300 and trigger the flip-flop circuit T202, which makes SW203 cut-off the main power circuit. Another input of SW203 is controlled manually. When plug P is inserted into the hole, the optical coupler L102 outputs positively, which sets SW203 for operation. Otherwise, SW203 does not act even when there is output from T202. From this description, it can be seen that the function of SW203 is to protect the transistor from excessive power consumption. During the background-current period, the arc voltage is low; therefore, the voltage drop across the transistor is high but the current passing through the transistor is low. During the pulse-current period, the current is high and the arc voltage also is very high so the voltage drop across the transistor is low. Therefore, in both cases, the power consumption in the transistor is not inevitably high. The protection circuit is designed to optimise the transistor capacity.

SW204 is controlled by T205, which consists of A205, T203 and T204. A205 controls the welding current. When the welding current exceeds a certain magnitude, it flips and triggers T203 and T204. When both the current magnitude and duration exceed preset limits, T203 and T204 trigger T205 via an AND gate and SW204 cuts off the current. It can be seen that the function of SW204 is to limit the maximum current but it acts only when both the magnitude and duration of the current exceed the preset limits. This design is also aimed at maximising the transistor's capacity.

The circuit described above also was applied to the protection circuit of the QH-ARC101 control.

5.3.2.3 Output-characteristic control circuit

The key technical characteristic of the QH-ARC 103 control is the output-characteristic control circuit. The present control method uses multi-segment and scanning output characteristics. The circuit is resolved into several parts to facilitate its description.

(i) *The preset welding-parameter circuit.* The essence of the QH-ARC 103 control method is to control the arc automatically by the specially designed output characteristics to obtain a stable arc and spray transfer without manual intervention. However, welding parameters should be preset for different wire diameters and different pulsed- and background-currents. In the present design, this requirement is met by setting different parameters of the output characteristics, keeping the principle of control and its form unchanged. A parameter-preset circuit was designed for this purpose.

In Block 1 of Fig. 5.14, 100, 104, 105, and 107 are DC power sources that provide bias for the control circuit. The output E_1 has positive polarity, E_2 is negative, and E_3 is positive. Their polarities are not indicated in the following description. Switch 106 is adjustable by the operator and selects one of four commonly used electrode-wire diameters, for example wires having diameters of 0.8 mm, 1.0 mm, 1.2 mm, and 1.6 mm. The switch output is a 4-bit word, K_1, K_2, K_3, or K_4. When the switch is turned to one of the four positions, a positive signal is sent from the switch (from the power source E_1 in this instance), while the output of the other three positions is 0 because they are grounded. From the circuit of Block 1, it can be seen that in all of the feedback loops there is an analogue switch for selecting a bias or reference value from the resistor and capacitor networks (see SW101, SW102, SW103, SW104, SW105, SW106, SW107). These switches select one set of bias or reference values according to the input word K_1–K_4.

(ii) *The closed-loop circuit.* In the QH-ARC 103 control method, the output characteristics consist of five segments, namely BC, CD, DE, EF, and FG. Each segment comprises one negative feedback loop; it is the same as in a conventional electronic welding power source. Some special measures have been taken, however, particularly those for connecting all of the segments together without breaching or overlapping and obtaining good dynamic properties without delay or oscillation.

A description of the QH-ARC 101 control and the method for accomplishing a double-step output characteristic were given in Chapter 4. The principle and method for producing multi-segment and scanning-output characteristics are discussed below.

If the parameter-selecting circuit shown in Block 1 of Fig. 5.14 is omitted, five closed-loop circuits connected in parallel can be distinctly seen. The parallel-connected devices of these loops are A101, A103, A104, A106, and A107. The five loops are connected by six diodes, namely D_1, D_2, D_3, D_4, D_5, and D_6. These diodes are critical for automatically transferring the output characteristics so they collectively might be called the automatic-transfer circuit. The five feedback loops and the automatic-transfer circuit can be simplified as shown in Fig. 5.15. One of the feedback loops forming the segment CD is illustrated separately in Fig. 5.16 to simplify the description

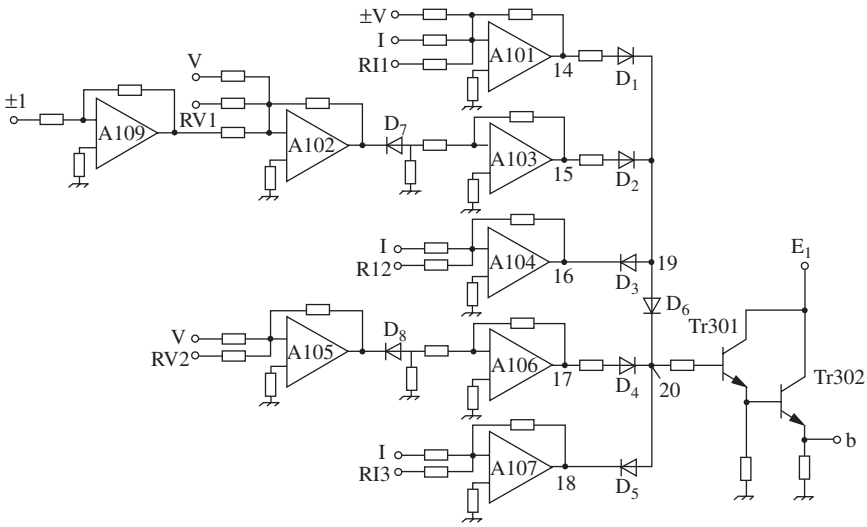

5.15 Automatic-transfer circuit

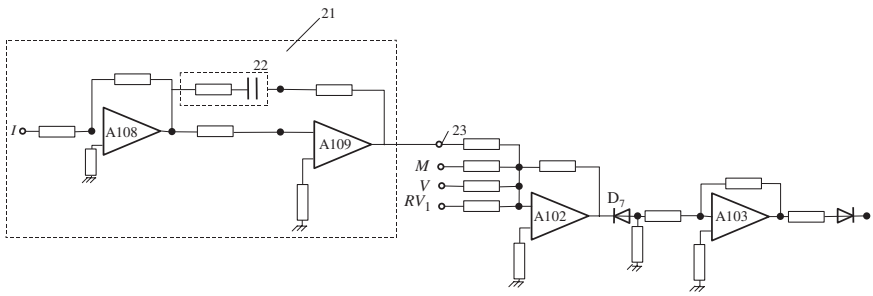

5.16 Circuit for scanning an output characteristic

of the scanning action of the characteristic. Reference to these two figures together with Fig. 5.14 is recommended while reading the following text.

(iii) *Segment BC.* The segment BC is controlled by an operational amplifier A101 (see Fig. 5.15). It has three inputs; one is the reference-current signal RI_1, which sets the background current. The second is the current-feedback signal I, which is used to obtain a constant-current output characteristic. The third is the arc-voltage feedback signal, which is used to raise the slope of the BC segment.

When a positive $+V$ is applied, the segment BC has a positive slope; when a negative $-V$ is applied, the segment BC has a negative slope. In the present design, the former is incorporated into the design because a higher current, which provides a more stable background arc, is preferred when the arc

voltage is higher. In this circuit, if $|I| < |RI_1|$, the output of A101 is positive at point 14, D_1 and D_6 are conducting, and the closed-loop circuit can operate. If $|I| > |RI_1|$, the output of A101 is negative, D_1 and D_6 are closed, and the closed-loop circuit is blocked off.

When the arc-operating point is on segment BC, only the loop of A101 is operating; the other four loops are automatically blocked because the arc voltage is high and current is low while it is on BC. For example, in loop A103, the output of A102 is positive, $|V| > |RV|$ and the output of A103 is negative. D_2 blocks off the loop. Diode D_7 is used to prevent electrical leakage from A102 to A103. In loop A104, the output is positive because $|I| < |RI_2|$ and thus D_3 blocks off the loop. In loop 106, the output of A105 is positive and the output of A106 is negative because $|V| > |RV_2|$. Thus D_4 blocks off the loop. In loop A107, its output is positive because $|I| < |RI_3|$ and thus D_5 blocks off the loop.

(iv) *Segment CD.* The circuit for the segment CD consists of A102, A103, A108, and A109. A102 and A103 are the main feedback loops for segment CD. There are four inputs for A102, namely, the reference voltage RV_1 that corresponds to the voltage at point C, the arc-voltage feedback signal V, the wire-feed rate signal M, and the arc-current feedback signal (see point 23). The current-feedback signal is supplied by A108 and A109 (see the square frame 21 in the figure). The two functions of this circuit are to feed the current signal to A102 according to a preselected proportion and to feed the current signal to A102 after it is differentiated. Among the four inputs, RV_1 and V configure the constant-voltage feedback loop. The proportional current signal is used to change the slope of the constant-voltage output characteristic. If I is positive, the slope is rising and if I is negative, the slope is drooping. In the present design, a positive signal is used. Therefore the CD segment rises. The wire-feed rate signal is used to adjust the magnitude of the voltage at C. If the wire-feed rate is increased, the arc current and voltage will increase; therefore segment CD should be raised. The wire-feed rate signal comes out from the terminal of the driving motor (M_1,M_2) via an optical coupler L101 to A102. The negative, differentiated arc-current signal (see frame 22 inside frame 21 in Fig. 5.16), or $\left(-\frac{dI}{dt}\right)$, feeds to A109. Therefore, when C jumps to D′, the welding current is increasing, $\frac{dI}{dt}$ is positive, the input to A109 is negative $\left(-\frac{dI}{dt}\right)$, and its output is positive, which makes the slope of CD steeper. That increases the speed of transfer of C to D′. When the welding current becomes stable, $\frac{dI}{dt} = 0$, and circuit 22 no longer plays a role. Similarly, when the arc-operating point jumps from D to C′, the welding current decreases,

$\frac{dI}{dt}$ is negative, the input to A109 from 22 is positive, and its output 23 is negative. Therefore, the slope droops very steeply and thus the welding current decreases very fast. When the welding current stabilises, circuit 22 no longer operates. In both cases, the output characteristics become steeper. Obviously, when the arc-operating point is at C, it scans counterclockwise around the axis at C. When the arc-operating point is at D, it scans clockwise around the axis at D. The circuit does not function during either the background- or the pulsed-current periods. From the description above, it is known that only points C and D of segment CD play a role in controlling the arc; they limit the minimum arc length L_2 (point C) and the maximum arc length L_1 (point D). When the arc-operating point reaches these points, it triggers a circuit so that CD scans and pushes the arc-operating point so that it jumps over. In other words, segment CD, in fact, does not exist; the arc-operating point does not move or stay on this segment. The aim of designing the segment CD is mainly to limit the arc lengths L_1 and L_2. The proportion of the feedback-current signal determines the parameters of this segment.

How the feedback loop is automatically selected for the segment CD is described in the following text. When the arc-operating point reaches C, the welding current increases and exceeds the magnitude of point C, the input to A101 $|I| > |RI_1|$, its output 14 is negative, and D_1 automatically blocks the feedback loop. In the circuit of A104, because the input $|I| < |RI_2|$ its output at 16 is positive, and D_3 also blocks the circuit. In the circuit of A106, because the reference voltage RV_2 is lower than the voltage of segment CD, the output of A105 is negative, D_8 blocks it, and the output of A106 is 0. In the circuit of A107, the output of point 18 is positive because $|RI_3| > |I|$, and D_5 blocks the circuit. Because the arc-operating point is on the segment CD, only the circuit of A103 operates; the other four circuits are automatically blocked.

(v) *Segment DE.* While the arc-operating point is jumping from C to D′, the circuit A103 controls the output characteristic of the power source. When the arc-operating point reaches D′, because the feedback signal of A104 changes from $|I| > |RI_2|$, its output at 16 changes from positive to negative, and D becomes conducting. In this case, although both A103 and A104 are conducting, the potential at 19 is clamped by the output of A104 at 16 because there is a resistance connected between 15 to D_2. Therefore A104 controls the circuit. There are two inputs for A104, namely I and RI_2. Therefore the output of the power source has constant-current characteristics.

In this case, the output of A101 is negative and D_1 blocks the circuit. The output of A105 is positive because its input $|V| > |RV_2|$. D_8 blocks the circuit and the output of 106 at 17 is zero. The output of A107 at 18 is positive because its input $|I| < |RI_3|$, D_5 blocks the circuit. It can be seen that only A104 operates to provide control; A101, A106, and A107 are all blocked. A103 also does not operate because of clamping by A104.

(vi) *Segment EF.* The segment EF is controlled by A105 and A106. The inputs to A105 are V and RV_2. In the present design, $RV_2 < RV_1$. When the arc voltage decreases to point F, because $|V| < |RV_2|$, the output of A105 is negative, D_8 is conducting, the output of A106 at 17 is positive, and D_4 becomes conducting. Therefore, the loop provides control. Because the inputs to A105 are V and RV_2, the output of the power source has a constant-voltage characteristic.

In this case, the output of A101 at 14 is negative because $|I| > |RI_1|$ and D_1 blocks the circuit. The output of A103 is positive, but because the input to A104 $|I| > |RI_2|$, its output at 16 is negative, and D_3 clamps the potential so that the output of D_2 plays no role. The output of A107 is positive because $|I| < |RI_3|$ and D_5 blocks the circuit. Only A106 functions and controls the circuit.

(vii) *Segment FG.* When the arc current reaches the segment FG, the output of A107 at 18 is negative because $|I| > |RI_3|$ and D_5 is conducting. Similar to the segment DE, the potential at 18 clamps the potential of 20, and A107 operates and controls the circuit. Under this condition, the output of A101 is still negative, the output of A106 is negative and clamps the output of D_2, and D_6 blocks all three feedback loops above it. None of the loops except A107 provides a control function.

Summary: From the description above, it is seen that the principle of the QH-ARC 103 control method is that five feedback-control loops are connected together by a network of diodes so that only one feedback loop at a time can be automatically selected for control of the power-source output characteristic while the others are automatically blocked. In the meantime, in transferring from one circuit to another, good dynamic properties without breach or overlaps of the output-characteristic segments can be obtained. This is the essential and key point of the invention.

5.3.2.4 Extension of the multi-segment circuit

In the QH-ARC 103 control method described above, the output is divided into five characteristics. This concept was developed especially for a new pulsed MIG welding process. From the view of electronic circuitry, it is possible to incorporate an arbitrary number of segments, as shown in Fig. 5.17. The prerequisite is that the reference value of each segment must obey the following rules. The first is that constant-current and constant-voltage characteristics should be alternated. The second is that the reference values for constant-current characteristics should be successively increased, i.e. $RI_1 < RI_2 < \cdots < RI_n$. The third is that the reference values for the constant-voltage characteristics should be successively decreased, i.e. $RV_1 > RV_2 > \cdots > RV_n$.

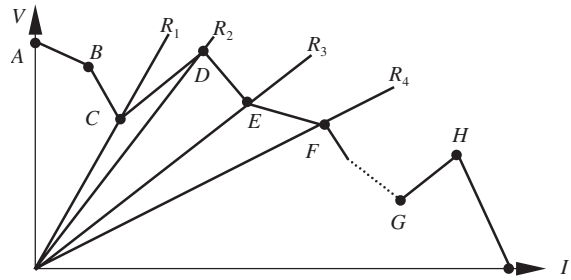

5.17 Extension of multi-segment output characteristics

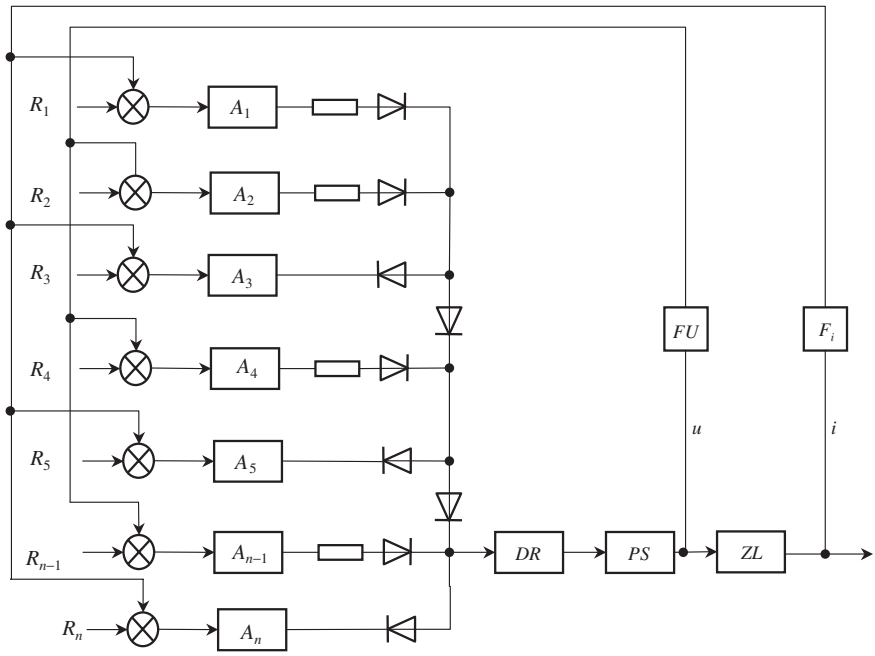

5.18 Extension of the multi-segment control circuit

In the circuit for the constant-current characteristic, the voltage-feedback signal can be added so that the slope of the constant-current characteristic can be inclined to an arbitrary angle. In the circuit for the constant-voltage characteristic, the current signal can be added so that the slope of constant-voltage characteristic can be positive or negative. All of the feedback loops are connected by a diode network so that only the circuit of the segment on which the arc-operating point is working is conducting while all other loops are blocked. Figure 5.18 is the configuration of the circuit. In this

figure, A_3 corresponds to A104 of Fig. 5.15, which plays the role of clamping. A_5 and A_n also play the same role of clamping as that of A107 in Fig. 5.15. It can be concluded that the author's invention is not only significant for developing a new arc-control method and welding process but also is instructive for the approach to developing a different kind of welding power source.

5.3.2.5 Circuit for the wire-feed mechanism

The circuit diagram for the wire feed mechanism is shown in Fig. 5.19. The motor T is driven by the transistor Tr601, which is driven by A602. There are two modes of wire feeding: constant wire-feed rate and pulsed wire-feed rate. When the switch is at C_1 and C_2, the mode is constant-feed rate, which is regulated by the resistor W601. When the switch is at P_1 and P_2, the mode is pulsed wire-feed. The control circuit consists of a multi vibrator T501, T502 and an electronic switch SW501. The pulsed wire-feed rate can be adjusted by potentiometers W503 and W504, as well as by the operator control. The durations of the higher- and lower-level feed rates are adjusted by potentiometers W501 and W502, respectively, and also by the operator. A603 is used for overload protection of the motor when the input current to the armature exceeds a certain limit. The signal from resistor 603 is fed to A603, which produces a negative potential, clamps Tr602, and cuts off its output. The potentials from terminals M_1 and M_2 are fed to the characteristic circuit to modify the parameters of the output segments, smooth the welding process under arbitrary conditions of wire-feed rate, and obtain a stable arc and spray transfer.

5.4 Mathematical analysis of arc operating-point movement

In conventional welding processes, the movement of the arc-operating point is due to the disturbance and restoration of the arc length while the disturbance happens, or due to the variation of wire-feed rate and wire-melting rate. This was discussed in detail in Chapter 1. In this section, the movement of the arc-operating point while the arc is on a steeply rising or scanning output characteristic of the power source is discussed.

In previous sections, the general idea of the segmented output characteristic and its function for limiting the upper and lower arc length to speed up the movement of the arc-operating point during transfer of pulsed to background current or vice versa was explained. Several question that remain unanswered are: Why not use a switching circuit to transfer the pulsed current to the background current or vice versa using a triggering

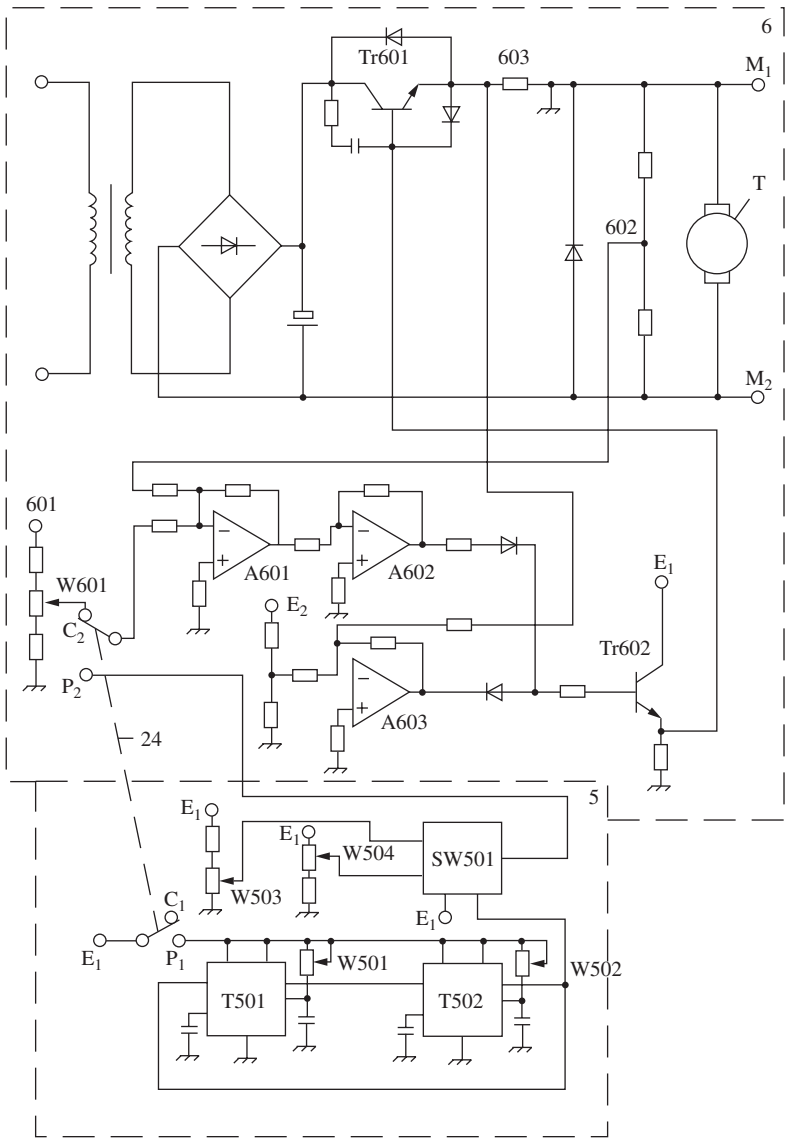

5.19 Wire-feed mechanism circuit

method based on preset upper and lower limits of the arc length? What is the difference between the QH-ARC 103 method and the triggering method? How is the QH-ARC 103 method superior? The discussion below about the arc-operating point movement under a rising slope and scanning output characteristics answers these questions.

5.4.1 On steep rising output characteristics

Assuming that the wire melting is continuous and neglecting the influence of wire-extension variation due to changes of arc voltage and melting rate, then the rules of arc operating-point movement on a steep rising output characteristic can be expressed by the following equations:

$$\begin{aligned} U_p &= L\frac{\mathrm{d}i}{\mathrm{d}t} + R_i + U_a \\ U_p &= U_0 + k_d i \\ U_a &= k_a L_a + K_p i + U_c \\ V_m - V_f &= \frac{\mathrm{d}L_a}{\mathrm{d}t} \\ V_m &= k_m i \end{aligned} \qquad [5.3]$$

where k_d is the rising slope characteristic and the other symbols are the same as mentioned in Section 1.2. The solution of Eq. [5.3] can be written as

$$i = Ae^{\lambda_1 t} + Be^{\lambda_2 t} + \frac{V_f}{k_m} \qquad [5.4]$$

where

$$\lambda_1 = \frac{-(R + k_p - d_d) + \sqrt{(R + k_p - k_d)^2 - 4Lk_a k_m}}{2L}$$

$$\lambda_2 = \frac{-(R + k_p - d_d) - \sqrt{(R + k_p - k_d)^2 - 4Lk_a k_m}}{2L}$$

If the initial conditions are $i = i_0$, $\frac{\mathrm{d}i}{\mathrm{d}t} = 0$, while $t = 0$, then

$$A = \frac{\lambda_2(k_m i_0 - V_f)}{(\lambda_2 - \lambda_1)k_m} \qquad B = \frac{-\lambda_1(k_m i_0 - V_f)}{(\lambda_2 - \lambda_1)k_m}$$

Therefore, in the case that $k_d < R + k_p$, λ_1 λ_2 are negative and the equation of arc movement is convergent; its steady value is $i = \frac{V_f}{k_m}$. In the case that $k_d = R + k_p$, the system is in a critical stable state, and in the case that $k_d > R + k_p$, the equation of arc movement is divergent, the arc operation point is unstable, and there is no steady value.

If the output characteristic is very steep, i.e. $k_d >> R + k_p$, the current changes very fast, the point moves very quickly, and the influence of melting rate can be neglected or need not be considered. Assuming that $k_m = 0$, then the solution of Eq. [5.3] is

$$i = \frac{(U_0 - k_a L_{a0} - u_c)(R + k_p - k_d) - k_a V_f L}{(R + k_p - k_d)^2} + \frac{k_a V_f}{R + k_p - k_d} t$$
$$+ \frac{i_0 (R + k_p - k_d)^2 - (U_0 - k_a L_{a0} - U_c)(R + k_p - k_d) + k_a V_f L}{(R + k_p - k_d)^2} e^{-\frac{R + k_p - k_d}{L} t} \quad [5.5]$$

Let $U_{a0} = k_a L_{a0} + U_c + i_0(R + k_p)$, $U_{p0} = U_0 + i_0 k_d$

$$\frac{\mathrm{d}i}{\mathrm{d}t} = \frac{k_a V_f}{(R + k_p - k_d)} + \left[\frac{k_a V_f}{k_d - (R + k_p)} - \frac{U_{a0} - U_{p0}}{L} \right] e^{\frac{R + k_p - k_d}{L} t} \quad [5.6]$$

The direction of movement is determined by the initial conditions:

When $U_{a0} \geq U_{p0} + \frac{k_a V_f L}{k_d - (R + k_p)}$, $\frac{\mathrm{d}i}{\mathrm{d}t} < 0$, point moves towards left.

When $U_{a0} < U_{p0} + \frac{k_a V_f L}{k_d - (R + k_p)}$, $\frac{\mathrm{d}i}{\mathrm{d}t} > 0$, point moves towards right.

When $t = 0$, the arc point is just on the steep output characteristic, or $U_{a0} = U_{p0}$, then

$$i = i_0 - \frac{k_a V_f L}{(R + k_p - k_d)^2} + \frac{k_a V_f}{R + k_p - k_d} t + \frac{k_a V_f L}{(R + k_P - k_d)^2} e^{-\frac{R + k_p - k_d}{L} t} \quad [5.7]$$

$$\frac{\mathrm{d}i}{\mathrm{d}t} = \frac{k_a V_f}{R + k_p - k_d} + \frac{k_a V_f}{R + k_p - k_d} e^{-\frac{R + k_p - k_d}{L} t} \quad [5.8]$$

Figure 5.20 illustrates the current change calculated from the derived equation of the arc-operating point under a steep rising output character-

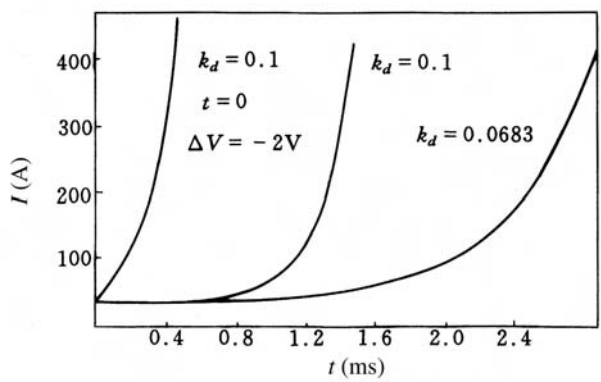

5.20 Current change of the arc under a steep rising output characteristic (calculated value)

Table 5.2 Arc and power-source parameters

R	23.56 mΩ	k_a	0.716 V/mm	V_f	65.8 mm/s
L	10 μH	U_c	14.7 V	i_0	35 A
U_0	19.8 V	k_p	0.0245 V/A		

Table 5.3 Arc-current increase rate under a steep-rising output characteristic

i (A)	38~85	85~135	135~185	185~235	235~285	285~335	335~385	k_d
Δt (ms)	1.1	0.12	0.08	0.056	0.04	0.036	0.03	0.1 V/A
$\Delta t/\Sigma t$	75%	8.2%	5.4%	3.8%	2.7%	2.5%	2%	
Δt (ms)	1.92	0.32	0.2	0.12	0.11	0.085	0.08	0.0683 V/A
$\Delta t/\Sigma t$	67.6%	11.3%	7%	4.2%	3.9%	3%	2.8%	

istic for different initial conditions. Table 5.2 gives the arc and power-source parameters used for the calculation.

From Fig. 5.20, it can be seen that the current increases very slowly initially; after some time, it increases rapidly. Table 5.3 quantitatively shows the increase of current from 35 A to 385 A under different conditions. From the table, it is seen that for $k_d = 0.1$ V/A, it takes 1.1 ms for the current to rise from 35 A to 85 A, which is 75% of the total time for the current rise (1.46 ms); it takes only 0.03 ms for the current to rise from 335 A to 385 A (also a 50 A increment), which is only 2% of the total time. The reason the current rises slowly initially is because there is a small difference between U_p and U_a; term 3 and term 4 of Eq. [5.7] offset each other. At this stage, if there is an arc-length disturbance so that the voltage difference is increased, the current-rise time can be greatly shortened. The curve at the left side of Fig. 5.20 is the current rise when the arc voltage is reduced 2 V by a random disturbance; obviously it is greatly shortened.

In order to observe the behaviour of the movement of the arc-operating point, an oscillograph was used to record the $I - t$ diagram, which is shown in Fig. 5.21. Obviously the measured results are very close to the calculated values shown in Fig. 5.20. For example, for $k_d = 0.1$, it took 0.6 ms for I to increase from 40 A to 200 A when recorded by the oscillograph, while the calculated value was 0.64 ms.

5.4.2 Scanning-output characteristics

In the QH-ARC 103 control method, a scanning-output characteristic is used. According to the electrical-circuit design, the relationship between current and voltage can be expressed by the following equation:

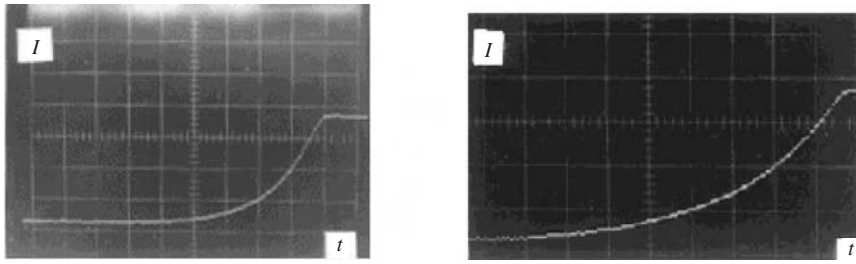

a) k_d = 0.1V/A b) k_d = 0.0683V/A

Abscissa t: 0.2 ms/Div, Ordinate I: 100 A/Div

5.21 Current increase recorded by an oscillograph

$$U_p = U_0 + k_d i + k_d T_1 \frac{\mathrm{d}i}{\mathrm{d}t} - T_2 \frac{\mathrm{d}U_p}{\mathrm{d}t} \qquad [5.9]$$

Similar to results given in the last section, assuming that wire melting is continuous and neglecting the influence of wire extension, the rule that governs the arc operating-point movement can be expressed by the following equations:

$$\begin{cases} L\dfrac{\mathrm{d}i}{\mathrm{d}t} + U_a + iR = U_p \\ U_p = U_0 + k_d i + k_d T_1 \dfrac{\mathrm{d}i}{\mathrm{d}t} - T_2 \dfrac{\mathrm{d}U_p}{\mathrm{d}t} \\ \dfrac{\mathrm{d}L_a}{\mathrm{d}t} = V_m - V_f \\ U_a = k_a L_a + k_P i + U_c \\ V_m = k_m i \end{cases} \qquad [5.10]$$

Because the duration of movement is very short, the wire in fact does not have time to melt, so it can be assumed that $V_m = 0$ and the solution of the equations is then obtained as follows:

$$i = D - BM + Mt + C_1 e^{\lambda_1 t} + C_2 e^{\lambda_2 t} \qquad [5.11]$$

where

$$\lambda_1 = \frac{-(RT_2 + k_p T_2 + L - k_d T_1)}{2T_2 L} + \sqrt{\left(\frac{RT_2 + k_p T_2 + L - k_d T_1}{2T_2 L}\right)^2 - \frac{R + k_P - k_d}{T_2 L}}$$

$$\lambda_2 = \frac{-(RT_2 + k_p T_2 + L - k_d T_1)}{2T_2 L} - \sqrt{\left(\frac{RT_2 + k_p T_2 + L - k_d T_1}{2T_2 L}\right)^2 - \frac{R + k_P - k_d}{T_2 L}}$$

$$B = \frac{RT_2 + k_pT_2 + L - k_dT_1}{R + k_p - k_d},\ M = \frac{k_aV_f}{R + k_p - k_d},\ D = \frac{k_aV_fT_2 + U_0 - k_aL_{a0} - U_c}{R + k_p - k_d}$$

If $i = i_0$, $\frac{\mathrm{d}i}{\mathrm{d}f} = 0$; when $t = 0$, then

$$C_1 = \frac{(i_0 + BM - D)\lambda_2 + M}{\lambda_2 - \lambda_1},\quad C_2 = \frac{-(i_0 + BM - D)\lambda_1 - M}{\lambda_2 - \lambda_1}$$

For different control parameters, there can be three different modes of movement:

let: $$\delta = \frac{RT_2 + k_pT_2 + L - k_dT_1}{2T_2L},\quad N = \sqrt{\frac{R + k_p - k_d}{T_2L}}$$

then: $$\lambda_1 = -\delta + \sqrt{\delta^2 - N^2},\quad \lambda_2 = -\delta - \sqrt{\delta^2 - N^2}$$

(i) In the case that $\delta > 0$, the solution is convergent, the arc point moves convergently.

(ii) In the case that $\delta < 0$, $\delta^2 > N^2$, the solution is divergent and the arc point moves divergently in one direction.

(iii) In the case that $\delta < 0$, $\delta^2 < N^2$ then

$$\lambda_{1,2} = -\delta \pm j\sqrt{N^2 - \delta^2} = -\delta \pm j\omega$$

The solution of Eq. [5.10] can be written as

$$i = D - BM + Mt + Ce^{-\delta t}\sin(\omega t + \theta) \qquad [5.12]$$

where $$\begin{cases} C_1 + C_2 = C\sin\theta \\ j(C_1 - C_2) = C\cos\theta \end{cases}$$

Equation [5.12] clearly states that the arc point will oscillate divergently with a sinusoidal waveform. To confirm this result, the author conducted experiments with proper setting of the parameters so that they conformed to the conditions of (iii). The trajectory of the arc-operating point on the $U - I$ plane and the current waveform on the $I - t$ plane were recorded using an oscilloscope. Figures 5.22 and 5.23 are the oscillograms that demonstrate that the experimental results fully coincide with the theoretical derivation.

According to case (ii), the conditions for divergent movement of the arc-operating point in one direction are

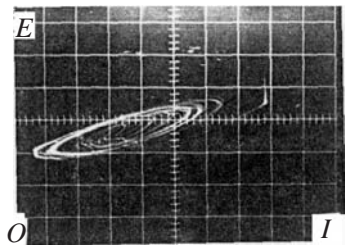

Abscissa I: 50 A/Div, Ordinate U: 10 V/Div

5.22 Trajectory of the arc-operating point during oscillation

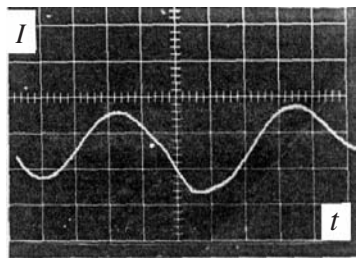

Abscissa t: 0.2 ms/Div, Ordinate I: 100 A/Div

5.23 Current waveform during oscillation of the arc

$$RT_2 + k_p T_2 + L - k_d T_1 < 0$$

$$(RT_2 + k_p T_2 + L - k_d T_1)^2 > 4T_2 L(R + k_p - k_d) \qquad [5.13]$$

These conditions can be satisfied using a proper set of the control parameters. The speed that the arc-operating point moves can also be adjusted by varying the magnitude of the parameters. Figure 5.24 gives the calculated results based on three different groups of control parameters; the circuit parameters are the same as those given in the previous section. Figure 5.25 shows the current change recorded by an oscilloscope. The figures are very similar to one another, which demonstrates that the theoretical analysis is correct. For example, curve (b) of Fig. 5.24 shows that 0.76 ms was required for the current to rise from 40 A ~ 300 A; the oscillogram (b) of Fig. 5.25 shows that 0.72 ms was required. Similarly, curve (a) of Fig. 5.24 shows that 0.72 ms was required for the current to rise from 80 A ~ 300 A while oscillogram (a) of Fig. 5.25 shows 0.8 ms.

From Eq. [5.13] it is known that use of scanning-output characteristics can lessen the requirement for the characteristic slope to speed up the movement of the arc-operating point. For example, in the case where $T_1 = 4.7$ ms, $T_2 = 1.54$ ms, and the arc and circuit parameters are those shown in Table 5.2, the required slope of the characteristic for divergent movement of the arc in one direction is $k_d \geq 0.026$ V/A. A welding experiment

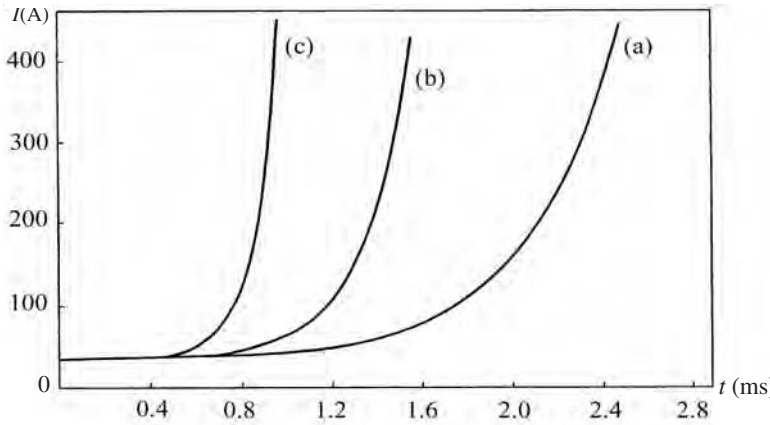

(a) $k_d = 0.034$, $T_1 = 6.1$ms, $T_2 = 2.56$ms
(b) $k_d = 0.034$, $T_1 = 4.7$ms, $T_2 = 1.5$ms
(a) $k_d = 0.0474$, $T_1 = 4.7$ms, $T_2 = 1.5$ms

5.24 Current changes for different parameters of scanning-output characteristics (calculated values)

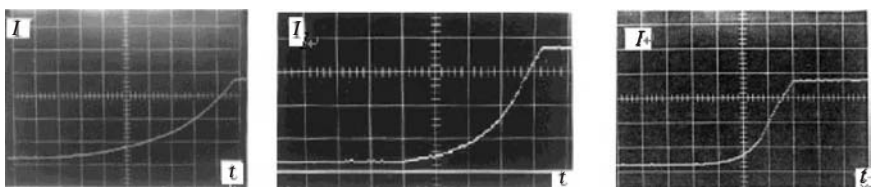

5.25 Oscillograms of current changes (by experiment)

demonstrated that, at this value of k_d, the speed of movement of the arc-operating point was fast enough between 35 A ~ 400 A that globular-droplet transfer did not develop. Under the same condition, if only a steeply rising characteristic was applied, a minimum value of $k_d = 0.0613$ V/A was required to avoid globular transfer.

From this analysis, it is known that the minimum upper limit of the arc length is determined by k_d (its intersection point with I_p). According to Eq. [5.9], the arc voltage is $U_p = U_0 + k_d I_p$. The lower limit of the arc voltage is U_0, and the minimum difference between the two limits is $\Delta U_p = k_d I_p$. This means that if the value of k_d is larger, the difference between the two limits of the arc voltage, and consequently T_b, T_p, also are larger. In that case, low-frequency sparkling of the arc can happen. Applying a scanning-output characteristic can speed up the movement of the arc-operating point, and avoid globular transfer and low-frequency sparkling.

In addition, the use of a scanning-output characteristic can improve the adaptability of the system to variations of loop resistance. If $k_d = 0.034$ V/A

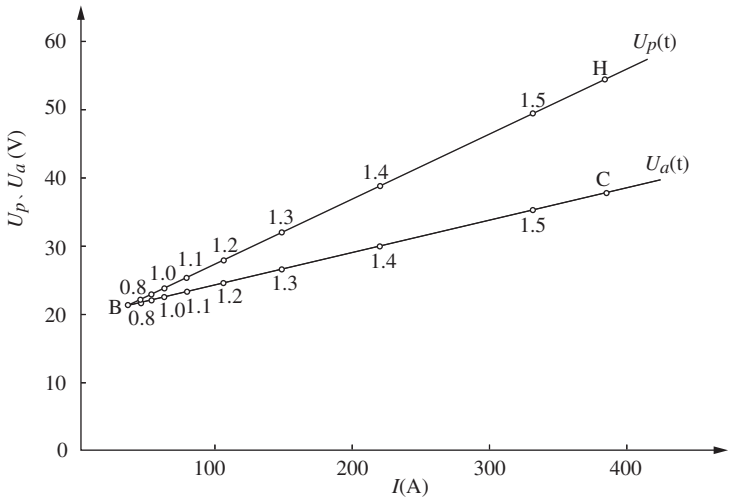

5.26 Moving speed of the arc-operating point (The parameters of the power-source output characteristics are the same as in Fig. 5.24b)

and the other parameters are as shown in Table 5.2, the resistance that can satisfy Eq. [5.13] for speeding up the arc operating-point movement is $R \leq 44\,\text{m}\Omega$, which is much higher than the resistance of a normal welding loop. That means the resistance of the welding loop has no influence on the arc operating-point movement while it passes through the globular-transfer region.

Figure 5.26 illustrates the speed that the arc-operating point moves under the action of the scanning-output characteristic and the corresponding voltage output of the power source on the $U - I$ plane. In this figure, each time division is 0.1 ms. From the figure it can be seen that $U_p(i)$ is approximately a straight line, which was proved by actual experiments. Also from this figure, it is known that the arc-operating point moves very slowly initially. It takes 1.0 ms for the current to rise from 35 A to 60 A because the potential difference $(U_p - U_a)$ is very small. In Eq. [5.11], the increase of items 4 and 5 is small. Later, the arc point moves faster; it takes only 0.35 ms for the current to rise from 100 A to 400 A. The rule mentioned above has been experimentally verified.

Obviously, the moving speed of the arc-operating point depends on the parameters of the power-source output characteristics. Table 5.4 shows the time required for various values of current change for the parameters shown in Fig. 5.24. The movement rule mentioned above is very advantageous for controlling the arc. Assume that point B in Fig. 5.26 corresponds

Table 5.4 Arc-current increase rate under scanning-output characteristics

***i* (A)**	38~85	85~135	135~185	185~235	235~285	285~335	335~385	Parameters
Δ*t* (ms)	1.66	0.26	0.16	0.11	0.088	0.072	0.06	$K = 0.034$
Δ*t*/Σ*t*	69%	10.8%	6.6%	4.6%	3.7%	3%	2.5%	$T_1 = 6.1$
								$T_2 = 2.56$
Δ*t* (ms)	1.12	0.144	0.088	0.056	0.048	0.04	0.03	$K = 0.034$
Δ*t*/Σ*t*	73%	9.4%	5.8%	3.7%	3.1%	2.6%	2%	$T_1 = 4.7$
								$T_2 = 1.5$
Δ*t* (ms)	0.75	0.072	0.044	0.032	0.028	0.024	0.016	$K = 0.047$
Δ*t*/Σ*t*	78%	7.5%	4.6%	3.3%	2.9%	2.5%	1.7%	$T_1 = 4.7$
								$T_2 = 1.5$

to point C of the output characteristic (segment CD, see Fig. 5.8) When the arc is approaching this point, the arc length is at its lower limit; it will move toward the right until it reaches D′. Because it moves very fast in the later stage, it almost bypasses the globular-transfer current region; no globular transfer can happen. On the other hand, in the initial stage, because $(U_p - U_a)$ is small, any random interference can change the direction of movement. For example, if the arc length is abruptly shortened a small amount, the potential difference increases, which would speed up the transition of the arc-operating point to the point D′. If the arc length is abruptly enlarged a small amount, the voltage difference $(U_p - U_a)$ can become negative and the arc-operating point can return to C. Therefore, the system has good dynamic properties on the one hand, and good resistance to random disturbances on the other. This is a significant benefit of the QH-ARC 103 control method over conventional arc-length control that uses electronic switching.

From the analysis in Section 5.3.1, it is known that the arc operating-point movement is the trajectory of the leading and trailing pulse edges. Therefore these edges are different from those of the pulse in normal pulsed MIG welding controlled by an activated switching method. Figure 5.29 shows the current waveform of the pulse in this control method. It can be seen that at its front edge it rises slowly at first and then rapidly. Similarly, at its back edge, it falls slowly at first and then rapidly. Moreover, the durations of both the front and back edges are small. Experiments show that arc noise comes mainly from the front and back edges of the pulse. Therefore, proper design of the output characteristic and the $\frac{\mathrm{d}i}{\mathrm{d}t}$ values at the front and back edges can decrease arc noise and produce a soft, pulsed MIG arc sound.

5.4.3 A second function of the scanning-output characteristic

Before proceeding with the text of this section, it must be pointed out that, in previous sections, the principle of the QH – ARC 103 method was illustrated for convenience using the static-output characteristic of the power source. The segment CD was used to control the arc length; C represented the lower limit and D represented the upper limit. The scanning-output characteristic was described as a measure for speeding-up the movement of the arc-operating point from C to D′ or from D to C′. But, as mentioned in last section, the scanning-output characteristic has another important function: stabilisation of the pulse length and the arc. Due to the function of the scanning-output characteristic, point D is, in fact, not fixed. This phenomenon is discussed in this section; this is, actually, a precise and thorough explanation of the control method.

In the following, the function of the scanning characteristic on arc control when the arc current $i = I_P$, or when it is on the segment DE, is analysed:

(i) *Movement of scanning-output characteristic on the segment DE*. When the arc-operating point arrives at segment DE, $i = I_P$. Substituting $i = I_P$ into Eq. [5.9], the following differential equation can be obtained:

$$T_2 \frac{\mathrm{d}U_p}{\mathrm{d}t} + U_p = U_0 + k_d I_p$$

If $U_P = U_{P0}$ when $t = 0$, then the solution of the equation is

$$U_p = U_0 + k_d I_P + [U_{p0} - (U_0 + k_d I_P)]e^{-\frac{t}{T_2}} \qquad [5.14]$$

Equation [5.14] represents the rule of scanning-characteristic movement when the arc-operating point is on the segment DE, or, more explicitly, the movement of the intersection point of the scanning-output characteristics with the segment DE, i.e. the intersection point of S_1 and DE: see Fig. 5.8.

(ii) *Movement of the arc-operating point on segment DE*. When the arc-operating point reaches DE, the wire melts in the droplet-transfer mode at the current I_P. The arc length gradually increases so that the arc-operating point ascends along I_P until it meets the descending intersection point of the scanning-output characteristic with the segment I_P. Then, the pulse period ends and the background period starts.

The ascending speed of the arc-operating point depends on the melting rate of the wire during the pulse period. Factors that affect the melting rate are reported differently in contemporary literature. Therefore, it is valuable to study this phenomenon further. The melting rate was measured directly

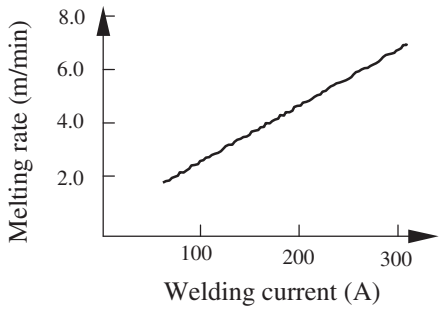

5.27 Relationship between melting rate and average welding current

by the author using an x, y recorder. The average welding-current (the pulsed current was filtered) signal was fed to the x-axis and the wire feed-rate signal, which represents the melting rate, was fed to the y-axis. The torch-to-work distance was kept unchanged but the arc length was increased in accordance with the welding current. The pulsing parameters were changed in accordance with the wire-feed rate. Both the average welding current and the melting rate were recorded. The results are shown in Fig. 5.27. It can be seen that the wire-melting rate was almost proportional to the average current and was independent of the pulsing parameters. The pulses visible on the line in Fig. 5.27 were due to filtering of the welding current. When the torch-to-work distance was within a certain range, the melting rate increased with the increase of wire extension, but only very slightly.

In the background-current period, the wire does not melt but it is preheated. This means that the duration T_b and current I_b affect the melting rate. The melting rate during the pulse period can be derived from Fig. 5.27.

Assuming that the average melting rate is k_m, which can be found from Fig. 5.27, let the melting rate during the pulse period be k_{mP}, as the melting is in fact taking place during this period. Then, the following equations can be written:

$$k_m I(T_P + T_b) = k_{mP} I_P T_P$$

$$k_{mP} = \frac{k_m I(T_P + T_b)}{T_P I_P}$$

as

$$I = \frac{I_P T_P + I_b T_b}{T_P + T_b}, \quad T_b = \frac{T_P(I_p - I)}{I - I_b} \qquad [5.15]$$

$$k_{mP} = \frac{k_m I(I_p - I_b)}{(I - I_b) I_p} \qquad [5.16]$$

From Eq. [5.16] it can be seen that if I_b, I_p, and I remain unchanged, or I_b and I_p and the pulse and background periods remain unchanged, then k_{mP} also will remain unchanged. Therefore, the change of the arc length during the pulse period can be calculated:

The arc length during the pulse period is

$$L_{ap} = L_{a0} + k_{mP} I_P t - V_f t \qquad [5.17]$$

Substituting Eq. [5.16] and $V_f t = k_m I$ into Eq. [5.17], we obtain

$$L_{ap} = L_{a0} + k_m I \frac{I_P - I}{I - I_b} t = L_{a0} + V_f \frac{I_P - I}{I - I_b} t \qquad [5.18]$$

$$U_{aP}(t) = k_a L_{a0} + U_c + (k_p + R) I_P + k_a V_f \frac{I_P - I}{I - I_b} t \qquad [5.19]$$

Equation [5.19] represents the arc-voltage increment while the arc-operating point ascends along segment DE.

(iii) *Pulse Width*. In the QH-ARC 103 control method, the pulse width is determined by the time needed for the descending point of the scanning-output characteristics to meet the ascending point of the arc characteristic on the segment DE. Mathematically, this can be expressed as:

$$U_p = U_0 + k_d I_P + [U_{p0} - (U_0 + k_d I_P)] e^{-\frac{t}{T_2}}$$

$$U_{ap} = k_a L_{a0} + U_c + (k_p + R) I_P + k_a V_f \frac{I_P - I}{I - I_b} t \qquad [5.20]$$

when $U_P = U_{aP}$, $t = T_P$

If the parameters of the arc and the circuit are as shown in Table 5.5, Eq. [5.20] can be calculated and illustrated as in Fig. 5.28, in which $U_p(t)$ is the descending voltage of the output characteristic along the segment DE and $U_{ap}(t)$ is the ascending voltage of the arc along the segment DE. The intersection point of these two curves determines the pulse width T_P. Figure 5.29 is the oscillogram of the pulsed current obtained experi-

Table 5.5 Arc and circuit parameters

k_d	0.034 V/A	U_0	21 V	I_b	30 A
R	0.019 Ω	k_m	0.43 mm/A.s	T_2	1.54 ms
k_p	0.0245 V/A	V_f	6.58 mm/s	U_{p0}	57 V
k_a	0.716 mm	I_p	385 A		

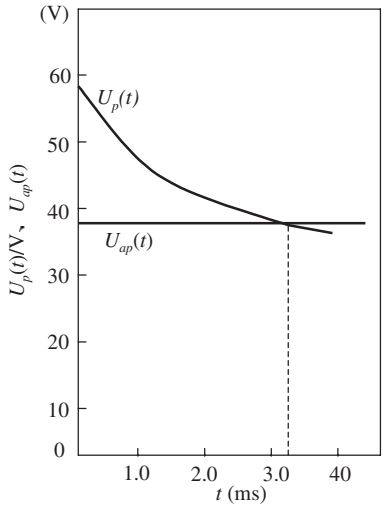

5.28 Control of the pulse width by the scanning-output characteristic

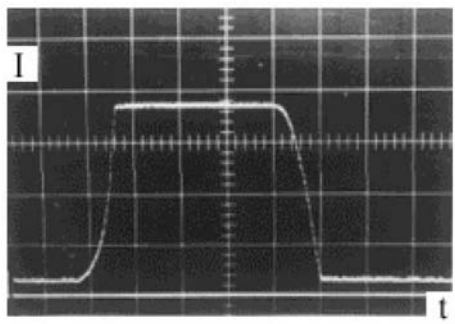

(100 A, 1 ms/Div)

5.29 Oscillogram of the pulsed current

mentally; it can be seen that the pulse width (width of the top horizontal line) is 3.4 ms. The figure corroborates the calculated value from Fig. 5.28.

After determining the pulse width T_P, the background width T_b can be obtained from the average current using Eq. [5.15]. The pulsed-current frequency is then $f = \dfrac{1}{T_P + T_b}$. The values of T_P, T_b, and f will adapt to changes of wire-feed rate and welding current. Experimental results show that for a wire diameter of 1.2 mm, the pulse frequency is in the range of 45 Hz~110 Hz for a welding-current range 80~300 A.

To compare the present control method to the arc-length threshold control method (i.e. when the pulsed current is switched on and off according to preset upper and lower arc-length thresholds), the pulsed-current frequency distribution range is discussed below:

Substituting $t = T_P$ into Eq. [5.18], one obtains

$$T_P = \frac{\Delta L_a (I - I_b)}{k_m I (I_P - I)} \qquad [5.21]$$

where $\Delta L_a = L_1 - L_2$, the difference between the two arc-length thresholds.

Because the wire does not melt during the background period, one obtains

$$T_b = \frac{\Delta L_a}{V_f} = \frac{\Delta L_a}{k_m I} \qquad [5.22]$$

$$f = \frac{1}{T} = \frac{1}{T_b + T_P} = \frac{k_m I (I_p - I)}{\Delta L_a (I_P - I_b)} = \frac{k_m I \; I_p - k_m I^2}{\Delta L_a (I_P - I)} \qquad [5.23]$$

If $\frac{\mathrm{d}f}{\mathrm{d}I} = 0$, one obtains $I = \frac{I_p}{2}$

and

$$\frac{\mathrm{d}^2 f}{\mathrm{d}I^2} = \frac{-2k_m}{\Delta L_a (I_p - I_b)} < 0$$

Therefore, the frequency has a maximum value at the average current $\frac{I_P}{2}$. It can be seen from Eq. [5.23] that the frequency depends on only two arc-length thresholds because the other parameter, such as k_m, I_P, I_b, cannot be changed. On the other hand, Eq. [5.21] shows that smaller values of ΔL_a give smaller values of T_P. However, too small a value of T_P is detrimental to achieving normal droplet transfer. The minimum value of ΔL_a should ensure a sufficient value of T_P and normal droplet transfer. It is known from experiments that the minimum value of T_P should be 3 ms. From Eq. [5.21] and the parameters given in Table 5.5, the minimum arc-length threshold difference can be obtained as ΔL_a = 1.0 mm. Using ΔL_a = 1.0 mm, T_P, T_b, and f can be calculated for different welding currents as shown in Table 5.6.

The data shown in Table 5.6 demonstrated that, for the same welding-current range, the pulse-frequency range is 23–11 Hz under the minimum arc-length threshold difference. Because there always are arc-length disturbances, the arc-length threshold difference should be much larger than 1.0 mm in order to ensure spray transfer. Therefore, the pulse frequency

Table 5.6 Pulse parameters under arc length threshold control

I (A)	T_P (ms)	T_b (ms)	f (Hz)
60	3.40	39.00	23.80
80	4.40	29.82	29.22
100	5.40	23.67	34.39
120	6.29	19.64	38.54
140	7.19	16.80	41.66
160	8.19	14.76	43.55
180	9.20	13.00	45.03
200	10.50	11.77	44.89
220	12.00	10.70	44.89
240	13.80	9.76	42.44
260	16.20	9.00	39.68
280	19.56	8.35	35.89
300	24.39	7.82	31.03
320	32.09	7.32	25.36
340	46.70	6.89	18.66
360	84.50	6.50	10.98

would be much lower than that given above. Such a low-frequency pulsed arc is harmful to people's sight. This phenomenon has been experimentally demonstrated.

(iv) *The influence of arc length and voltage disturbances on the stability of droplet transfer*. The application of scanning-output characteristics to control the pulse width can increase the stability of spray transfer. Figure 5.30 shows the change in the voltage of a scanning-output characteristic and the arc characteristics on segment DE. In the figure, two random arc-length or arc-voltage disturbances are shown (see $U_{ap}(t)$). Under normal conditions when there are no arc-length disturbances, the pulse width is T_p. In the following text, two control methods are compared, namely scanning-output characteristic control and arc-length threshold control.

Suppose that U_{aP2} and U_{aP1} are upper and lower arc-length thresholds, respectively. It can be seen from the figure that if the threshold method is applied, the first interference voltage peak of U_{aP} will trigger the circuit and the pulse width will be T'_P because the voltage peak is larger than the upper threshold U_{aP2}. Because T'_P is very small, spray transfer cannot occur. If scanning-output characteristics are used for pulse-width control, the first voltage peak will not result in misfiring of the circuit because the upper arc-length limit is $U_p(t)$, which is much larger than the first peak at that moment. It can be seen from the figure that the sooner the disturbance peak appears, the higher the value of $U_p(t)$ will be at that moment and the safer the control

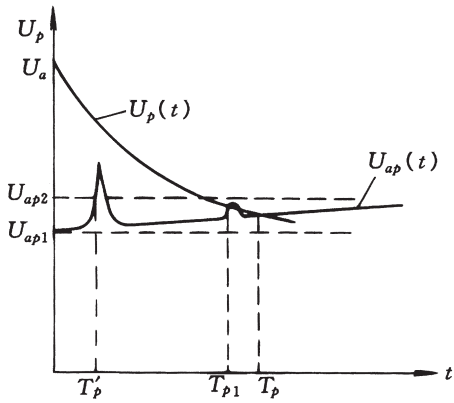

5.30 Pulse width under scanning-output characteristic control and threshold control

will be. An even higher voltage peak would not lead to improper triggering of the circuit, so that the pulse width T_p could be ensured. It also can be seen from Fig. 5.30 that after the arc stays on segment DE for a certain period of time, the scanning-output characteristic control will be more sensitive than the threshold-control method because, at this moment, the upper limit $U_p(t)$ is even lower than U_{ap2}. The second voltage-peak disturbance shown in the figure triggers the circuit in the former control circuit but not in the latter; the pulse width will be T_{p1}.

(v) *The adaptability of the control method to the change of welding-loop resistance*. Scanning-output characteristic control has much better adaptability to welding-loop resistance changes. It is known that the wire extension and welding-loop resistance inevitably vary during welding. Figure 5.31 shows that scanning-output characteristic control has stronger resistance to variation of the welding-loop resistance. The arc-length characteristic $U_{ap}(t)$ shifts upward when the welding-loop resistance increases. If the characteristic becomes $U'_{ap}(t)$, the pulse width decreases to T_{p1} with threshold control. If the characteristic becomes $U''_{ap}(t)$, which is higher than the upper threshold, the control system would not operate. Therefore, in this control method, either the pulse width will be greatly shortened or the control system will cease operating. In scanning-output characteristic control, the pulse width will be T_{P3} even when the arc-length characteristic moves up to $U''_{ap}(t)$, and the system can operate normally.

Quantitative analysis of the influence of the welding-loop resistance on the pulse width is discussed in the following paragraph:

When the arc-length threshold control method is used, the pulse width can be found from the following equations:

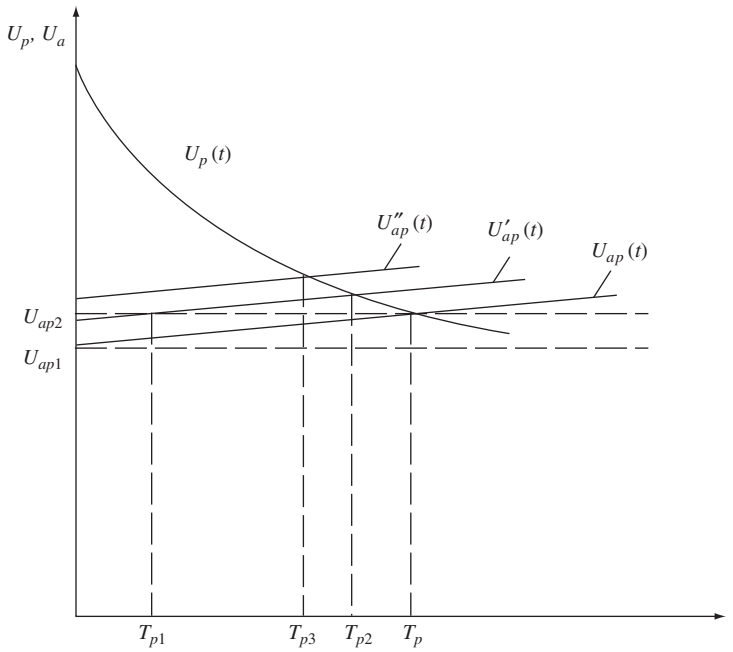

5.31 Influence of welding-loop resistance on pulse width

$$\begin{cases} U_{aP} = k_a L_{a0} + (k_p + R) I_P + U_c + k_a V_f \dfrac{I_P - I}{I - I_b} t \\ U_p = U_{p0} + \Delta U_P \\ \text{when} \quad U_{aP} = U_p, \; t = T_P \end{cases} \qquad [5.24]$$

From Eq. [5.24] one obtains $\dfrac{\mathrm{d}T_P}{\mathrm{d}R} = \dfrac{-I_P(I - I_b)}{k_a V_f (I_P - I)}$ [5.25]

Equation [5.25] represents the effect of variation of the welding-loop resistance R on the pulse width. Substituting the parameters of Table 5.5 into Eq. [5.25] gives

$$\frac{\mathrm{d}T_P}{\mathrm{d}R} = -4.16\,\mathrm{s}/\Omega$$

This means that an increase of the loop resistance of 1 mΩ decreases T_P by 4.16 ms. Obviously the loop-resistance variation produces a large change of pulse duration T_P. Consequently, it results in changes of T_b and f as well.

With scanning-output characteristic control, T_P is determined by Eq. [5.20] from which the following equation is obtained:

$$U_0 - k_a L_{a0} - U_c + (k_d - k_p) I_P - R I_P = k_a V_f \frac{I_P - I}{I - I_b} T_P - [U_{p0} - (U_0 + k_d I_P)] e^{-\frac{T_P}{T_2}}$$

Taking the derivative of both sides of the equation above with respect to the parameter R gives

$$\frac{\mathrm{d}T_P}{\mathrm{d}R} = \frac{-I_P}{k_a V_f \dfrac{I_P - I}{I - I_b} + \dfrac{U_{p0} - (U_0 + k_d I_P)}{T_2} e^{-\frac{T_P}{T_2}}} \qquad [5.26]$$

Taking the calculated data shown in Fig. 5.28, $U_{p0} = 57\,\mathrm{V}$, $T_P = 3.4\,\mathrm{ms}$, and the parameters indicated in previous sections, and substituting them into Eq. [5.26], gives $\mathrm{d}T_P/\mathrm{d}R = -0.23\,\mathrm{s}/\Omega$. This means that T_P decreases by 0.23 ms when R increases 1 mΩ.

This analysis demonstrates that scanning-output characteristic control has much greater resistance to variations of welding-loop resistance; its capability is 17 times greater than that provided by the threshold-control method. Moreover, the scanning-output characteristic control method can automatically adjust the arc length when the loop resistance changes. According to the analysis given in Section 5.3, the arc-operating point will automatically drift upward; the magnitude is ΔU_a where

$$\Delta U_a = \Delta R \cdot I_P$$

The line L_{a1} rotates to ($L_{a1} = \Delta R$) by an angle α, shown in Fig. 5.32 as L'_{a1}.

$$\alpha = \frac{\Delta U_a}{I_P - I_b}$$

Because $\Delta R = \dfrac{\Delta U_a}{I_P}$ and I_b is small, $I_p >> I_b$, then $\alpha \approx \Delta R$. This means that the change of resistance is compensated for automatically so that the arc length does not change.

In summary, the scanning-output characteristic control method offers stable spray transfer, a stable arc length, and good resistance to disturbances. Practical experiments have demonstrated that it has good resistance to arc-length disturbances, welding-loop resistance changes, wire-extension variations, etc. It continuously sustains spray transfer and an optimum arc length.

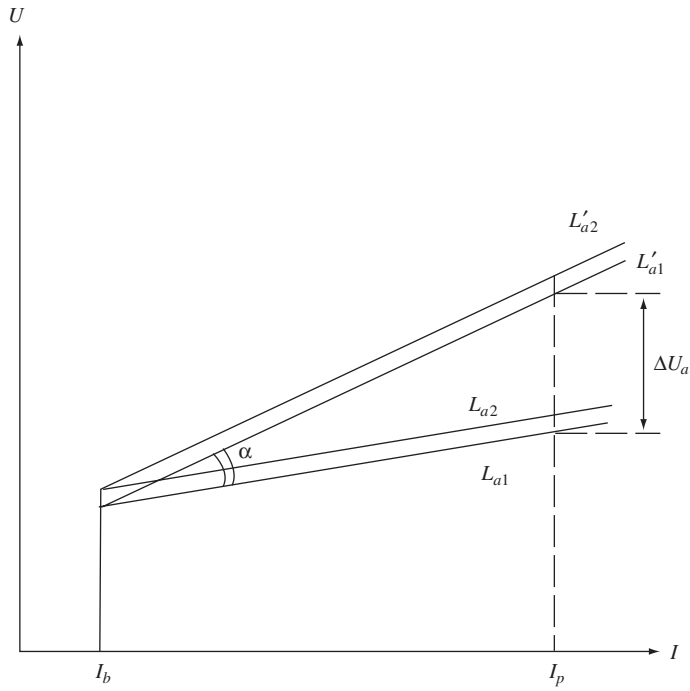

5.32 Influence of welding-loop resistance on arc-length variation

5.5 Closed-loop control of weld penetration

5.5.1 Introduction

Most service failures of pressure vessels are due to inadequate weld quality, particularly incomplete penetration of the first weld pass. Due to restrictions imposed by a vessel's diameter or high preheating temperature, root-side welding often is impossible or impractical. Therefore, one-sided welding with backside penetration is needed. This technique requires a very skilled welder. Even with a skilled welder, ensuring weld quality is difficult. Therefore, developing a one-sided welding process with adequate root penetration and root profile is an important project that has attracted the interest of welding researchers worldwide.

There are several penetration-control methods that are already applied in industry, for example, the pulsed TIG and plasma-arc processes.[49,122–124] In pulsed TIG welding, the welding speed is used as the control variable for ensuring penetration because the welding current is restricted by the current limitation of the tungsten electrode. Because the welding tractor in automated welding usually has large inertia, the dynamic behaviour of this

control method is poor. Plasma-arc welding is based on the keyhole phenomenon, which can ensure penetration but not weld-root formation. In both methods, there are no metal transfers to the welding pool (the electrode is not consumed during welding), so the productivity is low. The QH – ARC 103 control method can automatically adjust the welding parameters while the wire-feed rate varies in any way. Therefore, it offers a good means for penetration control and root-bead formation. A penetration control and root-bead formation process has been developed by the author and his colleagues Chen, Liu, and Wang.[254,324]

5.5.2 Bead penetration control

During the MIG welding process, the arc introduces heat and exerts force on the weld pool. In the meantime, melted droplets fall into the weld pool; the process is complicated. Experiments demonstrate that fusion-zone penetration is related to the heat input for a given groove size. However, due to the inertia of heat flow, penetration is not a linear relationship but more like a system with an inertial element: See Fig. 5.33 in which I represents welding current and Y represents penetration. This relationship can be used in the model for penetration control.

The control system can be designed for two welding modes, namely varying welding speed with constant welding current and varying welding current with constant welding speed. The dynamic behaviour of the first mode interferes with good control because welding tractors or turning rolls have high inertia. The following problems accompany the second mode.

(i) The welding-current range is small for conventional MIG welding; for example, the minimum welding current for 1.2 mm wire diameter and spray transfer is 250 A.

(ii) The welding-current range is large for pulsed MIG welding but the pulse parameters are complicated and not easy to adapt to large variations of welding current.

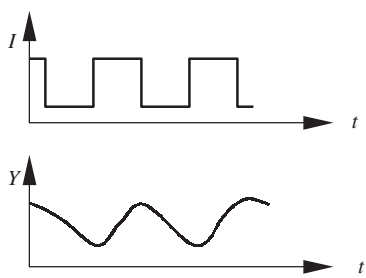

5.33 Relationship between penetration and welding current

(iii) Different metal transfer modes can be used for regulation of heat input, e.g. both high and low welding currents can be used with spray and short-circuiting metal transfer to change the heat input,[125] but this produces poor bead formation and requires accurate synchronization of the wire-feed rate and welding current.

Application of the QH – ARC 103 control method can solve these problems concerning the regulation of heat input.

5.5.3 Principle of the control system

The block diagram of the penetration-control system is shown in Fig. 5.34. The major components are described in the following sections.

5.5.3.1 Penetration sensor

An accurate and reliable sensor is the key element of the control system. Good penetration should have sufficient area of melting on the back side of the bead without suck back of weld metal, which leaves a depression in the root bead. In this control system, a photoelectric device is used for detecting the temperature and molten area.

From the principles of heat radiation, the full-wave radiation power can be expressed by the following equation:[126]

$$M = \varepsilon\sigma T^4 \qquad [5.27]$$

where M is the full wave radiation power per unit of area
σ is the Stefan–Boltzmann constant
T *is* the absolute temperature
ε is the full wave emissivity

If the radiation area is A, the total power is:

$$A \cdot M = A \cdot \varepsilon\sigma T^4$$

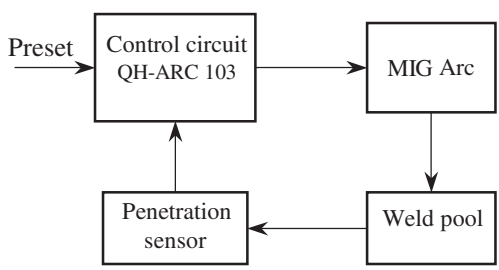

5.34 Block diagram of the penetration-control system

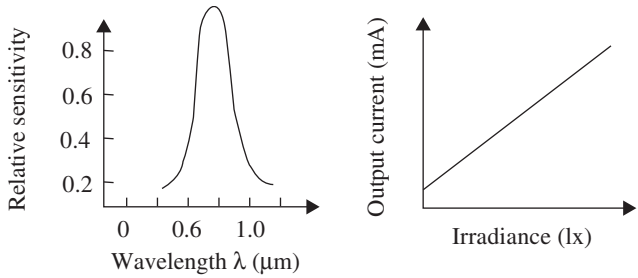

5.35 Characteristics of the 3DU photo-sensitive transistors

5.36 Appearance of sensor

This equation shows that the total radiation power is proportional to the fourth power of temperature and the first power of the radiated area. The output of most photoelectric devices is proportional to their irradiance, which, in turn, is proportional to their total radiation power. Therefore the temperature increase of the molten metal and its area increase the output of the photoelectric device. In the present system, a 3DU silicon photoelectric transistor is used. The characteristics of it are shown in Fig. 5.35.

Obviously, the amount of radiation that the photoelectric device receives depends on both the temperature and area of the molten pool and thus reflects the degree of penetration of the back bead. Because this device has high sensitivity and small volume, it can be installed in different ways to adapt to different designs of welded pressure vessels (see Fig. 5.36).

The problem with this sensor is that its output depends on the distance between it and the weld pool. Therefore it must be calibrated before use for each application. To solve this problem, Chen[324] has developed another kind of sensor using a linear CCD camera and a selected-wavelength filter as the sensing element. At the same time, he assumed that the temperature field obeyed the following rule:

$$T(y) = K\exp(-\zeta y^2)$$

By proper data processing of the signals received, the absolute temperature and degree of penetration can be recognised independently of the

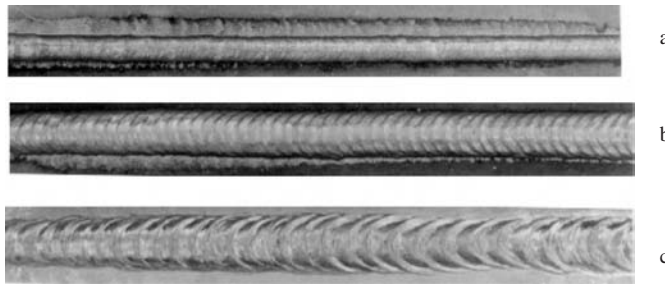

a) Constant wire-feed rate b) Fast pulsed wire-feed rate c) Slow pulsed wire-feed rate

5.37 Appearance of bead formation under different wire-feed modes

distance and without calibration.[324] Later, the author and his colleagues Su[295] and Zhang[296] developed a sensor using an ICCD camera, which can measure the temperature field without calibration at high speed (every field for 0.15 s), as the sensing device. The device can accurately measure both the temperature and area of the molten pool. This device has been applied successfully (see Section 14.7).

The descriptions in the following paragraphs are based on using the 3DU sensor as its volume is small, it is simple to control, and easy to calibrate. Therefore it is useful for practical applications.

5.5.3.2 Heat input control

For control of heat input and weld penetration, the power source designed for the QH – ARC 103 method[127] and a rapid-response wire feeder[128] were used as the basis of the system. Because the QH-ARC 103 power source can automatically regulate its parameters while wire-feed rate varies, the power source can ensure stable spray transfer in the welding current range of 60~350 A. Therefore the heat input can be easily regulated. Figure 5.37 shows the bead appearance obtained using different wire-feed rates. Figure 5.38 shows the current waveform taken by an oscilloscope while the wire-feed rate was pulsed. From the figure, it can be seen that the magnitudes of both the pulsed and background currents were not changed, but the pulse width and frequency changed adaptively with the variation of the wire-feed rate.

At the present time, almost all wire-feeding mechanisms are designed for constant wire-feed rate. Their dynamic properties are poor when the wire-feed rate changes, e.g. it takes more than 200 ms for the feed rate to increase from its lowest to its highest level. Obviously, it does not meet

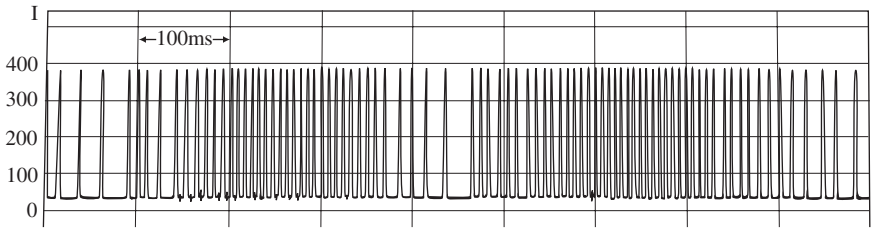

5.38 Welding current waveform under pulsed wire-feed rate

the requirement of the present control system. For this reason, the author has developed a wire-feeding mechanism having improved dynamic properties. A torque motor is used without a reducing gearbox instead of a servomotor. A tachometer is mounted on the axle of the wire-drive motor to provide closed-loop control of wire feeding. The transient time from the lowest feed rate to the highest feed rate is reduced to 30 ms from 300 ms. Figure 5.39 shows the control system. An arrow indicates the torque motor.

5.5.3.3 Configuration of the control system

The physical configuration of the control system is shown in Fig. 5.40. It can be seen by analysis of its transfer function that there are two inertia elements; one is the wire-feed motor and the other is the melting process of the weld pool. Figure 5.41 shows the block diagram of the control system. Its transfer function can be derived easily as follows.

$$G(s) = Y(s)/U_g(s) = \frac{k_x k_y k_m}{T_x T_y s^2 + (T_x + T_y)s + 1 + k_x k_y k_m k_f} \qquad [5.28]$$

where

$U_g(s)$ is the input signal
T_x is the time constant of motor
k_m is the wire melting rate
k_y is the penetration gain factor
$Y(s)$ is the penetration
k_x is the motor gain factor
$V_f(s)$ is the wire feed rate
$I(s)$ is the welding current
T_y is the time constant for penetration
k_f is the feedback factor

Equation [5.28] is for a Type 2 control system; its natural oscillation frequency is

$$\omega_n = \sqrt{\frac{1 + k_x k_y k_m k_f}{T_y T_m}} \qquad [5.29]$$

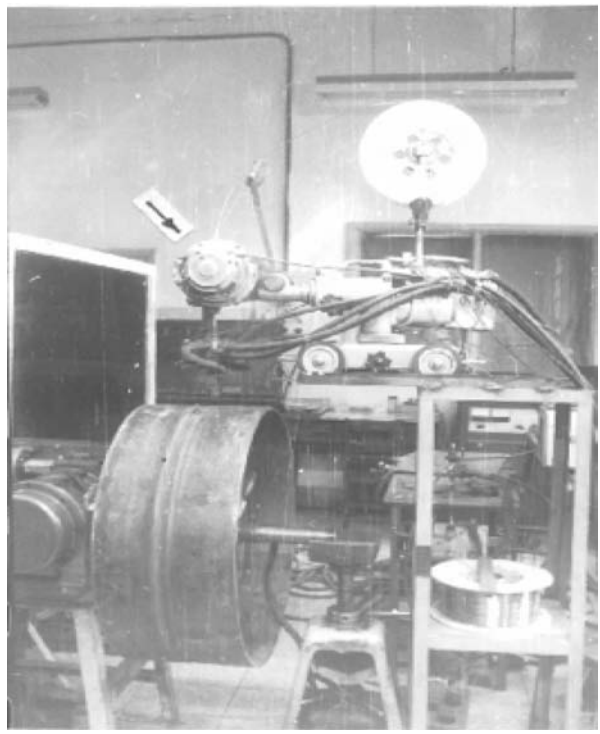

5.39 Apparatus for closed-loop penetration control

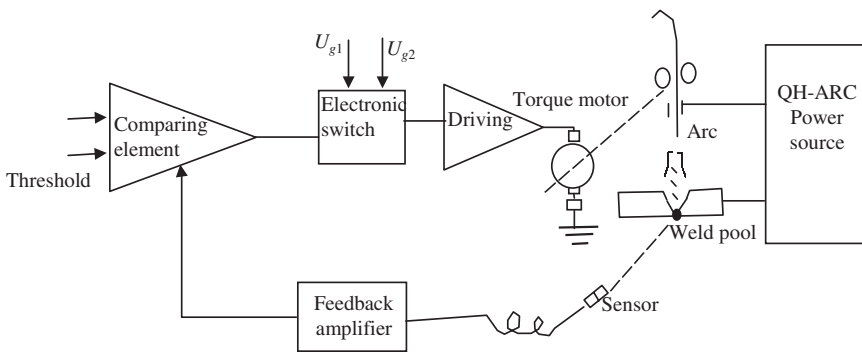

5.40 Configuration of the control system

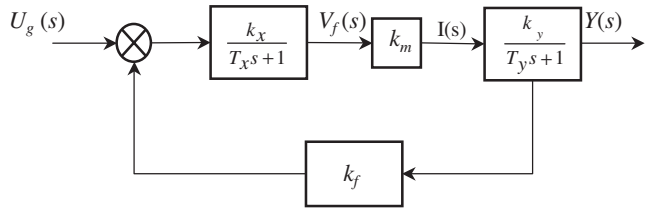

5.41 Block diagram of the control system

The damping factor is

$$\zeta = \frac{T_x + T_y}{2\sqrt{T_x T_y (1 + k_x k_y k_m k_f)}} \qquad [5.30]$$

In order to obtain optimum results, compensation can be incorporated into the design. In this system, however, there are special features. First, the time constant T_y for the degree of penetration and heat input varies with welding conditions. Second, arc forces can oscillate the molten pool; this oscillation can propagate throughout the whole system. Third, excessive molten metal in the pool can prevent control of penetration by heat input. For these reasons, a linear control system can hardly satisfy the control requirements. Therefore, in the present system, a non-linear control system or threshold-control method was applied: see Fig. 5.40. The principle of this control is explained as follows:

The lower threshold was selected so that the root side of the joint is just melted and the upper threshold is selected so that the root side is sufficiently melted but without suck back. A comparing element is used as a flip-flop circuit. The system will remain in its current state of operation while the input signal is between the lower and upper threshold so that oscillation or loss of control will be avoided and good robustness can be obtained. If the penetration input signal is lower than the lower threshold, the comparing element will connect the circuit with U_{g1} (Fig. 5.40) so that wire-feed rate will be V_{fH} and a high welding current I_H will be produced. If the penetration input signal is higher than the upper threshold, the comparing element will connect through U_{g2} to the control circuit and thus give a low wire-feed rate and low welding current. The heat input to the weld pool is regulated by adjusting I_H, I_L and T_H, T_L. The inputs U_{g1} and U_{g2} are preset so that during pulsed-wire feeding, there is not too much molten metal in the weld pool, which will cause loss of control. This also provides a stable arc with minimum welding current when the wire-feed rate is low.

A weld-root appearance obtained with this control method is shown in Fig. 5.42. It consists of a series of melted spots that overlap each other. Each

5.42 Bead formation on the root side

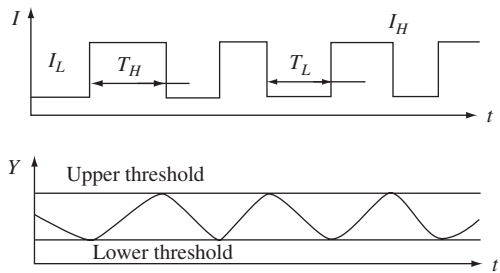

5.43 *I* and *Y* recorded in practice

spot is formed at the high welding current for penetration at first and subsequent low welding current for solidification of the pool. T_H and T_L are varied automatically according to the penetration input signal. Practical experiments demonstrated that although the volume of each weld pool may be different, good penetration could be ensured. Figure 5.43 is the record taken by an $X - Y$ recorder in practice.

5.5.4 Experiment and application

In order to examine the behaviour of the control system, a series of technological experiments have been conducted. The parameters used were as follows:

Work piece: 400 × 100 × 8 mm plate of steel 16 Mn. Single V-butt joint
Wire: 08Mn2Si, ϕ1.2 mm
Welding current: $I_H = 170 \pm 10$ A, $I_L = 60 \pm 5$ A
Shielding gas: 850 L/h · Ar + 150 L/h · CO_2

The groove shape is shown in Fig. 5.44. For experimental purposes, the groove angle β, root face δ, root gap c, mismatch ('high-low') d, and welding speed V_w were varied. The results are summarised as follows:

(i) Too small a value of β results in too much reinforcement, which is unfavourable for the stress distribution under loading. Moreover, too small a value of β makes penetration more difficult. A long T_H is needed to achieve sufficient penetration; in turn, more molten metal

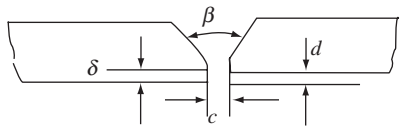

5.44 Groove shape of specimen

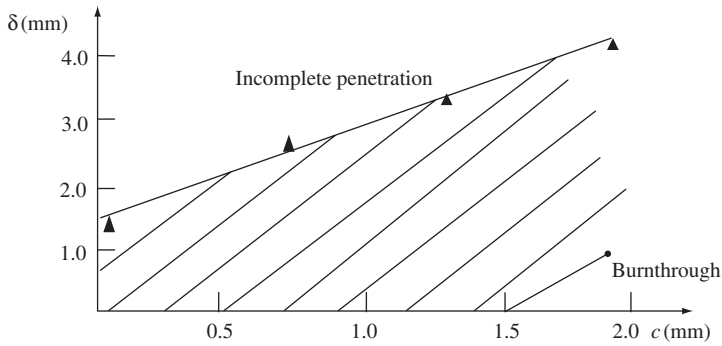

5.45 Allowable range of groove dimensions

will be deposited in the weld pool. Once the arc burns through the plate, a very large depression in the weld metal can result. On the other hand, larger β will reduce T_y, which is favorable for penetration control and bead formation. But the amount of machining for preparation of the groove and the number of subsequent weld passes will be larger. Therefore β = 80°~90° is usually recommended.

(ii) The experimental results related to the root face and root gap are shown in Fig. 5.45. It can be seen that T_y should be increased when δ is increased and T_y should be decreased when c is increased. Therefore, a larger value of c should be used for larger δ and smaller c used for smaller δ. It is difficult for the arc to penetrate when δ is large and c is small. On the other hand, small δ and large c produce a depression in the weld pool and cause loss of control. Normally it is not difficult to meet the requirement shown in the shadow area of Fig. 5.45 in practice. The mismatch d plays a role like that of δ. Increases of d increase T_y. Normally, the system can operate successfully if d is less than 1 mm.

(iii) From the point view of productivity, using high welding speed is desirable but due to the thermal inertia in weld-pool formation, too high a welding speed V_w will cause incomplete penetration so that overlap of the weld pools (individual beads) on the root side of the joint cannot be obtained. Experimental results demonstrated that good root-bead formation can be obtained in the welding-speed range of

5.46 Appearance of liquid acetylene vessel welded using the present method

0.18~0.25 m/min, which is 50~70% higher than the welding speed of pulsed TIG welding during the first pass.

(iv) The present development had been applied in industry. The circumferential seam of a liquid-acetylene vessel and a liquid-chlorine vessel was welded using the control system. The dimensions of the liquid-acetylene vessel were 250 mm inner diameter, 4.5 mm wall thickness, and 160 N/cm^2 working pressure. The technology used previously was pulsed TIG welding for the first pass and submerged arc welding (SAW) for subsequent passes. In the present technology, pulsed MIG was used for the root pass and MIG was used for subsequent passes. The method was not only more efficient in root-pass welding but also saved a lot of time due to the elimination of the changing of the welding process and welding location on the shop floor. The productivity was obviously improved. The entire length of all of the joints was nondestructively tested(100%) and 98.7% of them met the standard for penetration. The experiments demonstrated that one-side welding with adequate root-bead formation is possible and reliable. This new process control can be recommended for application in practice. Figure 5.46 shows the appearance of the circumferential seam of the liquid-acetylene vessel welded using this method. No data are available for the liquid-chlorine vessel.

6

Arc control of CO_2 welding and AC MIG welding

6.1 CO_2 welding

In CO_2 welding, force is exerted on the anode spot of the weld wire by the arc column, which impels the molten drop to fall to the weld pool. Therefore, it is very hard to achieve spray transfer. A short-circuiting method was invented in the 1950s to solve this problem. In this method, low arc voltage and a short arc length are used. When a molten drop is formed on the tip of the wire, short circuiting occurs, which causes high current and pushing of the droplet by the axial force accompanying the pinch effect. Advantages of CO_2 welding are its low cost and small molten pool. It is applicable to all-position welding but there are shortcomings also. The process produces significant spatter, excessive reinforcement, and poor bead formation. It is used mainly for all-position welding of thin plate.[21,30,129,131,132,134–137]

A constant-voltage output characteristic and a constant wire-feed rate are used. The inductance of the welding loop is used to control the current-rise rate during short circuiting. There is no means to control arc initiation and the current varies violently during welding. The range of allowable current for some wire diameters is very small.[138–140] In order to overcome these shortcomings and improve the quality of weldments made by CO_2 welding, much study has been carried out by welding researchers.[57,141,142,144] Zhang and Chen proposed to control CO_2 welding using the QH-ARC principle, concretely two methods were developed, i.e. QH-ARC CO_2 (A) and QH-ARC CO_2 (B).[130] The main idea was to use droplet transfer or droplet plus short-circuiting transfer instead of pure short-circuiting transfer. The transfer is controlled using a constant-current output characteristic. The droplet transfer keeps the arc initiated and thus produces deeper penetration. Constant-current, short-circuiting transfer produces less spatter and gives a more stable arc. This method is discussed in the following text.

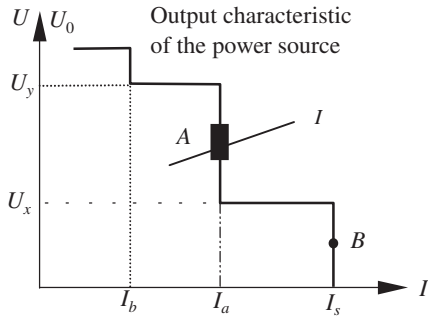

6.1 Schematic diagram of the arc-operating point

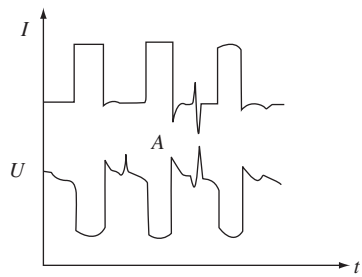

6.2 Current and voltage waveforms

6.1.1 Principles of control method QH-ARC CO_2(A)

Triple-step output characteristics are applied in the QH-ARC CO_2 control method. Figure 6.1 is a schematic diagram of the power-source output characteristic and the arc-operating point, in which U_0 is the open-circuit voltage, I_b is the background current, I_a is the operating current, I_s is the short-circuiting current, and U_x and U_y are the thresholds for limiting the range of arc length. U_x also controls the current-rise rate. U_y prevents burning of the weld-torch tip. Normally, the arc characteristic intersects I_a at A. However, in practice, the arc-operating point jumps between A and B. Figure 6.2 shows the current and voltage waveforms schematically. The arc operates at A when it is long and it is a short-circuit when the arc length becomes short. The arc successively alternates between two transfer modes. Both modes take place at constant current and the process proceeds smoothly. At certain wire-feed rates, the proportion of each transfer mode can be regulated by presetting the output-characteristic parameters. In this way, bead formation can be properly predesigned for different welding positions and plate thicknesses.

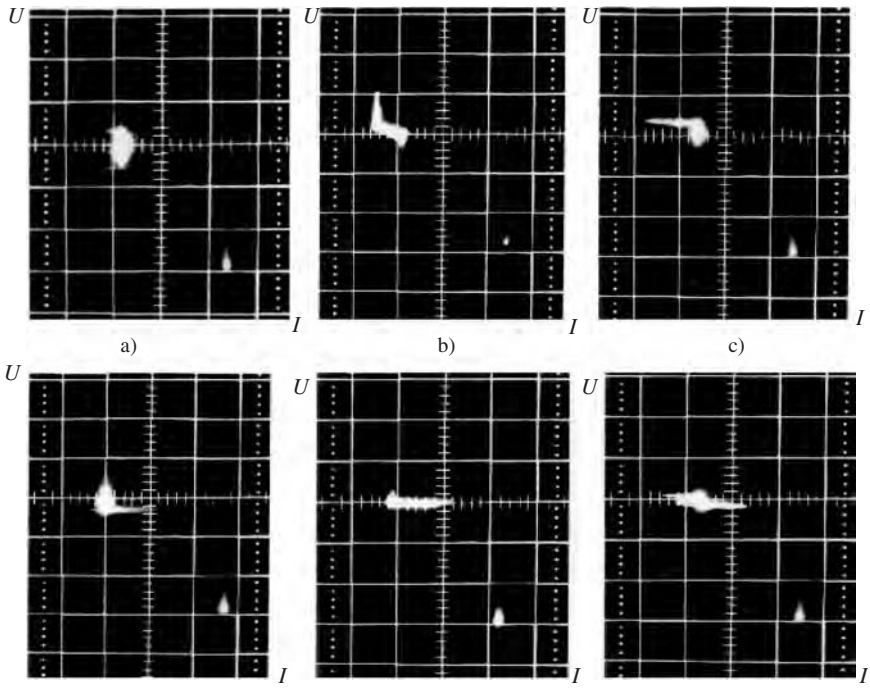

6.3 Oscillograms of arc-operating points on the *U-I* plane

Properly presetting the output-characteristic parameters is important for this control method. Figure 6.3 shows trajectories of the arc-operating point on the *U–I* plane for different presets of characteristic parameters.

a) The arc-operating point is on the constant-current segments I_a and I_s, the desired state for this control method.
b) The arc-operating point is between I_b, U_y, and I_a; it jumps to B during short-circuiting.
c) The arc-operating point is on the corner of I_b and U_y.
d) The arc-operating point is at the corner of I_a and U_x.
e) The arc-operating point is mostly on U_x.
f) The arc-operating point oscillates between U_y, I_a, U_x.

When the welding speed is held constant, the results shown in Figures 6.3a–f can be obtained by presetting different sets of parameters of the triple-step output characteristic. For example, from Fig. 6.3a, Fig. 6.3b can be obtained by increasing I_b and decreasing I_a and U_y. Figure 6.3c can be obtained by decreasing U_y. Figures 6.3d can be obtained by decreasing I_a,

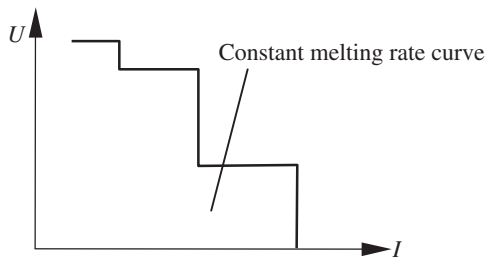

6.4 Power-source output and wire melting-rate characteristics

etc. From experimental observations it was seen that the arc-operating points represented by Figures 6.3b, c, and f give normal, long CO_2 arcs, which have poor self-adjustability and stability. Those represented by Figures 6.3d, and e are normal, short-circuiting transfer arcs, which are quite violent. That of Fig. 6.3e is the worst because it is on a constant-voltage segment; that of Fig. 6.3f is better because it is partly on a constant-voltage segment and partly on a constant-current segment. In all cases, I_s has the function of limiting the maximum short-circuiting current; this reduces the amount of spatter compared to conventional CO_2 welding. It can be concluded that Fig. 6.3a represents the most nearly ideal arc; therefore, the QH-ARC CO_2 control method was developed on the basis of this mode.

Constant-current and constant wire-feed rate are used in the QH-ARC CO_2 control method. The prerequisite is that the current corresponding to the preset wire-feed rate should be slightly larger than I_a (see Fig. 6.4) and I_s must be properly chosen so that the droplets formed during arcing will be pushed into the pool by gravity, the plasma-column force, and pinch off. During feeding, the part of the wire that is melted by droplet transfer is transferred during the short-circuit period because $I_s > I_a$ and the melting rate is larger than the wire-feed rate. When the wire-feed rate is disturbed, the ratio of droplet transfer to short-circuiting transfer automatically changes to maintain the balance between the wire-feed rate and the melting rate. Obviously, short-circuiting transfer is not only a mode of metal transfer but also a means for automatic regulation of arc length.

In conventional CO_2 welding, there are two categories of electrical parameters; one is small current and low arc voltage, and the other is large current and high arc voltage. The former is used for welding thin work pieces and the latter is used for welding thick work pieces. In the middle range of welding currents, the arc is not stable. Droplet transfer is driven mainly by gravity. Occasionally, there are short circuits but these are accompanied by a violent arc and spatter. One of the aims of developing the QH-ARC CO_2 control method was to facilitate the middle range of welding current for welding of medium- gauge plates.

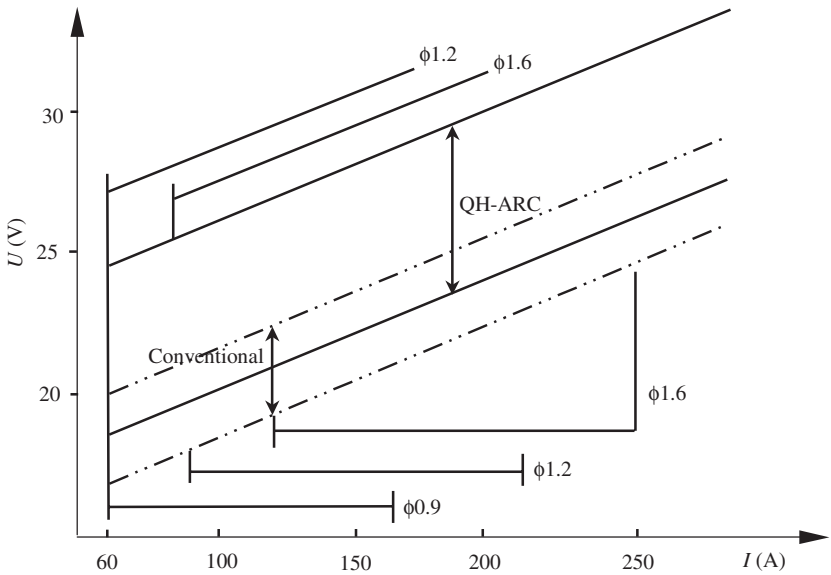

6.5 Ranges of welding parameters (The dotted line indicates the reasonable range for conventional CO_2 welding; the solid line indicates the reasonable range for QH-ARC CO_2 welding)

Applying I_s, effectively decreased spatter generation by restricting the maximum short-circuiting current.

6.1.2 Technological effects

A series of experiments that demonstrated successful results are described as follows:

Large applicable range of welding current. Figure 6.5 shows the applicable range of welding parameters for both the QH-ARC CO_2 and conventional CO_2 welding. It can be seen that the applicable current range for the newer method is very wide and almost the same range for both wire diameters ϕ1.2 mm and ϕ1.6 mm. That means that it is not necessary to change the wire diameter for different plate thicknesses, which greatly facilitates the welding job in practice. Experimental observations demonstrated that larger-diameter wire was preferred for stable wire feeding; the arc spot in the molten pool was large and a better bead-shape formed.

The wide range of welding parameters that are allowable using this control method can be attributed to the following reasons:

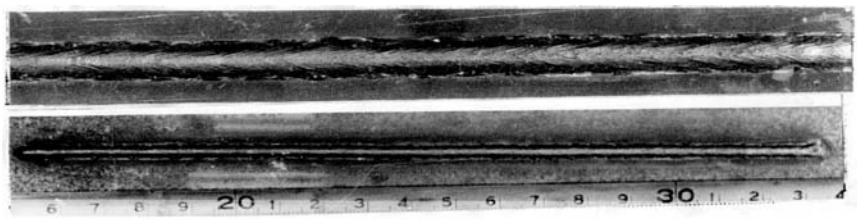

a) $I = 60$A, $\delta = 1.3$ mm (Upper image is magnified)

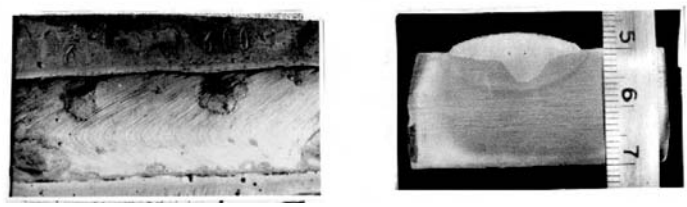

b) $I = 300$ A, $\delta = 20$ mm

6.6 Appearance and cross-sections of welds

(i) A soft and stable arc, obtained due to the constant-current control. Droplet transfer can be obtained at very low current (approximate 60 A). Figure 6.6 shows the appearance of a weld made at 60 A on 1.3 mm thick plate (see Fig. 6.6a) and a weld made at 300 A on 20 mm thick plate (see Fig. 6.6b).

(ii) Appropriate allocation of heat energy. Because the fusion zone and the metal transfer are automatically regulated in accordance with the wire-feed rate, there is much less spatter in both droplet and short-circuiting transfer, and bead formation is improved. Thus, the range of welding current bridges the gap between usable currents with conventional CO_2 welding.

Arc Stability. The allowable range of arc-voltage variation is 6 V, which is twice as large as that of conventional CO_2 welding (3 V). Arc voltage represents, in fact, the arc length and the metal-transfer mode. A large arc-voltage range means that the range of allowable arc length also is large. The system then has good stability and robustness. There is an abundant range for control because the ratio of droplet to short-circuiting transfer can be regulated in a large range.

The average arc voltage is determined by U_y and U_x. By regulating U_y and U_x, different arc voltages, U, can be obtained to meet the requirements of different welding situations. The arc current remains constant between the limits U_y and U_x. When the arc voltage exceeds either limit, the current and wire-melting rates change so that the arc-operating point returns to I_a. The

difference between the arc-length self-regulation mechanisms of conventional CO_2 welding and the present control method is that the current fluctuates during arc-length regulation in the former case but remains constant in the latter case. It limits arc-length variation without change of arc current. In control theory, this means that for the latter case there is a 'dead zone' for a small amount of arc-length variation but sensitive and fast response to arc-length change when it exceeds the limit. Experiments have been conducted to verify the ability for arc self-adjustment. The wire extension was varied from 12 mm to 36 mm under a given set of welding parameters (for simulation of an arc-length disturbance). It was found that the arc could always be kept stable while average values of I, U, and f varied accordingly.

Good bead formation. Bead formation during conventional CO_2 welding has the following features:

(i) sharp and deep penetration
(ii) high, hump-like reinforcement with narrow width; the form factor of the weld $\varphi = \dfrac{B}{H}$ is less than 3
(iii) a large toe angle that is a stress concentration
(iv) excessive molten metal in the weld pool
(v) insufficient penetration, D. For some welding currents, the pentration coefficient $\left(Z = \dfrac{H(\text{mm}) \times 100}{I(\text{A})}\right)$ is 0.8~1.2.[131]

Bead formation with the QH-ARC CO_2 process is much better than that of conventional CO_2 welding described above. A comparison of bead shapes made by the two control methods is shown in Fig. 6.7. It can be seen that for the QH-ARC CO_2 method, the form factor $\varphi \geq 4$, the bead width is larger, the reinforcement is smaller (which illustrates that the fluidity of the molten metal is better), the weld-toe angle is smaller and there is less possibility of undercut, and the penetration coefficient $Z \geq 1.6$, which means that the energy-consumption efficiency is higher and the process is more productive. Particularly because the arc is elastic, metal transfer is smooth and stable, and the bead has an attractive appearance with very fine ripples on the face with no hump.

Low spatter production. The amount of spatter produced in QH-ARC CO_2-controlled welding is much less than that produced using conventional CO_2 welding. There are many factors that affect spatter formation but it is reduced with soft and smooth arcs, and especially with even metal transfer.

A stable arc, good bead formation, and little spatter are important signs of high-quality welding. These can be achieved with the QH-ARC CO_2 control method. This is why this method is superior and why its application is significant.

a) b) c)

n.b. Units are centimetres

a) Conventional CO_2 welding b) QH-ARC welding c) QH-ARC welding I = 330 A δ = 12 mm

6.7 Comparison of weld bead appearances

6.1.3 Welding parameters and one-knob control

The QH-ARC CO_2 control method is controlled by six parameters, namely, U_0, I_b, U_y, I_a, U_x, and I_s. Different combinations of these parameters produce different behaviour of the welding process, e.g. arc initiation, droplet transfer, bead formation, spatter. In the previous section, the influence of parameters was discussed generally. However, for practical application of the control method, more concrete data are needed. To acquire these data, a series of experiments was conducted. All the parameters, except U_0, which is fixed, were regulated by a graduated dial on which each graduation was 1 V with ±0.1 V accuracy. Each graduation for current was 10 A with ±1 A accuracy. The selection of the combination of parameters was made on the principle that the welding process would be stable. The results are given as follows.

Arc current. Among the three current parameters, I_a plays the major role. Most of the time, the arc operates at I_a; I_s is used for regulation of the arc length, which controls the short circuiting frequency, metal transfer mode, and amount of spatter. Very occasionally, the arc jumps to I_b when the arc length is too long.

The allowable current ranges for I_a, and I_s for different wire-feed rates are shown in Figures 6.8 and 6.9. They explain on the one hand the allowable ranges of current for certain wire-feed rates, and, on the other hand, the allowable ranges of wire-feed rate for certain ranges of I_a or I_s, i.e. the wire feed-rate disturbance range the arc can tolerate.

From Fig. 6.8 it can be seen that the allowable range of V_f increases when I_a increases. Increasing of V_f results in the decrease of the average arc voltage, increase of the welding current, and increase of the short-circuit frequency. The proportion of short-circuit transfer also is increased.

I_s has a very strong influence on short circuiting and arc-length self-regulation. It can be seen from Fig. 6.9 that, with an increase of I_s, the allowable range of V_f shifts to the right, and vice versa. When I_s is lower, there is less spatter but arc self-regulation and arc ignition are less reliable. In the opposite way, there is better arc-ignition ability, but greater spatter,

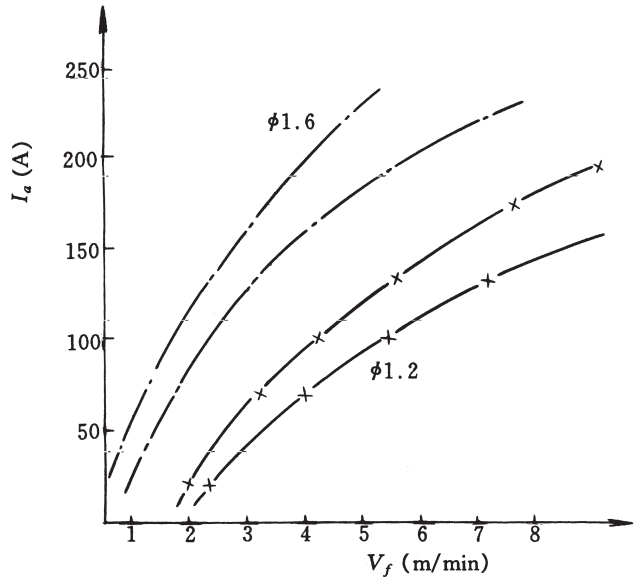

6.8 Allowable ranges of I_a and V_f

even explosion of the wire, when I_s is larger. With the newer control method, the rate of current rise toward the short-circuit current is very high and, therefore, I_s is needed much less than it is in conventional CO_2 welding.

From Fig. 6.8 it also can be seen that I_a does not increase linearly but more slowly with increasing V_f. Observations illustrated that, with increase of current the arc root climbed up the wire, which contributed to melting of the wire; the droplet-transfer rate increased, and the pinch effect increased. The proportion of globular transfer also increased.

Examination of the weld cross-section illustrated that the penetration increased with increasing I_a but not with I_s. This was due to the increase of arcing time as I_a increased.

The function of I_b is mainly to prevent arc breakdown when the arc length becomes exceptionally long. If I_b is too low or nonexistent, frequent arc breakdowns can occur and discontinuities can be introduced into the weld seam (see Fig. 6.10). Experimental results illustrated that the minimum level for I_b for ϕ1.2 mm-diameter wire was 10 A and for ϕ1.6 mm wire was 20 A. Larger values of I_b help maintain the arc but too large a value of I_b (for example over 80 A) can cause burning of the welding-torch tip. It was found that 30~70 A was a suitable range.

Arc voltage. Once the wire-feed rate and current are selected, the arc voltage and arc length depend on U_y and U_x; both their magnitude and their difference affect weld quality.

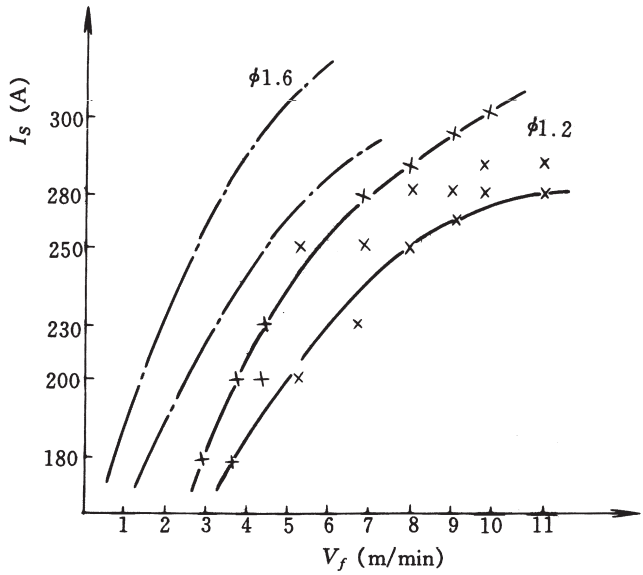

6.9 Allowable ranges of I_s and V_f

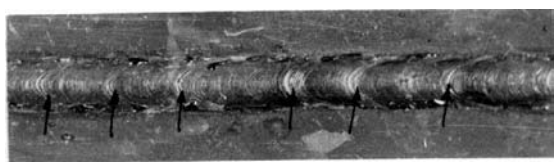

6.10 Discontinuity of the weld seam due to arc breakdown

The relationship between wire-feed rate, and U_y and U_x are shown in Figures 6.11 to 6.14. If U_y is too low, the arc-operating point can jump to I_b after the droplet transfer because the arc length is increased suddenly. Thus, the energy during the arc duration is decreased, the rate of droplet transfer decreases, and the rate of short-circuiting transfer increases. Too low a value of U_y destroys the arc form and can allow the wire to enter into the molten pool. If U_y is too high, then only I_a and I_s play roles in the arcing process; the arc may burn back to the weld tip. The arc also has less resistance to disturbances.

If U_x is too low, the rate of the short-circuiting current rise is lower, the short-circuit duration is increased, and the ability to ignite the arc is poor. Too low a value of U_x can result in $I_S \geq \frac{U_x}{R_e}$ where R_e is the resistance of the wire extension, so that the droplet in contact with the molten

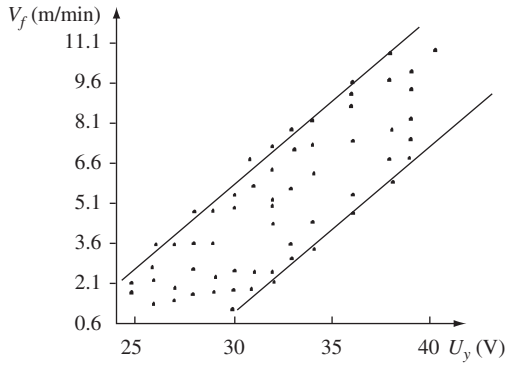

6.11 Allowable range of the V_f and U_y for ϕ1.2 mm wire

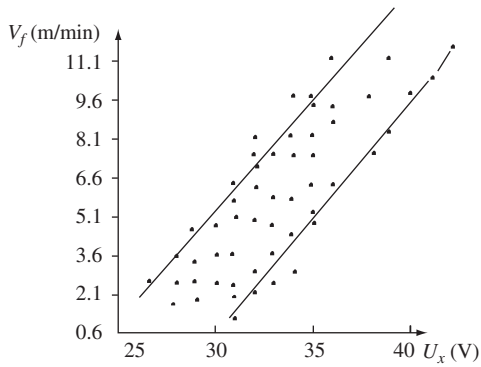

6.12 Allowable range of V_f and U_x for ϕ1.2 mm wire

pool cannot be broken down and the welding process is interrupted. If U_x is too high, the arc remains on when the current changes to I_a from I_s, the droplet will grow very big due to the large current and will be lifted upward by the arc-column force. That is the undesirable phenomenon of long-arc CO_2 welding. Moreover, too high a value of U_x results in the short-circuiting current rising rapidly, which produces heavier spatter.

The influence of U_y and U_x on bead formation also has been observed. Generally, increasing U_x and U_y will increase the average arc voltage and bead width. Between these parameters, U_y has the stronger influence. As in conventional CO_2 welding, an increase of arc voltage slightly decreases the reinforcement height, H. Penetration, D, increases with the increase of arc voltage at first but gradually decreases above a certain value of the arc voltage. The reason for this is that with too long an arc, heat energy is lost to the surroundings, which then does not contribute to the weld-pool

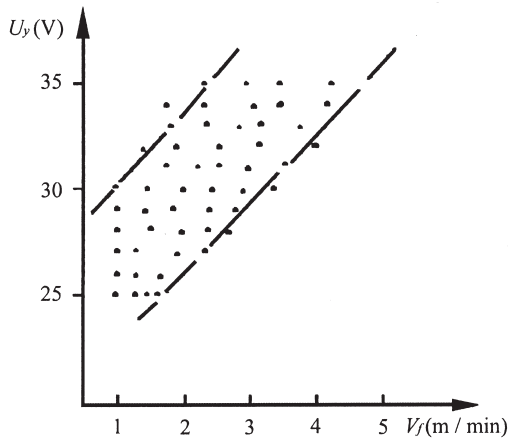

6.13 Allowable range of V_f and U_y for ϕ1.6 mm wire

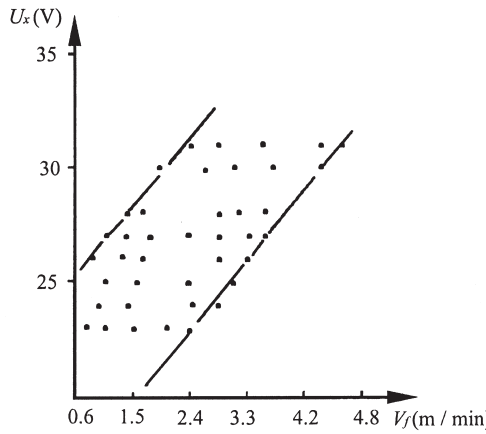

6.14 Allowable range of V_f and U_x for ϕ1.6 mm wire

penetration. The change of the metal-transfer mode and heat loss due to spatter loss caused by the variation of arc length also may explain the phenomenon of penetration variation.

The difference between U_y and U_x has a great effect on the control system. Too large a difference results in a large variation of arc length and less self-regulation ability; too small a difference shortens the duration of the arc on I_a so that the droplet transfer can hardly be controlled. An analogy is that a large difference between U_y and U_x makes the control behave like a constant wire-feed rate plus a constant-current welding system, whereas a small difference makes it behave like a constant wire-feed rate plus a constant-voltage welding system. Experimental results

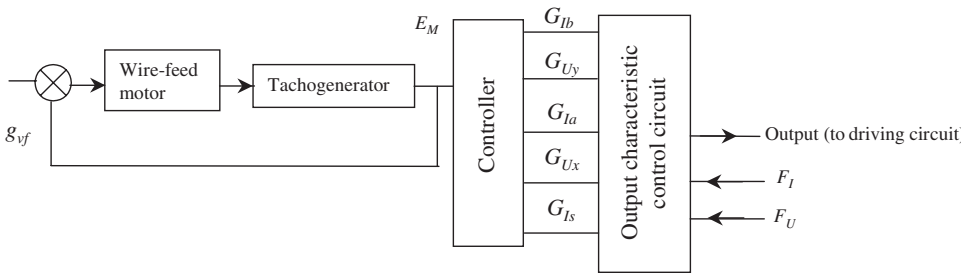

6.15 One-knob control system

demonstrated that a reasonable range of ΔU is 8 V, U_y should not exceed 38 V and U_x should not be less than 10 V. Obviously, for good bead formation and to avoid spatter, much more careful presetting of the parameters is required than that required for maintaining a stable arc.

One-knob control. Presetting of output-characteristic parameters using a graduated dial is satisfactory for research purposes but not convenient for an operator in practice. Therefore, a one-knob control system has been designed. Figure 6.15 shows the block diagram in which g_{vf} is the set value for the wire-feed rate and E_M is the back electromotive force of the wire-feed motor. The controller output G_{Ib}~G_{Is} is determined by the input E_M for setting the triple-step output-characteristic parameters to suit the wire-feed rate.

As discussed previously, all parameters (I_a, I_s, U_x, U_y) except I_b are determined by the wire-feed rate V_f. Theoretically, the functions representing the relationships of the parameters with V_f should first be found so that function generators can be constructed according to these functions. However, for simplicity, linear relationships were used to approximate the functions and, to remedy the inadequacy, a trimming controller was designed for use in practice. The linear relationships used in the present system are as follows:

$$I_b = 30\sim50 \text{ (A)} \quad [6.1]$$

$$U_y = U_x + 8 \text{ (V)} \quad [6.2]$$

$$I_a = \begin{cases} 74.1V_f - 17 \text{ (A)} & --\phi 1.6 \text{ mm wire} \\ 25.6V_f + 10 \text{ (A)} & --\phi 1.2 \text{ mm wire} \end{cases} \quad [6.3]$$

$$U_x = 0.04I_a + 16.6 \text{ (V)} \quad [6.4]$$

$$I_s = \frac{3}{5}I_a + 150 \text{ (A)} \quad [6.5]$$

where V_f is the wire-feed rate (m/min).

a) Wire-feed rate changed abruptly

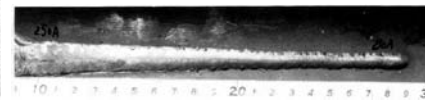

b) Wire-feed rate changed gradually

c) Enlargement of b)

6.16 Appearance of bead welding using one-knob control

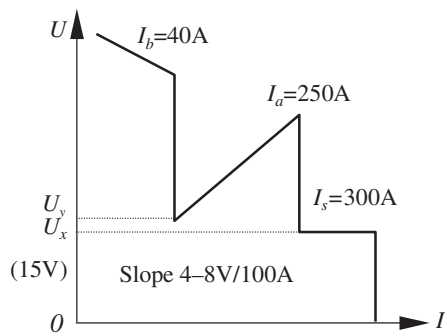

6.17 Principle of QH-ARC CO_2 (B) control

Figure 6.16 shows the appearance of a weld made using the one-knob control system. The wire-feed rate during welding was intentionally varied abruptly (Fig. 6.16a) and gradually (Fig. 6.16b and c). The results demonstrated that the system was excellent and could be applied in practice.

6.1.4 Control method QH-ARC CO_2(B)

The QH-ARC CO_2(A) control method was based on two modes of metal transfer, namely droplet transfer and short-circuiting transfer. The inadequacy of this method related to the short-circuiting transfer (for example, spatter formation) remained. Zhang and Chen have proposed another control method in which the central idea is to eliminate the short-circuiting transfer and achieve droplet transfer with no spatter. Figure 6.17 illustrates the control principle. I_b is the current that maintains the arc, I_a is the current for droplet transfer, and I_s is used for igniting the arc and preventing too large a current during short circuiting. U_x and U_y are used to control the droplet diameter and arc length. Figure 6.18 is an oscillogram showing the trajectory of the arc-operating point on the *I*–*U* plane.

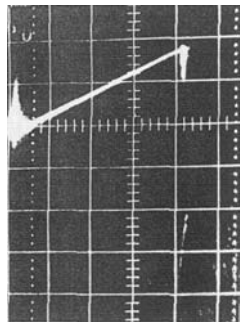

6.18 Trajectory of the arc-operating point on the *I-U* plane

Experimental results illustrated that for a wire feed-rate change from 1.6 m/min to 9.7 m/min, acceptable welds can be fabricated simply by regulating U_y between 22 V to 27 V; the average arc current was 80~240 A and the average arc voltage was 28~35 V. Small spatter loss and smooth bead formation could be obtained. The arc-operating point moved back and forth on the line connecting I_b and I_a, and the frequency was 30~50 Hz. The arc length varied periodically with clatter. When the arc-operating point reaches U_x, it jumps to I_a; sparks were observed at the center of the conic arc.

From this discussion, it is obvious that the line between I_b and I_a is a rising line, basically parallel to the static arc characteristic, as that described in Chapter 5 for the QH-ARC 103 control method. Therefore, the arc-operating point never stays on the line between I_b and I_a, U_y serves as a threshold. When the arc-operating point reaches U_y, a current pulse appears. As the wire-feed speed increases, the frequency of the pulse also increases so that the melting rate and wire-feed rate are automatically balanced. However, too long an arc length can interrupt the welding process; the arc-operating point jumps to I_b and finally breaks down the arc: see Fig. 6.19.

6.1.5 Summary

A constant-current and constant wire feed-rate welding process can be achieved by application of a triple-step or multi-segment output-characteristic power source. The process has the following advantages:

- Smooth, stable, and elastic arc. A large range of welding parameters is possible; the allowable current range for ϕ1.2 mm-diameter wire is 60~350 A, for ϕ1.6 mm-diameter wire is 80~400 A. The process can be used successfully for middle-gauge plate welding.

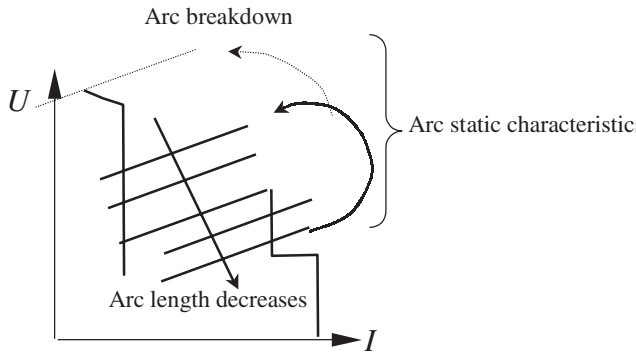

6.19 Automatic regulation of arc length

- Mixed-droplet transfer and short-circuiting transfer or simply droplet transfer can be obtained. The diameter of the droplets is less than 2~3 times the diameter of the wire. The droplets project down along the axis of the arc column. The ratio of droplet and short-circuiting transfer can be regulated as required.
- Bead formation is improved. The form factor of the weld is >4, and the penetration factor is <1.6. The bead surface is smooth and even. The spatter-loss coefficient is decreased.
- One-knob control of welding parameters can be realised.

6.2 AC MIG welding

MIG welding of both ferrous and non-ferrous metals has been widely applied in industry because it produces good quality weldments. The emergence of pulsed MIG welding has further widened its field of application.[146,147] It is an open-arc, spray-transfer welding process that is suitable for all-position welding. It facilitates automation and robotic welding. Due to the influence of electromagnetic forces and arc forces on the metal transfer, only reversed polarity DC can be used.[72,73,78,79,152] However, arc blow is troublesome in DC welding of ferrous alloys, particularly for semiautomatic and automatic welding because the torch angle cannot be adjusted quickly enough to compensate for the changing arc-blow direction, in contrast to manual arc welding.[21]

Arc blow is detrimental to the welding process and weld quality. It causes arc instability, undercut, porosity, overlap, bad appearance, and other weld defects.[153–156] In particular, it prevents maintaining the proper arc length and, therefore, the arc-voltage feedback in a closed-loop control system.

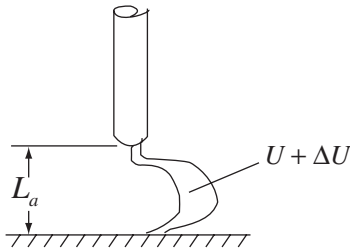

6.20 Arc length and arc voltage accompanying arc blow

Basically there are two kinds of MIG welding control systems. One is a constant-voltage and constant wire feed-rate system; the other is a constant-current and constant-voltage feedback control wire-feed system. The typical pulsed MIG arc-control systems currently available in the world are *Synergic* control, threshold control, arc-length feedback control, and QH-ARC control.[3,34,36,89,110,143,157,159] The common feature in all of them is that the arc length is detected and used for feedback control, which varies t_p and t_b to obtain a stable arc length. According to the technological requirement, the arc length should be the straight distance between the wire tip and the work piece, but in actual control systems the arc voltage is detected to give a measure of arc length. Therefore, the wrong information will be obtained when there is arc blow: see Fig. 6.20.

Using threshold control as an example, the arc voltage will increase to $U + \Delta U$ when arc blow occurs but, in fact, the arc length does not change. In this case the control system will lower the welding current so that the wire tip may touch the weld pool and result in a short circuit. The arc would not be stable.

In fact, arc blow is a very complicated phenomenon. The arc is an electrical discharge that acts as a flexible conductor so that the magnetic field of the arc and the residual magnetic field of the workpiece, that are both induced by the welding current, can act on the flexible conductor. For an infinitely long conductor with an evenly distributed electric field, the induced magnetic field also is evenly distributed and is directional. The force exerted on it is zero; therefore it will not move. The welding-current loop is short and finite but the route is variable. The current distribution in the parent metal, as well as its induced magnetic field, are uneven and unsymmetrical. Therefore it causes arc blow. The factors that affect arc blow are the surrounding magnetic body, the grounding point of welding loop, the direction of welding current, the presence of a root-pass weld, and the relative position of the arc to the workpiece, etc.[25] The effect of these factors on both the magnetic-field intensity and direction is random. The

common feature is that there is always arc blow during root-pass welding particularly during the background current period.

To resolve this problem, both domestic and foreign researchers have proposed different measures. Not all of them are effective. The author and his colleague, X. D. Jiao, proposed to change the MIG welding operation from DC to AC to completely solve the problem.[145,148–151] Trials demonstrated that it was very difficult to MIG weld using AC. No successful results using AC MIG welding have been reported anywhere in the world. The author made important progress in this endeavour, which is described in the following sections.

6.2.1 Study of DC pulsed MIG welding

The AC pulsed MIG process essentially is accomplished by alternating between reverse-polarity DC pulsed MIG (abbreviated to DCRP pulsed MIG) welding and straight-polarity DC pulsed MIG (abbreviated to DCSP pulsed MIG) welding. Therefore, the properties of both the DCRP and the DCSP pulsed MIG processes will affect the behaviour of the AC MIG process. Before studying the AC MIG process, it is wise to study DCRP and DCSP separately. For this purpose, a high-speed camera has been used to observe the arc form and droplet transfer.

The experimental apparatus is shown in Fig. 6.21. A strong backlight was used to obtain a shadow of the arc and droplets. Greater depth of focus and a distinct picture were obtained using a suitable filter and a small aperture. A green filter and a 500 W xenon lamp were used. A telephoto lens was used to enlarge the arc in the field of view. The aperture chosen was f16~f18. The film speed was 4000 frames/s. The film was made in China by Arial Photographic Company.

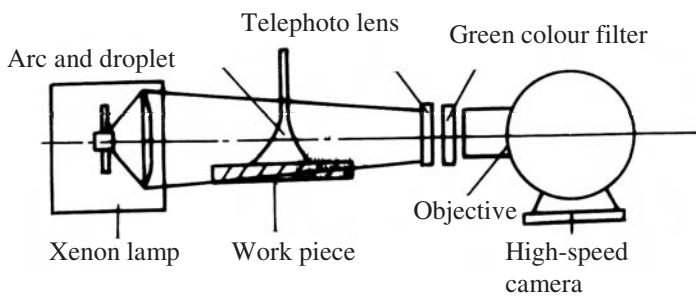

6.21 Apparatus for high-speed photography

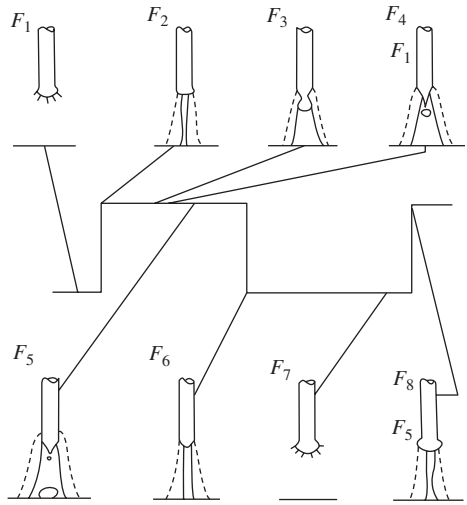

6.22 Arc form and metal transfer in DCRP pulsed MIG welding

6.2.1.1 DCRP pulsed MIG

DCRP pulsed MIG is the conventional pulsed MIG process applied in industry. A transistorised power source was used for the experimental study. The wire diameter was ϕ1.0 mm. The arc form and droplet transfer were observed by the high-speed camera at a film speed of 4000 frames/s. Figure 6.22 shows the arc form schematically.

During the background period, because the current was low, no twinkle area could be observed in the arc; only the area surrounding the wire tip was slightly bright. This phenomenon means that the arc temperature was low and there was little metallic vapour around the anode (see Fig. 6.22 F_1). A twinkle part appeared near the wire tip when the pulsed current started; it gradually elongated and became thicker as the pulsed-current time extended (see Fig. 6.22 F_2). This showed that the arc temperature and the amount of metallic vapour near the anode increased. After approximately seven frames, the amount of molten metal on the wire tip increased and the anode spot became larger. The twinkle area became a conic shape, a droplet formed, and a neck was produced by the pinch effect (see Fig. 6.22 F_3). Immediately after this (after one frame) the twinkle area jumped from the droplet to the neck (see Fig. 6.22 F_3), and forced the droplet to fall down (see F_4). The separated droplet became a sphere with a diameter as large as the wire diameter. The residual molten metal on the wire tip became sharp like a pencil tip, which could form small particles under the plasma force (see F_5). It took about 1 ms for the droplet to reach the molten pool, a distance of 3.5 mm. The metal transferred smoothly without spatter. When

the current pulse ended, the twinkle area became thin very rapidly and the sharp tip returned to a round shape (see F_6 and F_7). F_8 is the same as F_2; a new cycle started at this point.

It can be concluded that because the wire tip is the anode, the arc force on the anode is small and spray transfer can easily be obtained. The process is suitable for all-position welding. Therefore it is a popular pulsed MIG process.

6.2.1.2 DCSP pulsed MIG

As mentioned above, only reversed polarity is used for both continuous MIG and pulsed MIG in order to achieve droplet transfer and satisfactory bead formation. Therefore almost no information about straight-polarity MIG has been reported in the world's literature. DCSP MIG welding has been studied by the author in order to obtain a better understanding of this process.

(i) Arc form and metal transfer.

The arc form and droplet transfer were first observed by the naked eye through a dark-colour filter. It was found that the arc was dispersed and climbed up the wire. There always was a spherical drop on the end of the wire. The arc then was observed using a high-speed camera. The welding conditions used were 130 A welding current, Ar at 1.2 m^3/hr and CO_2 at 3 L/min shielding gas, and 1.0 mm-diameter H08Mn2Si wire. The process was stable without spatter.

Figure 6.23 shows the arc form at various times during the current pulsing. During the background period, the arc was weak, the droplet fell down with a diameter about 1.5 times that of the wire diameter, and the sharp wire tip quickly changed to a round tip after the droplet fell (see F_2). The twinkle area of the wire tip increased and fluttered rapidly when the pulsed current began. The central part of the twinkling region became a beam (see F_3). The beam diameter then increased while the shape remained unchanged. The arc climbed far up the wire and the droplet grew and tended to fall (see F_4 and F_5). When the current pulse ended, the arc form and forces exerted on the molten droplet changed; the droplet fell down by gravity and the electromagnetic force (see F_6). The volume of the droplet increased. As in DCRP welding, the wire tip became sharper but longer. The anode spot on the parent metal was relatively fixed. Essentially, one droplet was transferred during each pulse.

In DCSP, the arc climbed up the wire tip much higher than in DCRP because, in the former case, the wire is at negative polarity on which the oxide film is broken more quickly than the oxide film

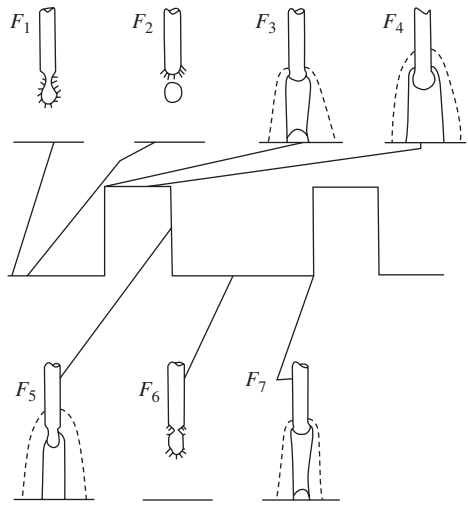

6.23 Arc form and metal transfer in DCSP pulsed MIG welding

forms. Therefore, the cathode cannot be kept at one point. The electron emission finds the spot where it has the minimum work function. As the welding current increases and the content of oxidizing elements in the shielding gas decreases, the arc climbs higher up the wire.

Under normal conditions the droplet in DCSP is larger than that of DCRP; the diameter is about 1.5 times the wire diameter. This phenomenon is caused by a different force exerted on the wire tip. It can be demonstrated that the force exerted on the cathode is larger than that on the anode, which impedes the falling down of the droplet and makes the droplet diameter bigger.

The shape of twinkle area of the arc is different in the two cases, which results in different forces on the plasma stream (see Fig. 6.24). The twinkle region of the arc in DCSP is like a column; that of DCRP is like a bell or a cone. In the case of a columnar arc, there is no axial force component and therefore no axial, static-force gradient and, therefore, no movement or convection of the plasma in the axial direction. In case of a conic arc there is an axial force gradient that therefore promotes droplet transfer.

Experimental results demonstrate that the CO_2 content in mixed gas affects the arc form and metal transfer in DCSP pulsed MIG welding. With 20 L/min Ar, the arc is stable whereas with less than 3 L/min CO_2, the droplets become smaller as the CO_2 content increases. A CO_2 flow-rate >5 L/min is detrimental to both arc sta-

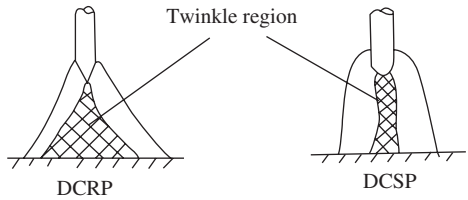

6.24 Twinkle region of DCRP and DCSP welding

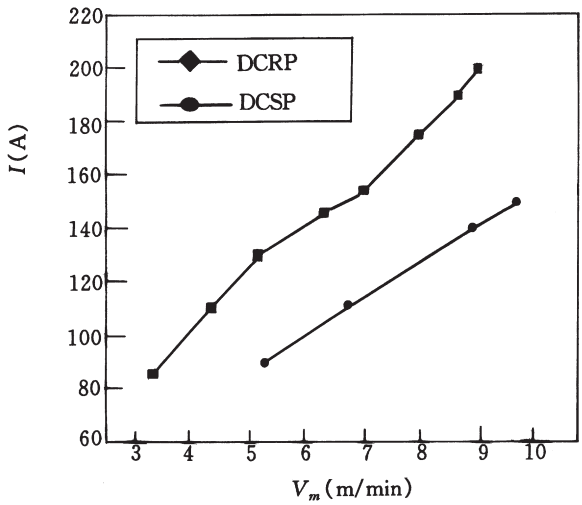

Wire diameter: 1.0 mm Ar + 20% CO_2

6.25 Steel-wire melting rate

bility and metal transfer; this is due to the cooling effect of the CO_2 gas.

The force that is exerted on the droplet can be observed by the speed of the droplets across the arc and into the weld pool in DCSP and DCRP welding. The droplet diameter is 1.5 times that of the wire, and the flight time is 5.25 ms in DCSP welding. The flight time is only 1 ms for a droplet during DCRP welding, although it has slightly smaller diameter. This phenomenon is obviously contrary to gravitational force.

(ii) Melting of the wire

The current density in MIG welding is over 250 A/mm^2; therefore the resistance heating of the wire extension cannot be neglected. For this reason, experiments were conducted with a constant wire extension. Figure 6.25 shows the results.

It can be seen that the melting rate for DCSP is 40–50% higher than that for DCRP. This difference arises because the mechanisms

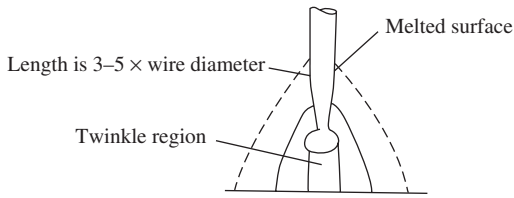

6.26 Schematic illustration of the high melting rate of DCSP

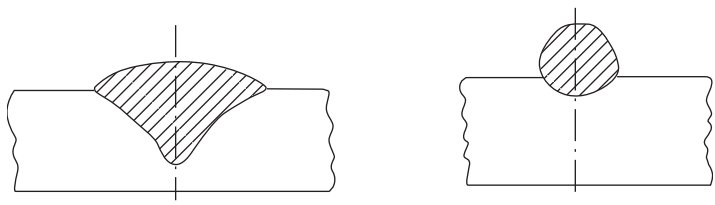

6.27 Cross-section of weld

of heat generation at the anode and cathode are different for these different processes.

It can be observed from the high-speed films that the outside surface of the wire above the droplet is melted in the case of DCSP (see Fig. 6.26). This obviously is not due to conduction of the arc heat from the tip of the wire, but rather due to the arc plasma climbing up the wire. This phenomenon surely contributes to the melting rate. The molten metal on the wire surface flows down the wire and joins with the formed droplet. From the high melting rate, it can be inferred that the temperature of the droplet in DCSP is lower that in DCRP.

(iii) Bead Formation

In MIG welding, the heat generated at both the anode and cathode are ultimately transferred to the parent metal. The molten metal of the parent metal together with the melted wire form the weld pool, which flows backward under the arc force, gravity and surface tension. This forms the bead. However, bead formation for DCSP is different from that for DCRP.

Figure 6.27 shows the cross-section of welds made by DCRP and DCSP. In DCRP the penetration is deeper, finger like, as the parent metal is negative, the arc is cone shaped, and the axial force of the plasma is larger than that of DCSP. At the same time, the force on the cathode also is larger than that on the anode.

Table 6.1 Comparison of DCRP and DCSP

	DCRP MIG	DCSP MIG
Metal transfer	Spray	Globular (1.5 times)
Penetration	Deep, finger-like	Shallow
Reinforcement	Small	Large
Melting rate	Small	Large
Anode atomisation	Yes	No
Arc blow	Yes	Yes

The reinforcement obtained by DCRP is smaller than that of DCSP because the molten metal is spread out. In DCSP, the reinforcement is higher, the bead is narrower, and the toe angle is larger because the wire-melting rate is higher. In DCRP, the cathode is on the parent metal. The cathode forms easily on the oxide-coated parent metal where the temperature is elevated. According to the theory of surface tension, the molten droplet spreads out on the pool easily. In contrast, when the anode is on the parent metal, the oxide film is stable and, therefore, the molten metal does not spread readily.

(iv) Comparison of the two pulsed MIG methods.

The advantages and deficiencies of two methods are listed in Table 6.1.

6.2.2 Control method for AC pulsed MIG welding

In the evaluation of a control system for AC MIG welding, the following items should be included: continuous existence of the arc, particularly at the moment of phase change, stable arc length, even metal transfer, little spatter, and good bead formation. Up to the present, two control methods have been reported in the published literature:

(i) High open-circuit voltage and high welding current with arc-stabilization chemicals or flux-cored wire.[15]

(ii) Square wave power source with a high-voltage arc-ignition pulse.[160–184]

The application of arc-stabilisation chemicals or a high-voltage pulse is inconvenient in practice. Completely different AC MIG control methods were developed by the author and X. D. Jiao in 1993.

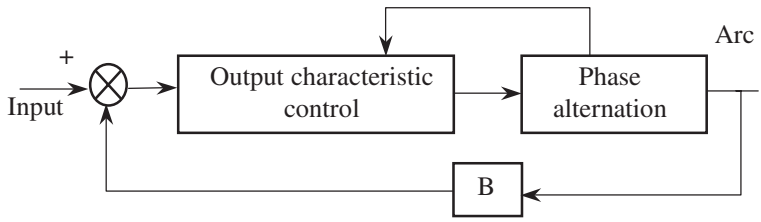

6.28 Block diagram of power source

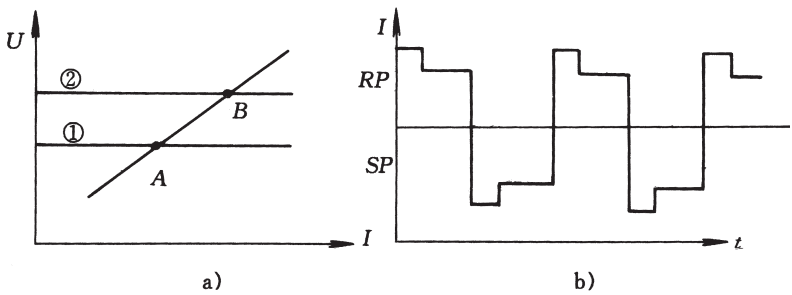

6.29 Output characteristics and current waveform for AC MIG welding

6.2.2.1 Control method for constant-current AC MIG welding

This method is applicable for MIG welding at high current, the magnitude of which is larger than the critical current for spray transfer. The block diagram of the power source is shown in Fig. 6.28.

The power-source output has a constant-voltage characteristic, which ensures good self-regulation of arc length. Two constant-voltage characteristics are applied: one is for maintaining the arc and the second is for facilitating arc re-ignition during phase changes. High-speed phase change is required to provide a stable arc. This requirement can be met easily using an inverter-type square-wave power source, which was built by the author for the present research. Figure 6.29a shows the output characteristic and Fig. 6.29b shows the current waveform under stable conditions. The arc-operating point normally is on characteristic ① at point A; at the moment the phase changes, the output characteristic is on characteristic ② at point B. An open-circuit voltage of 55 V is used for ② to facilitate re-ignition of the arc. After the phase change, the output characteristic switches to ①. The magnitude of voltage ① is linked to the wire-feed rate to allow one-knob system control.

The advantage of this system is that the frequency and ratio of RP and SP durations can be regulated independently. The arc voltage can be linked

to the wire-feed rate. The deficiency of the system is that the arc-re-ignition voltage is the same for all welding currents; therefore, the arc may not be stable at low welding currents.

6.2.2.2 *Control method for pulsed-current AC MIG welding*

Normally, spray transfer is used for MIG welding; for that, the welding current must be larger than the critical current in order to achieve transfer. Droplet or short-circuiting transfer may develop if the welding current is too low. For AC MIG welding, an additional problem is the stability of the arc at the moment the phase changes. Reducing the welding current for welding thin-gauge metal and stabilising the arc at the moment the phase changes are two important problems that need to be solved.

Four different control methods have been proposed by the author for study. The differences among these are mainly in the relationship of the instant of the phase change and the pulse-current duration. The stability of the arc was emphasized in these studies.

Method I. The current phase changes at the end of the background-current period. The output characteristic of the power source is shown in Fig. 6.30a and the current waveform is shown in Fig. 6.30b. The double-step output characteristic (‘⌝’) is used for the pulsed current and the double-step characteristic (‘⌞’) is used for the background current. The arc-operating point for the pulse duration is at point B of the constant-voltage characteristic, which ensures self-regulation of arc length; I_d is the current limit for short circuiting. The arc-operating point for the background duration is at A on the constant-current characteristic, which ensures arc stability. As shown in Fig. 6.30, at the end of the background-current period when the current changes its phase from RP to SP, the high-voltage pulse is started in order to facilitating re-ignition of the arc. After that, it follows the background current. Similarly, the pulsed current starts when the arc changes its phase from RP to SP. Both the pulsed current and the background current are linked to the wire-feed rate to achieve one-knob control. Using this control method, the droplet is transferred before the end of the background-current period. Therefore, only a small amount of molten metal is left on the wire tip, which cannot produce spatter when the pulsed current starts. On the other hand, the pulsed current facilitates re-ignition of the arc when the current phase changes.

Method II. The current phase changes at the end of the pulsed-current period. The output characteristics are the same as those shown in Fig. 6.30a. The current waveform is shown in Fig. 6.31. Supposing that the arc polarity is RP, the current starts from the background value and

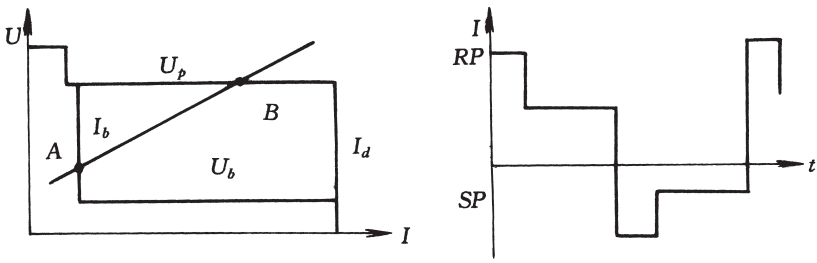

a) b)

6.30 Output characteristics and current waveform for Control Method I

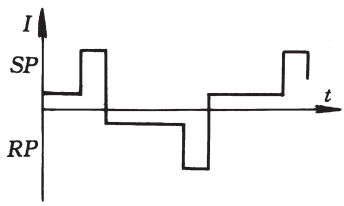

6.31 Current waveform, Method II

changes to pulsed-current value at the arc-operating point B. At the end of the current pulse, the arc polarity changes to SP. Similarly, as in RP, the current starts from the background value and changes to the pulsed-current value. To obtain a stable arc length, the electrical parameters of the arc are linked to the wire-feed rate. The special feature of this control method is that the droplet transfer happens mainly during the pulsed-current period of the RP regime but partly also in the background-current period of the SP regime. The droplet grows only during the pulsed-current period of the SP phase. At the end of the pulsed-current period, the heat energy generated by the high-current arc can facilitate re-ignition of the arc when it changes phase.

Method III. Current phase changes in the background-current period. The output characteristics are the same as those shown in Fig. 6.30a. The arc is present and droplets transfer mainly in the RP phase (see Fig. 6.32). The short duration of the SP phase is used to maintain the AC behaviour of the arc. The contribution of the arc in the SP regime to the melting of the wire is insignificant because the current is low in spite of the high melting rate during the SP period. For this reason, the duration of the SP period can be regulated over a wide range.

Method IV. Current phase changes in the pulsed-current period. The output characteristics are the same as those shown in Fig. 6.30a and the

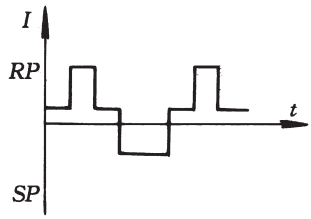

6.32 Current waveform, Method III

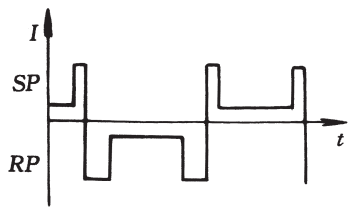

6.33 Current waveform, Method IV

current waveform is shown in Fig. 6.33. The current is high both before and after the phase change; therefore it contributes to arc stability. Because the melting rate for the RP and SP periods are different, the relationship between the average welding current and the melting rate is important for the design of the control system. The average current can be expressed as Eq. [6.6] (see Fig. 6.33).

$$I_{av} = \frac{I_p(t_{pr1} + t_{pr2} + t_{ps1} + t_{ps2}) + I_b(t_{br} + t_{bs})}{t_{pr1} + t_{pr2} + t_{br} + t_{ps1} + t_{ps2} + t_{bs}} \qquad [6.6]$$

The melting rate can be expressed as Eq. [6.7].

$$V_m = C_1 \frac{I_p(t_{pr1} + t_{pr2}) + I_b t_{br}}{t_{pr1} + t_{pr2} + t_{br}} + C_2 \frac{I_p(t_{ps1} + t_{ps2}) + I_b t_{bs}}{t_{ps1} + t_{ps2} + t_{bs}} \qquad [6.7]$$

where C_1 and C_2 are the melting rates during the RP and SP periods, respectively. All of the current parameters significantly affect the metal transfer and arc stability. Normally, $t_{pr1} + t_{ps1}$ and $t_{pr2} + t_{ps2}$ are kept constant for a given wire-feed rate. Shortening the SP duration improves the metal transfer. For that, $t_{pr1} > t_{ps1}$, $t_{pr2} > t_{ps2}$, but t_{ps1} and t_{ps2} should not be too short in order to ensure a stable arc before and after the phase change.

For better system properties, a forward control for the wire-feed rate is used. The pulsed-current magnitude and duration are increased slightly with an increase of wire-feed rate. The main control variable is the background-current duration.

All of these control methods have been experimentally studied. It was proved that the arc can be kept continuous and stable only in Method IV. It can be concluded that special measures for stabilising the arc must be taken for a sinusoidal waveform AC MIG process and the current magnitude must be sufficiently large. A high current also is required for square-wave AC MIG welding. Theoretical analyses demonstrated that three conditions should be satisfied for ensuring a stable AC MIG arc, namely sufficient current and heat energy of the arc before the phase change, sufficiently high voltage after the phase change, and rapid phase change. Method IV satisfied all three of these requirements. Therefore, a stable arc can be obtained. A power source that was designed for implementing this method and the technological experiments that were conducted are described in the following sections.

6.2.3 Power source for AC pulsed MIG welding[151]

6.2.3.1 Overall design

(i) *Requirements of the power source.*

- The output current should be high enough for spray transfer under all conditions. For a wire diameter of ϕ1.6 mm, the critical spray-transfer current is 380–420 A, the average current is 350 A, and the minimum capacity of the power source is 500 A.
- The current waveform should be square or quasi-square and the time for the phase change of the current and voltage across zero should be very short.
- Reasonable output characteristics and good control ability are necessary.

(ii) *Type of power source.* There are three main types of power sources for generating a square-wave output, namely diode-reactors, SCR reactors, and inverters. If the ratio of the maximum current magnitude to its effective value is defined as the wave-ripple coefficient, then the coefficients for the different types of power sources can be given as in Table 6.2.

Table 6.2 Current wave-form ripple coefficient

Type of power source	Ripple coefficient
Inverter	1.00
SCR + Reactor	1.15–1.30
Diode + Reactor	1.30–1.35
Normal sine wave	1.41

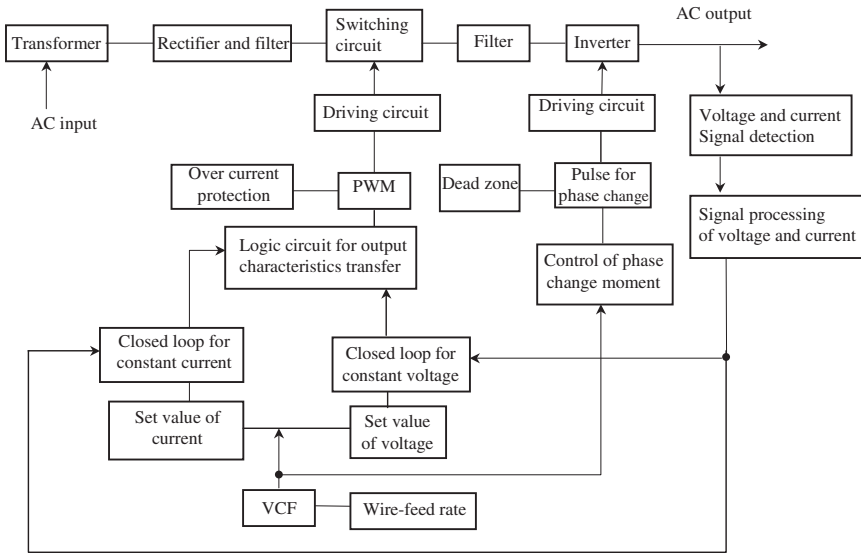

6.34 Configuration of AC pulsed MIG power source

Obviously, the waveform would be closer to a square wave if the coefficient were close to 1. This means that the speed that the current crosses zero is fast and the heat efficiency of the arc is high. It is seen from the table that DC rectifier plus inverter power sources meets the requirements listed above.

(iii) *General configuration*. The principle design concept is to make the power source in two parts, namely the part for controlling the output characteristics and the part for producing the alternating current. The control system and power source for the QH-ARC 101 were used for the first part (see Chapter 4). Two alternating double-step output characteristics are generated. (The difference between the present design and the power source described in Chapter 4 is that a switching-mode power transistor is used for the former and an analogue-mode power transistor is used for the latter). A full-bridge inverter circuit is used for the second part, which alternates the current phase according to the technological requirements. Figure 6.34 shows the block diagram of this system.

The special features of the power source are as follows:

- Stepless frequency regulation.
- Nonsymmetrical current-output magnitude and duration.
- Phase change can be preset at any moment during the high-current period.

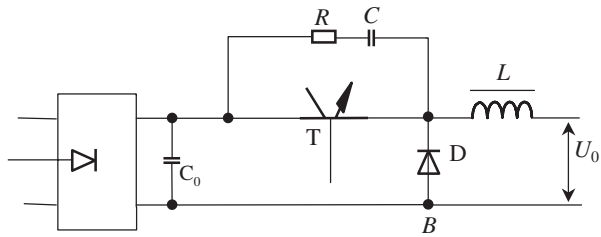

6.35 Diagram of a switching-mode transistorised DC power source

6.2.3.2 Main power circuit

(i) *DC power circuit*. The main DC power circuit consists of a transformer, a three-phase rectifier, switching circuit, and filter. Its main function is to supply the invertor with the required output characteristic. Because the power is very high, a switching-mode, transistorised circuit is used, as shown in Fig. 6.35, which consists of transistors T (due to the high load, hundreds of transistors are connected in parallel with resistors for equalising the current); diodes for continuing current D, filter L, a three-phase rectifier, and an RC protection circuit. The main circuit is controlled by PWM mode with a working frequency of 16–20 kHz. The transistor array is saturably conducting during the T_{on}, when the electrical energy is accumulated in the inductance. The transistors are blocked off during T_{off}, when the inductance discharges via diode D. The inductance plays the role of a filter; its effect is larger when the frequency and current are high. In the present design, 30 μH was chosen for the inductance on the basis of two considerations, namely the effect of filtering and the dynamic properties of the system. The inductance also influences the safety of the inverter's bridge transistors.

(ii) *Inverter*. The function of the inverter is to transform DC into AC. The principle of operation is shown in Fig. 6.36. Switches K_1 and K_4 are one group and K_2 and K_3 are another group. When K_1 and K_4 are conducting, K_2 and K_3 are blocked off, and the output has positive polarity. At another moment when K_1 and K_4 are blocked, K_2 and K_3 are conducting, and the output has negative polarity. In this way, square-wave AC current can be obtained when the process repeats continuously.

As mentioned above, the square-wave current should cross zero as fast as possible, which imposes rigorous requirements on the bridge elements, namely

- Fast switching speed
- Low switching energy consumption
- Good parallel connection properties
- A simple driving circuit and low driving power
- Resistance to voltage and current peaks

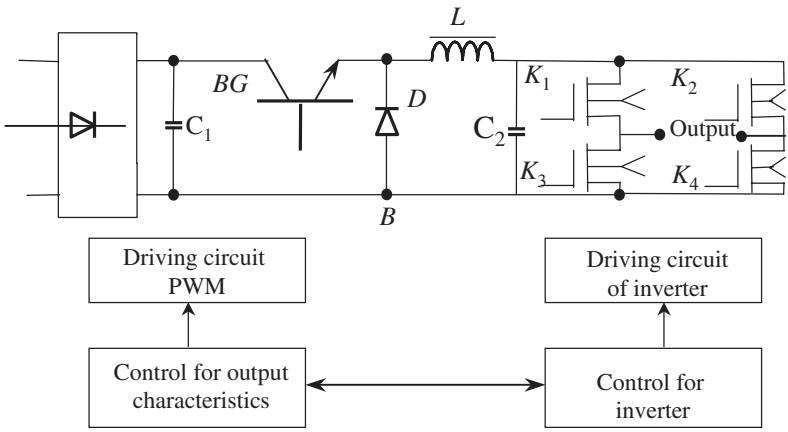

6.36 Main circuit of an AC MIG power source

The power element for the inverters can be thyristors (SCR and GTO), large power bi-directional thyristors (GTR), or V-groove MOS field-effect transistors (VMOSFET).

Thyristors have good resistance to dv/dt and di/dt, large capacity, and good over-current capacity, but their switching speed is low and the control circuit is complicated. GTRs have large capacity, good controllability, and high switching speed but their fatal weakness is the secondary breakdown problem and the capability for parallel connection. Power MOSFETs have many advantages compared with SCRs and GTRs; they provide high switching speed, simple driving circuits, wide safe-working ranges, ease of parallel connection, and no problems due to secondary breakdown.

In the present design, MTM40N20 power MOSFETs were chosen. These have a drain-pole voltage $V_{DSS} = 200\,\text{V}$, gate-pole voltage $V_{GS} = \pm 20\,\text{V}$, drain-pole continuous current $I_D = 40\,\text{A}$, drain-pole pulse current $I_{DM} = 200\,\text{A}$, power consumption $P_{DM} = 250\,\text{W}$, and resistance in the conducting state $P_{DS}(on) = 0.08\,\Omega$. Considering that the characteristics of the transistors can vary widely, and there is a powerful impact on the power source due to arc ignition, 15 MOSFETs were used for each bridge.

(iii) *Parallel connection of MOSFETs*. Because MOSFETs have a positive temperature coefficient, their thermal stability is good, their working range is large, and they are very easy to connect in parallel. However due to a difference between the static and dynamic properties of the transistors, even of the same type, special measures must be taken for their connection.

- Equalisation of current in the static state. The equalisation of current between transistors in the static state depends on the conducting resistance $P_{DS}(on)$ and its temperature coefficient. As mentioned above, the

temperature coefficient of the resistance is positive so if any transistor has a smaller value of $P_{DS}(on)$ and higher current, the temperature rise due to the current will increase the resistance and reduce the current; therefore, parallel-connected transistors can automatically equalise the current between themselves. For still better results, transistors having nearly the same characteristics should be selected for parallel connections and, preferably, be mounted on the same cooling plate.

- Equalisation of current in the dynamic state. The equalisation of current in the dynamic state is important for the circuit. Fortunately, in the present design, the inverter works at low frequency so the problem is not too serious. The most important factors that affect the equalisation are the trans-conductance g_{ts}, the threshold voltage $V_{vs(th)}$, and the output impedance of the driving circuit. Transistors of similar transconductance and threshold voltage should be selected for parallel connection, the output impedance should be made smaller, and an adequate resistance should be connected in parallel with the gate pole.

6.2.3.3 Driving circuit

Because the arc is extinguished during the phase changes, the frequency should not be too high in order to ensure arc stability. Moreover, the working duration of the two bridges is not symmetrical; a separate circuit should drive each bridge but they should have the same characteristics.

The relationship between the conducting and blocking periods of the two bridges is the key problem for ensuring the normal and safe operation of the inverter. The control circuit is shown in Fig. 6.37. The circuit consists of resistors, capacitors, and NAND and AND gates. If both bridges conduct simultaneously, the inverter will be destroyed. On the other hand, if both bridges are blocked simultaneously, the arc will be extinguished. Moreover the duration of blocking affects the magnitude of the induced voltage peak; too long a block duration also can destroy the transistors.

The principle of the control circuit is as follows. In Fig. 6.37, U_1 is the pulse input a to AND gate 1 (the input at terminal b is the opposite value

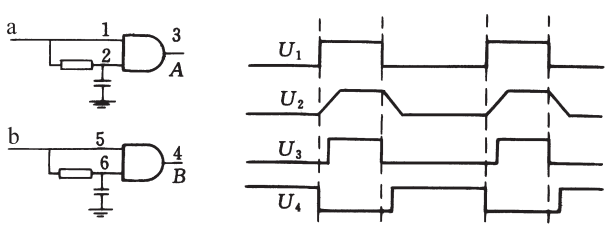

6.37 Circuit for obtaining the simultaneous blocking duration

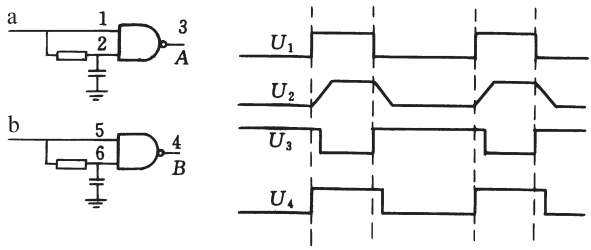

6.38 Circuit for obtaining the simultaneous conducting duration

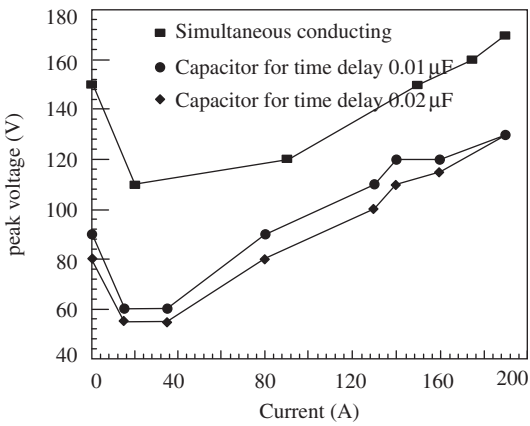

6.39 Voltage peak on MOSFET under different circuit parameters

of *a*), U_2 is the integrated value of *a* and is sent into gate 2 of the AND gate. U_3 is the output of AND gate 3 and U_4 is the output of another AND gate. By comparing U_3 and U_4, the simultaneous blocking duration can be obtained (U_3 and U_4 are the control signal for the two bridges of the inverter). Similarly if NAND is used instead of AND, the simultaneous conducting duration can be obtained: see Fig. 6.38.

The magnitudes of the simultaneous blocking and simultaneous conducting durations have a great affect on the voltage peak exerted on the transistors. This problem has been experimentally studied. The results are shown in Fig. 6.39.

The following conclusions can be drawn from the figure:

- The magnitude of the voltage peak is proportional to the current. Because the voltage peak results from the inductance discharge, higher current will cause higher energy to be accumulated in the inductance.
- An adequate simultaneous-blocking duration is advantageous because it decreases the magnitude of the voltage peak.

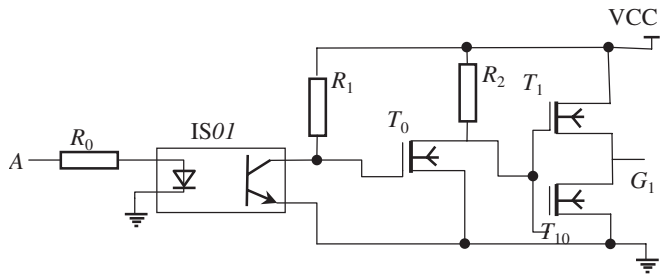

6.40 Driving circuit for inverter

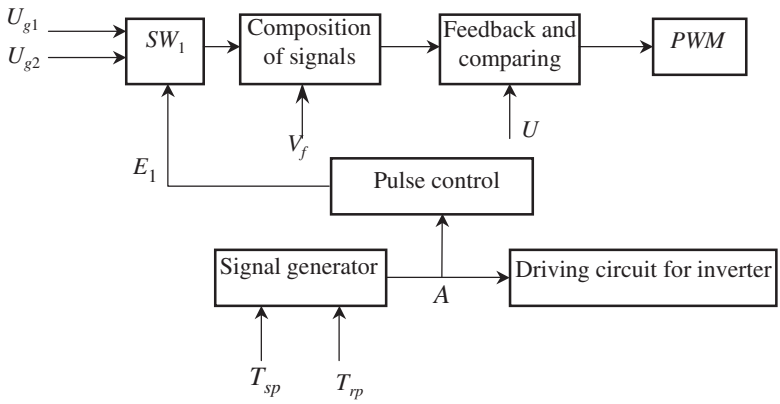

6.41 Block diagram of the control circuit

One branch of the driving circuit is shown in Fig. 6.40. Signal A is input via an optical coupler and a shaping circuit is used for driving the transistor of the push-pull inverter. Experimental study demonstrated that the designed circuit had good properties.

6.2.3.4 Control circuit

(i) *AC MIG welding with constant current*. One feature of this process is that the current magnitude does not change during welding (except for current fluctuations due to arc-length disturbances); a higher voltage (the open-circuit voltage) is applied to the arc only when the current phase changes for re-ignition. The output characteristic and the current waveform are shown in Fig. 6.29. The control circuit is shown in Fig. 6.41.

Two square-wave signals with opposite current phases are emitted by a signal generator, which controls the driving circuit of the inverter. The durations of the SP and RP periods are controlled by T_{sp} and T_{rp}; they also

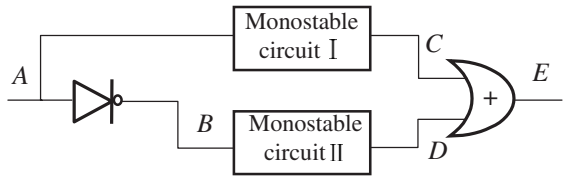

6.42 Principle of the pulse-control

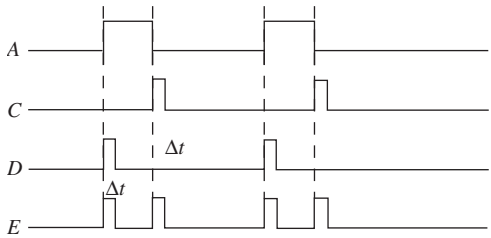

6.43 Waveform at different points of the control circuit

control the electronic switch SW_1, via the pulse-control element. The switch SW_1 selects a strobe signal U_{g1} or U_{g2} depending on the potential level of E. A low potential level of E selects U_{g1} and a high potential level selects U_{g2}. The U_{g1} output characteristic is on ① and the U_{g2} output characteristic is on ②. V_f is the wire-feed signal, which adjusts the vertical position of the output characteristic.

Figure 6.42 shows the principle of the pulse-control circuit. The signal for driving the inverter A and $\overline{A}$ separately triggers monostable trigger-action circuits I and II. Their output, C and D, are fed to an OR gate, which sends out the signal E. The waveform at different points in the circuit is shown in Fig. 6.43. The duration of the high-voltage (open-circuit voltage) output is controlled by the monostable circuits I and II. Thus the AC MIG process can operate with a stable, continuous arc without arc blow.

(ii) *AC MIG welding with pulsed current*. In order to obtain spray transfer, the magnitude of the current should exceed the critical value for spray transfer, which is high and limits the application of the AC MIG process for thin-gauge plates. For this reason, the author proposed AC pulsed MIG welding.

Figure 6.44 shows the electrical diagram of the AC pulsed MIG power source. VFC is a voltage frequency converter and SW is an electronic switch. Operational amplifiers A_3 and A_4 control the frequency and pulse width of the VFC. IC_4 and IC_5 are optical couplers. The AC pulsed MIG process is controlled by the joint actions of an 'AC control unit' and the VFC. Different pulsed AC waveforms are obtained using different 'AC

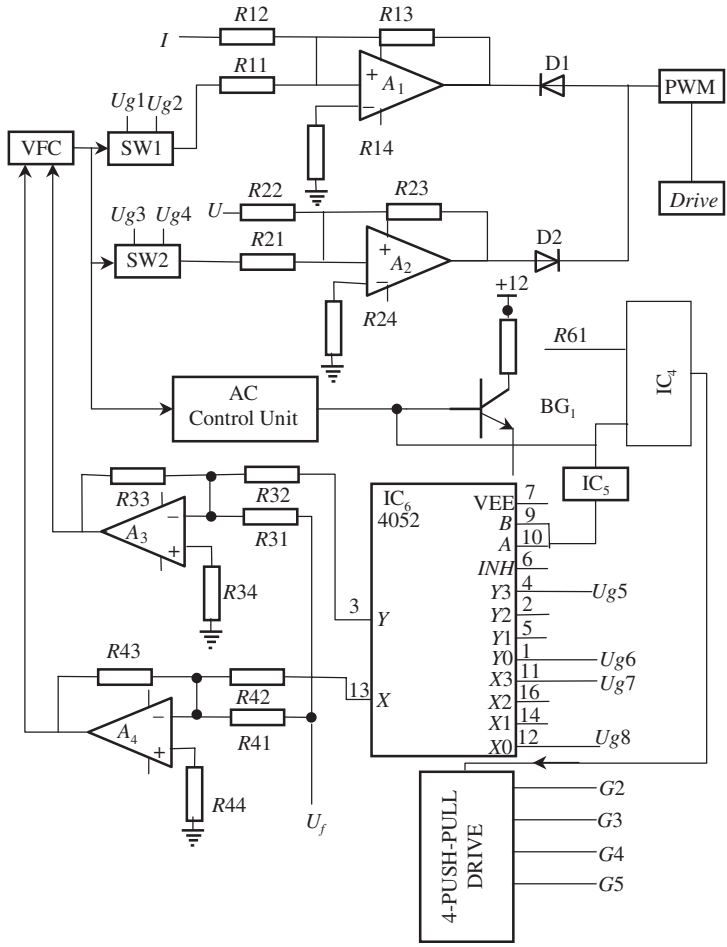

6.44 Electrical circuit for controlling a pulsed AC MIG power source

control units'. Different control units are described in the following paragraphs.

Figure 6.45 shows the electrical diagram for controlling a 'double-concavity current waveform'. The optical coupler is connected so that it sends out a signal that has the reverse phase of its input. Figure 6.46 shows the waveform at different points in the circuit. The circuit operates as follows (see the output characteristics of the power source in Section 6.2.2): The output of the VFC controls the output characteristics of the power source. It selects SW_1 or SW_2 for constant-current or constant-voltage output, respectively. U_{g1} and U_{g2} are for the background current I_b and the protection current I_d. U_{g3} and U_{g4} are for the background voltage U_b and the pulse voltage U_p.

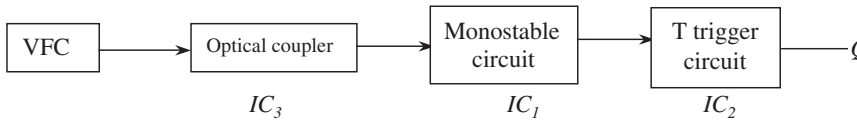

6.45 AC control unit for Method IV

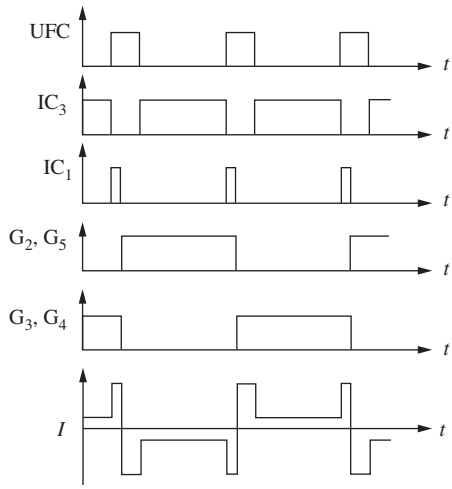

6.46 Waveform at different points for Method IV

The output signal of the VFC also controls the phase change via the optical coupler IC_3, monostable circuit IC_1, and the triggering circuit T (see Fig. 6.45). The frequency of the VFC is controlled by U_{g5} and U_{g6}, and the pulse width is controlled by U_{g7} and U_{g8}. The frequency and pulse width are linked with the wire-feed rate to provide one-knob control. When the output of the VFC is at a high potential, the power source emits a high-voltage pulse. After a time delay of $\Delta t'$, the inverter changes phase and the welding current changes its polarity. This process repeats continuously so that a 'double-concavity current waveform' is generated. The delay times Δt and $\Delta t'$, which are controlled by IC_1, are important parameters.

- Circuit for Method I. The control unit that produces a phase change at the same moment that the current pulse initiates is shown in Fig. 6.47. The waveforms at various locations are shown in Fig. 6.48.
- Circuit for Method II. To produce the phase change at the end of the pulse, IC_3 is connected so that its output is the same phase as its input. Figure 6.49 shows the waveforms at various locations in the circuit.
- Circuit for Method III. For the phase change to occur during the background-current period, it is necessary to connect the optical

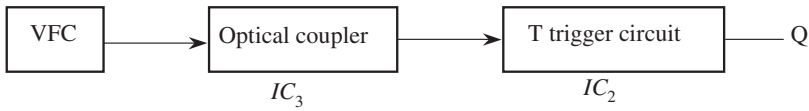

6.47 AC Control unit for Method I

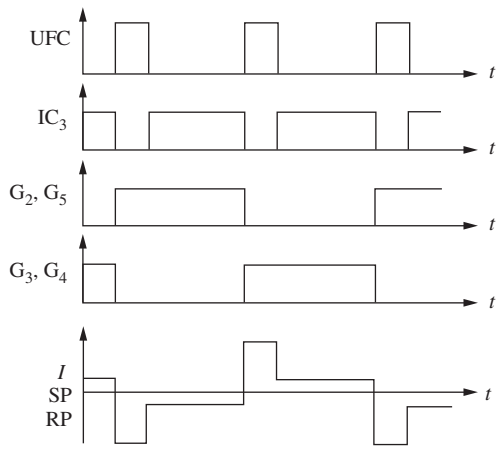

6.48 Waveforms at different locations for Method I

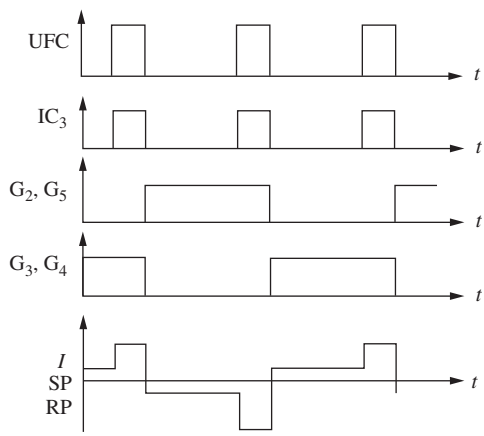

6.49 Waveforms at different locations for Method II

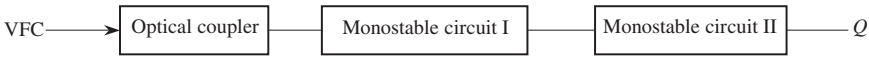

6.50 AC control unit for Method III

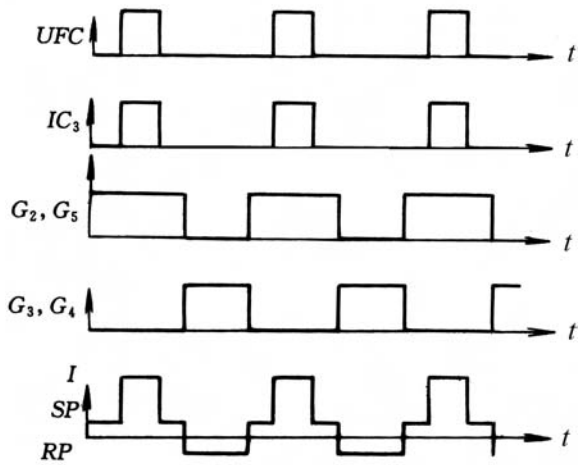

6.51 Waveforms at different locations for Method III

coupler so that its output has the same phase as its input as shown in Fig. 6.50.

Figure 6.51 shows the waveforms at various locations in the circuit. The time between when the pulse ends and the phase changes at t_1 is controlled by the monostable circuit I. The duration of the SP polarity is controlled by the monostable circuit II.

(iii) *Sampling and processing of current and voltage signals*. Detection, transfer and processing of the current signal are important for current control and over-current protection. There are two categories of sampling devices; one comprises conventional low-response speed-detection instruments such as AC mutual inductors and the other comprises high-response speed-detection instruments such as Hall-effect devices and inductance-free resistors.

In the present design, a Hall-effect device, which is isolated from the main power circuit, is used. An optical coupler, which also is isolated from the main power circuit, is used for measuring the voltage by means of resistor. To correct the nonlinear characteristics of the device, a compensating circuit has been designed and implemented. Practice has proved that both sampling methods are fast and accurate.

6.2.3.5 Protection circuit

(i) *Prevention of over-voltage and protection of switch elements*.

- In the AC MIG power source, there are two circuits that use switching devices, namely the output-characteristic control unit and the AC phase-change circuit. Due to inevitable inductance in the circuit, the switching transistors are subjected to a high-voltage peak. To protect the transistors, a resistor-capacitor network was used to absorb the energy.
- When the resistance between the gate and the source pole is too high, the sudden voltage change between the drain and the source pole can couple across the poles and produce an over voltage V_{GS} at the gate pole. The over voltage can destroy the oxide films in the gate pole. A 20 V Zener diode was connected in parallel with the gate and the drain pole to provide protection. An open circuit of the gate is prohibited.

(ii) *Over-current protection*. The main power circuit was designed with ample capacity. A current-feedback loop was used to liming excessive current ('over-current') during short circuiting. In the DC part of the circuit, a current sampling device was used that can cut off the power source when the welding-current diode is destroyed or the inverter circuit fails. A suitable sized capacitor should be connected between the output terminals. Too large a capacitance can introduce a current peak during arc ignition.

(iii) *Prevention of direct current conducting in one bridge of the inverter*. A conducting-current dead period was designed into the inverter to prevent the conducting of direct current through one bridge of the inverter. To ensure that the transistor is blocked in an open-circuit condition, a fixed resistor was connected between the output terminals.

6.2.3.6 Arc-ignition control

The AC MIG arc is good for avoiding arc blow, but its stability is poorer than that of the DC MIG arc, particularly when starting the arc.

As mentioned before, the stability of the AC MIG arc is attributed to the inertia of the heat energy of the arc. When starting the arc, both the wire and parent metal are cold, the arc is weak, the heat-energy inertia is low, and, therefore, the arc can be extinguished easily, particularly during the phase change. This problem also arises when the arc breaks down and is re-ignited.

To solve this problem, an ignition and re-ignition circuit was designed as shown in Fig. 6.52.

The normally closed contact K is linked to the 'start' knob. The monostable circuit I is triggered by the back edge of the pulse and emits a pulse

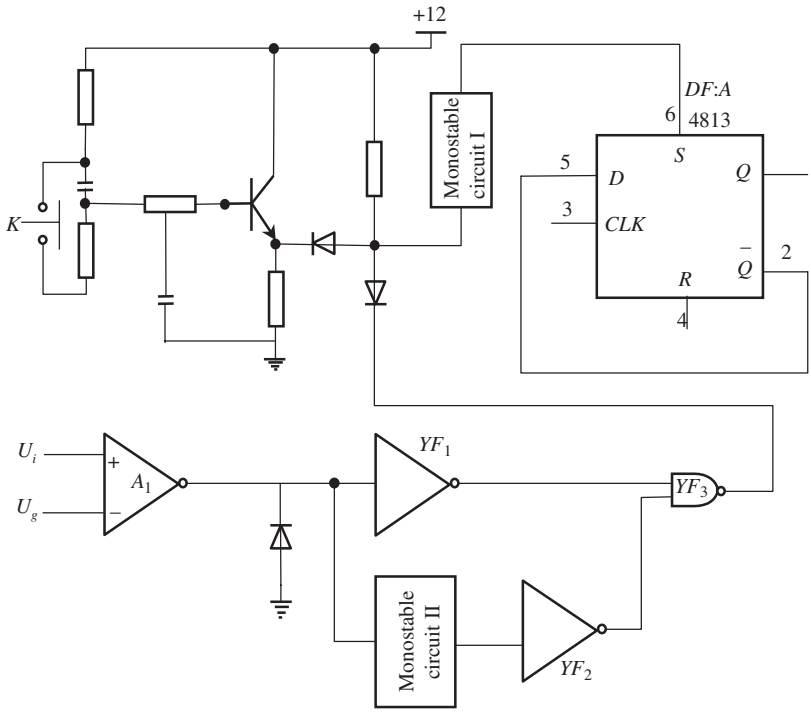

6.52 Ignition and re-ignition circuit

of duration τ, which forces the *D* flip-flop output logic 1 at Q. Then the power-source output is RP, which helps make the ignition of the arc reliable. Similarly, if the welding voltage $|U_1|$ is lower than the reference $|U_g|$ and the duration is longer than the pulse duration of the monostable circuit II, NAND gate YF_3 emits a back edge of a pulse, which triggers monostable circuit I and forces the power-source output to be RP for a duration of τ.

Figure 6.53 is the sequential waveform of the circuit, which illustrates the principle of the re-ignition control. At the moment of the phase change, there is no output from either YF_3 or monostable I; they emit a signal only when the arc breaks down, which forces the arc to convert to DCRP for a certain duration to facilitate arc re-ignition. The pulse duration of monostable II needs to be preset longer than the duration of the phase change.

The integration of the circuits described above, together with the ignition circuit, constitutes a reliable AC pulsed MIG power source. The phase change is fast: 100 A/50 μS. The AC frequency, ratio of the durations of SP and RP, and the magnitude of the current and voltage can be regulated independently and arbitrarily.

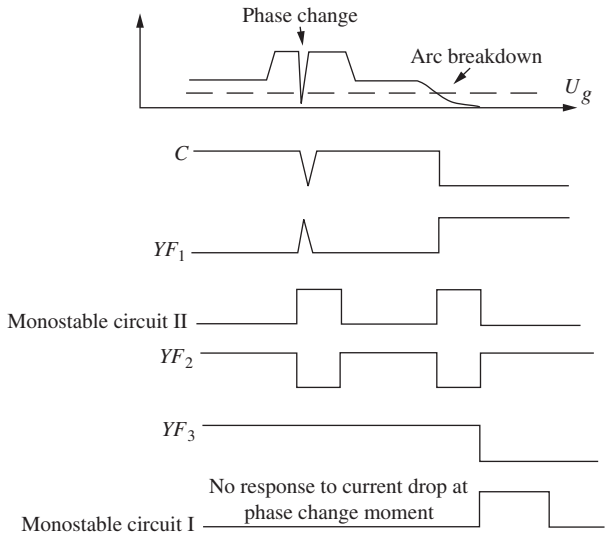

6.53 Time sequence for the ignition and re-ignition circuit

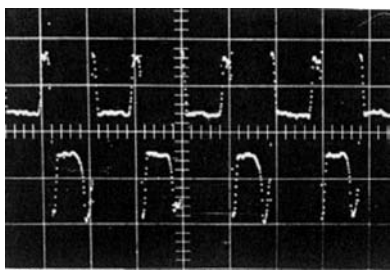

6.54 Current waveform for Method IV

6.2.4 Experiments

The conditions for the experiments that were conducted were: ϕ1.0H08Mn2Si wire, Ar = 1.2 m^3/h+ adequate CO_2 (3 L/min) shielding gas, and 55 V open-circuit voltage. No circuit for stabilising the arc was used. The results demonstrated that the arc was unstable when Methods I–III were used; short circuits and arc breakdown occurred frequently. The arc was stable only when Method IV (the 'double-concavity current waveform') was used; no arc breakdown was observed. Figure 6.54 shows the current waveform and Fig. 6.55 shows the trajectory of the arc-operating point on the *U-I* plane.

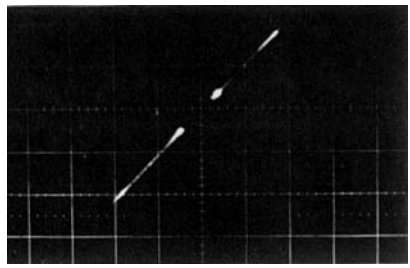

6.55 Trajectory of the arc-operating point on the *U-I* plane

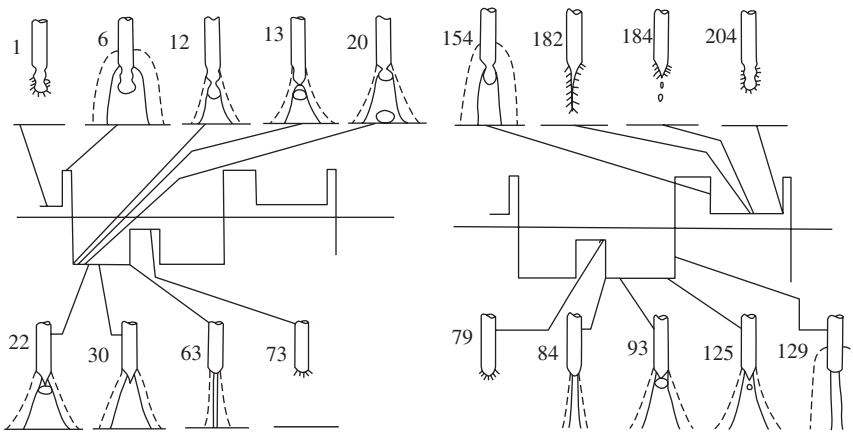

6.56 Arc forms and metal transfer of the AC pulsed MIG welding

6.2.4.1 Arc form and metal transfer of AC pulsed MIG welding

Many high-speed films of the welding arc have been reviewed. The arc form or shape and metal transfer can be divided it into four stages; see Fig. 6.56.

Stage I – The current changes from SP to RP. The arc is weak and dispersed; only a small twinkle ring surrounds the gourd- or bottle-shaped molten metal on the wire tip. There is no twinkle on the solid wire: see Fig. 5.56, image 1. This shows that the arc temperature is low, and there is very little metal vapour and a small degree of ionisation. When the SP pulse appears, the arc climbs up the wire, twinkle appears around the wire end, and a cylindrical twinkle region appears on the wire tip. As long as the pulse continues, the diameter of the cylindrical twinkle increases and the arc continues to climb (see Fig. 6.56, image 6). It can be seen that the cathode spot wobbles on the tip and the volume of molten metal increases, but no metal transfer occurs. When SP changes to RP, the twinkle region moves down to the wire tip quickly. The twinkle region weakens slightly at first but then becomes stronger very quickly. During the RP pulse period, the twinkle

region at the center of the arc become a cone shape from a cylindrical shape, a neck produced by the pinch effect appears on the wire, (see Fig. 6.56, image 12) and then a droplet transfers to the pool (Fig. 6.56, image 13). The volume of the droplet is bigger because of the heat accumulated during the SP period. The diameter of the droplet is 1.5 times that of the wire diameter and the time required for the first droplet to form is 1 ms faster than in the normal case.

Stage II – The role of the RP pulsed current. After the first droplet forms, 3–5 more droplets can transfer successively. The diameters of the droplets gradually decrease; the maximum diameter is less than the wire diameter. The forces exerted on the droplet include the plasma stream, electromagnetic force, and droplet gravity force (see Fig. 6.56, images 20, 22, and 30). When the background current starts, the small amount of molten metal left on the wire tip shrinks and becomes a sphere, the arc is weakened, and only a weak twinkle spot remains on the wire tip (Fig. 6.56, images 63 and 73).

Stage III – The welding current changes from RP to SP. The phenomena in this stage are variable and complicated but are important. When the background current ends (Fig. 6.56, image 79), the pulsed current starts again, the arc concentrates in the middle of the wire tip, the twinkle part becomes cone shaped, 1 or 2 droplets may transfer to the molten pool, and the arc and plasma reach their highest temperatures (Fig. 6.56, images 84, 93, and 125). When the phase of the current reverses, the arc rapidly climbs and moves along the periphery of the wire at its end. The shape of arc is no longer conical but is cylindrical (Fig. 6.56, image 129). If the droplet has not fallen to the molten pool during the RP period, it may wander left and right under the cathode-spot force. The cathode spot wanders simultaneously and the droplet continues to grow and finally falls into the pool when its diameter reaches 1.5 times the wire diameter (Fig. 6.56, image 154). After this drop falls, the melted metal on the surface of the wire end flows down, the wire tip becomes very sharp like a needle as if the wire skin had been stripped away (Fig 6.56, image 182), and after this, 2–3 fine droplets may transfer to the weld pool. The cathode spot does not wander as violently at the later stage of the SP period as it did at the beginning of this stage.

Stage IV – The background duration during the SP period. The needle-like part of the wire breaks up into short or long segments and falls into the pool (Fig. 6.56, image 184). The residual molten wire shrinks and becomes spherical. A neck forms between the molten sphere and the solid wire. A slightly bright spherical cathode spot can be observed on the spherical droplet but it is not as bright as it was during the background period of the RP stage because the arc is more dispersed (Fig. 6.56, image 204).

The current waveform shows that AC MIG welding constitutes alternating DCRP pulsed MIG and DCSP pulsed MIG welding. But in view of the

Table 6.3 Experimental results of the spatter-loss coefficient while $\Delta t = 2$ ms

Welding current (A)	Deposited metal (g)	Spatter loss (g)	Spatter-loss coefficient (%)
110	50	2	4.0
120	35	2	5.7
140	45	1.5	3.3
160	55	2.2	4.0

arc form and metal transfer, the AC MIG process is not a simple superposition of these two welding methods. In the DCRP portion of AC MIG, the arc form is not very different from the simple DCRP pulsed MIG welding arc form although the number droplets transferred is greater (3–4 droplets) and the volume of the first droplet is larger. The arc form in the DCSP portion of AC MIG welding is different from the simple DCSP pulsed MIG arc form. First, the cathode spot wanders very violently immediately after the phase changes and second, the arc climbs much higher. A droplet may transfer during the pulse. Because the current magnitude is large, the droplet size is small. The droplet size during the background period also is very small because the skin of the wire has been stripped off during the SP period and the solid wire that remains and can be melted has a smaller diameter.

6.2.4.2 Spatter in AC pulsed MIG Welding

In conventional MIG welding using RP, the arc and metal transfer are stable and there is little spatter. In SP MIG welding, the arc also is stable, the metal transfers in large drops, and there is little spatter as well. However, if the welding current varies widely, very large drops form and heavy spatter is deposited.

The current variation in AC pulsed MIG welding is larger than that in DC pulsed MIG welding. Therefore, the spatter loss is larger than that in DC pulsed MIG welding.

The amount of spatter was measured directly during AC pulsed MIG welding. The spatter particles were collected in a vessel. The difference between the work-piece weights before and after welding was taken as the weight of the deposited metal. The ratio of the weight of the spatter particles and the deposited metal was defined as the spatter-loss coefficient. The results are shown in Table 6.3. The time delay between the moment of the phase change and the start of the pulse was 2 ms, as shown in Fig. 6.57.

The table shows that the spatter-loss coefficient is almost as large as in CO_2 welding. The reasons for this can be described as follows:

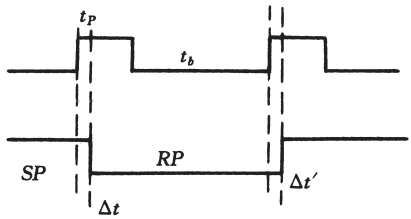

6.57 Time sequence of the phase change and current-pulse waveform

(i) Large current variation
In order to ensure arc stability, 280 A pulsed current was chosen at the phase change for a wire diameter of 1.0 mm. The current variation was 560 A during the phase change. Therefore, there is a large variation of arc force and heat energy; the droplet formed in the SP period accelerates very rapidly, impacts on the molten pool, and produces spatter. It can be seen from the high-speed film that the spatter particles fly vertically upward. A lot of spatter accumulates in the torch nozzle, which helps demonstrate the mechanism. On the other hand, the droplets formed during the SP period are very big, they cool during the phase change, and are heated rapidly during the RP period. Gas produced by metallurgical reactions expands and produces spatter.

(ii) Larger droplet volume
The droplet volume in AC MIG welding is larger than that in DCRP MIG welding. Spatter is generated when large droplets fall into the molten pool. High-speed film shows that a series arc can form between wire tip, droplet, and the parent metal. The forces exerted on the droplet by two arcs can push it away from the normal vertical path to form spatter.

(iii) The arc wanders violently when it changes from RP to SP.
When the current changes from RP to SP, the wire tip becomes the cathode and the arc wanders and climbs up the wire. Because the droplet forms during the RP period, it has been present for 2 ms. It remains until the SP period starts. The strong arc during the SP period makes the droplet grow rapidly, wander, and create spatter.

(iv) Spatter is generated mainly when RP changes to SP.
The high-speed film shows that the arc form and its surrounding atmosphere change violently when it changes from RP to SP. This produces spatter and explosion of droplets. But they are quite smooth while the current changes from SP to RP. According to the observation and analysis made above, a practical experiment was carried out to measure the spatter-loss coefficient when Δt was

Table 6.4 Experimental results of the spatter-loss coefficient while $\Delta t = 2.5$ ms

Welding current (A)	Deposited metal (g)	Spatter loss (g)	Spatter-loss coefficient (%)
110	65	0.6	0.9
120	35	0.5	1.0
140	55	0.5	0.9
160	60	0.6	1.0

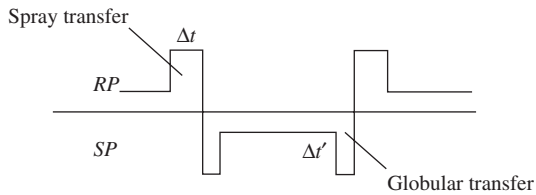

6.58 Effect of Δt on the mode of the metal transfer

regulated. The coefficient decreased greatly when Δt was extended to 2.5 ms. Table 6.4 shows the experimental results. The phenomena can be explained as follows. First, because $t = 2.5$ ms, there is time for the droplet to grow and separate from the wire tip so that after changing from RP to SP, there is not much molten metal left on the wire tip for transferring to the weld pool or generating spatter. Also, there is oxide film on the solid wire surface (but no oxide film on the melted droplet), so the cathode spot will not wander violently after changing from RP to SP. Second, in simple SP MIG welding, the diameter of the droplet does not exceed 1.5 times the wire diameter. Therefore in AC pulsed MIG welding, the droplet formed in the period $\Delta t'$ will not become spatter (see Fig. 6.58). The droplet formed in this period can be transferred in the successive RP period. Experiments were conducted by the authors with $\Delta t = 2.5$ ms and $\Delta t' = 1$ ms. The metal transfer improved and the amount of spatter decreased. Longer Δt and shorter $\Delta t'$ improve the mode of metal transfer; the greater portion of metal transfer takes place during the RP period.

6.2.4.3 *Melting rate during AC pulsed MIG welding*

The experimental conditions were 1.0 mm diameter H08Mn2Si wire, 1.2 m^3/hr Ar with 3 L/min CO_2 shielding gas, 22 mm wire extension, and con-

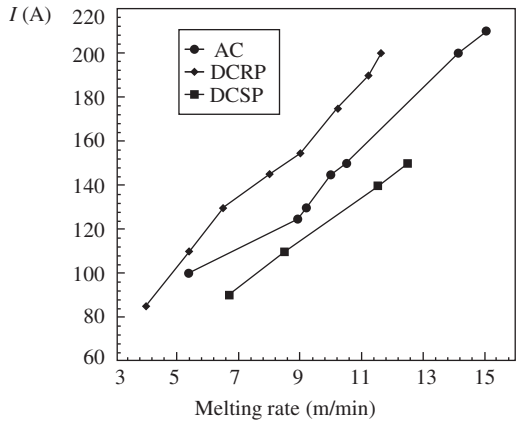

6.59 Melting rate of steel wire

stant arc length, which was regulated by the wire-feed rate. The results are illustrated in Fig. 6.59, from which it can be seen that SP produces the highest melting rate, RP produces the lowest, and AC MIG welding is in between. These results are understandable based on the nature of metal transfer that was described in previous sections. It can be concluded that one of the advantages of AC pulsed MIG welding is the higher productivity it provides. In other words, less energy input is needed for melting a given quantity of metal.

6.2.4.4 Bead formation in AC pulsed MIG welding

Experiments were conducted to measure the bead reinforcement during DCRP, DCSP, and AC MIG welding. The results are illustrated in Table 6.5, where B represents the bead width, a is reinforcement, and V_w is welding speed. These results show that the reinforcement coefficient (B/a) of DCSP welding is less than 3, while that of AC pulsed MIG welding is more than 3. Therefore, AC pulsed MIG welding meets the technological requirement regarding bead formation.

6.2.4.5 AC DCRP welding

Arc blow occurs most often during root-pass welding in a groove. Experiments demonstrated that AC pulsed MIG welding effectively avoids arc blow. However, for root-pass welding, small currents are normally used and the weld-toe angle is large due to less wetting of the groove surface by the arc. A new welding process was proposed by the author, namely an alternative AC plus DCRP welding method. Figure 6.60 shows an oscillogram

Table 6.5 Bead width and reinforcement, V_w = 135 mm/min

DCRP						
B	14	15	14	14.5	13.5	15
a	3	3.5	3	3.2	3.5	3.2

DCSP				
B	14	14	14.5	14
a	5	5	5.8	5

AC pulsed MIG welding				
B	12.5	14	13.5	12.5
a	4	4.2	4.5	5
B/a	3.1	3.3	3.0	2.5

(Ar = 1.2 m^3/min, CO_2 = 3 L/min)

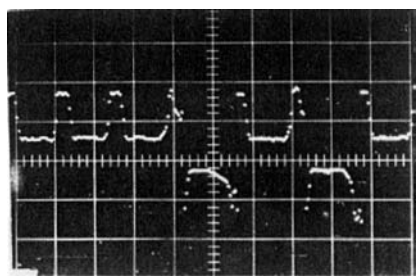

6.60 Current wave-form for AC/DCRP process

of the current taken during welding. The problem that should be considered for the present method is how to determine the moment that the current changes from AC to DCRP or vice versa. The principle that should be followed in the determination is that the moment of the change should be during the pulse period in either case. Figure 6.61 is the electrical diagram for implementation of the control. Figure 6.62 is the time sequence of the control.

The logic relation may be expressed as

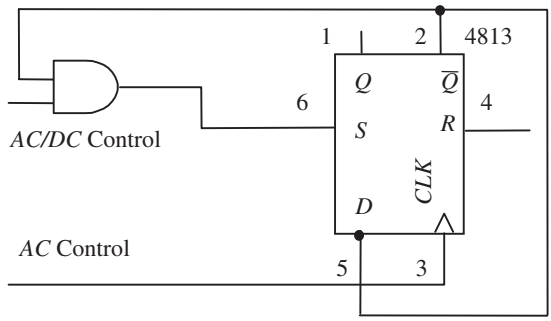

6.61 Control circuit for AC/DCRP

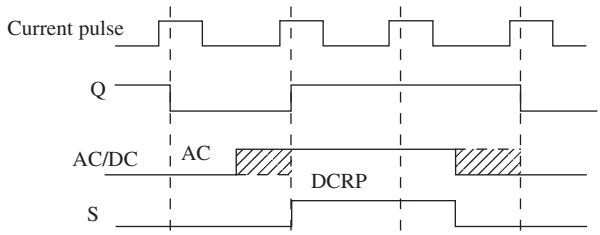

6.62 Time sequence of the control circuit in Fig. 6.61

$$S = AC/DC \cdot Q^n$$

$$Q^{n+1} = CP \cdot \overline{Q}^n + S$$

The shadow duration is for regulation; the circuit will be triggered only when the next pulse appears.

Because the melting rates for AC and DCRP welding are different, ripples which are coarser than those seen in the normal welding process can be observed on the bead surface. The bead penetration also is different. Penetration can be controlled by using different ratios of AC and DCRP periods. This is useful for developing welding technology for one-sided welding with back-bead formation.

6.2.4.6 *Effect of pulse parameters on AC MIG welding arc stability*

In AC pulsed MIG welding, the parameters are set according to certain rules; see Fig. 6.63. The pulse duration during AC MIG welding, $t_{pr1} + t_{ps1} = t_{ps2} + t_{pr2}$, is longer than the pulse duration during normal DC MIG welding. Because of the need for phase changes, t_{br} and t_{bs} are regulated according to the wire-feed rate. T_{br} is set to ≥2.5 ms in order to facilitate the droplet transfer before RP changes to SP and stabilises the arc during the transition. Improper setting of this parameter can produce globular transfer, an

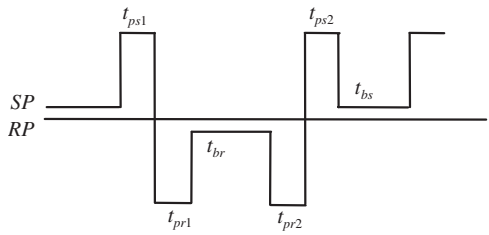

6.63 Pulse parameters of AC pulsed MIG welding

unstable arc, spatter, and even arc breakdown. t_{ps1} should not be too short (normally 1 ms); too short a value of t_{ps1} will not ensure that sufficient heat energy is generated to maintain a stable arc before entering into the background current. The function of t_{ps1} is to create a strong arc that ensures an ionized atmosphere and facilitates arc re-ignition. From the view of metal transfer, t_{ps1} should not be too long, as this can result in large globular droplets (larger than 1.5 times the wire diameter). Only when t_{ps1} is set correctly (about 1 ms) is it possible to avoid an excessive amount of molten metal and ensure good metal transfer when the arc changes to RP. When t_{ps1} is chosen, then t_{pr1} will naturally be determined. There may be 3–4 small droplets transferred successively in this period due to the heat accumulated in the SP period. The parameters t_{br} and t_{bs} can be varied according to the wire-feed rate. One-knob control is facilitated on the basis of the description in Section 2.2 about the relationship between wire-feed rate and pulse parameters.

6.2.4.7 *Effect of other factors*

The effect of shielding gas is obvious. Because CO_2 is ionised at high temperature, which can cool the arc, in this sense it is better to use pure Ar. However, experimental results demonstrated that the bead formation when Ar is used is bad; the reinforcement and weld toe are too high and the arc is less stable. Increasing the amount of CO_2 increases the oxidizing character of the arc atmosphere and forms an oxide film on the wire and parent metal so that the cathode spot can be stably located on the oxide film, which has a lower work function. When the CO_2 content is increased to 5 L/min while the Ar flow rate is 20 L/min, the arc becomes unstable because the cooling effect plays a major role. Too much CO_2 produces too much of an oxide film on the bead surface, which wastes not only materials, but also can interfere with succeeding operations. Serious spatter was observed when too much CO_2 was used; gas that was produced by metallurgical reactions in the droplet exploded. After balancing the factors mentioned above, a CO_2 content >3 L/min was chosen.

Stabilisers improve arc stability. Experiments were conducted with K_2CO_3 which was spread over the surface of the work piece. Greater arc stability and less spatter were observed but the melting rate of the wire was lower. The K_2CO_3 dissociated and ionised during welding, the K^+ ion was absorbed in the arc, and the work function for electron emission on the cathode was decreased. This allowed easier re-ignition but less heat was generated on the cathode and the melting rate was lower.

6.2.5 Summary

1) AC pulsed MIG welding has been successfully developed by application of the 'double-concavity current waveform' without use of flux-cored wire, stabiliser, or high-voltage arc-stabilising pulses. The arc was stable and arc blow was absent.
2) The metal transfer is a mixed mode of spray and droplets, and good bead formation can be obtained.
3) The pulsing parameters are important factors that affect the arc stability and metal transfer. A small spatter-loss coefficient (less than 1%) can be obtained by properly setting the pulsing parameters.
4) An appropriate amount of CO_2 added to the shielding gas can ensure good bead formation.
5) Stabilisers can improve the arc stability but they decrease the melting rate. The melting rate of AC pulsed MIG welding is in between that of DCRP and DCSP welding.
6) AC DCRP is effective for avoiding arc blow, and beneficial for the bead formation on the backside.
7) AC pulsed MIG welding is a new welding method. It has many advantages such as control of bead formation, allowing root-pass welding in deep grooves without arc blow, and raising productivity.

Part III

Arc sensors and seam tracking

7
Sensors for weld-seam tracking

7.1 Status of research and development

Research and development on automatic and intelligent control is the future direction of arc welding because it is an important means for ensuring weld quality, raising productivity, and improving labour conditions.[185–187] Many renowned research institutes and manufacturing firms devote substantial effort to this field.[186–205] The first problem that should be solved for the automation of welding processes is weld-seam tracking.[206] Substantial progress has been made after several decades of study and practice; emerging seam-tracking sensors have marked that progress.[207]

Sensors for weld-seam tracking can be categorised into the types according to their sensing mechanism, shown in Fig. 7.1. Most of the sensors used in industry are attached to the welding torch for detecting the groove position, namely mechanical, electromagnetic, and optical devices. The principles and features of these sensors are described in the following sections.

7.1.1 Contact sensors

The typical construction of a contact sensor is shown in Fig. 7.2. A probe, which detects the deviation of the torch from its position in the groove, slides or rolls in the groove. A micro switch detects the direction of deviation.[208] An electrical potentiometer, electromagnetic device or electro-optical device also can be used for determining the degree and direction of deviation.[209–210] This type of sensor is applicable to welds having X and Y grooves provided there is a reliable contact surface in the grooves, particularly for long and straight first-pass root-pass welds or corner welds.[211] The design and operation of such sensors are simple so they are widely used at the present time.[212] The problem with this type of sensor is that they need different probes for different groove shapes, the probes wear and deform, and tack welds pose an obstacle to the probe. The probes are not suitable for high-speed welding.

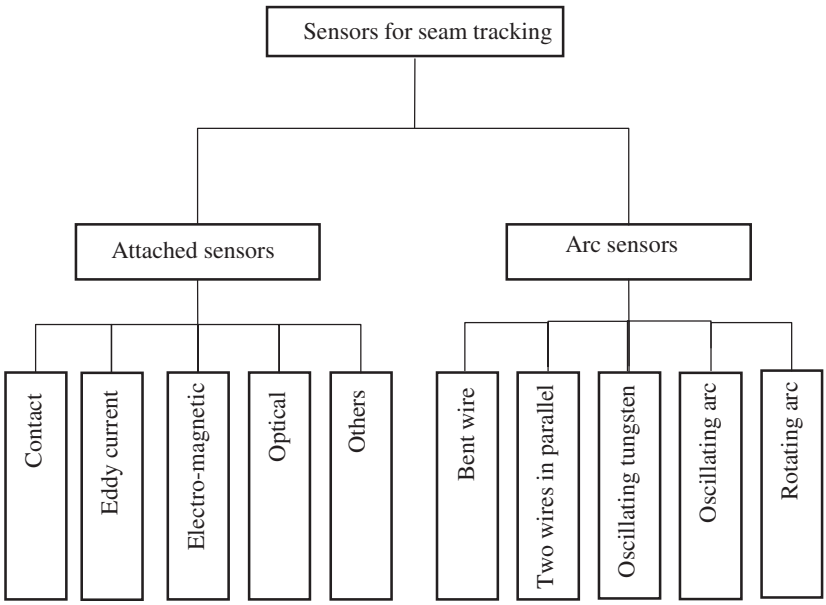

7.1 Types of sensors for seam tracking

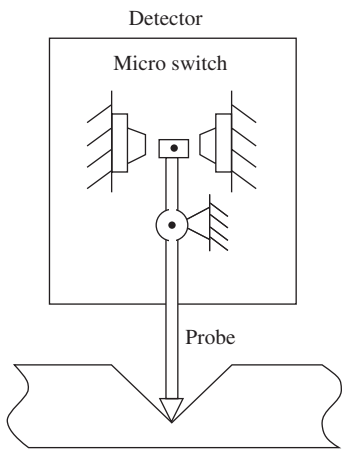

7.2 Contact-type sensor

7.1.2 Electromagnetic sensors

The principle of an electromagnetic sensor is shown in Fig. 7.3. A high-frequency exciting current is sent to the primary coil U_1, which induces a potential in the secondary coils U_{21} and U_{22}. The deviation δ_x results in

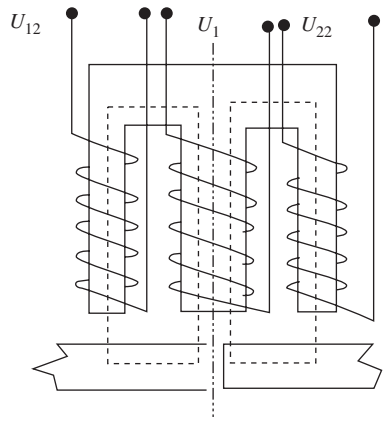

7.3 Magnetic-type of mutual inductance

asymmetry of the magnetic path. The difference between U_{21} and U_{22} reflects the degree and direction of δ_x. In order to overcome interference due to misalignment of the work piece and the presence of tack welds, magnetic flux-breakage restrain type, potential restrain type, and scanning-magnetic type sensors have been developed.[209,213–216]

This type of sensor is suitable for butt welds, lap welds, and corner welds. However, due to their large volume, they are less flexible than others and are sensitive to magnetic interference and assembly accuracy. This type of sensor is applied only under non-rigorous conditions.

7.1.3 Optical sensors

Major progress has been made in optical sensors. There are a variety of operating principles and types of optical sensors. Optical sensors can detect not only the relative position but also the shape of the groove, arc, and molten pool.

On the basis of their principle of operation, the object, the light source, and so on, optical sensors can be categorised as follows:

(i) Single-spot light sensors.
A simple photoelectric device is used to detect the groove or line marker designated A. A laser-spot light sensor for detecting the edge of a groove is shown in Fig. 7.4.[217–219,226] There also are sensors that use infrared, visible, or the arc as a light source.[219–222]

(ii) Linear light sensors.
A line of light is projected through a lens and slit in the envelope containing the light source onto the surface of the workpiece, per-

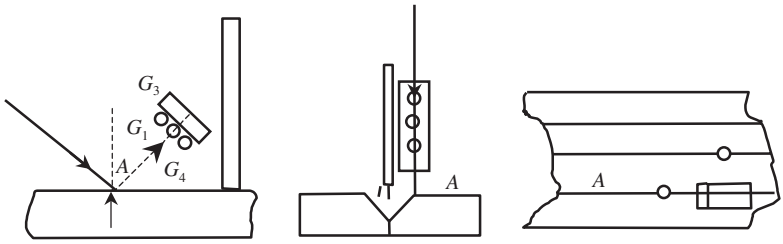

7.4 Laser sensor for detecting groove edges

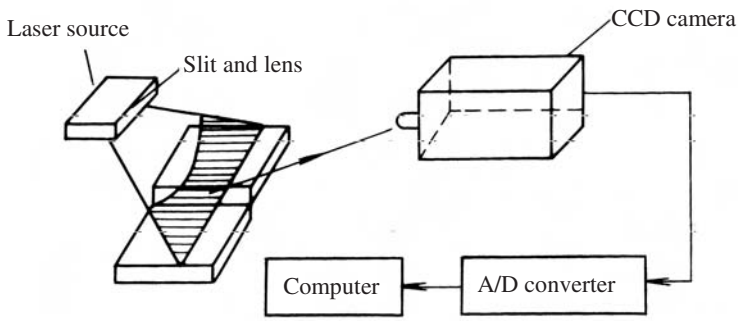

7.5 Principle of a linear laser sensor

pendicular to the weld seam. Operating at an angle from above the weld seam so that a curved line is formed on the surface, the groove shape is defined by the form of the curved line. The image of the projected line is taken by a CCD camera and processed by a computer to locate the centreline and the width of the groove,[223–224] as shown in Fig. 7.5.

(iii) Scanning-light sensors.

A laser beam scans the workpiece across the groove. The image is obtained synchronously by a CCD camera and processed by a computer to detect the groove shape, size, and centre line, as shown in Fig. 7.6. Because the spot of light has greater brightness than a line of light, the system has a larger signal-to-noise ratio and better resistance to arc-light interference.[213–214]

(iv) CCD-image sensor.

The arc, molten pool, torch, and wire tip are imaged by an ICCD. This image is processed by computer to measure the width of the groove, the relative position of the wire to the groove, and the wire extension.[41,225]

Optical sensors have high accuracy, good repeatability, and they can be used not only for seam tracking but also for detecting the groove shape,

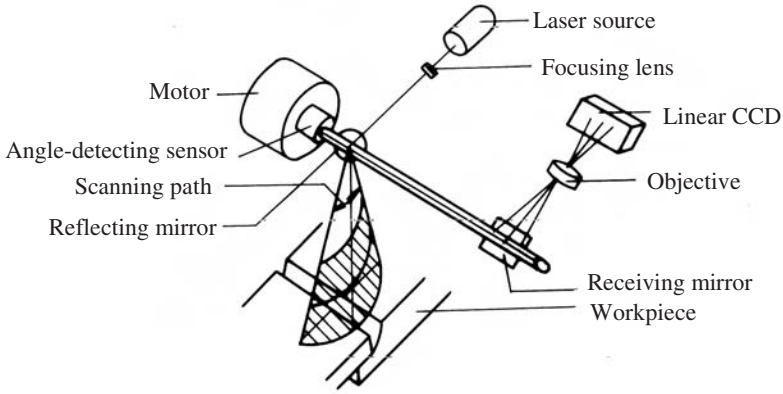

7.6 Scanning-laser sensor

width, and cross-sectional area to provide adaptive control of the welding parameters. Optical sensors are ideal sensors for welding processes.

7.1.4 Features and problems for attached sensors

Although there are many advantages associated with optical sensors, they are attached sensors, whose shortcomings are discussed below.

- The sensor is ahead of the arc. Except for some arc imaging systems, the detection point for optical sensors is 50 ~ 100 mm ahead of the arc, which may prevent accurate seam tracking in the case of seams that change direction significantly over short distances. To overcome this problem, memory, time delay, and a restoring system must be incorporated in the control circuit. Sometimes, two separate driving mechanisms, one each on the torch and sensor, can be used for welding. The separation between the torch and the sensor has to be measured by another means. All of these requirements increase the complexity of the system.[23]
- The sensor will not track properly if there is arc blow or cast (permanent plastic deformation due to bending) in the welding wire. While the attached sensor detects, in fact, the deviation of the welding torch from the groove centreline, the measured data are taken as the deviation from the arc to the groove centreline. When there is arc blow or wire cast, the arc is not coincident with the centerline of the torch.[227]

Both of these constraints can be overcome only by using a sensor having an arc-image processing system; no other type of attached sensor can track a welding groove accurately.

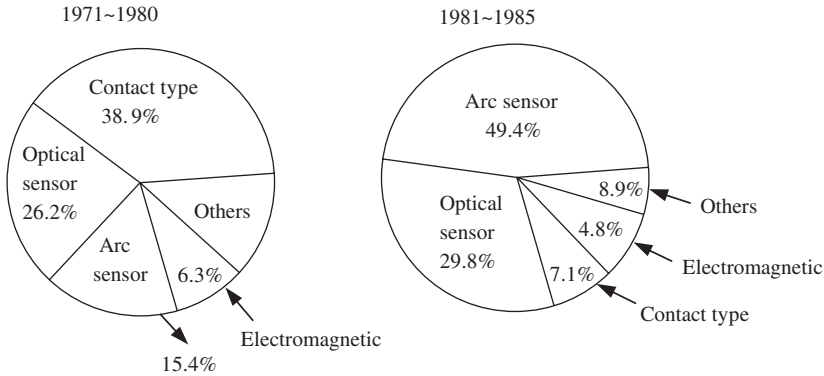

7.7 Trends of sensor development for weld-seam tracking in Japan

While an arc-imaging system is good for overcoming the above-mentioned problems, it is sensitive to arc-light interference, ICCD cameras are expensive, and application conditions are limited. Arc-imaging sensors are not popular in industry at this time. The arc-sensing systems invented over the last 30 years are good approaches to solving all of the problems mentioned above.

Arc sensors have the following advantages:

- The detection point is exactly at the point of welding; there is no problem caused by the separation between the position of the arc and the detection point.
- The sensor is not attached to the torch and therefore there is good accessibility of the torch to the weldment.
- There is no influence of arc blow or wire cast on the sensing.
- Arc sensors are inexpensive and reliable.

Great attention has been paid to joint sensing by welding personnel since the 1980s. The principal types of industrial arc-welding sensors that have been employed, particularly in Japan, are optical sensors and arc sensors,[228] as shown in Fig. 7.7. In China, however, arc-welding sensors are still under development.

7.2 Status of the application of arc sensors in industry

It is known that a variety of arc sensors which are suitable for TIG, MIG, MAG, etc. have been developed around the world, some of which are presently used successfully in welding production.[229–231]

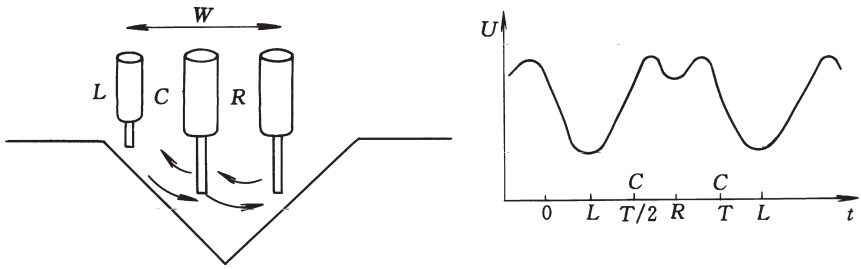

7.8 Oscillating-arc sensor for MIG/MAG welding

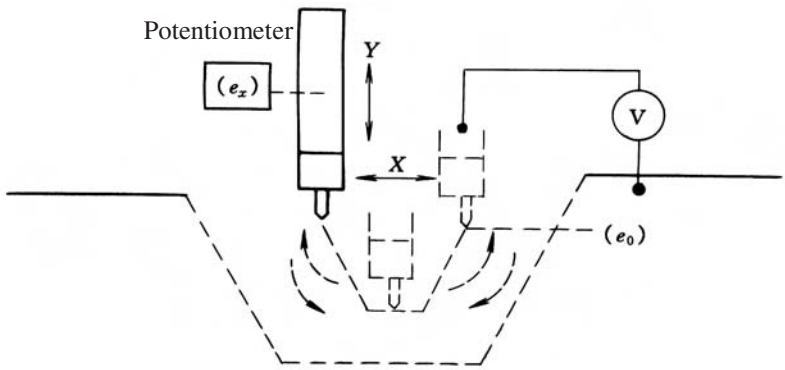

7.9 Principle of an oscillating sensor for TIG welding

7.2.1 Oscillating arc sensors for MIG/MAG welding

The earliest type of arc sensor was the mechanically oscillating sensor.[232] The torch oscillates across the groove at a low frequency, as shown in Fig. 7.8, in which L is the left point of torch movement, R is the right point of torch movement, and C the centre point of the oscillation. By comparing the arc voltage or current waveform between CL and CR, the deviation of the torch from the groove centre-line can be detected. This type of sensor also has been used with the wire bending method (mainly for narrow-gap welding[233]), the double wire method, and the twist-wire method.[234,235]

7.2.2 Oscillating sensors for TIG welding

Normally, constant-current or steeply dropping characteristics are used for TIG welding. The voltage variation caused by torch height variation is used for sensing the groove shape. Figure. 7.9 shows the principle of operation. An arc-voltage feedback control circuit (AVC) is used for this system. The height of the torch is automatically adjusted while the torch scans across

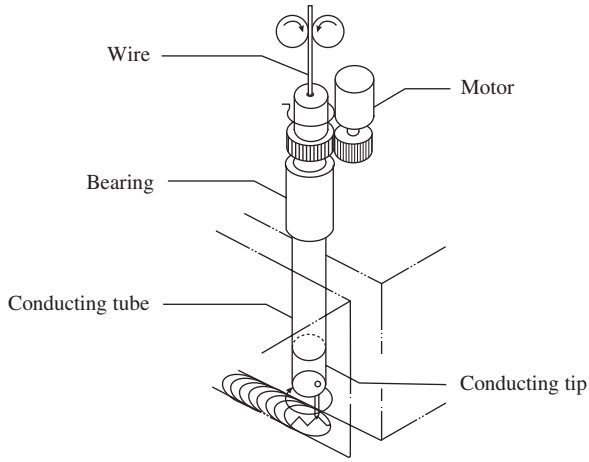

7.10 Rotating-arc sensor for MIG/MAG welding

the groove. A potentiometer is mounted on the torch, the output of which is compared with a preset reference value e_0. The potential difference is used as the measure of the torch-oscillation range. The method can keep the oscillation center coincident with the groove centreline. Moreover, it can automatically change the oscillation range as the groove width varies.[229–236]

7.2.3 Rotating sensors for MIG/MAG welding

The rotating arc sensor shown in Fig. 7.10 was reported first by the NNK Company of Japan for narrow-gap welding.[236,237] The rotational movement is achieved using an electrically-conducting tube with an eccentric hole for passing the welding wire. The principle is the same as an oscillating arc sensor but its frequency can easily be raised and therefore, higher sensitivity can be obtained. This kind of sensor has been applied up to the present for narrow-gap welding and fillet welding.[239,240]

Research on control of bead height by sensing the oscillation range or by scanning an area has been reported. The application of arc sensors in pulsed MIG/MAG welding is under development.[241,242]

Arc sensors differ from all other kinds of weld seam-tracking sensors. They are not independent of the arc-welding power source but are closely related to the characteristics of the power source. However, up to now, published papers and reports worldwide have been qualitative in regard to understanding and research on these sensors. Another problem with arc sensors is their application field; they are suitable for fillet welds, butt welds

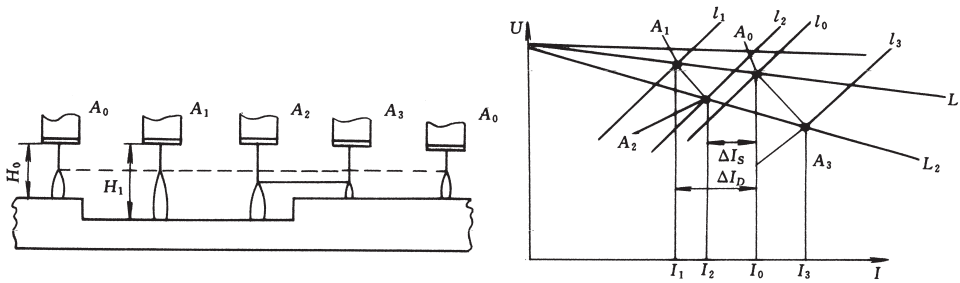

7.11 Principle of arc sensor

with grooves or narrow-gap welds. But they cannot recognise the seam centreline when the seams are lap joints, when they do not have grooves, or when the grooves are unsymmetrical. These restrictions limit the application of arc sensors in production welding.

7.3 Principles of seam tracking with arc sensors

7.3.1 Fundamentals

The fundamentals of arc sensors lie in the variation of welding current while the arc oscillates across the groove. Figure 7.11 shows the current variation due to the variation of the torch-to-plate distance (H_0). Taking a slightly drooping power source characteristic as an example, the analysis for a constant-current characteristic is similar. Suppose that the arc is stable at the arc-operating point A_0, arc length l_0, wire extension L_1, and current I_0. If a step change in the torch-to-plate distance occurs, for example, it moves to H_1, the arc length increases to l_1 abruptly, but the wire extension is not able to follow the change and remains at L_1. The arc-operating point jumps to A_1 and the current changes to I_1. After the time required for the arc length to shorten and the wire extension to increase, the electrical resistance of the welding loop increases. The arc-operating point moves to a new stable point A_2 where the arc length is l_2, the wire extension is L_2, and the current is I_2. The final result is that both the arc length and wire extension are longer than they were originally.

Similarly, if a step change happens again, the torch-to-plate distance changes abruptly from H_1 to H_0, the arc-operating point jumps from A_2 to A_3 (because the wire extension cannot follow the change), the arc length becomes l_3, and the current changes to I_3. After the time required for the arc length to readjust, the arc-operating point returns from A_3 to A_0. From this description, it is known that both the arc-operating point and the current change while the torch-to-plate distance changes. However, there

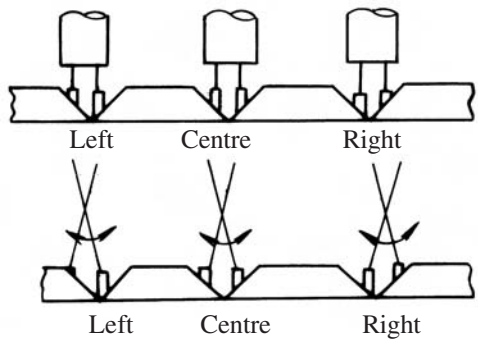

7.12 Scheme for left and right tracking

are two states, namely static and dynamic states. For example, the dynamic change of current is ΔI_D and the static change of current ΔI_S when the torch-to-plate distance changes from H_0 to H_1. In presently available control systems, the static change of current normally is used whereas the dynamic change is not used (because the oscillation speed is low). The dynamic phenomena of these sensors have not been studied up to the present. Experiments demonstrate that for Φ1.2 mm wire diameter, 215–280 A welding current, and 26-30 V arc voltage, a 1 mm change of the torch-to-plate distance can change ΔI_S by 5 A; in other words, a 1.4–2.4% current change may be obtained for a 1 mm change of the torch-to-plate distance. This means that seam-tracking control can be achieved by monitoring the static-current change.

The seam-tracking trajectory in welding is three dimensional and can be resolved into up and down, and left and right movements. Up and down tracking can be realised simply by moving the welding torch up and down according to the current variation. Special measures must be taken to recognise the centre-line of the groove and control the left-right movement of the torch. Figure 7.12 shows two examples used in practice. Two parallel wires were used in the first example and an oscillating wire was used in the second example.

From the figure, it can be seen that if the centre point between the two wires does not coincide with the groove centre different wire extensions and thus different welding currents will be carried by the two wires. The deviation of the torch from the groove centre can be judged by the difference of current, by which left and right movement of the torch can be controlled. Similarly for the oscillating wire, if the centre of the torch is not on the centre-line of the groove, the wire will have different extensions and thus different currents when it reaches the left and right sides of the groove. Seam tracking can be realised by comparing the current on the left side

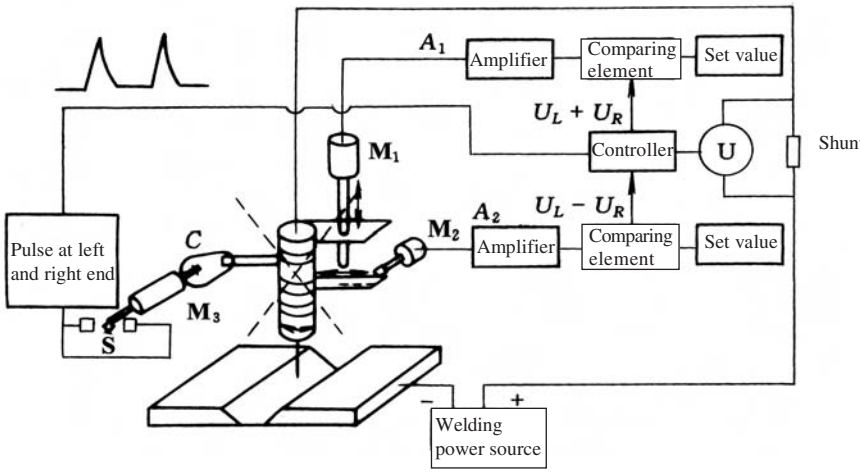

7.13 Schematic diagram of the seam-tracking mechanism

with that on the right side. Better bead formation can be obtained and a simpler control circuit can be used for the first example but synchronous feeding of two wires and electrical isolation of the two wires from one another are more complicated. The second example does not have these shortcomings but it needs an oscillation mechanism. Bead formation depends on the oscillation so that proper design of the oscillation is helpful for obtaining better bead formation. Both examples have been applied successfully in practice.

7.3.2 Principle of operation

The author, in co-operation with J. Platz,[243] successfully developed a seam tracking system in 1978 on the basis of the second scheme mentioned above. Only the hardware for three-dimensional seam tracking has been built. This development is described in more detail in this section to illustrate the principle of operation of a seam tracking system in general.[243] Figure 7.13 is a mechanical diagram of the system. There are four motors on the welding tractor. One drives the tractor itself (not indicated in the diagram), one (M_1) controls up and down movement, the third (M_2) controls left and right movement, and the fourth (M_3) drives a cam (C) and oscillates the torch. The oscillating frequency is about 3 Hz. The oscillating range is about 4–6 mm. On the other end of M_3, an electronic switch is mounted, which sends a pulse to the control circuit when the torch comes to the left or right end, so that the current is sampled at those moments. The current signal is taken from a shunt (200 mV/600 A). The control circuit takes the sum of

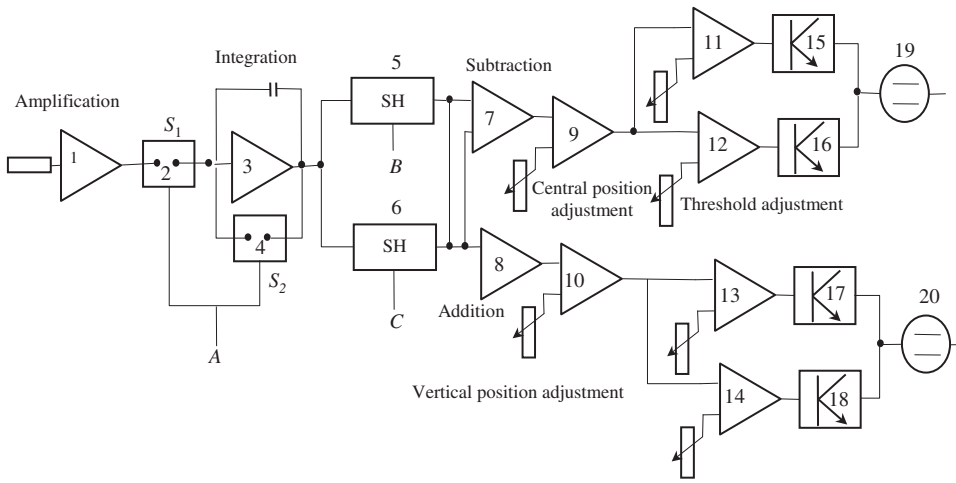

7.14 Electrical circuit diagram (1)

currents ($U_L + U_R$) to control the up and down movement, and the difference of the currents ($U_L - U_R$) to control the left and right movement.

The block diagram of its electrical circuit is shown in Fig. 7.14. The current signal is amplified first in 1 (60 times) and then is sent to the integration element 3 via an electronic switch 2. The integration element is an important part of the control circuit. Whenever the arc oscillates to the left or right side of the joint, a signal from A is sent to the electronic switches 2 and 4, and starts the integration. The time for integration is controlled by an electronic switch that is fixed at 25 ms. After the integration, the result is sent, according to arc position, from left to right, to the sample and hold circuit (S + H), either 5 or 6. When a signal goes to B, the signal input is 'sampled' by the circuit 5. When the signal to B ceases, circuit 5 'holds' the integrated value. Similarly a signal at C is sampled by circuit 6 and when the signal to C ceases, circuit 6 holds the last integrated value. When the welding current fluctuates violently, if the instantaneous current value is taken at the moment when the arc is at the left or right side of the joint, a large error will be introduced. Therefore, in the present design, the current signal is integrated for 25 ms, which greatly reduces the error due to current fluctuation and provides more accurate seam tracking. This design philosophy is important.

The signals produced by 5 and 6 are added and subtracted in the operational amplifiers 7 and 8. The sums are sent to 10, 13, and 14 to control the up and down movement of the welding torch. The preset value of the potentiometer at 10 is compared to this sum. When a positive signal is generated by 10, the output of 13 drives 17 and makes the motor rotate in one direc-

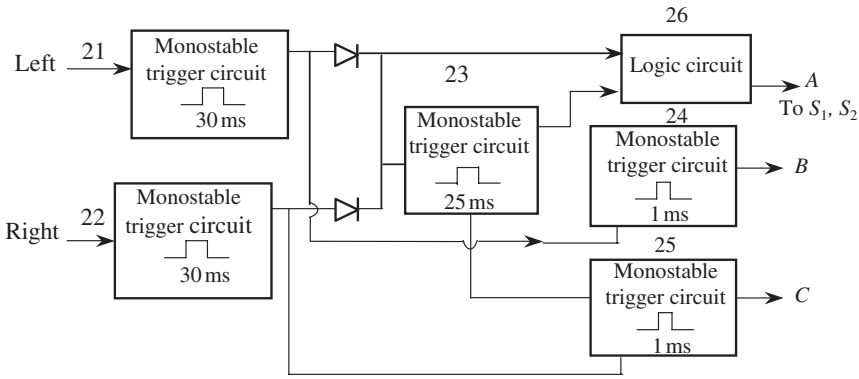

7.15 Electrical circuit diagram (2)

tion. When the signal generated by 10 is negative, the output of 14 drives 18 and makes the motor 20 rotate in the other direction, which produces vertical movement of the torch. There is an adjustable potentiometer on amplifier 9 whose value is compared to the value obtained by subtraction in 7, which adjusts the centre position of the torch. When the output of 9 is positive, 11 will send a signal to drive 15 to rotate the motor in the positive direction. When the output of 9 is negative, 12 sends a signal to drive 16 that rotates the motor in the reverse direction.

The locations A, B, and C shown in Fig. 7.14 are controlled by the electrical circuit shown in Fig. 7.15. A 30 ms pulse is generated by 21 when the torch oscillates to the left side of the joint and another pulse having a 30 ms width is generated by 22 when the torch reaches the right side of the groove. The front edge of both pulses triggers 23, which produces a 25 ms pulse. Signals from 21, 22, and 23 are received by logic circuit 26, the output of which controls the electronic switches 2, and 4 (see Fig. 7.14). Whenever the torch reaches the left or right side of the joint, S_1 switches on for 25 ms to operate the integration element and then switches off. The integration element holds its potential for 5 ms. When S_2 switches on, the potential on 3 discharges and returns to zero. The back edge of 23 triggers 24 and 25, which produce a 1 ms pulse and triggers 5 or 6 for sampling and holding. The trigger 24 can be activated only when there is an output signal from 21, and 25 can be activated only when there is output signal from 22. Therefore 24 sends a signal to B, when the arc reaches the left side of the joint and 25 sends a signal to C when the arc reaches the right side of the joint. The signals from B and C are sent to 5 or 6, respectively, so that the sampling operates for 1 ms and then initiates the hold. It is obvious that the output of 5 changes its value whenever the arc reaches the left side of the joint and the output of 6 changes its value when the arc reaches the right

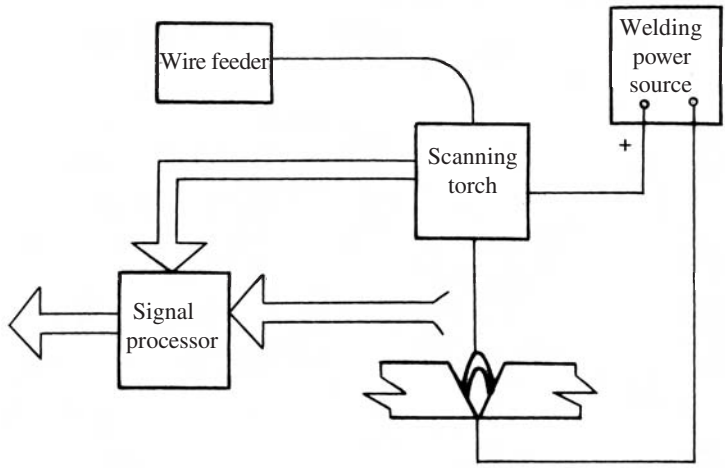

7.16 Arc-sensing system for MIG welding

side of the joint. Therefore, the new data from the addition element and the subtraction element are obtained every half cycle of oscillation.

7.4 Scanning arc-welding torches

7.4.1 Osallating-arc torch

The arc-sensing system for MIG welding consists of a welding power source, the arc, the scanning mechanism, a signal processor, and a wire feeder as shown in Fig. 7.16. The difference between this and conventional MIG welding is the torch. As described in previous sections, the arc-sensing system is based on the current variation that accompanies the scanning of the torch. Therefore, the core of the arc-sensing system is the scanning torch. The characteristics of the system depend on the properties of the torch. A good scanning torch should have the following functions:

- Scanning function. The arc should oscillate across the groove and the range of oscillation should be adjustable for practical applications.
- Sensing function. The arc current and its corresponding position should be detectable.
- Usual functions. The torch should provide the usual functions for MIG welding including conducting electricity, circulating cooling water, feeding welding wire, and supplying shielding gas.

In the first stage of its development, the oscillating type of arc sensor was used most often. Figure 7.17 shows the oscillating arc sensor produced by

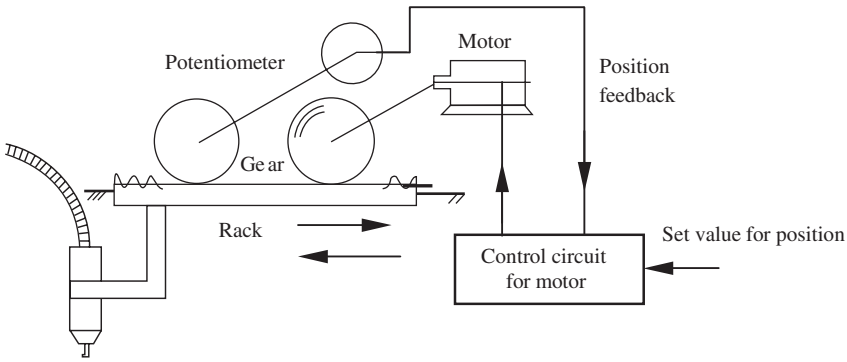

7.17 Oscillating welding torch

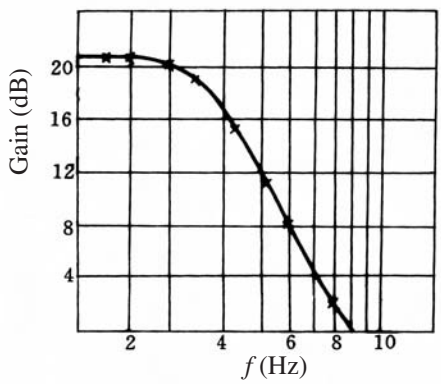

7.18 Frequency-response characteristic for an oscillating torch

OTC of Japan. In this apparatus a rack and pinion are used for the oscillation mechanism, and a multi-turn potentiometer is used to detect the arc and torch positions, the output of which is used for closed-loop position control. The sinusoidal or triangular trajectory of the torch movement can be obtained by sending a sinusoidal or triangular signal as a set value to the control system. The features of this system are as follows:

- Easy to control; the range of oscillation can be regulated.
- Because the rack is much longer than the oscillation range, the centre of oscillation can be adjusted.
- The frequency response of the system is limited to 5 Hz. The gain of the system decreases greatly if the oscillation frequency is higher than 5 Hz; this is shown in Fig. 7.18.

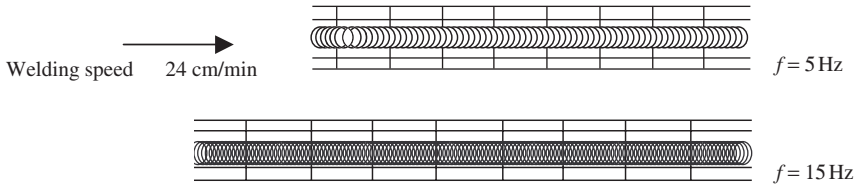

7.19 Arc trajectory

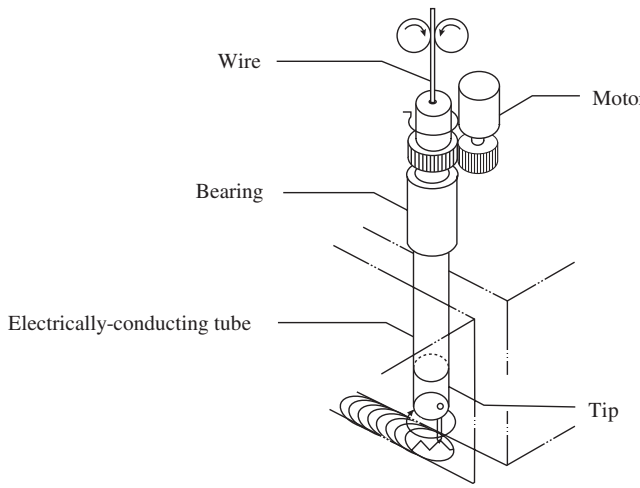

7.20 Rotating-arc torch developed by Nomura

7.4.2 Rotating-arc torch

The rotating-arc torch is a new development for overcoming the shortcomings of the oscillating-arc torch. In this concept, the arc and the wire rotate around the centreline of the torch. Figure 7.19 shows the trajectory of the arc. Obviously, if the rotational speed is much higher than the travel speed, the arc movement may be interpreted as scanning across the groove, just like an oscillating arc.

The rotating torch should have all the functions of a normal welding torch. In addition to these, the primary function of the torch is to rotate the arc. Figure 7.20 shows a schematic diagram of the rotating torch developed by H. Nomura.[238]

Inside the torch, a motor rotates an electrically conducting tube. An eccentric hole is incorporated in the torch tip where the wire passes through, so that the wire and arc rotate around the centre of the torch. This torch has been successfully applied in industry. However, there are some

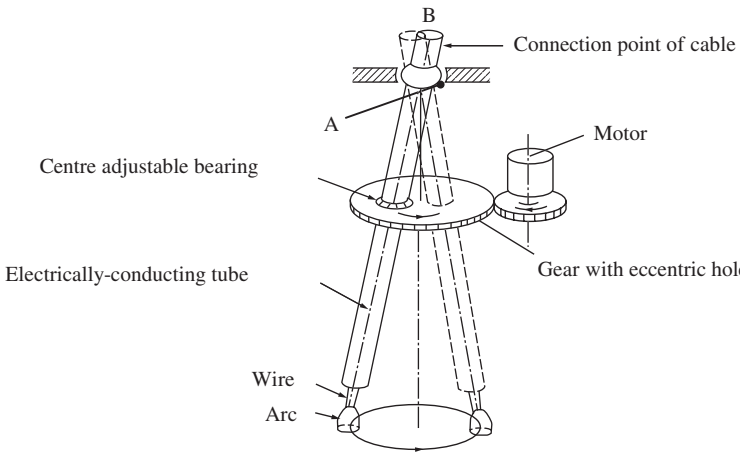

7.21 Rotating-arc torch developed by Pan and Fei

problems with it. First is the way that electrical power is connected to the torch. Because the conducting tube is rotating at high speed, a sliding graphite block is used to transmit current to it. This structure is difficult to manufacture and has a short service-life. Second, because the wire itself does not rotate, there is excessive wear of the torch tip so that even when wear-resistant material is used for making the tip, its the service-life is short. Third, it is difficult to connect the cooling-water tube to the electrically-conducting tube. In order to overcome these problems, a new design of rotating-arc torch was developed by the author and Y. N. Fei in 1980. This torch was named the RAT-I and is shown in Fig. 7.21.[244] The electrically-conducting tube does not rotate itself but is mounted on a spherical hinge made of a ball bearing steel and located at the upper end of the torch. At the lower end, the tube passes through an eccentric hole of a gear, which is driven by a motor. Thus, the tube itself does not spin but rather moves as a generating line of a cone. This design has the following advantages:

(i) There is no relative movement between the conduction tube, wire tip, and wire, and therefore no friction and wear.
(ii) Because the upper end of the conducting tube B is near to its hinge A, there is a very small amplitude of rotation at the end of the tube and, therefore, the power cable can be connected to it directly without a graphite brush or other means.
(iii) The cooling-water tube can be connected easily to the electrically-conducting tube.

Figure 7.19 shows the trajectory of the wire tip made by this kind of torch.

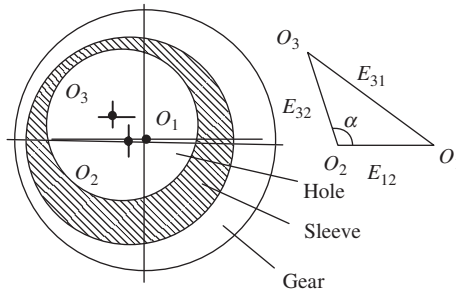

7.22 Regulation of the rotation centre

7.4.2.1 Regulation of diameter of rotation

The diameter of rotation or the oscillation range of the arc should be adjustable for production and experimental purposes. It can be seen that the rotation diameter of the arc can be adjusted easily by adjusting the eccentricity of the hole in the gear but this adjustment is rather inconvenient. The author and his colleague have developed a simple mechanism for adjusting the rotation diameter. That mechanism is called a 'double-eccentric adjustment mechanism' and is shown in Fig. 7.22. 0_1 is the axial centre of the gear and 0_2 is the axial centre of the hole on the gear. The distance between them is E_{12}. A sleeve with an eccentric hole is inserted into the hole in the gear. The axial centre of the inner hole in the sleeve is 0_3; the distance between 0_3 and 0_2 is E_{23}. A ball bearing is installed in the inner hole in the sleeve. Then, the distance between axial centre of the ball bearing and the axial centre of the gear is E_{31}. The relationships among them can be written as

$$E_{31}^2 = E_{12}^2 + E_{23}^2 - 2E_{12}E_{23}\cos\alpha \qquad [7.1]$$

Let $E_{12} = E_{23} = E$

then $$E_{31} = \sqrt{2}E\sqrt{1-\cos\alpha} \qquad [7.2]$$

which means that the eccentricity E_{31} can be regulated by α. $E_{31} = 2E$ when $\alpha = 0°$. Therefore the range of regulation is 0–2E. In the present design, E was chosen to be 1 mm. This means that the rotation diameter of axial centre of the sleeve is in the range 0 ~ 2 mm and accordingly the range of the rotation diameter of the arc is 0 ~ 8 mm.

7.4.2.2 Detection of arc position

The so-called 'arc position' is the relative position of the arc or wire end with respect to the welding torch central axis at a given moment t; see $\beta(t)$

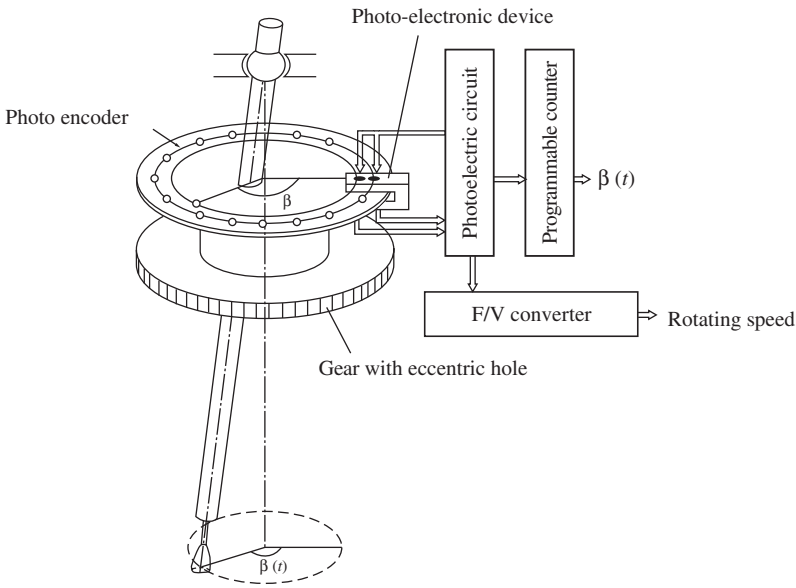

7.23 Photoelectric device for detecting angle and speed

in Fig. 7.23. This is a very important parameter for arc-signal processing. For this purpose, the author has designed a photoelectric device for detecting the rotation angle and rotation speed, which is shown in Fig. 7.23. It consists of an optical encoder attached to the gear, and an infrared emitter and receiver and its electronic circuit. There is one hole for detecting the position of the arc and 90 holes for detecting the angle of rotation; neighbouring holes are 4° apart. The electronic circuit output 0/1 is determined by a shaping circuit according to the infrared signals received. For one rotation of the arc, a position pulse and 90 angle pulses are emitted, as shown in Fig. 7.24. The position hole is drilled on the vertical plane formed by the torch axis and the vertical axis of the gear. Then the number of angle pulses N counted after the appearance of the position pulse represents the angle between the arc or the torch and the position of the photoelectric device, i.e. the angle of rotation of the torch $\beta(t_N) = N \times 4°$.

The counting is performed by an external interrupt of a single-board 8031 computer and a counter.

Another function of the photoelectric device is to measure the rotation speed. The F/V converter generates a potential signal proportional to the pulse frequency received by the photoelectric element. This signal is used as a feedback signal to the drive motor. This method of controlling rotation is much more accurate than the conventional closed-loop control based on the armature-voltage signal.

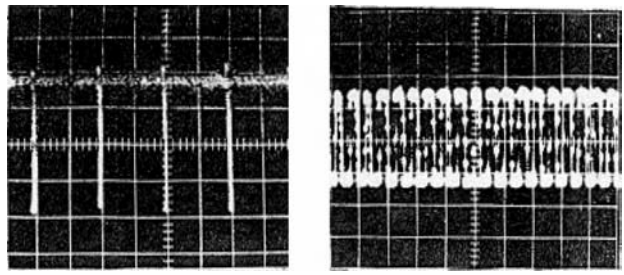

Position pulse Angle pulse

7.24 Output pulse of the photoelectric detector

The parameters of the RAT-I are as follows: the rotating frequency is 1–50 Hz, the rotation radius is 0–4 mm, the rated current is 500 A, the drive-motor power is 25 W, and the torch is water-cooled.

7.4.2.3 Rotating-arc torch RAT-II

A DC servomotor and a gear-reduction mechanism are used for the RAT-I rotating-arc torch. The accessibility of the torch is poor due to its bulky and heavy gearbox. Moreover, the transmission gears are noisy, particularly when they are contaminated by welding fumes or are improperly assembled. To overcome these shortcomings a more reliable and lighter rotating-arc torch, designated RAT-II, was developed by the author and B. J. Liao in 1993.[245,246] The special feature of this torch was a driving motor with a hollow shaft that was used as the main body of the torch.

To make the connection of the power cable, the cooling-water tube, and the shielding gas lines more convenient, the design based on rotating on a generating line of a cone was considered best for a rotating-arc torch. The problem was how to eliminate the gearbox. For this purpose, a new type of rotating-arc torch was designed as shown in Figures 7.25 and 7.26.[245,246]

The construction of the torch can be described as follows. A hollow-shaft motor is used as the main body of the torch; the electrically-conducting tube is inserted with a tilt through the hollow shaft. Similar to the RAT-I, a ball bearing is used as a hinge for the electrically-conducting tube, which is fixed on the upper end of the motor body. Similar to that of RAT-I, a disc with an eccentric hole is mounted on the lower end of the motor. A sleeve with another eccentric hole is inserted into the hole in the disc. The electrically-conducting tube passes through the eccentric hole in the sleeve, via a ball bearing. The eccentricity of the electrically-conducting tube can be adjusted by the angular position of the sleeve (see also Fig. 7.22). Thus, when the armature of the motor rotates, the electrically-conducting tube rotates on the line that generates a cone.

Because both the upper and lower supporting points of the electrically conducting tube are ball bearings, they are free to rotate. The power cable,

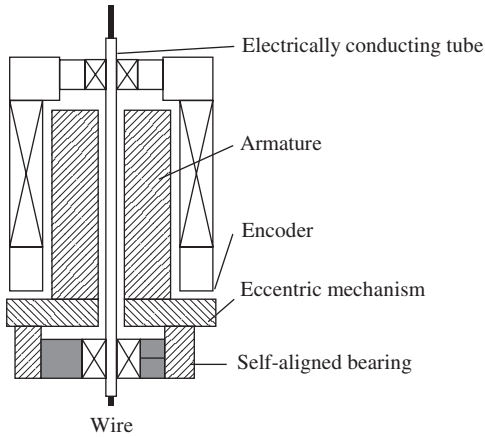

7.25 Schematic diagram of the rotating-arc torch RAT-II

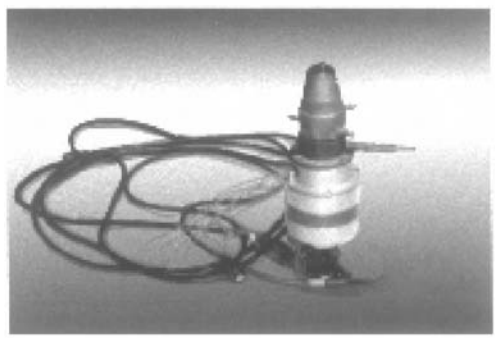

7.26 Appearance of the rotating-arc torch RAT-II

cooling water line and gas line are connected to the electrically-conducting tube at its upper end, which is very near to its hinge point.

A double-shield gas nozzle was designed for the torch to provide better shielding to overcome disturbances of the arc-shielding gas caused by rotation of the wire and arc.

To develop an effective torch, the key problem was how to design the motor and its speed-control circuit. Detection of the angular position of the arc is the basic requirement.

7.4.2.4 Hollow-shaft motor

There are two requirements for the motor used in the present design. The first is that the diameter of the shaft should be large enough and the outer diameter of the motor should be as small as possible in order to minimize

the torch diameter. It is hard to find this kind of motor commercially and it was also impossible to design and manufacture such a special type of motor. The diameter of the commutator of a conventional DC motor is too small and making a hollow shaft is impossible. The rotor and commutator of DC torque motors are larger but their speed is too low and they are too expensive. Therefore, a conventional single-phase capacitance motor for axial-flow air pumps was used for this purpose. The motor was a squirrel-cage type, which has no commutator in its rotor and the armature was made by casting. Therefore it was possible to incorporate a hole in the center of the armature. According to a theoretical analysis, in order to drive the torch, a motor having a torque of 500–700 g/cm, a maximum rotating speed of 3000 r/min, and a rated power of 20 W was required. A suitable axial-flow air-pump motor was therefore chosen. This motor had a fan diameter of 200 mm, 62 W maximum power, 220 V rated voltage, and 2700 r/min rated rotation speed.

Speed control and the reduction of the cross section of the magnetic circuit of AC motors are the two main problems associated with the motor that was chosen. An insufficient cross-sectional area of the magnetic circuit can increase the armature temperature. Voltage control of the motor speed is not acceptable because the mechanical-output characteristics are too soft. The first problem was solved by properly choosing the motor so that it had abundant power and used lower voltage so that the magnetic circuit would not be saturated. Designing a closed-loop speed feedback-control system using a photoelectric system for speed measurement and a switching mode for speed control solved the second problem.

7.4.2.5 Measurement of arc position and rotation speed

The angular position of the torch is the relative position of the torch with respect to the groove centre-line. It is important for seam tracking. Rotational-speed detection is important for feedback control of the rotation speed.

A potentiometer and an angle-synchronising motor are normally used to detect angular position. However, the potentiometer is not suitable for high rotation speeds and the angle-synchronising motor is too complicated for this welding application. Moreover, its analogue output is not conveniently fed to a computer.

Similar to Section 7.4.3, the photoelectric-encoder detection system was applied to this design. There are two methods for encoding the position. In the first method, a code is given to each angular position; in the second method, the position signal of a rotating disc is taken as the starting point for encoding and then the code is progressively increased for each signal received subsequently. The first method requires numerous sensors and

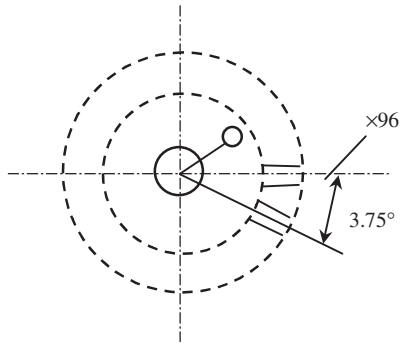

7.27 Schematic diagram of the encoding disc

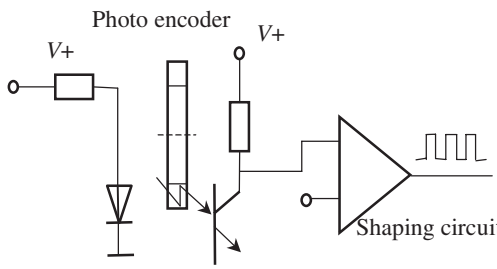

7.28 Amplifying and shaping circuit

accurate engraving of the graduations on the encoding disc. Therefore the second method was used for this new design. An encoding disc was designed as shown in Fig. 7.27; 96 rectangular teeth were cut on the outer ring of the disc so that 96 pulses would be emitted by the photoelectric device that used an infrared beam passing through the gaps between the teeth for each turn. Only one hole, which produces a pulse used as the starting point for encoding, called a starting pulse, was fabricated in the inner ring of the disc. For accurate control, the pulses are amplified and shaped by a circuit shown in Fig. 7.28.

Figure 7.29 shows the relationship between the pulse and the rotational angle of the torch. When the torch rotates counter clockwise, the angular position of the torch is taken as 0° when the torch is at the right side of the joint; thus the angular position of the torch is 135° when it reaches the front and middle of the path. This point is taken as the sequence number 0. This means that there is a deviation angle between the starting pulse and the angular position of the torch.

The frequency of the pulse output by the outer ring represents the frequency of the motor.

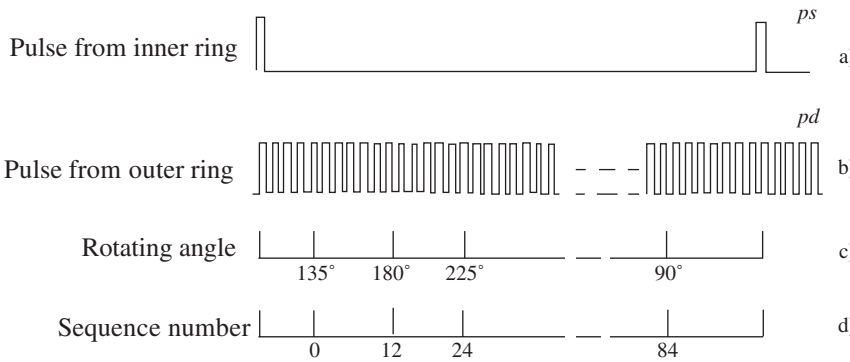

7.29 Relation of angular position with the pulse sequence

$$f_r = f_s = \frac{f_d}{96}; \quad n = 60 f_r \qquad [7.3]$$

f_r Rotational speed (Hz),
n Rotation speed (r/min)
f_s Frequency of starting pulse (Hz)
f_d Frequency of angular-position pulse (Hz)

7.4.2.6 Circuit for regulation of rotation speed

The synchronous rotation speed of the motor is 3000 r/min and the rated rotation speed is 2700 r/min. There are two methods for regulation of the AC motor, namely regulation by frequency or by voltage. The output mechanical characteristics of AC motors are too soft; therefore a speed feedback-control circuit was incorporated. Considering that, at low rotation speeds, decreasing the voltage is necessary to avoid magnetic-circuit saturation and that a frequency regulation circuit is more complicated, voltage regulation was used instead. Closed-loop feedback could solve the soft output mechanical characteristics intrinsic to voltage control.

Accurate rotational speed control can be obtained using a phase-lock or frequency-lock circuit but these circuits are too complicated, and unstable rotation can result from loss of steps.

For DC servomotors, series-controlled rectifier circuits are practical. For AC servo motors, the rectifier circuit and the control device (e.g. transistor, FET, or SCR) should operate using DC. If bi-directional control is used, then no rectifier is needed but the triggering and switching circuits are more complicated and the dynamic properties are poorer.

In the present design, an FET was used in the diode bridge, which is connected in series with the motor as shown in Fig. 7.30. The adjustment device

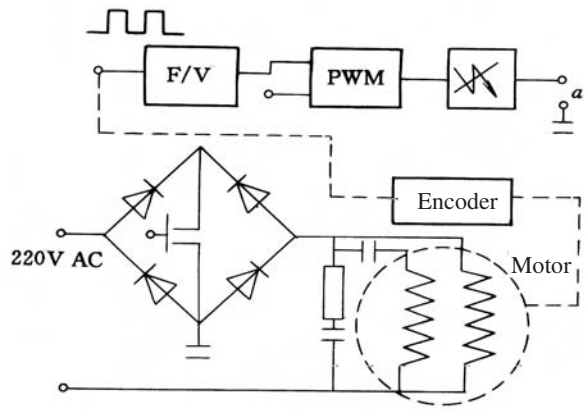

7.30 Closed-loop rotational speed control

works in an ON-OFF mode so that small capacity is needed and less power is consumed.

The angular pulses from the encoder are the signals representing the rotational speed; they are converted by an F/V into an analogue potential ω_r, which is compared with the set value ω_g. The difference between them is again converted into pulse width, which controls the on-off duration of the adjustment device and thus the rotation speed. An LM2907 was used for the F/V converter and a CA3524 was used for pulse-width control. Because the adjustment FET was connected in the high-voltage circuit, its control signal was input via an optical coupler. The working frequency of the circuit was 1 kHz.

7.4.2.7 Parameters and operating results

The specification for the rotating-arc torch RAT-II is as follows:

Outer diameter ϕ80 mm, rotation frequency 14.5 Hz ~ 36 Hz, maximum rotation radius 4 mm, maximum welding current 350 A. Motor shaft: outer diameter ϕ20 mm, inner diameter ϕ17 mm. Electrically conducting tube: outer diameter ϕ12 mm, inner diameter, ϕ7 mm, which is the diameter of the wire-feed tube.

Practical experiments demonstrated that the speed-detection system was reliable; the speed-control circuit had good properties. The motor operation was stable between 5 Hz ~ 45 Hz and it started quickly. For the practical requirements of welding technology, the range of rotational-speed regulation was set to 15 Hz ~ 35 Hz. Long-term observations showed that the reduced magnetic-circuit cross-section did not impair the motor's working, mainly because the actual voltage across the motor was much

Table 7.1 Voltage across armature at different rotation speeds

f_r (Hz)	15	20	25	30
U (V)	65	90	121	150

lower than the rated voltage. Table 7.1 shows the effective voltage across the armature at different rotation speeds. It can be seen that in the range of 15 Hz ~ 30 Hz rotation speed, the arc sensor had good sensitivity and the voltage across the armature was low.

The RAT-II rotating-arc sensor has several advantages compared to RAT-I; they are as follows:

- It is compact and lightweight; it is very convenient for practical application.
- The gear box is eliminated; thus, there is less torsional friction, less resistance, and less uneven loading due to improper assembly.
- It produces less noise.
- The speed-detection system and control are reliable.

The fields of application of RAT-II may be as follows:

- Tracking vertical and horizontal weld joints
- Detecting groove shape.
- Providing a dynamic load for measuring welding power-source characteristics.
- Improving bead formation and molten pool solidification.

8

Mathematical models of arc sensors

8.1 Introduction

Design of a highly accurate, sensitive, and multi-functional arc sensor requires an explicit understanding of the physical mechanism of arc sensors and the mathematical relationships between the output and input signals. This means that establishing a mathematical model of the arc sensor is necessary. No information regarding this subject has been published outside China up to the present. The author and Y. N. Fie presented a theoretical analysis and an experimental study in 1990.[244,247,379] The principal contents of this report are described in this chapter.

8.2 Static model

The principle function of either oscillating or rotating arc sensors is to generate a signal representing the variation of the torch-to-plate distance from the variation of welding current during the torch travel along the groove. From the information about the torch-height variation, the relationship of the torch centre to the groove centreline is detected and the resulting signal is used as the input for seam tracking. Therefore, the transfer rule relating torch height to arc current is the basic input and output relationship of these arc sensors. The discussion of the static and dynamic models of arc sensors in this chapter is a description of this relationship. In this section, a static mathematical model, i.e. the relationship between the arc current and the torch height under stable arc conditions, is discussed. The significance of this study is as follows:

- The relationship represents the mathematic rule relating torch-height variation to the arc sensing system, which is the basis for torch-height control.
- The relationship between the output and input reflects the characteristics of the system (linear or non-linear), which is useful for establishing the dynamic mathematical model.[248]

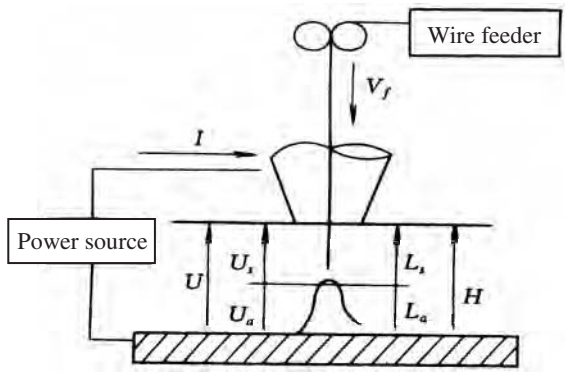

8.1 Physical model of an arc sensor

An arc sensor is not a single, separate element; it consists of the scanning welding torch, the welding machine, etc. The so-called mathematical model is, in fact, the model of the entire system.

The transfer rule relating torch height to the arc current is performed through the physical phenomena of the arc. Theoretically, the transfer function can be derived from the physical parameters of the arc, but, in fact, it is very difficult to obtain such a quantitative description of the physical parameters. Therefore, it is impossible to establish a mathematical model theoretically. For this reason, a mathematical model has been established by the author in two steps. The first step was to set up the structure of the model using a theoretical analysis. The second step was to experimentally determine the coefficients of the derived equations. These experiments showed that the relationship between the torch height and the arc current under static conditions was linear. Therefore a simple, linear static model was established.

8.2.1 Theoretical derivation

In order to explicitly represent the problem, the arc-sensing system was simplified as shown in Fig. 8.1 in which all of the physical parameters are indicated. There are two equilibria in the system, namely, the energy supply and demand between the welding power source and the welding arc, and the wire-melting rate and wire-feed rate.

According to the first equilibrium, the output characteristics of the power source U_p and the static characteristics of the arc U are required to intersect at a point, which is shown in Fig. 8.2. For convenience in the theoretical analysis and the experimental study, the resistance of the welding cable is included in the internal resistance of the power source and the resistance

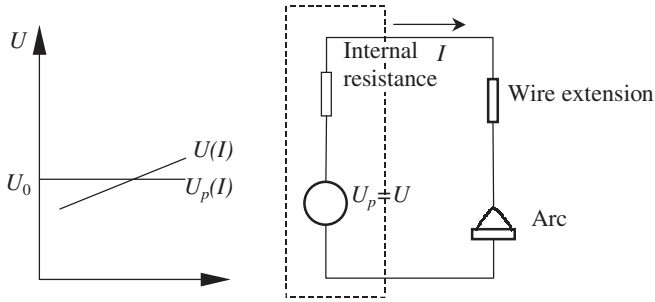

8.2 Equilibrium between an arc and a power source

of the wire extension is included in the resistance of the arc. U_p represents the output characteristic of the power source, which is normally constant voltage or slightly drooping for DC MIG welding. It can be expressed as

$$U_p = U_0 - k_d I \quad [8.1]$$

where U_0 is the open circuit voltage and k_d is the drooping slope. The voltage drop across the torch tip and weld pool consists of the voltage drop along the wire extension U_s and the voltage drop through the arc U_a.

$$U = U_a + U_s \quad [8.2]$$

The voltage drop in the wire extension can be written as[74]

$$U_s = k_s L_s I \quad [8.3]$$

where k_s is the resistance for a unit length of wire extension.

According to the results of previous studies on static arc characteristics,[249,250] the relationship of arc voltage, current, and arc length can be simplified as

$$U_a = k_a L_a + k_p I + U_c \quad [8.4]$$

where k_a is the potential gradient across the arc column, k_p is the equivalent resistance of the cathode and anode spots, and U_c is a constant.

Synthesising Equations [8.1] to [8.4] gives

$$U_0 = k_d I + k_p I + k_s L_s I + k_a L_a + U_c \quad [8.5]$$

The second equilibrium, i.e. the equilibrium of the wire-melting rate and the wire-feed rate can be expressed as

$$V_m = V_f \quad [8.6]$$

which is the necessary condition for a stable arc. The operator normally presets the wire-feed rate V_f and the melting rate depends on the arc

current and wire extension. The results of a study carried out by L. D. Zhang and his colleague[114] demonstrated that the wire melting consisted of two parts. One was the melting due to the energy of the arc, which is proportional to the welding current. The second part was due to the resistive heating of the wire extension, which is proportional to the length of wire extension. An empirical formula was set up by A. Lesnewich as follows:[119,252,253]

$$V_m = k_m I + k_\eta I^2 L_s + C_m \qquad [8.7]$$

where K_η is the contribution of resistive heating to melting rate and k_m is the contribution of arc heating to the melting rate. Combining Equations [8.6] and [8.7] gives

$$V_f = k_m I + k_\eta I^2 L_s + C_m$$

or

$$L_s = \frac{1}{k_\eta I^2}(V_f - k_m I - C_m) \qquad [8.8]$$

Substituting Eq. [8.8] into Eq. [8.5], the arc length can be written as

$$L_a = L_0 + k_0 I - \frac{k_s(V_f - C_m)}{k_\eta \cdot k_a} \qquad [8.9]$$

where

$$L_0 = \frac{1}{k_a}\left(U_0 - U_c + \frac{k_s k_m}{k_\eta}\right), \quad k_0 = -\frac{k_d + k_p}{k_a}$$

Obviously, the torch height is the sum of Equations [8.8] and [8.9]

$$H = L_a + L_s = L_0 + k_0 I - \frac{k_m}{k_\eta} I^{-1} - \frac{k_s}{k_\eta k_a} V_f I^{-1} - \frac{C_m}{k_\eta} I^{-2} + \frac{1}{k_\eta} V_f I^{-2}$$

which can be written as

$$H = L_0 + k_0 I + k_1 I^{-1} + k_2 V_f I^{-1} + k_3 I^{-2} + k_4 V_f I^{-2} \qquad [8.10]$$

where

$$L_0 = \frac{1}{k_a}\left(U_0 - U_c + \frac{k_s k_m}{k_\eta}\right)$$

$$k_0 = -\frac{k_d + k_p}{k_a}, \quad k_1 = -\frac{k_m}{k_\eta}, \quad k_2 = -\frac{k_s}{k_\eta k_a}, \quad k_3 = -\frac{C_m}{k_\eta}, \quad k_4 = \frac{1}{k_\eta}$$

Equation [8.10] is the static mathematical model of an arc sensor that was sought, where $k_i (i = 0, \ldots 4)$. These coefficients can be determined experimentally, as described below. Once these coefficients are determined, the

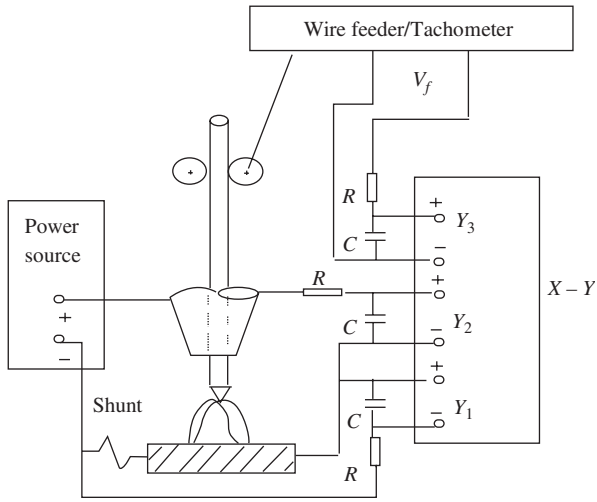

8.3 Circuit diagram for the study of a static mathematical model

torch height can be calculated if the values of welding current and wire-feed rate are given. It can be seen from Eq. [8.10] that it is a non-linear model. The degree of non-linearity is discussed later, after the coefficients are known. A method for simplifying this model is also proposed.

8.2.2 Experimental study

In order to determine the coefficients of Eq. [8.10], the author conducted an experimental study. The experimental data regarding torch height H, current I, and wire-feed rate were processed by regression analysis. Because a static model was being investigated, all of the data were measured while the arc was stable. The welding-current signal was taken from a shunt connected in series in the welding loop, the wire feed-rate signal was taken from a tachometer installed on the wire-feed motor, and the torch height was manually preset for each series of experiments. The circuit diagram for the experiment is shown in Fig. 8.3. The RC network was used to filter the noise and disturbance of the arc current and wire-feed motor during the experiments.

The experimental procedure was as follows. The wire-feed rate was set first and then the torch height was manually varied, one step at a time. The welding current then was recorded for each step of the torch-height variation, as shown in Fig. 8.4a. After the experiments were completed, welds were made at another wire-feed rate. The data were recorded using the

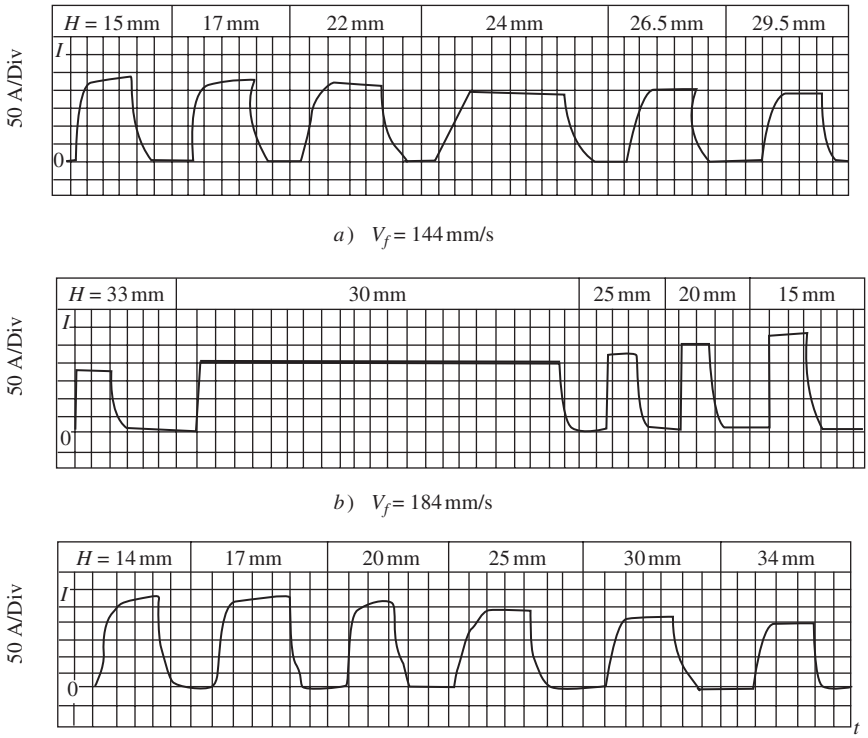

8.4 Experimental data for the static model

same procedure as that described above and shown in Figures 8.4b and 8.4c. The data obtained for the conditions, $U_0 = 38\,\text{V}$; $k_d = 2.25\,\text{V}/100\,\text{A}$ are listed in Table 8.1. I^{-1}, $I^{-1}V_f$, I^{-2}, and $I^{-2}V_f$ were calculated using these data and are listed in the same table.

Let $X_1 = I, X_2 = I^{-1}, X_3 = I^{-1}V_f, X_4 = I^{-2}, X_5 = I^{-2}V_f$

Because V_f and I are variables, $X_i (i = 1, \ldots 5)$ are irrelevant to the linearity and, therefore, the coefficient of Eq. [8.10] can be determined by regression analysis.[80–82]

Therefore, the regression function can be obtained using the data listed in Table 8.1 as

$$H = -189 + 0.015I + 5.11 \times 10^4 I^{-1} - 2.89 \times 10^6 I^{-2} + 99.0 I^{-1}V_f - 1.63 \times 10^4 I^{-2}V_f \quad [8.11]$$

The correlation coefficient is 0.99 and the error is ±1.14 mm.

Table 8.1 Experimental data for the static model

V_f (mm/s)	H (mm)	I (A)	I^{-1} (10^{-3}/A)	I^{-2} (10^{-5}/A^2)	$I^{-1}V_f$ (mm/sA)	$I^{-2}V_f$ (10^{-3}mm/sA^2)
144	15	250	4.00	1.60	0.576	2.31
144	17	238	4.20	1.76	0.605	2.54
144	22	225	4.44	1.97	0.640	2.85
144	24	215	4.65	2.16	0.670	3.21
144	26.5	208	4.81	2.31	0.692	3.34
144	29.5	190	5.26	2.77	0.758	4.00
144	15	270	3.70	1.37	0.681	2.52
184	20	250	4.00	1.60	0.736	2.94
184	25	230	4.35	1.89	0.800	3.47
184	30	205	4.88	2.37	0.898	4.35
184	33	185	5.41	2.92	0.995	5.36
204	14	285	3.51	1.23	0.740	2.59
204	17	270	3.70	1.37	0.755	2.80
204	20	265	3.77	1.42	0.796	2.99
204	25	242	4.31	1.70	0.847	3.48
204	30	225	4.44	1.97	0.911	4.03
204	34	205	4.88	2.37	1.000	4.85

When $V_f = 144$ mm/s,

$$H = -189 + 0.105I + 6.54 \times 10^4 I^{-1} - 5.27 \times 10^6 I^{-2} \quad [8.12]$$

When $V_f = 184$ mm/s,

$$H = -189 + 0.105I + 6.93 \times 10^4 I^{-1} - 5.89 \times 10^6 I^{-2} \quad [8.13]$$

When $V_f = 204$ mm/s,

$$H = -189 + 0.105I + 7.13 \times 10^4 I^{-1} - 6.21 \times 10^6 I^{-2} \quad [8.14]$$

The results of the calculation of the three functions above are plotted in Fig. 8.5. Experimental data also are included in the figure. The two sets of results are close to each other in the practical applied range of $H = 15$ mm–30 mm. The difference of the value of H between them is about 1 mm, individual data reach 2 mm. It can be concluded that Eq. [8.11] is reliable for representing the static model of an arc sensor.

8.2.3 Analyses of the model

8.2.3.1 Linearity of the model

It can be see from Fig. 8.5 that a linear relationship exists between H and I over a wide range. It can be proved that non-linearity is small by a Taylor-series expansion of Equations [8.12], [8.13], and [8.14] at $I = 240$ A.

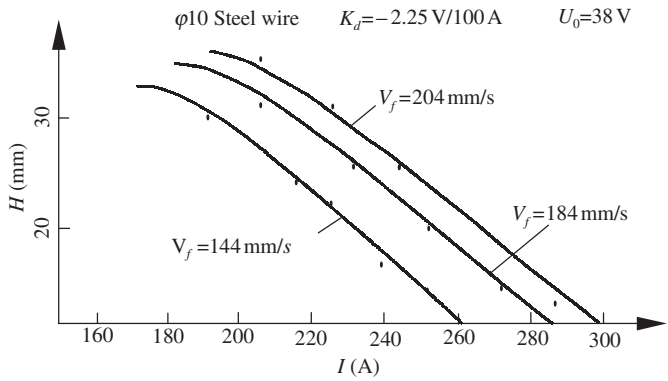

8.5 Comparison of the regression function with the experimental data

For example, according to Eq. [8.12], $H(240) = 17.7$ mm, the first order derivative of $H(I)$ at (240, 17.7) is $H'(240) = -0.272$, and the second order derivative $H''(240) = 1.44 \times 10^{-5}$.

Therefore the first three terms of the Taylor-series expansion formula of Eq. [8.10] is

$$\begin{aligned} H &= 17.7 - 0.272(I - 240) + 1.44 \times 10^{-5}(I - 240)^2 \\ &= 83.0 - 0.272I + s \end{aligned} \quad [8.15]$$

In the rectangular frame of the H,I diagram, H = [15 mm, 30 mm], I = [200 A, 280 A]

$$s_{max} = 1.44 \times 10^{-5}(280 - 240)^2 = 0.02 \text{ mm}$$

Therefore s can be neglected and the linear form of Eq. [8.12] can be written as

$$H = 83.0 - 0.272I \quad [8.16]$$

If the experimental data for (H, I) at $V_f = 144$ mm/s indicated in Table 8.1 are taken for a single variable regression, Eq. [8.17] is obtained and they are found to be very close.

$$H^* = 82.1 - 0.27I \quad [8.17]$$

Similarly if Equations [8.13] and [8.14] are expanded using the Taylor series and the corresponding data are processed by a single variable regression, the following results are obtained:

$$V_f = 184 \text{ mm/s}, \quad H = 81.9 - 0.246I \quad [8.18]$$

$$H^* = 82.3 - 0.243I \quad [8.19]$$

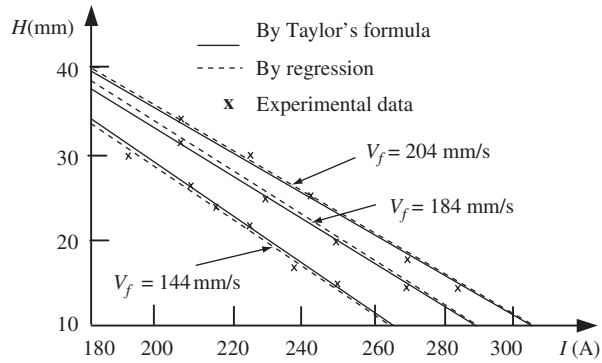

8.6 Single-variable regression function

$$V_f = 204\,\text{mm/s}, \quad H = 81.3 - 0.231I \qquad [8.20]$$

$$H^* = 82.1 - 0.234I \qquad [8.21]$$

The curves of Equations [8.16] through [8.21] and the experimental data are illustrated in Fig. 8.6. They are close to one another.

If Eq. [8.11] is expanded according to Taylor's formula, taking the first order at $I = 240$ A, within the range $V_f = 144$ mm/s, to 204 mm/s, one obtains

$$H = (-0.364 - 6.39 \times 10^{-4} V_f)I + 86.3 - 2.39 \times 10^{-2} V_f \qquad [8.22]$$

This is the static mathematical model of the arc sensor that is sought. More generally the static mathematical model can be written as

$$H = (a_1 + b_1 V_f)I + a_2 + b_2 V_f \qquad [8.23]$$

According to Eq. [8.23] and the experimental data for I, V_f, and IV_f, the regression function of the arc sensor is

$$H = 87.9 - 0.371I + 7.3 \times 10^{-4} V_f I - 4.72 \times 10^{-2} V_f \qquad [8.24]$$

This is plotted in Fig. 8.7 together with the experimental data. They agree closely. In conclusion, there is a linear relationship between H and I and the system can be regarded as linear.

8.2.3.2 Applicable conditions for the model

The mathematical model given by Eq. [8.24] was obtained by regression analysis of experimental data. Therefore it is applicable only under the conditions that were used for the experiments, i.e. a drooping characteristic

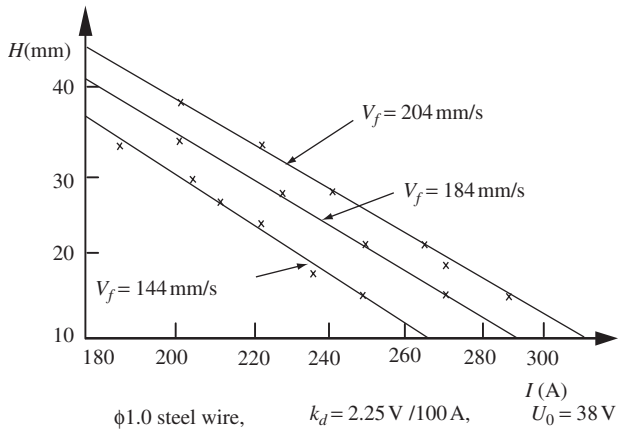

8.7 Linear model and experimental data

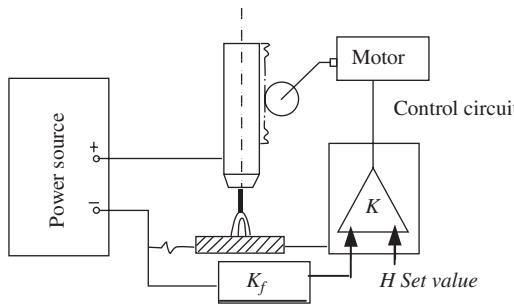

8.8 ACC control system

with a slope of 2.25 V/A and an open-circuit voltage of 38 V. The torch height can be calculated from Eq. [8.24] only under these conditions. The analysis of Eq. [8.10] shows, however, that the open-circuit voltage U_0 and the drooping slope k_d affect only the linear coefficients of Eq. [8.10] and do not affect the linearity of the function. Therefore, it can be concluded that Eq. [8.23] is valid universally for all MIG welding.

8.2.3.3 Application of the model for torch-height control

Figure 8.8 shows the torch-height control system. It controls the torch height and thus the arc current. Therefore it is called an Automatic Current Control (ACC).[33]

The feedback coefficient K_f can be determined from the mathematical model expressed by Eq. [8.25].

$$K_f = \frac{\Delta I}{\Delta H} = (a_1 + b_1 V_f)^{-1} \quad [8.25]$$

According to the analysis given above, K_f is related to the wire-feed rate and the slope of the power-source output characteristic, the value of which under the experimental conditions applied in the present case can be given as follows.

$$V_f = 144\,\text{mm/s}, \quad K_f = 3.7\,\text{A/mm}$$

$$V_f = 184\,\text{mm/s}, \quad K_f = 4.0\,\text{A/mm}$$

$$V_f = 204\,\text{mm/s}, \quad K_f = 4.3\,\text{A/mm}$$

Obviously, V_f does not noticeably affect K_f, which means that its effect can be neglected and the system can be designed as a linear system.

8.2.4 Summary

- The static mathematical model of an arc sensor is a linear time-invariant system, which can be expressed as

$$H = (a_1 + b_1 V_f) I + a_2 + b_2 V_f$$

- When the open-circuit voltage is 38 V, and the drooping slope of the power source is 2.25 V/100 A, the quantitative expression of the model can be written as

$$H = 86.3 - 0.367 I + 6.39 \times 10^{-4} V_f I - 2.39 \times 10^{-2} V_f$$

- The ACC control is a linear time-invariant system; the feedback coefficient is related to the drooping slope of the power-source output characteristic, which is 4 A/mm when the slope is 2.25 V/A.

8.3 Dynamic model

An elaborate experimental design for studying the dynamic behaviour of the arc sensor was developed by the author. The description of the dynamic behaviour was derived from the quantitative description of the dynamic relationship between the output and input of the arc sensor. The effect of welding conditions on the sensitivity of the arc sensor was studied. The results of the study provided both theoretical and experimental bases for designing highly accurate and highly sensitive arc sensors.

8.3.1 Introduction

The dynamic mathematical model describes the variation of welding parameters (or, more specifically, welding current) when the torch height is varied in the arc sensing system. The significance of the study and the establishment of the dynamic model are described as follows:

- The model provides the relationship between the gain and working frequency or between the sensitivity and working frequency of the system, which are important bases for designing the system.
- The model explains the effect of power-source dynamic properties on the sensitivity of the arc sensor and thus puts forward the requirements of the power source for the design of the sensor system.
- The model explains the effect of welding parameters such as average welding current, average arc voltage, average torch height, and shielding-gas composition, on the sensitivity of the system and thus provides guidelines for choosing welding parameters.
- The model gives a quantitative description of the properties of the system and thus provides a deeper understanding of the system, which makes it possible to further develop it on the basis of theoretical guidelines. The numerical simulation of the system for groove-line recognition described in Chapters 9 and 10 is based on the dynamic mathematical model established in this chapter.

As discussed in the last chapter, where H and I are linearly related, the relationship can be written as $H = KI + b$. Evidently, the change of input ΔH and change of output ΔI will have a linear relationship as well, i.e. the homogeneous linear equation $\Delta H = k\Delta I$ is tenable. Therefore, it is reasonable to establish the dynamic mathematical model using a transfer function.

Similarly to the static model, both the theoretical analysis and the experimental method were used for the derivation of the model. For this purpose, an experimental method was proposed. This approach can be used not only for the present study but also for quantitative study of arc length self-adjustability.

8.3.2 Theoretical derivation

Equations [8.2] to [8.4] describe the static relationship of the physical parameters of the system. In order to study the dynamic model it is necessary to rewrite them in dynamic-equation form. Equations [8.2] and [8.4] can be expressed as

$$U(t) = U_a(t) + U_s(t) \quad [8.26]$$

$$U_a(t) = k_a L_a(t) + k_p I(t) + U_c \quad [8.27]$$

Equation [8.27] is, in fact, a mathematical model of the arc but it is tenable based on the following three assumptions:

Assumption 1: The arc is not an energy-storage element. This means that the current is proportional to its voltage without any phase difference. Actually, there is heat-energy inertia but it is small for cold-cathode MIG welding. The transient process is completed within 1 ms; in other words, the response frequency is 1 kHz. In the case of an arc sensor, the scanning frequency is much lower than this and, therefore, it is reasonable to neglect it.

Assumption 2: The working range of the arc sensor $I(t)$ and $L_s(t)$ is within a small area around (I_0, L_{so}). Therefore small-signal theory is justifiable for this analysis. The function can be expanded according to a first-order Taylor series.

According to this assumption, Eq. [8.3] can be expressed in linear form as

$$U_s(t) = k_l I(t) + k_i L_s(t) + C_1 \quad [8.28]$$

where $k_l = k_s L_{s0}$, $k_i = k_s I_0$, C_1 is constant.

Equation [8.7] can be simplified as

$$V_m(t) = k_c I(t) + k_r L_s(t) + C_2 \quad [8.29]$$

where $k_c = k_m + 2k_\eta L_{s0}$, $k_r = k_\eta I_0$, and C_2 are constants.

Equation [8.29] is a dynamic function describing the wire melting. The description can be accepted only on the basis of the following third assumption.

Assumption 3: The wire melts continuously as small particles in the spray-transfer mode. The melting rate varies according to the arc-heating and resistance-heating variation, without any delay. In DC MIG welding, the metal transfer conforms to this assumption.

For maintaining a stable arc in MIG welding, $V_m = V_f$ is an important equilibrium condition. However, when the arc length varies in the dynamic state, this equilibrium no longer exits. Substituting it into the dynamic equation gives

$$\frac{dH}{dt} + V_m(t) - V_f(t) = \frac{dL_a}{dt} \quad [8.30]$$

This means that the arc-length rate of change is the vector sum of torch-height rate of change, wire-feed rate, and melting rate.

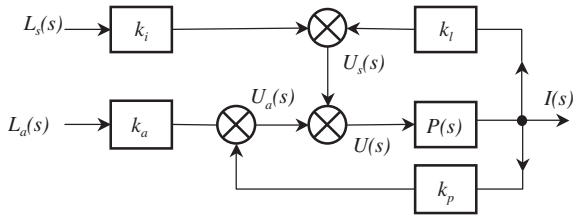

8.9 Block diagram of the electrical parameters of a welding loop

Taking the Laplace transformation of Equations [8.26] to [8.30], the following equations are obtained:

$$U(s) = U_a(s) + U_s(s) \quad [8.31]$$

$$U_a(s) = k_a L_a(s) + k_p I(s) \quad [8.32]$$

$$U_s(s) = k_l I(s) + k_i L_s(s) \quad [8.33]$$

$$V_m(s) = k_c I(s) + k_r L_s(I) \quad [8.34]$$

$$sH(s) + V_m(s) - V_f(s) = sL_a(s) \quad [8.35]$$

where k_a, k_p, k_l, k_c, k_r, are constants.

Equation [8.35] can be rewritten as

$$L_s(s) = H(s) - L_a(s) = \frac{1}{s}(V_f(s) - V_m(s)) \quad [8.36]$$

Equations [8.31] to [8.33] describe the relationships of the electrical parameters of the welding loop, which can be illustrated by the block diagram shown in Fig. 8.9.

$P(s)$ in the figure represents the relationship of the output current and the input voltage of the power source.[84] $P(s)$ can be expressed in a general form as

$$P(s) = \frac{I(s)}{U(s)} = P_0 \frac{1 + a_1 s + a_2 s^2 + \ldots + a_m s^m}{1 + b_1 s + b_2 s^2 + \ldots + b_n s^n} \quad [8.37]$$

where $P_0 = \lim_{s \to 0} P(s)$, i.e. the static output of the power source $\Delta I/\Delta U$, or the reciprocal of the output characteristic slope k_d of the power source.

$$P_0 = \frac{1}{k_d} \quad [8.38]$$

On the basis of Equations [8.34], [8.35], and [8.36], a block diagram regarding the arc-length variation can be constructed as shown in Fig. 8.10.

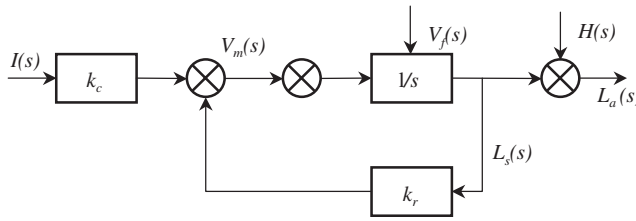

8.10 Block diagram of arc-length variation

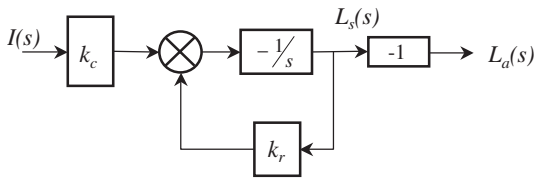

8.11 Simplification of Fig. 8.10

Let $V_f(s) = 0, H(s) = 0$, i.e. the wire-feed rate and torch height do not vary, then the block diagram changes to that shown in Fig. 8.11.

This means

$$L_a(s) = -L_s(s) = \frac{k_c}{s + k_r} \cdot I(s) \qquad [8.39]$$

Figure 8.11 and Eq. [8.39] manifest the following two points:

(i) Under conditions where the wire-feed rate and torch height do not change, increasing the welding current results in an increase of arc length and a decrease of wire extension. This is the well known and very important rule about arc-length self-adjustability.

(ii) The change of arc length and wire extension lag behind the welding-current change. This inertial element determines the time constant of the arc-length adjustability and affects the intensity of the output signal of the arc sensor.

Combining Figures 8.9 and 8.10, a block diagram of the arc-sensing system can be obtained, as shown in Fig. 8.12.

If only input $H(s)$ and output $I(s)$ are considered, the system can be simplified as shown in Fig. 8.13. From this diagram, the transfer function between $H(s)$ and $I(s)$ can be derived as

$$G(s) = \frac{I(s)}{H(s)} = \frac{k_a(s + k_r)P(s)}{(1 - k_N P(s))s + k_q P(s) + k_r} \qquad [8.40]$$

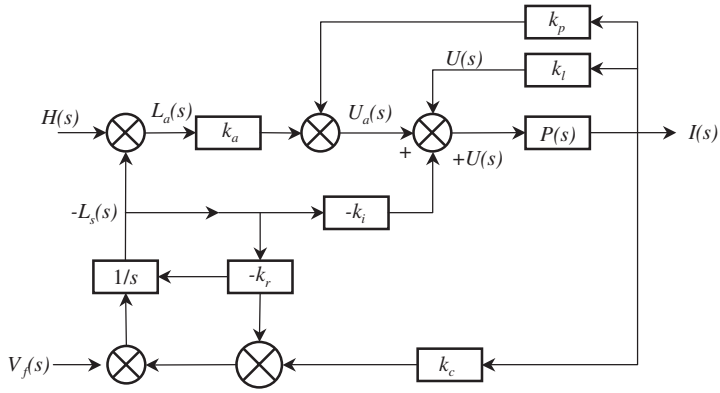

8.12 Block diagram of arc sensor

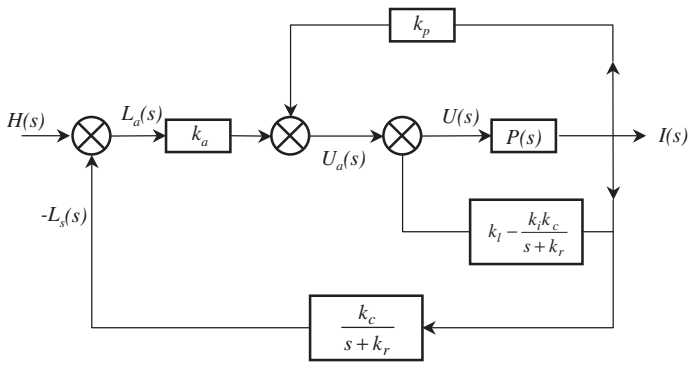

8.13 Simplified block diagram of arc sensor

where $$k_N = k_P k_l, \quad k_q = k_i k_c - k_r k_N - k_a k_N k_m$$

Equation [8.40] is the theoretically-derived mathematical model of the arc sensor. The order of the function depends on the output characteristic of the power source $P(s)$. Supposing that $P(s)$ is an n-order system as expressed by Eq. [8.37], substituting it into Eq. [8.40] gives

$$G(s) = \frac{P_0 k_a (s + k_r)}{[(1 + b_1 s + b_2 s^2 + \ldots + b_n s^n) - k_N P_0 (1 + a_1 s + a_2 s^2 + \ldots + a_m s^m)]s} \\ \frac{(1 + a_1 s + a_2 s^2 + \ldots + a_m s^m)}{+ k_q P_0 (1 + a_1 s + a_2 s^2 + \ldots + a_m s^m) + k_r (1 + b_1 s + b_2 s^2 + \ldots + b_n s^n)} \quad [8.41]$$

In this equation, the maximum order of the denominator is $(n + 1)$ and the maximum order of the numerator is $(m + 1)$. Therefore, it can be concluded that the structure of the mathematical model depends on the

dynamic characteristic of the power source. The order of the mathematical model equals the order of the transfer function of the power source plus 1. The number of zeros and the pole of the arc sensor are equal, respectively, to the number of zeros and poles of the power source plus one.

For example, in the case of a power source having good dynamic properties, it can be regarded as a proportional element, i.e. $P(s) = P_0$. Then, the mathematical model of the arc sensor can be written as

$$G(s) = K \times \frac{1 + T_1 s}{1 + T_2 s} \qquad [8.42]$$

where $K = \dfrac{k_a k_r P_0}{k_q P_0 + k_r}, T_1 = \dfrac{1}{k_r}, T_2 = \dfrac{1 - k_N P_0}{k_q P_0 + k_r}$

The coefficients in the equation are determined by experiments that are described in the following paragraphs.

8.3.3 Experimental study

When a sinusoidal exciting signal is fed into a system, the ratio of the output and input amplitudes (the gain of the system) and the phase difference between them change with the change of the input-signal frequency. The rule by which these parameters change represents the dynamic properties of the system. The former is called the magnitude-frequency characteristic and the latter is called the phase-frequency characteristic of the system. On the basis of these characteristics, the gain, and the position of zeros and poles, can be found directly and thus the transfer function of the system can be determined.[5] The author and his colleague have carried out an experimental study on the mathematical model. A key problem in these experiments was how to excite the variation of torch height according to a sinusoidal waveform.

Two schemes were developed for solving this problem. The first scheme was based on the mechanism used for oscillating the torch illustrated in Fig. 7.17. The oscillation rack was oriented vertically as shown in Fig. 8.14, and a sine-wave signal was fed into its controller so that the torch oscillated up and down. The current was recorded during the experiment. The magnitude-frequency characteristic that was constructed on the basis of the experimental data is illustrated in Fig. 8.15. As the frequency response of the rack was low, the output was insignificant when the frequency was more than 5 Hz. Therefore, the magnitude-frequency characteristic of an arc sensor can be obtained only below 5 Hz.

In order to raise the torch-height exciting frequency, a new experimental apparatus was proposed by the author and his colleague. The rotating torch RAT – 1 (Chapter 7) was installed in an inclined position: its axis was

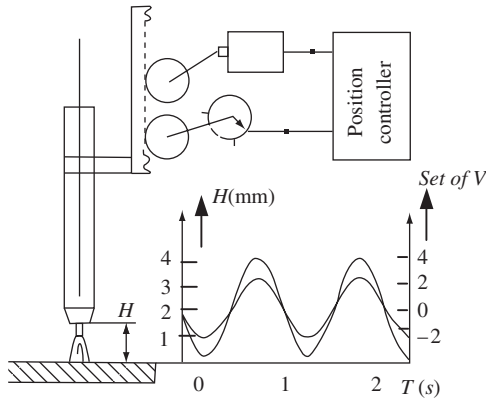

8.14 Vertical oscillation of torch

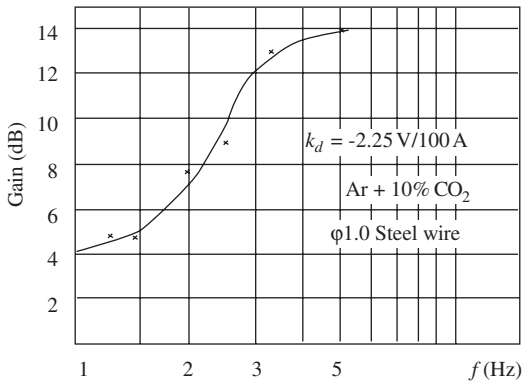

8.15 Magnitude-frequency characteristic of the arc sensor

inclined 45° to the horizontal steel plate, as shown in Fig. 8.16. Then the torch height varied according to a sinusoidal waveform while the torch rotated.

Supposing that the rotating speed is n and the rotation diameter is D, then the rule of torch-height movement is

$$H = \frac{D}{2}\sin\left(\frac{2\pi}{60}nt + \beta_0\right) + H_0 \qquad [8.43]$$

Where β_0 is the initial angular position of the torch when $t = 0$, and H_0 is the average height of the torch. The frequency and magnitude variation were stable within 50 Hz, which fully satisfied the requirement of the experiments.

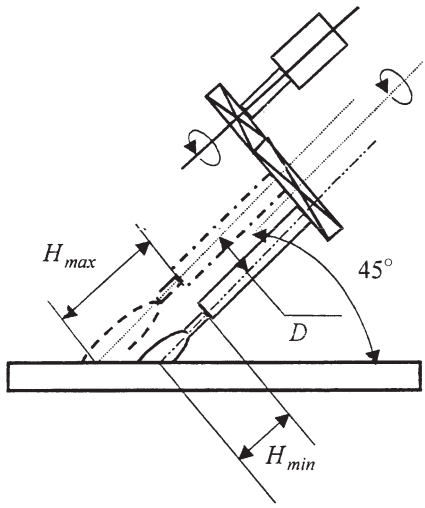

8.16 Apparatus for obtaining sinusoidal variation of torch height

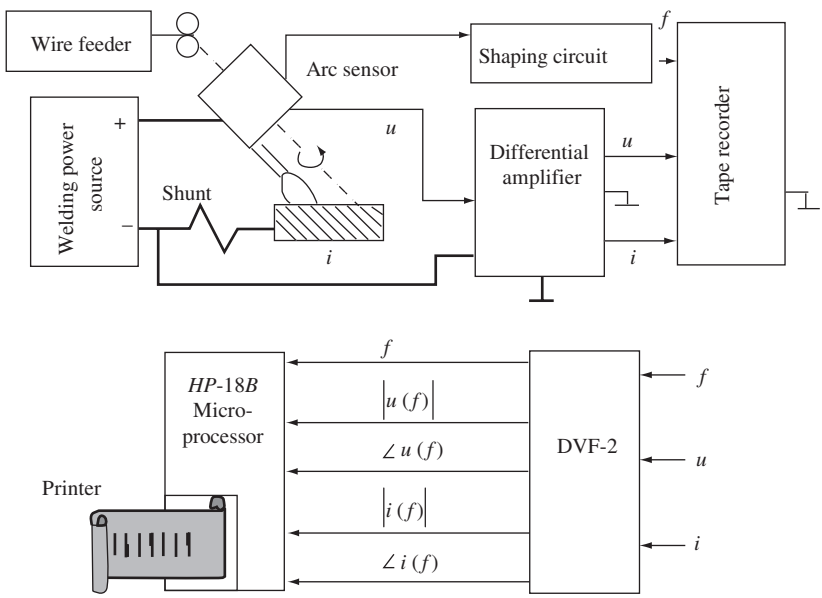

8.17 Block diagram of experimental apparatus

The experimental system is illustrated in Fig. 8.17. A transistorised welding power source and an electronic control were used: these allowed easy regulation of its output characteristics.[127] A torque motor drove the wire feeder and a tachometer was mounted on its shaft for feedback control

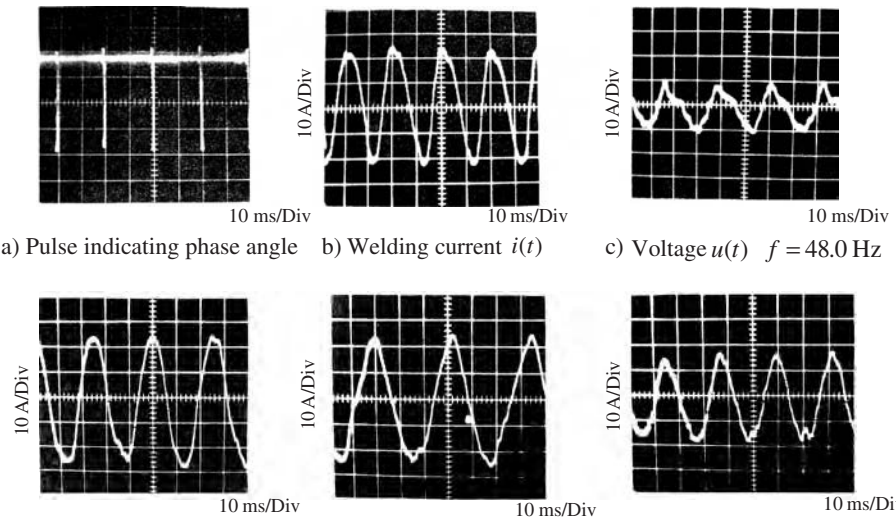

a) Pulse indicating phase angle b) Welding current $i(t)$ c) Voltage $u(t)$ $f = 48.0$ Hz

d) $i(t)$ $f = 38.2$ Hz e) $i(t)$ $f = 30.2$ Hz f) $i(t)$ $f = 22$ Hz

8.18 Current and voltage waveforms during dynamic-model experiments (1)

of the wire-feed rate. A stable wire-feed rate could be obtained in this manner.[254] A tape recorder and a photoelectric speed detector were used to measure some of the data so that the time and materials required for the experiments would be economical.

Because the variation of the welding current and voltage is much smaller than that of their DC components, two differential amplifiers were used to eliminate the DC components.

After setting the welding parameters and the output characteristic of the power source, the welding arc was rotated at different frequencies and the welding current, voltage, and the torch angle were recorded, as shown in Figures 8.18 and 8.19.

These figures show that the current amplitude increases with frequency. The magnitude-frequency characteristic can thus be roughly obtained. However, the recorded current and voltage waveforms consist of many waveforms having different frequencies. The arc-current change due to arc rotation is needed. Therefore, an analytical method or apparatus has to be used. Two ways to solve the problem are described below.[255–258]

(i) Correlation analysis. Mathematical analysis can be used to define the correlation function between the torch-height movement and the arc-current output to obtain the component of the current output that is related to excitation movement and thereby eliminate any unrelated factors.

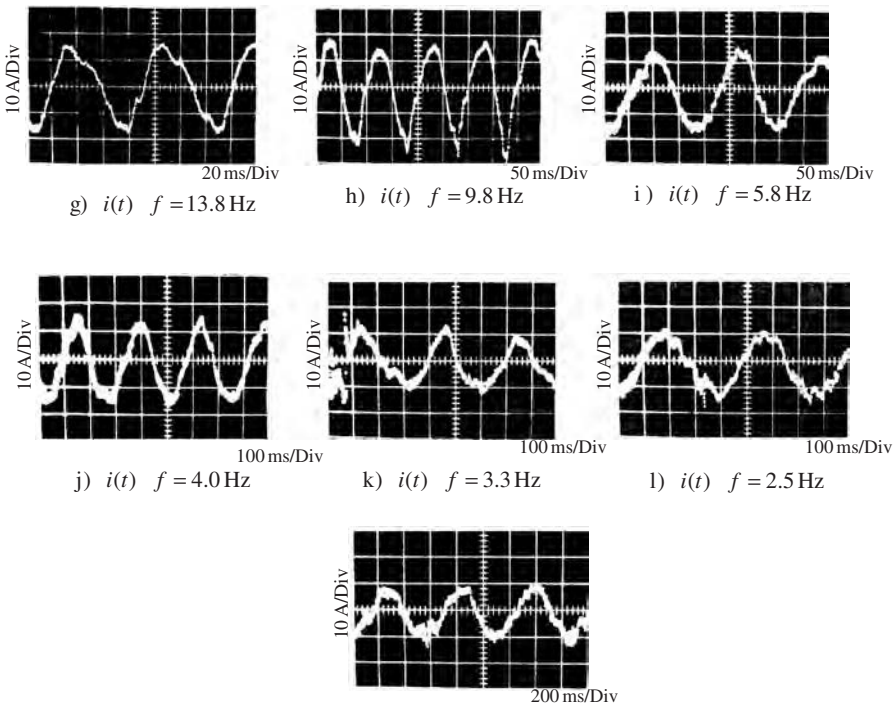

8.19 Current and voltage waveforms during dynamic model experiments (2)

(ii) Power-spectrum analysis. The power spectrum of the excitation movement and the output are calculated, from which the magnitude-frequency and phase-frequency characteristics can be obtained directly.

Although an accurate characteristic can be obtained by both methods, in practice there are two problems. The first is that it needs sufficient time to generate a large amount of data, particularly for low-frequency excitation (0~10 Hz). Five minutes are necessary, which introduces experimental difficulty. The second problem is that the analytical instruments (7T17 or HP3582) are expensive. For these reasons, a third method was used by the author:

(iii) Tracking filtering. In this technique, the central frequency of a filter automatically follows the excitation frequency established by the torch rotation. The digital-vector filter DVF – 2 is a tracking filter. The bandwidth of the filter is 0.2 Hz. It can separate a selected frequency from the signal and generate the magnitude and phase of the

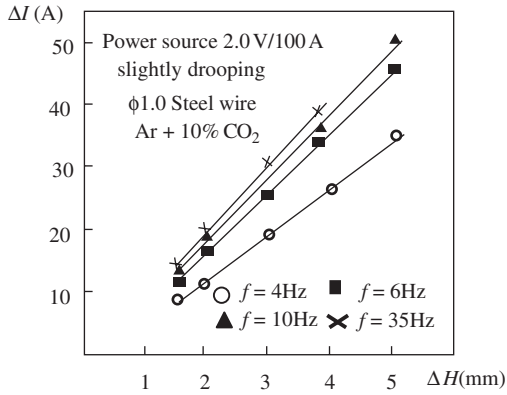

8.20 Analysis of arc sensor linearity

selected frequency 4 times per second (4 Hz). For convenience of recording and processing the signals, a microprocessor HP – 18B was connected to the DVF – 2, which provided an arc-signal analyser. A signal having the same frequency as the rotation frequency, measured using a photoelectric detector, could be separated and recorded.

8.3.4 Analysis of experimental results

A series of experiments having the following purposes was carried out:

(i) To verify the validity of the theoretical derivation of the mathematical model.
(ii) To establish the coefficients of the mathematical model.
(iii) To study the effect of various parameters in the system on the mathematical model and the sensitivity of the arc sensor.

Because a transfer function is used as the expression of the mathematical model, it is necessary to discuss the linearity of the system or to prove that the relationship between the output and the input does not depend on their magnitude.

8.3.4.1 Linearity of the arc-sensing system

In Section 8.1 it was proved that the arc-sensing system was linear. In the theoretical analysis given in previous sections, the non-linear elements were linearised. To verify the correctness of this linearisation, experiments were carried out to investigate the relationship between ΔH and ΔI; the results are shown in Fig. 8.20. The excitation frequencies were 4, 6, 10, and 35 Hz. It was shown that the relationship between ΔH and ΔI was linear when

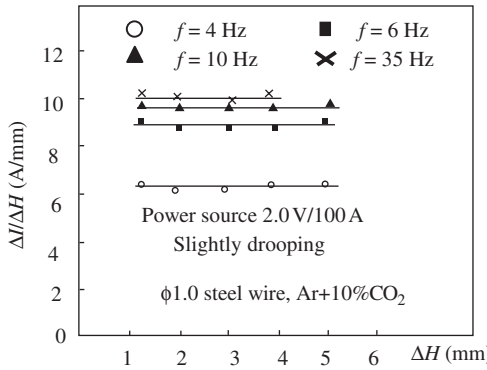

8.21 Effect of input magnitude on sensitivity

$\Delta H < 5$ mm. Therefore, it can be concluded that the system can be treated as linear. This conclusion has the following significance:

- For a linear system, a transfer function can be used to describe its dynamic behaviour. Magnitude-frequency and phase-frequency characteristics can be used to establish its mathematical model.
- The magnitude of the input does not change the gain or the sensitivity of the system, which is shown in Fig. 8.21. This inference facilitates the design of the system.

8.3.4.2 A Type 1 arc sensor

It was pointed out in Section 8.3.2 that the order of an arc sensor's mathematical model is one order larger than the order of the welding power source. In order to elucidate the behaviour of the arc sensor, experiments were performed using a highly responsive, transistorised power source. After these experiments are described, the effect of the dynamic properties of the power source on the mathematical model of the sensor is discussed.

A torch-height excitation of 4 mm and a power source having a drooping characteristic (–1.4 V/100 A), were used for the experiment. The current changes were measured and are listed in Table 8.2. To measure the frequency characteristics of the power source, the ratio of its current change to its voltage change was detected and plotted against the frequency, as shown in Fig. 8.22. It can be seen from the figure that the ratio of current change to voltage change was essentially constant and the phase angle difference was –180°. These results demonstrated that the power source was a Type 0 system or a proportional element. It should be pointed out also that due to magnetic leakage by the power-source transformer and inductance in the welding loop, the gain curve in Fig. 8.22 drops a small

Table 8.2 Experimental data for a first-order model

f (Hz)	ΔI (A)	$\angle I$ (°)	ΔU (mV)	$\angle U$ (°)	$\Delta I/\Delta H$ (A/mm)
1.5	13.4	–169	191	9	3.35
2.2	11.7	–166	163	14	2.92
3.7	19.2	–135	287	44	4.97
5.0	28.3	–146	404	33	7.08
6.7	28.3	–140	348	40	7.08
8.5	32.5	–139	449	39	8.13
11	33.3	–152	481	27	8.32
12	36.1	–153	487	27	9.02
14	46.4	–155	619	22	11.6
15	40.0	–144	533	36	10
18	47.6	–157	620	21	11.9
20	40.8	–149	538	30	10.2
23	40.4	–150	539	29	10.1
24	40.0	–158	552	21	10
25	39.1	–168	565	11	9.77
29	38.6	–163	545	12	9.66
32	40.0	–170	572	7	10
38	43.1	–170	576	3	10.8
42	39.1	–173	571	1	9.77
47	42.4	–178	592	0	10.6

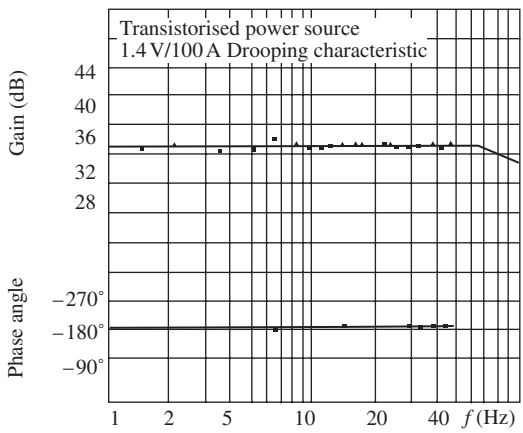

8.22 Frequency characteristics of the power source

amount but from the tendency of the curve, the corner frequency is high. Therefore,

$$P(s) = \frac{I(s)}{U(s)} = \frac{\Delta I}{\Delta U} = P_0$$

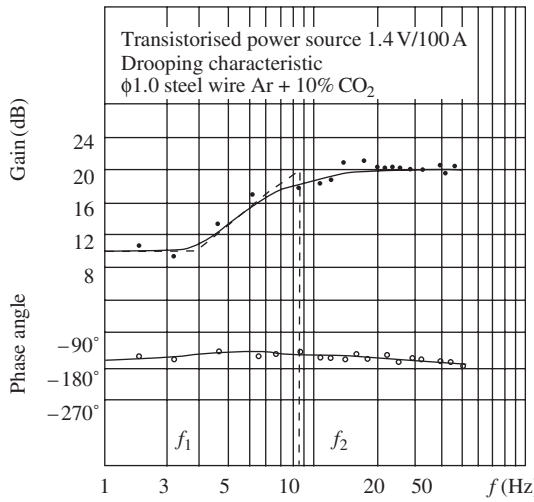

8.23 Frequency characteristics of the arc sensor

According to Eq. [8.24] the mathematical model can be written as

$$G(s) = K \cdot \frac{1 + T_1 s}{(1 + T_2 s)} \qquad [8.44]$$

It has one zero and one pole, which is denoted an arc sensor fitting a first-order mathematical model. The frequency at zero is $f_1 = \dfrac{1}{2\pi T_1}$, and frequency at the pole is $f_2 = \dfrac{1}{2\pi T_2}$. If the frequency trends to zero, one obtains

$$\lim_{s \to 0} G(s) = \lim_{s \to 0} K \cdot \frac{1 + T_1 s}{1 + T_2 s} = K$$

where K is the gain of the system in a static state.

From the data of Table 8.2, the magnitude-frequency and phase-frequency characteristics can be drawn as shown in Fig. 8.23. In the figure, the abscissa of the magnitude-frequency characteristic is the gain of H to I; the unit is dB.

$$dB = 20\mathrm{Log}A,\ A = |I(s)| / |H(s)|$$

The frequency characteristic can be regarded as a measure of the arc sensor's sensitivity. Because it is known that the curves on its frequency characteristic can be approximated by segments of a line for a linear, time-invariant system, the slope of these segments should be either

0 or a multiple of ±20 dB/10 times the frequency range. The corner points of these segments are either zero (where the slope increases) or pole (where the slope decreases). The magnitude-frequency characteristic shown in Fig. 8.23 was approximated by dotted-line asymptotes. The frequencies at the corner were

$$\text{Zero: } f_1 = 2.9\text{Hz}, \quad T_1 = 0.055\text{s}$$

$$\text{Pole: } f_2 = 8.5\text{Hz}, \quad T_2 = 0.019\text{s}$$

$$\text{Static gain: } K = -\text{ant} \quad \text{Log}(10.2/20) = -3.24\,\text{A/mm}$$

A negative value was taken for K because the phase difference between the output and input is 180°. Using the parameters obtained, Eq. [8.44] can be written quantitatively as

$$G(s) = -3.24 \cdot \frac{1 + 0.05s}{1 + 0.019s}$$

This is a first-order model of an arc sensor. It is worth noticing that the model is affected by the slope of the power-source output characteristic. From the theoretical derivation described in previous sections, it is known that if the slope is $k_d(V/A)$, the coefficients of Eq. [8.44] are

$$P_0 = 1/k_d, \quad K = \frac{k_a k_r k_d^{-1}}{k_q k_d^{-1} + k_r} = \frac{k_a k_r}{k_q + k_d k_r} \qquad [8.45]$$

$$T_1 = 1/k_r, \quad T_2 = \frac{1 - k_N k_d^{-1}}{k_q k_d^{-1} + k_r} = \frac{k_d - k_N}{k_q + k_d k_r}$$

From Eq. [8.45] it can be seen that if the power source has a flat output characteristic, i.e. $k_d = 0$, then

$$K = \frac{k_a k_r}{k_q} \qquad [8.46]$$

It is well known that the current decreases when the torch height is increased in the static state, i.e. $K < 0$. As it is known that $k_a > 0$, $k_r = k_\eta I_0 > 0$, therefore $k_q < 0$. Thus, when $k_d < 0$, the larger $|k_d|$ is, or the steeper the drooping characteristic becomes, the larger $|k_q + k_d k_r|$ is. The static gain K of the arc sensor will be larger.

It can be seen from Eq. [8.45] that T_1 is independent of k_d. This means that it does not depend on the slope of the output characteristic of the power source. T_2 is affected by k_d bi-directionally, which can be found only from experiments.

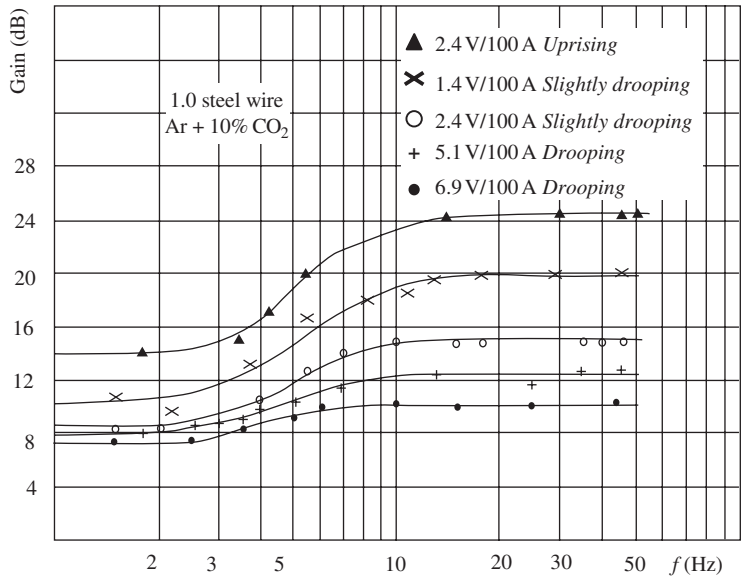

8.24 Magnitude-frequency characteristics for different power sources

Table 8.3 Effect of power source output characteristics on the parameters of the model

Slope of output characteristics (V/100 A)	Parameters of the model		
	T_1 (s)	T_2 (s)	K (A/mm)
Rising 2.4	0.055	0.016	–5.2
Slightly drooping 1.4	0.055	0.019	–3.3
Slightly drooping 2.4	0.055	0.025	–2.6
Drooping 5.1	0.055	0.029	–2.4
Drooping 6.9	0.055	0.036	–2.3

The magnitude-frequency characteristics for different power sources are shown in Fig. 8.24. The parameters of the model are listed in Table 8.3.

From these experiments, the following conclusions were drawn:

- When a responsive power source is used, the mathematical model of the sensor agrees with Eq. [8.42], which proves that the theory and the assumptions that were used are correct.
- It is seen from the model expressed by Eq. [8.42] that the frequency of zero is lower than that of the pole so that the system has 'high pass'

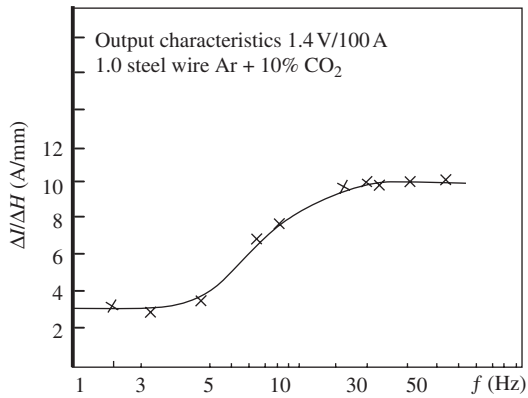

8.25 Relationship between sensitivity and rotation frequency

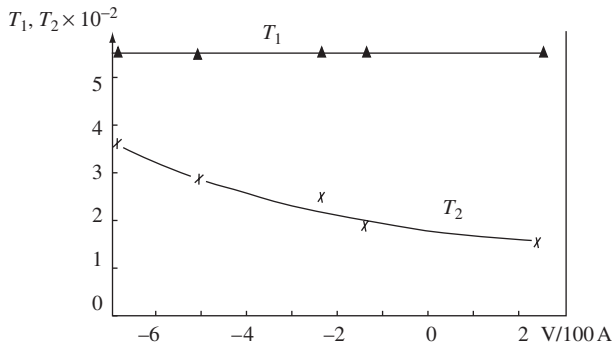

8.26 Effect of output-characteristic slope on the parameters of the model

character. This means that the gain at low frequency is lower and the gain at high frequency is higher but it remains flat at the high-frequency end. The sensitivity depends on the rotation frequency; it increases with the increase of rotation frequency (see Fig. 8.25) but it shows 'saturation' after f_2 such that the sensitivity no longer changes. This sensitivity is called the 'saturation sensitivity' in this book.

- The effect of the slope of the output characteristic on the parameters of the model expressed by Eq. [8.42] is illustrated in Fig. 8.26. Its effect on sensitivity at the low-frequency end (or static sensitivity), and on the saturation sensitivity, is shown in Fig. 8.27. This shows that the effect on saturation sensitivity is significant.
- From the experimental data it can be seen that the corner frequency is around 5~10 Hz depending on the welding power source that is used.

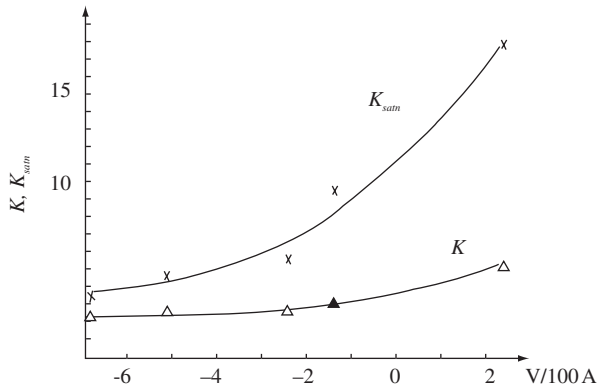

8.27 Effect of output-characteristic slope on sensitivity

To obtain the maximum possible sensitivity, using a frequency 2–3 times higher than the corner frequency is recommended. It is seen from Fig. 8.27 that the sensitivity increases with the slope of the output characteristic. But the margin of stability of the arc decreases as the slope increases. Therefore, using a slightly drooping characteristic is recommended.[3] In this case, the sensitivity is about 10 A/mm.

8.3.4.3 Second-order mathematical model of an arc sensor

It was pointed out in the previous text that the power source is taken as a proportional element, which is true for highly-responsive transistorised power sources. For most conventional power sources, however, the current-output change lags the voltage change. To study the mathematical model of an arc sensor with this kind of power source, experiments were conducted using transistorised power sources, but having an inductance connected in series in the welding loop. The effect of inductance on the model structure and parameters were then studied.

Table 8.4 lists the experimental data obtained with inductances L_1 = 0.2 mH and L_2 = 0.4 mH. The slope of the output characteristic of the power source was –1.4 V/100 A. From these data, magnitude-frequency and phase-frequency characteristics of the power source were drawn as in Fig. 8.28. Due to the limitation of the experimental conditions, the maximum frequency that was used was 50 Hz. Even though the ratio of the current and voltage decreased markedly, the current obviously lagged. All of the data showed that the power source was a first-order inertial element, which can be expressed as

Table 8.4 Experimental data for the second-order model

(a) Inductance 0.2 mH

f (Hz)	ΔI (A)	$\angle I$ (^{0})	ΔU (mV)	$\angle U$ (^{0})	$\Delta I/\Delta H$ (A/mm)
1.5	12.9	–180	229	5	3.24
2.0	13.2	–175	235	13	3.35
3.5	15.0	–172	283	28	3.76
4.6	19.2	–165	383	37	4.79
6.0	22.0	–160	439	50	5.50
9.0	24.1	–185	509	43	6.03
16	24.1	–192	619	38	6.03
25	24.5	–200	921	37	6.17
32	23.0	–225	988	25	5.75
42	17.5	–230	997	18	4.37
50	14.5	–252	997	3	3.63

(b) Inductance 0.4 mH

f (Hz)	ΔI (A)	$\angle I$ (^{0})	ΔU (mV)	$\angle U$ (^{0})	$\Delta I/\Delta H$ (A/mm)
2.0	12.9	–165	217	15	3.23
3.5	17.9	–160	301	21	4.47
6.0	25.8	–160	448	24	6.46
9.0	29.3	–175	509	17	7.33
16	33.3	–177	664	31	8.32
25	32.5	–190	835	33	8.13
32	30.4	–202	928	29	7.59
42	27.0	–210	954	17	6.76
50	23.8	–232	993	3	5.96

$$P(s) = I(s)/U(s) = P_0/(1+T_p s) \qquad [8.47]$$

When $L = L_1 = 0.2\,\text{mH}, \quad P_0 = -64\,\text{A/V}, \quad T_P = 0.008\text{s}$

$L = L_2 = 0.4\,\text{mH}, \quad P_0 = -64\,\text{A/V}, \quad T_P = 0.011\text{s}$

According to the results presented in previous sections and Eq. [8.41], the mathematical model of the arc sensor should be a second-order transfer function that has two poles and one zero, and can be written as

$$G(s) = K\frac{1+T_1 s}{(1+T_2 s)(1+T_3 s)} \qquad [8.48]$$

The frequency at zero is $f_1 = 1/2\pi T_1$, the frequency at the poles $f_2 = 1/2\pi T_2$, $f_3 = 1/2\pi T_3$, and

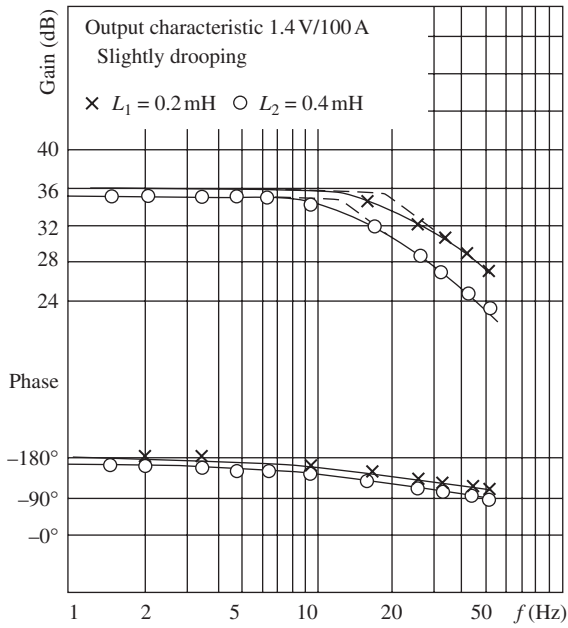

8.28 Frequency response of power-source

$$\lim_{s\to 0} G(s) = \lim_{s\to 0} K \cdot \frac{1+T_1 s}{(1+T_2 s)(1+T_3 s)} = K \qquad [8.49]$$

K is the gain at the low-frequency end, which corresponds to the static sensitivity.

From Fig. 8.29, the parameters of the model can be obtained as follows:

When $L = L_1 = 0.2\text{mH}$

$$f_1 = 2.9\text{Hz}, T_1 = 0.055\text{s}, f_2 = 7.1\text{Hz}, T_2 = 0.022\text{s}, f_3 = 38\text{Hz}, T_3 = 0.004\text{s}$$

When $L = L_1 = 0.4\text{mH}$

$$f_1 = 2.9\text{Hz}, T_1 = 0.055\text{s}, f_2 = 5.4\text{Hz}, T_2 = 0.029\text{s}, f_3 = 34\text{Hz}, T_3 = 0.05\text{s}$$

Comparing these results with the first-order model, the following conclusions can be drawn:

- In cases where there is an inductive element in the power source, the mathematical model of the arc sensor is second-order, as given by Eq. [8.48]. The magnitude-frequency and phase-frequency characteristics are shown in Fig. [8.29]. Obviously it has 'band pass' character; the

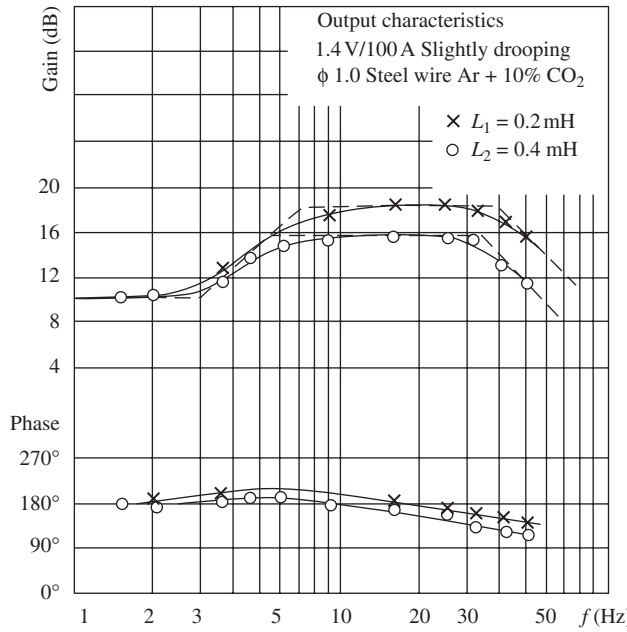

8.29 Effect of inductance on frequency characteristic of arc sensor

Table 8.5 Effect of power-source dynamic properties on the mathematical model

Power-source dynamic characteristics T (s)	Parameters of the mathematical model			
	T_1 (s)	T_2 (s)	T_3 (s)	K (A/mm)
0	0.055	0.019	0	–3.2
0.008	0.055	0.021	0.004	–3.2
0.013	0.055	0.029	0.006	–3.2

gain remains constant in the frequency range of 10~35 Hz. The gain drops when the frequency is higher than 35 Hz. Therefore using this frequency range is recommended.

- The effect of the dynamic response of the power source was observed; both the corner frequency and gain change due to the dynamic properties of the power source were affected as shown in Table 8.5. Both pole frequencies (T_2, T_3) shifted to the left (increase) and the maximum gain also decreased. Therefore the dynamic properties of the power source are an important factor in the design of an arc-sensing system.

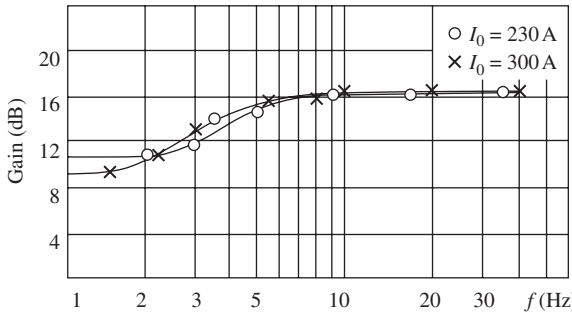

8.30 Effect of I_0 on the magnitude-frequency characteristic of the sensor

8.3.4.4 *Effect of welding conditions on the parameters of the mathematical model and the sensor's sensitivity*

The parameters of the model described by Eq. [8.42] can be expressed as

$$K = \frac{k_a k_r P_0}{k_q P_0 + k_r}, \quad T_1 = \frac{1}{k_r}, \quad T_2 = \frac{1 - k_N P_0}{k_q P_0 - k_r}$$

where $$k_r = k_\eta I_0, \quad k_q = k_i k_c - k_r k_N - k_a k_m, \quad k_N = k_p k_s L_{s0},$$

It can be seen that the static operating point of the arc (I_0,H_0) affects, to a certain extend, the model parameters and the sensor's sensitivity, in which H_0 plays a role via L_{s0}.

The magnitude frequency of the sensing system was experimentally determined for I_0 = 230 A and I_0 = 300 A as shown in Fig. 8.30. It can be seen that I_0 affects the 'zero' frequency but not the 'pole' frequency or the sensitivity. The effect of the static value of H_0 on the sensitivity is shown in Fig. 8.31. The saturation sensitivity decreases as the torch height increases. The reason can be explained as follows:

$$k_{satn} = \underset{s\to\infty}{\text{Lim}} G(s) = \underset{s\to\infty}{\text{Lim}} K \frac{1 + T_1 s}{(1 + T_2 s)} = \frac{T_1}{T_2} \cdot K = \frac{k_a P_0}{1 - (k_p k_s L_{s0}) P_0} \qquad [8.50]$$

Because $p_0 < 0$ in the formula and L_{s0} increases with H_0, consequently the denominator $1 - (K_P K_S L_{s0}) P_0$ increases with H_0, so that k_{satn} decreases with the increase of H_0. The formula also indicates that k_{satn} is independent of I_0.

According to Equations [8.42] and [8.50], the system gain is proportional to the potential gradient k_a, which depends mainly on the shielding-gas composition. Increasing the amount of CO_2 in the gas mixture raises the heat consumption in the arc plasma and thus increases the potential

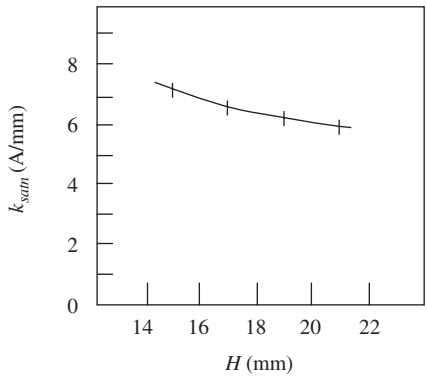

8.31 Effect of H_0 on the sensor's sensitivity

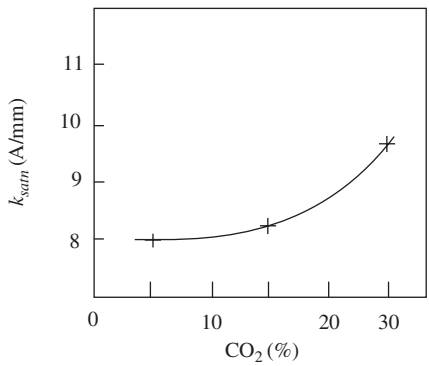

8.32 Effect of gas composition on the sensor's sensitivity

gradient so that the system gain increases. Experimental results shown in Fig. 8.32 prove this finding.

8.3.5 Summary

From the study of the arc sensor's mathematical model, the following conclusions were drawn.

- The mathematical model of the arc sensor depends on the dynamic properties of the power source. The order of the sensor's mathematical model equals the order of the power source's transfer function plus one.

  The number of zeros and poles in the arc sensor's transfer function equals the number of zeros and poles of the power source's transfer function plus one. In the case of a sensitive, transistorised power source,

the mathematical model of the sensor can be expressed by a first-order transfer function, as shown by Eq. [8.42]. When inductance is included in the welding loop, the mathematical model is expressed by a second-order transfer function, as indicated by Eq. [8.48].

- The effect of the static and dynamic properties of the power source, the welding conditions, shielding-gas composition, etc. on the parameters of the mathematical model have been studied. The pole frequency f_2 and the saturation sensitivity increase with the increase of the output-characteristic slope of the power source. The pole frequency f_3 decreases with an increase of the power source's time constant. H_0 and I_0 have a limited effect on the parameters of the model and the sensitivity, but an increase of the CO_2 content in the shielding gas will increase the sensitivity considerably.
- The highest sensitivity is obtained using a scanning frequency of 15~35 Hz, a sensitive power-supply, and a flat power-source output characteristic. In such cases, the sensitivity can reach 10 A/mm.
- The experimental method and apparatus developed by author were suitable. They have been used widely for other investigations of welding power sources and arc-welding processes.

9
Processing of arc-sensor signals

9.1 Introduction

Important features of a properly functioning arc-sensing system are resistance to arc light, high temperature, and intensive magnetic fields. It also is important for the sensor to be readily integrated with the torch and that the output signals are coincident with the time of any event and the position of the torch. Potential weaknesses are poor groove recognition and low resistance to current disturbances. Many researchers around the world have studied this problem. In 1978, the author applied the method of determining the integral difference of current at both sides of groove and clipping of the short-circuit current to increase the sensor's sensitivity.[243] The author and Y. N. Fei first studied the sensor's ability to recognise the groove line by numerical simulation in 1990. Simulation of the input and output relationship was studied in more detail by the author and S. D. Wu in 1997. The author proposed spatial transformation of signals, recognition of the groove line by harmonic vectors, and digital filtering methods. A breakthrough in signal processing was made. The theory and methods of these new techniques are described in this chapter.[260,263–280,379]

9.2 Signal processing of an ideal welding arc

9.2.1 Introduction

To obtain the deviation of a torch from the central line of a groove from the signals generated by a scanning arc is the goal of an arc-sensing system. Therefore, understanding the production and conversion of the signals and the mechanism of detecting torch deviation from these signals is important. It helps to know the character of the signals and to determine an effective signal-processing method for detecting the torch deviation. In this chapter, the practical procedure for signal conversion in the sensing system is discussed first. A numerical-simulation technique based on the mathematical

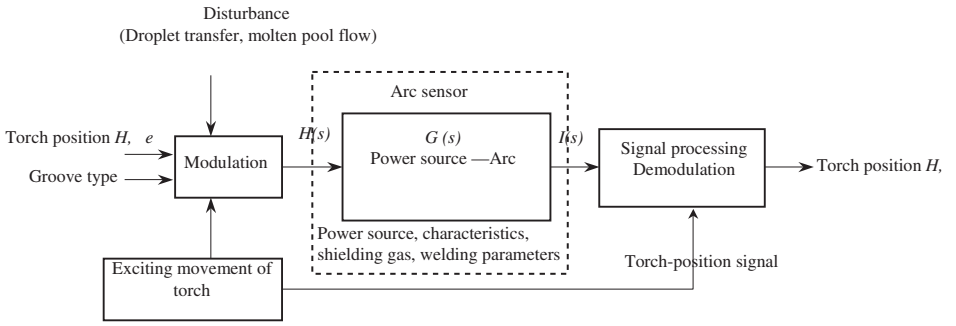

9.1 Principle of detecting torch deviation by an arc-sensing system

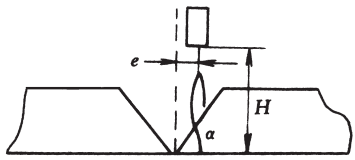

9.2 Schematic diagram of torch position

model of the arc sensor described in Chapter 8 are established next. Finally, the results are analysed.

The procedure for detecting the groove line using an arc-sensing system can be divided into three steps, which are shown in Fig. 9.1.

9.2.1.1 Modulation of signals

The relative position of the torch can be expressed by two parameters, namely, the torch height H and its deviation from the central line of the groove e: see Fig. 9.2. In order to determine e, scanning or rotating the torch across the groove is necessary. From the viewpoint of signal processing, the parameters H and e are regarded as modulated by the scanning or rotating of the torch to produce the torch-height variation $h(t)$. Because the volume of a rotating torch is more compact and has a higher frequency than a scanning torch, the study of signal processing is based on the modulation of $h(t)$ by rotation in the following paragraphs.

9.2.1.2 Signal conversion

After the torch position parameters H and e are modulated into a function of $h(t)$, this function is converted via the power source – arc system into a function of current $i(t)$. If the conversion function of the power source –

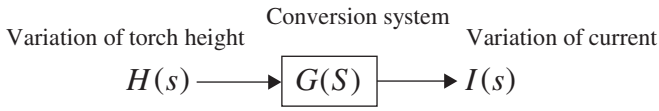

9.3 Block diagram of signal conversion

arc system is written as $G(s)$, then the process of signal conversion can be expressed as shown in Fig. 9.3.

9.2.1.3 Signal processing

In the process of signal conversion, interference will inevitably be introduced by various kinds of noise and disturbances including the following items:

(i) Droplet transfer, (ii) molten-metal flow in the pool that alters the shape of the groove, and (iii) an unstable arc and unstable wire-feed rate. All of these factors are incorporated into the torch-variation signal $h(t)$. The conversion function $G(s)$ is inherent to the system; it transforms $h(t)$ into $i(t)$. In order to determine e by demodulation of $i(t)$, filtering is necessary to eliminate noise. Then an effective signal-processing method should be used to determine e. The study of the method for accomplishing this is the most important problem for developing an effective arc-sensing system.

9.2.2 Mathematical model for numerical simulation

9.2.2.1 Introduction

The signal-processing method used at the present time is based on time domain. Using an actual welding process to study the problem introduces several difficulties:

- The parameters involved in the welding process, such as the power-source characteristics, welding parameters, scanning frequency and range, and groove shape, all fluctuate during sensing and disturb the analysis of the sensor's parameters.
- Melting of the groove surface and molten-metal flow alter the mathematical function of the modulated signal $H(s)$.
- Too many experiments are needed to determine the mathematical function (rule) of the signal conversion.

Therefore, the fastest, simplest and most direct way to study the effect of various factors on the mathematical function of the arc sensor's signal con-

version is the numerical-simulation method, which is helpful for both theoretical study and the analyses of experimental results.

9.2.2.2 *Determination of the coefficients of the sensor's model*

The first step for analysing the sensing system is to establish the mathematical model. The model was established using control theory and experimental methods, as described in Chapter 8. The following discussion is based on this model.

The character of the model can be summarised as follows: the order of the mathematical model depends on the order of power source $P(s) = U(s)/I(s)$. For a highly dynamic (responsive) power source (for example, a transistorised power source), its dynamic characteristics can be regarded as a proportional element, or $P(s) = I(s)/U(s) = P_0$. The transfer function of the sensor can be simplified (see Chapter 8) as

$$G(s) = \frac{I(s)}{U(s)} = K\frac{1+T_1 s}{(1+T_2 s)} \qquad [9.1]$$

It has one pole and one zero; this is called a first-order model of the arc sensor.

Frequently, when there is inductance in the welding loop, the power source can be regarded as a first-order inertial element, $P(s) = P_0/(1 + T_p s)$. The mathematical model of the arc sensor is second order; there are two poles and one zero. The transfer function $G(s)$, which converts torch height $H(s)$ to current $I(s)$, can be expressed as follows:

$$G(s) = \frac{I(s)}{H(s)} = K\frac{1+T_1 s}{(1+T_2 s)(1+T_3 s)} \qquad [9.2]$$

where K is the gain of the system in the static state, which depends on the output characteristic of power source $k_d (k_d = \Delta U/\Delta I)$, the welding materials, shielding gas composition, and welding parameters. The parameters in Equations [9.1] and [9.2] can be experimentally determined as described in the last chapter, i.e. by exciting the torch-height movement using a sine wave and measuring the magnitude and phase angle of the current.

The experiments were conducted as described in Section 8.3.3 of Chapter 8. A transistorised power source was used for the first-order model and an inductance of 20 mH was connected in series with the power source for the second-order model. The Bode diagrams then were plotted to fit them with Equations [9.1] and [9.2]. For the first order model, the coefficients are $T_1 = 0.09\,s$, $T_2 = 0.021\,s$, and for the second order model the coefficients are $T_1 = 0.09\,s$, $T_2 = 0.019\,s$, $T_3 = 0.0045\,s$.

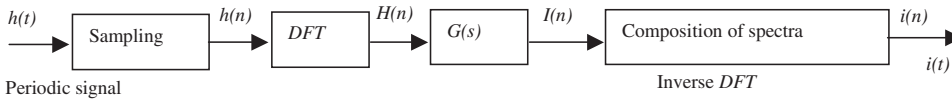

9.4 Schematic diagram of signal conversion in the digital mode

9.2.2.3 Numerical simulation equations

Theoretically the current output $i(t)$ of the arc sensor can be obtained by the equation $I(s) = G(s)H(s)$, and the inverse transformation of $I(s)$. However, because the function $h(t)$ is not a continuous function, applying a Laplace transformation is not possible so that a solution cannot be derived analytically.

Obviously the input signal $h(t)$ is a periodic function and the output of the arc sensor also is a periodic function if the conversion is via a linear function. Therefore, it would be more convenient to solve the problem in frequency domain rather than in time domain. Specifically, the input signal $h(t)$ can be expressed by a Fourier series and a few of its initial terms can be used as an approximation. The value of each term is obtained and summed to determine the approximate solution of the sensor's output. The error of the solution depends on the number of terms taken for the approximation; the solution becomes more accurate as the number of terms increases. For convenience of numerical simulation, the input signal is converted into digital information by DFT (Digital Fourier Transform) and the output digital signal is processed by Inverse Digital Fourier transform (Inverse DFT) to restore it to analogue information. In the following analysis, 256 discrete signals were taken for one cycle of the input and output, and 128 terms of the Fourier series were used for the approximation. The process is shown in Fig. 9.4.

The input signal $h(t)$ is determined by the groove shape and torch deviation. To simplify the analysis, it was assumed that the groove kept its shape during the scanning of the arc without molten metal and the arc axis was always coincident with the torch centreline. In the following paragraphs, three typical groove types are analysed, namely single V-groove, I-butt joint, and a lap joint (see Fig. 9.5). In this figure, the groove and rotating arc, together with the physical meaning of all of the symbols used in the following text, are illustrated.

Assume that the arc rotates with radius r and period T. At the starting moment $t = 0$, it is at the 3 o'clock position of the circle. The variation of torch height in one period ($-T/2 \le t \le T/2$) under the condition that the deviation of the arc from the groove central line is e ($-r \le e \le r$) can be expressed by the following equations:

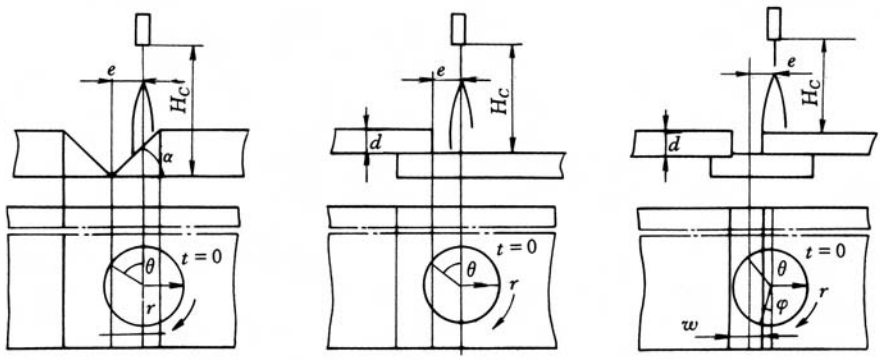

a) V-groove b) Lap joint c) I-butt joint

9.5 Schematic diagram of rotating arc in the groove

For a single V-groove joint, T-joint, or corner joint,

$$h(t) = H_C - |\cos\omega_t + \sin\theta| r \cdot \tan\alpha$$

$$= \begin{cases} H_C - (\cos\omega t + \sin\theta) r \cdot \tan\alpha & |t| \le \dfrac{T}{4} + \dfrac{\theta}{\omega} \\ H_C + (\cos\omega t + \sin\theta) r \cdot \tan\alpha & \dfrac{T}{2} \ge |t| > \dfrac{T}{4} + \dfrac{\theta}{\omega} \end{cases} \quad [9.3]$$

where $\theta = \arcsin(e/r)$, $-\pi/2 \le \theta \le \pi/2$, $\omega = 2\pi/T$, H_c, r, a are constant.
For a lap joint

$$h(t) = \begin{cases} H_C & |t| < \dfrac{T}{4} + \dfrac{\theta}{\omega} \\ H_C - d & \dfrac{T}{4} + \dfrac{\theta}{\omega} \le |t| < \dfrac{T}{2} \end{cases} \quad [9.4]$$

For an I-butt joint

$$h(t) = \begin{cases} H_C & \dfrac{T}{4} + \dfrac{\varphi}{\omega} < |t| < \dfrac{T}{4} + \dfrac{\theta}{\omega} \\ H_C - d & |t| \le \dfrac{T}{4} + \dfrac{\varphi}{\omega} \\ H_C - d & \dfrac{T}{4} + \dfrac{\theta}{\omega} \le |t| \le \dfrac{T}{2} \end{cases} \quad [9.5]$$

The simulation procedure was as follows. The input signal $h(t)$ was converted into an N ($N = 256$) discrete data series (see Eq. [9.6]), which was processed using a discrete Fourier transform (DFT) and converted via the sensor's function $G(s)$ so that the discrete data series $I(n)$ was obtained. Summing up the data series $I(n)$, the output-current data $i(n)$ was derived using the inverse DFT (see Fig. 9.4).

$$h(n) = h\left((n+0.5)\frac{T}{64}\right) \qquad (n = 0,1,2,\ldots 255) \qquad [9.6]$$

The sensor's transfer function $G(s)$ can be rewritten in the zero and pole form.

$$G(s) = K\frac{(s-z_0)}{(s-p_0)(s-p_1)} \qquad [9.7]$$

For the angular frequency $j\omega$, the amplitude response is

$$A(\omega) = |G(j\omega)| = K\sqrt{\frac{\omega^2 + z_0^2}{(\omega^2 + p_0^2)(\omega^2 + p_1^2)}} \qquad [9.8]$$

and the phase response is

$$\varphi(\omega) = \arctan\left(\omega/z_0\right) - \arctan\left(\omega/p_0\right) - \arctan\left(\omega/p_1\right) \qquad [9.9]$$

The results can be written in vector form as

$$G(j\omega) = A(\omega)e^{j\varphi(\omega)}$$

For a first-order transfer function, the term p_1 can be neglected.
The flow chart can be illustrated as in Fig. 9.6.

(i) Preset the coefficients of the sensor's transfer function T_0, T_1, and T_2 and the type of groove, e.g. V-groove, lap joint, or I-butt, and the deviation e.
(ii) Derive the function $h(t)$ according to Equations [9.3], [9.4], and [9.5].
(iii) Formulate 256 data discrete values of $h(t)$ according to Eq. [9.6].
(iv) Apply DFT to the input signal and take the initial 128 harmonics.
(v) Calculate all 128 harmonics of the output of the sensor's element according to Equations [9.8], and [9.9].
(vi) Derive 256 discrete data values of $i(t)$ by using the inverse DFT of the results obtained from step 5. The analytical value also can be obtained directly from step 5.

9.2.3 Results and analysis

Using the model described above, the torch-height variation $h(t)$ and output current $i(t)$ for three groove types, two types of power sources, different rotation frequencies, and different magnitudes of arc deviation were numerically calculated.

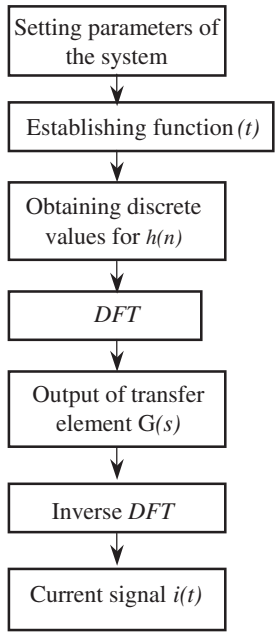

9.6 Flow chart of numerical simulation

9.2.3.1 Output signal

Figures 9.7a to 9.12a show the variation of the torch height; drawings b and c of these figures are the output of the sensor for two different sensing models.

The following observations are made first on the first-order transfer function, and are depicted in Figures 9.7b to 9.12b showing the output current variation for different scanning frequencies, different groove types, and different arc deviations.

(i) The sensing system had a differential effect; it distorted the input signal and the output-current phase led the input torch-height variation. This was particularly apparent for low-frequency scanning (see the solid line). The maximum current value appeared to lead the torch-height variation.

(ii) Due to the differential effect, a current peak appeared. Because the current waveform was distorted, the symmetry was lost even for a V-groove without arc deviation.

(iii) The change of the current waveform depended not only on the magnitude of the pole and zero of the transfer function but also on the scanning frequency.

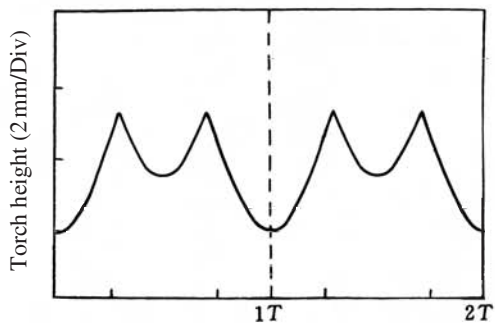

a) Variation of torch height

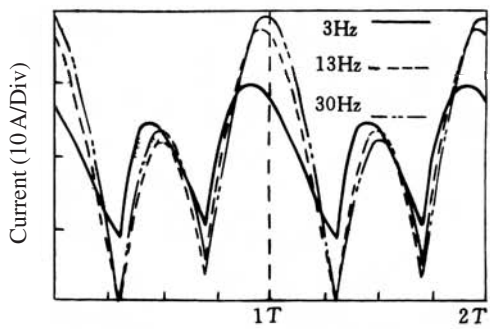

b) Current waveform for a first-order system

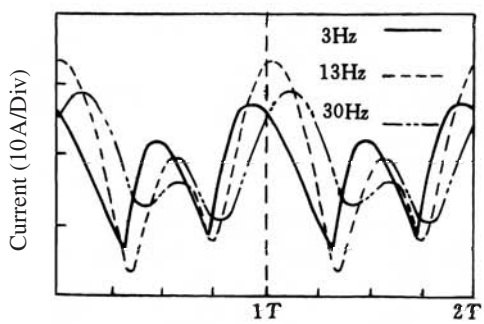

c) Current waveform for a second-order system

9.7 V-groove (corner groove) with deviation

Due to the distortion that resulted from the transfer function, the current waveform was different from the torch-height variation. Therefore, misinformation could be obtained if the deviation of the arc was judged by the current signal. For a first-order system, however, the distortion decreased

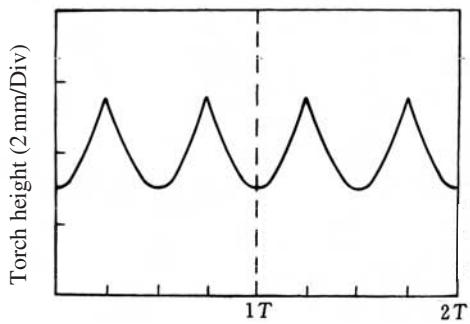

a) Variation of torch height

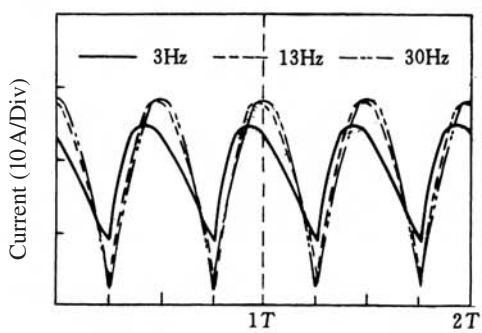

b) Current waveform for a first-order system

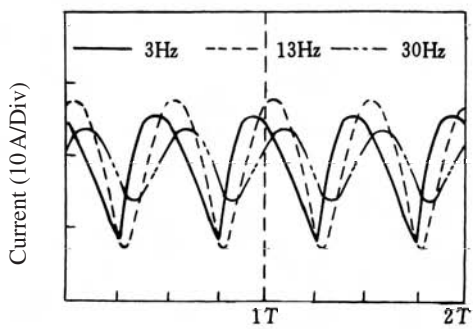

c) Current waveform for a second-order system

9.8 V-groove (corner groove) without deviation

when the scanning frequency was increased. If the rotation frequency was much higher than the zero and pole frequencies, large gain and high sensitivity could be obtained. Should the zero and pole coincide with each other, their effects compensate one another, the phase response would be near

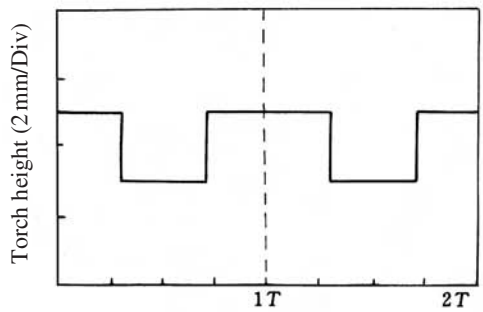

a) Variation of torch height

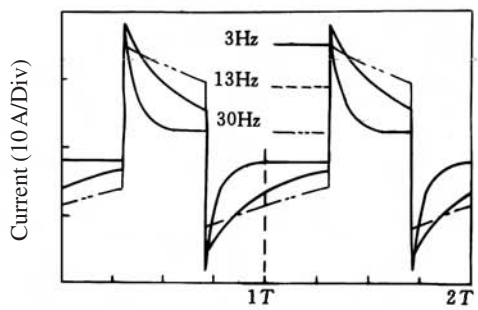

b) Current waveform for a first-order system

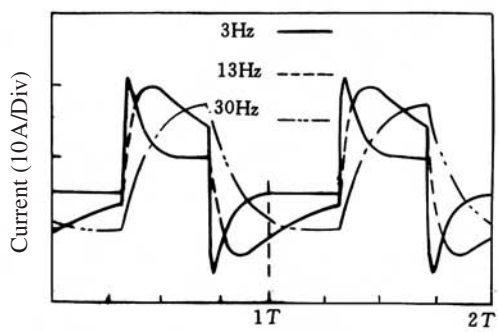

c) Current waveform for a second-order system

9.9 Lap joint with deviation

180°, and the output signal of the sensor would have no distortion. The scanning frequency for this case depends on the parameters of the sensing system.

Results of analysis of a second-order system are illustrated in Figures 9.7c to 9.12c. The torch-height variation is shown in figure 'a', respectively.

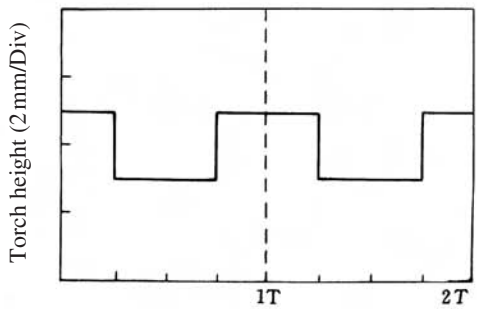

a) Variation of torch height

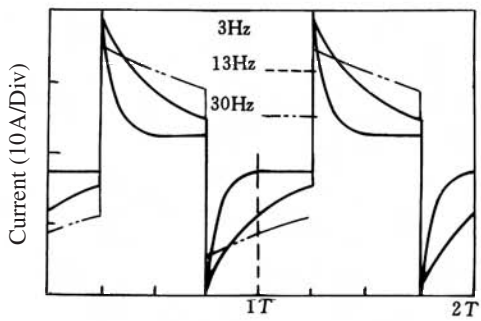

b) Current waveform for a first-order system

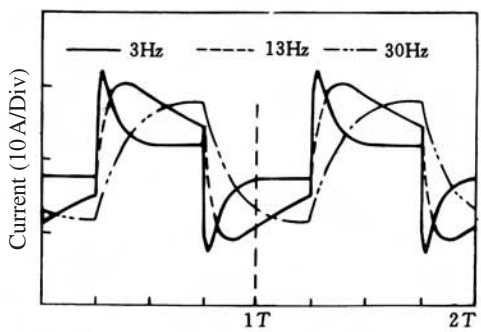

c) Current waveform for a second-order system

9.10 Lap joint without deviation

Comparing these results with the results for a first-order system, it is seen that the effect of a second-order sensing system on current output is much greater than with the former. Concretely, the phenomena may be described as the following four points:

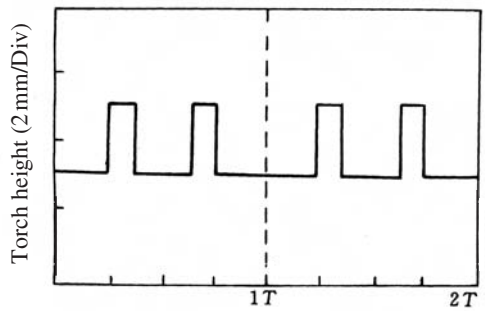

a) Variation of torch height

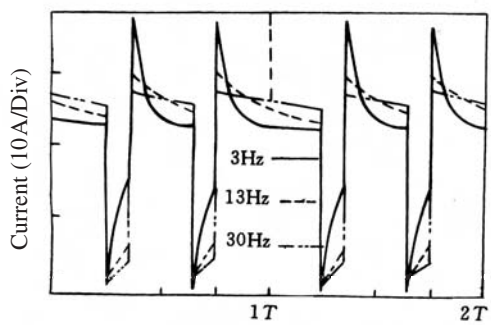

b) Current waveform for a first-order system

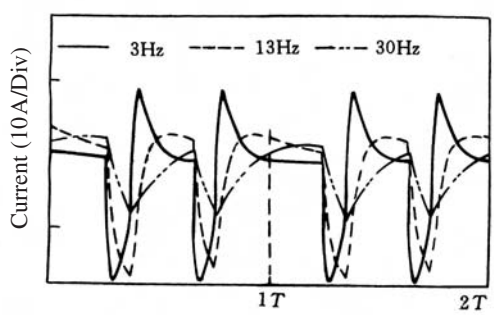

c) Current waveform for a second-order system

9.11 I-butt joint with deviation

(i) Because the frequency response of a second-order system is poorer than that of a first-order system, the gain was decreased and the phase lagged more. The output current waveform was smoother. The sharp angle on the waveform was eliminated and distortion was much greater.

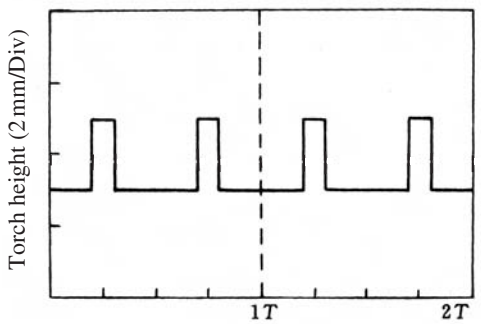

a) Variation of torch height

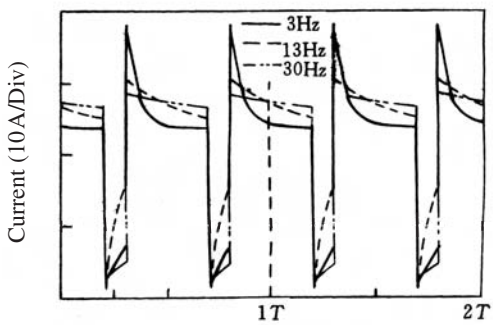

b) Current waveform for a first-order system

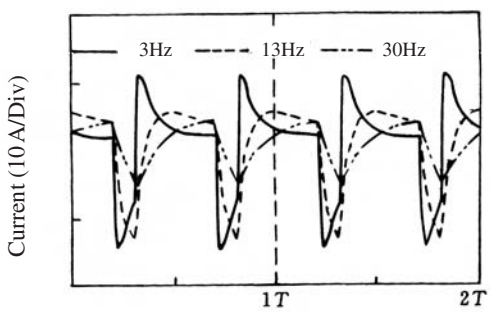

c) Current waveform for a second-order system

9.12 I-butt joint without deviation

(ii) At a low scanning frequency, the system presented a differential effect similar to that shown by a first-order system (see the solid line in the figure).

(iii) With an increase of frequency, the output current lagged more. There was greater loss of high and middle-frequency harmonics. The system

behaved like a low-pass filter and significant distortion can be seen (the dot-dash line in the figure). For the V-groove it appeared like a low-frequency sinusoidal waveform (see Figures 9.7c and 9.8c); for lap joints and I-butt joints the waveform had a saw-tooth shape (see Figures 9.7c to 9.12c). The waveform was quite different from a square waveform.

(iv) The phase-angle change was complicated. For the same system, a different scanning frequency can cause leading or lagging of the phase. The phase-angle change can reach 45° for the fundamental frequency at 3 Hz to 30 Hz. The phase change should be determined for specific cases. Predicting the current signal of the arc from the rule of torch-height variation is difficult.

Normally the most representative arc sensing system is second-order; therefore, phase shift is inevitable in the signal conversion.

The analyses described above were based on an ideal groove shape; the phenomena are much more complicated if the groove surface melts and the influence of molten metal is considered.

9.2.3.2 Analysis of results

The variation of torch height is modulated by scanning frequency; it consists of a series of harmonics. The harmonics of the modulated signal ($H(s)$) depend on the groove shape and the torch deviation. The response of the sensing element $G(s)$ to the input signal is different for different harmonics. Both the magnitude and phase angle of the harmonics are changed by the transfer (conversion) function depending on the zero and pole of the function.

In actual welding, the coefficients of the transfer function can be varied along with the scanning frequency. Therefore, judging the deviation of the arc from the output signal of the sensing system in time domain by the magnitude and phase angle of the signal is not reasonable.

9.2.3.3 Integral difference method and its limitation

As described in Section 7.3.1 and 7.3.2 of Chapter 7, the author successfully developed automatic seam tracking in 1978. The method is applied at present in most arc sensing systems used in industry. The current signal is integrated for a short duration when the arc reaches the right side and left side of the groove. Then the difference between these integrals is used as the indication of arc deviation and the sum of these integrals is used as the

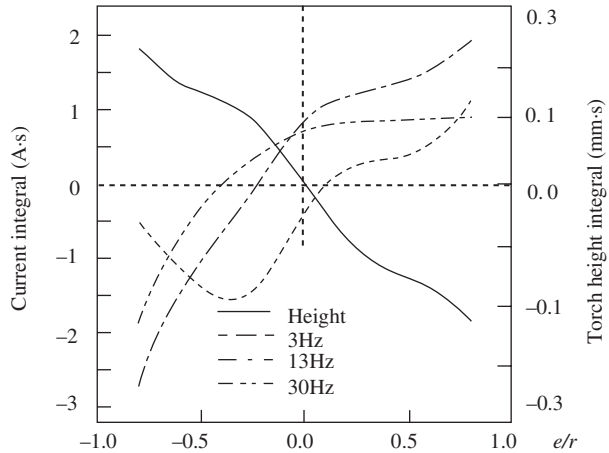

9.13 Integral difference of current and height for a second-order system – I-butt

indication of torch height. The basic idea of this method is to avoid the interference caused by noise in the arc current; integrating the current eliminates the effect of accidental current peaks that might be sampled. In order to investigate the validity of this method, the integral difference of current at the right and left sides of the groove was calculated by the numerical method for different groove shapes and different torch deviations, using the results obtained in Section 9.2.3.1. The data that were obtained are plotted in Figures 9.13 to 9.15.

The equations used for these calculations are as follows:

For the integral difference of current variation

$$\Delta I = \int_0^{T/4} i(t)d(t) - \int_{T/4}^{T/2} i(t)d(t) = \sum_{n=0}^{\frac{N}{4}-1} \left(I(n) - I\left(n + \frac{N}{4}\right)\right)\frac{T}{N} \qquad [9.10]$$

For the integral difference of torch-height variation

$$\Delta H = \int_0^{T/4} h(t)d(t) - \int_{T/4}^{T/2} h(t)d(t) = \sum_{n=0}^{\frac{N}{4}-1} \left(H(n) - H\left(n + \frac{N}{4}\right)\right)\frac{T}{N} \qquad [9.11]$$

In Equations [9.10] and [9.11], T represents the period of the scanning and N represents the number of samples in one period.

The results demonstrated that, in most cases, the integral difference did not represent the actual deviation of the torch except in the case of a first-

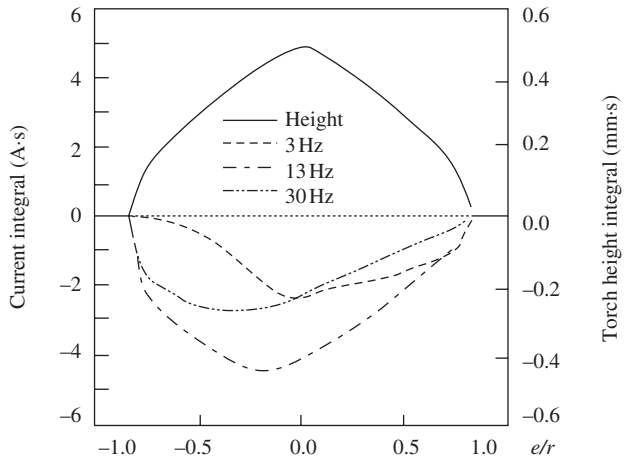

9.14 Integral difference of current and height for a second-order system – Lap joint

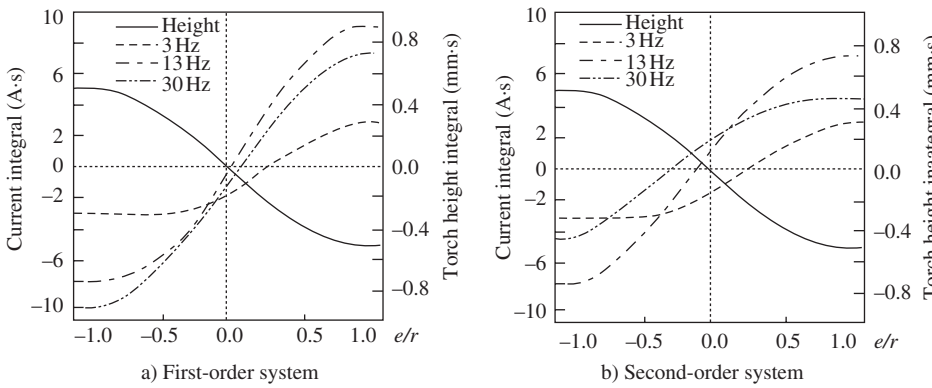

9.15 Integral difference of current and torch height for a V or corner groove

order system with a high scanning frequency. Due to the transfer function, the integral difference method showed a large error. Taking the second-order system as an example, the calculated integral difference for a V-groove can be near to the actual deviation (see Fig. 9.15b, 13 Hz) only when the scanning frequency is in the proper range. It does not reflect the actual deviation when the scanning frequency is higher or lower. In such cases, incorrect information about the deviation may be obtained if an improper scanning frequency is selected.

For an I-butt groove (Fig. 9.13), due to the distortion of the signal in the conversion process, the results at low frequency lost their monotonic character and those at high frequency had considerable inherent error. The calculated values for a lap joint did not represent the actual deviation at all (Fig. 9.14); they were not monotonic and could not be used for seam tracking.

It is necessary to point out that the analysis above was based on an ideal groove shape and welding occurring without various kinds of disturbances. The analyses of actual welding processes is much more complicated than the theoretical analysis so it is hard to apply the integral-difference method for seam-tracking control. A new concept and theory are needed for developing a suitable signal-processing method.

9.3 Analysis of signal characteristics

The aim of signal-characteristic analysis is to find some characteristic value that can be used for designing the sensor's parameters and processing the signals from the sensor so that closed-loop feedback control of seam tracking can be realised.

9.3.1 Introduction

Arc-sensing systems were first studied by welding scientists in the time domain, i.e. the variation of (U, I) with time. The studies were direct, easy to understand, and acceptable to technologists. However, due to the distortion of signals by transfer elements, determining the deviation of the arc directly by current-time signals was difficult and unreliable. In fact, the groove shape has fixed parameters; it is not a function of time but becomes a function of time by the scanning operation having excitation. Therefore, to study the deviation in time domain is an indirect method, which may complicate the problem. A better way is to transform the signal in time domain into a function in another domain that can be directly related to the deviation.[262,263]

Theoretical study[261] demonstrated that if orthogonal linear space were chosen as the transformation space, the transformation error was least and the solution of the problem would be easiest. The choice of space form depends on the variation rule of the object studied. For periodic functions or periodic digital data, there are different space forms that can be used. The space form that can satisfy the study of an arc-sensing signal should be determined so that it can be used for the mathematical solution of the problem.

9.3.2 Space transform

9.3.2.1 Choice of space form

There is a lot of distortion and noise in the signal from an arc sensor. Filtering can be used but it is still a complicated function of time and is difficult to express by an analytical function. This is the reason why an ideal input function representing the torch-height variation was used for study in the sections above. This was done, even though the current output of the sensor was quite different from the torch-height variation rule because of the transfer function of the system $G(s)$. The detected signal from the arc sensor in time domain was the result of the convolution of the transfer function to the variation of the torch height.

Based on the linearity of the mathematical model, the following condition must be satisfied in the choice of a space transform, namely, the character component in the space keeps its orthogonal property after the signal transfer by the sensor so that the character component can be operated on during processing of the response signal $i(t)$. Otherwise there would of no reason to use a space transform and serious error would be introduced. For example, the integral-difference method can be regarded as a square-wave transform of the Walsh method. After the sensor's transfer, it does not maintain the square waveform and cannot be operated on. That is why it introduces error (see Section 9.2.3).

A trigonometric sine transform was first proposed be the author and S. D. Wu in 1996, because among all of the transform methods used for periodic signals, such as Fourier, slant (ST), Walsh, Legendre, and digital cosine transforms (DCT), only the Fourier transform can satisfy the requirement. Moreover, it has explicit physical meaning.

9.3.2.2 Fourier transform

Suppose that $f(x)$ is a periodic integrable function with 2π as its period; then it can be expressed by a trigonometric polynomial as an optimum square approximation.

$$S_n(x) = \frac{1}{2}a_0 + a_1\cos x + b_1\sin x + \ldots a_n\cos nx + b_n\sin nx \qquad [9.12]$$

Because the trigonometric-function family $\{\cos x, \sin x \ldots, \cos kx, \sin kx, \ldots\}$ are orthogonal function groups in $[0, 2\pi]$, the coefficients of the polynomial $S_n(x)$ can be obtained as

$$a_K = \frac{1}{\pi}\int_0^{2\pi} f(x)\cos kx dx \quad (k = 0, 1, \ldots, n)$$

$$b_K = \frac{1}{\pi}\int_0^{2\pi} f(x)\sin kx dx \quad (k = 1, \ldots, n) \qquad [9.13]$$

where a_k, b_k are coefficients of the Fourier series, $S_n(x)$ is the Fourier formula of $f(x)$.

If the value of the function $f(x)$ is known in its discrete set form $\left\{x_1 = \frac{2\pi}{N} j, j = 0, 1, \ldots, N-1\right\}$, then the set is an orthogonal system and discrete Fourier function coefficients can be obtained. For a general case, suppose that $f(x)$ is a function of a complex variable with 2π as its period; then its values at equally divided N points are $f_1 = f\left(\frac{2\pi}{N} j\right)$, $j = 0, 1, \ldots, N-1$.

As $e^{ijx} = \cos(jx) + i\sin(jx)$ $(j = 0, 1, \ldots, N-1)$, it can be proved that the function family $\{1, e^{jx}, \ldots, e^{j(N-1)x}\}$ is orthogonal at the discrete point set $x_k = \frac{2\pi}{N} k, (k = 0, 1, \ldots, N-1)$. Thus, the least-square Fourier function of $f(x)$ at the N discrete set $\left\{x_i = \frac{2\pi}{N} j, j = 0, 1, \ldots, N-1\right\}$ is:

$$S(x) = \sum_{k=0}^{n-1} C_k e^{jkx}, \quad n \le N \qquad [9.14]$$

where

$$C_k = \frac{1}{N}\sum_{j=0}^{N-1} f_i e^{-jkx\frac{2\pi}{N}}, \quad (k = 0, 1, \ldots, N-1) \qquad [9.15]$$

When $n = N$, then $S(x)$ is the interpolation function of $f(x)$ at the point $x_j (j = 0, 1, \ldots\ldots N-1)$, or $S(x_j) = f(x_j)$. Then Eq. [9.14] can be written as

$$f_i = \sum_{k=0}^{N-1} C_k e^{jk\frac{2\pi}{N}j}, \quad (j = 0, 1, \ldots, N-1) \qquad [9.16]$$

Equation [9.15] is the formula to obtain $\{C_k\}$ from $\{f_i\}$, which is called a discrete Fourier transform or abbreviated as DFT. Equation [9.16] is the formula for obtaining $\{f_i\}$ from $\{C_k\}$, which is called an inverse transform. For $N = 2^m$, there is a rapid calculation method called a fast Fourier transform (FFT).

9.3.3 Characteristic of input signal

As pointed out previously, analysis of the signal characteristic starts with the input signal, or more specifically, starts from the torch-height variation

$h(t)$. Due to different dimensions and shapes of grooves, input signals are greatly different from one another. This is obvious in time domain. In frequency domain, however, the possibility of identifying the torch-deviation signal is of interest. Studying these problems is important for clarifying whether it is feasible to apply the frequency-domain method to practical welding processes.

To establish the characteristic vector of the signals, the torch-height variation for three typical and ideal grooves is analysed.

The schematic diagrams of the scanning arc above the groove are shown in Fig. 9.5 with the scanning period T and rotating radius r. All of the symbols and their physical meanings related to the analysis are indicated in the figure. For explicitness, the torch-height variation functions are rewritten as follows. For Fig. 9.5a.

$$H(t,\theta) = H_c - |\cos\omega t + \sin\theta| r \cdot \tan\alpha$$

$$= \begin{cases} H_c - (\cos\omega t + \sin\theta) r \cdot \tan\alpha & |t| \le \dfrac{T}{4} + \dfrac{\theta}{\omega} \\ H_c + (\cos\omega t + \sin\theta) r \cdot \tan\alpha & \dfrac{T}{2} \ge |t| > \dfrac{T}{4} + \dfrac{\theta}{\omega} \end{cases} \quad [9.17]$$

where $\theta = \arcsin(e/r)$, $-\pi/2 \le \theta \le \pi/2$, $\omega = 2\pi/T$, H_c, r, α are constants. The periodic function $H(t, \theta)$ can be written in trigonometric form as

$$H(t,\theta) = \frac{a_0}{2} + a_k \cos k\omega t + b_k \sin k\omega t \quad (k = 1, 2, \ldots) \quad [9.18]$$

Because $a_k = \dfrac{2}{T}\int_0^T H(t,\theta)\cos k\omega t.dt$,

one can obtain $a_0 = \dfrac{2\theta}{\pi}\sin\theta + \dfrac{2}{\pi}\cos\theta, \quad a_1 = \dfrac{2\theta + \sin 2\theta}{\pi}$

$$a_k = \frac{2\sin\left(\dfrac{k-1}{2}\pi + (k-1)\theta\right)}{(k-1)\pi} + \frac{4\sin\theta\sin\left(\dfrac{k}{2}\pi + k\theta\right)}{k\pi} + \frac{2\sin\left(\dfrac{k+1}{2}\pi + (k+1)\theta\right)}{(k+1)\pi} \quad (k = 2, 3, \ldots) \quad [9.19]$$

Because $H(t, \theta)$ is an even function, so $b_k(\theta) = 0$ $(k = 1, 2, \ldots)$.

Similarly, for a lap joint (Fig. 9.5b), the torch-height variation is

$$H(t,\theta) = \begin{cases} Hc & |t| \le \dfrac{T}{4} + \dfrac{\theta}{\omega} \\ Hc - d & \dfrac{1}{2}T \ge \dfrac{T}{4} + \dfrac{\theta}{\omega} \end{cases} \quad [9.20]$$

$$H(t,\theta) = Hc + \left(\frac{\theta}{\pi} - \frac{1}{2}\right)d + a_n \cos n\omega t \qquad [9.21]$$

The following can be derived.

$$a_n = \frac{2d}{n\pi}\sin\left(\frac{n}{2}\pi + n\theta\right) \qquad [9.22]$$

In the case of an I-butt joint, the derivation is more complicated; the torch-height variation is

$$H(t,\theta) = \begin{cases} Hc & \frac{T}{4} + \frac{\varphi}{\omega} < |t| \le \frac{T}{4} + \frac{\theta}{\omega} \\ Hc - d & |t| \le \frac{T}{4} + \frac{\varphi}{\omega} \\ Hc - d & \frac{T}{4} + \frac{\theta}{\omega} \le |t| \le \frac{T}{2} \end{cases} \qquad [9.23]$$

Because the torch-height varies over the full range of $|e|$, the Fourier series equation is given in the following text only for $|e| \le |r - 0.5w|$. In cases when the deviation is greater than this range, the formula can be derived with reference to a lap joint (for the variation, see Fig. 9.16).

$$H(t,\theta) = Hc + \left(1 - \frac{\theta - \varphi}{\pi}\right)d + a_n \cos n\omega t \quad (-(r - 0.5w) \le e \le r - 0.5w) \qquad [9.24]$$

$$a_n = \frac{2d}{n\pi}\left[\sin\left(\frac{n}{2}\pi + n\theta\right) - \sin\left(\frac{n}{2}\pi + n\varphi\right)\right] \qquad [9.25]$$

$$\theta = \arcsin\left(\frac{2e + w}{2r}\right), \quad \varphi = \arcsin\left(\frac{2e - w}{2r}\right)$$

It is seen from the formulae above that $\theta = \arcsin(e/r)$, and that the harmonic magnitude a_n is a function of θ; consequently a_n also is a function of e. The relationship between the harmonic magnitude for different frequencies and the deviation e is given in Fig. 9.16 (only the magnitude of several low-frequency harmonics are given; those of the high-frequency harmonics are not given because they are of no significance to recognising the deviation). The figures show that for a V-groove or corner groove, the vector magnitude of the first and third harmonics varies according to the same rule as the deviation e (a_1 varies from positive to negative, a_3 varies from negative to positive); see Fig. 9.16a. For a lap joint, the vector magnitudes of the first and third harmonics do not reflect the deviation, but that of the second harmonic does; see Fig. 9.16b. In the range $|e| \le \frac{\sqrt{2}}{2}r$, a_1 has a

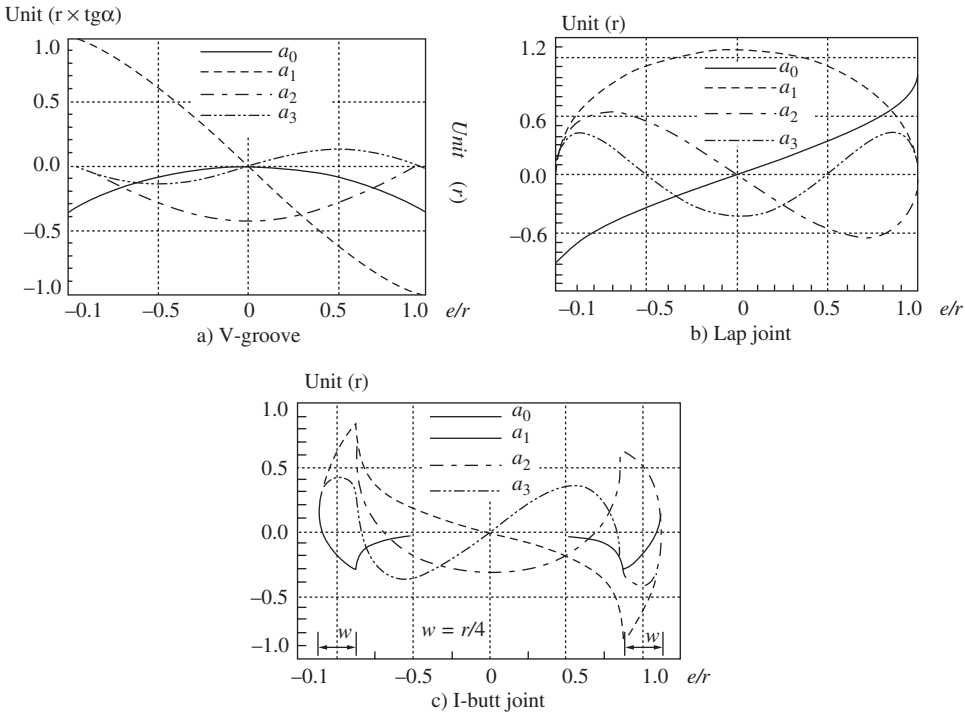

9.16 Relationship of harmonic magnitude to arc deviation

linear relationship with e. For butt joints, the rule is similar to that of a V-groove; see Fig. 9.16c. It is necessary to point out that the starting point for arc scanning is defined at the side half of the scanning circle so the magnitude of the harmonic b_n is zero. The effect of the deviation on the average torch height a_0 is also shown in Fig. 9.16.

Therefore it can be considered that the first-order harmonic of the input signal is the characteristic harmonic for a V-groove; its magnitude and phase angle are

$$a_T = a_1 = \frac{2\theta + \sin 2\theta}{\pi} \quad \theta = \arcsin\left(\frac{e}{r}\right) \qquad [9.26]$$

The second-order harmonic is the characteristic harmonic for a lap joint; its magnitude and phase angle are

$$a_T = a_2 = \frac{2r}{\pi}\sin(\pi + 2\theta) \quad \theta = \arcsin\left(\frac{e}{r}\right) \qquad [9.27]$$

For an I-butt joint, the first-order harmonic reflects the deviation. The third-order harmonic also shows an obvious effect for a small deviation,

which can be used for reference. The magnitude of the characteristic harmonic is closely related to the gap width w.

When $|e| \leq |r - 0.5w|$,

$$a_T = a_1 = \frac{4r}{\pi}\left[\sin\left(\frac{1}{2}\pi + \theta\right) - \sin\left(\frac{1}{2}\pi + \varphi\right)\right]$$

$$a_3 = \frac{4r}{3\pi}\left[\sin\left(\frac{3}{2}\pi + 3\theta\right) - \sin\left(\frac{3}{2}\pi + 3\varphi\right)\right]$$

$$\theta = \arcsin\left(\frac{2e + w}{2r}\right) \quad \varphi = \arcsin\left(\frac{2e - w}{2r}\right) \qquad [9.28]$$

If the characteristic harmonic is expressed in vector form as H_T according to Eq. [9.14], then

$$H_T = a_e e^{j\theta_i} \qquad [9.29]$$

Because $b_n = 0$, then $a_e = a_T$, $\theta_i = 0°$.

It can be seen from the description above that when the groove type is known, the arc deviation can be represented by the characteristic harmonic; the harmonics at higher frequencies are small and can be neglected. Among the low-frequency harmonics, only the characteristic harmonic is significant for recognition of the deviation. For the characteristic harmonic, there are two parameters, namely, magnitude and phase angle. The magnitude depends on the sensitivity of the sensing system and the phase angle depends on the phase-frequency characteristics of the system. Therefore, it is only necessary to analyse the characteristic harmonic without consideration of the frequency response of the entire system and vectors of other harmonics. Thus, a lot of labour can be saved and obtaining the solution is easy.

It should be mentioned that, particularly for lap joints, the optimum scanning frequency will not give the optimum gain for the second-order harmonic. In the opposite way, a reduced scanning frequency will give better response of the second-order harmonic. Therefore, for lap joints, a lower scanning frequency is recommended. A lower frequency also can improve the stability of the arc. Because the torch height can vary abruptly as the arc crosses the joint, a larger scanning diameter also is recommended to increase the stability of the arc. Both of these recommendations are important for the application of the sensor.

9.3.4 Detection method by characteristic harmonic

As anticipated at the beginning of this chapter, the characteristic component of the input signal was found. This gives the necessary information regarding the deviation of the arc. As described above, the starting point

for $t = 0$ was arbitrarily chosen for the convenience of analysis. With the proper choice of the starting point, only the cosine components of the Fourier series remained and a simple series function was obtained.

For convenience of discussion, the characteristic harmonic vector is defined as the specific harmonic vector that has an exact phase relation with the input signal and reflects the arc deviation. According to Equations [9.19], [9.22], [9.25], and the characteristic harmonic vector function expressed by Eq. [9.29], the magnitude of the vector is expressed by Equations [9.26], [9.27], and [9.28]. The phase angle is 0°.

As discussed previously, the sensing system can be simplified into a linear system, viz. $I(s) = G(s)H(s)$.

According to the superposition principle of linear systems, the output signal of the sensor is the sum of the responses of all of the individual harmonic components of the input signal. In other words, the output signal is determined only by the variation of the torch height. Therefore, the harmonic vector of the output-current signal has the same relation with the deviation e, which can be determined for seam tracking. The harmonic that reflects the arc deviation is defined now as the characteristic harmonic and subsequently defines the way to detect the arc deviation as the detection method using a characteristic harmonic. No matter how the dimensions of the groove change the deviation of the arc will be reflected only by this harmonic. Therefore, detecting this harmonic is necessary for obtaining e. In this way, any kind of interference other than this harmonic can be avoided and a high signal-to-noise ratio can be obtained.

The method may be summarised briefly as follows.

- The arc deviation can be detected by two parameters, namely, the magnitude and phase angle of the characteristic harmonic (or abbreviated as a characteristic vector).
- Because the phase angle of the harmonic will be changed by the transfer element, so the phase angle should be detectable for compensation.
- The deviation also can be detected directly by the response of the characteristic vector. It is known from the theoretical analysis of Section 9.3.3 that the deviation is determined only by the characteristic harmonic.

The method may be expressed more explicitly, i.e. the magnitude of the arc deviation is proportional to the magnitude of the characteristic harmonic and the direction of the deviation is judged by the phase angle of the harmonic; theoretically it is either $\theta_i = 0°$ or $\theta_i = 180°$, which means the output-vector magnitude is the negative of the input vector magnitude. However, the phase angle would not be exactly 0 or 180° for the following reasons:

(i) The phase angle changes due to the transfer function $G(s)$ and the magnitude of the phase-angle change, θ_s, depends on the harmonic frequency.

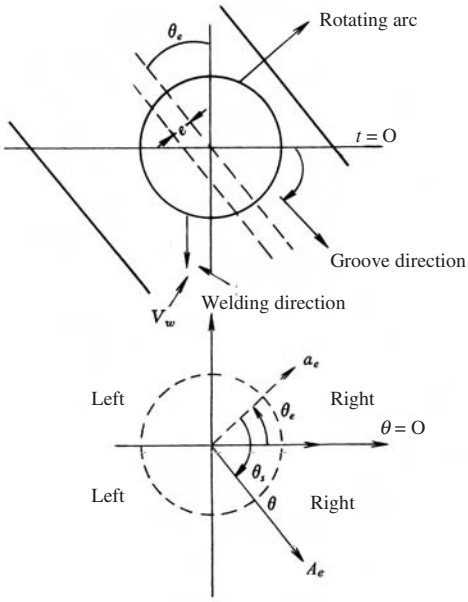

a) Phase-angle change when the groove line is inclined

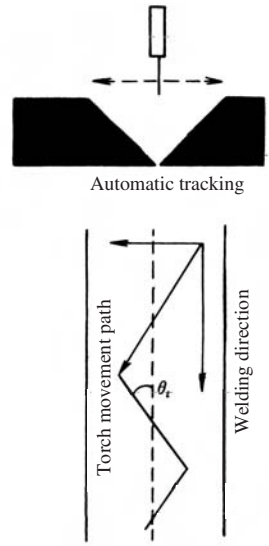

b) Phase-angle change during automatic tracking

9.17 Phase-angle change of the input signal

(ii) In the case when the welding direction does not coincide with the groove centreline, the angle between them θ_e changes the input signal $H(s)$. Thus the phase angle of the characteristic harmonic θ_I is no longer 0, but is θ_e: see Fig. 9.17a.

(iii) Because the regulation is automatic, the tracking path of the torch is composed of two parts, namely, the welding direction and the direction of the regulation: see Fig. 9.17b. The angle between the groove centreline and the path of the torch movement is $\theta_i = \theta_t$.

Therefore the initial phase angle of the characteristic harmonic is θ_i but not 0.

It is obvious that only the torch-deviation angle θ_e or the regulation angle θ_t can operate in a practical case. Assuming that the phase change due to the transfer function is θ_s, then the phase angle of the output harmonic will be

$$\theta_0 = \theta_s + \theta_i = \theta_s + \theta_e$$

in open-loop control and

$$\theta_0 = \theta_s + \theta_i = \theta_s + \theta_t$$

in closed-loop control, which can be represented by Fig. 9.18.

$$a_e \cdot e^{j\theta_t} \rightarrow G(s) \rightarrow A_e \cdot e^{j\theta_0}$$

9.18 Change of the characteristic harmonic vector by the transfer function

Suppose that the deviation is e and the magnitude of the characteristic harmonic is a_e, which becomes A_e after the transfer function. According the theoretical analysis and practical experiments, it can be confirmed that $45° < \theta_s < -45°$, and normally $|\theta_e| < 45°$, and $|\theta_t| < 45°$. Therefore, the final phase angle change would be within ±90°. Thus, it is possible to judge the deviation of the arc without a specific determination of the degree of the phase-angle change. To detect the deviation direction, only a qualitative evaluation of the harmonic phase angle is necessary.

The description given above can be summarised as follows. The deviation of the arc can be determined by the characteristic harmonic vector $A_e \cdot e^{j\theta_0}$; the magnitude A_e indicates the magnitude of the deviation. The direction of the deviation can be judged by θ_0. When $|\theta_0| < 90°$ (or the vector is in the first or fourth quadrant), the deviation is on the right side; see Fig. 9.17a. When $-180° \le \theta_0 \le 180°$ (or the vector is in the second or third quadrant), the deviation is on the left side.

This method solves the difficult problem of signal processing in time domain and is simple and easy to handle.

9.3.5 Adaptability of the method to pulsed-MIG welding

The characteristic-harmonic method was derived for ideal scanning-arc input and transfer function of the sensing system. It is adaptable to spray-transfer MIG welding, which will be proved later by experiment. However, the question arose whether it could be used for arc welding processes in which the current fluctuated violently and substantial noise existed. In this section, pulsed MIG is analysed as an example.

9.3.5.1 Periodic rectangular pulse

Suppose that the period of the pulse is T and the pulse width is τ ($\tau < T$), then the pulse can be expressed by the equation

$$f(t) = \begin{cases} A & |t| < \dfrac{\tau}{2} \\ 0 & \dfrac{\tau}{2} \le |t| \le \dfrac{T}{2} \end{cases} \qquad [9.30]$$

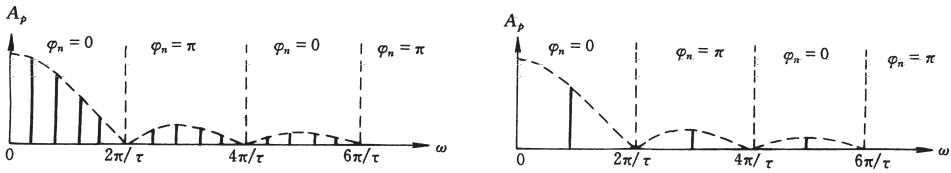

a) $T = 5\tau$ b) $T = 2\tau$

9.19 Frequency spectrum of periodic pulse signal

According to Equations [9.12] and [9.13], the Fourier series of the equation in trigonometric form and vector form can be written as follows.

$$f(t) = \frac{A\tau}{T}\left[1 + 4\sum_{n=1}^{\infty}\frac{\sin(n\omega\tau/2)}{n\omega\tau/2}\cos n\omega t\right] = \frac{A\tau}{T}\sum_{n=-\infty}^{\infty}\frac{\sin(n\omega\tau/2)}{n\omega\tau/2}e^{jn\omega t} \qquad [9.31]$$

The frequency spectrum of the equation can be plotted as in Fig. 9.19. The frequency magnitudes, which depend on the ratio τ/T, are expressed by Eq. [9.32]. The phase angle is either 0 or π, which is indicated in the figure.

$$A_n = \frac{2A\tau}{T}\left|\frac{\sin(n\pi\tau/T)}{n\pi\tau/T}\right| \qquad [9.32]$$

9.3.5.2 *Modulated waveform*

A modulated waveform is obtained by superposing a given signal on the modulated waveform. Suppose that the periodic signal is expressed by $e(t)$.

$$e(t) = E_0 + \sum_{n=1}^{\infty} E_n \cos(\omega_n t + \phi_n) \qquad [9.33]$$

Then the modulated signal can be expressed as

$$\begin{aligned} a(t) &= e(t)\cos(\omega_c t + \varphi_n) \\ &= E_0\cos(\omega_c t + \varphi_0) + \sum_{n=1}^{\infty}\frac{E_n}{2}\cos[(\omega_c + \omega_n)t + \varphi_0 + \phi_n)] \\ &\quad + \sum_{n=1}^{\infty}\frac{E_n}{2}\cos[(\omega_c - \omega_n)t + \varphi_0 - \phi_n)] \end{aligned} \qquad [9.34]$$

where ω_c is the frequency of the carrier and φ_0 is the initial phase angle of the carrier; they are constants.

Using the previous equations, the frequency spectrum of $e(t)$ and $a(t)$ can be plotted as in Fig. 9.20. Comparing Figures 9.20*a* and *b*, it can be found that the frequency spectrum is shifted by ω_c. The component spectral line

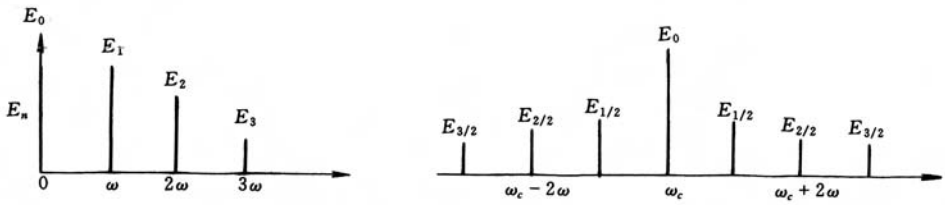

a) Original periodic signal b) Modulated periodic signal

9.20 Frequency spectrum of the original and modulated signals

of the original signal is split into two lines located on the left and right sides of ω_c, but their magnitudes are half of the original. This phenomenon is called the frequency-shift characteristic of the modulated signal. The spectral lines on both sides are called the upper and lower components of the frequency-spectral line.

The rule given above also can be obtained from the frequency-spectrum transformation. Suppose that the frequency spectrum of the function $f_1(t)$ is $F_1(\omega)$, then the frequency-spectrum function of $f(t) = f_1(t)e^{j\omega_c t}$ can be written as

$$F(\omega) = F_1(\omega - \omega_c) \qquad [9.35]$$

which can be expressed symbolically as follow:

If $$f(t) \leftrightarrow F(\omega), \text{ then } f(t)e^{j\omega_c t} \leftrightarrow F(\omega - \omega_c).$$

Because $$\cos\theta = \frac{e^{j\theta} + e^{-j\theta}}{2},$$

therefore $$f(t)\cos\omega_c t \leftrightarrow \frac{1}{2}[F(\omega + \omega_c) + F(\omega - \omega_c)] \qquad [9.36]$$

In a situation in which the carrier signal is not a sine wave but rather a square wave, of frequency ω_c, that consists of series of sine waves with frequencies 0, ω_c, $2\omega_c$, $3\omega_c$ . . . etc, then the frequency spectrum of the signal being modulated will be shifted to 0, ω_c, $2\omega_c$, $3\omega_c$ . . . etc. and split into half-magnitude spectrum lines on both sides of ω_c. This is the change rule for the spectral line when the signal is modulated.

9.3.5.3 Arc scanning signal in pulsed MIG welding

The current signal of the scanning arc is shown in Fig. 9.21. It consists of three parts, namely a constant current I_a, a periodic square-wave current I_b, and the current change due to torch-height variation I_c.

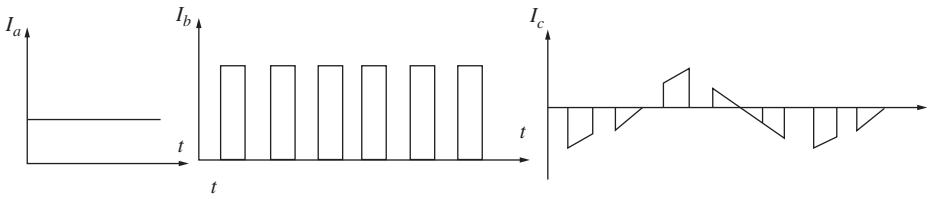

a)

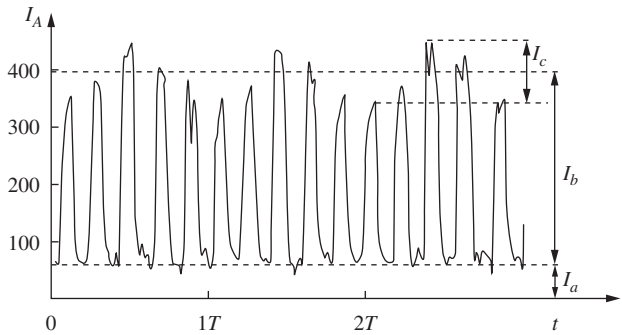

b)

$U = 29\ V$, $I = 220\ A$, Pulse frequency 95 Hz, Scanning frequency 19 Hz

9.21 Schematic diagram of pulsed current and resolved components

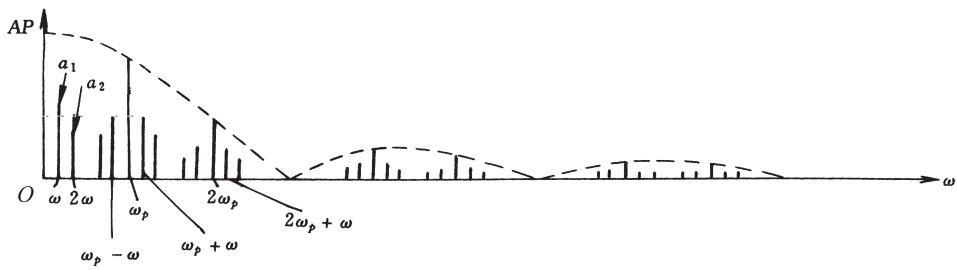

9.22 Frequency spectrum of the modulated pulsed current

The frequency spectrum of the current is the sum of the frequency spectra of these three current components. I_b is a periodic pulse, which can be resolved into a series of sine components; its frequency spectrum was illustrated in Section 9.3.5.1. Let I_b be the carrier and I_c be the modulated signal. Then, according to the frequency-shift rule, each frequency component of the scanning arc will move to each frequency-spectral line of the carrier and on both sides of it. The resulting frequency spectrum is illustrated in Fig. 9.22.

In the figure, ω_p is the pulse frequency and ω ($2\pi f_s$) is the arc-scanning frequency. a_1, a_2 are the first- and second-order harmonic magnitudes of the scanning-arc current. They are located on both sides of the carrier spectral lines 0, ω_p, $2\omega_p$ . . . etc. The frequency separation between them is an

integral multiple of ω. The magnitude of the spectral line on both sides is proportional to the product of the magnitude of the corresponding harmonic of the scanning arc current and the magnitude of the corresponding harmonic of the pulsed current. The phase angle of the spectral line is the sum or the difference of the phase angles of the above-mentioned two harmonics of the corresponding signals.

From the figure, it is seen that the spectral line of the scanning-arc signal ω_n still exists (when $\omega_p = 0$). The characteristic harmonic component also exists, but it is mixed with the spectral lines of the carrier. It can also be seen that, for a normal groove shape, the magnitudes of the high-order harmonics are small and can be neglected. But the magnitude of first, second and third harmonic components are close to the spectral line of the carrier so they might be mixed and overlapped.

In order to clarify the phenomena and analysis given above, experiments were conducted by the author and his colleagues on pulsed-arc welding using different pulse frequencies and a fixed scanning frequency of $f = 20$ Hz. The current waveform and its spectrum are shown in Fig. 9.37, in which Figure 9.37a is for a welding current I = 210 A, and a *V*- groove with torch deviation and Figure 9.37b is for a welding current $I = 130$ A, under the same conditions ($f = 20$ Hz). The ordinate is a logarithmic scale. It can be seen that the contour lines of the spectra a and b obviously are similar to the dotted contour line in Fig. 9.22. Nonetheless, the phase angle changes due to the effect of the mix of spectra of the two signals. The experimental results agree with the theoretical analysis.

From the analysis above, it is known that the arc sensor's signal in pulsed welding in time domain is the result of the multiplication of the scanning-arc signal and the carrier pulsed current signal. In frequency domain it is the convolution of the scanning-arc signal and the carrier signal, which is a phenomenon of frequency shifting.

In order to prevent the mixing of the signal-frequency spectrum with the carrier-frequency spectrum, the frequency of the carrier signal must be much greater than the frequency of the arc-sensing signal. In actual applications, the frequency of the former should be 10 times larger than the latter. Supposing that the arc-scanning frequency is $f_s = 10$ Hz and the frequency spectrum within $5f_s$ is considered, which means the maximum frequency considered is 50 Hz, then the pulsed-current frequency should be greater than $f_p = 500$ Hz. Obviously this is not acceptable for practical applications.

Depending on the method of detecting the characteristic harmonic vector, only the first- or second-order harmonic vectors are needed. Therefore the requirement for the pulsed-welding current frequency can be relaxed. Under the same conditions mentioned above, $f_p = 10f_s = 100$ Hz, which is quite possible for welding applications. However this requirement

is hard to meet for pulsed-arc welding when the average current is low. In this case, the method used to detect the characteristic harmonic vector is not reliable. In order to solve this problem, digital filtering of the signal is helpful. This will be introduced in Section 9.4.

9.3.6 Summary

- For studying a sensing system, an analytical method that can give the correct output signal on the basis of the input signal is required. Handling the variables in time domain will not meet this requirement. Space transformation of the signal from time domain into frequency domain using a trigonometric function can satisfy the requirements and provide the theoretical basis for the signal processing of the sensing system.
- The input signals for different groove shapes have different characteristic harmonic components representing the torch deviation. This rule does not change after the sensing process; therefore, the magnitude and phase angle of the characteristic harmonic vector can be used as the criterion for detecting the deviation of the arc.
- On the basis of the theoretical analysis, a signal-processing technique is proposed, namely, a characteristic harmonic-vector detection method. The method is simple and practical. It has a high signal-to-noise ratio.
- The spectral order of the characteristic harmonic is different for different groove shapes; therefore the choice of the scanning frequency depends on the groove shape. Lower frequencies are recommended for lap joints.
- The output of the sensing system in pulsed-arc welding can be regarded as the scanning-arc signal modulated by the carrier, i.e. a pulsed-current signal. The characteristic harmonic component will not be changed during the sensing process. Therefore the characteristic harmonic-vector method still can be used for detection of the arc deviation. However, there might be interference due to spectrum mixing. This problem can be solved by digital filtering.

9.4 Filtering of signals

9.4.1 Introduction

In Section 9.3, the characteristic harmonic vector was studied assuming arc scanning in an ideal groove. In actual welding, the arc current constantly fluctuates, which inevitably interferes with the signal transfer and reduces the quality of the output signal. The interference may be random or inherent from the scanning process. Therefore, filtering is important for signal processing. The aim of filtering is to magnify the useful part of the signal

and suppress the noise to improve the quality of the signal and facilitate signal processing.[380]

This section is directed toward improving the quality of the signal and the reliability of the detection method in CO_2 welding and pulsed-arc welding. Digital filtering has the advantages of flexibility, reliability and effectiveness. Different digital-filtering methods have been used for different welding situations and have given good results. The description presented below is universally useful. It is used as the basis for processing the signals from an arc sensor.

Because the number of data samples per rotation of the arc is fixed (64), implementation of the method described in this chapter does not depend on the scanning frequency of the arc.

9.4.2 Principle of digital filtering

In this section, some of the conventional linear and nonlinear digital-filtering methods that are effective are studied. The principles, advantages, and shortcomings of these methods are described.

9.4.2.1 Local average (smoothing) filtering

Local average filtering can be used either in time domain or in space domain. Both are easy to use and give good results.

Suppose that the noise $\eta(n)$ is white noise, its mean value is zero, and the variance is σ^2. The signal $f(n)$ is independent of the noise. The signal plus the noise can be expressed as $f'(n) = f(n) + \eta(n)$.

After local average filtering, it becomes the signal $g(n)$, which can be written as

$$g(n) = \frac{1}{N}\sum_{i\in s} f'(i) = \frac{1}{N}\sum_{i\in s}[f(i)+\eta(i)]$$
$$= \frac{1}{N}\sum_{i\in s} f(i) + \frac{1}{N}\sum_{i\in s}\eta(i) \qquad [9.37]$$

where S is the N-point set at the point n.

Two examples are shown in Fig. 9.23.

Besides the assumption given above, it is assumed that the values of the signals are close to one another. This assumption coincides with the actual phenomena of arc-scanning signals. Equation [9.37] is the algorithm for obtaining a new value of a point by averaging the values of its neighbour points. Suppose $E\{\bullet\}$ is the statistical average and $D\{\bullet\}$ is the variance, then

a) Two neighbouring points

b) Four neighbouring points

9.23 Two kinds of neighbourhoods

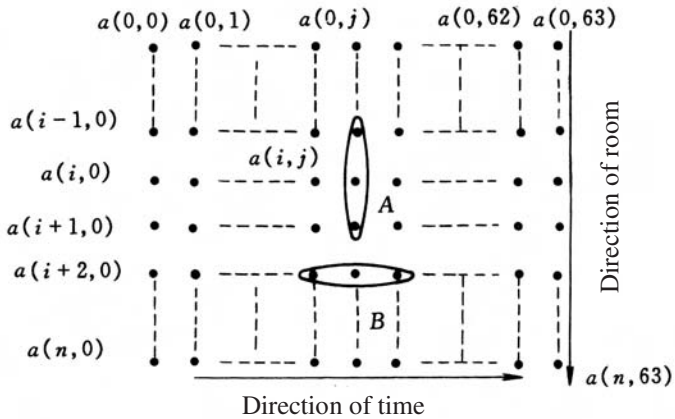

9.24 Data structure of the signal

$$E\left\{\frac{1}{N}\sum\eta(i)\right\}=\frac{1}{N}\sum E\{\eta(i)\}=0$$

$$D\left\{\frac{1}{N}\sum\eta(i)\right\}=\frac{1}{N^2}D\{\eta(i)\}=\frac{1}{N}\sigma^2 \qquad [9.38]$$

The equation illustrates that the average value of the residual noise is still zero, the variance σ^2 is reduced to $\frac{1}{N}\sigma^2$, but the signal $f(n)$ is changed to $\frac{1}{N}\Sigma f(i)$. The change results in distortion of $g(n)$. The signal becomes smooth and the sharp part becomes indistinct. The degree of indistinguishability depends on the size of neighbourhood taken. In order to overcome this shortcoming, average values can be filtered in space domain. Figure 9.24 shows the data structure of the sampling during the arc scanning.

In Fig. 9.24 there are 64 points in each row, which are the data sampled in one revolution of the arc. In each column, the data were sampled during

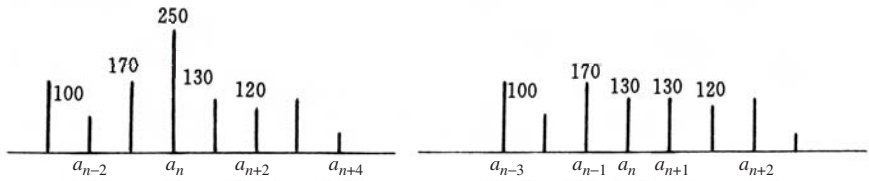

a) Original signal b) After filtering

9.25 Principle of mean-value filtering (neighbourhood of 5)

different rotations of the arc, but they are at the same position of the arc in relation to the groove. Region A is the neighbourhood in space, (or an average of several revolutions of the arc) and region B is the neighbourhood in time.

The effect of filtering depends on the number of data in the neighbourhood. In the choice of N, the filtering speed should be considered. The larger the value of N, the longer will be the time required for filtering, which is detrimental to the closed-loop control properties of the system. Normally, 2 to 8 rotations are taken for different scanning speeds. The average filtering method is effective for eliminating the noise of a statistical character but is not as effective for eliminating the noise caused by factors due to rotation during scanning.

9.4.2.2 Mean-value filtering

Mean-value filtering is based on an older statistical theory of mathematical statistics, which is a nonlinear signal processing method proposed by J.W.Takey in 1971. This method is particularly effective for suppressing the noise but the characteristic relationship between the output and input has not been found to date. The method is based on the actual phenomenon that noise appears predominately in the form of isolated events. The number of events is small and the actual signal consists of a more continuous data set.

In the case of one-dimensional data, a neighbourhood of odd-number signals is taken. In the filtering process, the datum at the middle point of the neighbourhood is replaced by the mean value of all the data in the neighbourhood. Figure 9.25 shows the data in the neighbourhood in which the value of the middle point is 250 and the other data are 100, 170, 130, and 120. The average of all of the data in the neighbourhood is 130; therefore, the value of the middle point 250 is replaced by 130. If 250 is a noise event, then it is eliminated, which is helpful, but if it is a real signal, the elim-

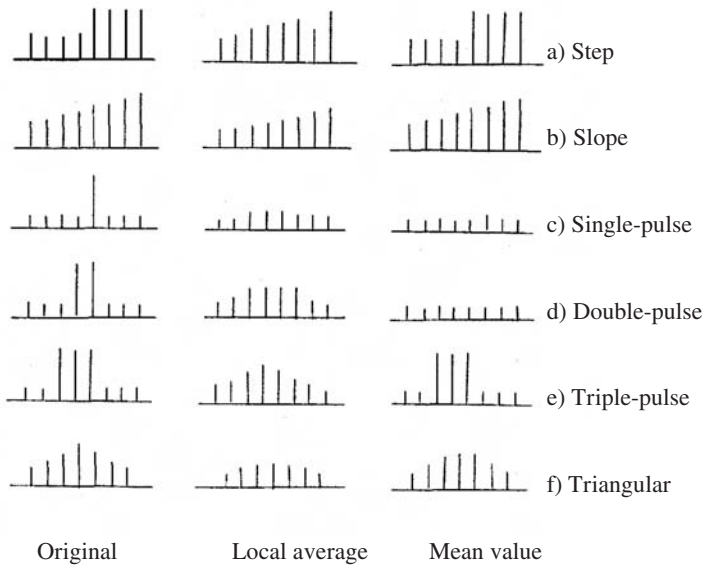

9.26 Results of filtering by two methods (Neighbourhood of 5)

ination is inappropriate. Therefore mean-value filtering is useful in some cases but erroneous in others.

Figure 9.26 shows the results of filtering by two methods, namely, the local-average method and the mean-value method. Figure 9.26a shows a step signal and the mean-value filtering retains the step character of the signal. In Fig. 9.26b, which shows a sloping signal, filtering retains the slope as well. In Fig. 9.26c, a single-pulse signal is eliminated by the filtering. In Fig. 9.26d, the double-pulse signal also is eliminated by filtering. In Fig. 9.26e, there is no effect on a three-pulse signal by filtering. In Fig. 9.26f, the triangular signal is distorted but basically retained. Figure 9.26 also shows the results of local-average filtering in the middle column. It can be concluded that mean-value filtering has no effect on the step signal and the sloping signal. It suppresses only those signals containing less than 2 pulses. It is superior to local-average filtering and is effective.

Let $Med\{\bullet\}$ represent mean-value filtering and k be a constant. The properties of the filtering can be expressed as follows:

$$\underset{j\in w}{\text{Med}}\{K\cdot f(j)\} = K\cdot \underset{j\in w}{\text{Med}}\{f(j)\}$$

$$\underset{j\in w}{\text{Med}}\{K+f(j)\} = K+\underset{j\in w}{\text{Med}}\{f(j)\} \qquad [9.39]$$

But

$$\underset{j\in w}{\text{Med}}\{f(j)+g(j)\} \neq \underset{j\in w}{\text{Med}}\{f(j)\}+\underset{j\in w}{\text{Med}}\{g(j)\} \qquad [9.40]$$

Normally three data points are taken as the neighbourhood. If no useful signal is lost, then the neighbourhood is expanded until the best filtering effect and the least loss of useful signals is obtained. Iteration also can be used and a fixed or variable number of data points in the neighbourhood can be applied. Generally, the width of the neighbourhood will not be changed once it is found to be suitable. For those neighbourhood widths that are less than 1/2, the filtering will be continued until its width is greater than 1/2.

Two-dimensional mean-value filtering also can be used for the data structure shown in Fig. 9.24. A two-dimensional $L \times L$ filter is more effective than two one-dimension filters that are $L \times 1$ and $1 \times L$ (for horizontal and vertical data sets). The problem is that an excessively complicated algorithm must be used. Mean-value filtering by hardware is feasible.

9.4.2.3 Morphologic filtering

Mathematical morphology is a special signal-processing method. It is based on set theory and tries to describe the signal form in a quantitative way. It is used to satisfy different applications by transforming, generating formulae, developing algorithms and combining. The concept of the theory is applied in this section to processing scanning-arc signals. A two-dimensional signal $f(x, y)$ can be regarded as a function; it corresponds to a three-dimensional point set $\{(x, y, f(x, y))\}$ of Euclidean space. The expanded third dimension corresponds to the value of the signal. Umbra is an important concept of morphology. The definition of Umbra is:

$$U(f) = \{D = (x, y, z); \quad z \le f(x, y)\} \qquad [9.41]$$

The function f is the surface of $U(f)$, which is the curved surface perpendicular to the z direction; side surfaces are not included.

It is easy to imagine that the result of a union and intersection operation is

$$U(f) \cup U(k) = U[\max(f, k)] \quad U(f) \cap U(k) = U[\min(f, k)]$$

$$\text{if } U(f) \subset U(k) \quad \text{or} \quad f(x, y) \le k(x, y) \quad \forall (x, y) \in R^{\Omega}$$

Figure 9.27 is the schematic diagram of these two equations. For simplicity, only two-dimensional space is shown. x corresponds to a spatial position and z is the value of the signal at the corresponding point. Obviously there is no mutual containing relationship between $U(f)$ and $U(k)$. If the two-dimensional signal indicated in the figure is the arc sensor's signal, the union and intersection operation applied to it become an operation to find their

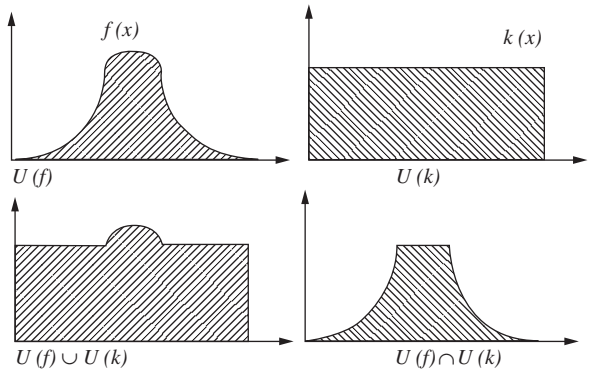

9.27 Intersection and union of umbra

upper and lower contour lines. In the case of the data structure shown in Fig. 9.24, the operation is to find the upper and lower contour surface of the signal, i.e. the filtering in space. Obviously it is a nonlinear filtering technique. Let min{•}, max{•} represent the minimum and maximum operations. Then the filtering of the arc sensor's output can be expressed by Eq. 9.42 for the intersection operation and Eq. 9.43 for the union operation.

$$a_j = \min\{a_{ij} \quad i = 0, 1, \ldots, N-1, \quad a_{ij} \neq 0\} \quad j = 0, 1, \ldots, 63 \qquad [9.42]$$

$$a_j = \max\{a_{ij} \quad i = 0, 1, \ldots, N-1, \quad a_{ij} \neq 0\} \quad j = 0, 1, \ldots, 63 \qquad [9.43]$$

where N is the width of the neighbourhood for filtering. In order to avoid the effect due to extinguishing of the arc, zero values of arc current are excluded from the operation.

The data processing described can be accomplished by computer programming using C language.

9.4.3 Signal filtering for CO_2 welding

In order to obtain a stable arc process, short-circuiting or small-droplet transfer normally are used for CO_2 welding. Short-circuiting transfer is used most often.

Due to frequent short circuits, the current fluctuates violently. A DC inductance is normally connected in the welding loop to control the rates of current rise and fall during short circuiting. The current waveform is therefore quite different from that obtained in MIG welding. In the following text, the filtering method for the process is described.

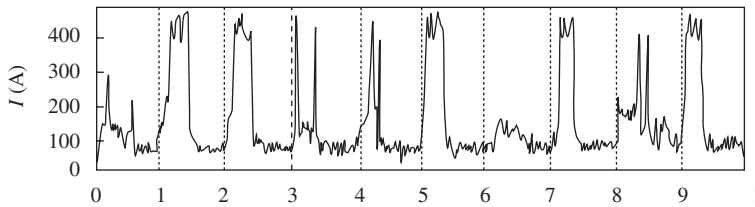

9.28 Current sampled during CO_2 welding ($f = 15$ Hz)

9.4.3.1 The current-signal output by the sensor

In CO_2 welding, the arc length is short and is sensitive to torch-height variation, and the arc stability is poor. Therefore there is a lot of noise.

Because the spatial-sampling method is used for the process and the sampling frequency depends on the rotation frequency of the arc, the influence of the short-circuiting current (frequency of 50–120 Hz) therefore will be different for different arc rotation speeds. Consequently, different filtering methods have to be used for different cases.

For a low scanning frequency ($f_s < 7$ Hz), the sampling frequency is low and the short-circuiting current appears like a sharp pike, which can be regarded as random interference. For high scanning frequencies, the sampling frequency is high and the short-circuiting current width is large. The groove shape has a stronger effect on the current waveform (see Fig. 9.28). Therefore, it should not be regarded as random interference. Suitable signal processing should be applied to it accordingly, otherwise a useful signal will be lost.

For a low-frequency scanning speed, clipping of the short-circuiting current was proposed by the author in 1978,[51] in which the short-circuiting current was suppressed completely. Good results were obtained. The technique was implemented using hardware, but with the development of computers, the method can now be implemented by software. The short-circuiting current can be detected from the change of arc voltage or by the current-rise rate. The variety of welding machines and different scanning frequencies make it hard to detect short-circuiting current from the current-rise rate.

The author proposed an improved method in 1996. In this method, the short-circuiting current, was clipped at the level of 1.5–2 times the welding current (for high welding current, the lower limit was taken while for low welding current, the higher limit was taken). In that way, the interference was eliminated and the variation rule for the current was retained. This method can be implemented easily using software because the data that are sampled are digital. Experiments demonstrated effective filtering, as shown in Fig. 9.29.

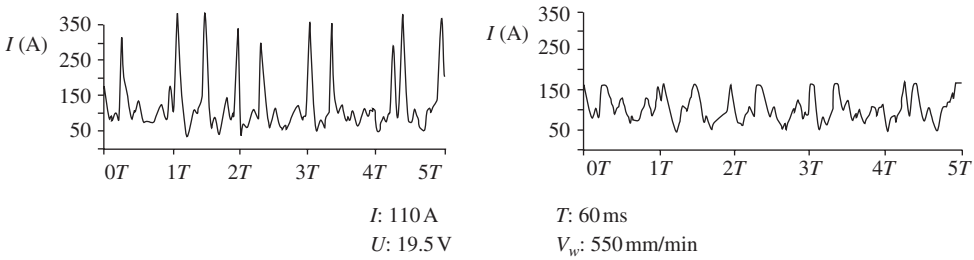

9.29 Sampled and filtered signal in CO_2 welding

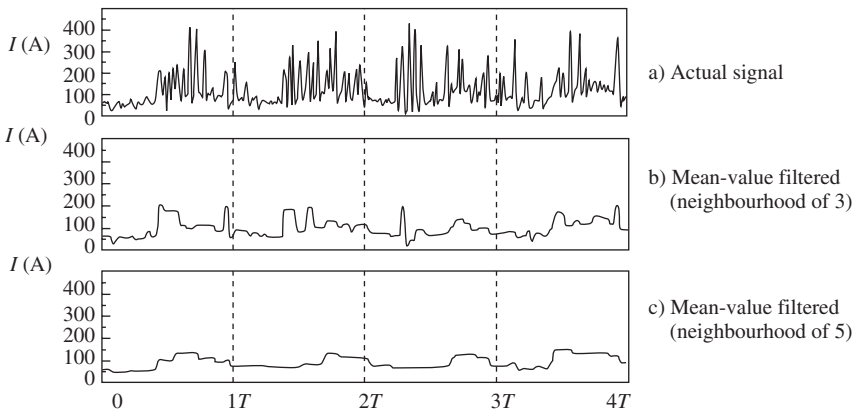

9.30 Welding current for CO_2 welding ($f = 3$ Hz)

Generally, for high welding currents, clipping the short-circuiting current is a simple and effective way of signal processing.

Several filtering methods and their effects are described in the following paragraphs. The clipping method was not used in these techniques.

9.4.3.2 Mean-value filtering for low scanning speeds

At low scanning speeds, the average filtering method can be used effectively but it causes a delay in the closed-loop control system. Therefore non-linear mean-value filtering was applied and satisfactory results were obtained, as shown in Fig. 9.30.

Figure 9.31 shows the frequency spectra of the current waveforms shown in Fig. 9.30, respectively. The scanning speed was $f = 3$ Hz and welding was performed on an inclined work piece. In the figure, a_n and θ_n represent the magnitude and phase angle of nth-order harmonic.

The figure shows that mean-value filtering eliminates the interference due to short circuiting and does not harm the useful signal. It was found

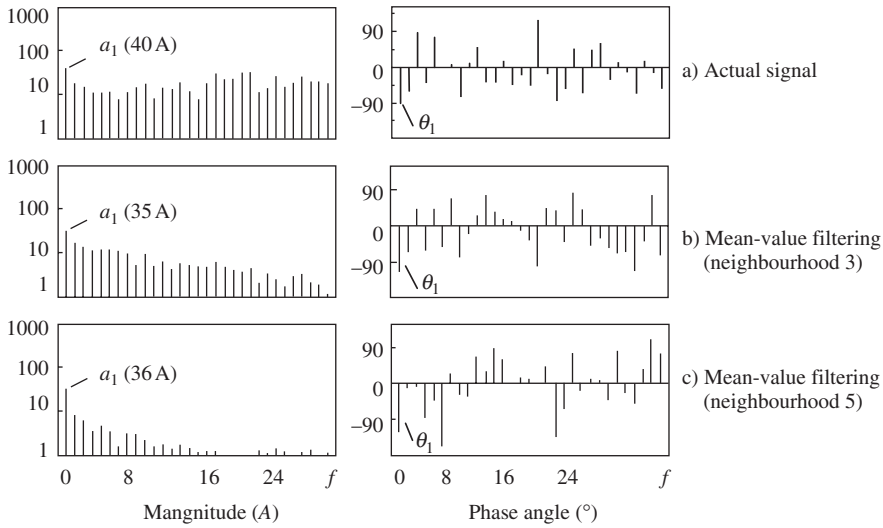

9.31 Frequency spectrum of current in CO_2 welding ($f = 3$ Hz)

that high-order harmonics were effectively filtered, the low-frequency characteristic harmonic remained unaltered, and, particularly, the first-order harmonic a_1 remained almost unchanged over the range from 35 A to 40 A. However its phase angle changed from –90° to –130°, which illustrated that mean-value filtering not only filtered the noise but also improved the waveform. In low-frequency scanning, short circuiting occurred more frequently when the arc length was shorter at the side of the groove. The distribution of the short-circuiting current changed the phase angle of the low-frequency harmonic, which made the phase lead and increased the magnitude of the low-frequency harmonic. These effects cannot be obtained using other filtering methods.

Figure 9.31 shows that the greater width of neighbourhood 5 eliminates high-frequency signals more effectively but does not affect low-order harmonics. The wider neighbourhood increases the amount of work and the processing time, which requires a greater hardware investment. Normally neighbourhoods 3 or 5 are effective for this purpose.

Figure 9.32 shows the current waveform and frequency spectrum for CO_2 welding at a scanning speed of 2 Hz. This figure shows that after mean-value filtering, the magnitude of a_1 has not changed while the phase angle has changed by 90°.

The discussion in Section 9.4.2.2, showed that mean-value filtering did not affect the signal, the duration of which is longer than the width of the neighbourhood. Therefore, its signal-to-noise ratio can be improved by mean-value filtering. Figure 9.33 shows the current waveform and frequency spectrum for CO_2 welding in a V-groove with arc oscillation at a scanning

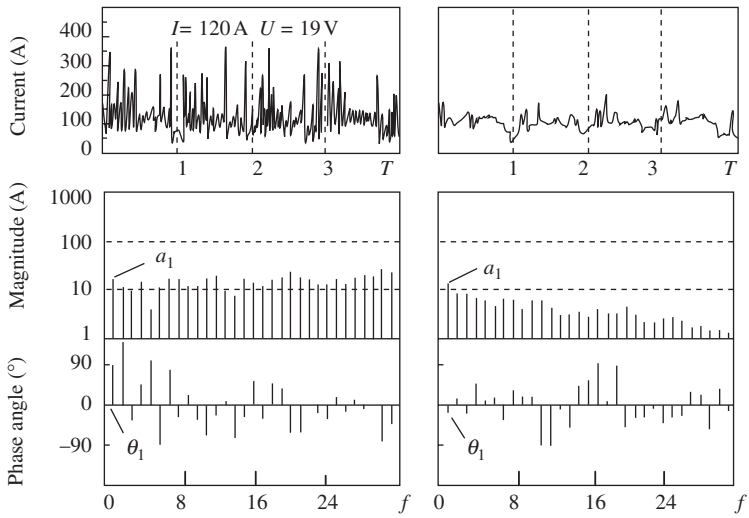

a) Actual signal b) Mean-value filtered (neighbourhood 3)

9.32 Current waveform and frequency spectrum for CO_2 welding ($f = 2$ Hz)

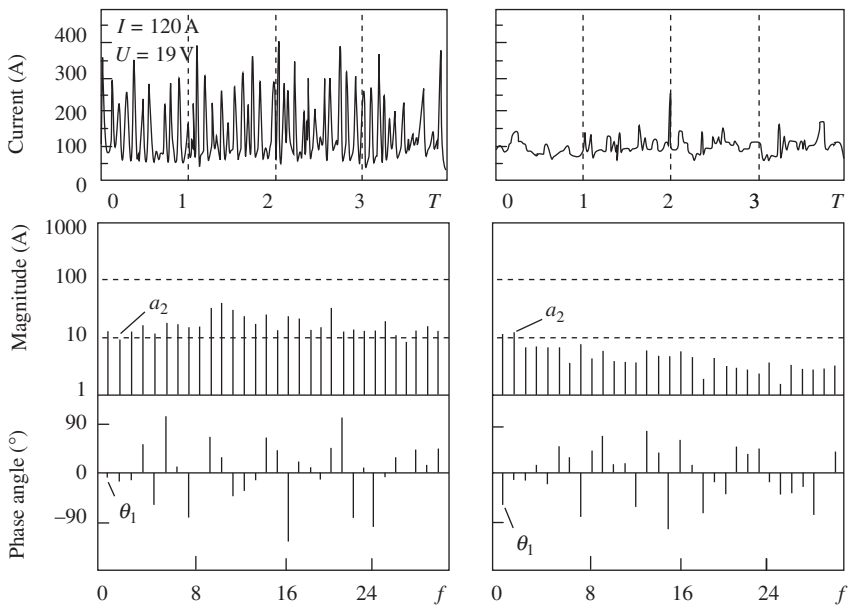

a) Actual signal b) After mean value filtering (3 turns)

9.33 Current waveform and frequency spectrum for CO_2 ($f = 5$ Hz)

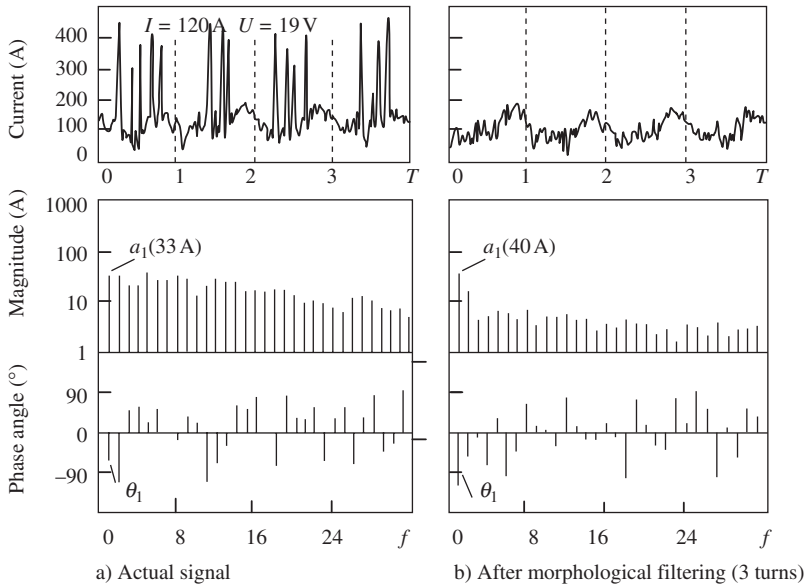

9.34 Current waveform and frequency spectrum for CO_2 welding (f = 12 Hz)

speed of 5 Hz. Although the sensor's second-order harmonic output changes most dramatically, the figure shows that mean-value filtering has no detrimental effect on this harmonic. Its magnitude is even larger (see a_2 in Fig. 9.33). The first-order harmonic remains the same as described before.

Normally, low-frequency scanning is not used with a rotating arc because the sensitivity is lower. However, with an oscillating arc, increasing the frequency is difficult and, therefore, mean-value filtering has practical significance.

9.4.3.3 Morphological filtering for a high-frequency scanning arc

When high-frequency scanning is used, the amount of data sampled during short circuiting is greater. Therefore, it requires a wider neighbourhood for mean-value filtering, which requires greater processing time on the one hand and suppresses the useful signal on the other hand. However, high-frequency scanning also allows multi-turn filtering. Taking the data sampled during two rotations of the arc for morphologic filtering can give useful results. At very high scanning frequencies, when the short-circuit waveform changes its appearance, multi-turn morphological filtering (by intersection of umbra) gives useful results (see Fig. 9.34).

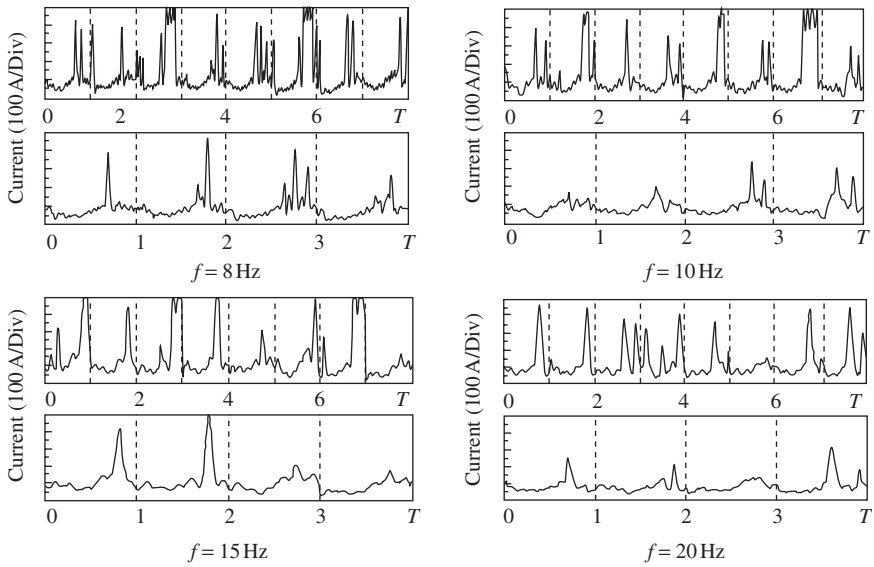

9.35 Current waveform before and after morphological filtering during CO_2 welding

Figure 9.34a shows the current waveform and its frequency spectrum during CO_2 welding on an inclined surface at a scanning speed of 12 Hz. Figure 9.34b is the waveform and frequency spectrum obtained after morphological filtering (take min operation). It is obvious, by comparison of these two figures, that a_1 is not decreased but, on the contrary, is increased. The phase angle is changed by 45°; this change obviously is due to the elimination of the interference of the peak current during short circuiting.

In morphological filtering, the number of turns taken depends on the scanning speed; two turns minimum at a scanning speed of 10 Hz gives good results. Interference due to globular metal transfer can be eliminated. Figure 9.35 illustrates the results of morphological filtering for frequencies of 8 and 10 Hz. Due to centrifugal force, globular droplet transfer becomes obvious and the frequency of transfer decreases. Two turns for morphological filtering are not enough; four turns are necessary for better results. For example, in Fig. 9.36 ($f = 25$ Hz), the upper figure shows the original signal and the lower figure gives the results of filtering. The interference of globular transfer is completely eliminated.

The discussion above can be summarised as follows. In the case of CO_2 welding, different filtering methods should be used for different scanning speeds. At low scanning frequencies, the short circuiting current can be regarded as an interference having a sharp current pike, which can be eliminated by mean-value filtering. At high scanning frequencies, the short-circuiting current is influenced by the arc length. Its effect on the output of

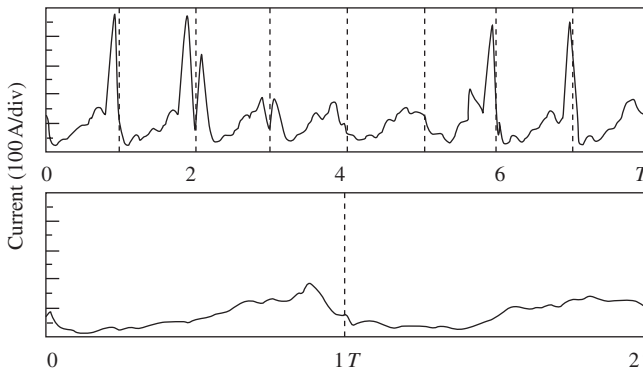

9.36 Current waveform before and after morphological filtering during CO_2 welding ($f = 25$ Hz)

the sensor is twofold. Although either multi-turn averaging, morphological filtering, or the clipping-current method can eliminate interference effectively, in practice a combination of all three filtering methods gives better results during CO_2 welding.

9.4.4 Signal filtering for pulsed-arc welding

In Section 9.3.5, the pulsed-arc signal was analysed and regarded as a modulated signal of the scanning arc by the carrier pulsed current (Fig. 9.37a). Due to the shifting and mixing of the frequency spectrum, the quality of the sensor's signal deteriorates, particularly at low welding current (see Fig. 9.37b). In this case, how to choose the filtering method and improve the signal quality becomes an important problem.

Figures 9.37a and b are the current signals and their frequency spectra for the same groove but different welding currents. It can be seen that at a low welding current (Fig. 9.37b), only two pulses appear in one turn and the current waveforms are quite different for different turns. Because serious frequency-spectrum mixing occurs and a poor output signal appears, this signal is hard to process. If the signal from several turns is synthesised, the situation is improved. Normal linear filtering does not improve the signal very much. Taking advantage of morphology and the union ($\cup$) of umbra of the pulsed current over several turns, the pulsed current component is enhanced and the signal quality is improved substantially. Thus, it becomes possible to use the sensor at a low welding current. Figure 9.37c shows the waveform after morphological filtering; not only are the magnitudes of the low-order characteristic harmonics improved, the phase angle due to fre-

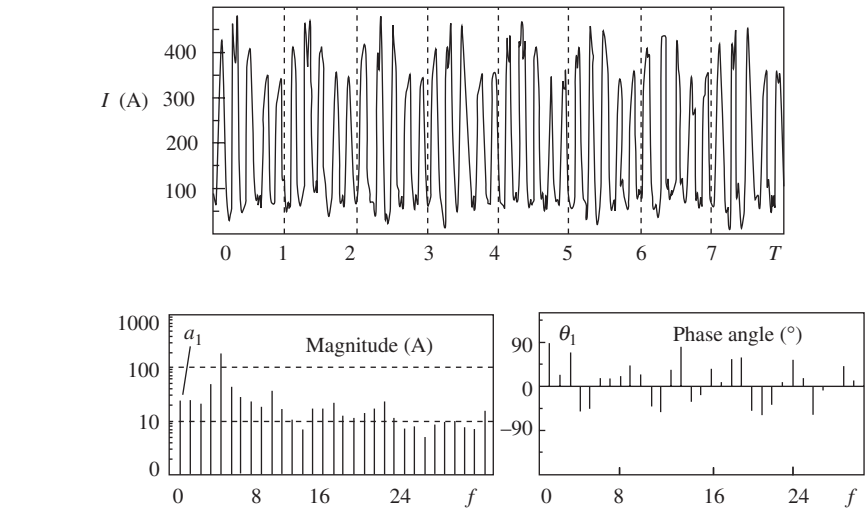

a) Actual signal (I = 210 A, U = 29 V)

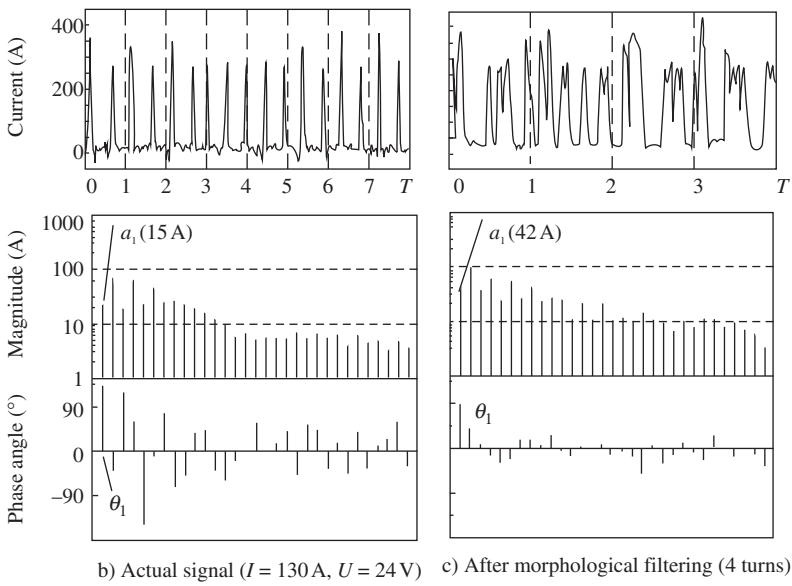

b) Actual signal (I = 130 A, U = 24 V)

c) After morphological filtering (4 turns)

9.37 Current waveform and frequency spectrum during pulsed-arc welding while I = 210 and 130 A

quency mixing also is corrected (see θ_1 in the figure). The phase angle change is shown more clearly in Fig. 9.38. It is obvious that without morphological filtering, picking up the characteristic harmonic of the arc signal is difficult.

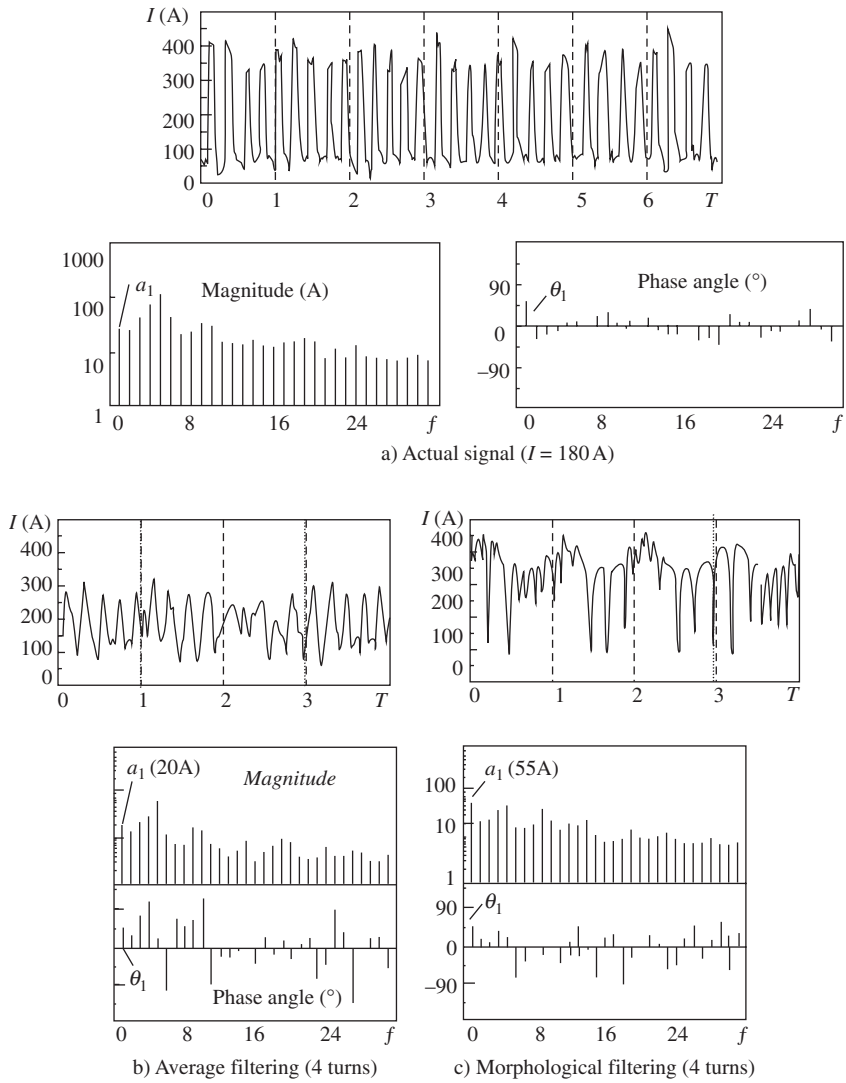

9.38 Current waveform and frequency spectrum during pulsed-arc welding while $I = 180$ A

Figure 9.38a is the waveform of the sensor's output at 180 A welding current. Comparing Figures 9.38a, b and c shows that the first-order harmonic magnitude has no obvious change after average filtering, but is greatly improved by morphological filtering; the magnitude was increased from 20 A to 55 A without any change of phase angle. These phenomena are significant for the sensitivity of a pulsed-arc sensor because they solve

the problem of frequency-spectrum mixing (see Section 9.3) while maintaining the gain of the system's response.

In summary, to avoid frequency-spectrum mixing, increasing only the scanning speed does not help. Choosing reasonable sensor parameters (scanning speed and diameter), and morphological filtering give satisfactory results.

9.4.5 Summary

In Section 9.4, the principles of filtering and several kinds of digital filtering methods (e.g. average filtering, mean-value filtering, morphological filtering and clipping) were introduced. The effects of their special features were studied experimentally.

(i) For low scanning-frequency CO_2 welding, mean-value filtering can eliminate the influence of short-circuiting current and give good results.
(ii) For high scanning-frequency CO_2 welding, clipping and multi-turn morphological filtering can eliminate noise and give good results.
(iii) For pulsed-arc welding, morphological filtering improves the signal waveform, reduces the effect of frequency-spectrum mixing, and raises the signal-to-noise ratio of the characteristic harmonic while maintaining the sensitivity of the sensor. This makes it possible to apply the sensor to low-current pulsed-arc welding at a high scanning frequency.

9.5 Signal processing in a practical welding process

In the sections above, studies of sensor signals and their transfer, and the method for obtaining the characteristic harmonic for an ideal groove were described. Different digital-filtering methods were applied for different welding processes, according to their special features. Good results have been demonstrated. In this section, practical experiments were conducted using different welding conditions in order to provide the basis for achieving closed-loop control of a seam-tracking system.

9.5.1 Orthogonalisation of the characteristic harmonic vector

9.5.1.1 Influence of the molten pool on the scanning signal

According to the theoretical analysis, the first-order harmonic for a V-groove should be zero, but practical experiments have shown that a

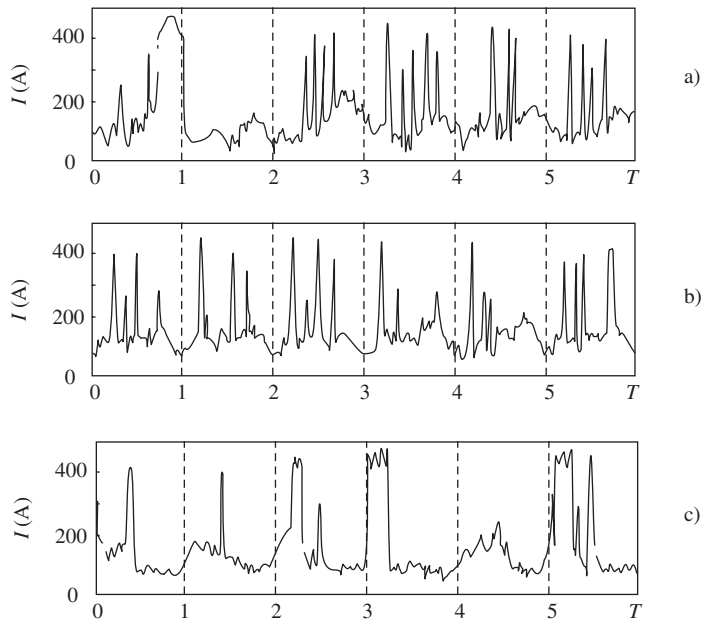

(a-deviation to the left, b-center, c-deviation to the right)

9.39 Current waveform during CO_2 welding in a V-groove

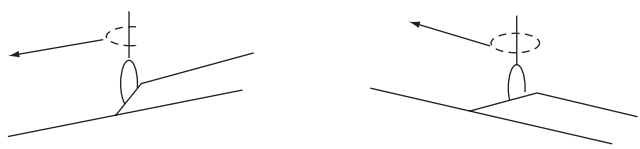

9.40 Welding on an inclined plate

certain magnitude of this harmonic vector exists (see Fig. 9.39b). It should not be regarded as an interference and neglected, otherwise it could result in an incorrect judgment of the arc deviation in practice.

In order to study this problem and to avoid the influence of groove shape, an experiment on a simple plate was carried out. It was found that this phenomenon still existed. Detailed observations demonstrated that the surface of the molten pool caused the first-order harmonic vector. To explain this phenomenon, the following experiments were performed (see Fig. 9.40).

Upward and downward welding were conducted on inclined plates. According to the analysis given above, the influence of the molten pool is larger in the case of downward welding and smaller in the case of upward welding. The results are shown in Fig. 9.41. Obviously the first-order harmonic (see the dotted line in figure a) is larger in the case of downward

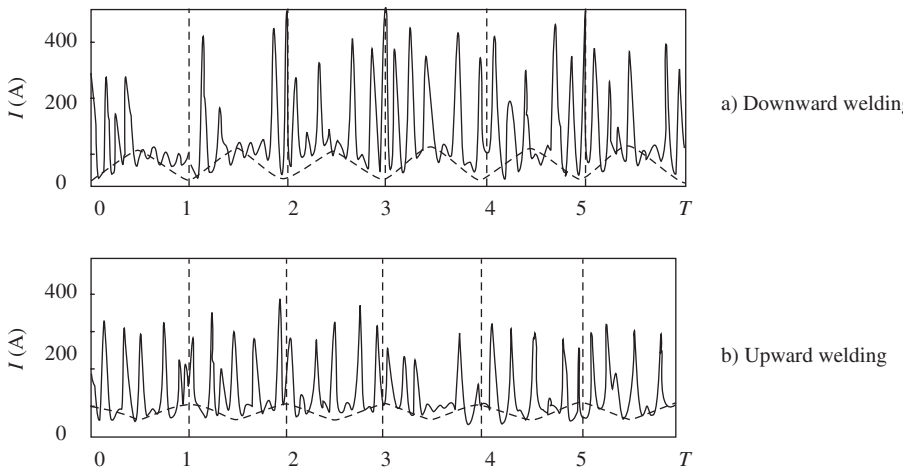

9.41 Current waveform of scanning arcs on inclined plates

welding. This phenomenon coincides with the analysis mentioned above. It proves that this harmonic is not a random interference but, rather, is a signal related to the scanning of the arc. Special measures must be taken to eliminate its influence.

9.5.1.2 Orthogonalisation of the characteristic harmonic vector

Figure 9.42 shows the actual form of the molten pool and the arc rotating above it. The torch-height variation can be resolved into two components. The first component is the variation due to the V-groove surface, $H_p(s)$. The second component is the variation due to the molten pool surface, or more specifically due to the molten-metal flow and the difference in the torch height between the front of the pool and in the body of the pool, designated $H_r(s)$. The variation of arc length is the superposition of these two components.

The torch-height variation Δh_p is symmetrical to an axis across the groove; the torch-height variation due to the molten pool is symmetrical to an axis parallel to the groove. At $t = 0$ as shown in the figure, the former can be written as the following equation:

$$H_p(t) = C_p + \sum_{n=1}^{\infty} k_{pn} \cos(n\omega t) \qquad [9.44]$$

where C_p is a constant that depends on the arc deviation from the groove centreline.

The latter can be written as the following equation:

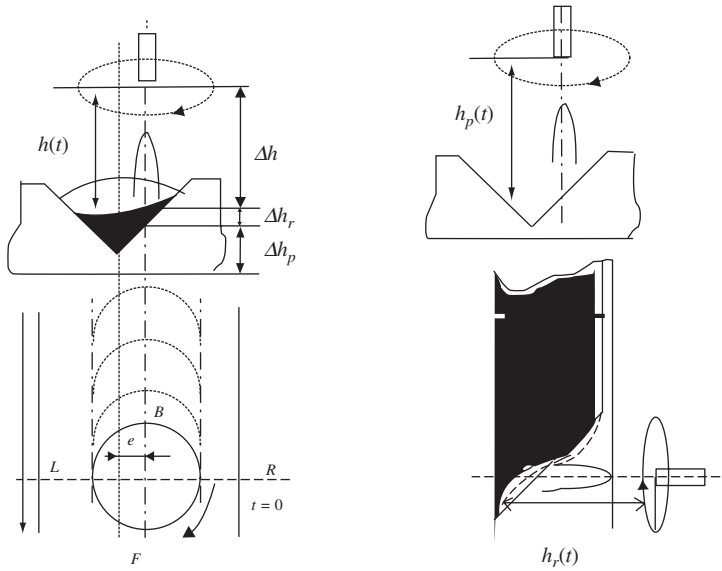

a) Rotation of arc b) Resolution of torch-height variation

9.42 Schematic diagram of scanning above the molten pool

$$H_r(t) = C_r + \sum_{n=1}^{\infty} k'_n \cos(n\omega(t + T/4))$$

$$= C_r + \sum_{n=1}^{\infty} k'_{2n} \cos(2n\omega(t + T/4)) + \sum_{n=1}^{\infty} k_{2n+1} \cos((2n+1)\omega(t + T/4))$$

$$= C_r + \sum_{n=1}^{\infty} k''_{2n} \cos(2n\omega t) + \sum_{n=1}^{\infty} k''_{2n+1} \sin((2n+1)\omega t) \quad [9.45]$$

If the molten pool is an inclined flat surface or a symmetrical dotted line surface, as shown in Fig. 9.42, then the even-order harmonic coefficient is zero. Only an odd-order harmonic will remain; it is an odd-harmonic function.

It can be shown that the odd-order harmonics of two functions are orthogonal. Assuming that the characteristic harmonic is first order, then the magnitude of the characteristic harmonic output by a sensor is the square root of the sum of the squares of the first-order harmonics of the two functions. Because Eq. [9.45] is not related to the arc deviation, the signal exists even when the arc has no deviation. Therefore, detecting the deviation by the magnitude of the harmonic would be inaccurate; the molten pool introduces error.

However, regardless of the magnitude of the deviation, the spatial relationships decide that the two components of the scanning signal are orthogonal. If the characteristic harmonic vector is expressed by the magnitude and

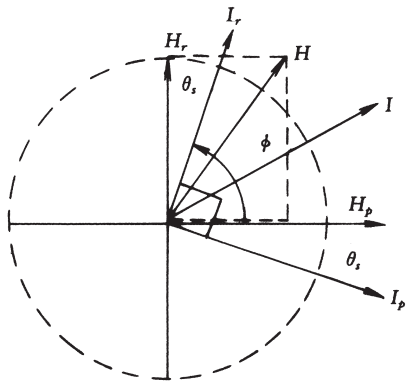

9.43 Relationship of the characteristic harmonic vectors in the case of no deviation

phase angle of the cosine function, and the characteristic harmonic vector of the groove is expressed by H_p (Fig. 9.43), the characteristic harmonic vector of the molten pool is expressed by H_r. The phase angle between them is 90°. After transfer of the sensing system, the characteristic harmonic vectors of the current I_p and I_r maintain the same relationship; that is, their phase-angle difference remains 90°. θ_s in the figure expresses the phase shift due to the transfer function. Because I_p and I_r are orthogonal, it is possible to find the component I_p, detect the deviation, and eliminate the interference due to I_r. Based on the fact that $I_p = 0$ when the deviation is zero, it is possible to determine θ_s using an open-loop experiment. The procedure, called orthogonalisation of the characteristic harmonic vector, is as follows.

The phase angle of the characteristic harmonic is measured and calculated for welding on a plate or in a groove without deviation. The angle obtained should be the phase angle ϕ for I_r. Then, according to Fig. 9.43 and the analysis of Section 9.3, the phase angle of the characteristic harmonic vector I_p for the groove weld is

$$\theta_s = \phi - 90° \qquad [9.46]$$

The magnitude of characteristic harmonic vector of the scanning arc, $e^{j\theta_s}$, represents the magnitude of the deviation. According to the theory of orthogonalisation, it can be calculated using the following equation:

$$A_p = \sum_{k=0}^{63}\left[I(k)\cdot\cos\left(\frac{2k+1}{64}\pi+\theta_s\right)\right] \qquad [9.47]$$

where A_p(A) represents the magnitude of the characteristic harmonic vector and $I(k)(k = 0, 1, 2, \ldots, 63)$ are the values of the sensor's current that were sampled.

According to the theoretical analysis, after the orthogonalisation by Eq. [9.47], the influence of the molten pool can be eliminated. Practical application of the method and its effect are demonstrated by experiments in the sections that follow.

9.5.2 Signal processing

The principle and method for detecting the arc deviation were discussed in Section 9.3 and the signal filtering method was discussed in Section 9.4. Signal processing during actual welding is discussed in this section. First, the characteristic harmonic should be determined according to the type of groove. Supposing that the order of the characteristic harmonic is n, then the filtering method should be chosen according to the welding technology and the scanning parameters. The practical procedure is as follows:

(i) Confine the current-signal amplitude according to a specific rule. For example, if the sampled data are $a_{ij} = I(j) = 0$ ($j = 1, 2, \ldots, 63$) (see the data structure in Fig. 9.24), then they are replaced by the sampled data obtained in a previous rotation, $a_{i-1,j}$. If a_{ij} is too large, then it is clipped, particularly for CO_2 welding.

(ii) For MIG/MAG welding, better results can be obtained using a multi-turn averaging method. Because the MIG/MAG arc is stable, a higher scanning frequency (for example $f_s = 20$~30 Hz) and a neighbourhood width $N = 2$~8 gave satisfactory results in experiments.

(iii) In CO_2 short-circuiting welding, mean-value filtering is used mainly at low scanning frequencies and multi-turn morphological filtering (minimum operation with $N = 2$~3) is used at high scanning frequencies. In the latter case, the average-filtering method also can be used in combination.

(iv) For pulsed MIG/MAG welding, multi-turn morphological filtering (maximum operation, $N = 2$~5) is used for eliminating the frequency spectrum mixing; average filtering can be used in addition.

After filtering, the characteristic harmonic component can then be found from a complete data series. Supposing that the data are ($a_j j = 0, 1, \ldots, 63$), let the sampled data start at $t = 0$ (see Fig. 9.42) and be expressed by $I(0)$, which is a_0 after filtering. Then the average welding current I can be written as

$$I = 1/64 \sum_{j=0}^{63} I(j) \qquad [9.48]$$

The imaginary part of the characteristic harmonic vector is

$$I_m = \sum_{j=0}^{63} a_j \sin(n(2j+1)\pi/64) \quad [9.49]$$

The real part of the characteristic harmonic vector is

$$R_e = \sum_{j=0}^{63} a_j \cos(n(2j+1)\pi/64) \quad [9.50]$$

The magnitude and phase angle of the vector can be obtained from Equations [9.48] and [9.49]

$$A_n = \sqrt{I_m^2 + R_e^2} \quad [9.51]$$

$$\theta_n = \arctan 2(I_m, R_e) \quad [9.52]$$

Equation [9.52] is the formula for the phase angle, the value of which is $|\theta_n| \leq 180°$. According to the degree of θ_n or the positive or negative sign of the real part R_e, the direction of the deviation can be determined. The magnitude of the deviation A_n can be obtained from Eq. [9.51].

The flow chart for the signal processing is illustrated in Fig. 9.44.

The basic steps in the flow chart are:

(i) Sampling of the current signal and writing to a data file (This step is described in Chapter 10).
(ii) Filtering using the methods described above.
(iii) Determining the characteristic harmonic vector using Equations [9.48] to [9.52] after sampling and filtering for the present turn.
(iv) Determination of the deviation e^* (digital signal) from the magnitude and phase angle of characteristic harmonic vector.

In Section 9.5.1.2, orthogonalisation of the harmonic vector to eliminate the interference of molten pool was introduced. With welding conducted on a plate or in a groove without deviation and signal processing according to Fig. 9.44, the phase angle ϕ of the interference (by the molten pool) and the harmonic vector can be determined. Subsequently, the phase angle of the characteristic harmonic vector θ_s can be obtained from Eq. [9.46]. Replacing Equations [9.49] to [9.52] of the flow chart by Eq. [9.47] to orthogonalise the characteristic harmonic vector, the result would be A_p (or e^* in the flow chart), which is the representation of the deviation e.

9.5.3 Detection of arc deviation

The relationship between the output of the signal-processing system and the actual deviation is called the detection characteristic of the system. In

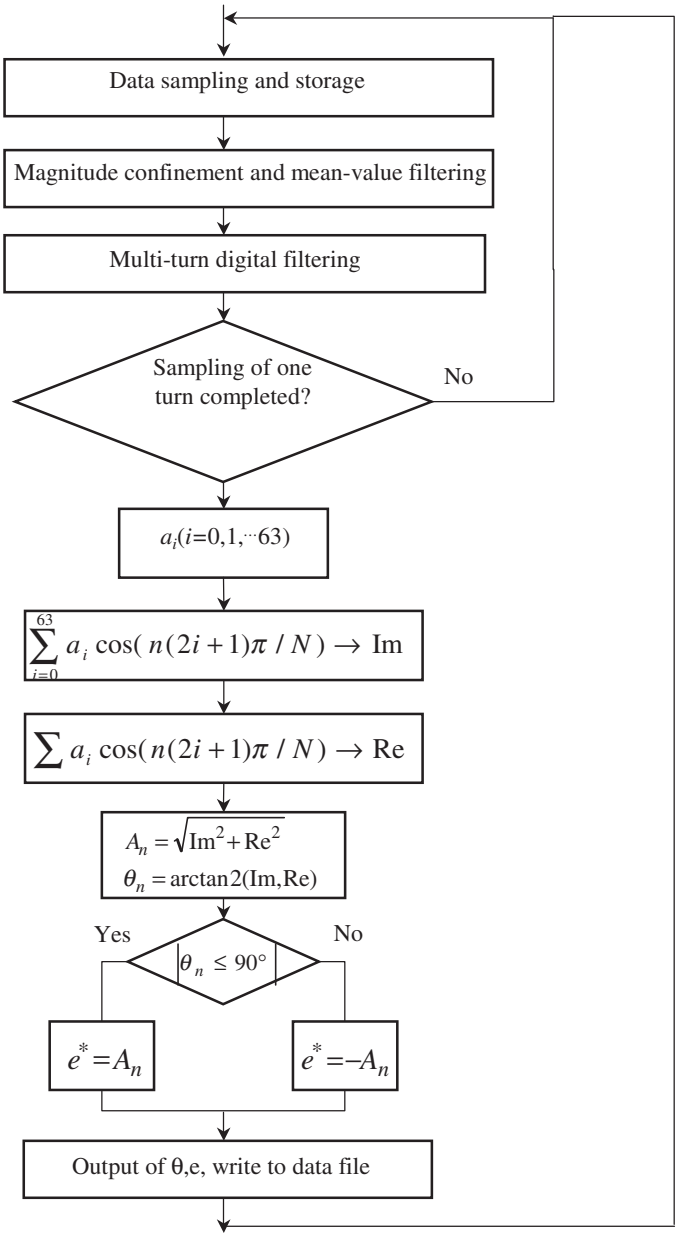

9.44 Flow chart of signal processing

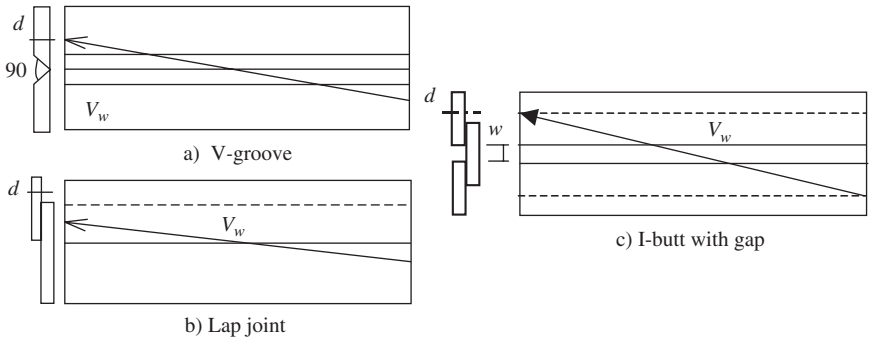

9.45 Schematic diagram showing calibration of the characteristic harmonic vector

order to verify the method, an experimental method has been designed as shown in Fig. 9.45. Keeping the welding speed V_W unchanged, the deviation of the arc changes from ($e > 0$) to ($e = 0$) and ($e < 0$). Thus, the characteristic harmonic vector A_p representing the deviation will be a time-variable function.

The unit of the sampled data and thus the magnitude of the characteristic harmonic is the ampere (A), which represents e (mm). The relationship between them depends on the sensitivity of the system (A/mm) and the type of groove.

The welding conditions that were used were CO_2 welding, a wire diameter of 1.2 mm, 130 A welding current, and 20 V arc voltage.

9.5.3.1 Detection in a V-groove or corner welding

The scanning torch travelled as shown in Fig. 9.45a. The diameter of rotation was $r = 2$ mm.

The characteristic harmonic of a V-groove or corner welding is first order. Figure 9.46 is the output of the sensing system based on the theoretical analysis. Figure 9.46a shows the change of the phase angle and Fig. 9.46b shows the detected deviation. It is known from the theoretical analysis that, $|\phi| < 90°$ when the deviation is on the right and $|\phi| > 90°$ when it is on the left.

Figure 9.47a is the actual phase-angle output without filtering. This shows that the response is lagging about –30°. Figure 9.47b is the output after filtering; the lagging angle is about –20°. It can be seen by comparison of Fig. 9.47b with Fig. 9.47a that the dispersion of the latter is smaller than that of the former. This is due to the effect of filtering, which suppresses the short-circuit spike. Moreover, it can be seen that the phase angle after filtering is

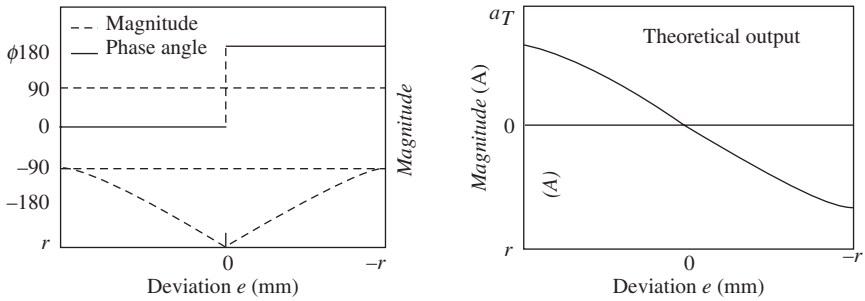

9.46 Theoretical detection characteristics

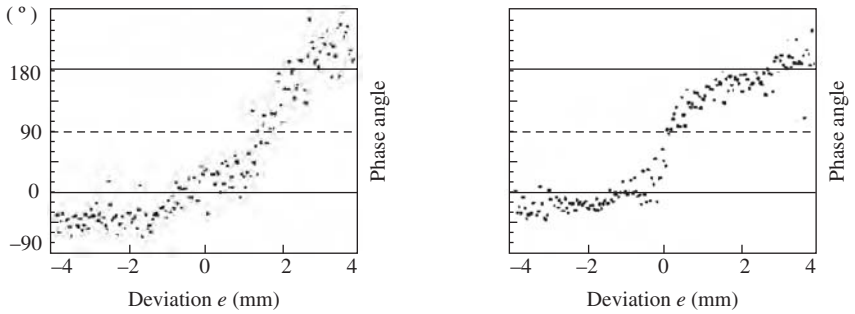

9.47 Detection by the phase angle of the characteristic harmonic

closer to the theoretical value, as shown in Fig. 9.46. When the direction of the deviation is changed, the phase angle does not have a step change. That is caused by the influence of the molten pool. Figure 9.48 shows the detection characteristics. Figure 9.48a is the result obtained by the orthogonalisation treatment for eliminating the effect of the molten pool. Figure 9.48b is the result obtained from the quadrant criterion to judge the direction of the deviation on the basis of the theory described in Section 9.5.

Figure 9.49 is the deviation output obtained directly by orthogonalisation, but without prior phase-angle correction. There is a difference between the detected error and the actual error. This phenomenon coincides with the analysis by simulation made in Section 9.3.

Therefore, if the gain of the sensing system is sufficiently large and the groove contour has obvious changes, the characteristic harmonic vector can be used to detect deviation without prior knowledge of the system, which is simpler and easier to perform.

Figure 9.50 shows the detection characteristics for a corner joint. For the corner joint, the output reaches maximum and is saturated while deviation $|e| > r$ ($r = 2\,\text{mm}$).

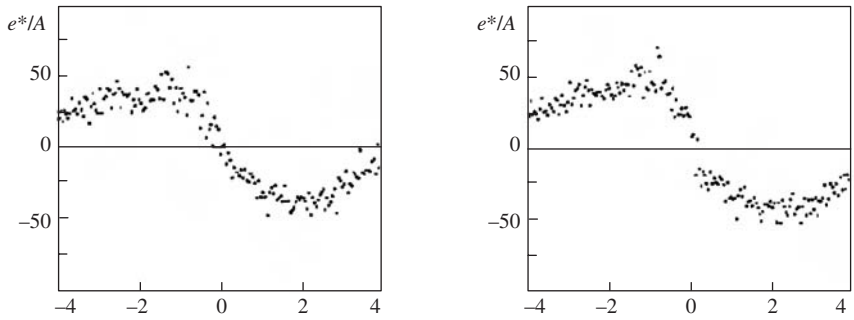

a) Orthogonalisation ($\phi = -24°$)

b) Quadrant criterion ($|\phi| < 90°$)

9.48 Detection characteristics of the sensor

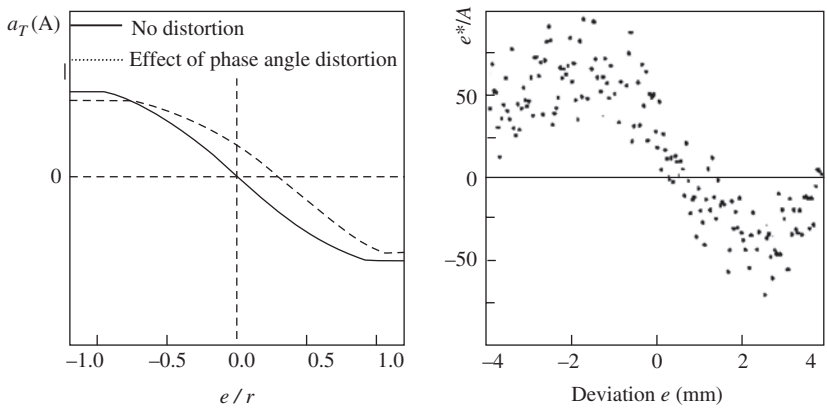

a) Output by simulation

b) Actually detected output

9.49 Detection output for a V-groove without orthogonalisation

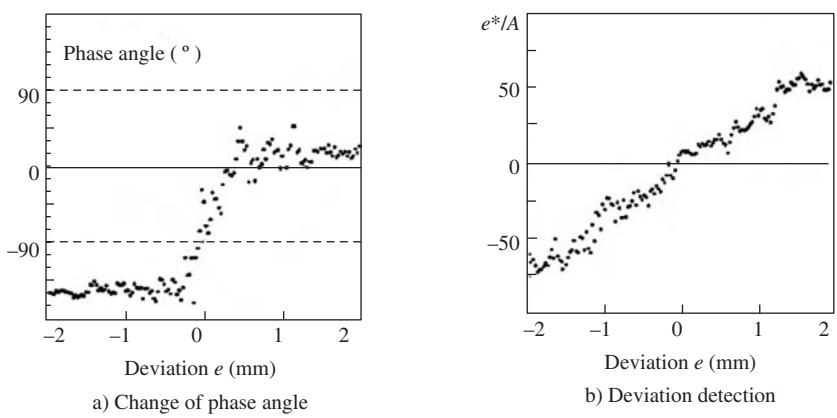

a) Change of phase angle

b) Deviation detection

9.50 Detection characteristics for a corner joint

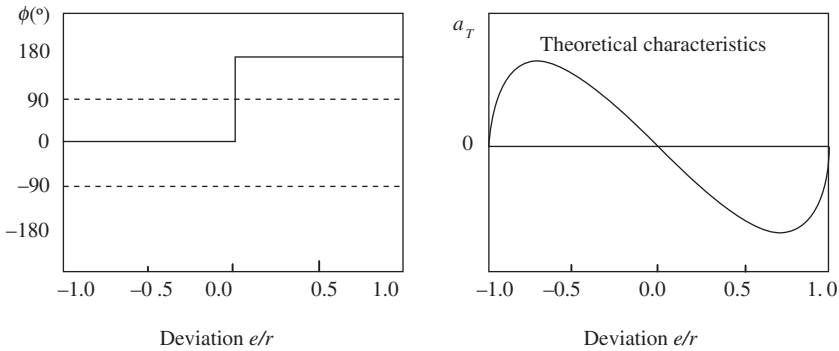

a) Phase-angle change of characteristic harmonic

b) Deviation output

9.51 Theoretical detection characteristics

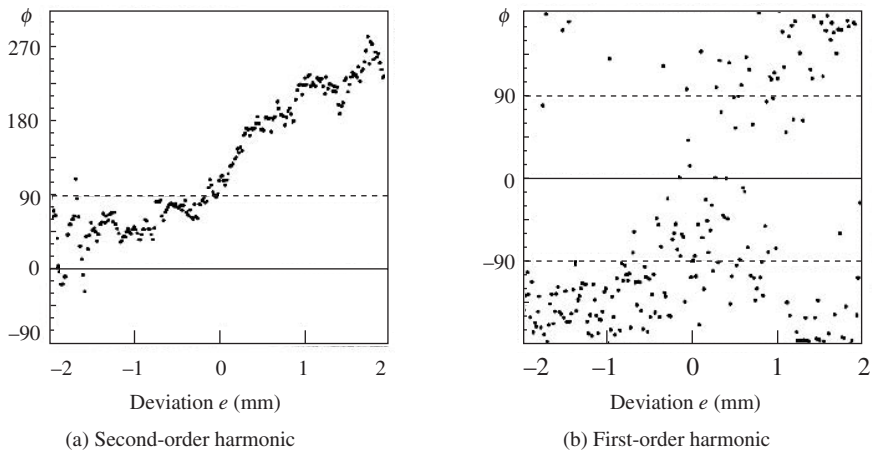

(a) Second-order harmonic

(b) First-order harmonic

9.52 Phase-angle change of harmonics for CO_2 welding of a lap joint

9.5.3.2 Detection in a lap joint

The schematic diagram for this experiment is shown in Fig. 9.45b. The scanning speed was 8 Hz and the plate thickness was $d = 2.0$ mm.

Figure 9.51 shows the variation of the second-order harmonic obtained by simulation on the basis of the theoretical analysis. Figure 9.52a shows the relationship between the phase angle of the second-order harmonic vector and the actually measured deviation e. This shows that the phase angle is leading. The phase-angle data were scattered when the deviation was on the left because there was more globular droplet transfer. The distribution did not change in this quadrant. Figure 9.52b shows the experimental data of the first-order harmonic. It coincides with the theoretical analysis in that the first-order harmonic does not represent the deviation

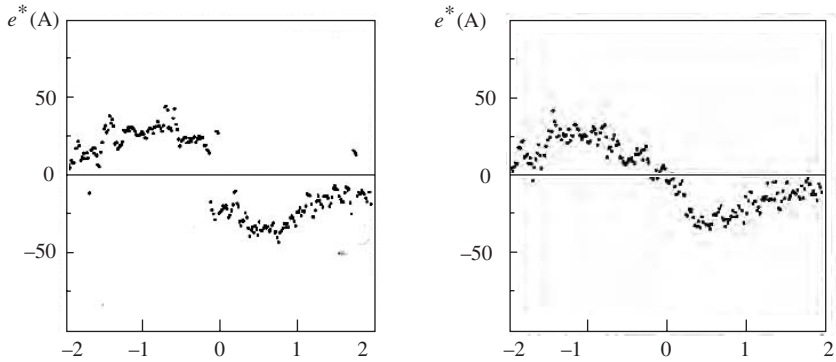

(a) Quadrant criterion (|Ø| < 90°)

(b) Orthogonalisation (Ø = 45°)

9.53 Sensing signal for CO_2 welding of a lap joint

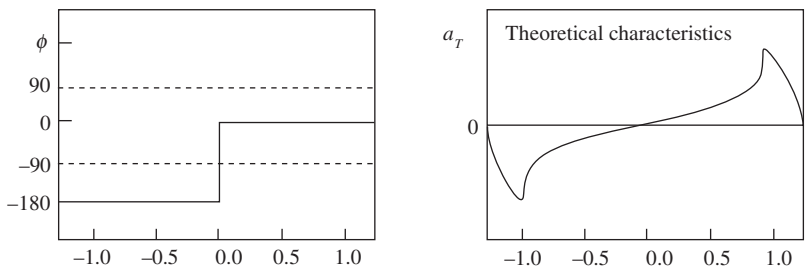

(a) Phase-angle change of the characteristic harmonic

(b) Deviation output

9.54 Theoretical detection characteristics

for a lap joint. The phase angles are close when the deviation is either on the left or on the right ($|\theta| > 90°$).

Figure 9.53 shows the results of the second-order harmonic. It coincides with the theoretical analysis shown in Fig. 9.51 and accurately represents the actual deviation. There is a step change near the centreline of the groove. The orthogonalisation gives good linearity between the harmonic and the deviation (see Fig. 9.53b). It represents the actual deviation.

9.5.3.3 Detection in an I-butt joint

The experiment was conducted as shown in Fig. 9.45c. The plate thickness was $d = 2$ mm and the gap was $w = 2$ mm. Figure 9.54 is the theoretical analysis of the deviation output showing the first-order harmonic. Figure 9.55 is the result obtained by experiments. It shows that the phase angle of the characteristic harmonic was leading. Because the plate thickness was

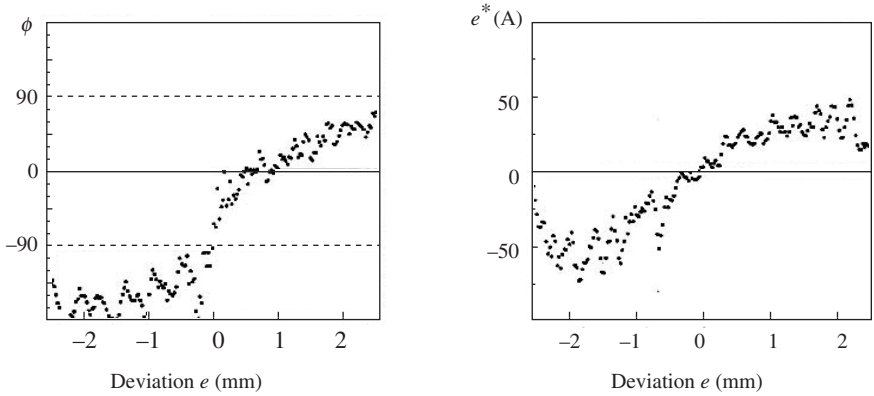

(a) Phase angle of the characteristic harmonic

(b) Deviation

9.55 Sensing signal for CO_2 welding of an I-butt joint

$d = 2$ mm, the molten pool exerted a greater effect on the characteristic harmonic. The phase-angle change was different from the theoretical prediction but, because the quadrant criterion ($|\phi| < 90°$) is still correct for judging the deviation direction, so the final results were correct and coincided with the theoretically predicted values.

Because the variation of the groove shape was small due to small plate thickness, the sensing current and the magnitude of the harmonics were small. However, the sensitivity of the system (a_T/e) reached 10 A/mm, which is quite satisfactory for detection purposes. Even though CO_2 welding involves short-circuiting transfer, the results illustrated a good signal-to-noise ratio for the system.

9.5.4 Signal processing for pulsed-arc welding

The experiment was conducted as shown in Fig. 9.45a. The current waveform that was recorded is shown in Fig. 9.56. The scanning speed was 20 Hz, the current was 180 A, the arc voltage was 28 V, the rotation diameter was 2 mm, and the groove angle was 90°.

It is known from Section 9.4 that for pulsed-arc welding, morphological filtering can improve the current waveform, reduce the effect of frequency-spectrum mixing, and increase the sensitivity of the system. Figure 9.58 shows the phase-angle change obtained directly from the sampled data and after its filtering. This shows that the filtering not only increased the magnitude of the characteristic harmonic but also eliminated the influence of frequency-spectrum mixing. Good results can be obtained using the characteristic harmonic detection method: see Fig. 9.59. Because pulsed-arc

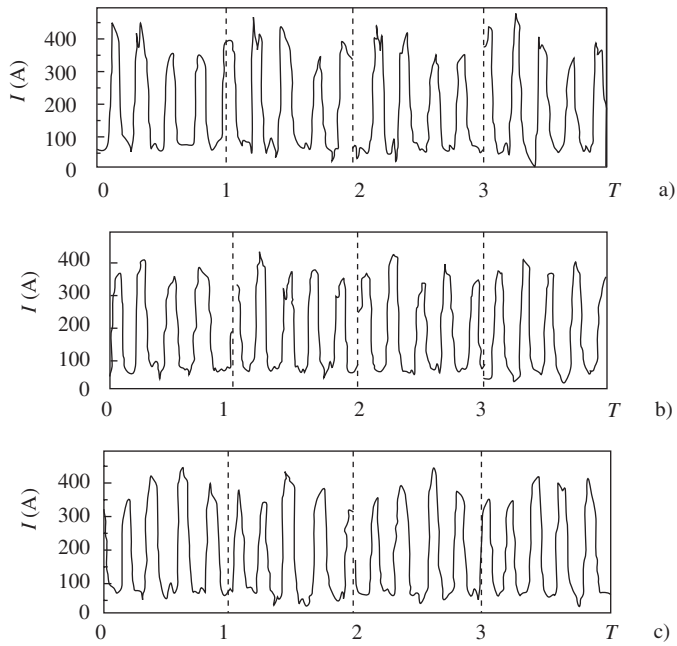

9.56 Current waveform for V-groove pulsed-arc welding (a, on left; b, central; c, right)

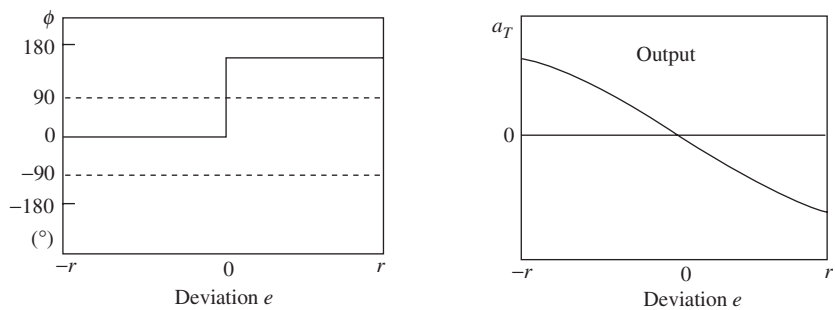

a) Phase-angle change of characteristic harmonce

b) Deviation output

9.57 Theoretical detection characteristics

welding is conducted in an argon-rich gas with a long arc length, the molten pool has less effect on the detection, which can be seen by comparing the phase-angle changes in Figures 9.57 and 9.58.

For comparison, results obtained by signal processing without morphological filtering are shown in Fig. 9.60. Figure 9.60a shows the results obtained by orthogonalisation of the characteristic harmonic, and Fig. 9.60b

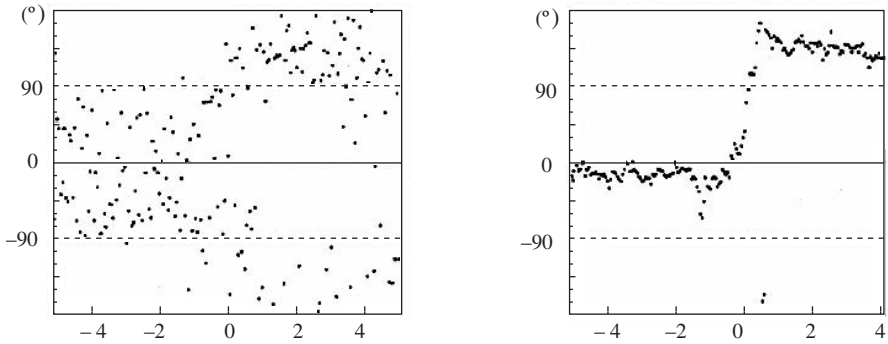

(a) Sampled signal (b) After filtering

9.58 Phase angle change of the first-order harmonic for pulsed-arc welding of a V-groove

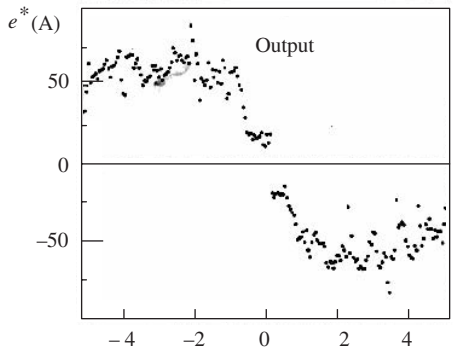

9.59 Arc-sensing characteristics (Quadrant criterion $|\Phi| < 90°$)

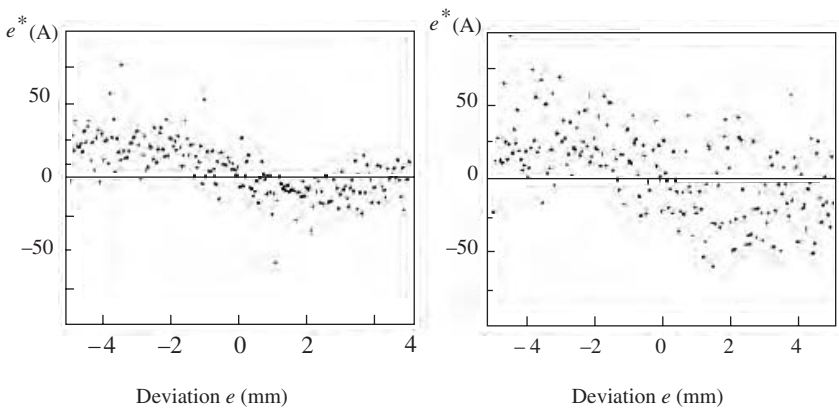

(a) First harmonic (b) By integral difference

9.60 Signal processing without filtering for pulsed-arc welding in a V-groove

was obtained from the integral difference of the first-order harmonic. Both cases give inferior results compared to those of signal processing with filtering and are not acceptable.

All of these results demonstrated that morphological filtering is effective for signal processing of pulsed-arc welding and can be applied in practice.

9.5.5 Summary

From the results described in this section (9.5), the following conclusions may be drawn:

- The effect of the molten pool on the sensing system is inherent in the scanning process. It is impossible to eliminate this effect by filtering. The orthogonalisation introduced in the text is an effective way to solve this problem.
- Experiments proved that the characteristic-harmonic detection method can be used for all kinds of grooves. It has good sensitivity for CO_2 welding, independent of the dynamic properties of the power source and is simple to perform.
- Experiments proved that morphological filtering was effective for signal processing during pulsed-arc welding.

10

An automatic seam-tracking machine with an arc sensor

10.1 Introduction

After several years of study, significant progress has been made in the development of an arc sensor. The volume and weight of the sensor have been greatly reduced and the ability of the sensor to recognise the arc position has been improved. This has enabled two types of automatic seam-tracking machines to be developed by the author, Liao, Liu, and Wu.[379] The first type of machine was constructed using the concept of a conventional arc-welding tractor. Cross-slides were mounted for guiding the torch up and down, and left and right. Because the design was simple, it could be used as the basis for designing a new type of automatic arc-welding machine or it could be used for modifying an existing automated arc-welding machine. The second type was designed to be a new type of automatic arc-welding machine without rails. It has two axes of freedom in the moving plane; therefore it can follow long and curved seams, even on upward or downward inclined planes. Three design features were problematic. The first was providing a suitable sensor, the second was designing a flexible travel mechanism, and the third was the control method. In this Chapter, the design developed by the author that overcame these difficulties is introduced.

10.2 Conventional automatic seam-tracking machine[251,260]

10.2.1 Configuration of a closed-loop control system

Figure 10.1 shows the schematic diagram of the system. It consists of three parts, namely, the arc sensor, a regulation mechanism, and a controller.

10.2.1.1 Arc sensor

The sensor consists of a rotating welding torch, an encoder for detecting the angle of rotation, its control circuit, and a driving mechanism. The fre-

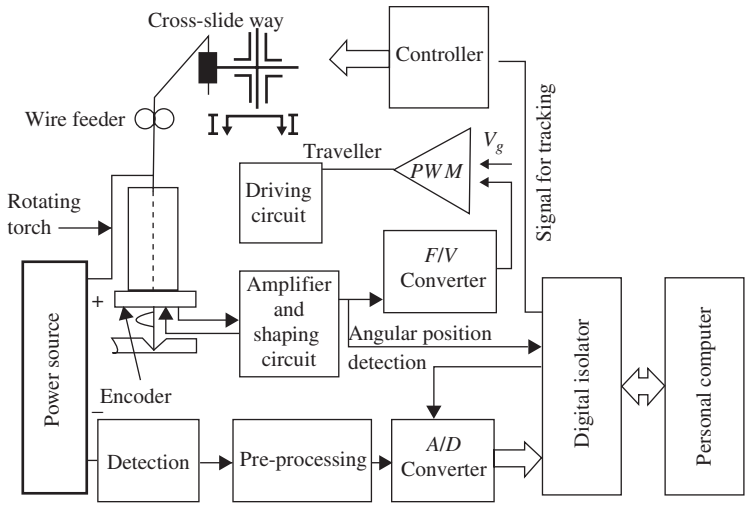

10.1 Schematic diagram of a tracking system using an arc sensor

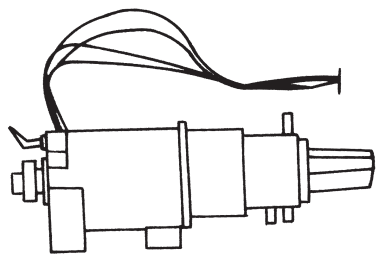

10.2 Schematic drawing of an arc sensor

quency and diameter of rotation of the arc can be regulated. The angular position of the arc is detected by the sensor used for signal processing. The arc sensor, power source, and wire feeder as a whole perform the sensing.

The arc sensor for the rotating arc is shown in Figures 10.2 and 7.26. A torque motor, made using a permanent magnet, is a special feature that was used for driving the torch that can satisfy the requirements for rotational speed and torque with low power-consumption. The design also was suitable for making a hollow shaft so that a compact and simple torch could be constructed. The torch was tightly sealed for reliable operation in the welding environment. It could be applied directly in production.

The design parameters of the arc sensor were as follows. The outside diameter was 62 mm, the length was 200 mm, the torque output was 254 mm, the arc-rotation diameter was 0–7 mm, the voltage was 27 V, and the rotational speed was 0–30 Hz.

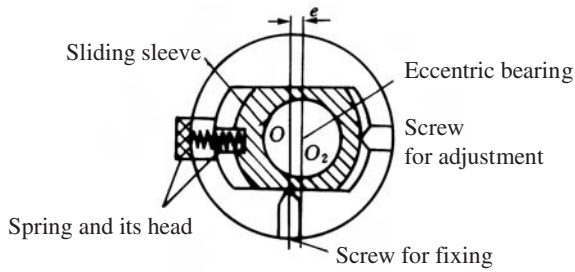

10.3 Principle for eccentricity regulation

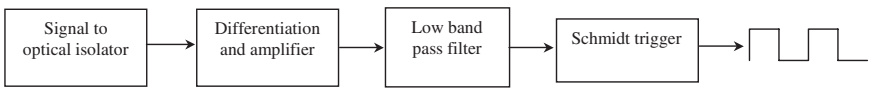

10.4 Signal processing for encoder output

The rotational speed was not the only parameter that was considered; the diameter of rotation should be considered also on the basis of technological requirements and groove type. This diameter can be regulated by an eccentric mechanism, as shown in Fig. 10.3, in which a ball bearing is inserted into a sliding sleeve, which can be moved horizontally and fixed by a screw. In this way the phase angle of the arc is not changed when the diameter is adjusted. The mechanism is simple, compact, and easy to adjust.

An optical encoder was used to detect the angular position of the arc and provide closed-loop control of the rotational speed. Because the characteristics of the optical device were inadequate at high frequency, a differentiation element was used to enhance the gain and a low band-pass filter was used to eliminate high-frequency interference. The pulse signal obtained is transmitted along one path to a computer and along another path to the motor circuit via an *f*/*v* converter (PWM) and an amplifier for closed-loop control of the motor. The principle of the electric circuit is shown in Fig. 10.4.

The rotational frequency of the torch f_s can be obtained from the pulse frequency of the angular position f_d. On the basis of this, a closed-loop system for control of speed using a variable PWM was designed, which showed satisfactory control characteristics. The electrical diagram and waveform of this are shown in Fig. 10.5.

The PWM control system greatly simplifies the hardware and has good control ability. It is robust, and the rotational speed is stable and capable of regulation. The starting characteristics are fast. The circuit operates well in the frequency range of 2–30 Hz.

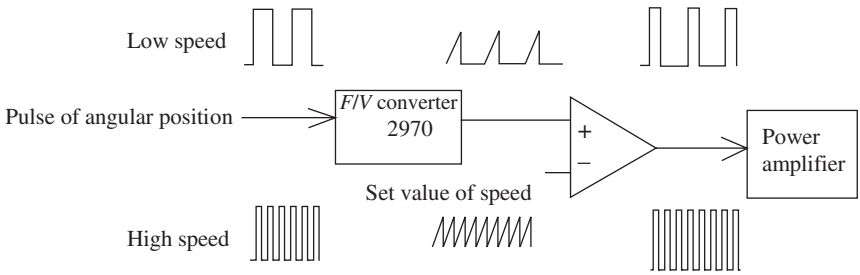

10.5 Speed-control circuit and waveform

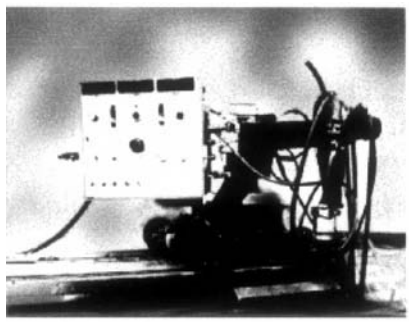

10.6 Automatic seam-tracking machine

10.2.1.2 Actuator

The actuator consisted of a DC servomotor and a cross-slide, made using a guide screw and nut, which moved the torch up and down, and left and right. The rotating-arc sensor, the cross slide and the tractor made up the complete seam-tracking system.

The actuator is an element of the closed-loop control system. Therefore the requirement for its drive system was not rigorous. An open-loop circuit was used for its drive mechanism. There were two windings in the armature. The motor direction was changed by changing the winding. Figure 10.6 shows the appearance of the tracking machine.

The travel distance of the moving nut depends on $s = v \cdot t$, where v is the motor's speed, and t the running time of the motor. Therefore, either v or t can be used to control the moving nut. In the present design, the running duration and direction of rotation of the motor were used for control. A DC-current drive (instead of PWM) system was implemented for simplicity and fast response. The duration was automatically regulated by the control system.

10.7 Computer control system

10.2.1.3 Seam-tracking control system

The welding current was sampled by a Hall-effect sensor that was completely isolated from the main power circuit for welding. The measurement has good linearity, high accuracy, and fast response. The detected current data were converted by an A/D converter and input to the computer. The computer sampled the data using an interrupt mechanism according to the angular position signal of the arc sensor. After proper signal processing, outputs were given to the actuator for seam tracking.

The core of the control system was a 386 DX40 computer, which performed sampling, processing, and control, as shown in Fig. 10.7. The real-time interrupt was used for sampling, processing, and data storage. It had the advantages of high speed, large storage capacity, ease of programming, and a convenient I/O interface. All of the inputs were isolated by an optical coupler. Therefore, it had good resistance to interference and could be used in a shop environment.

The angular-position signal guaranteed evenness of sampling and the starting-point signal guaranteed the space relationships of the signal data. The real-time sampling was performed by an interrupt request. DOS was used as the operating system because some of peripherals allocated by the interrupt were not working while sampling was proceeding, so they could be used as the I/O port for sampling the starting pulse and the angular position pulse. INTR7 and INTR5 were used for this purpose.

Because the optical coupler takes a certain amount of time for data processing, the sampling speed depended on the transfer speed of the optical isolator (The transmission frequency was about 5 kHz). Considering the time needed for the interrupt and data processing, the transfer speed of the optical coupler was not satisfactory. In particular it was hard to use the query mode. In order to solve this problem, time-sharing and multiple operations were used as shown in Fig. 10.8.

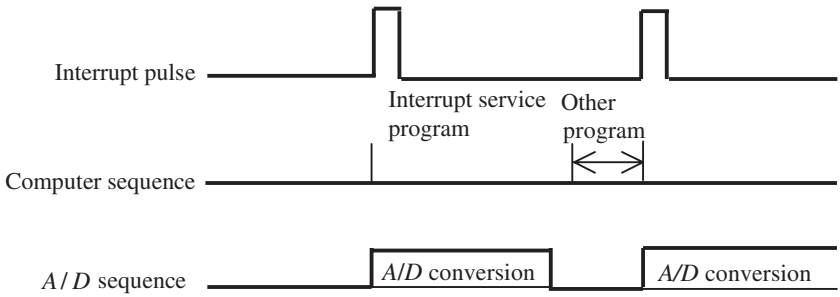

10.8 Time-sequence for digital sampling

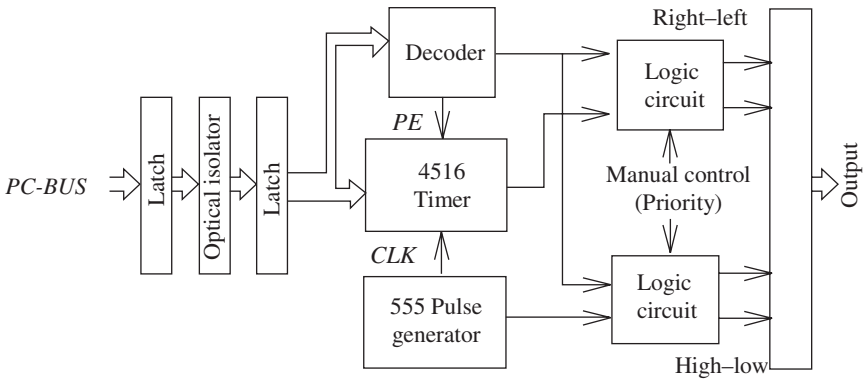

10.9 Schematic diagram of output circuit

When the angular position pulse was received, the computer sampled and pre-processed the data, including A/D starting, resetting, reading A/D and converting data. In order to avoid the waiting time for completion of the A/D conversion, the initial interrupt was used to start and the next interrupt was used to reset and read the data. The duration between the two interrupts was sufficient for A/D conversion and establishment of a data file for the photoelectric device. With the demand on the computer speed reduced, there was no waiting for a query and more time was available for the sensor's signal processing and real-time control.

The output circuit is shown in Fig. 10.9. In order to simplify the hardware, the outputs were digital (8 bit). They were sent to an MC4516 decoder and 555 timer, via a latch and optical coupler. The current duration and direction were input to the servomotor. The logic-control circuit controlled the direction of the motor but there also was manual control, which was a priority.

The schematic diagram of the closed-loop control seam-tracking system is shown in Fig. 10.10. The input to the system was the groove position and

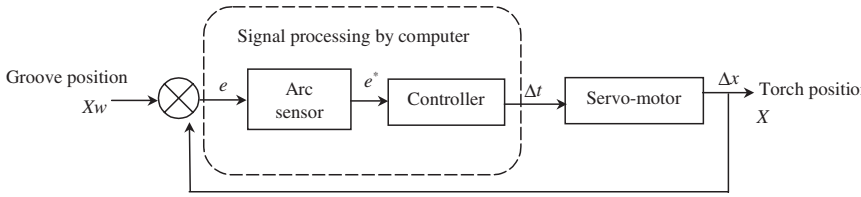

10.10 Schematic diagram of the closed-loop seam-tracking control

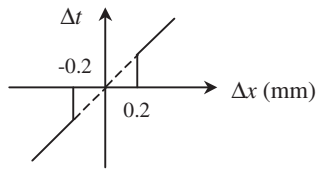

10.11 Output of the control system

the output was the torch position. When there was a deviation between the torch and groove position, e, the control system would produce an output current with a certain duration and direction to move the torch in the direction to decrease the deviation e.[380]

The features of the system were as follows:

- A high rotational speed of the arc that increased the sensitivity of the sensor.
- The characteristic harmonic-vector method that increased the accuracy of detection.
- A 386 computer-based control system that had a large memory, high operation speed, and real-time interrupt handling, and which could effectively process and operate the signals.

The system met all of the requirements for seam tracking and the hardware was simple. Moreover the I/O interface was available and convenient for other uses.

10.2.2 Control method

It is known from the experiments described in Chapter 9 that the signal generated by the sensor is linear. Therefore according to the control rule, $\Delta t = ke^*$, Δt was used for PID control of the system. Considering interference, which may come from the droplet transfer, gaps in the mechanical parts of the actuator, etc., the control rule shown in Fig. 10.11 was applied.

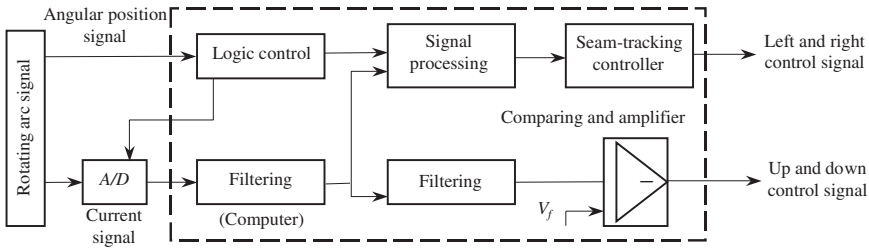

10.12 Schematic diagram of the signal-processing circuit

It can be seen that there was a dead zone of 0.2 mm. When the detected deviation was between ±0.2 mm, the torch was considered to be on the centreline of the groove; no output was sent to the actuator.

Control of the vertical position of the torch was simpler. The torch height is proportional to the current under a given arc voltage and wire-feed rate,[244] which can be written as $H = kI + b$, where k and b are constants, $k < 0$.

The torch-height variation can be obtained from the average current variation and thus be controlled.

Because the detected deviation data can be obtained only once after each oscillation of the torch, the duration between two output signals depended on the rotational speed of the torch. Fortunately, the travel speed during welding was low. Experiments proved that an output frequency of about 3~5 times per second was enough for seam tracking.

10.2.3 Software design

The schematic diagram of the signal-processing circuit is shown in Fig. 10.12. The main task of the circuit was to take the angular-position signal, sample the current signal, judge the short-circuit current, filter the signal, obtain the deviation signal, and deliver an output-control signal. All of these processes including sampling, processing, and output were performed using a personal computer.

The flow chart of the control system is shown in Fig. 10.13. The initial program performed the following tasks.

- Allocation of data and main variables in memory.
- Setting up a data file.
- Setting up control ports, interrupt vector, and protection system.
- Setting up characteristic values and control data.

The initial program for starting the angular-position pulse was

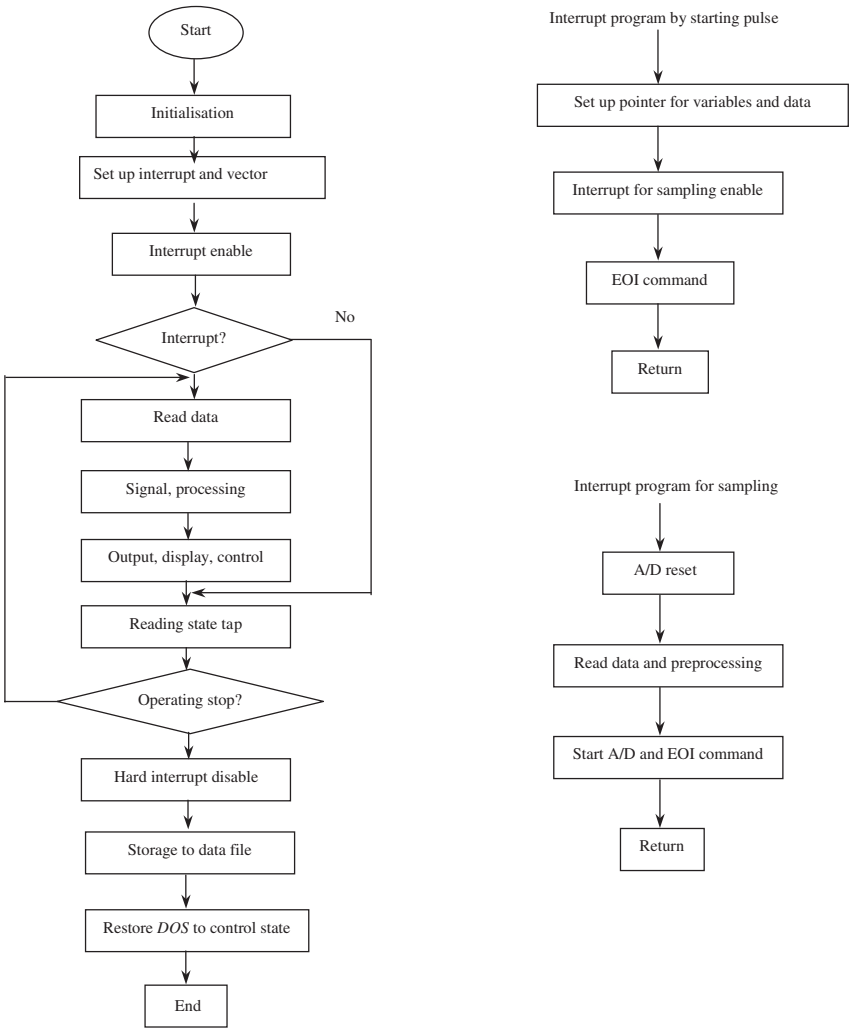

10.13 Flow chart of the control system

- Setting up the data pointer and main variables.
- Enabling the interrupt for sampling.

This guaranteed the location of the memory for the data and the integrity of sampled data for each rotation.

The software provided digital filtering, analysis of harmonic vectors, data display, operation of data files, real-time data sampling, and processing and transmission of output control signals, etc.

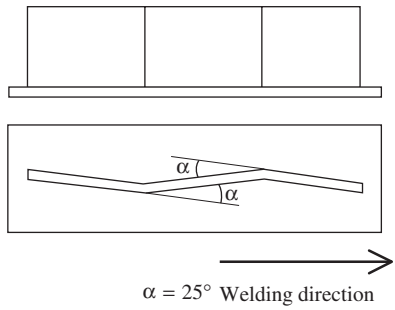

10.14 Workpiece

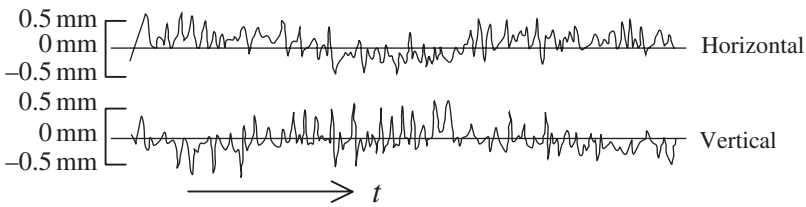

10.15 Output of error signal

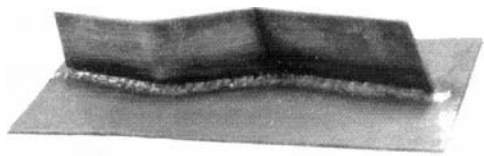

10.16 Appearance of weld obtained by automatic seam tracking

10.2.4 Experimental results

A zigzag three-dimensional groove, shown in Fig. 10.14, was used for experiments with CO_2 welding. The angle α was 25°. Both the horizontal and vertical angles of the weld path were 18°. Figure 10.15 shows the output of the control system for tracking the seam. Figure 10.16 is a photograph of the weld, which demonstrated good control characteristics. The welding parameters were: plate thickness d = 2.0 mm, welding current I = 120 A, arc voltage U = 19.5 V, and welding speed V = 550 mm/min.

Figure 10.17 is a schematic drawing of a sheet butt joint. Figure 10.18 is the weld that was obtained. Lap joints also were welded using sheet thicknesses of 2.0 + 2.0 mm and 1.5 + 1.5 mm (Fig. 10.19). The results demonstrated good control. The bead obtained was wide with good formation (see

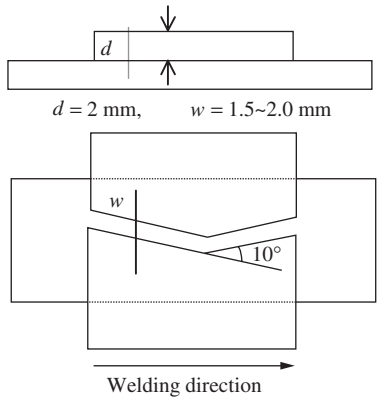

10.17 I-butt weld

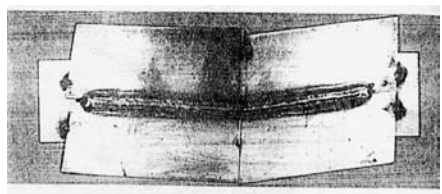

10.18 I-butt weld obtained with automatic seam tracking

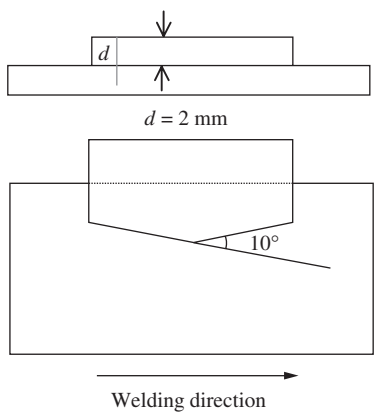

10.19 Lap joint

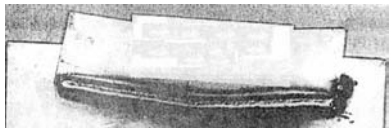

$\phi = 1.0\,\text{mm}$, $I = 110\,\text{A}$, $U = 19\,\text{V}$
$d = 2.0\,\text{mm}$, $r = 2.0\,\text{mm}$, $f_s = 10\,\text{Hz}$
$V_w = 430\,\text{mm/min}$

a) Lap joint ($d = 2.0\,\text{mm}$)

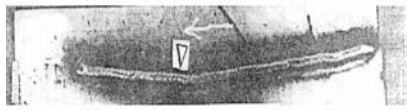

$\phi = 1.0\,\text{mm}$, $I = 110\,\text{A}$, $U = 19\,\text{V}$
$d = 1.5\,\text{mm}$, $r = 2.0\,\text{mm}$, $f_s = 10\,\text{Hz}$
$V_w = 430\,\text{mm/min}$

b) Lap joint ($d = 1.5\,\text{mm}$)

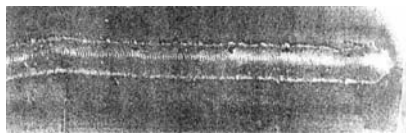

c) Appearance of weld obtained using a rotating arc

10.20 Results of automatic seam tracking

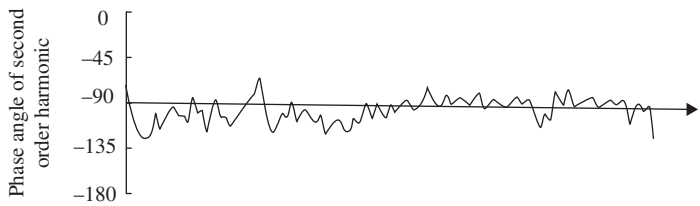

10.21 Change in the phase angle of the characteristic harmonic vector during seam tracking

Fig. 10.20). In the picture there is a triangle indicating the location of the tack weld, which means that satisfactory seam tracking could be obtained without failure even across the tack weld. Figure 10.21 shows the phase angle of the characteristic harmonic vector. In the first half of the weld, the torch was closer to one edge of the seam and in the second half of the weld, the torch was farther away from the edge of seam, so the phase angles had opposite signs. It can be observed that the phase angle changed significantly due to the presence of the tack weld.

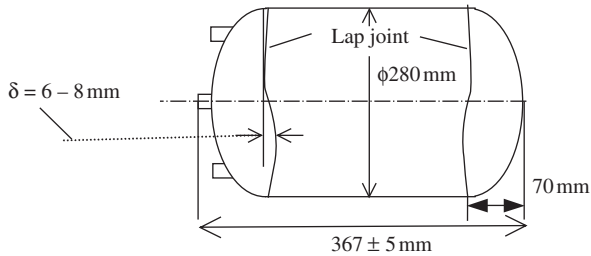

10.22 Schematic drawing of the product

10.2.5 Practical application

10.2.5.1 Introduction to a product

A gas storage vessel, shown in Fig. 10.22, was manufactured by an automobile company. Two heads were welded to the body using lap joints and automatic CO_2 welding. The torch was stationary and the workpiece rotated. The geometrical variations of the assembly were as follows. Out-of-roundness was ≤10 mm, plate thickness was 2–2.5 mm, the groove deviation was δ = 6–8 mm, the error of the vessel's body edge was ≤3 mm, and the gap between the head and the vessel body was ≤2 mm. The requirements of the weld were good appearance, a bead width >5 mm, no undercut, and 100% qualification by leak testing to an internal pressure of 0.8 MPa.

There was inevitable error in the assembly and fixturing of the workpiece. The turntable may shift the workpiece to the right or the left due to its own inaccuracy. Therefore, the application of automatic seam tracking was significant. In the present production line, the torch position was adjusted manually using visual judgment. The labour intensity was high and the welding speed was limited to 600~700 mm/min. The quality of the welds could not be guaranteed and the amount of repair work to salvage rejected vessels was significant.

Up to the present, no report could be found in the literature worldwide regarding automatic seam tracking of such a product. The difficulties to that must be surmounted are as follows:

- Conventional sensing systems do not work well under conditions of high temperature, high-intensity light, high current, and welding fume that is generated.
- Interference and spatter are more prominent in CO_2 welding.
- Due to the small diameter of the vessel, an attached type of sensor could not be used readily, particularly for high-speed welding.

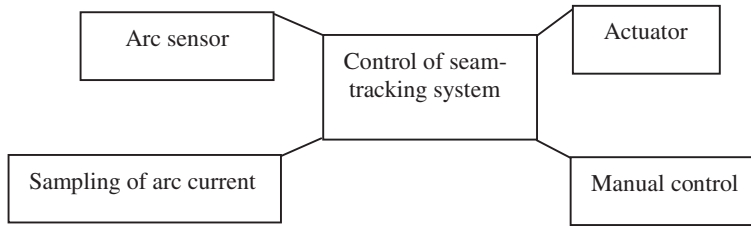

10.23 Schematic diagram of the system

- Because the sheet was thin, it was hard to detect the groove-shape variation.
- The small working space required a compact sensor and torch.
- Two-directional seam tracking was required.

The welding parameters used in present experiments were a wire diameter of ϕ1.6 mm, an arc current of 180~250 A, and an arc voltage of 20~25 V.

10.2.5.2 Description of the design

An arc sensor was chosen for this application. Because the sensor and the welding arc were combined, there was no additional attachment. Its resistance to heat, light interference, etc. was high. High welding current could be used for high welding speed and thus ensure high efficiency. A special design was made by Tsinghua University; the schematic diagram is shown in Fig. 10.23.

10.2.5.3 Configuration of the system

(i) *Control system.* A single-board computer (Intel 8089) was chosen as the core of the control system; it performed sampling, data processing and output control-signal transmission. Compared to other types of single board computers, the 8089 had the following advantages.

- 10 bits for the A/D converter and 22 μs speed.
- Multi-pass high-speed input (HSI) and high-speed output (HSO). The input signal's variation could be recorded and the output port's level could be changed in real time without the intervention of the CPU.
- Multiplication and division commands at 16 bits, speed 6 μs.
- The master-clock frequency was 12 MHz, a high speed of data processing. An STD bus and modular construction were used for the computer.

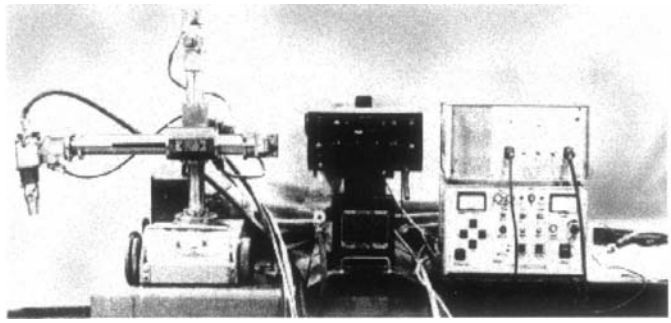

10.24 Machine for industrial application

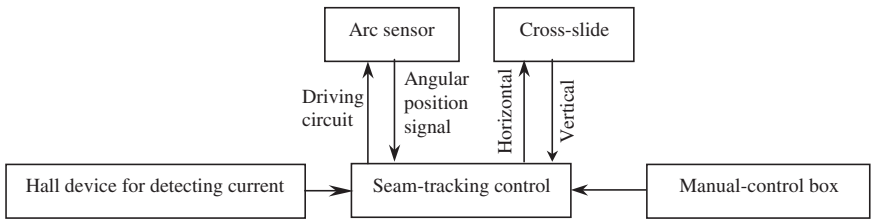

10.25 Schematic diagram of the system

(ii) *Arc sensor.* The construction of the sensor was described in Section 10.2.

(iii) *Measurement of arc current.* Because there was an A/D converter inside the 8089, it was simpler. The current was measured by a Hall device and input into the computer via an optical coupler.

(iv) *Actuator.* A cross-slide was used for automatic adjustment of the torch. Because fume was generated by the arc, the mechanism was sealed: see Fig. 10.24.

(v) *Manual control.* Manual control is incorporated into the design. All of the switches were mounted on the control box as shown in Fig. 10.24. The schematic diagram is shown in Fig. 10.25.

In addition to the parts mentioned above, there was the welding power source, wire feeder, and tractor, which are the basic components for CO_2 welding.

The machine showed good performance in practice.

10.3 Crawling type of tractor[245]

For welding long seams in the field, conventional welding tractors are difficult to use, particularly for curved seams or seams that have up and down

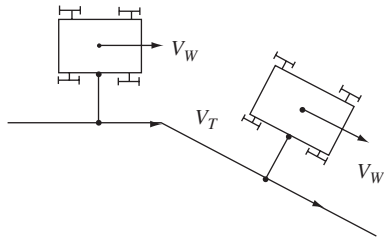

10.26 Schematic diagram showing turning of the tractor

slopes. Developing a crawling type of welding tractor is an important area of welding automation for the future.[349] To realise this goal is difficult because the sensor, tractor and control system are complicated. The sensor has been described in detail in the previous three chapters. Therefore only the tractor and control system are discussed in this chapter.

10.3.1 Structure of the tractor

According to the aims of the design, the tractor should be able to travel up and down on an inclined surface. It should be able to follow the seam whether the seam is curved or turns abruptly, using the signal from the arc sensor while the speed of the welding torch is kept constant (see Fig. 10.26). Moreover, the attitude of the torch should be changed according to the position of the torch. In the present design, the attitude in the left and right direction was adjusted manually and the attitude toward the front and rear was adjusted by a motor that was controlled manually. In addition, the tractor should support itself on an inclined surface to overcome its own weight.

10.3.1.1 Structure of the tractor and the motion analysis

According to the requirements given previously, the following choices can be considered:

(i) Automobile construction: see Fig. 10.27a. The front wheels are manipulated by a multi-rod mechanism so that their axes intersect the axis of two rear wheels. The intersection point is the instantaneous centre of movement. The rotational speed of two rear wheels is adjusted by a differential gear mechanism so that the tractor turns around the centre. The direction and speed can be adjusted independently. The shortcomings are that it is a complicated mechanism and has only a limited turning radius.

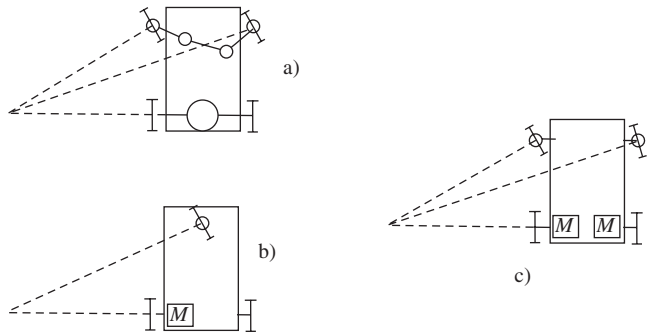

10.27 Construction concepts for the tractor

(ii) Tricycle construction as shown in Fig. 10.27b. A single front wheel controls the direction. One of the rear wheels is driven and the instantaneous centre of turning is the intersection of the axis of the front wheel and the rear wheel. Both the direction and speed are controllable but there is a dead zone; it is impossible to turn the car near the rear wheel. The problem can be overcome by driving from the front wheel. The mechanism is complicated because the driving mechanism and direction control mechanism are on one wheel.

(iii) Two-wheel drive construction: see Fig. 10.27c. Two front or rear wheels are driven separately; two other wheels are universal. From kinematics, if two wheels are moving in the same direction, then the instantaneous centre is on the line (or extended line) connecting the centre of these two wheels. Changing the speed of the two wheels can change the travel speed and direction of the carriage. This kind of mechanism is simple, there is no dead zone of the movement, and the carriage can turn around any arbitrary instantaneous centre on the axis line between the two wheels. The driving circuit and control are the same for both wheels.

As described above, the two-wheel drive mechanism is effective and very simple in construction and control, but the movement of the carriage on the plate is by reaction to a frictional force. Therefore, the accuracy of movement control is poor. In order to improve the precision of torch-movement control, a cross-slide was designed and mounted on the carriage to hold the torch so that control of the torch movement was based on the slide together with the carriage movement.

In the design of the mechanism, there were two motors for driving each of the two wheels, two motors for driving the cross-slides, one motor for adjusting the altitude of the torch in the front and rear direction, and one

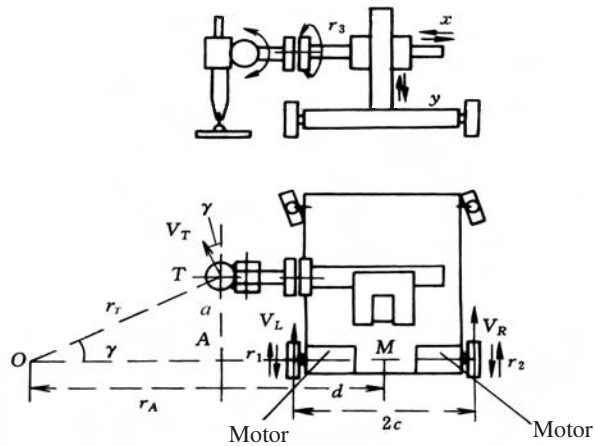

10.28 Schematic drawing of the tractor's construction

motor for the arc sensor. Altogether there were six motors for five axes of freedom. To work on an inclined surface, permanent magnets were used for the wheel. Rubber wheels, which could be used when magnetic wheels are not needed, were also available.

The schematic diagram of the tractor's construction is shown in Fig. 10.28. The distance between the two wheels is $2c$, the torch-to-car centreline distance is d, and the torch-to-wheel axis distance is a. The movement of the car can be analysed as follows:

To perform a qualified welding process, the machine is required to follow the seam automatically on the one hand and keep the welding velocity constant on the other hand. Assuming that the effect of cross-slide regulation for the torch movement is small and can be neglected, then for a given welding speed V_T, the velocity of the two wheels while the tractor is turning around the center 0 can be calculated from the following equations.

$$r_A = \frac{a}{tg\gamma}, \quad r_T = \frac{a}{\sin\gamma}, \quad r_m = r_A + a, \quad V_L = \frac{r_m - c}{r_T} V_T, \quad V_R = \frac{r_m + c}{r_T} V_T \quad [10.1]$$

where γ is the angle between the travel direction of the torch and the tractor's longitudinal axis. It can be seen that in the case where $a = 0$, it is impossible to have $\gamma \neq 0$. This means if the torch is on the axis of the wheel, its velocity direction cannot be changed abruptly. Its trajectory is a curve of a continuous tangent line, i.e. it is impossible to follow a sharply turning seam. If $a > 0$ or if the torch is in front of the wheels, it is possible for the tractor to follow a sharply turning groove line. If $a < 0$, or the torch is behind the wheel, the direction of torch movement will deviate from the groove

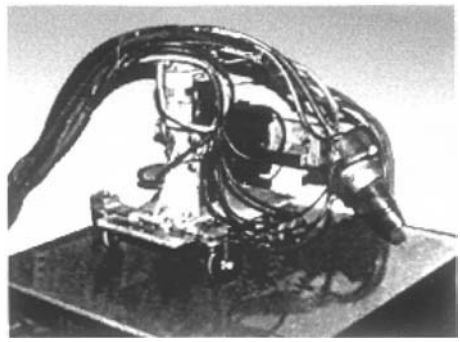

10.29 Outside view of the multi-axis tractor

line when the tractor is turning. Therefore, it is preferable to set the torch in front of the wheel axis.

The distance d was determined by the construction of the tractor and preferably is small; $d = 455$ mm was taken for the nut on the center of the slide and the attitude of torch ϕ was inclined to the right at 45°. The distance $2c$ was determined by the requirement for stability and the magnetic force needed for the tractor. In the present design, $2c = 222$ mm. Figure 10.29 shows the outside view of the tractor.

10.3.1.2 Description of the driving mechanism

The normal welding speed is 0.2~0.6 m/min, so 1.2 m/min was taken as the upper limit of the tractor speed. According to the kinematics principles for two-wheel drive systems, the wheel velocity is much higher than the welding velocity when the instantaneous centre of turning is very near to the tractor. It can be derived (see Fig. 10.29 and Eq. [10.1]) as the following equations:

$$\frac{r_L}{r_T} = A_1 \sin(\gamma + \varphi_1); \quad \frac{r_R}{r_T} = A_2 \sin(\gamma + \varphi_2)$$

where A_1 and A_2 are the maximum ratios of wheel velocities (left and right) to the welding speed;

$$A_1 = \sqrt{1 + \left(\frac{l_1}{a}\right)^2}, \quad A_2 = \sqrt{1 + \left(\frac{l_2}{a}\right)^2}$$

$$\varphi_1 = \arcsin\frac{1}{A_1}, \quad \varphi_2 = \arcsin\frac{1}{A_2}$$

where $l_1 = d - c$, $l_2 = d + c$. When $a = 100$, $2c = 220$, $d = 436$ mm, the ratio of the right-wheel velocity to the welding speed can reach $A_2 = 5.6$ when

the turning angle (to the left) $r = 72.90$ or $r_A = 31$ mm. If a is changed to 50 mm and the other parameters remain unchanged, the ratio A_2 reaches a maximum value of 11.0 when $r = 81.4°$. Obviously a has great influence on the ratio. Smaller values of d are preferable but is the values are restricted by the tractor's construction. Therefore, it is appropriate to use a larger value of a.

The wheels were driven by a motor that provided a maximum rotational speed of 30 r/min and a velocity of 7.5 m/min for a wheel diameter of 80 mm. A suitable reduction gearbox was used for the driving wheel. The power of the motor was about 40 W.

The possible choices for the motors are DC servo motors, DC torque motors, step motors and AC servo motors. Although the last two types of motors introduce complications, they are suitable for light loads and a wide range of velocities. DC torque motors have lower speed but they have a large diameter, which increases the height of the tractor, which makes it inconvenient to travel on a vertical surface. DC servomotors were chosen for the present design. A closed-loop control circuit was used for the speed control, which increases accuracy and the response characteristics of the tractor.

The 70SZ54 motor specification includes $n_e = 3000$ r/min and $M = 1.7$ N·cm.

The reduction mechanism had a velocity ratio = 90, one pair of reduction gears, and a pair of worm gears.

10.3.1.3 Closed-loop control circuit

It can be seen that the velocity of the wheels is an important parameter for the tractor. In order to obtain accurate control of the tractor, an optical velocity measuring system and a closed-loop control system were incorporated. The velocity is stable even at low speed. The system consisted of the following parts:

- Velocity set value. The output of the computer is the set value for the velocity after D/A conversion. The tractor also can be controlled manually. There are four modes of movement, namely, (i) travelling along a straight line; (ii) turning around the centrepoint of the axis between the two wheels; (iii) turning around any point on the axis of the two wheels; and (iv) moving according to the set value of the computer.

  The set value was $-5\,V$ to $+5\,V$ for speeds between -7 m/min and $+7$ m/min.

  The control circuit is shown in Fig. 10.30a. V_W is the set value for the welding speed. V_{gl} and V_{gr} are the signals that control the speed of the left and right wheel, respectively. S_1 and S_2 are the control signals for

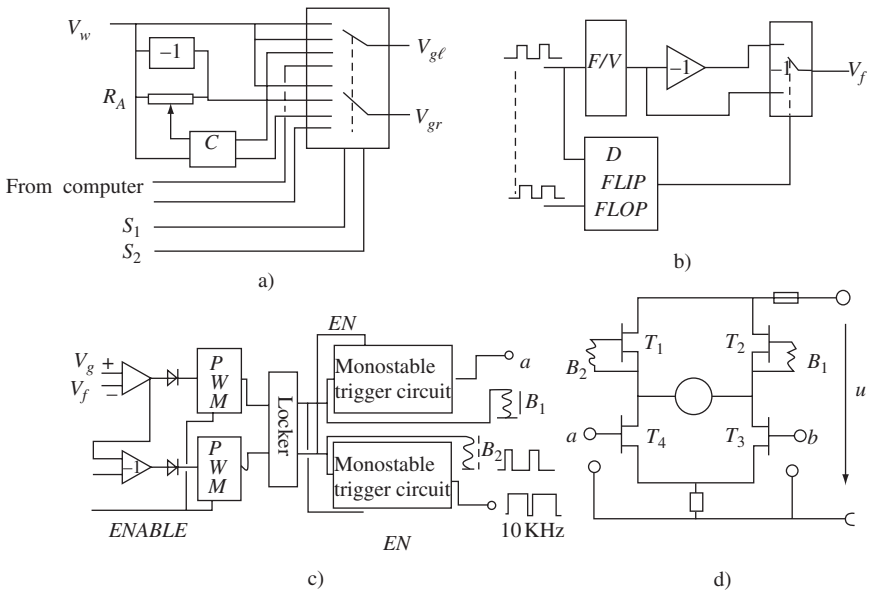

10.30 Wheel-velocity regulation circuit

selecting the mode of movement; they change V_{gb} and V_{gr} (the set value for left and right wheel speeds) via an electronic switch and network. B_1 and B_2 represent primary coils of pulse transformers, both lower ends are connected to the ground. When the first channel is connected, V_{gb} and V_{gr} are equal to V_w and the tractor moves forward along a straight line. When the second channel is connected, $V_{gl} = V_w/k$, $V_{gr} = -V_w/k$, the tractor turns around the centre M (see Fig. 10.28), where $k = \frac{}{\sqrt{a^2 + d^2}}$, which is preset for keeping the welding speed V_w constant. When the third channel is connected, the tractor turns around a centre depending on the set value R_A. When the fourth channel is connected, the velocity of the wheels depends on the commands of the computer.

- Velocity measurement. There were two choices for measuring velocity, namely, a tachometer and an encoder. In the present design, a low-cost, lightweight encoder was chosen. The device is similar to the arc sensor but the motor can turn in either direction. Therefore, the detecting pulses should be able to be sensed in some way. Two pairs of optical couplers were installed in the motor with a phase-angle difference of 90°. The direction of rotation can be detected by the phase angle. In the present design, trigger D was used for judging the direction of rotation.

  The optical encoder was made of a disc with teeth and mounted directly on the motor to obtain greater accuracy. There were 72 teeth

on the disc, which can satisfy the design requirement even at low speeds. For example, if the wheel velocity is 168 mm/min, (a rotational speed of 60 r/min, or 1 turn/s) 72 signals can be obtained per second. Increasing the number of teeth is obviously good for accuracy but manufacturing the disc is more difficult.

The pulse frequency was converted into an analogue signal by an F/V device. Taking the pulse series of either phase and connecting with the F/V circuit, the rotational speed can be obtained. To recognise the direction of rotation, the output pulses of the two phases were connected respectively to the data input (D) and the clock input of a D-type flip-flop (see Fig. 10.30b). The D flip-flop was triggered by the leading edge of the pulse and its output Q was taken for control. If the signal at D was leading the signal at the clock, the output was logic 1; in the reverse case the output was logic 0. This output controlled the electronic switch V_f, so that the positive or negative value of F/V was connected to the motor's closed-loop control circuit.

- Reversible driving circuit (Fig. 10.30c). When the turning radius is small, reverse rotation of the motor is necessary. It was produced by reversing the voltage polarity across the armature. A full-bridge circuit with a MOSFET device was designed for this purpose. The MOSFET worked in the switching mode and the PWM was used for power regulation. A pulse transformer was used to isolate the control circuit with power elements. The parameters of the MOSFET were 9 A, 450 V. The working frequency of the MOSFET was 10 kHz and the voltage across it was 48 V at 2 A.
- PWM and interlock circuit (Fig. 10.30d). This circuit performs subtraction of the set value from the feedback velocity signal, and amplifies and transforms it to the pulse width. When $V_g - V_f$ was positive, the upper PWM operated and output a pulse making the motor rotate in the positive direction. When $V_g - V_f$ was negative, the opposite was the case. T_1 and T_3 were conducting when the motor was driven in the positive direction. Because T_1 was in the switching mode, T_3 was required to switch on during the entire duration of the cycle to ensure continuous current flow. A monostable trigger circuit was used for control. T_1 was driven by the PWM signal from the pulse generator B_2. T_3 was driven directly by the corresponding PWM signal. The duty cycle was nearly 100% so that T_3 continued conducting at any time when T_1 was triggered. To prevent simultaneous conducting of T_1 and T_4 or T_2 and T_3, an interlock circuit was designed. The PWM signal of one path was allowed to input only when the PWM signal of another path reached a low level and after a certain delay. This means that once there was a driven signal on T_1 or T_2, the monostable trigger circuit was prohibited from inputting to the MOSFET on the same bridge arm.

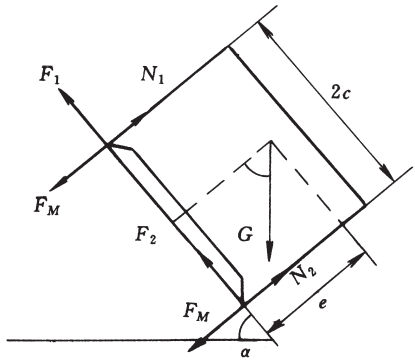

10.31 Forces on the tractor on an inclined surface

Experimental results demonstrated good reliability. The circuit could adapt to a wide range of load and was stable at low speed. The velocity range was 90~2700 r/min. The MOSFET worked without a heat sink.

In order to obtain perfect symmetry of both the left- and right-wheel control circuits, debugging was necessary. In the case of closed-loop control, however, the requirement for symmetry is not rigorous. To ensure the accuracy of travel along a straight line, a circuit was specially designed on the basis of the signal $V_{fL} - V_{fR}$.

10.3.1.4 The magnetic force

One important aim of the design was to enable the tractor to travel on inclined or vertical surfaces. Therefore, it needed to have a normal force to the work-piece from the tractor. A magnetic wheel was designed for this purpose.

Suppose that the tractor is travelling on an inclined surface, as shown in Fig. 10.31. The condition for not slipping is

$$f(N_1 + N_2) \geq G \sin\alpha$$

where f is the friction coefficient, G is the tractor's weight, and N_1 and N_2 are the reaction forces of the inclined surface to the tractor.

Because $$N_1 + N_2 = G\cos\alpha + 2F_m,$$

where F_m is the magnetic force of the two left or right wheels, the following equation can be derived:

$$F_m \geq \frac{G}{2}\left(\frac{1}{f}\sin\alpha - \cos\alpha\right) = \frac{G\sqrt{1+f^2}}{2f}\sin(\alpha - \beta) \qquad [10.2]$$

where $\sin\beta = \frac{f}{\sqrt{1+f^2}}, \cos\beta = \frac{1}{\sqrt{1+f^2}}$

The required F_m is given by: $F_m = \frac{G}{2}\frac{\sqrt{1+f^2}}{f}$ (10.3)

According to available data $f = 0.1$~0.15. We can show that $F_m \geq 5G$ when the tractor is in an almost vertical position because

$$\beta = \arccos\frac{1}{\sqrt{1+f^2}} = 5.7°$$

$$\alpha = 95.7°$$

To avoid tipping over, another condition for equilibrium should be considered: see Fig. 10.31.

$$F_m 2c \geq N_1 2c + G(e\sin\alpha - c\cos\alpha)$$

At the critical point of tipping over, $N_1 = 0$, therefore

$$F_m \geq \frac{G}{2}\left(\frac{e}{2}\sin\alpha - c\cos\alpha\right) = \frac{G}{2}\frac{\sqrt{1+(c/e)^2}}{c/e}\sin(\alpha-\gamma) \quad [10.4]$$

where $\gamma = \arccos\frac{1}{\sqrt{1+(c/e)^2}}$

The F_m required is

$$F_m = \frac{G\sqrt{1+(c/e)^2}}{2c/e} \quad [10.5]$$

It can be seen that decreasing the height of the center of gravity and increasing the distance between the two wheels are effective. In the case of horizontal welding, the distance between the two wheels is important.

Comparing Equations [10.3] and [10.5], we find that the magnetic force should be calculated by the principle that sliding should not take place, as $c/e >> f$,

Supposing that the tractor weight is $G = 10$ kg, then the magnetic force should be 100 kg, or 25 kg per wheel in the case where $f = 0.1$. The force should be larger if the speed variation of a wheel on a curved path and acceleration are considered.

The specification for the electromagnet can be calculated according to a reference.[282] The results were a 0.56 mm wire diameter with 2500 turns, an outside diameter of the wheel of 84 mm, and a pole thickness of 4 mm. The

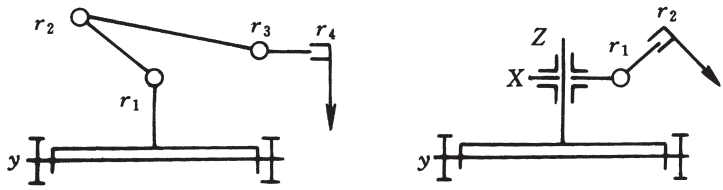

10.32 Mechanism for horizontal and vertical regulation

actual magnetic force obtained and experimentally measured was 65 N, which was sufficient for a tractor on a 20° inclined surface.

The connection of electrical power to the magnetic wheels is difficult because the wheels rotate. There is a risk that the tractor may fall down once the electricity is disconnected. Therefore, it is more reliable to use high-quality permanent magnets. A larger wheel diameter and a suitable wheel width are recommended for improved performance.

10.3.1.5 Cross-slide and control circuit

Theoretically the tractor can follow the seam in a horizontal direction but, due to the large inertia of the tractor, the accuracy of the horizontal tracking is poor. Therefore additional horizontal and vertical movement mechanisms are necessary for tracking purposes.

There were two choices for the design of the mechanism. The first was an arm type, shown in Fig. 10.32a. The three rotating pairs r_1, r_2, and r_3 can control horizontal, vertical and attitude positions by their co-ordinated movements. However, the control system to accomplish this was complicated. The second choice was a cross-slide mechanism that is shown in Fig. 10.32b. The regulation range was smaller than in the former concept but the horizontal and vertical movements were regulated independently of one another. This made the controller simpler. As the tractor already had two axes of freedom, a large range of regulation by the mechanism was not required. Therefore the second choice was selected for the present design.

The mechanism consisted of DC servomotors, ball screws, and nuts. A Type DG-12 motor was used for this mechanism. This kind of motor is normally used for avionics. It was incorporated with a reduction gear and an internal brake system that can quickly stop the motor. The motor voltage was 27 V, the torque was 15 N·cm, and the speed was 38 r/min. The ball screws had low friction. The range of regulation for both vertical and horizontal movement was ±44 mm and the maximum speed was 20 mm/s. Figure 10.33 shows its external appearance.

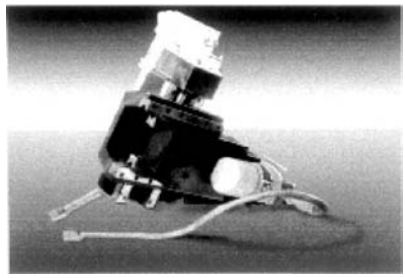

10.33 Outside view of the cross-slide

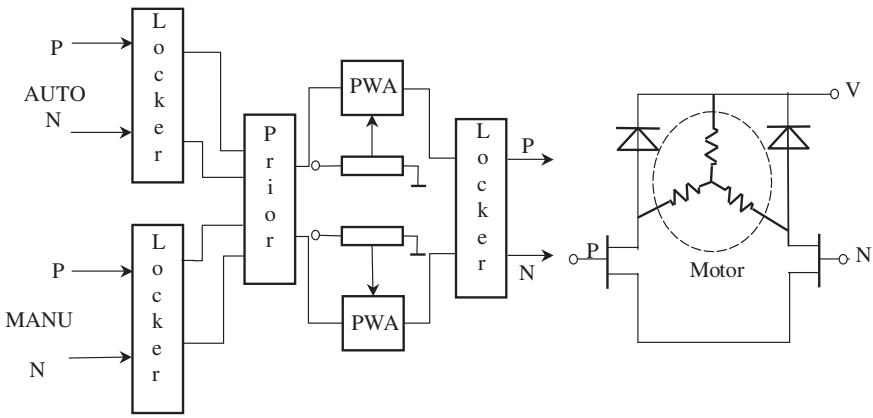

10.34 Circuit diagram for the cross-slide motor

Because the servomotor was an element in the closed-loop control system, there was no necessity to design a complicated control circuit. In the present design, an open-loop circuit was used. A certain voltage was applied to the motor and the direction of rotation was changed by reversing the electrical polarity. The motor speed was controlled by the duration of the current flow.

The motor had two armature windings. The direction of motor rotation was changed by changing the armature winding. There can be three states: 1 – positive rotation, 2 – stop, and 3 – reverse rotation. There were two input terminals. For safety there was an interlock circuit so that only one of the windings could be connected to the power. Figure 10.34 shows the schematic diagram of the circuit. The features of the circuit are (i) the speed in both directions of rotation could be regulated separately, (ii) the MOSFET worked in a switching mode at 10 kHz, (iii) the signals for forward and reverse rotation were interlocked so that the motor could not

conduct current if both signals appeared, and (iv) the manual control had priority for the purpose of correcting any incorrect operation of the closed-loop control system. Experiments demonstrated good system characteristics.

In the figure, AUTO, P, and N are signals from the computer; P means positive and N means reverse. MANU, P, and N are from the manual control knob. The interlock, as well as the priority circuit, are made using logic gate devices. When the manual knob is pushed, the motor rotates in the direction dictated by the signals that come from the computer. If two manual knobs are pushed at the same time, the motor will not rotate at all. PWA is the duty-ratio controllable pulse generator made by the time-base circuit. The priority circuit enabled and disabled the PWA.

10.3.1.6 Attitude regulation and control circuit

As described above, the left and right attitudes of the torch were not needed for regulation during welding but the front and rear attitude had to be regulated when the tractor was on an upward or downward inclined surface. The following paragraphs describe the front and rear attitude regulation mechanism and control circuit.

A requirement is that the arc position should not change when the attitude of the torch is regulated. Therefore, an arch rail or a multi-rod mechanism could be designed for this purpose. However, both kinds of mechanisms are complicated so that a pivot at the top of the torch was designed, which was applicable for small inclination angles of the plate, particularly when slow rates of regulation were needed. This mechanism was much simpler because the motor could then be mounted on the pivot.

Supposing that 20° of attitude has to be regulated in 1 ms, the speed of the motor will be

$$n = 60\frac{20}{360} = 3.3\,\mathrm{r/min}$$

A hysteresis synchronous motor at a speed of 4 r/min was chosen for this purpose. The motor is small and has high torque. The motor direction is controllable. The angle of regulation is controlled by the duration of current conduction. No automatic regulation is necessary.

The nominal voltage of the motor was 110 V AC. There were two windings inside the motor; one of the windings was connected to the AC power line directly and the other was connected to the power line via a capacitor. The phase difference between the two windings was π/2. The motor direction is changed by reversing the main winding, i.e. by the phase angle change between the two windings, which can be leading or lagging.

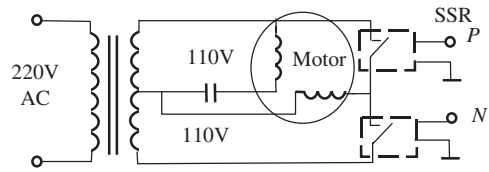

10.35 Circuit diagram of a magnetic synchronous motor

Because an AC power supply was used, the reversal of the direction of the motor was not as simple as with a DC motor. Figure 10.35 shows the circuit in which an AC solid-state device was used for the power element. In the figure, P represents positive rotation and N means reverse rotation P and N interlocked. Manual regulation was designed according to the 'Priority' principle. Both the horizontal and vertical regulation were similar. When P was at a high level, N was at a low level. The upper winding of the transformer was connected to the major winding of the armature. The secondary winding of the armature was supplied an AC voltage via a capacitor, which shifted its phase angle, and the motor rotated in the positive direction. When P was at a low level, and N was at a high level, the lower winding of the transformer was connected to the major winding of the armature, the phase angle of the current was just opposite to that of the former situation, but the phase angle of the secondary winding of the armature remained the same. Therefore, the motor rotated in the reverse direction.

10.3.2 Microcomputer control

In the tractor there were two driving motors for the wheels, two cross-slide motors, and one attitude regulation motor that are controlled. The signal from the arc sensor was complicated and had to be properly processed to obtain the deviation data of the arc. Because the control was a multi-input and multi-output system, only a computer could perform the required functions.

10.3.2.1 Configuration of computer control system

Because the system is used at industrial production sites, the environment is often bad. Moreover the arc produces a large amount of interference; therefore, a robust controller that can resist various kinds of interference without malfunctioning is required. The function of the controller is mainly sampling, data processing, and generating output signals for-closed loop control. There is little exchange of information with the operator; therefore, a single-board computer was chosen for the controller. This type of com-

puter is used frequently for industrial intelligent control. A single-board computer provides input and output interfaces, RAM, and EPROM, in addition to a CPU. Numerous commands are available. Because all of the functions can be performed on one IC chip, it is reliable and has strong resistance to interference. The controller-based single-board computer is convenient.

At the present time, popular, inexpensive, and high-quality single-board computes applied in intelligent instruments or industrial control are the MCS series of the Intel Co. The MCS96 has a larger arithmetic unit, higher speed, and better control characteristics than available single-board computers, and therefore an 8098 chip from that Intel series was chosen as the control unit.[283–289] It has the following features:

- 256 registers. Except for some special function registers, all of the other registers can be used as accumulators and execute commands, while in conventional CPUs there is only one Acc register that can execute arithmetic commands such as add, subtract, multiply, and divide.
- A 16-bit bus inside and an 8-bit bus outside. They ensure the accuracy of arithmetic operation on the one hand and a convenient I/O interface on the other hand.
- 16 bit multiply and divide commands with 6 μs speed.
- 10 bit conversion for the A/D converter; speed 22 μs.
- Multi-channel high-speed input (HSI) and output (HSO); it can record the input data variation and transmit output data on time without the intervention of the CPU.

The clock frequency is 12 MHz. Due to the features mentioned above, the quantity of data transfer during operation is very small; the speed is high. The high-speed output is very adaptable to PID control.

One of the special features of the industrial computer is its modular construction. There are modules for various functions, e.g. analogue input, digital input, display control, power switching, and output. The socket connecter for all of the modules is the same, which is convenient for including a variety of modules. It has the most popular industrial standard STD bus, which has 56 leads including addresses, data, and control buses. Because it allows convenient expansion of the system, an 8098, modular single-board computer with a STD bus was chosen as the controller. System design involved selecting proper modules according to the requirements of the control system.

The CPU module included the following circuits and devices: major IC, address decoding and an allocation circuit, EPROM for programming, RAM for data, serial and parallel I/O interfaces, an A/D converter, and a power circuit for setting the reference value.

The signal in or out of the CPU should be transmitted via buffers. For industrial purposes, an optical isolator is necessary. There were analogue-signal input and output modules, and digital-signal input and output modules.

- The digital-signal input module. The digital-input data included the control signal from the isolator, and the detected value of the horizontal position of the cross-slide. It also included the 'nonaddress' external interrupt and signals coming from the HSI via isolators.
- The analogue-signal input module. This included the A/D converter. The analogue signal was isolated outside this module before it entered the module. The analogue signals were the preset value of the welding current, the welding speed, and the wire-feed rate. This module also accepted the signal from the arc sensor.
- The digital-signal output module. This module included the buffer and the optical isolator. The signals from this module are mainly the signals that control the cross-slide and the signal for displaying the state of the program's progress. When the HSO was used, only the driving and isolator parts functioned without a buffer.
- The analogue-signal output module. This module included the A/D converter and the optical isolator on the digital side. The signals that were received were mainly the values of the velocities of the two wheels.

Figure 10.36 shows the circuit diagram of the control system, based on an 8098 IC and an STD bus.

The microprocessor performed the closed-loop control. Capability of the I/O interface, reliability and operational speed were the main requirements. There was no requirement for human–computer interaction. Therefore, no keyboard or CRT was needed. But in developing the software for the system, monitoring the execution of the programme and making corrections were necessary. Therefore, a microcomputer was connected to it. After debugging, the software was installed in the EPROM. The microprocessor worked independently.

10.3.2.2 Manual-operation circuit

Although there is little human-computer interaction, starting and stopping the software and setting values should be input into the controller by humans. This circuit is used mainly for setting and programming welding parameters.

The programme circuit initiates and stops the MIG welding process and the running of software simultaneously. The 'start' and 'stop' were fed into the computer by an interrupt so that a corresponding 'pulse' would be gen-

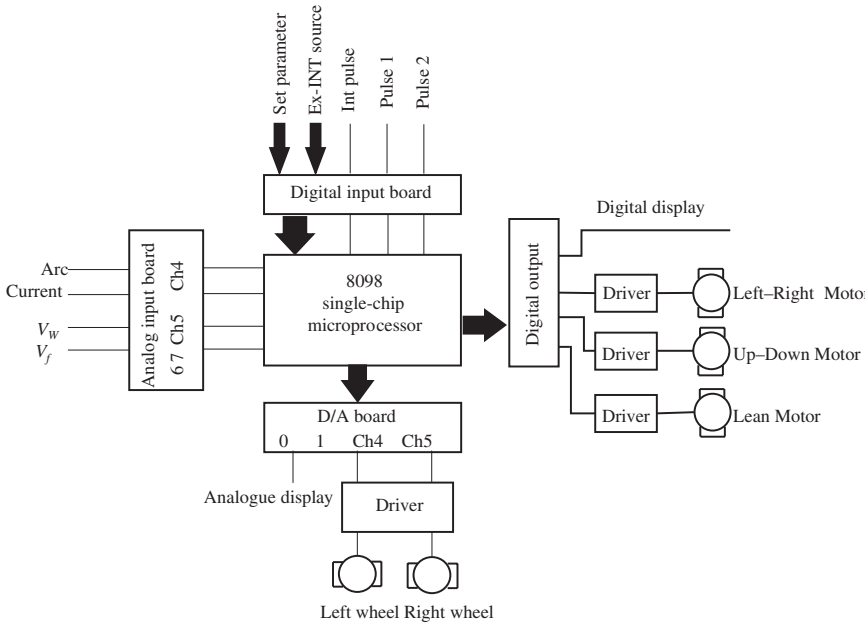

10.36 Configuration of the microprocessor or control system

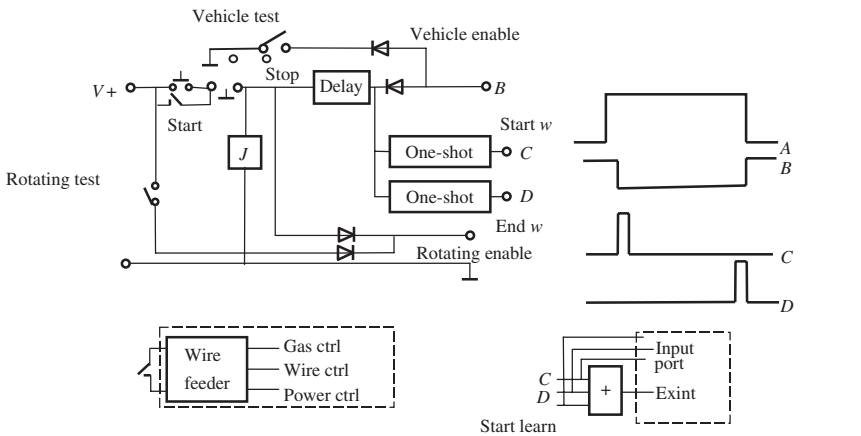

10.37 Control circuit for the welding program

erated. Because the number of Ext interrupt leads was limited, all of the interrupt input signals were connected to the module via an OR logic circuit so that the CPU could recognise their functions. Figure 10.37 shows a part of the schematic circuit diagram. The control circuit for the wire feeder provided the gas supply in advance of initiating the wire feed.

The circuit for setting the functions and parameters included a selection switch for the control programme, the tractor travel mode (straightforward manual control, and computer control), the welding-speed and wire feed-rate regulation, the initiation of sampling, and the processing of the calibrated interrupt signals.

There were 10 software-programme selections, which were chosen using a switch having four codes. The different software programmes were for different ways (calibrated methods) to obtain the character quantities. The identities of these programmes were as follows:

0: Enquiry method for a symmetric groove
1: Same as 0
2: Enquiry method for a lap joint
3: Gradient method for a lap joint
4: Oscillating welding with variable groove width
5: Variable-speed method for variable groove width
6: Judge method using maximum and minimum values
7: Same as 6
8: Teaching mode
9: According to previous parameters

The last two methods were studied in detail.

All of the software selections above had tractor-turning control. In cases when the tractor turning control was not needed, the travel control switch could be turned to 'open' so that the computer would not control the tractor speed.

Software selection No.8, the teaching mode, was obtained by sampling and processing data while the welding was stable with an arc on the groove centreline. The operation was started manually, i.e. a push knob produced an external interrupt, which was called a 'start learn'.

10.3.2.3 Circuit for the analogue input signal

As described in previous sections, there was a high-speed A/D converter inside the microprocessor but there was no isolator in it. Therefore, the signal had to be isolated before it was fed into the computer in order to avoid a direct power connection between the welding loop and the microprocessor.

The main requirement for signal isolation was linearity and stability. In computers used for industrial control, isolation normally is on the digital side. There was no problem with linearity and little influence of temperature and other kinds of interference.

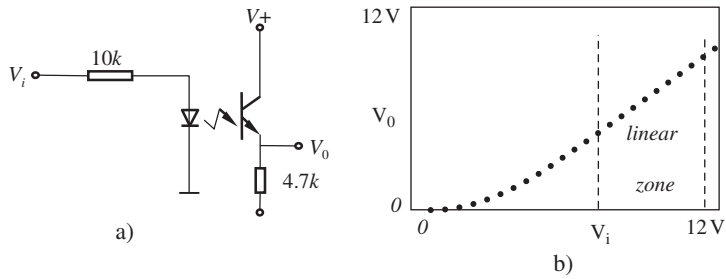

10.38 Characteristics of an optical coupler

For analogue-signal isolation, a transformer or an optical coupler normally is used. However, a conventional transformer obviously is not adaptable for a low-frequency signal. In order to use a transformer, the low-frequency signal is converted into a high-frequency signal before it is fed into the transformer; then it is converted back to low frequency after leaving the transformer. Transformers are not applicable for very high frequency signals as well because they contain a magnetic core. In the present design, an optical coupler was used. The problem with using an optical coupler is its small range of linearity (see Fig. 10.38) and sensitivity to temperature. A special circuit was designed for overcoming these two problems. Two similar optical couplers were sealed into a single unit. A circuit based on feedback-control theory was designed as shown in Fig. 10.39.

The principle of the circuit can be described as follows. Supposing that the output and input relation of the coupler is $V_a = f(V_i)$, then, for the second coupler, $V_b = f(V_{01})$.

For operational amplifier A_2, one can obtain

$$V_{01} = (V_a - V_b) \cdot K$$

Because K is very large and V_{01} is a finite value, $V_a = V_b$, i.e. $f(V_i) = f(V_{01})$.

Because resistor R_b provides a bias potential, $f(V_i)$ provides a monotonically increasing function in the range $V_i > 0$, thus

$$V_i = V_{01}$$

Obviously, the ratio of signal transfer is 1:1. Figure 10.39b shows the measured results, which demonstrate good linearity in the range $V_i \in [0, 12\,\text{V}]$.

According to the arc sensor's working principle, the average welding current is needed for torch-height control and the instantaneous current change is needed for horizontal-position control. The two signals are

V_{01} Average welding current
V_{02} Instantaneous current

The magnitudes of both signals were designed to be 0~5 V so they could adapt to the reference signal from the A/D converter.

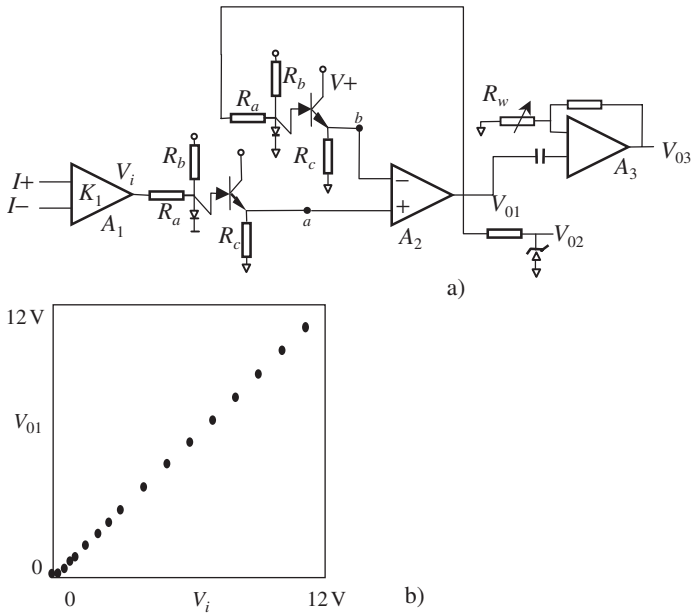

10.39 Circuit for an optical coupler

For a stable welding current, $V_{02} = 2.5\,\text{V}$ DC.

The resistor for sampling the welding current was 4 mΩ, which was amplified by the operational amplifier A_1 with a gain of 3. Therefore, the amplification coefficient was

$$K_{iA} = 1.2\text{V}/100\text{A} = 0.012\,\text{V}/\text{A} \qquad [10.6]$$

After 10 bit A/D transform (the reference is 5 V), the amplification coefficient becomes

$$K_I = K_{iA} \cdot K_{AD} = 0.012\text{V}/\text{A} \cdot 400HI/\text{V} = 2.457\text{I}/\text{A}$$

The gain of amplifier A_3 was 5; the amplification coefficient for the instantaneous current was

$$K_{i1A}. = 5 \cdot K_{iA} = 0.06\text{V}/\text{A}$$

The overall amplification coefficient was

$$K_{I1} = K_{i1A} \cdot K_{AD} = 61.5629\text{I}/\text{A} \qquad [10.7]$$

The set value of the welding speed and wire-feed rate were input simply by their corresponding potential and isolation.

10.3.2.4 Allocation of I/O signals

The output and input signals (addresses or leads) were allocated on the hardware as follows:

Welding current I, ACH4 (Input 4 of the 8098 chip)
Variation part of the welding current I_1: ACH5
Set value of the welding speed V_w: ACH6
Set value of the wire-feed rate V_f: ACH7
The start position pulse of the rotating torch P_1: HSI.1
The angular position pulse of the rotating torch P_2: HSI.0
Selection word of the software and welding condition: 1000 H unit
Welding start, stop, start learn, and interrupt: EXINT
Recognition of the external interrupt, slide position: 1002 H unit
Horizontal tracking signal: To the left, HSO.0 acts at high level; To the right, HSO.1 acts at high level
Vertical tracking signal: Upward, HSO.2; Downward, HSO.3
Front and rear attitude: Towards front, HSO.4; Towards rear, HSO.5
Wheel velocity: left, D/A4; right, D/A5.
Display: 1004 H unit

Among the above signals, the high-speed signals were effective at high potential levels, i.e. the corresponding motor moved according to the set direction. An 8-bit D/A was used for wheel velocity, which can satisfy the industrial requirements. The output magnitude was 0~5 V, corresponding to the range from the maximum reverse rotation speed to the maximum positive rotation speed, i.e. –3 m/min to +3 m/min.

10.3.3 Principle of fuzzy control[290–294]

Fuzzy control is applied in contemporary industrial applications. The objective of this type of control is to control complicated systems that are difficult to analyse. In the present study, the multi-freedom welding machine with an arc sensor included two wheel controls, a cross-slide control, and signal processing by an arc sensor. All of the elements are complicated and difficult to describe accurately. Therefore, using fuzzy control was beneficial. The dynamic response and accuracy of fuzzy control are poorer than those of normal control but its robustness is greater. It is not sensitive to the control model and parameter changes. Therefore, it has good adaptability and reliability, which are valuable for industrial applications. Moreover, it does not need an accurate definition of the control model and is easily implemented.

For the present purpose, the principle of fuzzy control can be described as follows. The relative position of the tractor with the weld groove is judged by the position of the nut on the horizontal screw of the cross-slide and the tendency of the movement of the nut. On the basis of the position signal, the turning angle of the tractor is controlled. The signals for controlling the tractor are delivered synchronously with the signal for controlling the nut on the screw. The welding torch is fixed on the nut and, therefore, the movement of the torch is the combination of the movement of the tractor and the nut on the cross-slide.

10.3.3.1 Output and input signals of fuzzy control

As described in last section, the control of the tractor was based on the position and signals of the motion tendency of the nut on the slide. In turn, the movement of the nut was based on the signal output from the arc sensor. Therefore, the integral value of the current on both sides of the arc EH (in the present design, the integral-difference method was used for signal processing of the arc sensor; see Section 7.3.2) and the position of the nut x_D could be used as the inputs.[380] If x_D is used as the input, the rate of change of x_D is difficult to determine because it requires very precise detection of x_D. When EH is used as the input, the change rate of x_D can be found directly by the microprocessor by computation. However, because the initial position of the nut is not certain, the nut position obtained by computation is not reliable. Therefore, both EH and x_D were chosen as inputs. The value of x_D was detected by a more or less rough method that is not critical for fuzzy representation. In order to eliminate random interference, EH was processed by an appropriate low-pass filter and was designated as EH_F.

In fuzzy control the first problem was to transform the input signal into a fuzzy representation or to define the membership function. For the nut position, rectangular-shaped membership functions were used for simplicity; the fuzzy set could be obtained by

(i) Binary value method: $x_D = \{L, R\}$
(ii) Triple value method: $x_D = \{L, Z0, R\}$

L represents Left, R represents right, $Z0$ represents middle. Figure 10.40a,b shows the membership function. The widths of the rectangles were determined on the basis of the mechanical conditions and the experimental results.

Input EH_F was obtained from the arc sensor as a 16-bit signal. It was more appropriate to use a triangular-shaped membership function. The fuzzy set can be obtained by

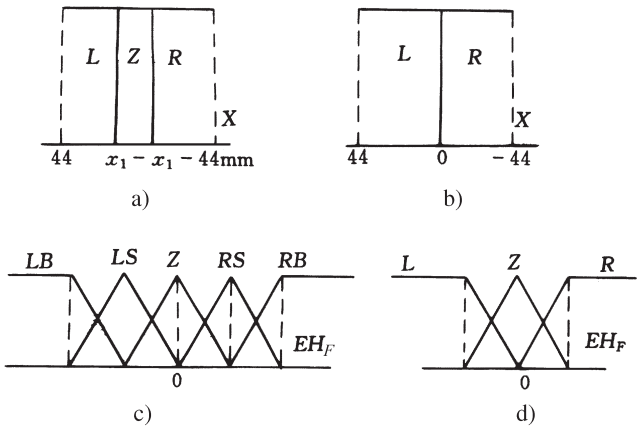

10.40 Transformation of input signals into fuzzy information

(i) Triple-value method: $x_D = \{L, Z0, R\}$
(ii) Five-value method: $x_D = \{LB, LS, Z0, RS, RB\}$

Figure 10.40c,d shows its membership function. The top point of the triangle means membership grade 1 when EH_F is on it. The abscissa of the figure is determined by the relationship between the groove-line deviation angle with EH_F and determined from the experimental results. From experience, the corresponding values of EH_F for LB, RB and LS were set at the groove centre-line deviation angles of ±10°, ±5°, and the corresponding values of EH_F were ±600 H, ±200 H.

A five-value fuzzy set was taken for the output signal Δγ

$$U = \{LB, LS, Z1, RS, RB\}$$

which meant turn to the left greatly, slightly, no turn, turn to the right slightly, greatly.

Experience demonstrated[10] that the five-value method was simpler and had satisfactory characteristics.

The triangular shape also was used for its membership function.

The tops of the triangles were ±2°, ±1°, 0°.

These values can be adjusted in practical experiments.

10.3.3.2 Fuzzy rule

The fuzzy rule is, in fact, a simulation of a human's mode of thinking. For example, if the nut (torch) is on the left and the groove line is inclined to the left greatly (EH_F is LS), the tractor should be turned to the left greatly

Table 10.1 Fuzzy-control rules

x_D \ EH_F	L	ZO	R
L	L	L	ZO
R	ZO	R	R

a)

x_D \ EH_F	L	ZO	R
L	LB	LS	ZO
ZO	LS	ZO	RS
R	ZO	RS	RB

b)

x_D \ EH_F	LB	LS	ZO	RS	RB
L	LB	LB	LS	ZO	RS
ZO	LS	LS	ZO	RS	RS
R	LS	ZO	RB	RB	RB

c)

or the extent of turning right should be reduced, i.e. let $\Delta\gamma$ be LS. The fuzzy conditional statements can be written as the following examples:

IF x_D is L AND EH_F is LB THEN $\Delta\gamma$ is LB
IF x_D is R AND EH_F is RB THEN $\Delta\gamma$ is RB

Using different methods of defining the fuzzy set, there are different fuzzy rules that can be illustrated, as in Table 10.1. These logic rules, of course, should be adjusted based on the results of experiments. For example, if inputs (x_D, EH_F) are (L, RB), the output can be $Z0$ or RS. The effect of the choice can be found only by experiment.

10.3.4 Fuzzy control system

The hardware and software of the control system are discussed in the following paragraphs.

10.3.4.1 Detection of parameters concerned

As described in the sections above, the nut position x is detected by a sensing device. An electro-optical method was used for this purpose. Two obstructing plates divide the nut's travelling range into four parts. Table 10.2 shows the two ways for defining the position. A two-bit signal was used for

Table 10.2 Coding of the nut position

x_D	×0	×1
x	L	R

a) Binary value

x_D	00	01	1×
X	L	R	ZO

b) Triple value

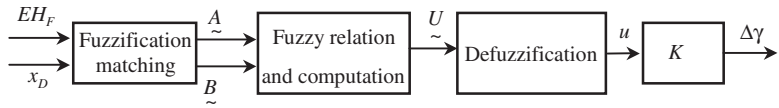

10.41 Structure of the fuzzy controller

expressing the position and was fed into the microprocessor via a parallel interface. Adjusting the length of the obstructing plate regulated the width of the control range.

Because there can be many random interferences in EH, digital filtering should be used. The method of filtering can be expressed by the following equation

$$EH_F(n+1) = \alpha EH(n+1) + (1-\alpha)EH_F(n); \quad 0 < \alpha \leq 1 \qquad [10.8]$$

The output $\Delta\gamma$ was executed by the wheel-drive mechanism, which had closed-loop control. The set value V_{g1}, V_{gR} was deduced from theory.

10.3.4.2 Fuzzy algorithm

Figure 10.41 shows the schematic diagram of the fuzzy control system. It consisted of three parts, i.e. fuzzification, fuzzy-relation computation, and deffuzzification.

There is a variety of algorithms based on fuzzy-control theory:

(i) Maximum–minimum composition.

The first step, on the basis of the defined membership function and input value of EH_F and x_D, is to determine the fuzzy set of EH_F and x_D. A column vector B can be set up according to its membership grade in the fuzzy set L, ZO, R for x_D.

$a_i = \mu_{x_1}(x_D)$; X_i is membership grade x_D at L, ZO, R.

For EH_F, a five-column vector B can be set up according to its membership grade in the fuzzy set LB, $LS \ldots RB$.

$b_1 = \mu E_j(EH_F)$; E_j is the fuzzy membership grade at LB, $LS \ldots RB$.

According to the fuzzy algorithm, the membership grade matrix of (x_D, EH_F) to their subset (L, LB), (L, LS). . . . (R, RB) is

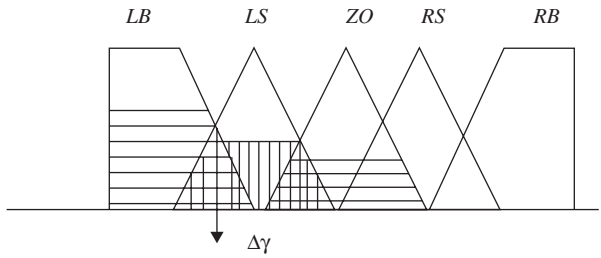

10.42 Principle of the centre-of-gravity method

$$C = A \wedge B; \quad C_{ij} = \min(a_i, b_j) = \mu_{XE_{ij}}(x_D, EH_F) \qquad [10.9]$$

C is a 3×5 matrix. It can be rewritten as a 15-column vector C'. Its elements are the membership grades of the subset in their corresponding positions.

The second step is to write the control rule in matrix form. That is the membership-grade matrix for input (L, LB), (L, LS). . . . (R, RB) and output LB, LS . . . RB. The matrix is a 5×15 array. According to the described rule, the element takes 0 or 1; there is only one 1 in each row.

The third step is to determine the output fuzzy vector.

$$U = R \cdot C'; \quad u_{ij} = \underset{k=1,\ldots,15}{\text{Max}}(\min(r_{ik}, c'_k)) \qquad [10.10]$$

R and C' are operated by composition. The result is a column vector of 5 rows, which represents the membership grade of $\Delta\gamma$ in its subset.

The fourth step is to determine an accurate value of $\Delta\gamma$ on the basis of U and the membership function of $\Delta\gamma$. Supposing that $\Delta\gamma$ is in the universe of discourse of m discrete values and D is the membership-grade matrix of $\Delta\gamma$, then the output membership-grade vector F is

$$F = D \cdot U \qquad [10.11]$$

The final, accurate value of $\Delta\gamma$ is the average of the discrete values using the element F as a weighting coefficient.

When $\Delta\gamma$ is a continuous membership function, the method can be illustrated by Fig. 10.42. Suppose that $U = (a_1, a_2, \ldots a_5)^T$, where $a_1 \ldots a_5$ are numbers between [0, 1], then the membership grade of the output $\Delta\gamma$ can be expressed by the shadow area. In the same triangle, for a given $\Delta\gamma$, the shadow line takes the value $\min(a_i, \mu_{ui}(\Delta\gamma))$, i.e. find the minimum value of $\Delta\gamma$ in $D \cdot U$ for a given value of $\Delta\gamma$. In a different triangle, it takes the highest shadow line, i.e. find the maximum value of $D \cdot U$.

The determination of $\Delta\gamma$ by calculating the cross-hatched area is reasonable using the centre-of-gravity method, i.e. the value of $\Delta\gamma$ at

the location of the centre of gravity. The other way to determine $\Delta\gamma$ is to take the point where it has the highest membership grade.

(ii) Modelling method for the fuzzy set.

A fuzzy number replaces the output of the fuzzy subset LB, LS . . . described above; the highest point of the triangle is taken as the centre point for $\Delta\gamma$. The algorithm is as follows

The first step is to find out the membership grade of EH_F, x_D. Because the triangular-shaped membership function is used, EH_F would not be zero except in two neighbouring subsets. Suppose they are $\mu_{E_1}(EH_F)$ and $\mu_{E_{i+1}}(EH_F)$. If a complementary membership function is used, then

$$\mu_{Ei}(EH_F)+\mu_{E_{i+1}}(EH_F)=1$$

Because a rectangular-shaped membership function is used for x_D, it is not zero but equal to 1 in only one of its subsets.

Linear interpolation is the second step. Under the conditions described above, it can be simplified into a one-variable linear interpolation

$$\Delta\gamma=\mu_i+(\mu_{i+1}-\mu_i)\cdot u_{E_{i+1}}(EH_F) \qquad [10.12]$$

μ_i, μ_{i+1} are the centre-point values of the output fuzzy subset corresponding to the input EH_F and $\mu(x_D) = 1$. The principle of the control method corresponds to the linear transformation of EH_F segments controlled by x_D.

$$\Delta\gamma=f_{x_D}(EH_F)$$

The method is easier to implement but the ability to correct the control rule and the model is limited.

(iii) Graphical method of max–min composition.

Suppose that the membership functions of x_D and EH_F are rectangular- and triangular-shaped, respectively. Any arbitrary x_D would have a non-zero number in one of its fuzzy subsets, and would be equal to 1 (see Fig. 10.43).

$$\mu_{x_i}(x_D)=1$$

EH_F is non-zero in its two neighbouring fuzzy subsets

$$\mu_{E_j}(EH_F)=b_j,\quad \mu_{E_{j+1}}(EH_F)=b_{j+i}$$

Therefore (x_D, EH_F) is non-zero only in two neighbouring fuzzy subsets of its region of influence.

$$\mu_{XE_{ij}}(x_D,EH_F)=b_j,\quad \mu_{XE_{ij+1}}(x_D,EH_F)=b_{j+1}$$

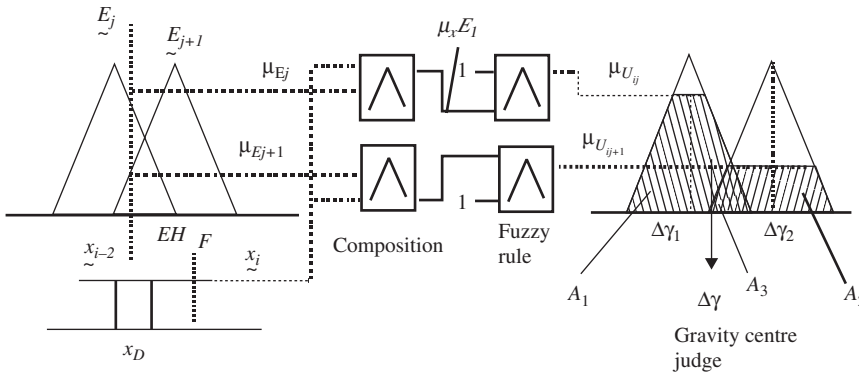

10.43 Schematic diagram for the fuzzy algorithm

According to the fuzzy rule, $\Delta\gamma$ would be non-zero in only two corresponding fuzzy subsets, XE_{ij} and XE_{ij+1}. One XE_{ij} is limited to emitting only one U_{ij}; this means that in the rule matrix R, there is only one element in each row that equals 1; other elements are zero. Thus

$$\mu_{U_{ij}}(\Delta\gamma) = \mu_{XE_{ij+1}}(x_D, EH_F) = b_j;$$
$$\mu_{U_{ij+1}}(\Delta\gamma) = \mu_{XE_{ij+1}}(x_D, EH_F) = b_{j+1}$$

The intercepted height of the triangular-shaped membership function is the membership grade of the corresponding subset of the output.

The most precise solution for the output normally is obtained by the so-called centre-of-gravity method. The centre-of-gravity method is shown in Fig. 10.43. Supposing that the membership grade of one of the output subsets U_{ij} is b_j, the membership grade of the subset of the defined point $\Delta\gamma$ is determined by the hypotenuse of the triangle as μ_r. Then the smaller of the values of b_j and μ_r will be the weight of the output $\Delta\gamma$. Taking the average of the $\Delta\gamma$ range according to its weight, the gravity value of $\Delta\gamma$ will be obtained as the cross-hatched area shown in the figure.

The arithmetical method for finding the centre of gravity is as follows:

The weight (cross-hatched area) is

$$A = A_1 + A_2 - A_3;$$
$$A_1 = t \cdot b_j(2 - b_j) \qquad [10.13]$$
$$A_2 = t \cdot b_{j+1}(2 - b_{j+1})$$
$$A_3 = \frac{1}{2} t \cdot b_m(2 - b_m), \quad b_m = \min(b_j, b_{j+1}, 0.5)$$

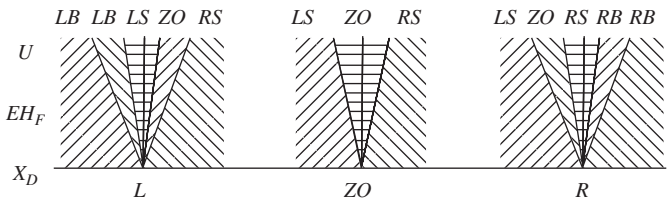

10.44 Schematic drawing showing simplified tabulation

where t is the distance between the highest points of the triangles
The weight moment (area moment) is

$$S = A_1 \cdot \Delta\gamma_1 + A \cdot \Delta\gamma_2 - A_3(\Delta\gamma_1 + \Delta\gamma_2)/2 \qquad [10.14]$$

The co-ordinate of the centre of gravity is

$$\Delta\gamma = \frac{S}{A} \qquad [10.15]$$

10.3.4.3 Fuzzy algorithm suitable for microcomputer control

Although all of the algorithms given above can be used for real-time computer control, a tabulation method is advisable for reducing the amount of operational work to obtain high speed. If the first algorithm is applied, the input and output are quantified, the solution is found in advance, and the results are tabulated. This is convenient for real-time control.

In the tabulation method, x_D, EH_F, and $\Delta\gamma$ are quantified. Then, a three-dimensional control table is created using the results of the computation and stored in the computer ROM using to a specific format. In the control operation, the inputs x_D and EH_F are rounded off to the level nearest to them in the table.

One of the advantages of this method is that it is possible to correct the table locally, according to the performance of the control system, without correcting the population plan.

This method simplifies tabulation. Because the ball screw of the cross-slide tracks position rapidly, high dynamic sensitivity of the tractor control system is not needed. The levels of x_D, EH_F, and $\Delta\gamma$ can be coarser in the tabulation and the membership function also can be simplified.

Figure 10.44 shows the schematic diagram of the control strategy. The output $\Delta\gamma$ depends on the position of the sliding nut (left, middle, and right) and the arc sensor's output EH_F. EH_F is represented by the slope of the line in the figure. The results for $\Delta\gamma$ are then LB, LS . . . RB, which can be precisely quantified. The division of the regions in the figure is determined by

analysis and experiment. The width of the central region of the nut is determined by the maximum travel range of the slide and an estimation of the tractor's turning speed. The control rule should ensure that the nut would not travel outside of the maximum range.

The slope of the line EH_F on the figure is determined by the possible angle between the groove centreline, and the travel direction and welding speed. The magnitude of $\Delta\gamma$ corresponds to the gain of the closed-loop control system. It greatly affects the static and dynamic characteristics of the system. The method used for filtering *EH* also has a strong effect on the dynamic properties. The filtering method should be experimentally debugged.

10.3.4.4 Implementation

As described above, the tabulation method is used for control. Therefore, the computer reads the input value x_D from the slide and the arc sensor's input *EH* (*EH* is, in fact, obtained inside the computer), filters the *EH*, and then chooses the $\Delta\gamma$ from the table. Based on $\Delta\gamma$, it calculates the speed of the left and right wheels. Floating-point operation is used for accuracy. The 8089 single-board computer has sufficient floating-point capacity. Because the CPU has 16 bits, its floating-point operation is very fast.

Both slide control and tractor control are time-based, i.e. after several rotations of the arc sensor, sampling is stopped for one turn during which period the CPU processes the input and output signals. They are controlled synchronously and with the same period.

The flow chart for the tractor-control software is shown in Fig. 10.45. This subprogram can be initiated after the slide control is completed. The signal *EH* is filtered according to Eq. [10.8], in which α is determined by its interference-suppressing effect and closed-loop dynamic characteristics.

x_D represents the position of slide nut. A change of x_D will change the parameters of the tractor's turning-velocity control (see Section 6.1 of [245]). However, if the movement range of the nut is small, the change is relatively small compared to the turning radius. Setting a different range of x_D values in the software does not have much influence on the precision of the control.

The set value of the welding speed is read by the computer using a 10-bit word. After calculation of right and left wheel velocity, the data is output by an 8-bit word via an I/O interface.

For a finer grade of tabulation, a query-table method was used for programming. The table is three-dimensional. Transforming this table into a two-dimensional table was necessary. The principle was as follows. x_D was transformed linearly into digits and used as the high field of the memory

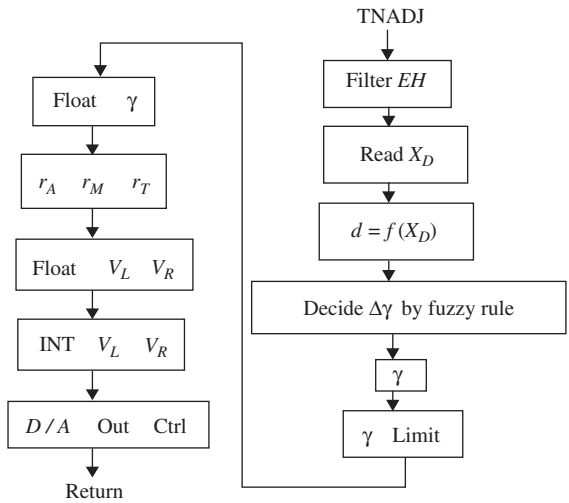

10.45 Flow chart for the tractor's turning control

address, and EH_F was transformed into digits and used as the low field of the memory address. Values of Δγ were then stored in the memory.

For a simple control table, comparing, judging and branching methods are used for programming.

10.3.5 Debugging and experiments

The main parameters that had to be debugged were the period of regulation, the definition of the input membership function, the filtering parameters of EH, and the definition of the output membership function Δγ. In addition, some structural parameters of the tractor were debugged as required by the experimental results.

As described above, regulation of tractor turning and the nut movement were simultaneous. The division of x_D was limited by the detection method. The center part of x_D was defined as 36 mm while the total slide range was 88 mm. If the tractor travelled straight and the groove was inclined 5°, the slide could regulate the torch alone without turning the tractor for a groove length of 207 mm.

Two structural parameters, a and b, were determined using the following considerations. If a was increased, the transverse speed of the torch during turning was increased. This meant that the amplification factor of the horizontal-tracking control loop should be increased. If a was too small, then r_A was small for the same value of γ. The ratios of V_L and V_R to V_W were larger, i.e. the ratio of wheel velocity to torch travel velocity was larger. If d was increased, the variation of wheel velocity was increased and its

required velocity range was larger. If d was too small, then the calculations of V_L and V_R were affected more strongly by the resolution of detection of x_D. Finally, the evenness of the torch travel speed was affected. Due to limitations dictated by torch construction, d could not be too small.

On basis of many experiments that were used to investigate γ, V_W, and the effect of a and b on V_L, and V_R, the parameters were selected as follows.

Range of γ ±48° a = 100 mm d = 455 mm

The first group of experiments was carried out under non-welding conditions. The torch travel was observed while the tractor moved straight and through turns. The second group of experiments was carried out under welding conditions. The torch travel and bead appearance were observed. The results were satisfactory using the parameters given above.

While x_D was divided into three regions, namely, left, middle, and right, the detector divided the middle into two additional parts. On the basis of debugging experiments, ±9 mm and ±26 mm were taken the ranges of subsets. This meant that the sliding nut was in the 'left' region if d was at d = 455 + 26 mm, while the sliding nut was in the "middle-left" region if d was at 455 + 9 mm. The other definition was analogous to this.

According to the simplified control table described in Section 10.3.4.3, EH_F was divided into 5 levels. On the basis of the relationship between EH_F and the inclination angle of the groove, it was defined in advance, as follows:

LB: $EH_F \leq -800$ H; LS: -800 H $\leq EH_F \leq -400$ H

ZO: -400 H $\leq EH_F \leq 400$ H; RS: 400 H $\leq EH_F \leq$ 800 H;

RB: 800 H $\leq EH_F$

For $\Delta\gamma$, it was defined as

$LB = +2°$; $LS = +1°$; $ZO = 0°$; $RS = -1°$; $RB = -2°$

Thus, the control table is as shown in Table 10.1c; the only difference was that the symbols were substituted by data. The main task of debugging was associated with the number of subsets for EH_F, $\Delta\gamma$, and the filtering coefficient α for EH_F.

In order to obtain the most suitable parameters, the following experiments were conducted:

- Experiment (i): EH_F dividing-point subsets were changed, the sensitivity of tractor's turning was observed, and the change of γ was recorded. After many experiments, the division points for the EH_F subsets were obtained as shown in Table 10.3.
- Experiment (ii): The effect of the filtering coefficient α for EH_F was observed. First, a horizontal corner joint was welded using α = 0.5, a groove line inclined at an angle of 20°, and welding conditions of 240 A and 28 V (Open circuit), a welding speed of 240 mm/min, and $\Delta\gamma$ divisions of ±2°, ±1°, 0°. The results are illustrated in Fig. 10.46 in which the ordinate indicates the turning angle γ (expressed by the phase-shift

Table 10.3 Fuzzy-control table

EH_F / Δ_γ / x_D	<–600 H	–600 H ~ –200 H	–200 H ~ 200 H	200 H ~ 600 H	>600 H
00 (*L*)	2^0	2^0	1^0	0^0	-1^0
1 × (*Z*)	1^0	1^0	0^0	-1^0	-1^0
01 (*R*)	1^0	0^0	-1^0	-2^0	-2^0

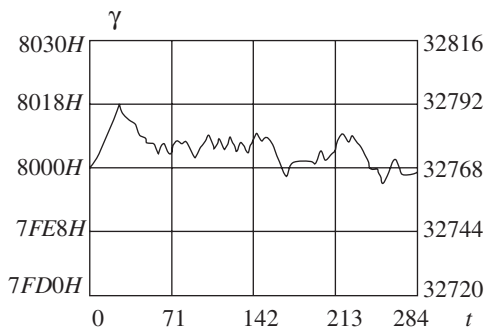

DIAGRAM OF *D:* 0091*G X*—71/Div *V*—24/Div

10.46 Process of tractor-angle regulation (1)

code, 8000 H corresponds to 0°). The value of γ should be zero if the tractor reaches a stable state and goes along the seam. It can be seen from the figure that there was some low-frequency oscillation; the high frequency oscillation was insignificant.

To investigate changing α and letting $\alpha = 0$, the welding was conducted under the same conditions as given above. The results are shown in Fig. 10.47. It can be seen that γ has less low-frequency oscillation but more high-frequency oscillation. The reason for this probably was the interference of *EH*, which had not been filtered.

The results were somewhat better than those using the former conditions. In both cases, the sliding nut was kept in the middle region. The time required for the tractor to turn to become parallel to the groove was 30–40 s. Therefore it can be concluded the value of α can be taken between 0.5 and 1.0.

- Experiment (iii): The amplification coefficient was determined. The amplification coefficient is the proportional ratio used to transform the fuzzy-signal output into a precise quantity. For a simplified control table,

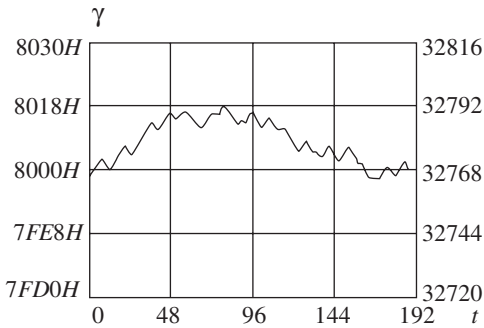

DIAGRAM OF *D*: 0092G X—48/Div V—24/Div

10.47 Process of tractor-angle regulation (2)

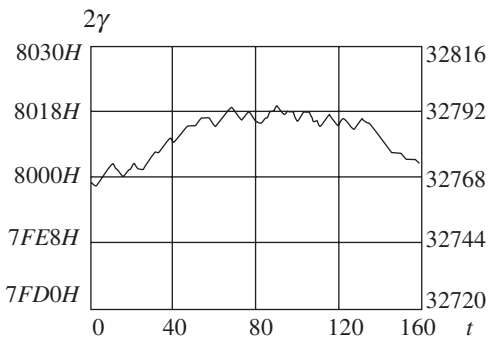

DIAGRAM OF *D:* 0093*G* *X*—40/Div *V*—24/Div

10.48 Process of tractor-angle regulation (3)

it is the magnitude of $\Delta\gamma$. In the case in which the values of $\Delta\gamma = \pm 2°$, $\pm 1°$, $0°$ were taken, the results were shown in Fig. 10.47. When the value of $\Delta\gamma$ was decreased to one half of the values given above and the welding experiments were conducted under the same conditions as in Experiment (ii), the results obtained were as shown in Fig. 10.48. The ordinate was expressed by the shift code of 2γ. It can be seen that in the latter case, the time for regulation was longer. It took a travel distance less than 220 mm to complete the regulation for the former while in the latter case, the regulation was far from completed in a travel distance of 215 mm. Therefore, it can be concluded that 0.8–2 times of $\pm 2°$, $\pm 1°$, $0°$ can be taken as the value of $\Delta\gamma$.

On the basis of these experiments, the final control table shown in Table 10.3 was obtained.

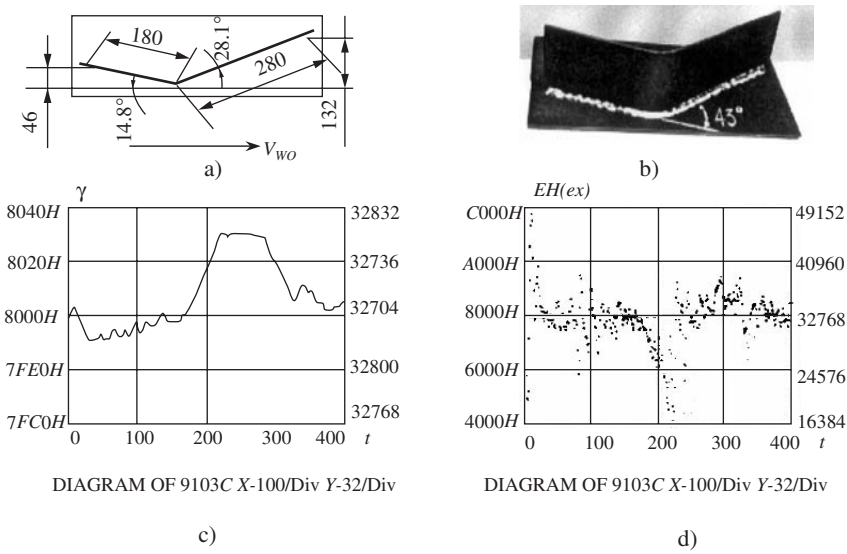

10.49 Seam-tracking test on an abruptly turning groove

To observe the effect of the closed-loop control system further, a corner joint work piece was designed with a large deflection angle of 43°, as shown in Fig. 10.49a,b. The first section of the groove had a length of 180 mm and was inclined to the right 14.8°. The second section of the groove had a length of 280 mm and was inclined to the left 28.1°. The maximum deviation at the starting point was 46 mm and at the end point was 132 mm, which was much greater than the range of the slide. The weld was satisfactory, as shown in Fig. 10.49b. Both the seam tracking and bead formation were satisfactory. Figure 10.49c is the record of variation of γ during the regulation process. The ordinate indicates γ, expressed by the shift code 8000 H means $\gamma = 0$. The abscissa indicates the number of the regulation. The time between two regulations was 0.2 s. Figure 10.49d shows the *EH* value detected by the arc sensor, expressed by the shift code. It can be seen that the negative value of *EH*, at abscissa 210, was large. It corresponded to the abrupt turning point of the groove. The turning angle at this point also quickly increased to 48°, which was the maximum value of the turning angle set by the design.

Part IV

Real time measurement of welding temperature-field

11

Principles of the colorimetric imaging method

11.1 Introduction

Welding is one of the most important manufacturing processes in modern industry. The requirements for weldment quality have become more rigorous. The only solution to these demands is to apply automation and intelligence techniques.[1–3] The first challenge is met by sensing technology; for example, detection of the geometric parameters of the work piece (joint gap, weld position, work piece temperature, etc.) and detection of quality parameters (penetration, bead formation, etc.) Among characteristics that merit sensing, temperature-field measurement is important because the temperature field and its dynamic process are key elements for ensuring weld quality. The temperature field determines the microstructure and mechanical properties, stresses and strains, and possible defects in the joint. The temperature field contains a large quantity of information regarding weld quality. Therefore, real-time detection and control of the temperature field is a basic project in the development of welding technology. In recent years, welding scientists and engineers have performed research in this field but, due to technical difficulties, practical application of the results was not possible. It is still a frontier area in welding-technology research, which needs to be solved urgently. In the following four chapters, the research work and the results obtained at Tsinghua University are described.[295,296]

11.1.1 Status of the research

The thermal process is central to the entire fusion-welding process. All of the physical and chemical reactions in welding are related to the thermal process. It determines the stress and strain fields and is closely related to the metallurgical reactions, crystallisation, and other phase transformations. The accurate measurement of the thermal process is a prerequisite for understanding and controlling metallurgical events, and strain and stress.

Welding researchers have attached great importance to research on this topic and have performed a lot of work. There are two approaches; the first is temperature-field calculation using heat-transfer theory and the second is based on temperature-field measurement.

11.1.1.1 Temperature-field calculation based on thermal-conduction theory

As early as the 1950s, Rykalin of the Soviet Union systematically studied the thermal processes in welding on the basis of the work of Rosenthal, who established the foundation of heat-transfer theory in welding processes.[297] Rykalin established a mathematical model using differential equations under certain conditions to describe the thermal field during fusion welding.

Adams *et al*.[298] made many measurements using different plate thicknesses and welding parameters. Then, on the basis of physical concepts, he summarised a series of heat-transfer formulae. Although this method was more accurate than the analytical method, it required a large quantity of experimental results and its accuracy depended on the measurement method.

With the development of the computer, the numerical method was an important advancement. The finite-difference method[299] and the finite-element method[300] were developed for solving the differential equations that describe heat transfer.

Generally speaking, the thermal processes in welding are complicated so that the nonlinear equations that describe them are difficult to formulate. In most studies, the thermophysical properties of the materials under consideration are assumed constant and the welding arc is considered as a point heat source. These assumptions are not realistic. Therefore, the results of mathematical analyses of various welding heat-transfer situations are not satisfactory. This is the biggest drawback of the mathematical-analysis method.

11.1.1.2 Welding temperature-field measurement

(i) Thermocouples.[301,302] This is the conventional high-temperature measurement method. Thermocouple measurements are accurate and are widely used in research; for example, measuring the thermal cycle at a point. This method is suitable for measuring temperature at a point but measuring a temperature field is difficult, particularly for welding processes, because many thermocouples are needed to map temperatures in three dimensions. Attaching thermocouples and measuring

temperatures are laborious activities. Moreover, too many thermocouples change the temperature distribution and, due to high temperatures, measuring the temperature near the arc is not possible. Therefore, real-time control using thermocouples is not possible.

(ii) Infrared radiation. This is a non-contact measuring method that is superior to thermocouples because contacting the object is not necessary. The temperature field is not altered by the measuring method and waiting for temperature equilibration between the sensor and the object is not necessary. In addition, infrared radiation propagates at the speed of light; the measuring speed depends only on the response of the measuring instruments. The particular advantage of this method is that measuring the temperature field and realising real-time control are possible. Before describing the status of welding temperature-field measurement, conventional temperature measurement methods of the non-contact type,[301,303] i.e. the brightness method, radiation method, and colorimetric method, are introduced first.

- Brightness method. The brightness method is based on the principle that the brightness of a body increases with its temperature. A standard calibrated light source, for example a heated lamp wire, is placed next to the object image for visual comparison. When the lamp wire blends with the object image, the body has the same temperature as the lamp wire, the temperature of which was known in advance by calibration.
- Radiation method. The radiation method is based on the principle that the radiation intensity of a body in a certain wavelength band corresponds to its temperature. Proper calibration also is important for this method.
- Colorimetric method. The colorimetric method is based on the principle that the ratio of the intensities of two different radiation wavelengths emitted by a body is a function of its temperature. If the object is an ideal black body or grey body, the method can give the true temperature of the object.

Up to now, there have been no reports about the application of the brightness and colorimetric methods for measuring temperature fields in welding. (The colorimetric method has been used for detecting temperature at a point or the average temperature of a small area but not for temperature-field measurement.) In Section 11.2, a theoretical analysis and a comparison of the radiation and colorimetric methods will be discussed. At the present time, most temperature measuring methods for welding are based on the colorimetric method.[204,304,306–323] Temperatures typically are measured only at specific points in the field.[204,304,306–311] In most cases, individual devices are used for measuring the field[312–323] from which charac-

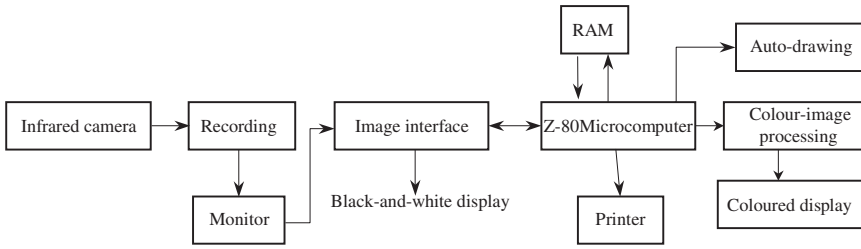

11.1 Temperature-field measurement system using infrared radiation

teristic data points in the temperature field are used for welding process control.

A direct measurement of a complete temperature field can be found in[304], in which an infrared camera was used. The configuration of the system is shown schematically in Fig. 11.1.

The measurement system consisted of four parts: an infrared camera (operating at a speed of 1/60 s per picture), an A/D image converter, a microcomputer, and a display. The measurement procedure was as follows. First, a thermal image was taken by the camera. The target surface was made of a semi-conductor material. When the radiation from a high-temperature location was projected onto the target, the resistance at that point decreased so that the output of the point on the target was at a higher potential when an electron beam scanned it. In contrast, if the temperature was low, the radiation intensity was lower, the resistance of the target point was higher, and thus the output was at a lower potential when an electron beam scanned the target. In this way, the camera tube generated a continuous electric-potential waveform that represented the temperature distribution. The potential waveform was recorded on a camcorder, which could be used to analyse the temperature at a single point or over an area.

The image information obtained by the camera was fed into a computer via an A/D converter. After processing, it was sent to a printer that printed the temperature values at various points of the field or to a drafting instrument that drew the temperature distribution as a colour image.

The calibration of the system was a big problem; two methods were applied:

(i) Special calibrator. A calibrator was designed as shown in Fig. 11.2. The calibrator material was the same as the material of the object. Current was conducted through it while cooling water was passed through both ends. The calibrator had a varying cross-section so that a temperature gradient was established when a current passed through it. The calibrator was placed with the object so that the images

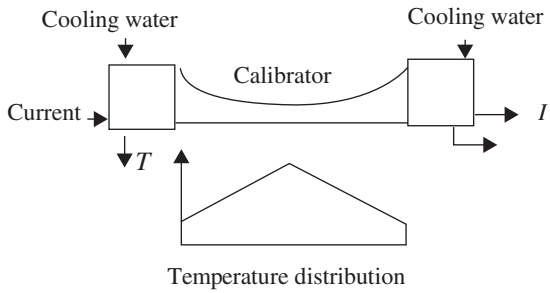

11.2 Schematic drawing of calibrator

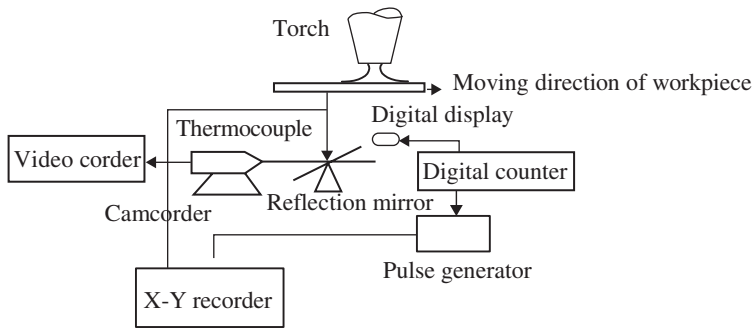

11.3 Calibration using a monitoring thermocouple

of the calibrator and the object were taken by the camera simultaneously. After computer processing, the temperature distributions of both pieces were printed or displayed. Because the temperature of the calibrator was known, the temperature of the object could be obtained. Although this method is simple, its accuracy is low. Also, because a calibrator must be used for each measurement, this technique is cumbersome.

(ii) Calibration using a thermocouple monitor. A thermocouple was mounted at the centre of the joint on the root side, as shown in Fig. 11.3, so that it experienced all of the temperatures of the field. The output of the thermocouple was recorded by an X – Y recorder. The position of the thermocouple was detected using two techniques. In the first technique, a small hole was drilled where the thermocouple was located and a sharp notch was machined in it. The light at the hole and the notch indicated the location of the thermocouple when an infrared camera took an image. In the second technique, a pulsed signal at a specific frequency was fed into a digital display tube and

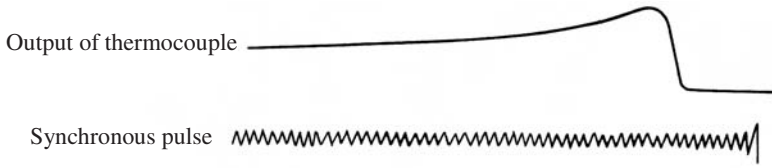

11.4 Calibration using synchronous pulse

one channel of an X – Y recorder. Thus, an oscillating curve was plotted on the X – Y diagram, see Fig. 11.4. The camera took the temperature image and presented it on the digital display. In this way, the temperature at a specific point could be measured. Because the thermocouple monitored the entire range of the temperature field, it could be used to calibrate the grey-scale range of the field.

The method was successfully used for measuring the temperature field during welding of 18-8 stainless steel. The results were compared with the data obtained from the mathematical method based on Rykalin's theory. Modifications made in recent times to this mathematical analysis of the temperature field during welding were incorporated.

In addition, an optical method has been developed for measuring the temperature field during welding without requiring calibration.[324] A linear charge-coupled device (CCD) camera was used, in conjunction with an optical system, to receive the full range of radiation wavelengths from the root side of the work piece. Assuming that the temperature distribution obeyed the rules of the theoretical analysis, after the data collected by the CCD were analysed, the absolute temperatures across the welding field were presented. In this detection method, the relationship between temperature and radiation intensity was not used. Rather, the relationship between the transverse distribution of the welding-temperature field and the thermal radiation law was used. Compared to the former methods, its advantage was its simplicity. A problem was that because the difference method was used for data processing, the bit number of the A/D converter had a significant effect on its accuracy. Moreover, it was based on the assumption that the temperature distribution obeyed the theoretical heat-transfer law, which, in fact, did not agree with the actual behaviour.

11.1.2 Problems with the existing methods using infrared radiation

For the image taken by an infrared camera to describe the temperature field, its calibration is critical. Without calibration, the image is only a

radiation intensity field but not the temperature field. Calibration is complicated because the grey levels of the image pixels depend on many factors such as the radiation wavelength, radiation intensity, conditions surrounding the detected point, parameters of the atmosphere through which the radiation travels, materials, distance, and surface condition. Among these, the wavelength and radiation intensity are related to the temperature while the other factors are not related to temperature but affect the grey level of the pixels.

All these factors make calibration difficult. All non-temperature factors must be understood or eliminated in order to calibrate the temperature accurately; this cannot be accomplished using a theoretical mathematical method.

Recently, the system was calibrated using an engineering method. In this method, the calibration was performed when non-temperature factors were either fixed or being converted. However, the problem exists that an instrument that has been calibrated under one set of conditions is not suitable for use under another set of conditions; recalibration is required.

It can be seen that calibration is the key problem for temperature-field measurement and should be solved to successfully implement this measurement method.

To overcome this problem, a colorimetric method using a CCD camera has been developed by the author with his colleagues, He and Su.[305,325] The special features of this method are as follows:

- Calibration is done using a mathematical method from which the real temperature field can be obtained without physical calibration.
- Materials, distance, and surface conditions do not affect the results.
- Because an infrared wavelength is used, it has good resistance to arc light and other interference.
- Information about the entire temperature field can be obtained quickly; the computer processes the data rapidly.

11.2 Fundamentals of the colorimetric imaging method

11.2.1 Electromagnetic wave spectrum

There are three modes of heat transfer, namely conduction, radiation, and convection. The contact type of temperature measurement is based on conduction and the non-contact type on heat radiation. Before going into the colorimetric imaging method, the theory of infrared radiation is described as follows:

Infrared radiation is electromagnetic radiation with a wavelength between visible light and microwave radiation; its wavelength is between 0.75~1000 μm. Its location in the electromagnetic spectrum is shown in Fig. 11.5; it is beyond red visible light and is therefore called infrared.

Infrared radiation is similar to visible light. It is electromagnetic radiation, propagates as a transverse wave, propagates at the same velocity in a vacuum, and exhibits wave-particle dualism. A heated body emits this kind of radiation. The infrared wavelength band can be divided into four parts,

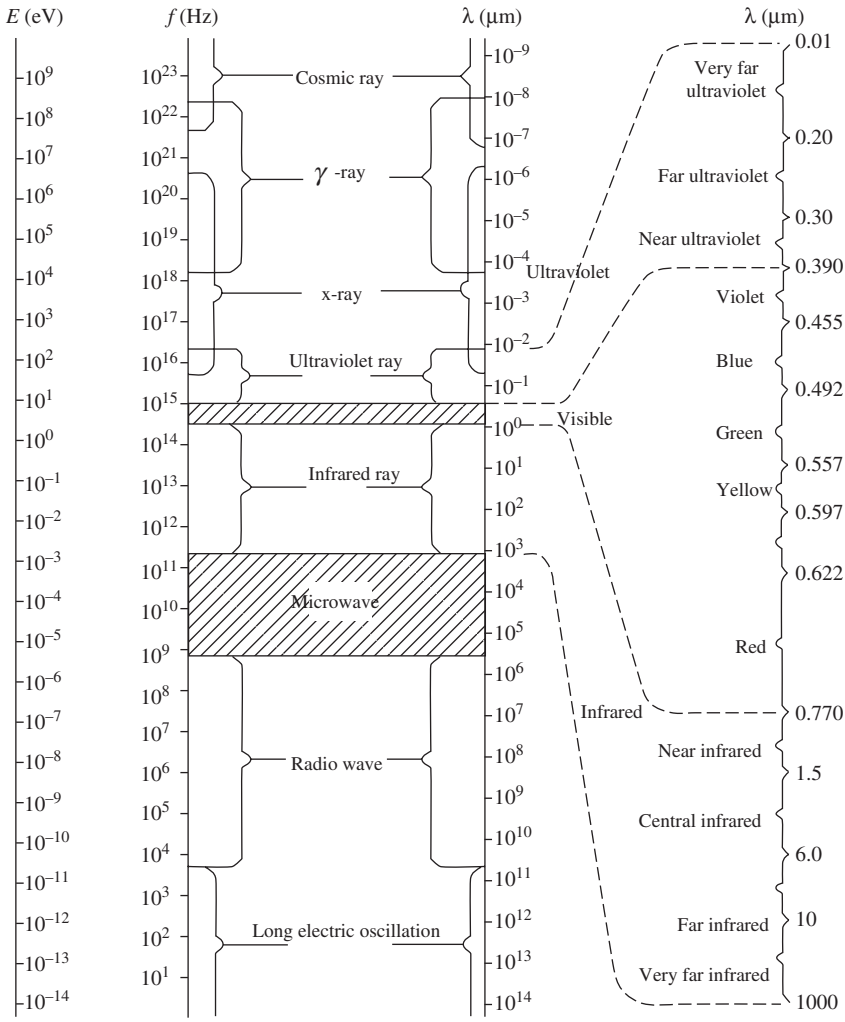

11.5 The electromagnetic spectrum

namely near infrared ($\lambda = 0.77\sim1.5\,\mu m$), central infrared ($\lambda = 1.5\sim6\,\mu m$), far infrared ($\lambda = 6\sim10\,\mu m$), and very far infrared ($\lambda = 10\sim1000\,\mu m$).

Infrared radiation commonly is called heat radiation; radiation in this wavelength range that is absorbed by bodies turns into heat.

11.2.2 The law of black-body radiation

11.2.2.1 Physical parameters describing a radiation field

(i) Radiation intensity. If the radiation power (or radiation flux) of a point radiation source in a small solid angle $\Delta\Omega$ in a certain direction is $\Delta\Phi$, then the limit of the ratio of $\Delta\Phi$ to $\Delta\Omega$ is defined as the radiation intensity of the point radiation source in that direction

$$I = \lim_{\Delta\Omega\to0}\frac{\Delta\Phi}{\Delta\Omega} = \frac{\partial\Phi}{\partial\Omega} \quad (\text{unit: W}/\text{m}^2) \qquad [11.1]$$

From this equation, the total radiation flux over all space is

$$\Phi = \int I d\Omega = \int_0^{2\pi} d\phi \int_0^{\pi} I(\Phi,\theta)\sin\theta d\theta \qquad [11.2]$$

If the radiation intensity I does not depend on direction, then $\phi = 4\pi I$.

Equation [11.1] shows that radiation intensity is the radiation power of a point source in a unit solid angle. It is a physical parameter that describes the spatial distribution of the radiation intensity power in space; it is expressed as W/sr.

As with most sources, radiation power varies with direction; therefore, to measure radiation intensity, the detector must be placed opposite to the direction that the radiation is propagating.

(ii) Radiant exitance. Radiation intensity is a parameter that describes the radiation power from a point source. For an extended source, the radiation power depends on the area of the radiation source, A. Radiant exitance is a parameter describing the extended source.

$$M = \lim_{\Delta A\to0}\frac{\Delta\phi}{\Delta A} = \frac{\partial\phi}{\partial A} \qquad [11.3]$$

It can be seen from this equation that radiant exitance is the radiation power by the extended source over the surface of a hemisphere; its units are W/m^2.

(iii) Radiance. Generally, the radiation of an extended source is not only related to the source area but also to the direction of the observation and the solid angle. Radiance is a parameter for describing this property. The radiance of an extended source in an arbitrary direction is defined as the

power over the unit area of observation in a unit solid angle; its units are $W/(m^2 \cdot sr)$.

$$L = \lim_{\substack{\Delta A \to 0 \\ \Delta \Omega \to 0}} \left(\frac{\Delta^2 \phi}{\Delta A_\theta \Delta \Omega} \right) = \frac{\partial^2 \phi}{\partial A_\theta \partial \Omega} = \frac{\partial^2 \phi}{\partial A \cos\theta \partial \Omega} \quad [11.4]$$

where θ is the angle between the line normal to the radiation surface ΔA and the observation direction. ΔA_θ is the projected area that is observed in the direction θ. This area is called the apparent area of the source; $\Delta A_\theta = \Delta A \cos\theta$.

(iv) Irradiance. This describes the power distribution on the receiving surface of a body.

$$E = \lim_{\Delta A \to 0} \frac{\Delta \phi}{\Delta A} = \frac{\partial \phi}{\partial A} \quad (W/m^2) \quad [11.5]$$

Irradiance is the radiation power received per unit area of the object.

(v) Spectrum radiation parameters. The radiation power implies that power consists of radiation at all wavelengths. Often, it is important to know the radiation properties at some arbitrary wavelength; then the symbol of the radiation property is the same as mentioned above but with a subscript λ, indicating that the properties are at a wavelength of λ.

Suppose that the radiation power in the wavelength range λ to $\lambda + \Delta\lambda$ is $\Delta\phi$, then the spectrum radiation power is

$$\phi_\lambda = \lim_{\Delta \lambda \to 0} \frac{\Delta \phi}{\Delta \lambda} = \frac{\partial \phi}{\partial \lambda} \quad [11.6]$$

where, ϕ_λ is the monochromatic radiation power at wavelength λ; it is a function of λ.

Similarly, one can obtain spectrum radiation intensity

$$I_\lambda = \lim_{\Delta \lambda \to 0} \frac{\Delta I}{\Delta \lambda} = \frac{\partial I}{\partial \lambda}, \quad [11.7]$$

Spectrum radiant exitance

$$M_\lambda = \lim_{\Delta \lambda \to 0} \frac{\Delta M}{\Delta \lambda} = \frac{\partial M}{\partial \lambda}, \quad [11.8]$$

Spectrum radiance

$$L_\lambda = \lim_{\Delta \lambda \to 0} \frac{\Delta L}{\Delta \lambda} = \frac{\partial L}{\partial \lambda}, \quad [11.9]$$

Spectrum irradiance

$$E_\lambda = \lim_{\Delta \lambda \to 0} \frac{\Delta E}{\Delta \lambda} = \frac{\partial E}{\partial \lambda}. \quad [11.10]$$

11.2.2.2 The radiation law for an absolute black body

A black body has the strongest emission power for a given temperature. An absolute black body is applied as a standard for evaluating emission power and is widely used for calibration of infrared instruments, thermometers, and for the measurement of radiation characteristics of various materials.

(i) Planck radiation formula. The experimental data for black-body radiation is plotted as shown in Fig. 11.6.

In order to explain the experimental curve for black body radiation, Planck hypothesised energy quantisation. Planck regarded the radiation of a black-body cavity as the electromagnetic radiation of a cluster of oscillating dipoles (or simply oscillators). The energy of the oscillator cannot have any value; for a dipole of oscillating frequency γ, the minimum energy unit is $h\gamma$. A dipole in a certain state would have the energy $nh\gamma(n = 0, 1, 2, \ldots)$ where h is the Planck constant, $h = 0.6262 \times 10^{-34}(J{\cdot}s)$ and $h\gamma$ is called an energy quantum. Planck considered that the probability that an oscillator will have a certain energy level is proportional to $\exp\left(-\frac{nh\gamma}{KT}\right)$ where K is the Boltzman constant, $K = 1.3806 \times 10^{-2}\,\mathrm{WsK^{-1}}$ and T represents the absolute temperature. On the basis of these two hypotheses, the famous Planck radiation formula is written as follows.

$$M_\lambda = \frac{C_1}{\lambda^5}\left(e^{\frac{C_2}{\lambda T}} - 1\right)^{-1} \left(\mathrm{W \cdot cm^{-2} \cdot \mu m^{-1}}\right) \qquad [11.11]$$

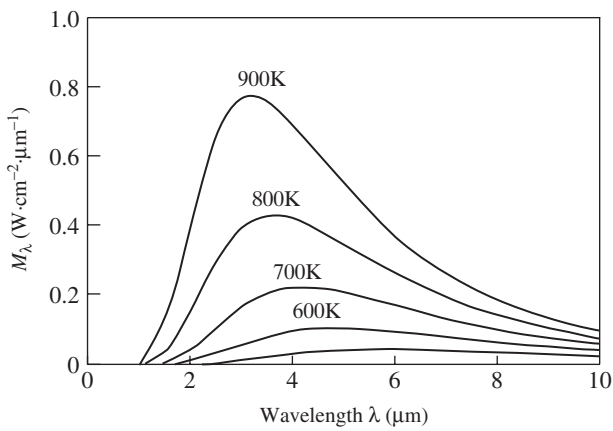

11.6 Experimental radiation curve of a black body

where M_λ is the spectrum radiant exitance. C_1 is the first radiation constant.

$$C_1 = 2\pi C^2 h = 3.7415 \times 10^{16}\ (\mathrm{W \cdot m^2})$$

where C is the velocity of light, $= 2.9979 \times 10^8\ (\mathrm{m \cdot s^{-1}})$

C_2 is the second radiation constant, $C_2 = \dfrac{hC}{K} = 1.4388 \times 10^{-2}\ (\mathrm{m \cdot K})$

The Planck hypothesis, which is contrary to classical physics, successfully explained radiation phenomena of black bodies. Planck assumed that the energy of an oscillator cannot be changed continuously but has discrete levels of energy. Classical physics cannot explain why the energy should have discrete values. Einstein popularised the quantum theory and pointed out that light also has a corpuscular property; a photon is a single quantum of energy. When matter emits or absorbs light, it emits or absorbs only by single-photon increments. Thus, this theory explains the photoelectric effect, which classical physics does not. The Planck radiation formula is an important fundamental from which many heat radiation laws can be derived.

(ii) Stefan–Boltzmann law. Stefan observed that the total energy of a black body is proportional to the fourth order of the absolute temperature of the black body. He derived the formulae on the basis of Maxwell's theory:

By integrating Eq. [11.11] over all wavelengths, the total power radiated by a black body over a half sphere of space can be obtained as

$$M_B = \int_0^\infty M_\lambda d\lambda = \int_0^\infty \frac{C_1}{\lambda^5}\left(e^{\frac{C_2}{\lambda T}} - 1\right)^{-1} d\lambda = \sigma T^4 \qquad [11.12]$$

This is the Stefan–Boltzmann law, where $\sigma = 5.670 \times 10^{-8}(\mathrm{W \cdot m^{-2} \cdot K^{-4}})$, which is called the Stefan–Boltzmann constant.

It can be seen from Fig. 11.6 that the spectrum radiation power for an absolute black body has a maximum value at a certain wavelength, which depends on the absolute temperature of the body. The corresponding wavelength is designated as λ_m. The relationship between T and λ_m is given by

$$\lambda_m T = b \qquad [11.13]$$

This is the Wien displacement law, where $b = 2.897 \times 10^{-3}(\mathrm{m \cdot K})$.

For temperatures normally encountered, the wavelength corresponding to its maximum radiation power is in the infrared region.

11.2.3 Grey-body radiation

Most matter generally is not a black body; it has selective absorption characteristics. The absorptivity is large for certain wavelengths of electromagnetic radiation. In some categories of matter there is no obvious selective absorptivity; their emissivity is less than 1 but approximately a constant. This kind of matter is called a grey body.

For a grey body, the radiation law of a black body is applicable but emissivity should be taken into consideration

Thus, the Planck formula becomes

$$M(\lambda, T) = \varepsilon(\lambda, T)\frac{C_1\lambda^{-5}}{\exp(C_2/\lambda T - 1)} \qquad [11.14]$$

and the Stefan–Boltzmann formula is

$$M_B = \varepsilon(T)\sigma T^4 \qquad [11.15]$$

11.2.4 A comparison of two measuring methods that use radiation

11.2.4.1 An existing method for measuring the welding temperature field using thermal radiation

Due to the limitation of spectrum response by the camera and the measured temperature range, radiation having a certain range of wavelength is used in existing measurement methods.

Assume that a radiation beam from the object is projected, via an optical system, onto the receiving element. Its output signal N can be expressed as the following equation:

$$\begin{aligned} N &= KF\eta(\lambda_m)\int_{\lambda_1}^{\lambda_2} \varepsilon(\lambda, T)M_\lambda \eta(\lambda)\gamma(\lambda)\varphi_1(\lambda)\varphi_2(\lambda)\ldots\varphi_n(\lambda)d\lambda \\ &= KF\eta(\lambda_m)\int_{\lambda_1}^{\lambda_2} \varepsilon(\lambda, T)M_\lambda \cdot \eta(\lambda)\cdot\gamma(\lambda)\cdot\varphi(\lambda)d\lambda \end{aligned} \qquad [11.16]$$

where:

λ_1, λ_2	Upper and lower limit of received wavelength
K	Conversion coefficient of heat to electricity
F	Geometric factor of the receiving element and object
$\varepsilon(\lambda, T)$	Emission coefficient
$\eta(\lambda_m)$	Maximum spectrum sensitivity of the receiving element
$\eta(\lambda)$	Relative spectrum sensitivity of the receiving element
$\gamma(\lambda)$	Transmissivity of the filter

$\varphi_1(\lambda)$	Transmissivity of the first optical element
$\varphi_2(\lambda)$	Transmissivity of the second optical element
$\varphi_n(\lambda)$	Transmissivity of the n^{th} optical element
$\varphi(\lambda)$	Product of transmissivity of all optical elements
M_λ	Radiance exitance of object

It is seen from Eq. [11.16] that the output signal depends on many factors including F – Geometric factors of the receiving element and object, and $\varepsilon(\lambda,T)$ – Emissivity of the object.

The other factors can be found for a given measurement system. Only these two factors F, and $\varepsilon(\lambda,T)$ are variables that depend on the distance, material, and surface conditions (see Chapter 13 for more details on Eq. [11.16]).

- The effect of distance. Suppose the other factors are kept constant, only distance is varied, the radiation intensity of the source S is I, and the angle between the normal line of the receiving surface and direction of the radiation is θ. Then the radiation power received can be written as (see Fig. 11.7)

$$d\phi = I \cdot d\Omega = I \frac{dA\cos\theta}{d_0^2} \qquad [11.17]$$

In this equation, d_0 is the distance between the point source S and dA. Therefore the irradiance on dA by S is

$$E = \frac{d\phi}{dA} = I\frac{\cos\theta}{d_0^2} \qquad [11.18]$$

The output signal N of the receiver is proportional to the irradiance

$$N \infty E, \quad N \infty \frac{\cos\theta}{d_0^2} \qquad [11.19]$$

It can be concluded, therefore, that the output potential of the receiver is proportional to $\cos\theta$ and inversely proportional to the square of d_0.

It is seen that there is a strong influence of distance and θ on the measurement. Normally it is arranged so that the normal line of the

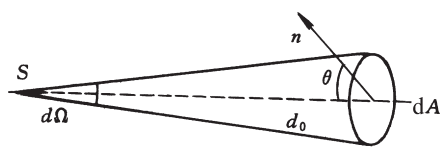

11.7 Radiance exitance on dA by point source S

receiving surface coincides with the radiation direction, so that the influence of θ can be eliminated.

- Influence of material and surface condition. It is seen that the output signal depends on the emissivity of the object ε(λ, *T*), which is, in turn, affected by many factors. It varies greatly. Table 11.1 lists the emissivity of various materials with different surface conditions.

Table11.1 Emissivity of conventional materials ε_n (in normal line direction)[326]

Material surface condition	Temperature (°C)	Emissivity e_n
Aluminium:		
Vacuum illuviated Al	20	0.04
Polished Al	50~500	0.04~0.06
Polished Al	225~575	0.039~0.057
Coarse surface Al	20~50	0.06~0.07
Frosted Al	26	0.055
Al plate	100	0.09
Polished Al plate	100	0.05
Oxidised at 600°C Al	200~600	—
Strongly oxidised Al	150~550	0.20~0.25
Heavily oxidised Al	93~504	0.20~0.25
Oxidised Al	500~827	0.42~0.26
Oxidised grey colour Al	25	0.28
Copper:		
Rolled brass, natural	22	0.06
Frosted brass	50~350	0.22
Highly-polished brass	100	0.03
Rolled brass, coarse sand wheel ground	22	0.20
Ground brass	100	0.05
Oxidised brass	100	0.61
Oxidised at 600°C brass	200~600	0.61~0.59
Polished	50	0.10
Fine ground, electrolytic copper	80~115	0.018~0.023
Near-mirror copper	22	0.027
Molten copper	1075~1275	0.11~0.13
Rolled, bright Mn-Cu	120	0.05
Copper with heavy oxide surface	25	0.78
Copper with heavy black oxide surface	5	0.88
Iron and steel:		
Polished steel	100	0.07
Polished ingot	770~1040	0.52~0.56
Rolled steel plate	21	0.66
Coarse steel plate	38~370	0.94~0.97
Steel with coarse surface	50	0.95~0.98
Newly-rolled steel	20	0.24

Table11.1 (cont.)

Material surface condition	Temperature (°C)	Emissivity e_n
Ground steel belt and plate	910~1100	0.52~0.61
Rolled belt	50	0.56
Molten mild steel	1600~1800	0.28
Rubbed 18-8 stainless steel	20	0.16
Stainless steel oxidised at 800°C	60	0.85
Polished stainless steel	25~30	0.13
Sand-sprayed stainless steel	700	0.70
Rolled stainless steel	700	0.70
Rolled stainless steel	700	0.45
Alloy steel (8% Ni, 18% Cr)	500	0.35
600°C alloy steel	200~600	0.79
Steel plate with coarse oxide film	24	0.80
Steel plate with dense luminous oxide film	24	0.82
Steel with red rust	20	0.60
Strongly oxidised steel	50	0.88
Steel with coarse oxide	40~370	0.94~0.97
Polished iron	420~1020	0.147~0.377
Smooth plate	900~1040	—
Fine-polished iron for welding	40~250	0.28
Hot-rolled iron	20	0.77
Iron with grey surface	130	0.60
Coarse cast iron	830~990	0.60~0.70
Cast iron ingot	1000	0.95
Molten pig iron	1300~1400	0.29
Polished iron	200	0.21
Polished iron	40	0.21
Non-operated cast iron	925~1115	0.87~0.95
Cutting cast iron	830~990	0.60~0.70
Old galvanised wrought iron	20	0.28
301 oxidised wrought iron	215~525	–
Completely oxidised iron plate	19	0.69
Non-luminous oxidised wrought iron	21~360	0.94
Iron oxide	500~1200	0.85~0.95
Oxidised iron surface	100	0.736
Smooth oxidised iron surface	125~525	–
Iron with red-rust surface	20	0.61~0.85
Cast-iron oxidised at 600°C	200~600	0.64~0.87
Coarse strong oxidised cast iron	38~250	0.95
Ferrous sulphate powder	—	0.60
Zinc galvanised steel plate	28	0.228
Zinc galvanised steel plate after oxidation	24	0.276

The table shows that emissivity varies greatly depending on the material and surface condition. The amount of variation can be several orders of magnitude. This is the main factor that affects the accuracy of the measuring method.

11.2.4.2 A new proposed method

As described previously, with measuring methods available currently, there is no corresponding relationship between the output potential and the temperature. The distance to the object and surface conditions affect it. In order to solve this problem, a colorimetric imaging method has been proposed. It uses a CCD camera to take the image, which is processed by computer to obtain the two-dimensional temperature field. The principle of the method is as follows:

From the Planck formula one can obtain

$$M_{\lambda 1} = \varepsilon_{(\lambda_1,T)} \frac{C_1}{\lambda_1^5}\left(e^{\frac{C_2}{\lambda_1 T}} - 1\right)^{-1}; \quad M_{\lambda 2} = \varepsilon_{(\lambda_2,T)} \frac{C_1}{\lambda_2^5}\left(e^{\frac{C_2}{\lambda_2 T}} - 1\right)^{-1}$$

Dividing the first formula by the second:

$$R = \frac{M_{\lambda 1}}{M_{\lambda 2}} = \frac{\varepsilon_{(\lambda_1,T)}}{\varepsilon_{(\lambda_2,T)}} \frac{\frac{C_1}{\lambda_1^5}\left(e^{\frac{C_2}{\lambda_1 T}} - 1\right)^{-1}}{\frac{C_1}{\lambda_2^5}\left(e^{\frac{C_2}{\lambda_2 T}} - 1\right)^{-1}} = \frac{\varepsilon_{(\lambda_1,T)}\lambda_2^5\left(e^{\frac{C_2}{\lambda_2 T}} - 1\right)^{-1}}{\varepsilon_{(\lambda_2,T)}\lambda_1^5\left(e^{\frac{C_2}{\lambda_1 T}} - 1\right)^{-1}} \qquad [11.20]$$

where R is called the colorimetric ratio, λ_1, λ_2 are two wavelengths, and T is the absolute temperature of the object.

From Eq. [11.20] it can be seen that describing the temperature using the colorimetric ratio is an improved way because two wavelengths can be chosen so that the emissivity of the matter at the two wavelengths is similar and an accurate relationship between R and T can be obtained.

11.2.4.3 The relationship of T *to* R *in the new method*

From Eq. [11.16], the output potential of the receiver in the wavelength band $\Delta\lambda_1$ near λ_1 is

$$N_1 = KF\eta(\lambda_m)\int_{\lambda_1}^{\lambda_1+\Delta\lambda_1} \varepsilon_{(\lambda_1,T)} \cdot \frac{C_1}{\lambda_1^5}\left(e^{\frac{C_2}{\lambda_1 T}} - 1\right)^{-1} \cdot \eta(\lambda_1)\gamma(\lambda_1)\varphi_1(\lambda_1)\varphi_2(\lambda_1)\ldots\varphi_n(\lambda_1)d\lambda$$

The output potential for the wavelength band $\Delta\lambda_2$ at λ_2 is

$$N_2 = KF\eta(\lambda_m)\int_{\lambda_2}^{\lambda_2+\Delta\lambda_2} \varepsilon_{(\lambda_2,T)} \cdot \frac{C_1}{\lambda_2^5}\left(e^{\frac{C_2}{\lambda_2 T}} - 1\right)^{-1} \cdot \eta(\lambda_2)\gamma(\lambda_2)\varphi_1(\lambda_2)\varphi_2(\lambda_2)\ldots\varphi_n(\lambda_2)d\lambda$$

Dividing the first formula by the second gives the colorimetric ratio

$$R = \frac{N_1}{N_2} = \frac{\varepsilon_{(\lambda_1,T)}}{\varepsilon_{(\lambda_2,T)}} \cdot \frac{\lambda_2^5 \cdot \Delta\lambda_1}{\lambda_1^5 \cdot \Delta\lambda_2} \cdot \frac{\left(e^{\frac{C_2}{\lambda_2 T}} - 1\right) \cdot \eta(\lambda_1)\gamma(\lambda_1)\varphi_1(\lambda_1)\varphi_2(\lambda_1)\ldots\varphi_n(\lambda_1)}{\left(e^{\frac{C_2}{\lambda_1 T}} - 1\right) \cdot \eta(\lambda_2)\gamma(\lambda_2)\varphi_1(\lambda_2)\varphi_2(\lambda_2)\ldots\varphi_n(\lambda_2)} \quad [11.21]$$

The following can be obtained for metals, because $\varepsilon_{(\lambda_1,T)} = \varepsilon_{(\lambda_2,T)}$:

$$R = \frac{\lambda_2^5 \cdot \Delta\lambda_1}{\lambda_1^5 \cdot \Delta\lambda_2} \cdot \frac{\left(e^{\frac{C_2}{\lambda_2 T}} - 1\right) \cdot \eta(\lambda_1)\gamma(\lambda_1)\varphi_1(\lambda_1)\varphi_2(\lambda_1)\ldots\varphi_n(\lambda_1)}{\left(e^{\frac{C_2}{\lambda_1 T}} - 1\right) \cdot \eta(\lambda_2)\gamma(\lambda_2)\varphi_1(\lambda_2)\varphi_2(\lambda_2)\ldots\varphi_n(\lambda_2)} \quad [11.22]$$

Equation [11.22] means that the potential response of the receiving element for a grey body is related to temperature and

$$\lambda_1, \lambda_2, \Delta\lambda_1, \Delta\lambda_2, \eta(\lambda_1), \eta(\lambda_2), \gamma(\lambda_1), \gamma(\lambda_2), \varphi_1(\lambda_1), \varphi_2(\lambda_1)\ldots \varphi_n(\lambda_1), \varphi_1(\lambda_2), \varphi_2(\lambda_2)\ldots\varphi_n(\lambda_2).$$

Among them, all of the factors except temperature are known and fixed for a given measuring system. Therefore, it can be concluded that temperature has a relationship with only the colorimetric ratio and has no relationship with material, distance, surface conditions, etc. Equation [11.22] is the general formula that describes the colorimetric ratio – temperature relationship for the colorimetric method.

12

Study of the colorimetric imaging method

12.1 Introduction

The principle described in Chapter 11 should be proved by practical experiments in order to see whether it is correct in reality. The facilities, experimental procedures, and results of such experiments are described in this chapter.[295] Figure 12.1 shows the parts that comprised the experimental system.

12.2 Facilities for acquisition of the infrared image

Designing and fabricating an infrared camera is the key challenge for achieving a sensitive measuring method.

During welding, the temperature range of the weld pool is about 1000~1600°C. According to the Wien displacement law, the wavelengths corresponding to the maximum radiance exitance are 2897/(1000 + 273)~2897/(1600 + 273) (see Eq. [11.3]), which is around 1.55~2.27 μm. This is in the near-infrared range. Therefore, it is reasonable to use a camera sensitive to infrared radiation. This wavelength range also is resistant to interference.

12.2.1 Comparison of different cameras

The infrared camera is a device that takes a picture in the infrared wavelength range and transforms it into a visible image. The principle is that it divides the image of the object into many small pixels using horizontal and vertical lines, scans all of the pixels, and generates output signals. Reconstruction of these signals creates the visible image.

There are three types of devices used for pixel division and scanning, namely

(i) Optical–mechanical camera. The construction of this camera is shown schematically in Fig. 12.2. An optical detection device deflects

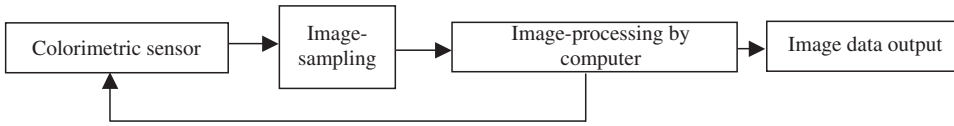

12.1 Colorimetric imaging system

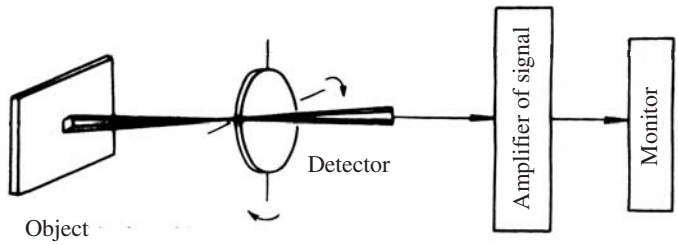

12.2 Schematic diagram of an optical–mechanical camera

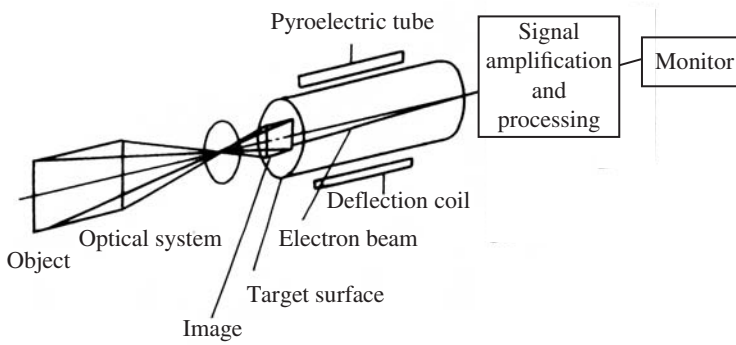

12.3 Schematic diagram of a pyroelectric camera

up and down, and left and right, so that it scans the full area of the object.

(ii) Electron-beam scanning camera. There are several types of cameras that use electron-beam scanning. The most common type is a pyroelectric camera. The optical system does not deflect. The whole object image is projected onto the target of the pyroelectric camera. An electron beam scans the target surface and picks out the signals using the pyroelectric effect (Fig. 12.3).

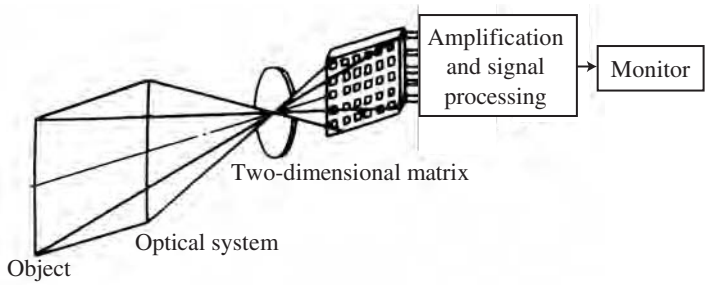

12.4 Schematic diagram of a solid-state scanning camera

(iii) Solid-state automatic scanning camera. This camera comprises a two-dimensional matrix of detection elements. It is manufactured as a large-scale integrated circuit. The image is projected onto the matrix, the signal from each pixel is detected, and the device automatically transmits an output signal (Fig. 12.4).

The solid-state type of camera was developed using large-scale integrated-circuit technology. The resolution increases with the density of the pixel array. Recently, charged-coupled devices (CCDs) have been used for this purpose.

Among these three types of cameras, the solid-state automatic scanning type is superior. Because there is no optical scanning or electron-beam scanning as used in the other types, the weight and size are smaller. These advantages favour its implementation.

12.2.2 The optical response of CCD cameras

CCD cameras are widely used for taking visible-light images. They give very clear grey (black and white) and colour pictures and have good spectrum response in the wavelength range of 0.4~1.1 μm. Therefore they can be considered for recording infrared images.

In the present study, a Type WV-BL200 black and white CCD camera manufactured by National of Japan was chosen. The camera specifications were as follows:

Pick up device: 577 (horizontal) × 581(vertical) pixel, line transform CCD

Device area: 6.4 mm (horizontal) × 4.89 mm (vertical)

Scan: 625 lines/50 fields/25 frames

Scan: 2 : 1 one-line partition

Signal to noise ratio: 48 dB

Focal length: 12 mm

12.3 Sensor for experimental use

12.3.1 Selection of filter

For the colorimetric method, two filters of different wavelengths and with narrow bandwidths should be used. The characteristics of the filters affect the measurement accuracy.

Principles for the selection of filters. (i) The wavelength of the filter should be within the spectrum-response range of the CCD and preferably not in the visible-light range. Therefore, the possible wavelength range is 0.75~1.1 μm. (ii) The colorimetric method can exclude the effect of neutral media such as fume, dust etc., but not the effect of selective absorbing media such as water vapour and CO_2. Therefore, avoiding the wavelength of the selective absorbing media is necessary. The sensor is normally used in air, which contains mainly symmetrical molecules such as N_2 and O_2. These gases do not absorb the infrared radiation over a wide range of wavelengths but H_2O, CO_2, and CO in the air absorb infrared radiation. For example, water vapour's absorbing wavelengths are 0.94, 1.13, 1.38, 1.87, 2.7, and 6.3 μm, and CO_2's absorbing wavelengths are 2.7, 4.3 and 14.5 μm. Therefore, the filters have to avoid these wavelengths. (iii) Emissivity $\varepsilon(T)$ generally is considered unrelated to wavelength but, in fact, there is an influence of wavelength on $\varepsilon(T)$. Therefore, selecting two wavelengths that are close to each other so that they have similar emissivities is appropriate to ensure measurement accuracy. (iv) The ratio of the radiation power at the two wavelengths should be within a certain limit in order that the signals are within the dynamic-response range of the CCD and bits of the A/D converter. For example, if the ratio is too high, the CCD output at one wavelength may be saturated while that at the other wavelength may be very weak so that the detection system has low sensitivity.

Filter specification. Based on the considerations above, filters having wavelengths of $\lambda_1 = 0.8046\,\mu m$ and $\lambda_2 = 0.8943\,\mu m$ were chosen. The transmissivity of the two filters are shown in Figures 12.5 and 12.6, respectively. It is necessary to mention that the transmissivity of the 0.8046 μm filter is very high at $\lambda > 1.2\,\mu m$ but it does not effect the measurements because the CCD has no response to wavelengths greater than 1.2 μm.

12.3.2 Construction of the sensor

Design requirements. The measurement system should ensure accuracy, have small volume and light weight, be inexpensive and have high speed for real-time measurement of rapidly varying temperature fields during welding.

Optical system. There are two design choices for the optical system. In the first design, one detection device is used. The radiation beam projects

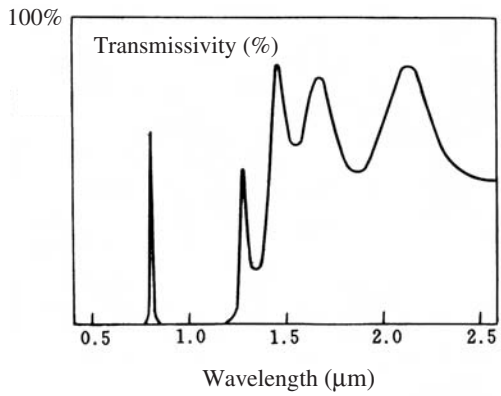

12.5 Transmissivity curve for the 0.8046 μm filter

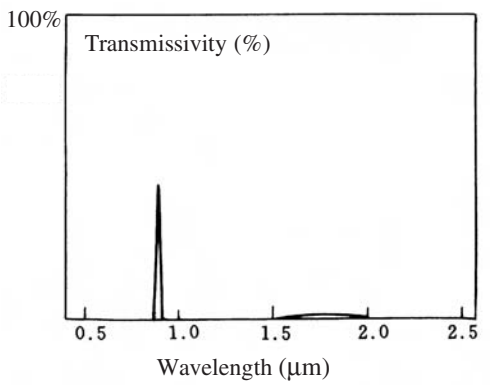

12.6 Transmissivity curve for the 0.8943 μm filter

to the device along a single path. In the second design, two detection devices are used; the radiation beam projects to the device via two optical paths, as shown in Fig. 12.7.

The advantages of the single-path design are that it is a small and compact sensor, it is stable, and optical-device adjustment is convenient. Its shortcomings are that its measuring speed is slower and a color modulator is required.

The advantages of the two-path design are that a color modulator is not needed and the measuring speed is high. The shortcomings are that the optical path is complicated, the design is hard to debug, it is heavier and has a larger volume, and it is more expensive. Moreover, the characteristics

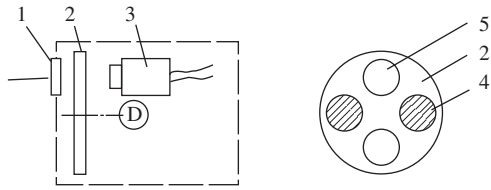

a) Single path

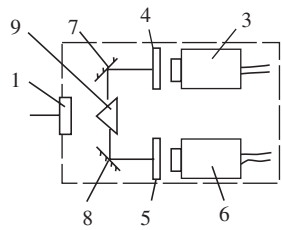

b) Double path

1. Protecting glass; 2. Colour modulator; 3. Video camera recorder; D. Motor; 4. Filter 1; 5. Filter 2; 6. Video camera recorder 2; 7. 8. Reflection mirror; 9. Spectroscope

12.7 Optical system of the sensor

of two CCDs used in this design are not the same; therefore the measurement accuracy cannot be ensured.

These comparisons show that the single-path design is superior. Considering the large inertia of the thermal process in welding, the available measuring speed of the single-path design can meet the actual requirements.

Colour modulator and control. The function of the colour modulator is to alternately change between the two color filters in the optical path so that the CCD camera can take two images at different radiation wavelengths. High speed and accurate positioning are required. Therefore a Model 36BF-003 stepping motor produced by Changzhou Micromotor Manufacturing Co. was chosen to position the filters.

In order to reduce the volume of the sensor, a 30° sector instead of a disc was used as the colour modulator. Two filters were placed in the image path, alternately, by positive and reverse rotations of the stepping motor. The control circuit of the modulator is shown in Fig. 12.8. Another design of the sensor is described in Section 13.6.

A command signal is sent to the pulse-allocation device CH250 via an I/O, which produces a pulse to control an MOS and drive the motor. The optical coupler detects whether the color modulator has reached the right position; if so, it sends a signal to the computer via an I/O.

Due to the torque-frequency characteristics of the stepping motor (see Fig. 12.9), the motor driving programme provides low-speed starting followed by acceleration so that the alternating between the filters can be completed within 40 ms. The construction of the sensor is shown in Fig. 12.10.

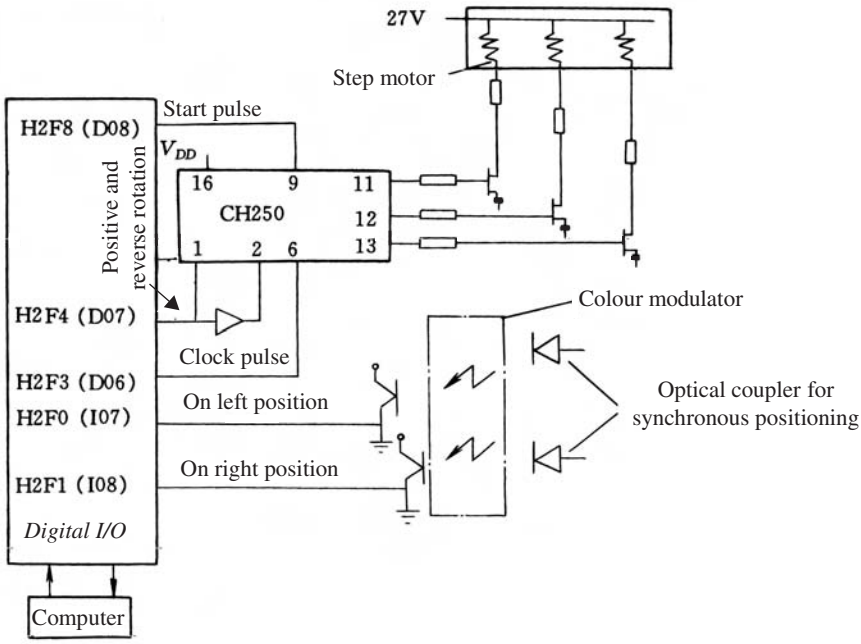

12.8 Control circuit for the colour modulator

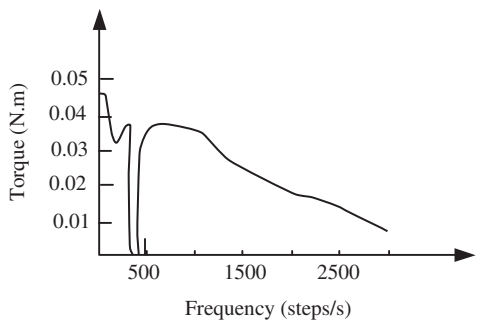

12.9 Torque-frequency characteristics for the stepping motor

12.4 The colorimetric imaging system

12.4.1 Configuration of the system

The system consists of the sensor, image-sampling board, computer, display, and colour modulator control, which are shown in Fig. 12.11.

(i) Sensor and colour modulator control
(ii) Image sampling board, the functions of which are:

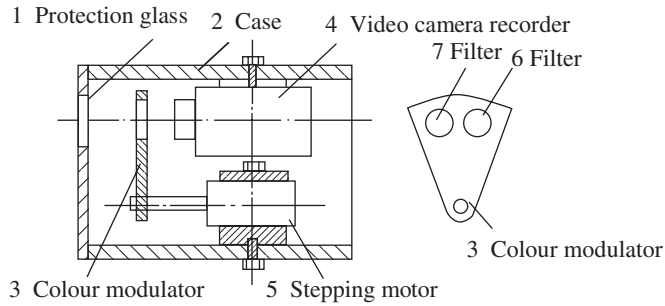

12.10 Construction of the sensor

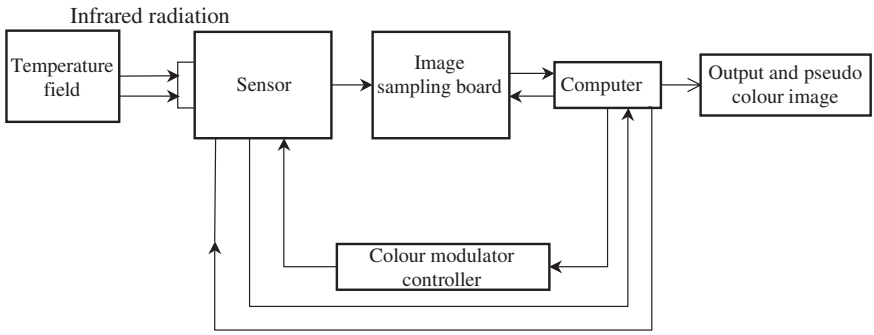

12.11 Colorimetric imaging system

- A/D conversion of the image signals.
- Storage of the signal into memory.
- Signal processing including smoothing, filtering, etc.
- Control of the monitor to display monochrome or pseudo-colour images.

An IP-8 pseudo-colour image board made by the Matrox Co. was used. The characteristics of this board are as follows: four input channels, superposition of grey images with VGA, single-screen display, 8× amplification by the hardware with independent X,Y-direction amplification, a single-channel 8-bit frame memory, high-speed write and read of each $1024 \times 1024 \times 8$ bit frame, 1/25 s frame duration, and 256 grades of pseudo-colour display.

(iii) Computer. A SUPIX 80386SX/16 computer with 2 M memory, 16 MHz master clock frequency, and 40 M hard disk was used. The computer output provided commands to control the colour modulator and the image-sampling board for performing the sampling. It performed pro-

cessing, colorimetric computation, and defined the temperature field. In addition, it controlled the hard disk and printer that stored, recorded and printed the temperature field that was obtained.

12.4.2 Measuring procedure

First the computer initiated the image-sampling board, and then sent a command to position the 0.8046 μm filter in the optical path. An image was taken when the filter reached the correct position. After that the 0.8046 μm filter was moved out of the optical path and the 0.8943 μm filter was positioned in the optical path. The second image was taken when this filter reached the correct position. After two images were taken, the data first were smoothed and filtered, and then the computer performed the colorimetry of the two images, i.e. division of each grey pixel of one image with the corresponding grey pixel of the second image. The colorimetric temperature field image thus was obtained and stored on the hard disk, from which it could be printed or displayed by the monitor in pseudo colour. The image could be processed further to define the characteristic parameters of the temperature field for control of the welding process. The flow chart for these operations is shown in Fig. 12.12.

12.4.3 Filtering of noise

Noise originated mainly from fluctuation of the power-source voltage, electromagnetic interference, thermal noise of the CCD, and noise of the processing circuit. Different measures could be taken to eliminate noise accompanying sensing temperature fields of different objects.

If the temperature gradient was small, a method that averaged nine points could be applied. For example, the nine data points can be expressed as:

$$\begin{matrix} a_{(i-1)(j-1)} & a_{(i-1)j} & a_{(i-1)(j+1)} \\ a_{(j-1)} & a_{ij} & a_{(j+1)} \\ a_{(i+1)(j-1)} & a_{(i+1)j} & a_{(i+1)(j+1)} \end{matrix}$$

The value of a_{ij} (row i and column j) can be calculated as

$$A_{ij} = \frac{1}{9}[a_{(i-1)(j-1)} + a_{(i-1)j} + a_{(i-1)(j+1)} + a_{i(j-1)} + a_{ij} + a_{i(j+1)} + a_{(i+1)(j-1)} + a_{(i+1)j} + a_{(i+1)(j+1)}]$$

This is a classical method for eliminating the noise associated with images. It is effective in cases where the temperature gradient is not

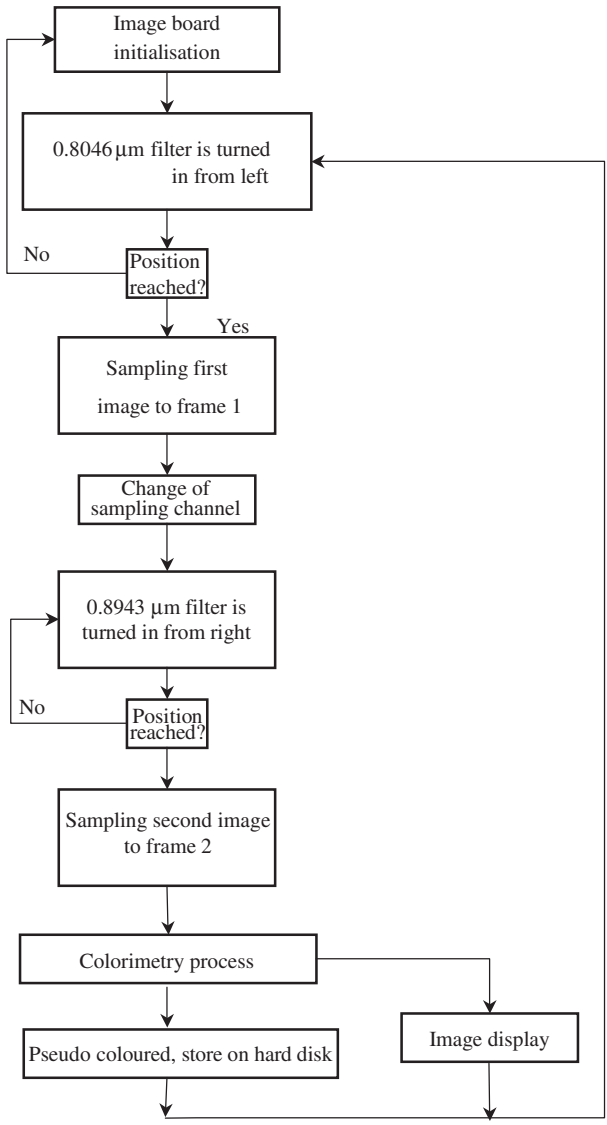

12.12 Flow chart of temperature-field measurement

large. This technique was used in the calibration experiment utilising a Gleeble machine for which the temperature gradient is not large. In welding, however, the temperature gradient is large and this method would distort the actual temperature-field image. This topic is discussed in later chapters.

12.5 Calibration of the system using a mathematical method

From Eq. [11.22] it is known that the colorimetric ratio is

$$R=\frac{\lambda_2^5\cdot\Delta\lambda_1}{\lambda_1^5\cdot\Delta\lambda_2}\cdot\frac{\left(e^{\frac{C_2}{\lambda_2 T}}-1\right)\cdot\eta(\lambda_1),\gamma(\lambda_1),\varphi_1(\lambda_1),\varphi_2(\lambda_1),\ \cdots\varphi_n(\lambda_1)}{\left(e^{\frac{C_2}{\lambda_1 T}}-1\right)\cdot\eta(\lambda_2),\gamma(\lambda_2),\varphi_1(\lambda_2),\varphi_2(\lambda_2),\ \cdots\varphi_n(\lambda_2)}$$

Because the temperature range measured is 1000~1600°C,

$$e^{\frac{C_2}{\lambda_1 T}}>>1,\quad e^{\frac{C_2}{\lambda_2 T}}>>1,$$

Equation [11.22] then can be written as

$$R=\frac{\lambda_2^5\cdot\Delta\lambda_1}{\lambda_1^5\cdot\Delta\lambda_2}\cdot\frac{\eta(\lambda_1),\gamma(\lambda_1),\varphi_1(\lambda_1),\varphi_2(\lambda_1),\cdots\varphi_n(\lambda_1)}{\eta(\lambda_2),\gamma(\lambda_2),\varphi_1(\lambda_2),\varphi_2(\lambda_2),\cdots\varphi_n(\lambda_2)}\cdot e^{\frac{C_2}{T}\left(\frac{1}{\lambda_2}-\frac{1}{\lambda_1}\right)} \qquad [12.1]$$

In the present system

$$C_2=14388\,\mu\text{m/K}\quad \lambda_1=0.8046\,\mu\text{m}\quad \lambda_2=0.8943\,\mu\text{m}$$

$\Delta\lambda_1=\Delta\lambda_2=0.01\,\mu$m (The band width is determined by measurement.) The bandwidth between the two half-transmissivity points on the transmissivity curve was taken as the bandwidth of the filter. The transmissivities of the protection glass used in the optical system for the two wavelengths were $\varphi_1(0.8046\,\mu\text{m})=\varphi_1(0.8943\,\mu\text{m})=82\%$, the transmissivities of the two filters were $\gamma(0.8046\,\mu\text{m})=62.38\%$ and $\gamma(0.8943\,\mu\text{m})=44.31\%$, and the spectrum-response curve (relative value) of the CCD camera is shown in Fig. 12.13. It is seen that $\eta(0.804\,\mu\text{m})=50\%$, $\eta(0.8943\,\mu\text{m})=24\%$.

Substituting these value to Eq. [12.1] gives

$$R=\left(\frac{0.8943^5}{0.8046^5}\cdot\frac{0.01}{0.01}\cdot\frac{50\%}{24\%}\cdot\frac{82\%}{82\%}\cdot\frac{62.38\%}{44.31\%}\right)\cdot e^{\frac{14388}{T}-\left(\frac{1}{0.8943}-\frac{1}{0.8046}\right)}$$

$$=4.97e^{-\frac{1793.6}{T}}$$

$$T=\frac{1793.6}{\ell n\frac{4.97}{R}}$$

This is the result obtained from the mathematical calibration.

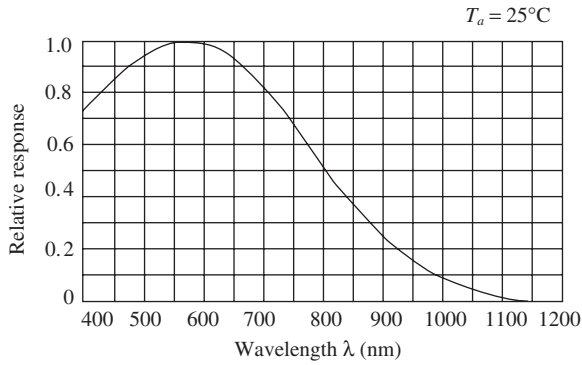

12.13 Relative response curve of the CCD camera

12.6 Experimental results and verification

The result obtained from the mathematical calibration should be verified by actual testing and corrected using experimental data. For this purpose, a precision heating facility was used. It is described below.

12.6.1 Gleeble-1500 thermal simulation

Figure 12.14 shows a schematic diagram of the machine. It consists of the body, heating transformer, hydraulic servo system, stress and strain detection devices, programming device, control board, recorder, computer, etc.

The stress and strain are controlled by a closed-loop servo-hydraulic system. It can be programmed on a time scale. The heating system also can be programmed on a time scale and synchronised with the stress-strain control. The temperature can be measured using either a thermocouple or an optical pyrometer. Resistance heating is used for heating the specimen. For this, the specimen is held between two water-cooled copper clamping blocks through which electricity is conducted. In order to avoid the influence of the heating current on the temperature measurement by the thermocouple, the heating current stops for a short duration in each cycle of the alternating current for measuring the temperature. The main characteristics of the Gleeble machine are shown in as follows:

Maximum heating speed	1700°C/s (Carbon steel, ϕ6 mm sample, distance between clamps 15 mm). ≥1000°C/s (Commonly the status of affairs)
Maximum cooling speed	140°C/s

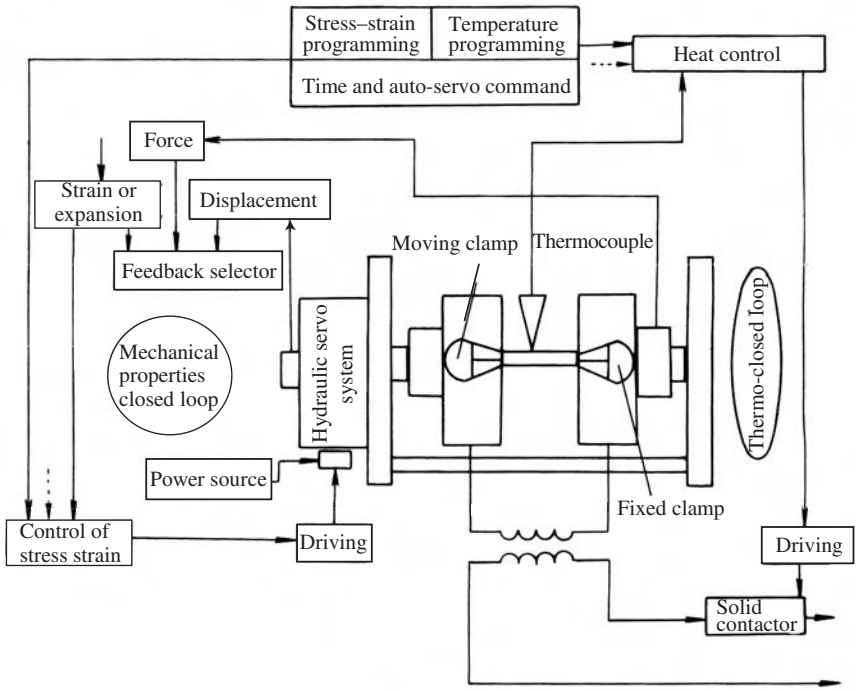

12.14 The Gleeble-1500 machine

12.6.2 Calibration using the mathematical method

Experimental verification was carried out on the Gleeble machine. The results obtained by both the colorimetric method and a thermocouple were recorded and compared:

Experiment conditions. Gleeble-1500, NiCr–NiAl thermocouple, 1Cr18Ni9Ti specimen material, $\phi 12 \times 100$ mm specimen dimensions, 475 mm distance between the specimen and the CCD sensor.

Results. Experiments were conducted in the temperature range of 1000~1300°C and measurements were taken each 50°C step. Table 12.1 gives the numerical data and Fig. 12.15 shows the calibrated mathematical data. Both the table and curves show that the results of the two methods were very close; the maximum error was +26.8°C, and the relative error was 2.64%.

Error analysis of the mathematical calibration method. Table 12.1 shows that the error was larger in the range of 1000~1150°C, as large as 26.8°C, than at higher temperatures. The reason for this result may be analysed as follows:

- The mathematical calibration was based on the theoretical formula which implies that the radiation power over the wavelength band

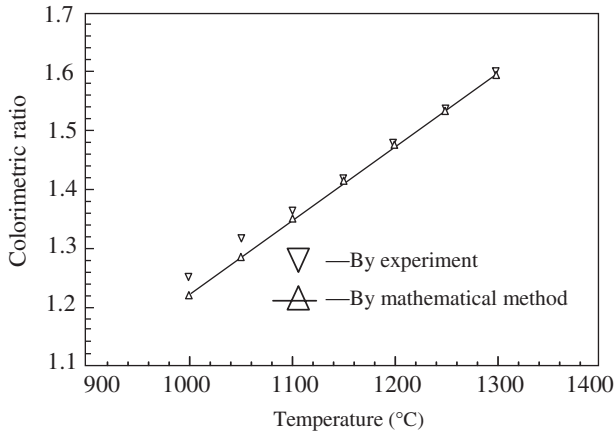

12.15 Comparison of results obtained by mathematical calibration and by experiments

Table 12.1 Mathematically calibrated and experimental results

Colorimetric ratio by experiment	Mathematically-calibrated temperature (°C)	Actual temperature (°C)	Error (°C)
1.602	1311.2	1300	+11.2
1.536	1254.5	1250	+4.5
1.480	1207.6	1200	+7.6
1.419	1157.9	1150	+7.9
1.363	1113.4	1100	+13.4
1.316	1076.8	1050	+26.8
1.25	1026.4	1000	+26.4

$\left(\lambda_1 - \frac{\Delta\lambda}{2}, \lambda_1 + \frac{\Delta\lambda}{2}\right)$ and $\left(\lambda_2 - \frac{\Delta\lambda}{2}, \lambda_2 + \frac{\Delta\lambda}{2}\right)$ is the same as the central wavelength λ_1 and λ_2, i.e.

$$M_1 = \varepsilon(\lambda_1, T)\frac{C_1}{\lambda_1^5}\left(e^{\frac{C_1}{\lambda_1 T}} - 1\right)^{-1} \cdot \Delta\lambda; \quad M_2 = \varepsilon(\lambda_2, T)\frac{C_1}{\lambda_2^5}\left(e^{\frac{C_1}{\lambda_2 T}} - 1\right)^{-1} \cdot \Delta\lambda$$

In reality, the formula should be

$$M_1 = \int_{\lambda_1 - \Delta\lambda/2}^{\lambda_1 + \Delta\lambda/2} \varepsilon(\lambda_1, T)\frac{C_1}{\lambda_1^5}\left(e^{\frac{C_1}{\lambda_1 T}} - 1\right)^{-1} d\lambda;$$

$$M_2 = \int_{\lambda_2 - \Delta\lambda/2}^{\lambda_2 + \Delta\lambda/2} \varepsilon(\lambda_2, T)\frac{C_1}{\lambda_2^5}\left(e^{\frac{C_2}{\lambda_2 T}} - 1\right)^{-1} d\lambda$$

Moreover the transmissivity in the interval $\left(\lambda_1 - \frac{\Delta\lambda}{2}, \lambda_1 + \frac{\Delta\lambda}{2}\right)$ and $\left(\lambda_2 - \frac{\Delta\lambda}{2}, \lambda_2 + \frac{\Delta\lambda}{2}\right)$ is distributed. Simplification of these factors in the mathematical calibration produced an error.

- Although $\varepsilon(\lambda_1, T) = \varepsilon(\lambda_2, T)$ was assumed in the mathematical calibration, in fact they are not equal, which also introduced an error.
- Eliminating all kinds of interferences in image processing was not possible.
- The D/A converter was limited because an 8-bit D/A was used; the relative error for one-half frame was 0.4%. Thus the sampling itself was not accurate. If a 12-bit D/A were to be used for conversion, the relative error would decrease to 0.023%, which would improve the measurement accuracy.

Experimental calibration of the system. The mathematical calibration formula is $T = 1793.6/\ln(4.97/R) - 273(°C)$, which is not convenient for fast calculation by a computer. For faster calculation and more accurate results, the experimental results might be fitted to a specific curve so that the temperature would be found using the curve obtained by experiments.

The experimental data above show that the colorimetric ratio had a linear relationship with temperature. Therefore, least squares linear fitting is possible.

Let $T = a + bR$.

From the least squares method,

$$\begin{cases} 7a + b\sum_{i=1}^{7} R_i = \sum_{i=1}^{7} T_i \\ a\sum_{i=1}^{7} R_i + b\sum_{i=1}^{7} R_i^2 = \sum_{i=1}^{7} R_i T_i \end{cases}$$

That is $\begin{cases} 7a + 9.966b = 8050 \\ 9.966a + 14.2822b = 11541.55 \end{cases}$

Solving the binary linear equation gives

$$a = -80.61 \quad b = 864.37 \quad T = 864.37R - 80.61(℃)$$

The results calculated using the fitting formula, and their errors, are shown in Table 12.2, which shows that that predicted temperatures were very close to the actual temperatures; the maximum error was +6.9°C.

12.6.3 The applicable temperature range for experimental calibration

Due to the limitation of possible experimental conditions, the experiments described above were conducted in the range 1000~1300°C. Afterward, the

Table 12.2 Results by experiment and fitting curve

Actual temperature T (°C)	Colorimetric ratio R	Error (°C)	Temperature obtained by fitting formula (°C)
1300	1.620	+4.1	1304.1
1250	1.536	–2.94	1247.06
1200	1.480	–1.34	1198.66
1150	1.419	+4.93	1154.93
1100	1.363	–2.47	1097.53
1050	1.316	+6.9	1156.9
1000	1.25	–0.15	999.85

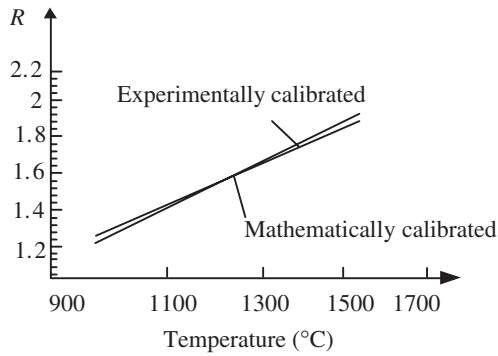

12.16 Calibration curve obtained by mathematical and experimental methods

temperature at the bond line of the weld was measured; its colorimetric ratio was 1.82. If this value was extrapolated on the experimental calibration curve, the corresponding temperature was 1493°C. The error was only 7°C. It can be concluded then that the applicable range was 1000~1500°C and it might be extrapolated to 1600°C. Figure 12.16 shows both the mathematically calibrated and experimentally calibrated curves. This shows that the mathematically calibrated curve also is nearly a straight line. There was only a slight difference between them. (The mathematically calibrated R at 1500°C was 1.807 and the experimentally calibrated R, by extrapolation, was 1.828.) Both implied that the applicable range was 1000~1600°C.

12.7 Calibration procedure

For any new measurement system, because the characteristics of the CCD, the wavelength of the filter, and the optical path are different, the ratio

R and temperature would have a different relationship, and therefore it should be calibrated. There are two calibration methods, namely, the mathematical method and the experimental method. Because some factors are neglected in the mathematical calibration, error is introduced. If higher accuracy is required, the experimental calibration method can be directly applied.

12.7.1 Mathematical method

First, determine the parameters of all of the elements concerned; the wavelengths of the two filters λ_1, λ_2; their transmissivities $\gamma(\lambda_1)$, $\gamma(\lambda_2)$; the bandwidths $\Delta\lambda_1$, $\Delta\lambda_2$; the relative response sensitivities of the CCDs $\eta(\lambda_1)$, $\eta(\lambda_2)$; and the transmissivities of all optical elements, $\varphi(\lambda_1)$, $\varphi(\lambda_2)\ldots\varphi_n(\lambda_1)$, $\varphi_n(\lambda_2)$.

Next, determine the relationship between R and absolute temperature T using the theoretical formula

$$R = \frac{\lambda_2^5 \cdot \Delta\lambda_1}{\lambda_1^5 \cdot \Delta\lambda_2} \cdot \frac{\left(e^{\frac{C_2}{\lambda_2 T}} - 1\right) \cdot \eta(\lambda_1)\gamma(\lambda_1)\varphi_1(\lambda_1)\varphi_2(\lambda_1)\cdots\varphi_n(\lambda_1)}{\left(e^{\frac{C_2}{\lambda_1 T}} - 1\right) \cdot \eta(\lambda_2)\gamma(\lambda_2)\varphi_1(\lambda_2)\varphi_2(\lambda_2)\cdots\varphi_n(\lambda_2)}$$

12.7.2 Experimental method

(i) Chose a qualified heating machine that can control the temperature of the specimen accurately (for example a Gleeble-1500).

(ii) Change the temperature of the specimen in 50°C steps on the machine, detect the temperature using a sensor, and determine the ratio R.

(iii) Repeat the detection n times (for example, five times) and calculate the average value of R: $R_i = \dfrac{R_{i1} + R_{i2} + \cdots R_{in}}{n}$.

(iv) Determine the relationship of R and T°K, using a linear fitting method. If the wavelengths of the two filters are close to each other, linear fitting can be used; otherwise fitting can be based on the formula $R = ae^{b/T}$.

12.8 Effects of measurement conditions

According to Boltzman's law, the ratio R is related only to temperature and does not depend on material, distance, and surface conditions. To verify this prediction the following experiments were conducted.

12.8.1 Materials

Experimental conditions: Gleeble-1500 machine, NiCr–NiAl thermocouple, 1000°C/s heating speed, 2 s temperature hold time, 1000~1300°C measured temperature range, 50°C measurement steps, and 475 mm distance.

Materials measured: Q235 mild steel, 18-8 stainless steel, and BHW alloy steel (German).

The results are shown in Fig. 12.17 and Table 12.3.

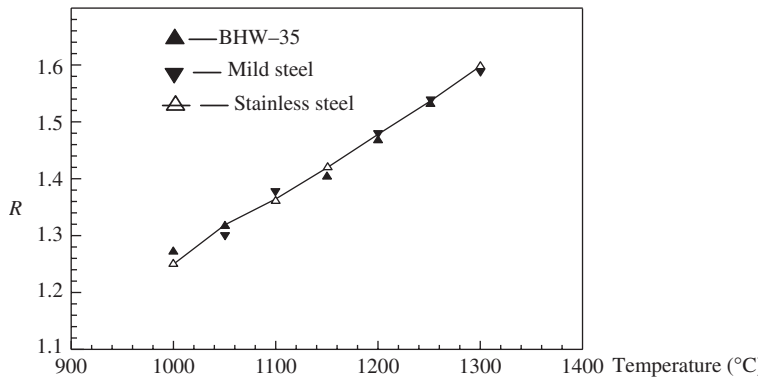

12.17 Relationship between colorimetric ratio and temperature for different materials

Table 12.3 Colorimetric ratio for different materials

Material	Temperature actual (°C)	1000	1050	1100	1150	1200	1250	1300
Mild steel	*R*	1.25	1.302	1.379	1.426	1.471	1.542	1.591
	Temperature obtained by *R* (°C)	1000	1045	1111	1152	1191	1252	1295
	Error (°C)	0	–5	+11	+2	–9	+2	–5
18-8 stainless steel	*R*	1.25	1.316	1.363	1.419	1.480	1.536	1.602
	Temperature obtained by *R* (°C)	1000	1057	1098	1146	1199	1247	1304
	Error (°C)	0	+7	–2	–4	–1	–3	+4
BHW – 35 alloy steel (German)	*R*	1.27	1.319	1.372	1.406	1.470	1.537	1.592
	Temperature obtained by *R* (°C)	1017	1059	1105	1135	1190	1248	1295
	Error (°C)	+17	+9	+5	–15	–10	–2	–5

The figure and table show that the maximum error of temperature was 17°C and the relative error was 1.7%. It can be concluded that the material had little effect on the measurement accuracy.

12.8.2 Distance

Experimental conditions: Gleeble-1500 machine, NiCr–NiAl thermocouple, ϕ10 mm Q235 steel, 1000°C/s heating speed, 2 s temperature hold time, 1000~1300°C measured temperature range, 50°C measurement steps.

Measurement distance: 395 mm and 475 mm.

The results are shown in Fig. 12.18 and Table 12.4.

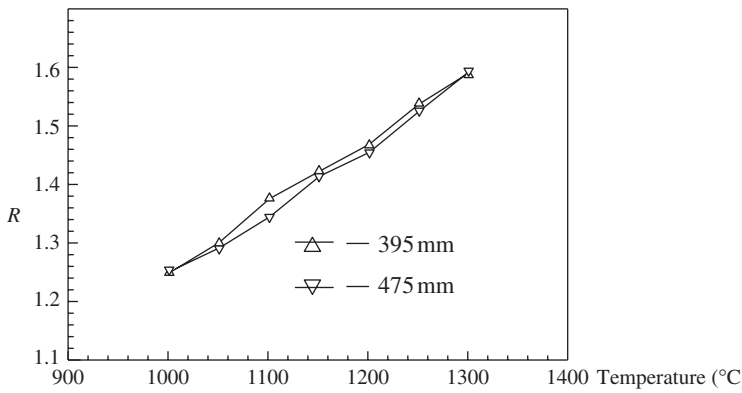

12.18 Relationship between *R* and *T* for different distances

Table 12.4 Colorimetric ratio for different distances

Distance (mm)	Temperature (°C)	1000	1050	1100	1150	1200	1250	1300
395	*R*	1.253	1.293	1.347	1.417	1.459	1.531	1.591
	Temperature obtained by *R* (°C)	1002	1037	1084	1144	1181	1243	1302
	Error (°C)	+2	−13	−16	−6	−19	−7	+2
475	*R*	1.25	1.302	1.379	1.426	1.471	1.542	1.591
	Temperature obtained by *R* (°C)	1000	1045	1111	1152	1191	1252	1295
	Error (°C)	0	−5	+11	+2	−9	+2	−5

Table 12.4 shows that the maximum error was –19°C and the maximum relative error was 1.58%. It can be concluded that the measurement distance had little influence on the measured results.

12.8.3 Surface condition

In order to study the effect of surface condition, one group of experiments was conducted in vacuum so that an unoxidized surface would be maintained. The second group of experiments was conducted in air and the temperature hold time was prolonged so that more surface oxide would form.

Experimental conditions: Gleeble-1500 machine, vacuum chamber, NiCr–NiAl thermocouple, BHW–35 low-alloy steel (German), 1×10^{-4} Torr vacuum, 1000°C/s heating speed, 2 s temperature hold time (normally).

The results of the first group of experiments are shown in Table 12.5.

The table shows that there was a large difference between the values measured by the colorimetric method and the values measured directly by

Table 12.5 Results of colorimetric measurement in vacuum

T (°C) by thermal couple	1000	1050	1100	1150	1200	1250	1300
R	1.366	1.427	1.483	1.518	1.579	1.649	1.706
T (°C) converted from *R*	1100	1153	1201	1231	1284	1344	1394
Corrected *R**	1.269	1.326	1.378	1.411	1.467	1.532	1.585
Corrected *T* (°C)*	1016	1065	1110	1139	1187	1244	1290
Error (°C)	+16	+15	+10	–11	–13	–6	–10

* Correction for the transmissivity of the vacuum-chamber wall

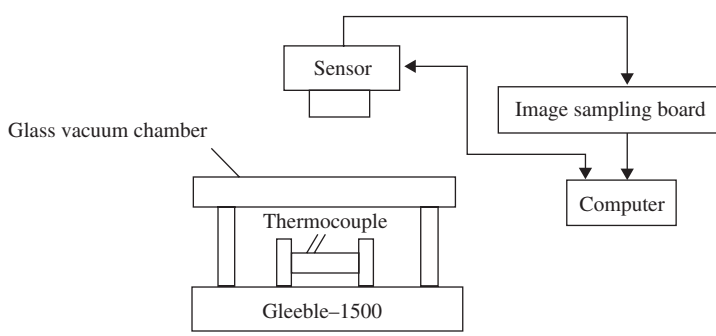

12.19 Facilities for colorimetric measurement in a vacuum

the thermo-couple. This was due to the transmissivity of the vacuum-chamber wall: see Fig. 12.19. Using a HILGE Analytical instrument, the transmis sivity of the wall at two wavelengths was found to be different; it was 90% at $\lambda = 0.8943\,\mu m$ and 83.64% at $\lambda = 0.8046\,\mu m$. Therefore, corrections had to be made according to the formula $R' = R \cdot \frac{83.64\%}{90\%}$. The corrected R and temperature are also listed in Table 12.5. Then, the maximum error was 16°C and the relative error was 1.6%.

Experiments were conducted in air with a prolonged hold time in order to increase the specimen's surface oxidation. It was found that, up to 10 s hold time, no difference in R was observed. When the hold time was extended to 15 s, however, the surface of the specimens was crazed and a big difference was measured between the colorimetric detection and the thermocouple's measurement. The temperature of the heavy oxide film may have been different from the temperature of the metal that the thermo-couple measured. Anyhow, it can be concluded that oxidation of the steel surface did not affect the measurement accuracy.

13

Design of a colorimetric imaging apparatus

13.1 Introduction

It was proved in the last chapter that the results obtained by the colorimetric method were accurate and they did not depend on the material, distance and surface conditions. It was concluded that the method was applicable in practice. For industrial application of the technology, however, there are more problems that need to be solved:

- The narrow dynamic response of CCDs causes the measurable temperature range, 1000–1300°C, to be too narrow. This limits the application of the method in practice.
- Although the wavelength of the maximum radiation intensity is in the infrared range, the wavelength range that gives optimum response of the CCD is the range of visible light. Therefore, choosing the wavelength that could be overlapped by both and choosing the wavelength for the filter so as to obtain optimum performance are problems that need to be studied.
- The volume and the weight of the sensor should be reduced further.

These three problems were the key issues for designing a suitable system. For this purpose the author and H. Zhang have conducted a systematic study. In this chapter the theory of the colorimetric method is discussed further. Then, the principles and the design of the sensor, including the characteristics, stability and reliability of the developed system, are described in depth.[296,357,379]

13.2 Formation of the thermal-radiation image

Figure 13.1 shows the process of thermal-image formation.[327] The optical system collects the infrared radiation of the object, via filters, and projects it onto a sensor's matrix. The sensor transforms the irradiance into an electrical signal. The system amplifies and processes the signal, and then transmits it to the display monitor.

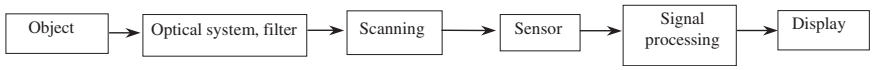

13.1 Thermal-image formation system

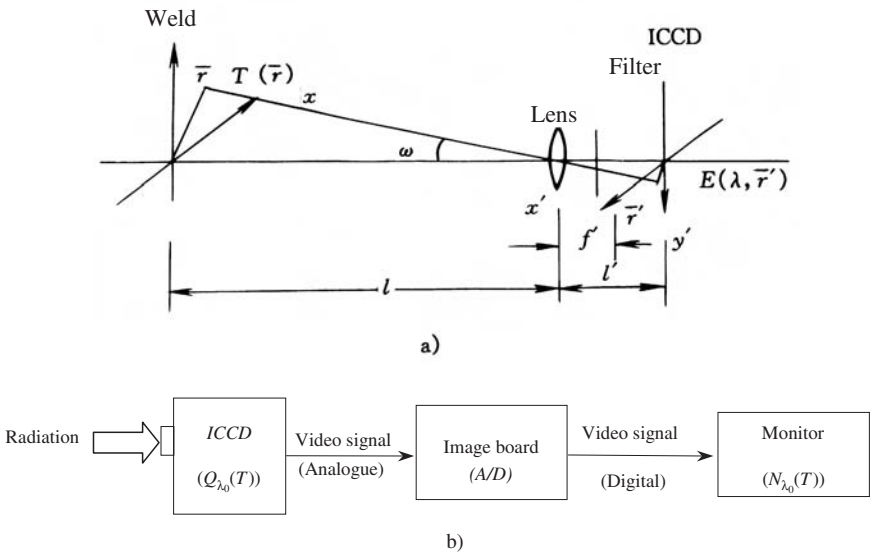

13.2 Formation of thermal image of the weld

In the present system, an ICCD was used to capture the image, as shown in Fig. 13.2. Suppose that the temperature field (on the back side of the weld bead) of the object is $T(\bar{r})$ and its image is projected onto the ICCD. The weld area can be regarded as the collection of points of incoherent infrared radiation source. Their radiation spectrum is different because of the different temperatures and reflectivities. The radiation of each point emits evenly in a spherical space. When it reaches the lens with a grating, a series of diffraction waves is produced. These diffraction waves are still spherical waves but the characteristics of the total wave are produced. The shape of the lens determines the wave front. The radiation field of an arbitrary point behind the lens is the superposition of all of the diffraction waves at that point. Therefore, the corresponding radiation point source on the ICCD surface is an extended radiation point image. All of such spots with different irradiance make up the thermal image.[328]

It is very complicated to determine the irradiance distribution of an ICCD surface by rigorous diffraction theory. However, the present system satisfies the condition of geometrical imaging $\left(\frac{a}{\lambda} >> 1\right)$. Therefore the irradiance on the ICCD surface can be found by geometrical optics.[329]

$$E(\vec{r}',\ \lambda)=\frac{\varepsilon(\lambda,T(\vec{r}))M_B(\lambda,T(\vec{r}))}{4F^2}\left(\frac{f'}{l'}\right)^2\varphi(\lambda)\xi H\gamma(\lambda)\cos^4\omega \qquad [13.1]$$

where $\vec{r}'=-\frac{l'}{l}\vec{r}$, l' = image distance, l = object distance, f' = focal length, F = aperture coefficient of the lens, $\varphi(\lambda)$ = transmissivity of the lens, ζ = stray light coefficient of the lens, $\gamma(\lambda)$ = transmissivity of the filter, (H) = vignetting coefficient, ω = angle between the light ray of the outer point and the optical axis, $\omega=tg^{-1}\frac{|\vec{r}'|}{l'}$.

Equation [13.1] shows that the irradiance depends not only on the transmissivity $\varepsilon(\lambda, T(\vec{r}'))$ and the radiant exitance $M_B(\lambda, T(\vec{r}'))$ of the corresponding temperature of the black body but also on the geometrical parameters of the optical system and the optical devices.

The factors that affect the irradiance may be listed as follows:

(i) The irradiance $E(\lambda, \vec{r}')$ is proportional to the fourth order of $\cos\omega$. The value of $E(\lambda, \vec{r}')$ with different values of ω would not be the same even when M_B is constant but if the irradiance at the centre has 255 grey levels, it would be 3~4 levels less on the periphery of the field, which introduces an error. However, when f' is large and the area imaged by the CCD is relatively small, $\cos^4\omega \approx 1$ and the effect can be neglected.

(ii) The irradiance $E(\lambda, \vec{r}')$ is inversely proportional to l', which shows that it is sensitive to the latter. The problem is the same for both monochromatic light and panchromatic light.

(iii) $E(\lambda, \vec{r}')$ is inversely proportional to the aperture coefficient. The choice of this coefficient can effectively regulate the irradiance on the ICCD.

(iv) $E(\lambda, \vec{r}')$ is proportional to the transmissivity of the filter $\gamma(\lambda)$. Proper design of transmissivity, including the peak wavelength and its band width, can determine the spectrum-radiation component and its magnitude so that it can match the response of the ICCD.

(v) The irradiance is proportional to the vignetting coefficient H, which can be approximated as 1 when the aperture is small.

The irradiance mentioned above is converted by the ICCD into an electrical-charge signal.

$$\begin{aligned}Q_{\lambda_0}(T)&=\int_{\lambda_0-\delta\lambda/2}^{\lambda_0+\delta\lambda/2}k\eta(\lambda)E(\vec{r}',\lambda)A\tau d\lambda\\&=\int_{\lambda_0-\delta\lambda/2}^{\lambda_0+\delta\lambda/2}k'\frac{\tau}{F^2}\frac{\cos^4\omega}{l'^2}\gamma(\lambda)\eta(\lambda)\varepsilon(\lambda,T)M_B(\lambda,T)d\lambda\end{aligned} \qquad [13.2]$$

where $\eta(\lambda)$ is the spectrum response of the ICCD, A is the area of the ICCD chip, τ is the exposure time, k is the quantum, λ_0 is the peak wavelength and $\delta\lambda$ is the bandwidth; k' is a constant.

The electrical charge $Q_{\lambda_0}(T)$ is transformed by the driving circuit of the ICCD into a standard video signal, which is converted by an 8-bit A/D into a 256-level grey image.

$$N_{\lambda_0}(T) = k_0 Q_{\lambda_0}(T) \qquad [13.3]$$

where k_0 is the transform coefficient.

13.3 Theoretical analysis of the colorimetric imaging method

Multicolour (including monochromatic, two-colour, three-colour, etc.) temperature-measuring methods are customary but their theoretical foundation and practical application have been research topics until now; the aim of these studies was mainly to study the dependence of the method on the emissivity. In the following paragraphs, the dependence of different methods on emissivity and the error that results from changes of emissivity are discussed first. Then, the two colour colorimetric imaging methods, developed on the basis of the two-colour colorimetric method, are described in detail.

13.3.1 Multi-colour thermal imaging detection methods

There are different advantages and disadvantages for the different multicolour methods. These methods are compared in the following text on the basis of the effect of emissivity on the apparent temperature that is detected.[53,54,80]

(i) *Full-colour detection*. Using the Stefan–Boltzmann law, suppose that the temperature of a real object is T and the object, which is a black body, has the full-colour radiation power as if it were at temperature T_p. Then T_p is called the apparent temperature of the body, which has a real temperature T. The difference between T and T_p, and the error that results from the difference of emissivity, can be expressed by the following formulae:

$$T_p = [\varepsilon(T)]^{\frac{1}{4}T} \qquad [13.4a]$$

$$\frac{\Delta T_p}{T} = \frac{T - T_p}{T} = 1 - [\varepsilon(T)]^{\frac{1}{4}} \qquad [13.4b]$$

$$\frac{dT_p}{T_p} = \frac{1}{4}\frac{d\varepsilon(T)}{\varepsilon(T)} \qquad [13.4c]$$

Equation [13.4a] shows that the apparent temperature is affected greatly by the emissivity, particularly for those bodies that have low emissivity. The real temperature can be obtained only when $\varepsilon(T) = 1$. Otherwise, the error is expressed by Eq. [13.4b] and the error of the detected value, i.e. T_p, would be that expressed by Eq. [13.4c].

(ii) *Monochromatic light detection*. On basis of Planck's formula, the radiation power at a certain wavelength can be detected by using a filter. Suppose the apparent temperature thus obtained is T_s and the real temperature of the object is T. Then the following equations can be expressed.

$$T_s = \left[\frac{1}{T} + \frac{\lambda}{c_2}\ln\frac{1}{\varepsilon(\lambda, T)}\right]^{-1} \quad [13.5a]$$

$$\frac{\Delta T_s}{T} = \frac{T - T_s}{T} = \frac{\lambda T_s}{c_2}\ln\frac{1}{\varepsilon(\lambda, T)} \quad [13.5b]$$

$$\frac{dT_s}{T_s} = \frac{\lambda T_s}{c_2}\frac{d\varepsilon(\lambda, T)}{\varepsilon(\lambda, T)} \quad [13.5c]$$

Equation [13.5a] means that the real temperature can be found by detection only when $\varepsilon(\lambda, T) = 1$. Otherwise, errors will be introduced that depend not only on the emissivity but also on the apparent temperature and the wavelength that was chosen. Equation [13.5c] shows the error in the apparent temperature that results due to the emissivity of the object. The error depends on the apparent temperature and chosen wavelength as well.

(iii) *Two-colour detection*. The ratio of the radiation power to the temperature can be obtained by calibration.

Derivation showed that

$$R_{12} = \frac{\varepsilon(\lambda_1, T)M_B(\lambda_1, T)\delta\lambda_1}{\varepsilon(\lambda_2, T)M_B(\lambda_2, T)\delta\lambda_2} \quad [13.6]$$

Substituting the Wein formula into the equation above and considering that $\delta\lambda_1 = \delta\lambda_2$, the temperature can be obtained as

$$T = \frac{c_2[1/\lambda_2 - 1/\lambda_1]}{\ln R_{12} - 5\ln(\lambda_2/\lambda_1) - \ln(\varepsilon(\lambda_1, T)/\varepsilon(\lambda_2, T))} \quad [13.7]$$

The apparent temperature, the error between the apparent temperature and the real temperature, and the error of the apparent temperature caused by the emissivity are as follows:

$$T_c = \left[\frac{1}{T} - \frac{\ln\varepsilon(\lambda_1, T) - \ln\varepsilon(\lambda_2, T)}{c_2(1/\lambda_2 - 1/\lambda_1)}\right]^{-1} \quad [13.8a]$$

$$\frac{\Delta T_c}{T} = \frac{T - T_c}{T} = \frac{T_c}{c_2(1/\lambda_2 - 1/\lambda_1)} \ln \frac{\varepsilon(\lambda_1, T)}{\varepsilon(\lambda_2, T)} \quad [13.8b]$$

$$\frac{dT_c}{T_c} = \frac{T_c}{c_2(1/\lambda_2 - 1/\lambda_1)} \frac{d[\varepsilon(\lambda_1, T)/\varepsilon(\lambda_2, T)]}{\varepsilon(\lambda_1, T)/\varepsilon(\lambda_2, T)} \quad [13.8c]$$

Equation [13.8a] shows that when $\varepsilon(\lambda_1, T) = \varepsilon(\lambda_2, T)$, the apparent temperature equals the real temperature or when $\varepsilon(\lambda_1, T)/\varepsilon(\lambda_2, T)$ is a constant, the error between the apparent and real temperatures is a constant. This characteristic makes it possible to obtain the real temperature under certain conditions. If the conditions are not satisfied, then the error is represented by Eq. [13.8b]; it depends not only on the emissivity but also on the apparent temperature and the wavelength that was chosen. Equation [13.8c] represents the error caused by emissivity, as well as the apparent temperature and wavelength.

(iv) *Three-colour detection*. Two colorimetric ratios are measured by two of the three wavelengths, R_{12} and R_{32}, and the temperature is obtained by calibration.

$$\ln(R_{12}R_{32}) = \ln\left\{\frac{\varepsilon(\lambda_1, T)\varepsilon(\lambda_2, T)}{[\varepsilon(\lambda_2, T)]^2}\right\} + 5\ln\left(\frac{\lambda_2^2}{\lambda_1\lambda_3}\right) + \frac{c_2}{T}\left[\left(\frac{\lambda_1 - \lambda_2}{\lambda_1\lambda_2}\right) - \left(\frac{\lambda_2 - \lambda_3}{\lambda_2\lambda_3}\right)\right] + \ln\frac{\delta\lambda_1\delta\lambda_3}{[\delta\lambda_2]^2} \quad [13.9]$$

Assuming that $\delta\lambda_1 = \delta\lambda_2 = \delta\lambda_3$, the measured temperature can be expressed as

$$T = c_2\left[\left(\frac{\lambda_1 - \lambda_2}{\lambda_1\lambda_2}\right) - \left(\frac{\lambda_2 - \lambda_3}{\lambda_2\lambda_3}\right)\right] \Bigg/ \left\{\ln\left(\frac{R_{12}}{R_{32}}\right) - \ln\left[\frac{\varepsilon(\lambda_1, T)\varepsilon(\lambda_3, T)}{\varepsilon^2(\lambda_2, T)}\right] - 5\ln\frac{\lambda_2^2}{\lambda_1\lambda_3}\right\} \quad [13.10]$$

Further, assuming that $\varepsilon(\lambda_1, T)\varepsilon(\lambda_3, T) = \varepsilon^2(\lambda_2, T)$, the apparent temperature is

$$T_a = c_2\left[\left(\frac{\lambda_1 - \lambda_2}{\lambda_1\lambda_2}\right) - \left(\frac{\lambda_2 - \lambda_3}{\lambda_2\lambda_3}\right)\right] \Bigg/ \left[\ln\frac{R_{12}}{R_{32}} - 5\ln\frac{\lambda_2^2}{\lambda_1\lambda_3}\right] \quad [13.11a]$$

If the condition $\varepsilon(\lambda_1, T)\varepsilon(\lambda_3, T) = \varepsilon^2(\lambda_2, T)$ is not satisfied, the error between the apparent and real temperatures is:

$$\frac{\Delta T_a}{T} = \frac{T_a\lambda_1\lambda_2\lambda_3}{(\lambda_2 - \lambda_1)(\lambda_3 - \lambda_1)(\lambda_3 - \lambda_2)} \left\{\lambda_1 \ln\left[\frac{\varepsilon(\lambda_2, T)}{\varepsilon(\lambda_3, T)}\right] + \lambda_2 \ln\left[\frac{\varepsilon(\lambda_3, T)}{\varepsilon(\lambda_1, T)}\right] + \lambda_3 \ln\left[\frac{\varepsilon(\lambda_1, T)}{\varepsilon(\lambda_2, T)}\right]\right\} \quad [13.11b]$$

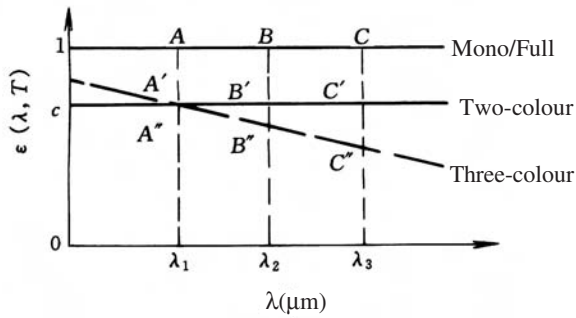

13.3 Requirements of emissivity for various detection methods

By comparing the four detection methods, it is found that the emissivity has different effects on different methods; this is illustrated by Fig. 13.3. For full-colour detection, if the emissivity is less than 1, there is an error between the apparent and real temperatures. The magnitude of the error does not depend on the measured temperature. If the real temperature has to be obtained, the emissivity for the whole wavelength range should be 1; see ABC in Fig. 13.3. The error caused by emissivity in the case of monochromatic light detection is smaller than that for full light. The required emissivity for the λ used should be 1. It corresponds to one point on ABC of Fig. 13.3. For the two-colour detection method, the dependence on emissivity is much less. In order to obtain the real temperature, only the emissivity of the two wavelengths chosen must equal one another. Two arbitrary points on A′B′C′ will satisfy this requirement. Dependence of the three-colour detection method on emissivity is even smaller. The only requirement is that $\varepsilon(\lambda_1, T)\varepsilon(\lambda_3, T) = \varepsilon^2(\lambda_2, T)$. This means that any three points on the line A″B″C″ will satisfy the requirement (see Fig. 13.3).

The greatest advantage of multi-colour (two or more) detection methods is the small dependence of their accuracy on emissivity. The full-colour or one-colour methods' advantage is their simplicity in operation; only one measuring operation is needed. They have high speed, high sensitivity, and high resolution. The disadvantages of multi-colour detection methods are that signal processing is more complicated, there is a strong influence of noise on the accuracy, and their speed is slower. With the development of high-quality CCD sensors, these disadvantages can be overcome to a certain extent.

13.3.2 Two-colour thermal-imaging detection method[342,343,347]

In the previous section, the advantages and disadvantages of multi-colour detection methods were discussed in view of the radiation properties of the

object. The influence of other factors was not considered. In this section, the principles and methods are discussed further. Suppose that the ratio of grey levels of two points is

$$R_{12}(T) = \frac{N_{\lambda_1}(T)}{N_{\lambda_2}(T)} \qquad [13.12]$$

Substituting Eq. [13.2] into Eq. [13.3] gives

$$R_{12}(T) = \frac{\int_{\lambda_1-\delta\lambda_1}^{\lambda_1+\delta\lambda_1} K' \frac{\tau}{F^2}\frac{\cos^4\omega}{l'^2}\gamma(\lambda)\eta(\lambda)\varepsilon(\lambda,T)M_B(\lambda,T)d\lambda}{\int_{\lambda_2-\delta\lambda_2}^{\lambda_2+\delta\lambda_2} K' \frac{\tau}{F^2}\frac{\cos^4\omega}{l'^2}\gamma(\lambda)\eta(\lambda)\varepsilon(\lambda,T)M_B(\lambda,T)d\lambda} \qquad [13.13]$$

where K' is a constant.

Cancelling all common factors, one obtains

$$R_{12}(T) = \frac{\int_{\lambda_1-\delta\lambda_1}^{\lambda_1+\delta\lambda_1} \gamma(\lambda)\eta(\lambda)\varepsilon(\lambda,T)M_B(\lambda,T)d\lambda}{\int_{\lambda_2-\delta\lambda_2}^{\lambda_2+\delta\lambda_2} \gamma(\lambda)\eta(\lambda)\varepsilon(\lambda,T)M_B(\lambda,T)d\lambda} \qquad [13.14]$$

For the purpose of this discussion, it was assumed that the wavelength was in a narrow band, and $\varepsilon(\lambda, T)$, $\eta(\lambda)$, $M_B(\lambda, T)$ are slow functions. The formula can be written as

$$R_{12}(T) = \frac{\varepsilon(\lambda_1,T)\gamma(\lambda_1)\eta(\lambda_1)\lambda_2^5\delta\lambda_1}{\varepsilon(\lambda_2,T)\gamma(\lambda_2)\eta(\lambda_2)\lambda_1^5\delta\lambda_2}\exp\left[-\frac{c_2}{T}\left(\frac{1}{\lambda_1}-\frac{1}{\lambda_2}\right)\right] \qquad [13.15]$$

Thus, from Eq. [13.15] the measured temperature is

$$T = -c_2\left(\frac{1}{\lambda_1}-\frac{1}{\lambda_2}\right)\left[\ln R_{12} - \ln\frac{\varepsilon(\lambda_1,T)\gamma(\lambda_1)\eta(\lambda_1)\lambda_2^5\delta\lambda_1}{\varepsilon(\lambda_2,T)\gamma(\lambda_2)\eta(\lambda_2)\lambda_1^5\delta\lambda_2}\right]^{-1} \qquad [13.16]$$

The apparent temperature detected is

$$T_c = -c_2\left(\frac{1}{\lambda_1}-\frac{1}{\lambda_2}\right)\left[\ln R_{12} - \ln\frac{\gamma(\lambda_1)\eta(\lambda_1)\lambda_2^5\delta\lambda_1}{\gamma(\lambda_2)\eta(\lambda_2)\lambda_1^5\delta\lambda_2}\right]^{-1} \qquad [13.17]$$

13.4 Division of the temperature field[336,340]

The temperature field in welding has a large range; the range of interest is at least 800~1400°C. But due to the limited response capability of the CCD,

it can detect only a small range of temperature. Therefore, it was proposed to divide the temperature field into several regions according to the temperature range. Using different exposure times for different regions, the radiation power of all regions could be limited to the response capability of the CCD and thus the temperature of the whole field could be obtained.

13.4.1 Dynamic response range of the ICCD

The most important characteristic of the ICCD is its dynamic response range. This is determined by the maximum electrical charge that can be stored in the potential pit Q_{max} and the minimum electrical charge due to the inevitable noise Q_{min}.[330] It can be seen that the charge in the pit depends not only on the irradiance at that point but also on the exposure time (the time integration of charge by the ICCD). The photoelectric characteristic of an ICCD is linear in the normal range, as shown in Fig. 13.4. Equation [13.2] can be rewritten as

$$Q_{\lambda_0}(T) = K'\tau E(T, \lambda_0) \qquad [13.18]$$

where K' is the coefficient decided by the optical imaging system. $Q' = \tau E(T, \lambda_0)$ is the exposure quantity; its units are lx.s. The co-ordinates of the point in space are replaced by its temperature.

In cases when the exposure quantity of the electrical charge is larger than Q_{max} or smaller than Q_{min}, the signal induced by the irradiance would be saturated or submerged, respectively, in the noise.

The exposure quantity, by which the quantity of electrical charge is determined, can be regulated by the irradiance $E(T, \lambda_0)$ and the exposure time τ, so that $Q_{min} < Q < Q_{max}$. The irradiance $E(T, \lambda_0)$ depends on the image distance l', aperture coefficient F, etc. For a case in which l' is unchanged and F is chosen, then the irradiance is a function of temperature only.

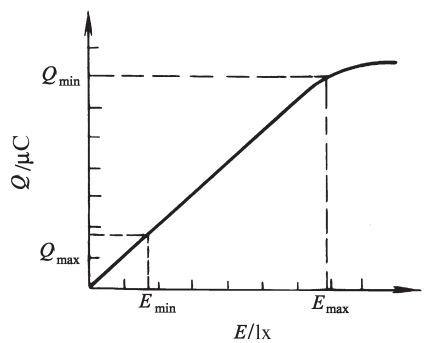

13.4 Photoelectric characteristics of an ICCD

Producing the quantity of electrical charge within the range $Q_{max} - Q_{min}$ for a different temperature range can be accomplished by using a different exposure time. This means the time should be taken as

$$\frac{Q_{min}}{K'} < \tau E(T, \lambda) \frac{Q_{max}}{K'} \qquad [13.19]$$

Obviously, when the welding temperature field has a large temperature range, satisfying this requirement using one exposure is difficult.[295]

13.4.2 Method

Assuming that the ICCD has a minimum electrical charge quantity Q_{min} and a maximum of Q_{max}, the corresponding grey level after 8-bit conversion is N_{min}~N_{max}. Assuming also that the conversion is linear, as shown in Fig. 13.5, then the dynamic-response range can be expressed as N_{max}/N_{min}. For the present system, $N_{min} \approx 50$, $N_{max} \approx 240$. The ICCD has good linearity in this range.

Suppose that the temperature range is T_1~T_2 and the wavelength is λ, then the ratio of irradiance on the ICCD can be obtained from Eq. [13.1] and Eq. [11.11] as follows (the emissivity is not taken into consideration):

$$c(\lambda) = \frac{E(T_2, \lambda)}{E(T_1, \lambda)} = \frac{M_B(T_2, \lambda)}{M_B(T_1, \lambda)} = \exp\left[-\frac{c_2}{\lambda}\left(\frac{1}{T_2} - \frac{1}{T_1}\right)\right] \qquad [13.20]$$

For example, for the temperature range $T_1 = 1073\,K$~$T_2 = 1673\,K$, $\lambda = 0.78\,\mu m$, $c(\lambda) = 1200$. Suppose that the irradiance due to T_1 makes up the Q_{min} and N_{min}, then the Q produced by T_2 would be 1200 times that of Q_{min} and the grey level would be $1200*N_{min} >> 255$; obviously the ICCD is saturated. Therefore, dividing the temperature field into several regions and using different exposure times is needed to keep the irradiance of the

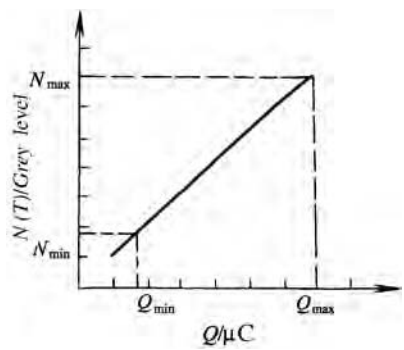

13.5 A/D conversion characteristics of an image

temperature range of all divisions within the dynamic response range of the ICCD.[336,340]

Suppose that the exposure times are $\tau_1, \tau_2, \ldots, \tau_{m+1}$, and the temperature T_1 to T_2 is divided into m segments, see Fig. 13.6a.

In order to fully use the dynamic response range of the ICCD, the temperature range T_1–T_2 is divided into m sections T_1~T_1', T_1'~T_2', . . . , T_m'~T_2, according to geometric ratios, and the corresponding exposure times are $\tau_1, \tau_2, \ldots, \tau_{m+1}$.

Then, the following conditions must be satisfied

$$\frac{M_B(\lambda, T_1')}{M_B(T_1, \lambda)} = \frac{M_B(\lambda, T_2')}{M_B(\lambda, T_1')} = \cdots = \frac{M_B(\lambda, T_2)}{M_B(\lambda, T_m')} = c'(\lambda) \le \frac{N_{max}}{N_{min}} \qquad [13.21]$$

Transforming the formula shows that $T_1', T_2', \ldots, T_m'$ are only functions of T_1, T_2 and are independent of λ.

$$\frac{1}{T_1'} - \frac{1}{T_1} = \frac{1}{T_2'} - \frac{1}{T_1'} = \cdots = \frac{1}{T_2} - \frac{1}{T_m'} = c_T \qquad [13.22]$$

Substituting Eq. [13.22] into Eq. [13.21] gives

$$c'(\lambda) = \exp\left(-\frac{c_2}{\lambda} c_T\right) \qquad [13.23]$$

The exposure times $\tau_1, \tau_2, \ldots, \tau_{m+1}$ should be chosen so that the dynamic responses on the ICCD for T_1~T_1', T_1'~T_2', . . . , T_m'~T_2 are within the largest linear range. The corresponding grey levels are shown in Fig. 13.6b.

For λ_1, the ideal case is:

$$\tau_1 E(\lambda, T_1) = \tau_2 E(\lambda, T_1') = \cdots = \tau_{m+1} e(\lambda, T_m') \qquad [13.24]$$

As to λ_2, because $\lambda_2 > \lambda_1$, then $c'(\lambda_2) < c'(\lambda_1)$, which satisfies the condition for division given by Eq. [13.21].

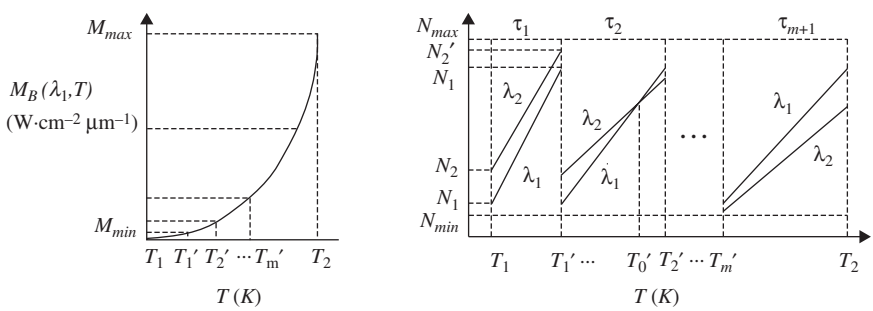

a) T_1~T_2 Division by geometric ratio

b) Grey levels for each region

13.6 Division of the temperature field

Transforming Eq. [13.23] and combining it with Eq. [13.21] gives

$$\frac{\tau_1}{\tau_2}=\frac{\tau_2}{\tau_3}=\cdots=\frac{\tau_m}{\tau_{m+1}}=c'(\lambda_1)\le\frac{N_{max}}{N_{min}} \qquad [13.25]$$

It is seen that, in order to satisfy the requirement of division of Eq. [13.21], the exposure time should be decided according to Eq. [13.25]. However, the exposure time of available ICCDs is discrete and the ratio of any neighbouring two values may not be equal. Anyhow, it is advisable to satisfy Eq. [13.25] as closely as possible. For a two-colour image, the irradiance of both wavelengths must be kept within the response range. Equation [13.13] shows that the related factors are wavelengths λ_1, λ_2, band widths $\delta\lambda_2$, $\delta\lambda_1$, transmissivities I_1, I_2 at the peak values of λ_1, λ, and the response values of the ICCD $\eta(\lambda_1)$ and $\eta(\lambda_2)$.

In order to fully use the dynamic range of the ICCD, locating the electrical-charge quantity in the middle range of the temperature for the two wavelengths being close to each other, i.e. $R(T_1)*R(T_2)=1$ was proposed, so that the electrical-charge quantity at the low-temperature and high-temperature ranges would not be too different for the two wavelengths, and a larger measurable temperature range could be obtained. In this case, the parameters of the filter could be found by transforming Eq. [13.15] as follows

$$\left[\frac{I_1\cdot\delta\lambda_1\cdot\eta(\lambda_1)}{I_2\cdot\delta\lambda_2\cdot\eta(\lambda_2)}\right]^2=\left[\frac{\lambda_1^5}{\lambda_2^5}\right]\cdot\exp\left[C_2\left(\frac{1}{\lambda_1}-\frac{1}{\lambda_2}\right)\left(\frac{1}{T_1}+\frac{1}{T_2}\right)\right] \qquad [13.26]$$

Thus, there is a temperature T_0 in the range T_1~T_2 where $R(T_0)=1$. From Eq. [13.15] T_0 can be determined by the following formula:

$$T_0=c_2\left(\frac{1}{\lambda_2}-\frac{1}{\lambda_1}\right)\left\{\ln\left[\left(\frac{\lambda_1}{\lambda_2}\right)^5\cdot\frac{\eta(\lambda_2)}{\eta(\lambda_1)}\cdot\frac{I_2\delta\lambda_2}{I_1\delta\lambda_1}\right]\right\}^{-1} \qquad [13.27]$$

The formula shows that T_0 can be determined by proper design of the peak value of the two-colour filter's transmissivity. In other words, the peak value of transmissivity is an important factor for the design of the filter.

Combining Equations [13.26] and [13.27], the relationship of T_0 and T_1, T_2 can be written as

$$\frac{2}{T_0}=\frac{1}{T_1}+\frac{1}{T_2} \qquad [13.28]$$

Substituting Eq. [13.27] into Eq. [13.15] gives

$$R(T)=\exp\left[-c_2\left(\frac{1}{T}-\frac{1}{T_0}\right)\left(\frac{1}{\lambda_2}-\frac{1}{\lambda_1}\right)\right] \qquad [13.29]$$

From this formula, $R(T)<1$ when $T>T_0$ and $R(T)>1$ when $T<T_0$.

13.4.3 Effect of the ICCD dynamic range

In the following paragraphs, the effects of the ICCD dynamic-response range on the measuring-temperature range, the division number, the choice of wavelength, and the requirement of exposure time are discussed on the basis of Equations [13.20], [13.21], [13.22], [13.24].

(i) *Exposure-time requirement*. The available exposure times for the ICCD applied in the present design were 16.7, 8, 4, 2, 1, 0.5, 0.25, 0.1 ms. The exposure time should be as short as possible; therefore, $\tau_1 = 8$, $\tau_2 = 2$, $\tau_3 = 0.5$, $\tau_4 = 0.1$ were chosen. Thus, $\tau_1/\tau_2 = 4$, $\tau_2/\tau_3 = 4$, $\tau_3/\tau_4 = 5$, which satisfy the requirement of Eq. [13.25]. Due to the exposure times available, dividing the temperature field into a maximum of four regions was allowed.

(ii) *The requirement of λ for a given range of T_1~T_2 and the division number N*. Supposing that a temperature field of T_1~T_2 is divided into n regions, c_T can be obtained from Eq. [13.22]. Substituting it into Eq. [13.23] and combining it with Equations [13.21] and [13.20] gives

$$\lambda \geq -\frac{c_2}{\ln \dfrac{N_{max}}{N_{min}}} c_T = -\frac{c_2}{n \ln \dfrac{N_{max}}{N_{min}}} \left(\frac{1}{T_2} - \frac{1}{T_1} \right) \qquad [13.30]$$

This equation shows that the smaller the dynamic range of the ICCD, the longer the λ should be.

(iii) *Requirement of n for given values of T_1~T_2 and λ*. Equation [13.30] can be transformed as

$$n \geq -\frac{c_2}{\lambda \ln \dfrac{N_{max}}{N_{min}}} \left(\frac{1}{T_2} - \frac{1}{T_1} \right) \qquad [13.31]$$

(iv) *The limitations on the lower temperature T_1 and the upper temperature T_2 when λ and n are given*. Similarly, Eq. [13.30] can be transformed as

$$\frac{1}{T_2} \geq \frac{1}{T_1} - \frac{\lambda n}{c_2} \ln \frac{N_{max}}{N_{min}} \qquad [13.32]$$

Obviously, as the dynamic-response range of the ICCD becomes larger, the measurable temperature range also can be larger.

13.5 Wavelength of the filter[337,341]

The choice of wavelength is important.[331–333] It determines the radiant exitance, the linearity and sensitivity of the colorimetric ratio, etc. The choice of wavelength was discussed in the last section in relation to how to divide the temperature region. This issue is discussed again in this section relative to the colorimetric-ratio response. The object radiation, light transmission

through filters, and the light received by the ICCD, were simulated using a computer. The optimum wavelength was derived for a given temperature range, which could give larger spectrum-radiant exitance, dynamic response of the ICCD, and larger and more even colorimetric-ratio response.

13.5.1 The grey ratio of the two images

The colorimetric ratio depends mainly on the radiation properties of the object, the transmissivity of the filter, and the spectrum response of the ICCD: see Eq. [13.14]. In Chapter 11 and previous sections, the radiation characteristics of the object have been discussed in detail. Numerical simulation was carried out in this section mainly in connection with the dynamic response of the ICCD and the transmissivity of the filters.

(i) *The dynamic-spectrum response of the ICCD*. The dynamic-spectrum response depends on the structure and material of the ICCD. In the case of a Si substrate, the dynamic-spectrum response range is 0.4~1.1 μm. Figure 13.7 shows the experimentally-determined dynamic-spectrum response curve. The curve was fitted to a polynomial by a least-squares error determination as

$$\eta(\lambda) = \sum_{j=0}^{N} a_i \cdot \lambda^i \qquad [13.33]$$

where N = number of terms and a_i = coefficient of fit. Specifically, the numerical values obtained were $a_0 = -1.222, a_1 = 1.11, a_2 = 7.639, a_3 = -6.944$, and $N = 3$.

(ii) *Characteristics of the interference filter.* The two-colour wavelength was obtained using an interference filter. The centre wavelengths were λ_1, λ_2 and their transmissivities are shown in Fig. 13.8. The transmissivity function $\gamma_i(\lambda)$ is[85]

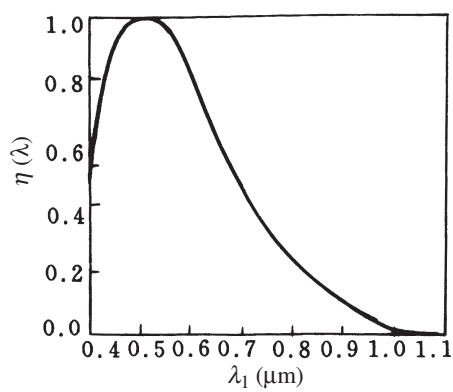

13.7 Specturm response of the ICCD

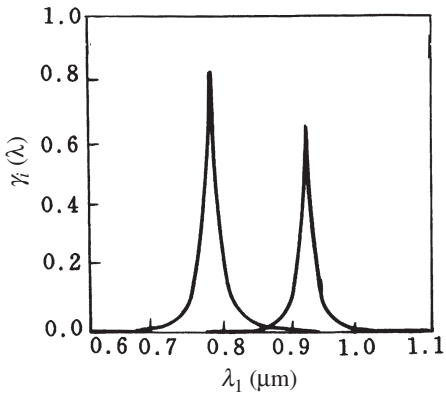

13.8 Transmissivity function of the filter

$$\gamma_i(\lambda) = I_i\left[1+\sin^2\left(\frac{\pi k\lambda_i}{\lambda}\right)\sin^{-2}\left(\frac{\pi k\lambda_i}{\lambda_i-\delta\lambda_i/2}\right)\right]^{-1} \qquad [13.34]$$

where $i = 1, 2$ filters and k = interference order. $\delta\lambda_I$ is determined by λ_I, etc. All of the parameters except k were experimentally measured after it was designed and manufactured.

(iii) *Algorithm*. For the calculation of Eq. [13.14], the product of three functions, namely Equations [11.14], [13.33], [13.34], was integrated using the approximation formula of a trapezoid:

$$\int_a^b f(x)dx = H\left\{x[f(a)+f(b)]/2+\sum_{k=1}^{N} f(x_k)\right\} \qquad [13.35]$$

where $H(b-a)/N, x_k = a + kH(k = 1, \ldots, N), a, b$ are upper and lower limits of the wavelength.

For λ_2, $a = \lambda_2 - \delta\lambda_2/2$, $b = \lambda_2 + \delta\lambda_2/2$, $dx = d\lambda$.

For λ_1, $a = \lambda_1 - \delta\lambda_1/2$, $b = \lambda_1 + \delta\lambda_1/2$, $dx = d\lambda$.

With the aid of this formula, the relationship of the system's dynamic response and temperature at an arbitrary wavelength and with a specific bandwidth, can be obtained by numerical simulation considering all of the factors concerned, e.g. the object's radiation properties, the filter's transmission, and the response property of the ICCD.

13.5.2 Selection of wavelength

In the measuring system, the sensitivity, or the ratio of $R(T)$ to T, reflects more clearly the response characteristics of the system. If the sensitivity is designated as $S(T)$, then

$$S(T)=\frac{\partial R(T)}{\partial T}=\frac{\displaystyle\int_{\lambda_1-\delta\lambda_1/2}^{\lambda_1+\delta\lambda_1/2}\frac{c_2}{\lambda T^2}\exp\left(\frac{c_2}{\lambda T}\right)\left[\exp\left(\frac{c_2}{\lambda T}\right)-1\right]^{-1}\varepsilon(\lambda,T)M_B(\lambda,T)\gamma_1(\lambda)\eta(\lambda)d\lambda}{P_{\lambda_2}(T)}$$
$$-\frac{P_{\lambda_1}(T)\displaystyle\int_{\lambda_2-\delta\lambda_2/2}^{\lambda_2+\delta\lambda_2/2}\frac{c_2}{\lambda T^2}\exp\left(\frac{c_2}{\lambda T}\right)\left[\exp\left(\frac{c_2}{\lambda T}\right)-1\right]^{-1}\varepsilon(\lambda,T)M_B(\lambda,T)\gamma_2(\lambda)\eta(\lambda)d\lambda}{P_{\lambda_2}^2(T)} \qquad [13.36]$$

where $P_{\lambda_i}(T)=\displaystyle\int_{\lambda_i-\delta\lambda_i}^{\lambda_i+\delta\lambda_i}\gamma_i(\lambda)\eta(\lambda)\varepsilon(\lambda,T)M_B(\lambda,T)d\lambda \quad (i=1,2).$

The selection of the central wavelength is based mainly on the object's radiant exitance, the spectrum response of the ICCD, the effect of surrounding light, the linearity and sensitivity of the system, the temperature range, and the range of dynamic response of the ICCD. The last two factors were discussed in the previous section. The wavelength of the maximum radiant exitance of the object at temperatures of 1100~1800 K are 2.616~1.599 μm. Obviously, they are not in the range of the ICCD's dynamic response. The optimum response wavelength of the ICCD is 0.5 μm, which cannot be used because of serious interference from ambient light (daylight). Therefore, the applicable wavelength is between 0.77~1.0 μm. In the following text, the rule and method for selecting the two-colour wavelengths is described in view of the system's response and sensitivity.

(i) *The requirement related to the system's response and sensitivity*. $R(T)$ must be linear with a steep slope in the measuring-temperature range T_1~T_2, so that the temperature scale is reasonably even and sensitive. More explicitly, $S(T_1) = S(T_2)$ and a large value of $S(T)$ is required. The wavelengths of the two colours that can meet these requirements in the temperature range of 1100–1800 K were obtained by numerical simulation and are shown in Fig. 13.9. Any two wavelengths on the figure could have a stable sensitivity of $S(T)$ in the assigned temperature range. Considering that the dynamic response of the ICCD should not be too small, and avoiding the visible light range as far as possible, then it is reasonable that λ_2 could be in the range of 0.90~0.948 μm and λ_1 in the range of 0.77~0.80 μm. The possible combinations are 0.77~0.905 μm, 0.780~0.920 μm, 0.790~0.934 μm, and 0.800~0.948 μm. Figures 13.10 and 13.11 shows the response $R(T)$ and sensitivity $S(T)$ of the four combinations, determined by numerical simulation. In the calculation, all factors including the radiation intensity, peak value, central wavelength and bandwidth of filters, and the

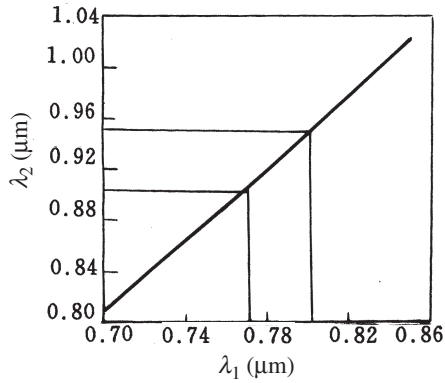

13.9 Curve for the selection of λ_1 λ_2

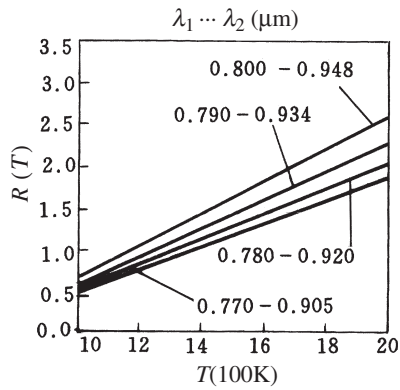

13.10 Relationship of $R(T)$ with T for different combinations of λ_1 and λ_2

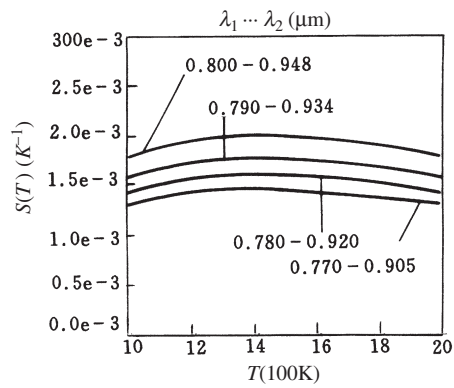

13.11 Relationship of $S(T)$ with T for different combinations of λ_1 and λ_2

response of the ICCD (as shown in Fig. 13.7) were considered. The temperature range for these calculations was 1000~2000 K.

Figures [13.10] and [13.11] show that with the increase of wavelength (combinations), the response ratio becomes larger and steeper, and the sensitivity becomes greater. But too large a wavelength may reach the decreasing end of the ICCD's response curve (Fig. 13.7). As a compromise between these two situations, 0.780 and 0.920 μm were chosen for λ_1 and λ_2.

(ii) *The effect of the central wavelength on* $R(T)$. The relationship between $R(T)$ and T depends on λ_1, λ_2 and $\delta\lambda_1$, $\delta\lambda_2$. $R(T)$ was obtained by numerical calculation for different values of λ_1, λ_2 , $\delta\lambda_1$, $\delta\lambda_2$. The results are shown in Fig. 13.12a, b, c.

In the case where $\Delta\lambda = \lambda_2 - \lambda_1 = 0.14\,\mu m$, $\delta\lambda_1 = 0.0235\,\mu m$, $\delta\lambda_2 = 0.0204\,\mu m$ were kept constant and λ_1 was varied between 0.68, 0.73, 0.78, 0.83 μm, the relationship between $R(T)$ and λ_1 was obtained and is shown in Fig. 13.12a. This shows that when λ_1 is small, the linearity between $R(T)$ and T was poorer at the low-temperature end and when λ_1 was large, the $R(T)$tended to be saturated in the high-temperature range. Therefore, choosing $\lambda_1 = 0.78\,\mu m$ for the assigned temperature range of 1000–18000 K was appropriate. In the case where $\lambda_1 = 0.78\,\mu m$, $\delta\lambda_1 = 0.0235\,\mu m$, $\delta\lambda_2 = 0.0204\,\mu m$ were kept constant and λ_2 was varied between 0.84, 0.88, 0.92, 0.96 μm, the relationship between $R(T)$ and T was obtained and is shown in Fig. 13. 12b. This shows that when λ_2 was large, $R(T)$ at the low-temperature end was poorer and when λ_2 was small, $R(T)$ tended to be saturated at the high-temperature end. Therefore, using $\lambda_2 = 0.92\,\mu m$ for the temperature range of 1000–1800 K was recommended. In the case where $\lambda_1 = 0.78\,\mu m$, $\lambda_2 = 0.92\,\mu m$ were kept constant and $\delta\lambda_1$, $\delta\lambda_2$ were varied as $\delta\lambda_1 = 0.0435$, 0.0335, 0.0235, 0.0135 μm and $\delta\lambda_2 = 0.0405$, 0.0305, 0.0205, 0.0105 μm, the relationship between $R(T)$ and T was obtained and is shown in Fig. 13.12c. This shows that $\delta\lambda_1$, $\delta\lambda_2$ exert an insignificant effect on the $R(T)$–T relationship. However, if $\delta\lambda$ is too large, the ICCD becomes saturated and if $\delta\lambda$ is too small, a small signal is produced and, hence, a low signal-to-noise ratio. Therefore, using 0.01~0.03 μm for $\delta\lambda_1$ and $\delta\lambda_2$ was recommended.

(iii) *The effect of the central wavelength on* $S(T)$. Similar to the discussion in the last section, the relationship of $S(T)$ to T was obtained for different values of λ_1, λ_2, $\delta\lambda_1$, $\delta\lambda_2$ and is illustrated in Fig. 13.13a, b, c. Figure 13.13a shows that $S(T)$, or sensitivity, increases with the increase of $\lambda_1 = 0.68$, 0.73, 0.78, 0.83 μm while keeping $\Delta\lambda = \lambda_2 - \lambda_1 = 0.14\,\mu m$, $\delta\lambda_1 = 0.0235\,\mu m$, $\delta\lambda_2 = 0.0204\,\mu m$ unchanged. But the variation of $S(T)$ is large for large and small values of λ_1. Therefore, taking $\lambda_1 = 0.78\,\mu m$ for the temperature range of 1100~1800 K, was recommended. Figure 13.13b shows that $S(T)$ increases when increasing λ_2 or $\Delta\lambda$ ($\Delta\lambda = \lambda_2 - \lambda_1$) while keeping $\lambda_1 = 0.78\,\mu m$, $\delta\lambda_1 = 0.0235\,\mu m$, $\delta\lambda = 0.0204\,\mu m$ constant. However, because too small or too large values of λ_2 causes unstable $S(T)$, $\lambda_2 = 0.92\,\mu m$ was

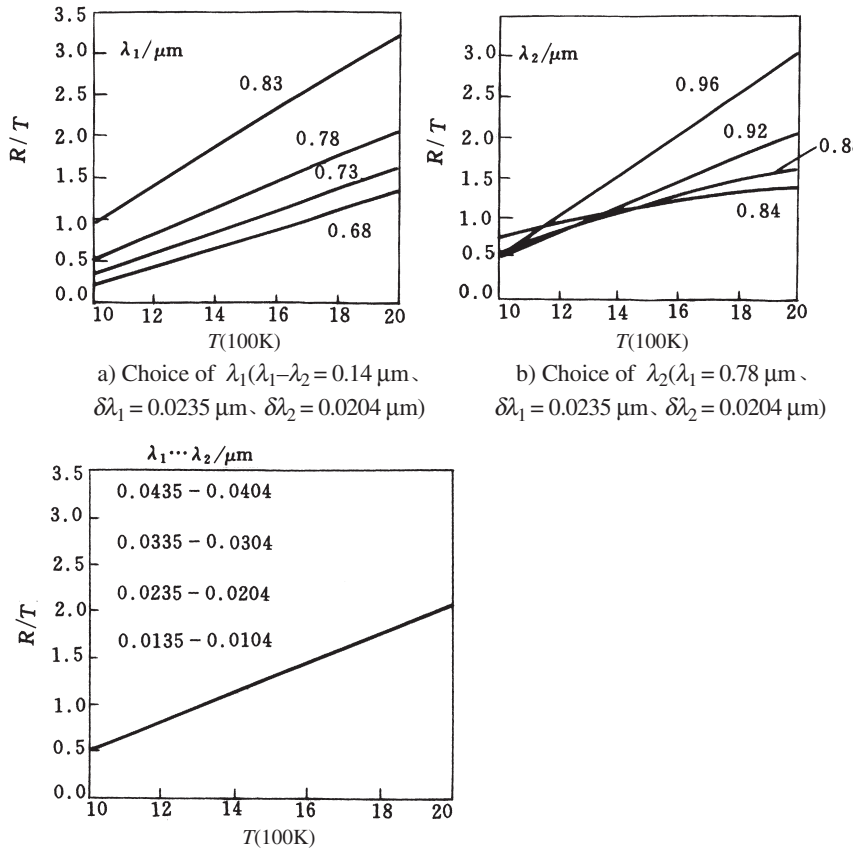

a) Choice of $\lambda_1(\lambda_1-\lambda_2=0.14\,\mu m$、$\delta\lambda_1=0.0235\,\mu m$、$\delta\lambda_2=0.0204\,\mu m)$

b) Choice of $\lambda_2(\lambda_1=0.78\,\mu m$、$\delta\lambda_1=0.0235\,\mu m$、$\delta\lambda_2=0.0204\,\mu m)$

c) Choice of $\delta\lambda_1$、$\delta\lambda_2$ $(\lambda_1=0.78\,\mu m$、$\lambda_2=0.92\,\mu m)$

13.12 Relationship of $R(T)$ with T for different central wavelengths λ_1, λ_2 and wave bandwidths $\delta\lambda_1$ and $\delta\lambda_2$

recommended. Figure 13.13c shows that changing $\delta\lambda_1$ = 0.0435, 0.0335, 0.0235, 0.0135 μm and $\delta\lambda_2$ = 0.0404, 0.0304, 0.0204, 0.0104 μm, had little effect on $R(T)$ when λ_1 = 0.78 μm and λ_2 = 0.92 μm were kept constant.

In order to get good linearity and a steep slope of the $R(T)$–T curve, $S(T)$ was required to be stable in the temperature range being measured. From the results described above, it can be concluded that λ_1 = 0.78, λ_2 = 0.92 μm satisfy the requirement.

(iv) *The effect of the central wavelength on the relative sensitivity* $(S_r(T))$ *of the system's response*. The relative sensitivity $S_r(T)$ is defined as

$$S_r(T)=\frac{\dfrac{\partial R(T)}{R(T)}}{\dfrac{\partial T}{T}}$$

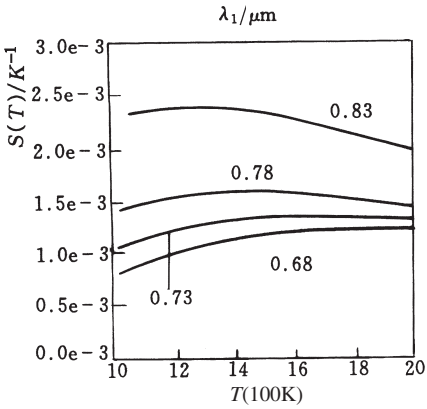

a) Choice of $\lambda_1(\lambda_1-\lambda_2 = 0.14\ \mu m$、$\delta\lambda_1 = 0.0235\ \mu m$、$\delta\lambda_2 = 0.0204\ \mu m)$

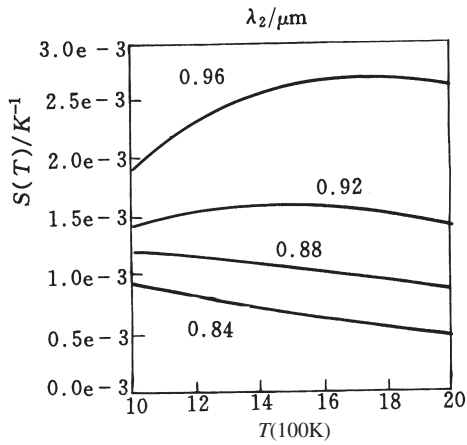

b) Choice of $\lambda_2(\lambda_1 = 0.78\ \mu m$、$\delta\lambda_1 = 0.0235\ \mu m$、$\delta\lambda_2 = 0.0204\ \mu m)$

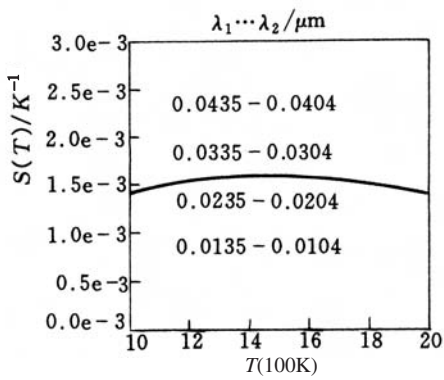

c) Choice of $\delta\lambda_1$、$\delta\lambda_2$ $(\lambda_1 = 0.78\ \mu m$、$\lambda_2 = 0.92\ \mu m)$

13.13 Relationship of $S(T)$ with T for different central wavelengths λ_1, λ_2 and wave bandwidths $\delta\lambda_1$ and $\delta\lambda_2$

This is an important parameter, which can reflect the properties of the system. It can be derived from Eq. [13.14] as follows:

$$S_r(T) = \frac{\dfrac{\partial R(T)}{R(T)}}{\dfrac{\partial T}{T}} = \frac{c_2}{T}\left[\frac{\displaystyle\int_{\lambda_1-\delta\lambda_1/2}^{\lambda_1+\delta\lambda_1/2}\frac{1}{\lambda}\varepsilon(\lambda)M_B(\lambda,T)\gamma_1(\lambda)\eta(\lambda)d\lambda}{P_{\lambda_1}(T)} - \frac{\displaystyle\int_{\lambda_1-\delta\lambda_1/2}^{\lambda_1+\delta\lambda_1/2}\frac{1}{\lambda}\varepsilon(\lambda)M_B(\lambda,T)\gamma_2(\lambda)\eta(\lambda)d\lambda}{P_{\lambda_2}(T)}\right] \quad [13.37]$$

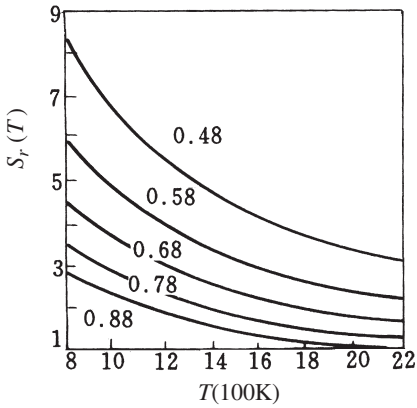

a) Choice of λ_1

(λ_1–λ_2 = 0.14 μm、 $\delta\lambda_1 = \delta\lambda_2$ = 0.01 μm)

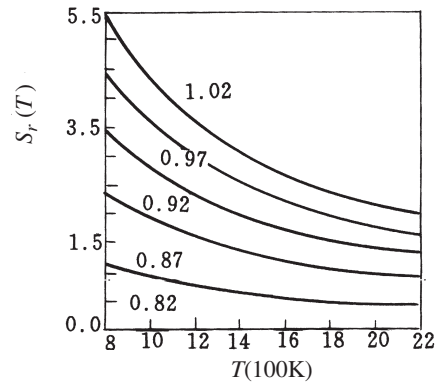

b) Choice of λ_2

(λ_1 = 0.78 μm、 $\delta\lambda_1 = \delta\lambda_2$ = 0.01 μm)

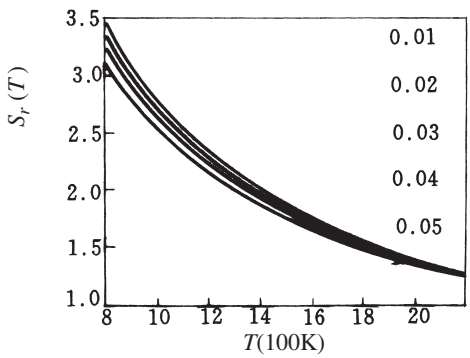

c) Choice of $\delta\lambda_1$、 $\delta\lambda_2$ (λ_1 = 0.78 μm、 λ_2 = 0.92 μm)

13.14 Relationship of $S_r(T)$ with T for different central wavelengths λ_1, λ_2 and wave bandwidths $\delta\lambda_1$ and $\delta\lambda_2$

The $S_r(T)$–T relationship was calculated by numerical simulation for different values of λ_1, λ_2, $\delta\lambda_1$, $\delta\lambda_2$. The results are shown in Fig. 13.14a, b, c. Figure 13.14a shows that $S_r(T)$ decreased with an increase of λ_1(0.48, 0.58, 0.68, 0.78, 0.88 μm) when holding $\lambda_1 - \lambda_2$ = 0.14 μm and $\delta\lambda_1 = \delta\lambda_2$ = 0.01 μm constant. $S_r(T)$ increased with an increase of λ_2 (0.82, 0.87, 0.92, 0.97, 1.02 μm) when λ_1= 0.78 μm, and $\delta\lambda_1 = \delta\lambda_2$ = 0.01 μm (see Fig. 13.14b). $S_r(T)$ slightly decreased when $\delta\lambda_1$ and $\delta\lambda_2$ were increased (0.01, 0.02, 0.03, 0.04, 0.05 μm) and λ_1 = 0.78 μm, λ_2 = 0.92 μm were kept constant.

13.6 Design of the sensor[295,296]

The design of the two-colour thermal-image sensor determines the quality of the image. It should be small, reliable, and have fast response. The main

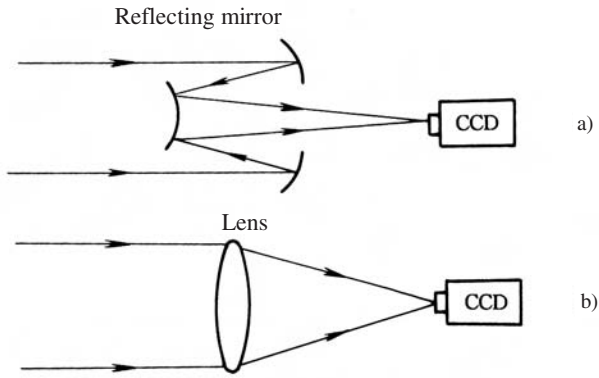

13.15 Optical path of the infrared image

design problem is how to sample two-colour images in as short a time as possible. The construction of the optical system, choice of devices, design of filters, image sampling, and time-sequence control, etc. are described in the following sections.

13.6.1 Structure

There are two possible types of optical systems for radiation-image formation as shown in Figures 13.15a and b, respectively, a reflection type and a refraction type.[334] Because the system works at $\lambda_1 = 0.78\,\mu m$, $\lambda_2 = 0.92\,\mu m$, all devices, including the lenses and filters, must have good transmissivity at these two wavelengths to ensure high image quality. Most, but not all, existing infrared imaging systems are of the reflection type because there are few materials that can satisfy the physical, chemical and mechanical properties needed for an infrared refraction system, and designing an achromatic optical system is difficult. The reflection type has no chromatism and a wider applicable working wavelength. The materials requirements are not rigorous. However, there are many shortcomings including a small field, bulkiness and eclipse in the major optical path. Therefore, the refraction type was chosen for the present design.

For the system, the main aim was to obtain two thermal images. There were two possible choices for this, namely, a single optical path and a binary path,[335] as shown in Figures 13.16a and b. In the binary-path design, a spectroscope was used that divided the radiation into two paths with different filters. Two ICCDs were used to form the image. In this way, two thermal images could be obtained simultaneously. However, very strict synchronisation and accuracy are required for all optical devices in establishing these two optical paths. Practical experience demonstrated that this type of sensor was hard to fabricate and also was bulky. The single-path design was much simpler to construct and had greater system stability but it required a precise color modulator and two filters.

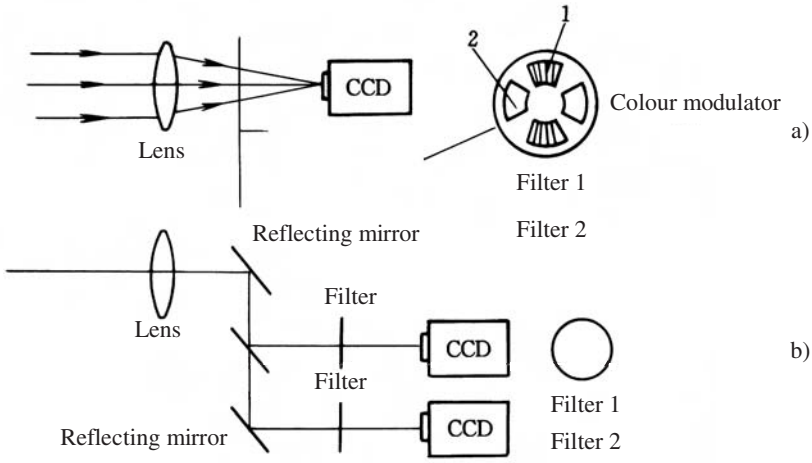

13.16 Optical paths for obtaining two thermal images

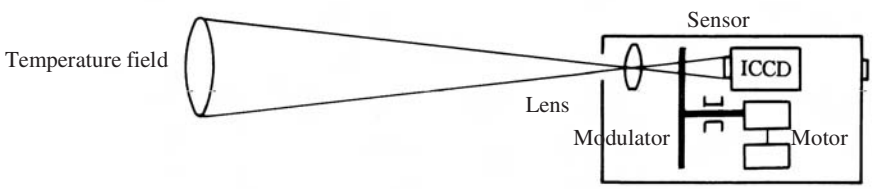

13.17 Single-path sensor

The optical system of the present design is shown in Fig. 13.17. Obviously this is an improved design on the basis of the structure described in Section 12.2.2 and Fig. 12.10. On the colour modulator there are two half-disc filters. The optical path and all of the devices included were identical except the wavelengths of the two filters. Therefore, it was simple and stable. The focal length of the lens was $f = 50$ mm. In the case in which the object field was 50×40 mm and the optically sensitive surface of the ICCD was 7.95×6.45 mm, the image distance l' and object distance l can be calculated as

$$l' = \frac{\alpha}{1+\alpha} f = 43.14(\text{mm})$$
$$l = \alpha l' = 271.32(\text{mm}) \qquad [13.38]$$

where α is the imagery magnification

A different image size can be obtained by regulating the image distance. Figure 13.18 shows the appearance of the actual sensor that was designed.

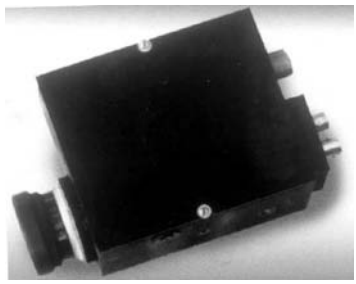

13.18 Appearance of the colorimetric sensor

13.6.2 Sensor components

The main components of the sensor are the lens and the ICCD; their characteristics determine image quality.

Lens. In the choice of a lens, the following factors are considered:

- The focal length is chosen according to the image and object distances, the image-field size and the space needed for mounting, the required temperature-field size, etc. For the present design, 50 mm was chosen.
- The aperture coefficient F is chosen according to the minimum and maximum irradiance acceptable to the ICCD and should be coordinated with the exposure time. In the present design, $F = 4.5$, 5.6, 8, 11, and 16 were chosen. The irradiance of the ICCD decreases by one half when the F-stop is increased by one step.
- Vignetting coefficient H. H affects the evenness of the irradiance on the ICCD surface when a uniform source emits and projects radiation to the lens.

$$H = \frac{D_\omega}{D} \qquad [13.39]$$

where D is the optical beam diameter projected by a point on the object located on the principle axis. D_ω is the actual beam width projected by a point located outside of the principle axis. The angle between the major optical line of the point and the principle axis is ω. The beam width is measured on the intersecting plane formed by the object point and the principle axis.

Due to the vignetting effect, the irradiance at the periphery of the image decreases; the bigger the viewing field, the more serious this phenomenon becomes. Because the viewing field is small in the present case, H may be neglected.

- Geometric parameters and lens quality.

ICCD. An ICCD has many advantages over other imaging systems including low weight and small volume, low-power requirement, and

Table 13.1 Characteristics of the ICCD

Item	Parameter
Image area	4.8 mm × 3.6 mm
Pixel	795 (Horizontal) × 596 (Vertical)
Horizontal frequency	15.625 KHz
Vertical frequency	50 Hz
Scanning system	CCIR Standard, 625 line, 50 field/sec
Minimum irradiance	0.0ℓx for output voltage –6 dB at f1.4 lens
Signal to noise ratio	>48 dB
Resolving power	Better than 600 line TV
Shutter	Discrete, 8 grades

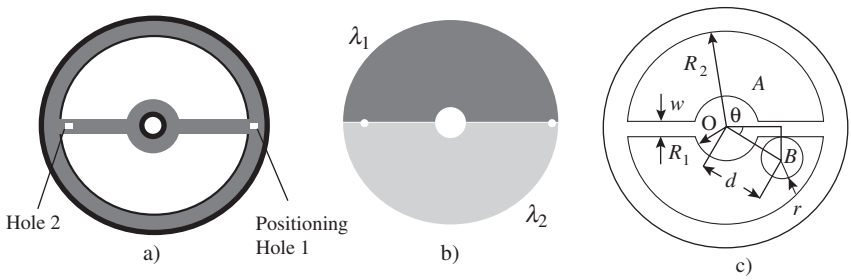

13.19 Construction of a two-colour modulator

robustness in operation. Moreover, its resolving power, dynamic response, sensitivity, and real-time scanning and signal transmission also are superior. The main function of the ICCD is to accumulate and transmit electric charge. In the present system, a model MTV1881EX was chosen, the characteristics of which are shown in Table 13.1.

13.6.3 Two-colour modulator and filter

The function of the colour modulator is to alternate between the filters in order to take two images at different wavelengths. Because the temperature field changes rapidly, high-speed switching between the two filters is required to minimise the displacement of the temperature field between images. Figures 13.19a and b show the construction of the modulator. It comprises a disc with two half-circle holes, as shown in Fig. 13.19a. On the frame of the disc are two small holes that are called location holes and are used for a photoelectric element. When the hole passes by the photoelectric element, a signal is produced that instructs the computer to take an image. Figure 13.19b shows the two half-circle filters having wavelengths λ_1 and λ_2. Suppose that the centre of the disc is O (see Fig. 13.19c), the outer diameters are R_1

and R_2, the width of the cross-beam between the two half-circles is w, the centre of the light-beam is at B and its radius is r, the distance between the disc centre and the centre of the light beam is OB = d, the angle between OB and the cross-beam is θ, and the angle used for taking the image is θ_0. Then the values of R_1, R_2 and θ should satisfy the following formula:

$$\theta_0 = \sin^{-1}\left(\frac{r + w/2}{d}\right), \theta_0 < \theta < \pi - \theta_0$$
$$R_1 < d - r, \quad R_2 > d + r \qquad [13.40]$$

It can be seen from these formulae that an appropriate design of the disc could increase the beam receiving-angle and the switching speed of the filters. If $r + w/2 = d/2$, then $\theta_0 = 30°$ and the effective beam receiving angle would be $180° - (2*30°) = 120°$

The maximum exposure time of the ICCD was 16.7 ms. In selecting the rotation speed of the colour modulator, 40 ms was considered a satisfactory time for taking an image. If the switching time of the filters was 20 ms, then the total time for taking two images would be $2*(40 + 20) = 120$ ms. Therefore $N = 8.33$ r/s was selected for the rotation speed of the modulator. A 6 V, 2400 r/min DC miniature motor having a belt drive was chosen to rotate the modulator.

Because the images are taken during high-speed rotation of the filter, the filters should have uniform quality. Two specially made interference filters were designed according to the principle described in Section 13.4 and Eq. [13.26]. The filter parameters were $\lambda_1 = 0.78\,\mu m$, $\delta\lambda_1 = 0.0235\,\mu m$, $I_1 = 0.83$, $\lambda_2 = 0.92\,\mu m$, $\delta\lambda_2 = 0.0204\,\mu m$, and $I_2 = 0.662$.

13.6.4 Acquisition of the image signals and control[345,352]

For dividing the temperature range, choosing several exposure times, which are controlled by the computer via an I/O interface, are necessary. The switching of the imaging is controlled by a photoelectric signal produced using two small holes. A schematic diagram of the operation is shown in Fig. 13.20.

Exposure-time control. The exposure time was determined by a four-bit logic circuit. The logic settings are shown in Table 13.2.

Acquisition of the image. Image acquisition was controlled by the signal generated from the holes on the modulator disc. When a hole reached a preset location, the photo-electric device transmited a signal to the computer and started the sampling of the image. The time sequence is shown in Fig. 13.21.

The image signal-processing system. This system, which is shown in Fig. 13.22, consisted mainly of an image module and a computer. The image was sampled according to the location pulse, which could be sent to the monitor for display or to the memory of the computer for processing. The

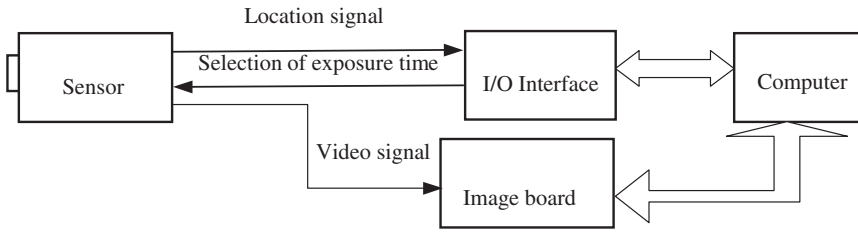

13.20 Two-colour sensor and computer *I/O* interface

Table 13.2 Exposure-time control

Shutter time	J_4	J_5	J_6	J_7
Close	0	×	×	×
1/60 (ms)	1	0	0	0
1/125 (ms)	1	0	0	1
1/250 (ms)	1	0	1	0
1/500 (ms)	1	0	1	1
1/1000 (ms)	1	1	0	0
1/2000 (ms)	1	1	0	1
1/4000 (ms)	1	1	1	0
1/10000 (ms)	1	1	1	1

Note: '1' Open-circuit, '0' Short-circuit

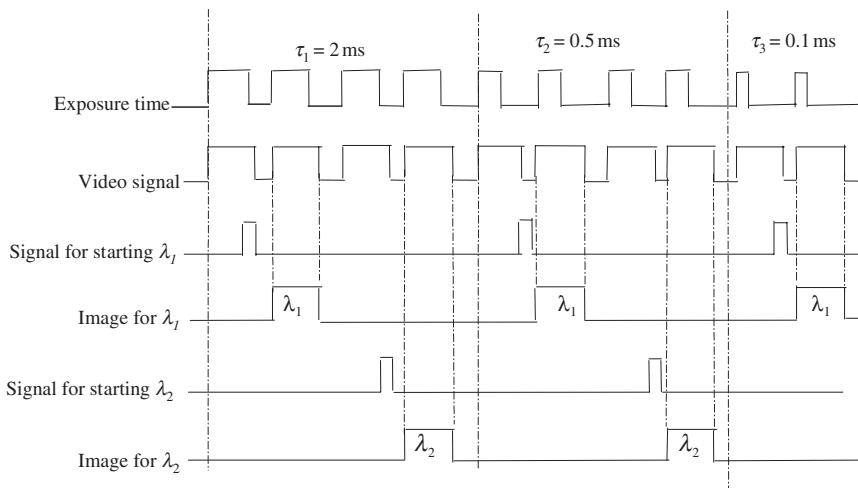

13.21 Time sequence for imaging

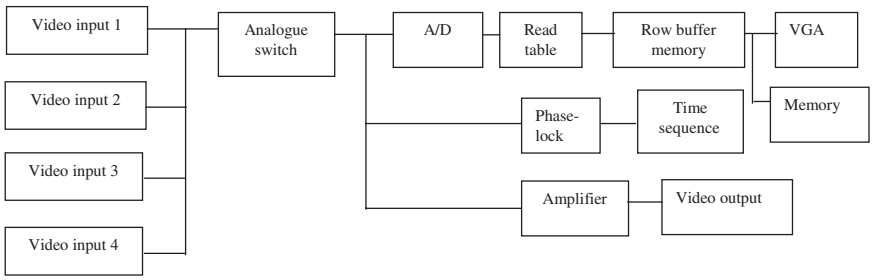

13.22 Schematic diagram of the image module

software selected one of the four channels and the signals were sent to an A/D converter. After reading the table, the 8-bit image signals were sent to the buffer memory. At the same time as the signals were sent to the row buffer memory, they were taken by the computer via a VESA bus and sent to the computer's memory or the display module of the VGA for further processing.

13.7 Effects of measuring conditions[338]

As described in Chapters 11 and 12, the results of measurements by the colorimetric method theoretically do not depend on the distance, exposure time, lens aperture, filter-material uniformity or surface conditions. This implication is verified in this section for further confirmation of the accuracy and reliability of the method. For this purpose, a Gleeble–1500 machine and NiCr–NiAl thermocouples were used. The effect of various factors, such as material, surface conditions, distance, exposure time, and aperture, were studied in detail.

13.7.1 Materials and surface conditions

Effect of spectrum emissivity. The colorimetric method has the least dependence on emissivity. If the object is a grey or black body, or the emissivity equals 1 or is a constant, the measured temperature T_c (or apparent temperature) is identical to the real temperature T. If the object does not satisfy these conditions, then there is an error between T_c and T. The error can be obtained by substituting Eq. [13.8a] into Eq. [13.8b].

$$\frac{\Delta T_c}{T} = \frac{T - T_c}{T} = \frac{\dfrac{\lambda_1 \cdot \lambda_2 \cdot T}{\lambda_2 - \lambda_1} \ln \dfrac{\varepsilon(\lambda_1, T)}{\varepsilon(\lambda_2, T)}}{\dfrac{\lambda_1 \cdot \lambda_2 \cdot T}{\lambda_2 - \lambda_1} \ln \dfrac{\varepsilon(\lambda_1, T)}{\varepsilon(\lambda_2, T)} - c_2} \qquad [13.41]$$

The emissivity of real matter depends on the material, surface condition, radiation direction, wavelength and temperature. For an engineering material, and a small difference of λ_1, λ_2, it can be regarded as a grey material. Then, the colorimetric temperature T_c is very close to its real temperature T. For the wavelengths $\lambda_2 = 0.78\,\mu m$, $\lambda_2 = 0.92\,\mu m$, the emissivities are not identical. $B = \varepsilon(\lambda_1, T)/\varepsilon(\lambda_2, T)$ is not equal to 1 and the absolute error $\Delta T_c(K) = T - T_c$ can be calculated as shown in Table 13.3. This table shows that when ($B < 0.85$) or ($B > 1.15$), the error is larger than 50 K. Moreover, the higher the temperature, the larger the error is when B is kept constant. Therefore it can be concluded that the key problem of ensuring measurement accuracy is to keep the emissivities of the materials at two wavelengths as close as possible.

Figure 13.23 shows the experimentally determined relationship between emissivity and wavelength for some metals. The figure shows that

Table 13.3 Difference between T_c and T due to different ε for λ_1, λ_2

B	T(K)								
	1000	1100	1200	1300	1400	1500	1600	1700	1800
0.85	54.7	65.9	78.0	91.0	105.0	119.9	135.7	152.3	169.9
0.90	36.2	43.6	51.7	60.5	69.9	80.0	90.6	102.0	114.0
0.95	18.0	21.7	25.8	30.2	34.9	40.0	45.5	51.2	57.3
1.00	0	0	0	0	0	0	0	0	0
1.05	−17.7	−21.4	−25.6	−30.1	−34.9	−40.2	−45.8	−51.2	−58.1
1.10	−35.1	−42.7	−51.0	−60.0	−69.9	−80.5	−91.9	−104.1	−117.2
1.15	−52.4	−63.7	−76.3	−90.0	−104.9	121.1	−138.5	−157.2	−177.2

Conditions: $\lambda_1 = 0.78\,\mu m$, $\lambda_2 = 0.92\,\mu m$, $B = \varepsilon(\lambda_1, T)/\varepsilon(\lambda_2, T)$

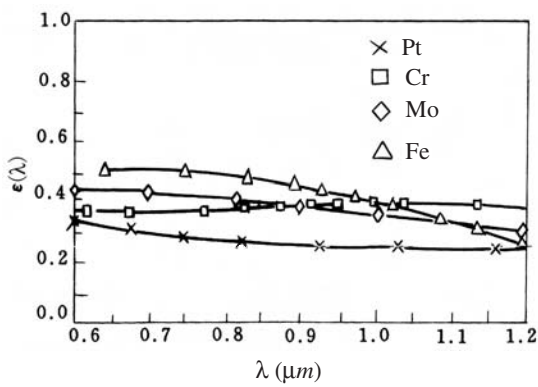

13.23 Emissivity obtained by experiment

$B = \varepsilon(\lambda_1, T)/\varepsilon(\lambda_2, T)$ is less than 1.033 for Pt, Cr, Mo and Fe. In the present design, λ_1, λ_2 were 0.78~0.92 μm; therefore the resulting error could be neglected.

Effect of materials. Two metal alloys, namely 1Cr18Ni9Ti stainless steel and Q235 mild steel, were tested in vacuum to avoid oxidation of their surfaces.

The experimental conditions were: An aperture of 8, exposure time of 2 ms, specimen dimensions of 10 × 10 × 150 mm, and 310 mm distance.

The measurements were repeated three times for each condition. The colorimetric ratios obtained are shown in Table 13.4.

The table shows that the sensitivity was 0.74×10^{-3}/°C and 0.92×10^{-3}/°C, respectively, for 1Cr18Ni9Ti and Q235. The difference between the two metals was 4.3°C at 900°C and 14.5°C at 950°C. Also, the grey level of 1Cr18Ni9Ti was greater than that of Q235. This means that the emissivity of 1Cr18Ni9Ti was greater than that of Q235. However, both were stable in repeated measurements. The results were reliable and acceptable for practical application.

Effect of surface condition. The emissivity depends strongly on the surface condition. Experiments with stainless steel were conducted with two different surface conditions. One was a bright surface and the other condition was an oxidised surface formed by holding at a high temperature for a long time. The results obtained at 1100°C and 1150°C are listed in Table 13.5.

The experimental conditions were: An aperture of 11, exposure of 0.5 ms, specimen dimensions of 10 × 10 × 150 mm and distance of 310 mm.

This table shows that the sensitivity was 0.7×10^{-3}/°C and 0.68×10^{-3}/°C for the bright surface and the oxidised surface, respectively. The difference

Table 13.4 Effect of materials on colorimetric ratios

Temperature (°C)	Test No.	Mild steel				1Cr18Ni9Ti				Difference of ratio
		Grey		Ratio	Average	Grey		Ratio	Average	
		λ_1	λ_2			λ_1	λ_2			
900	1	64	71	0.904	0.919	129	140	0.916	0.915	0.004
	2	65	70	0.930		129	140	0.921		
	3	66	71	0.923		128	140	0.907		
950	1	100	104	0.962	0.965	182	192	0.952	0.952	0.013
	2	101	104	0.964		182	192	0.951		
	3	102	105	0.969		183	192	0.954		

(Conditions: Distance 310 mm, Aperture 8, Exposure 2 ms)
n.b. λ_1 and λ_2 are nearest whole numbers

Table 13.5 Effect of surface condition

Temperature (°C)	Test No.	Bright stainless steel				Oxidised stainless steel				Difference of colorimetric ratio
		Grey		Ratio	Average	Grey		Ratio	Average	
		λ_1	λ_2			λ_1	λ_2			
1100	1	138	130	1.062	1.062	189	180	1.047	1.056	0.006
	2	138	130	1.061		189	178	1.064		
	3	138	129	1.064		189	179	1.057		
1150	1	178	162	1.096	1.097	242	222	1.090	1.090	0.007
	2	179	162	1.097		241	222	1.089		
	3	179	163	1.097		241	221	1.090		

(Conditions: Distance 310 mm, Aperture 11, Exposure 0.5 ms)
n.b. λ_1 and λ_2 are nearest whole numbers

Table 13.6 Effect of ω on the irradiance ratio

ω	0°	5°	10°	12°	15°	20°	25°	30°
$E(\lambda, \vec{r})/E(\lambda, 0)$	1	0.985	0.94	0.915	0.87	0.78	0.675	0.563

between these two surfaces was 8.6°C at 1100°C and 10.0°C at 1150°C. These results showed as well that the grey level of the oxidized surface was higher than that of the bright surface. Obviously, the oxide film increased the emissivity. The grey level for repeated experiments was stable, with little variation.

13.7.2 Distance

The influence of different measuring points on the object. It is known that the irradiance at a point depends on the angle ω between its principal ray and the optical axis. When the radiant exitance values of both points is equal, the ratio of the irradiance between these two points is

$$E(\lambda,\vec{r}\,')/E(\lambda,0) = H \cdot \cos^4 \omega \qquad [13.42]$$

The effect of ω was calculated and is shown in Table 13.6 (for $H = 1$). This table shows that the resulting difference was significant when ω > 12°.

Because only the ratio of grey level was used for the assessment of temperature, the grey-level change due to the angle ω would not play a significant role. However, if an aberration (for example a chromatic aberration) or a difference of image location existed, the grey level change due to ω would play an important role in the value of the error of R. In the present system, $\omega < 6°$, $\Delta\lambda = 0.14\,\mu m << \lambda_1$ and λ_2, and the location error between the two images was less than 2 pixels. Therefore, the error due to the location of the point in the viewing field could be neglected. In fact, its influence was hard to experimentally verify because rigorous experimental conditions were needed to obtain precise measurements.

Effect of distance. It was demonstrated that in the colorimetric measuring method, the effect of distance on the measured value was theoretically eliminated: see Eq. [13.15]. To verify this rule, the following experiments were conducted. The experimental conditions were: An aperture of 8, exposure for 0.5 ms, specimen dimensions of $10 \times 10 \times 150$ mm, 1Cr18Ni9Ti stainless steel material, distances of 290, 310, 355, and 488 mm. The grey levels, their ratios, and the average values were measured three times. The results are shown in Table 13.7. This table shows that the sensitivities were 0.68×10^{-3}, 0.46×10^{-3}, 0.64×10^{-3}, and 0.6×10^{-3}/°C, for distances of 290, 310, 355, and 480 mm, respectively. If the data at a distance of 310 mm is taken as the standard, the error for distances of 290, 355, and 480 mm were –8.7, –10.9, and –52.2°C at 1100°C and +32.6, +8.71, –37.0°C at 1150°C. These results also show that the grey level and grey-level ratio decreased when the distance increased but the error was within only 11°C for a distance of 310~355 mm, which is a great advantage of this method.

13.7.3 ICCD and lens parameters

Theoretically, the exposure time of the ICCD and the aperture coefficient have no effect on the grey level ratio but, in fact, the signal-to-noise ratio changes when the exposure time and aperture coefficient change and, consequently, the grey-level ratio changes.

Effect of aperture coefficient. The aperture coefficient represents the area of the optical path. A larger aperture coefficient means the area of the optical path is smaller; the area decreases by one half when the aperture coefficient increases one grade. Experiments were conducted using two aperture coefficients at two different temperatures, 1100°C and 1150°C. The results are shown in Table 13.8. The experimental conditions were: Apertures of 8 and 11, exposure for 0.5 ms, specimen dimensions of $10 \times 10 \times 150$ mm, 1Cr18Ni9Ti stainless steel material, and a distance of 355 mm.

This table shows that the sensitivities were 0.63×10^{-3}/°C, and 0.75×10^{-3}/°C for apertures of 8 and 11, respectively. The error at 1100°C was 30.2°C and at 1150°C was 44.0°C. It is known from Equations [13.2] and

Table 13.7 Effect of distance on measuring results

Temperature (°C)	Test No.	Distance (mm)															
		290				310				355				488			
		Grey		Ratio	Average	Grey		Ratio	Average	Grey		Ratio	Average	Grey		Ratio	Average
		λ_1	λ_2			λ_1	λ_2			λ_1	λ_2			λ_1	λ_2		
1100	1	169	176	0.962	0.956	156	163	0.956	0.952	155	164	0.945	0.947	130	140	0.924	0.928
	2	169	177	0.956		156	164	0.954		155	164	0.944		130	141	0.925	
	3	169	178	0.950		156	166	0.945		155	163	0.952		131	141	0.934	
1150	1	222	224	0.988	0.990	205	209	0.981	0.975	203	206	0.984	0.979	173	181	0.957	0.958
	2	222	225	0.987		205	211	0.972		203	207	0.981		175	180	0.968	
	3	222	223	0.996		205	211	0.973		203	209	0.971		172	181	0.950	

(Conditions: Stainless steel with bright surface, Aperture 8, Exposure 0.5 ms)
n.b. λ_1 and λ_2 are nearest whole numbers

Table 13.8 Effect of aperture on measuring results

Temperature (°C)	Test No.	Ap. 8				Ap. 11				Difference of ratio
		Grey		Ratio	Average	Grey		Ratio	Average	
		λ_1	λ_2			λ_1	λ_2			
1100	1	155	164	0.9450	0.9470	110	115	0.9553	0.9660	0.019
	2	155	164	0.9442		111	115	0.9646		
	3	155	163	0.9517		111	114	0.9781		
1150	1	203	206	0.9837	0.9785	145	145	1.0047	1.0035	0.025
	2	203	207	0.9807		146	146	1.0014		
	3	203	209	0.9711		146	146	1.0044		

(Conditions: Stainless steel with a bright surface, Distance 335 mm, Exposure 0.5 ms)
n.b. λ_1 and λ_2 are nearest whole number

Table 13.9 Effect of exposure on measuring results

Temperature (°C)	Test No.	2 ms				0.5 ms				Difference of ratio
		Grey		Ratio	Average	Grey		Ratio	Average	
		λ_1	λ_2			λ_1	λ_2			
1000	1	165	172	0.962	0.963	65	68	0.955	0.958	0.005
	2	164	170	0.969		64	68	0.948		
	3	162	169	0.959		65	67	0.971		
1050	1	228	219	1.039	1.028	97	94	1.029	1.030	0.002
	2	226	221	1.023		98	95	1.031		
	3	226	221	1.021		96	93	1.029		

(Conditions: Stainless steel with a bright surface, Distance 310 mm, Aperture 11)
n.b. λ_1 and λ_2 are nearest whole numbers

[13.3] that the grey level for an aperture of 8, theoretically, is 2 times that for an aperture of 11 at the same temperature (in fact, it is not 2 times). The data shown in Table 13.8 demonstrates that there is an influence of aperture on the measurements. In order to eliminate the influence of the relationship between temperature and colorimetric ratio, calibrating the sensor using a fixed aperture and storing the results in the computer is recommended for practical applications.

Effect of exposure. Two exposure times, namely, 2 ms and 0.5 ms at an aperture of 11 were selected for the experiments. Measurements were carried out at 1000°C and 1050°C. The results are shown in Table 13.9.

The experimental conditions were: An aperture of 11, exposure for 2 ms and 0.5 ms, specimen dimensions of $10 \times 10 \times 150$ mm, 1Cr18Ni9Ti stainless steel material, and a distance of 310 mm.

This table shows that the sensitivities were 1.3×10^{-3}/°C and 1.46×10^{-3}/°C for exposure times of 2 ms and 0.5 ms, respectively. The errors introduced were 3.8°C at 1000°C and 1.5°C at 1150°C.

The grey-level ratios for the two different exposures of 2 ms and 0.5 ms at the same temperature should be 4 according to Equations [13.2] and [13.3], but actually they were less than 3. In practical applications of the measuring method, the system is calibrated for each exposure so that the effect of exposure will be eliminated.

13.8 Calibration of the system[344,350]

After temperature-measuring instruments are built, they should be calibrated to establish the relationship between the output and temperature, which is called the calibration function or calibration curve. For conventional instruments, a standard reference should be used, either near the object or inside the photoelectric scanning device. This requirement is hard to satisfy, particularly for temperature-field measurements.

The author has proposed a special calibration method. First, off-line calibration was carried out with a known temperature reference so that the relationship of the grey ratio and temperature was obtained. In subsequent actual applications, the instrument was calibrated on-line to establish the relationship between grey level and temperature. Then the temperature-field data can be quickly acquired in actual measurements.

13.8.1 Off-line calibration

As described in Section 13.7, a small distance variation within 40 mm does not greatly affect the grey ratio–temperature relationship. Proper selection of λ_1, λ_2 confines the error due to surface conditions to a certain range. Therefore, the factors that should be calibrated are the exposure of the ICCD and the aperture of the lens.

The conditions for calibration were: Gleeble–1500 thermal-cycle simulation machine, a lens of aperture 8, an ICCD exposure of 0.1, 0.5, and 2 ms, stainless steel material, specimen dimensions of $12 \times 12 \times 60$ mm, and a distance of 310 mm. The schematic diagram of the calibration system is shown in Fig. 13.24.

Procedure: Two thermal images were taken at the centre of a uniform temperature field, the data were processed and the grey-level ratios were determined.

In order to avoid the thermocouple influencing the temperature field, the athermocouple was mounted on the back of the specimen opposite the measured point. Measurements were then taken every 50°C. The grey-level

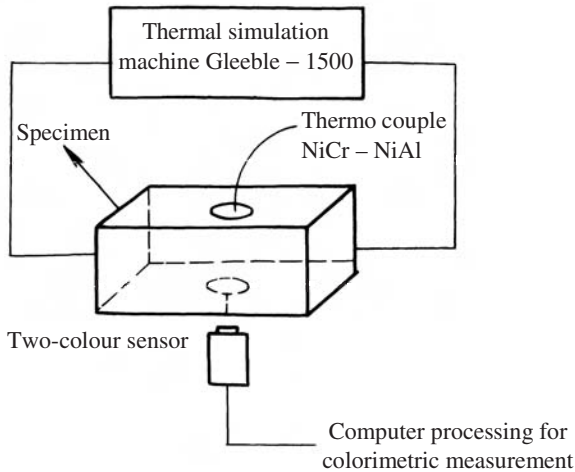

13.24 Off-line calibration

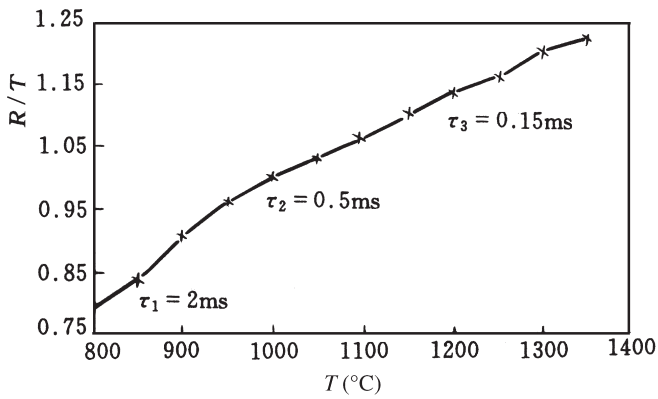

13.25 Relationship between grey ratio and temperature

ratio to temperature relation was recorded for each exposure. Three calibration curves were obtained by fitting the data as shown in Fig. 13.25.

13.8.2 On-line calibration

In the colorimetric method, a lot of time is needed for data acquisition and processing for each temperature field. The first step is the sampling of two thermal images, which requires 40 ms including the switching of the optical path. The second step is filtering the image data, which also takes 40 ms if a (3 × 3) pixel average is used. This duration can be shortened if signals of

only local parts of the temperature field are necessary. The first duration may be greatly shortened if a single image is used instead of two images. However, the grey level of a single image is sensitive to distance and cannot be used directly for assessment of the temperature.

It is known that the grey-level ratio has a definite relationship to temperature, independent of the measurement distance. If the distance and material are kept constant, there is a definite relationship between the grey-level ratio and the grey level. In other words, there is a definite relationship between the grey level $N_{\lambda_1}(T)$ of the image λ_1 and the temperature. This relationship can be calibrated on line for all three exposures. The method is shown in Fig. 13.26. Thus, the temperature-field data can be established directly from its grey level from one image. The method is called a 'two-colour calibration and one-colour measuring method'. In this way, the process becomes simple and quick. Figure 13.27 shows an on-line calibration curve obtained under the following conditions: a distance of 310 mm, stainless steel, an aperture of 16, and exposure times of 0.1, 0.5, and 2 ms. By using these curves, the measuring time is shortened to one half of that for the two-colour measurement method.

13.8.3 Conclusion

- The core of the colorimetric temperature-field measuring facility is the two-colour sensor developed by the author and described in

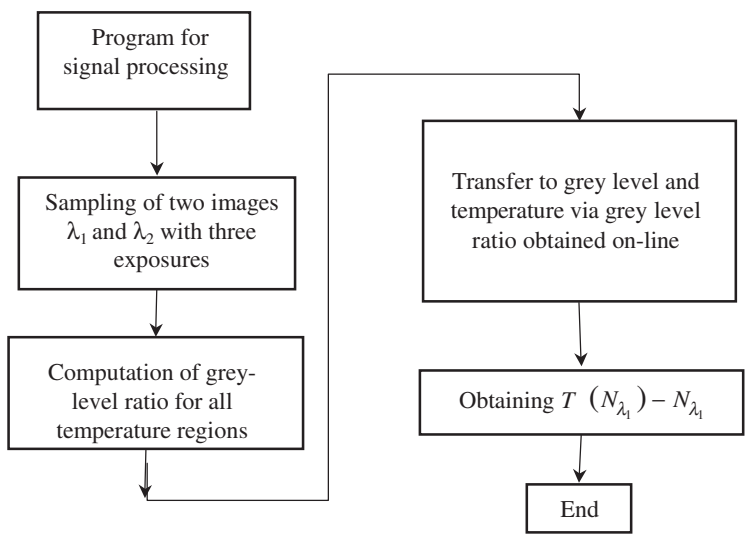

13.26 Procedure for on-line calibration

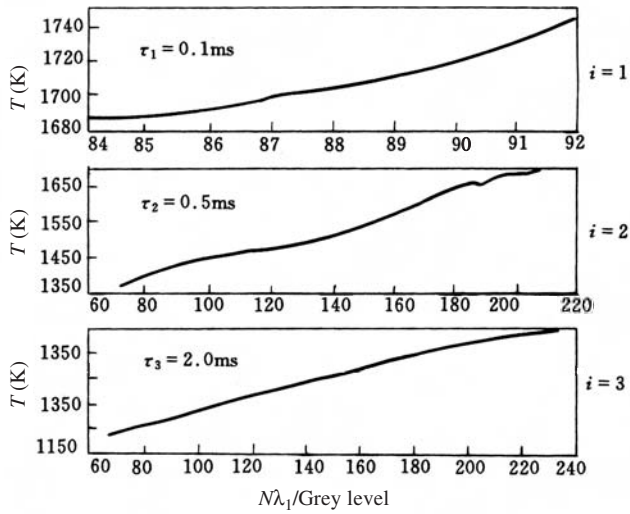

13.27 On-line calibrated temperature and grey-level curves

Section 13.6. It is compact, lightweight and reliable. The time needed for measuring one temperature field is less than 120 ms, which is satisfactory for real-time detection.

- The effects of different factors on the measurement accuracy are discussed in Section 13.7. The results demonstrated that the distance and emissivity have little effect; this is the greatest advantage of the method that was developed. The effect of other factors can be eliminated by calibration.
- A two-colour calibration and one-colour measuring method has been developed by the author. It possesses the advantages of the two-colour measuring method and the results are independent of measuring distance, emissivity, etc. It also possesses the advantage of the one-colour measuring method, i.e. high speed. This method provides a good means for real-time measurement and weld-quality control.

14

Practical measurement and application

14.1 Experimental apparatus

The system described in Chapter 12 was applied in an automatic welding machine in which TIG welding was used with the QHT-80 power source developed by Tsinghua University (see Chapter 4). A two-colour sensor was mounted toward the back of the weld, which was moving simultaneously with the welding torch. The temperature field was measured in real time while welding was in progress. Various parameters of the thermal process during welding could be monitored and used for closed-loop control of the welding process, as shown in Fig. 14.1.[339,351,379]

14.2 Measurement of the welding temperature field

The main problems for real-time measurement of a welding temperature field are the measuring speed and measurable temperature range. Applying combined off-line and on-line calibration can shorten the measuring speed for one image to 40 ms. Applying several exposures has extended the measurable range from 250°C to 600°C. Therefore, adequate information about the welding temperature field can be obtained within 0.5 s, which makes real-time control possible.

The measuring procedure includes sampling the thermal image, data processing and connection of the temperature regions to form a complete field.

14.2.1 Acquisition of temperature-field signals

Measurements were conducted using TIG welding. The experimental conditions were flat welding without filler-wire addition, mild steel having dimensions of $60 \times 150 \times 2$ mm, argon shielding gas at a flow rate of 0.5 m^3/h, 128 A welding current, 14 V arc volts, 7.07 mm/s travel speed, ϕ2.5 mm tungsten electrode, a measuring distance of 310 mm, an aperture setting of 11, and exposure times of 0.1, 0.5, and 2 ms.

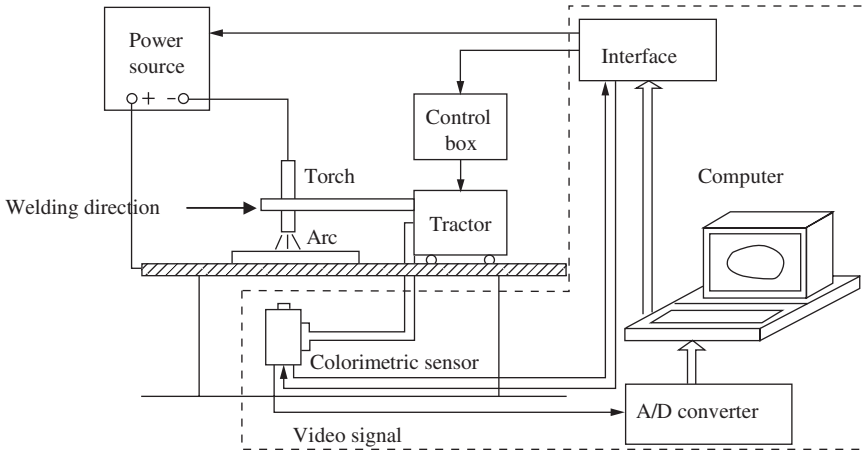

14.1 Welding machine with a colorimetric sensor

Two images were taken through the filters designed for wavelengths λ_1 and λ_2 at an exposure time of 0.1 ms for the high-temperature region, at an exposure time of 0.5 ms for the medium-temperature region, and at an exposure time of 2.0 ms for the low-temperature region. The time sequence for imaging is shown in Fig. 13.21 and the flow chart is shown in Fig. 14.2. Because the total imaging time was less than 60 ms, the influence of torch movement could not be determined. Using a two-colour calibration method and a one-colour measuring method, three images were obtained for λ_1 at three different exposures times. Figures 14.3a, b, and c show the three images for λ_1 at exposure times of τ_1, τ_2, and τ_3.

14.2.2 Procedure for signal processing

Signal processing can be divided into three procedures: preprocessing of the thermal image, calibration of the grey level of each of the three regions, and connection of the three temperature regions.

(i) *Preprocessing of the image*. In practical measurements, there is contamination on the object's surface and noise produced by the optical system itself. Both of these cause error in the measurements; the grey-level ratio is particularly sensitive to noise. Therefore, filtering the signals is necessary. The average grey level of 9 neighbouring pixels normally is used, namely

$$\begin{aligned} N'(i,j) = [&N(i-1,j-1)+N(i-1,j)+N(i-1,j+1)+N(i,j-1) \\ &+N(i,j)+N(i,j+1)+N(i+1,j-1)+N(i+1,j) \\ &+N(i+1,j+1)]/9 \end{aligned} \qquad [14.1]$$

where, $N'(i,j)$ is the grey value of the row i, column j pixel.

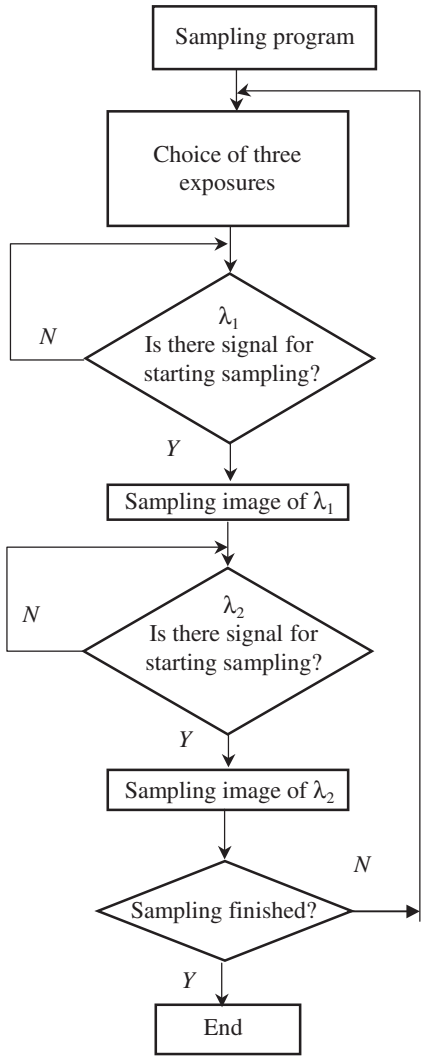

14.2 Flow chart of image sampling

(ii) *Detection of the temperature in different regions*. After filtering of the signals, two images in the high-temperature region, $N(\lambda_1)$ and $N(\lambda_2)$, are selected. The pixels that have the same grey level, N_1, in image λ_1 are selected and the pixels in image λ_2 that correspond to the pixels of N_1 in image λ_1 are identified. The average grey value of these pixels, $N_2(N_1)$, is calculated using the following formula:

$$R(N_1) = \frac{N_1}{N_2(N_1)} \qquad [14.2]$$

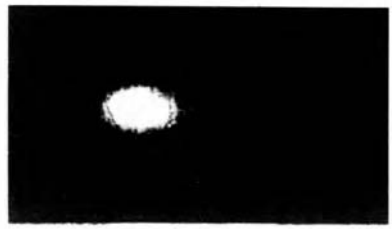

a) $\tau_1 = 0.1$ ms

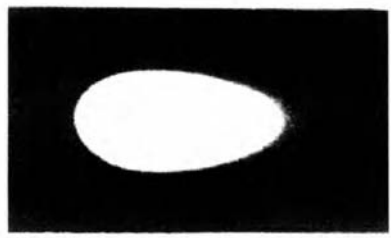

b) $\tau_2 = 0.5$ ms

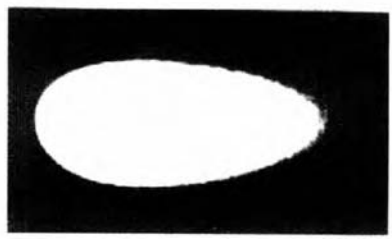

c) $\tau_3 = 2.0$ ms

14.3 Images of λ_1 for τ_1 τ_2 and τ_3

Taking advantage of the off-line calibration curve (the R–T relationship curve), the temperature corresponding to N_1 can be found as $T(R(N_1))$.

In order to eliminate the misalignment of images λ_1 and λ_2 (in the present design, it would be no more than two pixels), the value of $T(N_1)$ is averaged with two neighbouring ratio values.

$$T(N_1) = \frac{T(N_1 - 1) + T(N_1) + T(N_1 + 1)}{3} \qquad [14.3]$$

Similarly, from images in the medium-temperature region and the low-temperature region, $T_2(N_1)$ and $T_3(N_1)$ can be obtained in the same way as $T_1(N_1)$.

It is seen that $T_1(N_1)$, $T_2(N_1)$ and $T_3(N_1)$ were obtained on the basis of $R(N_1)$. However, on the basis of it, the temperature values of the field can be evaluated directly from N_1 obtained from the three λ_1 images.

(iii) *Connection of the temperature regions*. In order to obtain the complete temperature field, the three regions are connected together. To make this connection, the borders of each region have to be defined. The location where the grey level $N_1 < 50$ in the high-temperature image λ_1 is defined as the border of the high-temperature region. Similarly, the location where $N_1 < 50$ in the medium-temperature image λ_1 is defined as the border of the medium-temperature region. The location where $N_1 < 50$ in the low-temperature image λ_1 is considered as a region that does not give reliable data. In order to put the temperature fields of the three regions together and display them as a single image, the temperature data are transformed into their grey levels. Supposing that the maximum and minimum temperatures obtained for the complete temperature field are T_{max} and T_{min}, transforming them into grey levels from 255 to 0 is required. The formula for transformation is:

$$N[T_i(N_1)] = 255\frac{T_i(N_1) - T_{min}}{T_{max} - T_{min}} \qquad [14.4]$$

where $i = 1, 2$, and 3 represent the high-temperature, medium-temperature and low-temperature regions, respectively.

If the grey level N is known, the temperature can be found using the following formula:

$$T = T_{min} + (T_{max} - T_{min})\frac{N}{255} \qquad [14.5]$$

After artificially colouring, the picture is obtained as shown in Fig. 14.4. The maximum temperature in the centre is 1700 K and at the periphery is 1200 K. Each colour band represents 50 K. A flow chart of the signal processing is shown in Fig. 14.5.

14.2.3 Connecting the temperature regions

Figures 14.6a, b, and c, show a three-dimensional diagram of the temperature distribution in the low-, medium- and high-temperature regions. Figure 14.6d is the whole picture that incorporates the three connected regions, where XOY is an isothermal plane. Each colour grade is 50 K.

14.3 Mathematical model of the temperature field in welding based on measurement

The analysis of the temperature field is based mainly on three factors; namely, the distribution of the heat source, heat transfer laws and the

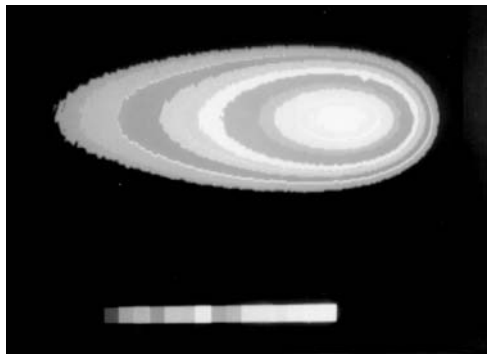

14.4 Artificially-coloured temperature field

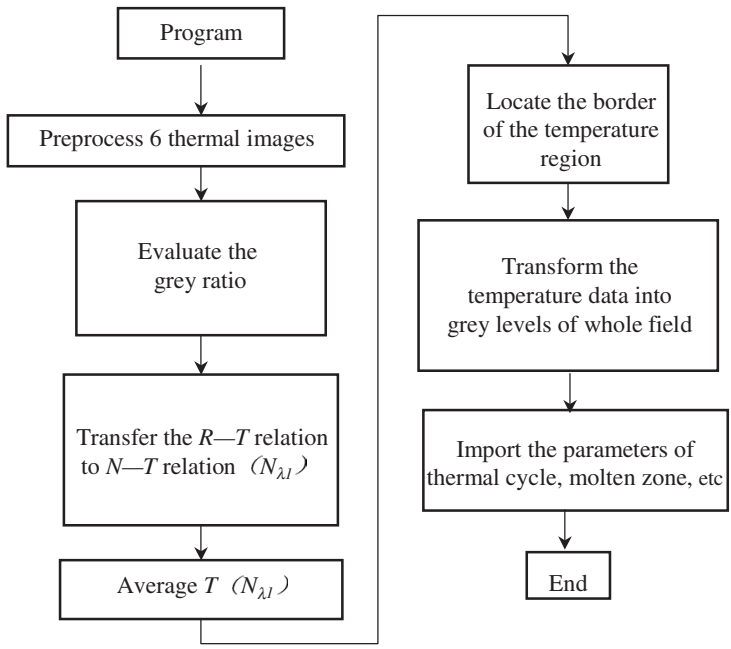

14.5 Flow-chart of signal processing of the temperature field

boundary conditions of the work-piece. An analytical solution can be obtained only for the case of a half infinitely thick, half infinitely large or infinitely long workpiece. The heat source is assumed to have a point, line or surface shape. Actually, the heat source is not ideally distributed; therefore the temperatures cannot be analysed even if the boundary conditions

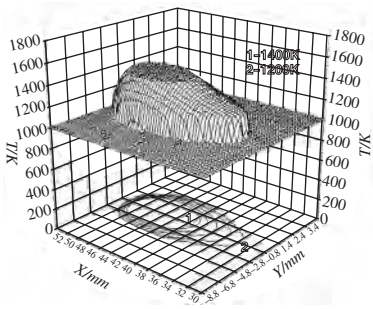

a) $\tau_1 = 2$ ms, Low-temperature region

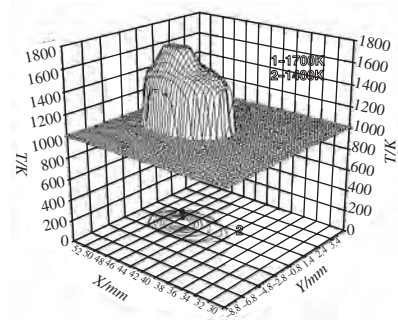

b) $\tau_2 = 0.5$ ms, Medium-temperature region

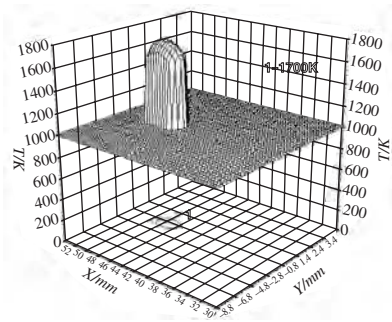

c) $\tau_3 = 0.1$ ms, High-temperature region

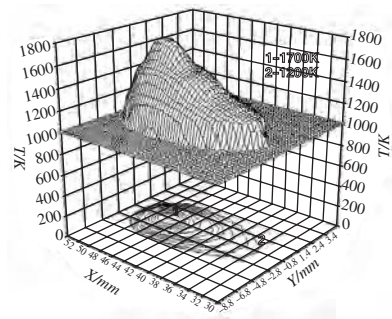

d) Complete temperature field

14.6 Temperature distribution of three regions and the complete field

of the work piece are ideal. Anyhow, an analytical function has been obtained when the heat-source distribution is assumed to obey a Gaussian model, which approximates to a real arc. Zhang proposed a heat source following a double elliptical Gaussian model that is closer to a real heat source than the simple Gaussian model. The analysis was performed using a finite work-piece thickness. The temperature distribution was obtained by numerical simulation and checked using the data obtained by actual measurements.[296] It was proved that the proposed heat-source model was closer to the actual conditions than the simple Gaussian model.

14.3.1 Bi-ellipse Gaussian model

(i) *The moving-line heat source and Gaussian-distributed heat source.* In the welding of thin plates, the heat source is close to a line heat source. Assume that the effective power is q, the plate being welded is infinitely large, the heat source moves from the point O_0 with constant speed and after t sec it reaches O, as shown in Fig. 14.7. The temperature distribution is[353]

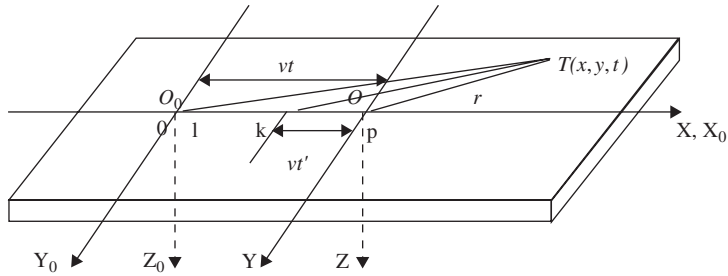

14.7 The co-ordinate system for calculation

$$T(x, y, t) = \frac{q}{4\pi\lambda h}\int_0^t \frac{dt'}{t'+\tau}\exp\left[-\frac{(x+vt')^2+x^2}{4a(t'+\tau)} - b(t'+\tau)\right] \qquad [14.6]$$

where $r^2 = x^2 + y^2$, $x = x_0 - vt$, $y = y_0$, h is the plate thickness, b is the heat-dissipation coefficient of the plate, v is the welding speed, q is the effective power of the welding power source, λ is the heat-transmission coefficient, a is the heat-diffusion coefficient, τ is the cooling time, and t is the total welding time.

The period $0 \sim t$ is divided into P subfields, the centre co-ordinate of the subfields is t_i, and its duration is $\Delta t = t/P$. The Gaussian integration is applied to each subfield. The numerical integration formula can be written as follows:[353]

$$T(x, y, t) = \sum_{i=1}^{P}\sum_{j=1}^{N}\frac{q}{4\pi\lambda h}\frac{H_j}{\sum N_i t_i' + \tau}\frac{\Delta t}{2}\exp\left[-\frac{(x+v\sum N_i t_i')^2+x^2}{4a(\sum N_i t_i' + \tau)} - b(\sum N_i t_i' + \tau)\right] \qquad [14.7]$$

$$\text{where } \sum N_i t_i' + \tau = \frac{-(1-\xi_j)\xi_j}{2}\left(t_i' - \frac{\Delta t}{2}\right) + (1-\xi_j^2)t_i' + \frac{(1+\xi_j)\xi_j}{2}\left(t_i' + \frac{\Delta t}{2}\right) \qquad [14.8]$$

where $j = 1, 2, 3$, $N = 4$, ζ_j is the coordinate of each Gaussian point, and H_j is the integration coefficient.

For a half-infinite thick plate and Gaussian heat source, the temperature-field distribution can be written as[356]

$$T(x, y, z, t) - T(x, y, z, 0) = \frac{q}{\rho c\pi}\int_0^t \frac{1}{[4\pi a(t-t')]^{1/2}[2a(t-t')+w^2]} \exp\left[-\frac{z^2}{4a(t-t')} - \frac{(x-vt')^2+y^2}{4a(t-t')+2w^2}\right]dt' \qquad [14.9]$$

where q is the effective power of the heat source, ρ is the material density, c is the specific heat capacity, w is the Gaussian distribution parameter, v is the welding speed, a is the thermal-diffusion coefficient, and t is the total welding time. Similarly, the duration 0~t is divided into P subfields, and a Gaussian integration is applied to each subfield. The numerical integration formula can be written as follows:

$$T(x,y,z,t)-T(x,y,z,0)=\sum_{l=-\infty}^{\infty}\sum_{i=1}^{P}\sum_{j=1}^{N}\frac{q}{\rho c\pi}\frac{1}{[4\pi a(t-\sum N_i t_i)]^{1/2}[2a(t-\sum N_i t_i)+w^2]}$$
$$\exp\left[-\frac{z^2}{4a(t-\sum N_i t_i)}-\frac{(x-v\sum N_i t_i)^2+y^2}{4a(t-\sum N_i t_i)+2w^2}\right]\frac{H_j}{2}\Delta t \qquad [14.10]$$

(ii) *The bi-elliptical heat source distribution*. The model of the heat source is shown in Fig. 14.8. The power density of the heat source is

$$Q(x',y',0,t')=\frac{f_f q}{2\pi w_{x1}w_y}\exp\left[-\frac{x'^2}{2w_{x1}^2}-\frac{y'^2}{2w_y^2}\right] \quad x'>0,$$
$$\frac{f_r q}{2\pi w_{x2}w_y}\exp\left[-\frac{x'^2}{2w_{x2}^2}-\frac{y'^2}{2w_y^2}\right] \quad x'<0 \qquad [14.11]$$

where q is the effective power of the heat source, f_f and f_r are the coefficients of the power distribution in the front and rear parts of the molten pool, $f_f + f_r = 2$, v is the welding speed, w_{x1}, w_{x2}, and w_y are the distributive coefficients of the bi-elliptical heat source, and $x'y'z'$ is the co-ordinate system moving with the heat source.

(iii) *The temperature distribution in a half-infinite thick body*. Substituting the heat-source formula into the heat-flow formula, the analytical expression for the temperature distribution can be written as

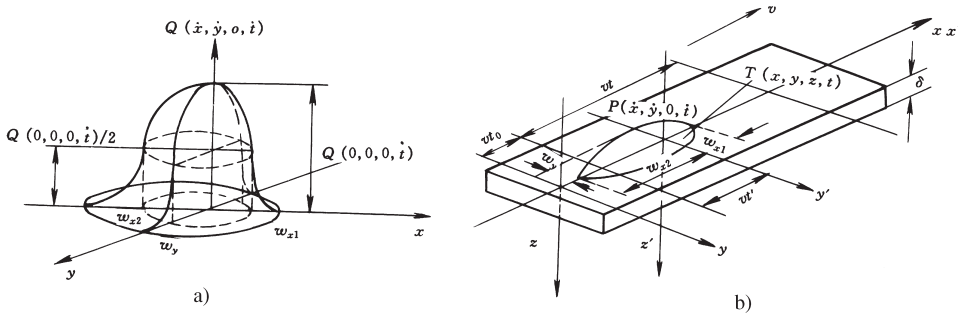

14.8 Bi-elliptical heat source distribution

$$dT(x,y,z,t) = \frac{2Q(x',y',0,t')dx'dy'dt'}{\rho c[4\pi a(t-t'-\tau)]^{3/2}}\exp\left\{-\frac{[x-x'-v(t'+t_0)]^2+(y-y')^2+z^2}{4a(t-t'-\tau)}\right\} \quad [14.12]$$

where ρ is the material density, c is the specific heat capacity, a is the heat-diffusion coefficient, vt_0 is the initial position of the heat source ($vt_0 = 0$), and τ is the cooling time ($\tau = 0$).

After integrating the heat source, the temperature distribution formula can be derived as follows:

$$\begin{aligned} dT(x,y,z,t)|_t &= dt'\int\int \frac{2Q(x',y',0,t')}{\rho c[4\pi a(t-t')]^{3/2}}\exp\left[-\frac{[x-x'-vt']^2+(y-y')^2+z^2}{4a(t-t')}\right]dx'dy' \\ &= \frac{dt'}{\rho c[4\pi a(t-t')]^{3/2}}\frac{q}{\pi w_y}\exp\left[-\frac{x^2+y^2+z^2}{4a(t-t')}\right]\left[\frac{f_f}{w_{x_1}}\Delta_1+\frac{f_r}{w_{x_2}}\Delta_2\right]\Delta_3 \end{aligned} \quad [14.13]$$

when Δ_1, Δ_2, and Δ_3 are as follows:

$$\Delta_1 = \left\{\frac{\pi^{1/2}}{2}\left[\frac{2a(t-t')+w_{x_1}^2}{4a(t-t')w_{x_1}^2}\right]^{-\frac{1}{2}} + \int_0^{\frac{w_{x_1}^2(x-vt')}{2a(t-t')+w_{x_1}^2}}\exp\left\{-\frac{2a(t-t')+w_{x_1}^2}{4a(t-t')w_{x_1}^2}x''^2\right\}dx''\right\}$$
$$\exp\left\{\frac{1}{4a(t-t')}\left[\frac{w_{x_1}^2(x-vt')^2}{2a(t-t')+w_{x_1}^2}+vt'(2x-vt')\right]\right\} \quad [14.13a]$$

$$\Delta_2 = \left\{\frac{\pi^{1/2}}{2}\left[\frac{2a(t-t')+w_{x_2}^2}{4a(t-t')w_{x_2}^2}\right]^{-\frac{1}{2}} - \int_0^{\frac{w_{x_2}^2(x-vt')}{2a(t-t')+w_{x_2}^2}}\exp\left\{-\frac{2a(t-t')+w_{x_2}^2}{4a(t-t')w_{x_2}^2}x''^2\right\}dx''\right\}$$
$$\exp\left\{\frac{1}{4a(t-t')}\left[\frac{w_{x_2}^2(x-vt')^2}{2a(t-t')+w_{x_2}^2}+vt'(2x-vt')\right]\right\} \quad [14.13b]$$

$$\Delta_3 = \pi^{1/2}\left[\frac{2a(t-t')+w_y^2}{4a(t-t')w_y^2}\right]^{-\frac{1}{2}}\exp\left\{\frac{w_y^2y^2}{4a(t-t')[2a(t-t')+w_y^2]}\right\} \quad [14.13c]$$

Integrating it over time, the temperature distribution can be found as:

$$T(x,y,z,t)-T(x,y,z,0)=\int_0^t \frac{1}{\rho c[4\pi a(t-t')]^{3/2}}\frac{q}{\pi w_y}\exp\left[-\frac{x^2+y^2+z^2}{4a(t-t')}\right]\cdot\left(\frac{f_f}{w_{x1}}\Delta_1+\frac{f_r}{w_{x2}}\Delta_2\right)\Delta_3 dt' \quad [14.14]$$

(iv) *The temperature-field distribution of a finite-thickness plate*. For a plate thickness δ, the temperature distribution can be obtained from the formula above by the mirror-images method[358] as follows:

$$T(x,y,z,t)-T(x,y,z,0)=\sum_{\ell=-\infty}^{\infty}\int_0^t \frac{1}{\rho c[4\pi a(t-t')]^{3/2}}\frac{q}{\pi w_y}\exp\left[-\frac{x^2+y^2+(z-2l\delta)^2}{4a(t-t')}\right]\cdot\left(\frac{f_f}{w_{x1}}\Delta_1+\frac{f_r}{w_{x2}}\Delta_2\right)\Delta_3 dt' \quad [14.15]$$

Dividing the time duration 0 ~ t into p subfields, the numerical formula for calculation of the temperature distribution by Gaussian integration is

$$T(x,y,z,t)-T(x,y,z,0)=\sum_{\ell=-\infty}^{\infty}\sum_{i=1}^{P}\sum_{j=1}^{N}\frac{1}{\rho c[4\pi a(t-\sum N_i t_i)]^{3/2}}\frac{q}{\pi w_y}\exp\left[-\frac{x^2+y^2+(z-2\ell\delta)^2}{4a(t-\sum N_i t_i)}\right]\cdot\left(\frac{f_f}{w_{x1}}\Delta_1+\frac{f_r}{w_{x2}}\Delta_2\right)\Delta_3\frac{\Delta t}{2}H_j \quad [14.16]$$

where Δ_1, Δ_2, and Δ_3 are as follows:

$$\Delta_1=\left\{\frac{\pi^{1/2}}{2}\left[\frac{2a(t-\sum N_i t_i)+w_{x1}^2}{4a(t-\sum N_i t_i)w_{x1}^2}\right]^{-\frac{1}{2}}+\frac{w_{x1}^2(x-v\sum N_i t_i)}{M[2a(t-\sum N_i t_i)+w_{x1}^2]}\sum_{m=0}^{M}\exp\left\{-\frac{2a(t-\sum N_i t_i)+w_{x1}^2}{4a(t-\sum N_i t_i)w_{x1}^2}\left\{\frac{mw_{x1}^2(x-v\sum N_i t_i)}{M[2a(t-\sum N_i t_i)+w_{x1}^2]}\right\}^2\right\}\right\}\exp\left\{\frac{1}{4a(t-\sum N_i t_i)}\left[\frac{w_{x1}^2(x-v\sum N_i t_i)^2}{2a(t-\sum N_i t_i)+w_{x1}^2}+v\sum N_i t_i(2x-v\sum N_i t_i)\right]\right\} \quad [14.16a]$$

$$\Delta_2 = \left\{ \frac{\pi^{1/2}}{2} \left[\frac{2a(t-\sum N_i t_i)+w_{x_2}^2}{4a(t-\sum N_i t_i)w_{x_2}^2} \right]^{-\frac{1}{2}} - \frac{w_{x_2}^2 (x - v\sum N_i t_i)}{M[2a(t-\sum N_i t_i)+w_{x_2}^2]} \right.$$
$$\left. \sum_{m=0}^{M} \exp\left\{ -\frac{2a(t-\sum N_i t_i)+w_{x_2}^2}{4a(t-\sum N_i t_i)w_{x_2}^2} \left\{ \frac{m w_{x_2}^2 (x - v\sum N_i t_i)}{M[2a(t-\sum N_i t_i)+w_{x_2}^2]} \right\}^2 \right\} \right\}$$
$$\exp\left\{ \frac{1}{4a(t-\sum N_i t_i)} \left[\frac{w_{x_2}^2 (x - v\sum N_i t_i)^2}{2a(t-\sum N_i t_i)+w_{x_2}^2} + v\sum N_i t_i (2x - v\sum N_i t_i) \right] \right\} \quad [14.16b]$$

$$\Delta_3 = \pi^{1/2} \left[\frac{2a(t-\sum N_i t_i)+w_y^2}{4a(t-\sum N_i t_i)w_y^2} \right]^{-\frac{1}{2}} \exp\left\{ \frac{w_y^2 y^2}{4a(t-\sum N_i t_i)[2a(t-\sum N_i t_i)+w_y^2]} \right\} \quad [14.16c]$$

The numerical-simulation formulae for calculating the temperature-field distribution under a bi-elliptical heat source have been defined. If the thickness is considered in Eq. [14.10], then Equations [14.7], [14.10], and [14.16] can be used to calculate the temperature field for a plate with finite thickness but an infinite work-piece size. In the following section, practical measurements that were carried out are described and the data that was generated are used to check the theoretical results.

14.3.2 Comparison of calculated results with measured data

(i) *Numerical simulation and real time measurement*. The conditions for numerical simulation and measurement are shown in Table 14.1.

Table 14.1 Condition for numerical simulation and experiment

Welding conditions	Parameters	Conditions for numerical simulation	Parameters
Workpiece	Mild steel ($60 \times 150 \times 2\,mm^3$)	Material density	$7.68\,g/cm^3$
Shielding gas	Argon ($0.5\,m^3/h$)	Heat diffusion	$0.08\,cm^2/s$
Voltage	12 V	Heat dissipation coefficient	0
Current	60 A	Specific heat capacity	0.679 J/(g.°C)
Welding speed	5 mm/s	Heat-conduction coefficient	0.377 J/(cm.s.°C)
Electrode	Tungsten (Φ2.5 mm)	Heating efficiency	0.75

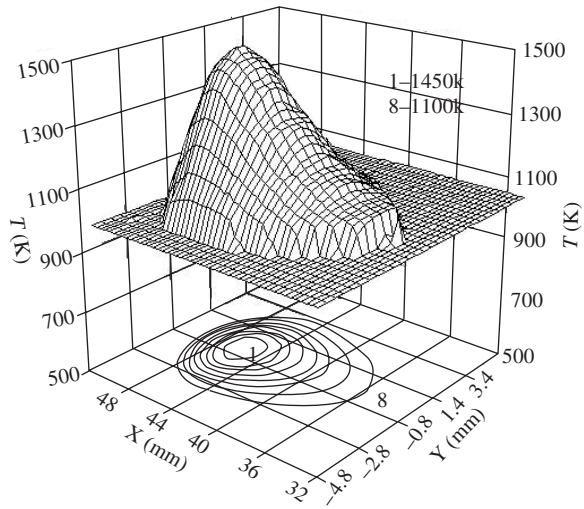

14.9 Experimental temperature distribution

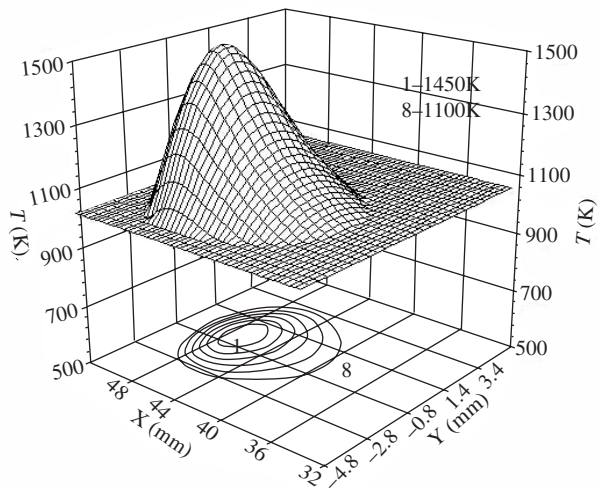

14.10 Numerical simulation results of a bi-elliptical Gaussian heat source

The experimental results are shown in Fig. 14.9 in which 8 isothermal planes (XOY) are illustrated. The interval was 50 K, the inner isotherm was at 1450 K and the outer isotherm was at 1100 K.

Numerical simulation was carried out for a bi-elliptical Gaussian distribution, a Gaussian distribution and a line heat source using Equations [14.16], [14.9], and [14.6]. The results are shown in Figures 14.10, 4.11, and

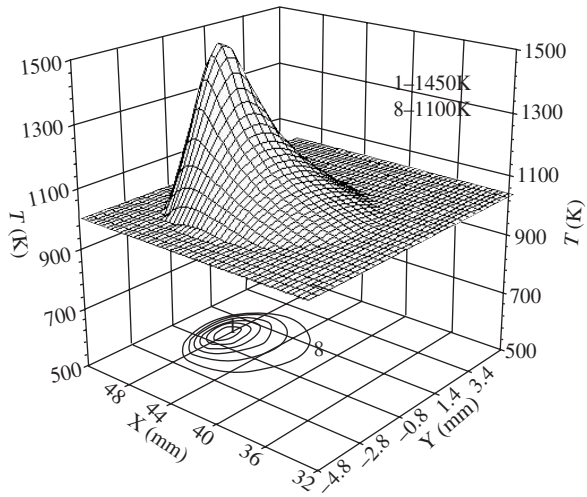

14.11 Numerical simulation results of a Gaussian heat source

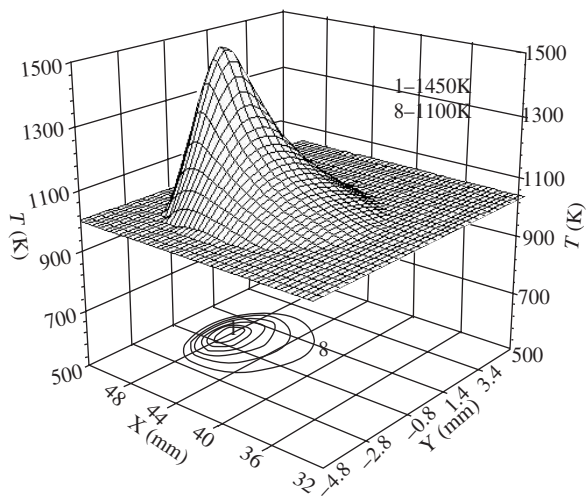

14.12 Numerical simulation results for a moving-line heat source

14.12, respectively. The parameters for the bi-elliptical Gaussian heat source were $w_{x1} = 0.10$ cm, $w_{x2} = 0.30$ cm, $w_y = 0.14$ cm, $f_f = 0.6$, and $f_r = 1.4$. The parameter for the Gaussian heat source was $w = 0.14$ cm. Eight isothermal planes designated XOY are shown in all of the figures. The intervals were 50 K, the inner isotherm was at 1450 K, and the outer isotherm was at 1100 K.

(ii) *Comparison of results*. Comparing Figures 14.10, 14.11, and 14.12 with Fig. 14.9 shows that the bi-elliptical Gaussian model was the closest

to the measured data. The difference between the results using the Gaussian model and the measured data was large. The difference between results for the line heat source and the experimental data was larger than that for the Gaussian model. In order to compare them in more detail, the isotherms are given in Table 14.2. The temperature distribution curves in the longitudinal and transverse directions across the weld pool are plotted in Fig. 14.13.

The same conclusion can be drawn if the curves in Fig. 14.13 are compared. The Gaussian heat source showed a large difference from the actual temperature distribution; the line heat source showed an even larger difference than the former. Therefore, simulating the temperature distribution using a line heat source is not useful.

Comparing the numerical-simulation results with the measured data is valuable. The measured results can be used to correct or modify the

Table 14.2 Comparison of isotherms

Temperature (K)	Width (mm)		Error (%)	Length (mm)		Error (%)
	Actual	Bi-elliptical		Actual	Bi-elliptical	
1100	6.11	6.04	–1.15	13.48	12.35	–8.38
1150	5.54	5.56	0.36	11.52	10.61	–7.90
1200	4.80	4.92	2.50	9.37	9.26	–1.17
1250	4.32	4.42	2.31	8.27	8.00	–3.26
1300	3.75	3.89	3.73	6.74	6.90	2.37
1350	3.18	3.22	1.26	5.39	5.60	3.89
1400	2.69	2.66	–1.12	4.31	4.39	1.86
1450	1.87	1.80	–3.74	2.94	3.10	5.44

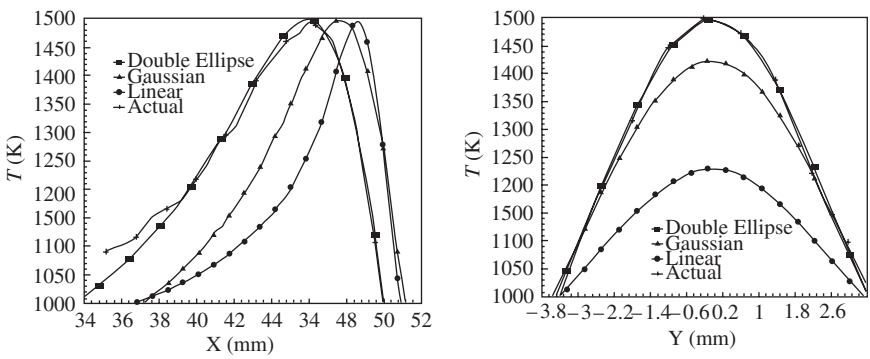

a) Longitudinal ($y = 0$ mm) b) Transverse ($x = 46$ mm)

14.13 Longitudinal and transverse temperature distributions for three different heat sources

numerical-simulation model. Also, the numerical-simulation model can be used to analyse the temperature-distribution phenomena for investigation of the metallurgical and physical processes in welding. For example, the numerical simulation can be used to find the three-dimensional temperature distribution or the temperature distribution at low temperatures, which is not possible using experimental measurements.

14.4 Theoretical results and measured data for different welding parameters

The factors that affect the welding temperature are the heat source, welding parameters, thermal properties of the materials, type of work piece, and heating time. For TIG welding, the current and welding speed have large effects on the temperature distribution. The temperature distribution during TIG welding with different welding currents and welding speeds has been measured. Numerical simulation using a bi-elliptical heat source also was conducted.

14.4.1 Influence of welding current

Two welding currents, 98 A and 120 A (the corresponding arc voltages were 13 V and 14 V) were chosen, with the welding speed held constant at 6.38 mm/s. The experimental and simulation conditions are the same as shown in Table 14.1. The experimental and numerical simulation results are shown in Figures 14.14 and 14.15. Figure 14.14 shows the results for a welding current of 98 A and voltage of 13 V. Figure 14.15 shows the results for a welding current of 120 A and voltage of 14 V. Isotherms are shown on the XOY plane. Each step is 50 K. Comparing these two figures shows that the widths and lengths of the isotherms increase with the increase of

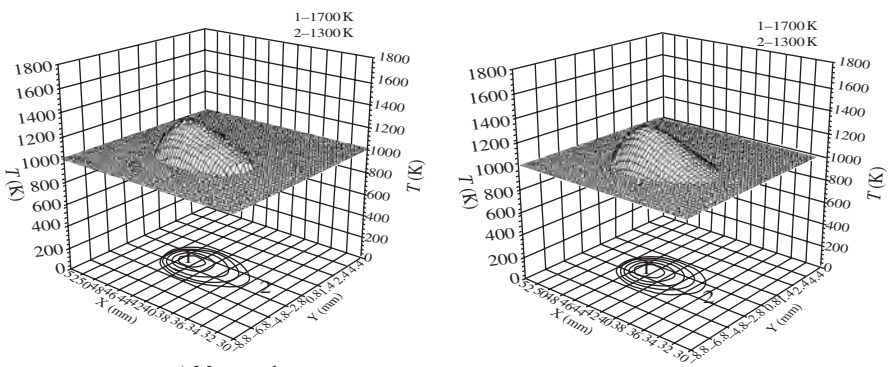

a) Measured

b) By numerical simulation

14.14 Temperature field for a welding current of 98 A and a welding voltage of 13 V in TIG welding

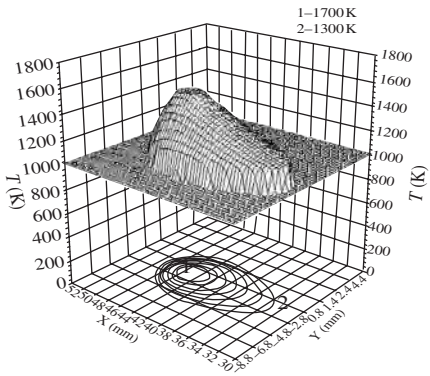

a) Measured

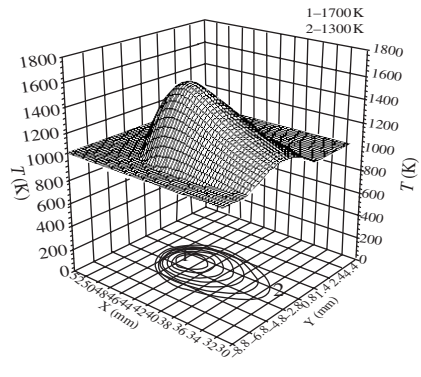

b) By numerical simulation

14.15 Temperature field for a welding current of 120 A and a welding voltage of 14 V in TIG welding

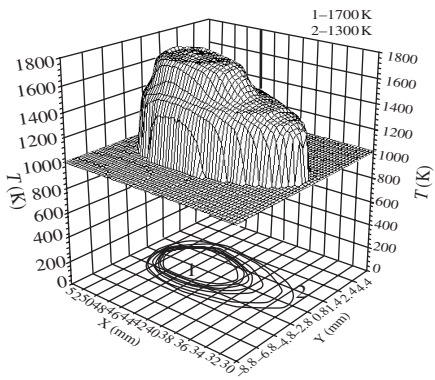

a) Measured

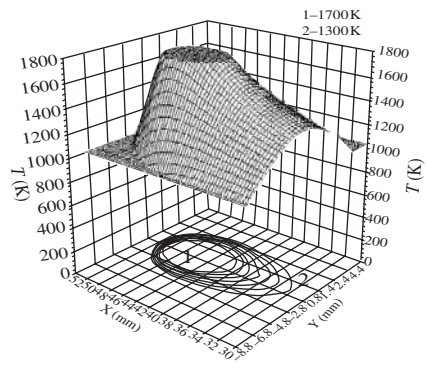

b) By numerical simulation

14.16 Temperature field for a welding speed of 6.7 mm/s

welding current. These results also show that the measured data and numerical-simulation results nearly coincide.

14.4.2 Influence of welding speed

Two welding speeds, 6.7 mm/s and 8.0 mm/s, at a constant welding current and voltage, 168 A and 15 V, were chosen for study. The conditions for the measurements and numerical simulation were the same, as shown in Table 14.1. The results are illustrated in Figures 14.16 and 14.17. Figure 14.16 shows the results for a welding speed of 6.7 mm/s and Fig. 14.17 shows the results for a welding speed of 8.0 mm/s. Isotherms are shown on the XOY plane. The isotherm intervals are 50 K. These figures show that the isotherms becomes narrower and longer as the speed is increased. They also show that the experimental and numerical-simulation results are similar.

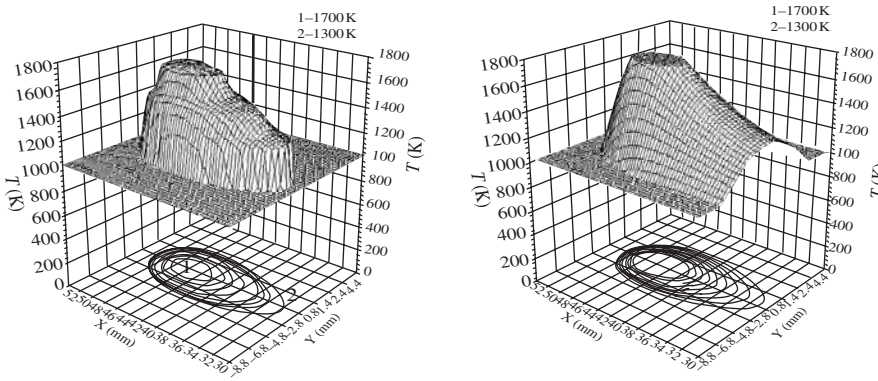

a) Measured

b) By numerical simulation

14.17 Temperature field for a welding speed of 8.0 mm/s

Table 14.3 Isotherm parameters

T/K	Width (mm)	Length (mm)	T/K	Width (mm)	Length (mm)
1050	6.76	15.52	1300	3.75	6.74
1100	6.11	13.48	1350	3.18	5.39
1150	5.54	11.52	1400	2.69	4.31
1200	4.80	9.37	1450	1.87	2.94
1250	4.32	8.27			

14.5 Extraction of the thermal-cycle parameters

14.5.1 Thermal-cycle parameters on the root side of the bead

A lot of information may be obtained from the temperature field on the root side of the bead; for example, isotherms and the temperature distribution in longitudinal and transverse directions, the thermal cycle at any arbitrary point in the temperature field, the width of the pool, and the characteristic parameters of the thermal cycle. In the following paragraphs, isotherm parameters, longitudinal and transverse temperature distributions, and thermal cycle parameters are extracted from the measured temperature field shown in Fig. 14.9.

(i) *Isotherm parameters*. The isotherm parameters are the width and length of the isotherm that reflect the energy input of welding. The isotherm near the melting point represents the shape of the molten pool. Table 14.3 lists the extracted isotherm parameters from Fig. 14.9.

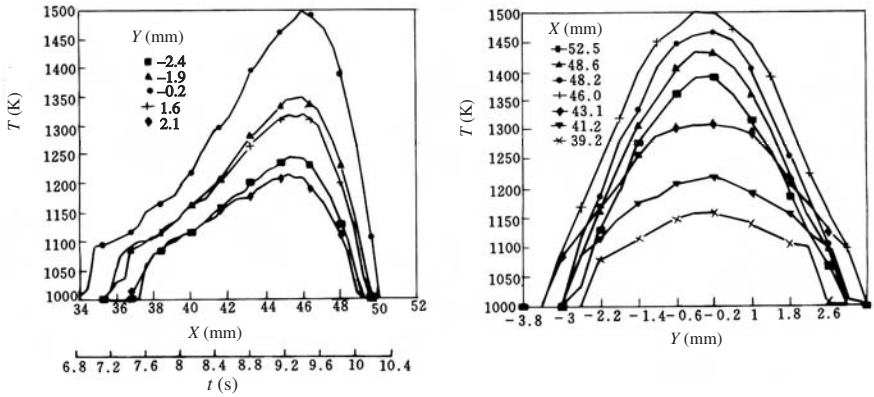

a) Longitudinal b) Transverse

14.18 Temperature distributions of a weld in longitudinal and transverse directions

(ii) *Longitudinal and transverse temperature distributions*. The longitudinal and transverse temperature distributions at the weld pool can be identified easily from Fig. 14.9 and are illustrated in Fig. 14.18. In part a) of the figure, the X abscissa designates the welding direction. The upper abscissa values represent the location on the work piece and the lower figures represent the travel time of the moving torch. The five curves are the temperature distributions of the point, the Y co-ordinates of which are –2.4, –1.9, –0.2, 1.6 and 2.1 mm. These show that the temperature gradient at the front is much larger than at the rear. In part b) of the figure, Y represents the transverse position of the point. The seven curves are the temperature distributions at different cross-lines, the X co-ordinate of which are 39.2, 41.2, 43.1, 46.0, 48.2, 48.6, and 52.5 mm. All of these distributions are symmetrical.

(iii) *Thermal cycle parameters*. When the welding parameters are kept unchanged during the welding process, the temperature field is a quasi-static field.

The temperature distribution along an arbitrary longitudinal line of the weld can be regarded as the thermal cycle of any point on the longitudinal line. Therefore, the five curves in Fig. 14.18a are the thermal cycles of various points on these five lines. The thermal-cycle parameters can thus be found easily from these curves: see Table 14.4. The heating rates and cooling rates are the values when the temperature is at 1100 K. The high-temperature hold duration is the time above 1100 K. These parameters are valuable for the study of the microstructure, stress and strain of the weld.

Table 14.4 Thermal cycle parameters

Y (mm)	–2.4	–1.9	–0.2	1.6	2.1
Heating rate ω_H (K·s^{-1})	427.35	732.60	1121.80	512.82	284.90
Maximum temperature T_m (K)	1243.75	1350.00	1500.00	1312.50	1218.75
High-temperature hold duration t_H (s)	0.74	2.34	2.72	2.34	0.74
Cooling rate ω_c (K·s^{-1})	111.48	128.20	106.80	128.20	111.48

14.5.2 Extrapolation of the two-dimensional temperature field

Taking advantage of the numerical simulation method, the temperature distribution in the low-temperature range (lower than the ICCD can measure by the colorimetric method) can be obtained by extrapolation. Figure 14.19a shows the results obtained by extrapolation using a measured temperature field (see Fig. 14.9). The extrapolation extends the temperature to 700 K. Figures 14.19b and c show the longitudinal and transverse temperature distributions obtained by measurement and extrapolation. Figure 14.19b shows that the cooling time $t_{8/5}$ is 3.6 s, which is one of the most important parameters that determines the microstructure of the heat-affected zone.

14.6 Three-dimensional welding temperature field

14.6.1 Results of extrapolation

The analytical model for numerical simulation was established using measurements of the temperature field on the root side of the weld bead. The three-dimensional temperature field can be derived by numerical simulation using this model but this temperature field cannot be experimentally measured. Figures 14.20 and 14.21 show the results obtained by the analytical model. They are based on the experimental results shown in Fig. 14.9. The welding and simulation parameters are listed in Table 14.1. The arc position was at $X = 50$ mm and $Y = 0$ mm. Figure 14.20a shows the temperature distribution on the transverse plane at $X = 46$ mm. Figure 14.20b shows 6 isotherms from 1500~1750 K at intervals of 50 K, and 5 isotherms from 700~1500 K at intervals of 200 K. Figure 14.21a shows the temperature distribution on the transverse plane at $Y = 0$ mm. Figure 14.21b shows 6 isotherms from 1500~1750 K at intervals of 50 K and 5 isotherms from 700~1500 K at intervals of 200 K.

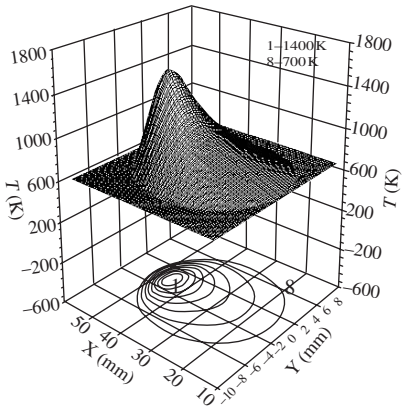

a) Entire field

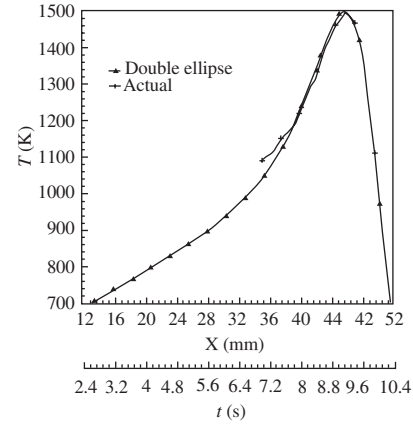

b) Longitudinal ($Y = 0$ mm)

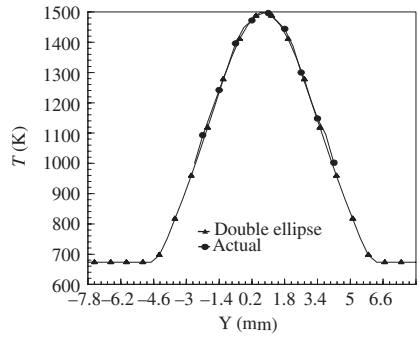

c) Transverse ($X = 46$ mm)

14.19 Temperature distributions obtained by extrapolation

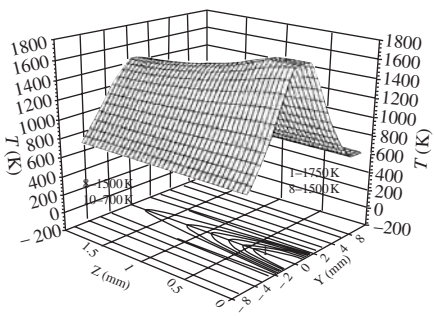

a) Three dimensional distribution

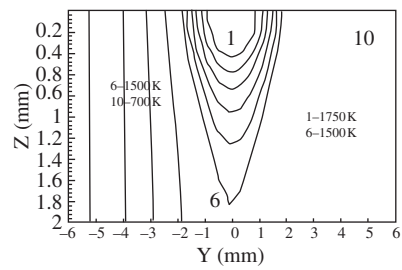

b) Isotherms

14.20 Temperature distribution on a cross-section (X = 16 mm)

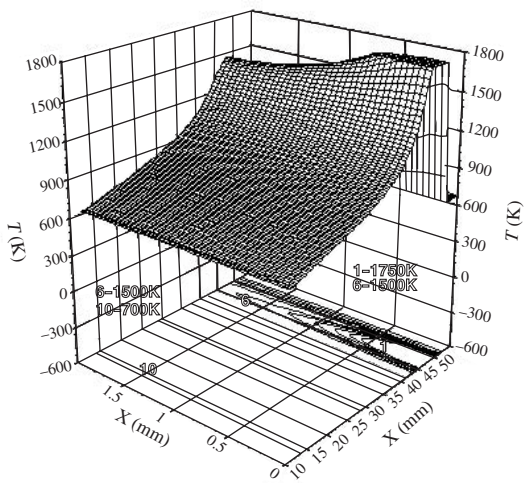

a) Three-dimensional distribution

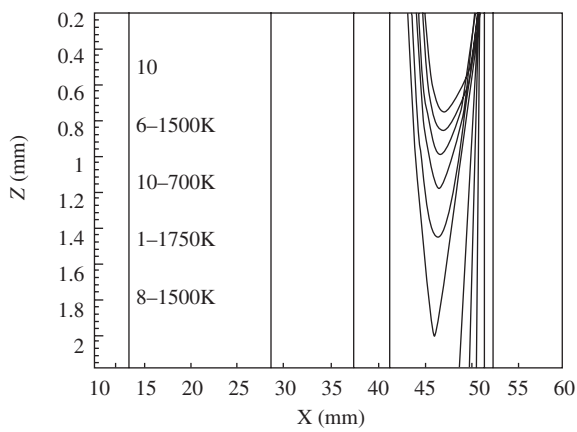

b) Isotherms

14.21 Temperature distribution on a longitudinal plane ($Y = 0$ mm)

14.6.2 Verification

It is difficult to compare the results obtained by the analytical method and the experimental method for the three-dimensional temperature field because there is no way to measure the three-dimensional temperature field. However, the results can be verified indirectly by comparing the two-dimensional temperature field obtained by numerical simulation. Figure 14.22 shows the isotherm width at the front and back of the weld obtained by both methods. The welding parameters with the welding speed held

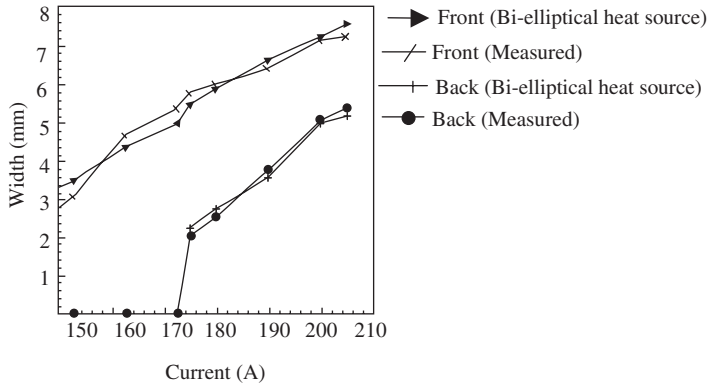

14.22 Calculated and measured width of the weld pool for different welding currents

Table 14.5 Welding parameters

No.	1	2	3	4	5	6	7	8
Welding current (A)	152.5	162.5	172.5	175.0	180	190	200	205
Welding voltage (V)	14.0	15.2	15.2	16.0	16.0	16.0	16.8	16.8
Total power (W)	2135	2470	2622	2800	2880	3040	3360	3444

constant are listed in Table 14.5. The conditions for the numerical simulation are: plate thickness of 2 mm, bi-elliptical heat source of $w_{x1} = 0.15$ cm, $w_{x2} = 0.35$ cm, $w_y = 0.25$ cm, and the conditions shown in Table 14.1.

The isotherm width also was measured and calculated for different welding speeds at constant welding current and power (165 A, 15.4 V, total power 2514 W). The experimental and simulation conditions were the same as those for Fig. 14.22. The results for 8 different speeds, namely 3.45, 4.08, 5.13, 5.17, 6.67, 7.41, 8.00, and 8.7 mm/s are shown in Fig. 14.23. The figure shows that the difference between the numerical values and the measured data at the front of the weld is greater than that at the back. The error is within 8%. Therefore, the numerical-simulation method can be used to define the width of the molten pool on the front side.

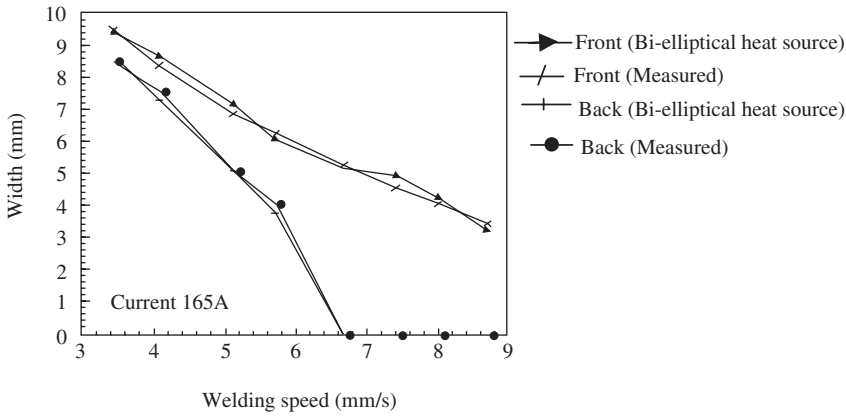

14.23 Calculated and measured width of the weld pool for different welding speeds

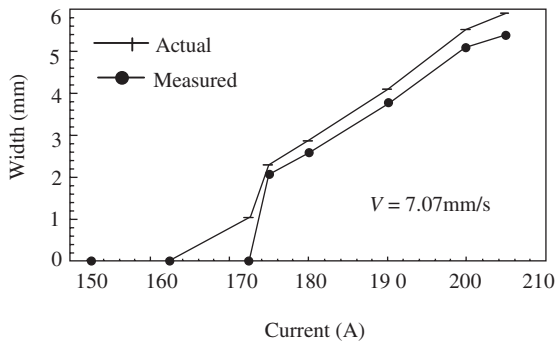

14.24 Isotherm width and molten-pool width

14.7 Closed-loop control of weld penetration[339,348,351]

14.7.1 Control system

A penetration-control system was introduced in Section 5.5 of Chapter 5. In this section, another penetration-control system, based on the width of the weld pool determined from the melting-temperature isotherm, is discussed. Figure 14.24 shows the width of the isotherm measured during welding using the colorimetric method, and the width of the molten pool measured after welding. They agree closely with each other, which suggests that controlling the penetration in real time using an isotherm width measured during welding is practical. Similarly, the heat affected zone also can be controlled using the isotherm width for a selected temperature.

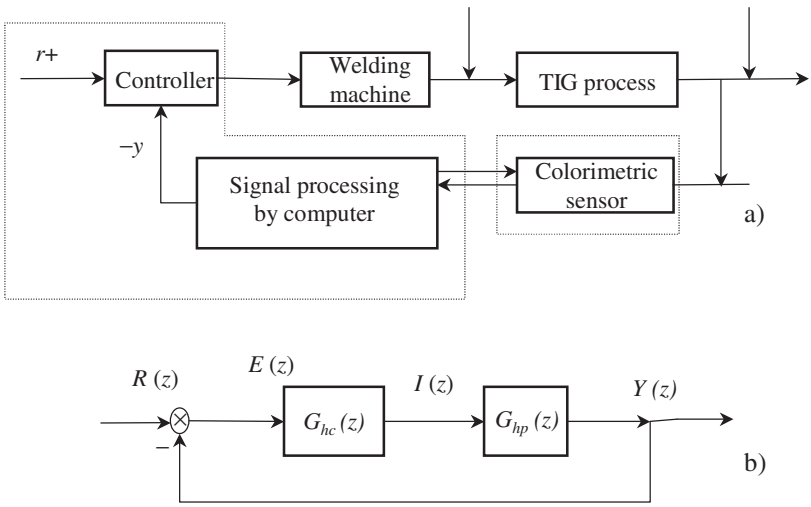

14.25 Closed-loop penetration control

(i) *Schematic diagram of the control system*. The system consists of a colorimetric temperature-measuring apparatus, a welding machine and the control loop, which are shown in Fig. 14.25. In part a) of this figure, the input signal is the isotherm's width y and the output signal is the temperature field $T(r)$. The colorimetric apparatus detects the isotherm's width. The error $e = r - y$ is used to vary the welding current I so that the isotherm's width can be maintained. Figure 14.25b is the simplified block diagram of the control system where $R(z)$, $Y(z)$, $E(z)$, and $I(z)$ are the z-transfer of r, y, e and i. $G_{hp}(z)$ is the z-transfer function of the control object and $G_{hc}(z)$ is the z-transfer function of the controller.

(ii) *Mathematical model of the control process*. Although welding is a complicated thermal process, the colorimetric temperature measuring system can acquire a variety of process information. Figure 14.26 shows the response of an isotherm's width to a step change of current. The experimental conditions were 5.0 mm/s welding speed, a 60 × 150 × 1.5 mm thick mild steel work piece, and shielding gas flowing at 0.5 m^3/hr. The welding current was increased from 71 A to 85 A at $t = 1.1$ s (in fact, the step output was performed by the computer via D/A conversion, which introduced a delay time at the power source). The isotherm width was monitored by the colorimetric measuring method. It was found that the isotherm width had a certain time delay, after which it increased gradually until it became stable.

The control system consisted of four parts, namely, the welding machine (power source and travel mechanism), heating process, colorimetric sensor and computer for data processing the images. Among these, the heating process and the signal processing are the key elements of the process.

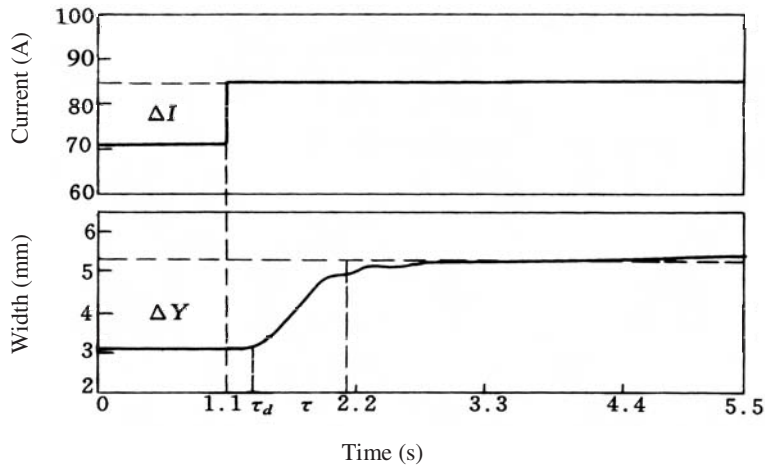

14.26 Step response of the control system

Figure 14.26 shows that the control object is an inertial element with a time delay. Its transfer function can be expressed as

$$G_P(s) = Y(s)/I(s) = k_p e^{-\tau_d S}/1+\tau s \qquad [14.17]$$

where k_P is the static gain, τ is the time constant and τ_d is the delay time.

By measuring the response curve directly, these parameters can be found approximately: $\tau_d = AB = 0.22\,\text{s}$, $\tau = BC = 0.77\,\text{s}$, $k_p = \Delta y(t)/\Delta i(t) = 0.23$, and the equivalent time delay $\tau_d = \tau_d + T/2 = 0.275\,\text{s}$, where T is the sampling period, which is 0.11 s in the present case.[354]

The z-transfer function of the process with the zero-order hold element $G_{hp}(z)$ can be written as

$$G_{hp}(z) = Z\left[\frac{1-e^{-Ts}}{s}\frac{k_p e^{-\tau_d s}}{1+\tau s}\right] = \frac{k_p(1-e^{-X/L})z^{-L}}{z-e^{-X/L}} \qquad [14.18]$$

(iii) *PID Controller and determination of its parameters*. The advantages of PID controls are their simplicity, stability and robustness. The object of control is a first-order inertial element with a time delay; the transfer function is as follows:

$$G_C(s) = \frac{I(s)}{E(s)} = k_c\left(1+\frac{1}{T_i s}+\frac{T_d s}{1+\frac{T_d}{k_d}s}\right) \qquad [14.19]$$

where k_c is a proportional constant, T_i is an integration constant, T_d is a differentiaton constant and k_d is the differential gain.

The control is performed by computer. The digital form of the formula is

$$\Delta I(n) = \Delta I_p(n) + \Delta I_i(n) + \Delta I_d(n) \qquad [14.20]$$

where $I_p(n)$, $I_i(n)$, $I_d(n)$ are

$$I_p(n) = k_p(E(n) - E(n-1)) + I_p(n-1); \quad I_i(n) = \frac{k_p T_0}{T_i} E(n-1) + I_i(n-1)$$

$$I_d(n) = \frac{T_d}{k_d T_0 + T_d}(I_d(n-1) + k_p k_d(E(n) - E(n-1)))$$

The z-transfer function of the PID can be obtained using a bilinear transformation

$$G_{hc}(z) = G_c(s)\Big|_{s=\frac{21-z^{-1}}{T_1+z^{-1}}} = \frac{g_0 + g_1 z^{-1} + g_2 z^{-2}}{(1-z^{-1})(1+fz^{-1})} \qquad [14.21]$$

where the four constants f, g_0, g_1 and g_2 can be derived as follows

$$f = \frac{k_d T - 2T_d}{k_d T + 2T_d}; \quad g_0 = k_c\left(1 + \frac{T}{2T_i} + \frac{2k_d T_d}{k_d T + 2T_d}\right)$$

$$g_1 = k_c\left(-1 + f + \frac{T}{2T_i} + \frac{T}{2T_i} f - \frac{4k_d T_d}{k_d T + 2T_d}\right);$$

$$g_2 = k_c\left(-f + \frac{T}{2T_i} + \frac{T}{2T_i} f + \frac{2k_d T_d}{k_d T + 2T_d}\right)$$

The important problem in PID control is the determination of parameters. A step-response method is used for this purpose. Substituting the parameters of the object into an emperical formula,[354] the preliminary parameters of the PID control are determined as k_c = 9.466, T_i = 0.676 s, T_d = 0.169 s and k_d is taken as 3.

In order to obtain good control characteristics, the parameters should be optimised. The controller parameters are optimised by determining the combination of its parameters so that the required dynamic properties of the system can satisfy the prescribed criteria for a specific object, control process and control rule. The optimised parameters are functions of the characteristic parameters of the controlled process. Normally, deviation integrals of the dynamic response are chosen as the index.

$$\text{ISE} = \sum_{n=0}^{N} e^2(n)t, \quad \text{IAE} = \sum_{n=0}^{N} |e(n)|t, \quad \text{ITAE} = \sum_{n=0}^{N} n|e(n)|t, \qquad [14.22]$$

The system is optimised by ensuring that the indexes above are minimum. This can be accomplished on line by the computer-controlled system shown in Fig. 14.25.

14.7.2 Simulation of the control system

In order to examine the properties of the system, choose the optimum parameters and know the adaptability of system, numerical simulation was carried out as follows:

(i) Figure 14.25 is a discrete control system; its z-transfer function can be written as

$$G(z)=\frac{Y(z)}{R(z)}=\frac{G_{hc}(z)G_{hp}(z)}{1+G_{hc}(z)G_{hp}(z)}$$
$$=\frac{z^{-L-1}(g_0'+g_1'z^{-1}+g_2'z^{-2})}{(1-b_0z^{-1})(1-z^{-1})(1+fz^{-1})+z^{-L-1}(g_0'+g_1'z^{-1}+g_2'z^{-2})} \quad [14.23]$$

where constants b_0, g_0', g_2' can be derived as

$$b_0=e^{-X/L};\quad g_0'=k_p(1-e^{-X/L})g_0;$$
$$g_1'=k_p(1-e^{-X/L})g_1;\quad g_2'=k_p(1-e^{-X/L})g_2$$

Let $L=\tau_d/T=2$ and, substituting it into Eq. [14.23], the difference equation of the input and output are

$$y(k)=a_1y(k-1)+a_2y(k-2)+a_3y(k-3)+a_4y(k-4)$$
$$+a_5y(k-5)+b_3r(k-3)+b_4r(k-4)+b_5r(k-5)$$

where $a_1=b_0+1-f$, $a_2=-(b_0-b_0f-f)$, $a_3=-(b_0f+g_0)$, $a_4=-g_1$, $a_5=-g_2$, $b_3=g_0'$, $b_4=g_1'$, $b_5=g_2'$.

For an isotherm-width step-input signal $r(k)=1$ $(k\geq 0)$, the output isotherm-width (response) signal is

$$y(k)=0\quad k<0 \quad [14.24]$$

The isotherm-width response signal can be derived from the input (isotherm width) signal and the initial conditions. Different control-process parameters and controller parameters will produce a different response, so that the controller parameters can be optimised for a certain control process. In other words, the robustness of the control system for a certain configuration and controller parameters can be determined.

(ii) *Numerical simulation of the optimisation of the controller parameters*. The optimum parameters of the controller can be determined by numerical simulation. Figures 14.27, 14.28 and 14.29 illustrate the step response of the system and the deviation-integral value.

Figure 14.27a shows six curves for $k_c=6$~11. Figure 14.27b shows that the deviation integration values of ISE and IAE change slightly with the change of k_c but ITAE varies greatly with the change of k_c. It can be found from these two figures that for the best step response, the optimum value

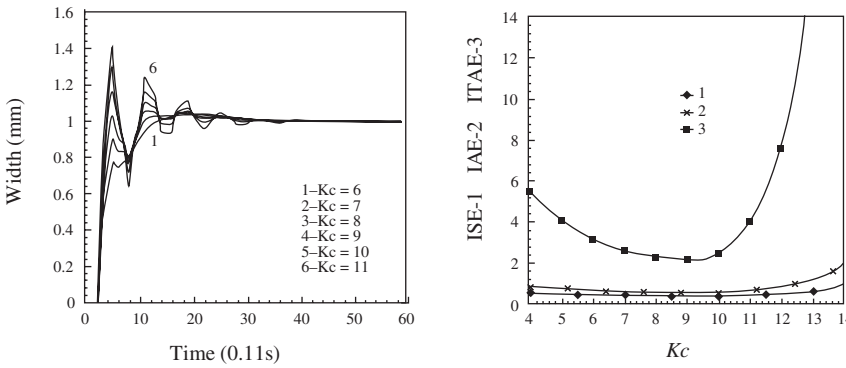

a) Step response b) Three deviation integrals

14.27 Numerical simulation for different values of k_c (t_i = 0.676 s, t_d = 0.169 s)

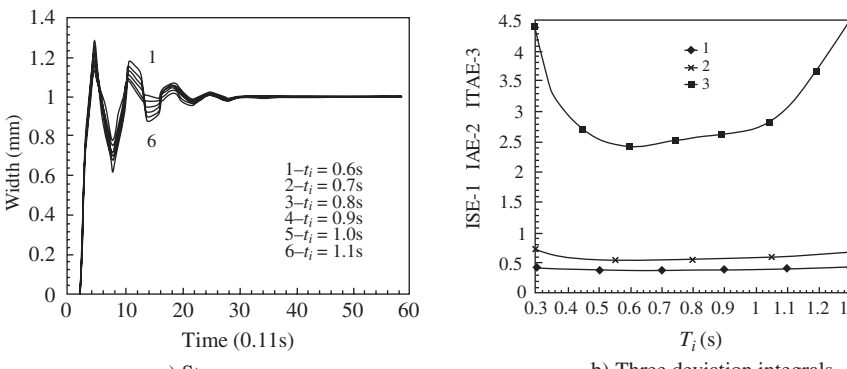

a) Step response b) Three deviation integrals

14.28 Numerical simulation for different values of t_i (k_c = 0.94, t_d = 0.169 s)

of k_c is 8–10 or, more precisely, 9.4. The six curves shown in Fig. 14.28a are for t_i = 0.6~1.1 s. It was found that there was only a slight difference in their step response. Figure 14.28b shows that all three kinds of deviation-integral values are satisfactory when t_i = 0.45~0.9 s; the optimum value was 0.6 s. Figure 14.29 shows six curves for t_d = 0.03~0.18 s. Their step responses were quite different but within the prescribed norm. From the deviation integral value shown in Fig. 14.29b, the optimum value of t_d = 0.05~0.2 s or, more precisely, 0.09 s.

(iii) *Numerical simulation of robustness*. The parameters of the control object often vary from time to time. These include, for example, variation

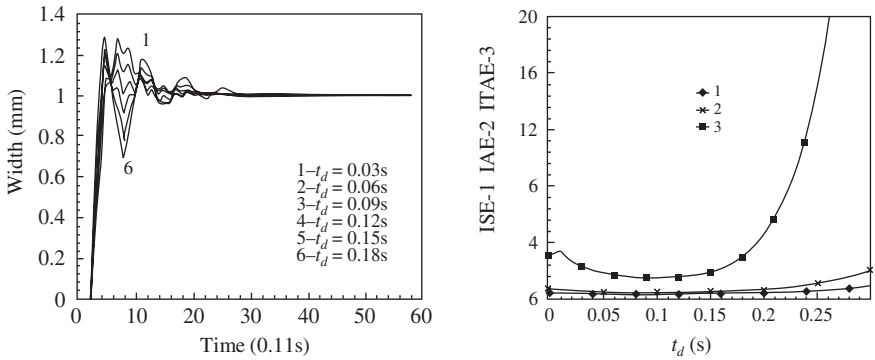

a) Step response

b) Three deviation integrals

14.29 Numerical simulation for different values of t_d (k_c = 9.4, t_i = 0.6 s)

of the welding travel speed and material thickness. The ability of the system to perform satisfactorily under varying parameters of the object is called the robustness of the system. Figure 14.30 shows the step response of the system when the controller parameters were held constant but the parameters of the control object were varied. The controller parameters were $k_c = 9.4$, $t_i = 0.6$ s, $t_d = 0.09$ s. The figures show that when k_p varied from 0.13~0.25, t_1 varied from 0.05~0.275 s and t_2 varied from 0.8~1.3 s. The step response was satisfactory. This means that the controller had good adaptability or good robustness. Experiments carried out in next section supported this conclusion when there were variations of welding parameters and plate thickness.

14.7.3 Performance of the system and a technological test

(i) *Performance test*. The performance test included tracking ability and resistance to interference.

- Command tracking ability. The tracking ability reflects the response speed of the system. Figure 14.31 shows the isotherm-width response to the input reference change. The reference value changed from 3~5 mm at t = 120 ms and from 5~3 mm at t = 220 ms. The response delay time was less than 1 s, which showed satisfactory dynamic behaviour of the system.

  Because welding is a complicated process with a lot of varying parameters such as plate thickness, welding speed, materials and so on, thickness and welding-speed variation were studied, as described in the following paragraph.
- Plate thickness. A special specimen was prepared for investigating the influence of plate thickness on penetration or isotherm width. A 0.5-mm

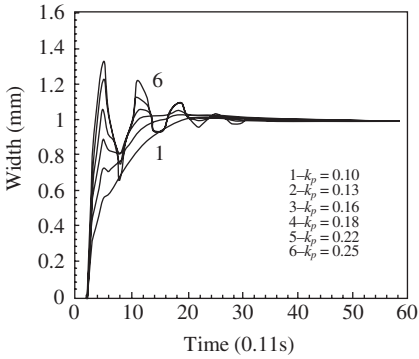

a) Different k_p ($t_1 = 0.27$s, $t_2 = 0.77$s)

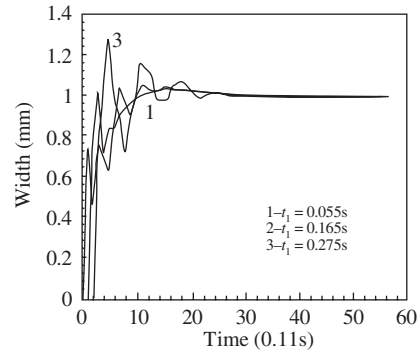

b) Different t_1 ($k_p = 0.23$s, $t_2 = 0.77$s)

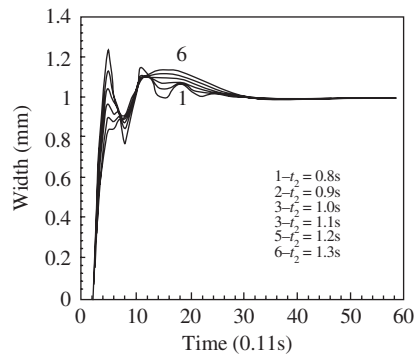

c) Different t_2 ($k_p = 0.23$s, $t_1 = 0.275$s)

14.30 Step response for different control-object parameters

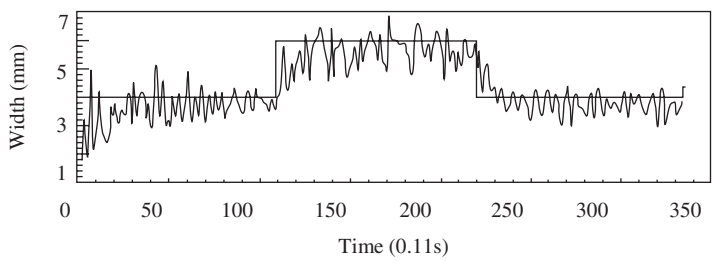

14.31 Step response of the control system

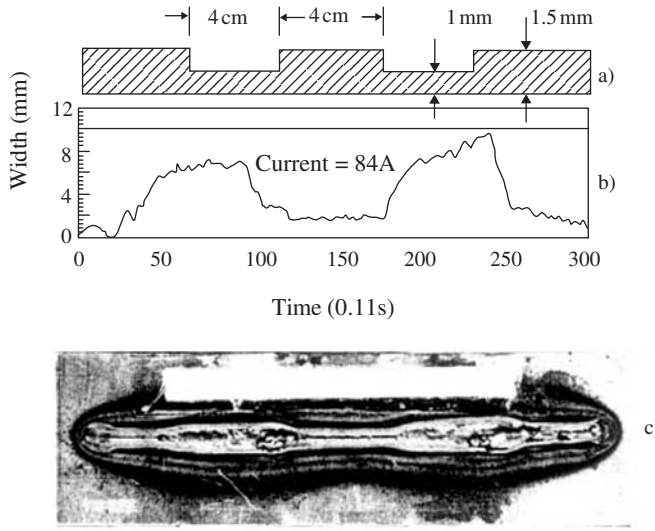

14.32 Effect of thickness variation (open-loop control)

deep by 4-cm wide groove was machined across a 1.5 mm thick specimen (see Fig. 14.32a) and a weld was made in the groove at constant current and travel speed. Figure 14.32b shows that the isotherm width varies greatly. Figure 14.32c shows the appearance of the root side of the welded beam.

In order to obtain uniform isotherm width, the welding current was controlled during welding. The results are shown in Fig. 14.33. Figure 14.33a is a longitudinal cross-section of the work piece, Figure 14.33b is the current-output variation by the control system, Fig. 14.33c is the variation of the isotherm width and Fig. 14.33d is the appearance of the root side of the bead. These results show that this control system gave satisfactory results for a plate having uneven thickness.

- Welding speed. Welding speed affects the isotherm width when the current is held constant. Figure 14.34 shows the welding process with varying welding speed but constant welding current. Figure 14.34a shows the step change of the welding-speed output by computer. Figure 14.34b shows the variation of the isotherm width (1350°C) that resulted from the speed change. Figure 14.34c is the appearance of the root side of the weld bead.
- Figure 14.35 illustrates the control effect. Figure 14.35a is the step change of welding speed set by the computer and Fig. 14.35b is the current variation due to the control system. This shows that the current rises with travel speed. Figure 14.35c is the isotherm width (1350°C)

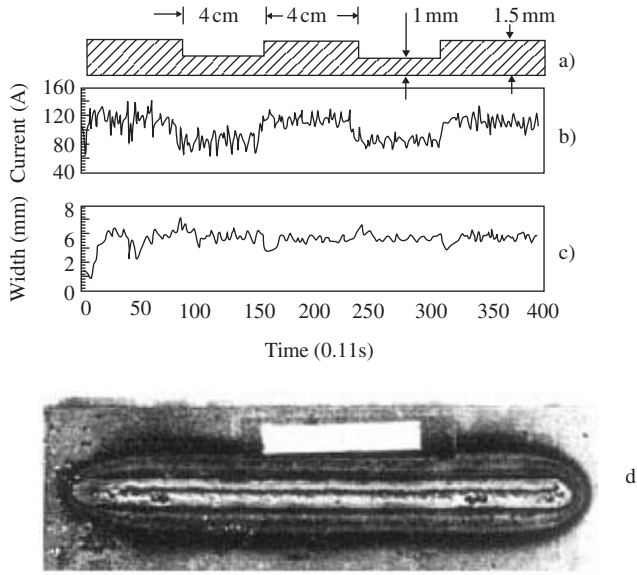

14.33 Effect of thickness variation (closed-loop control)

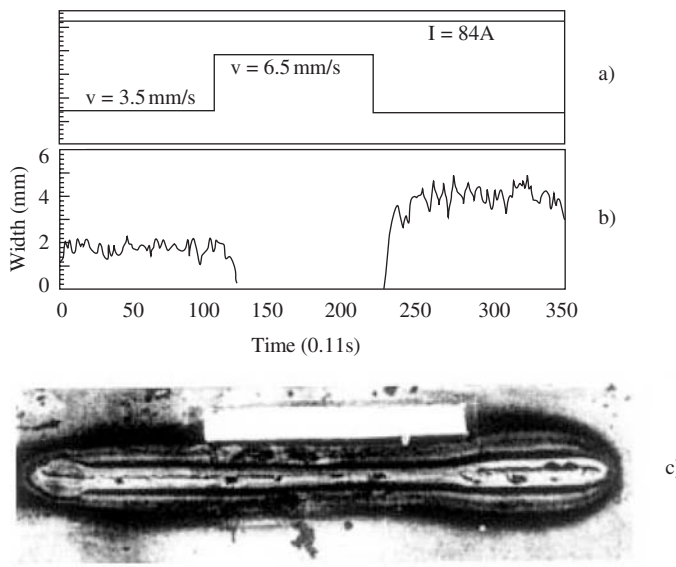

14.34 Effect of welding-speed change (open-loop control)

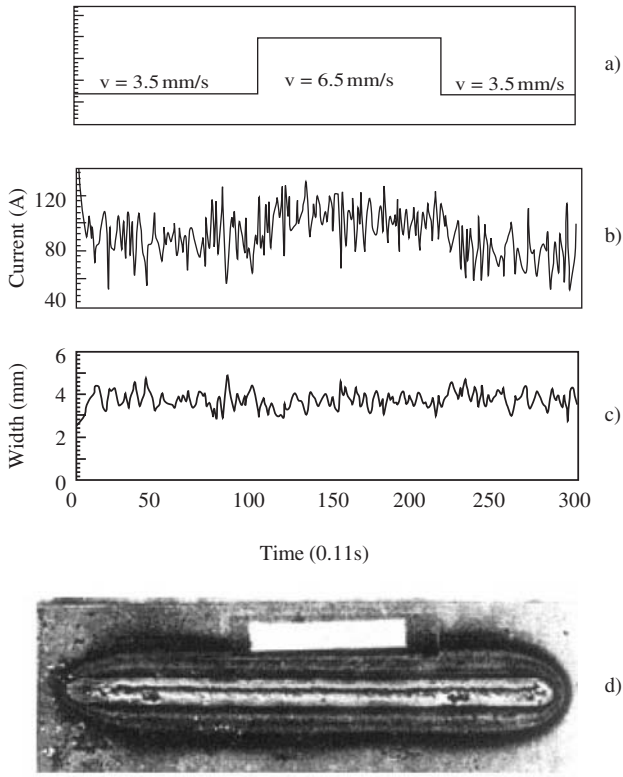

14.35 Effect of welding-speed change (closed-loop control)

obtained by the closed-loop control, and Fig. 14.35d is the appearance of the root side of the bead, which is uniform.

(ii) *Welding test with a closed-loop control system*.

- Varying plate thickness. Plates having three thicknesses, 0.8, 1.5 and 2.5 mm were welded. The results are shown in Figures 14.36a, b and c. In the figure, (1) indicates the variation of current and (2) indicates the variation of the isotherm width. This shows that the current increased with the increase of thickness while the isotherm width was held constant.
- Varying welding speed. Welds were made at 3.9, 5.4 and 7.5 mm/s travel speed. The results are shown in Figures 14.37a, b and c. In the figure, (1) indicates the variation of current and (2) indicates the variation of the isotherm width (1350°C). The figure shows that although the welding speed changed significantly, the isotherm width was stable.

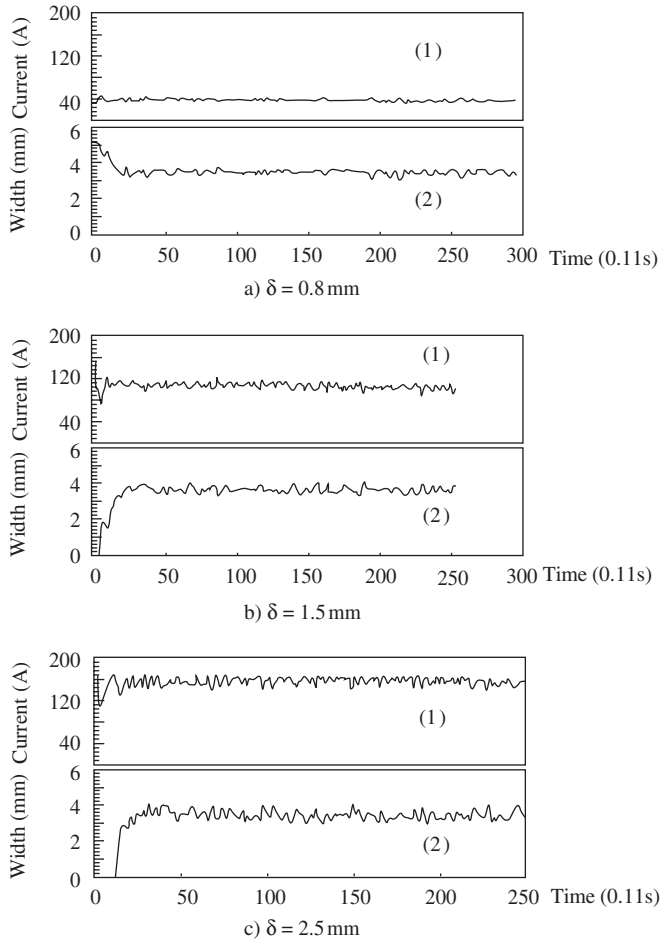

14.36 Closed-loop controlled welding with different thicknesses

- Varying isotherm width. The isotherm width W_0 (1350°C) was set separately to 3, 4, 5 and 6 mm for welding at a constant speed of 5.6 mm/s. The results are shown in Figures 14.38a, b, c, and d in which (1) indicates the variation of current and (2) indicates the variation of the isotherm width. This figure shows that the welding current increased to achieve increasing isotherm width.

(iii) *I-Butt welding with different specimens and gaps.*

- An unsymmetrical plate. One plate had a uniform thickness and the other plate had transverse grooves, as shown in Fig. 14.39a. The results

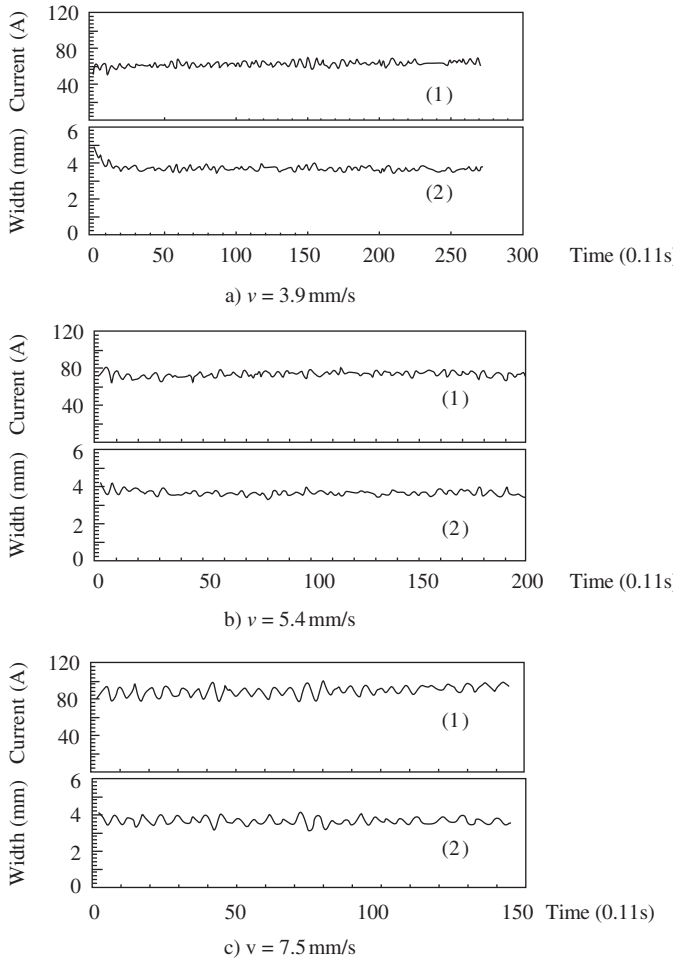

14.37 Closed-loop controlled welding with different welding speeds

are shown in Figures 14.39b, c and d in which b shows the variation of current, c shows the variation of the isotherm width (1350°C) and d shows the appearance of the root side of the weld. These results show that although there were abrupt changes of thickness along the seam, the isotherm width remained uniform.

- I-butt joint without a gap. A 210 × 40 × 1.2 mm specimen was welded. The results are shown in Fig. 14.40 in which *a* indicates the variation of current, *b* indicates the variation of the isotherm width and *c* shows the appearance of the weld.

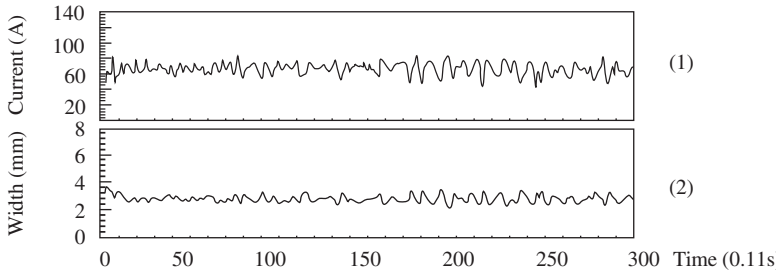

a) $W_o = 3\,mm$

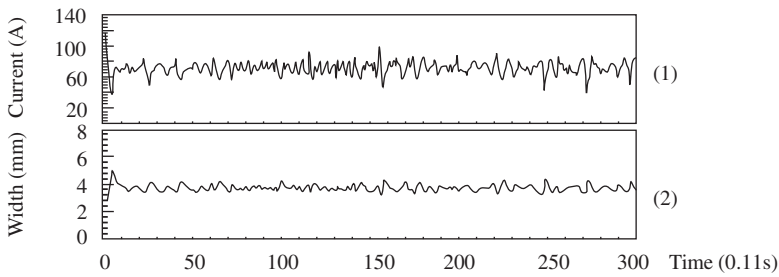

b) $W_o = 4\,mm$

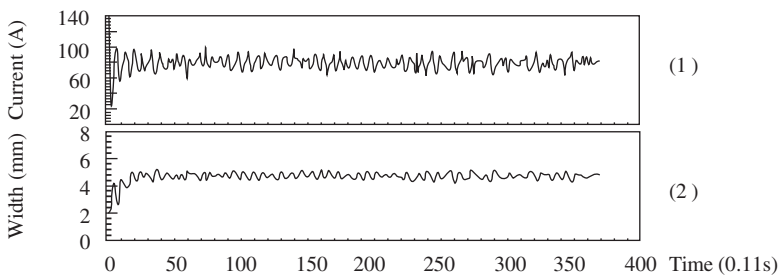

c) $W_o = 5\,mm$

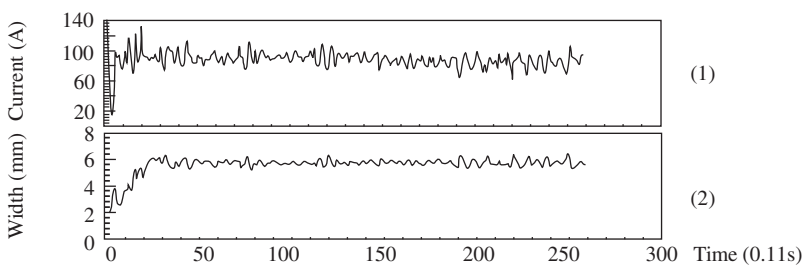

d) $W_o = 6\,mm$

14.38 Closed-loop controlled welding with different isotherm widths

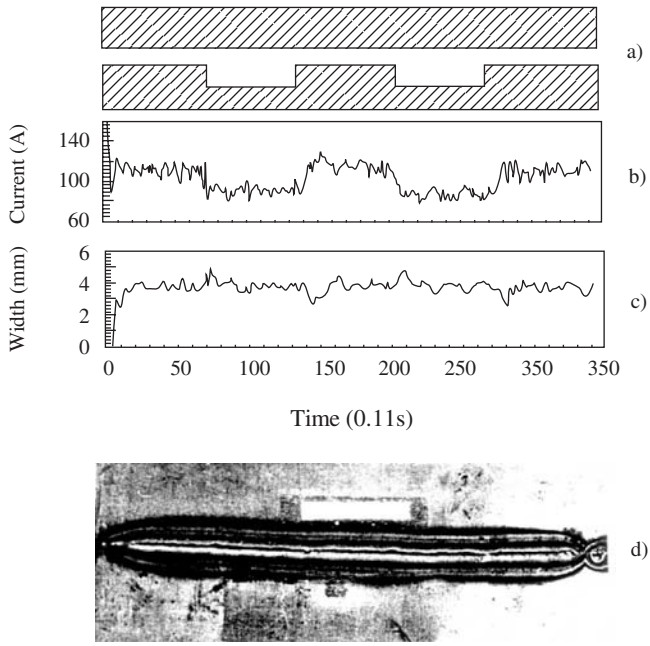

14.39 Closed-loop controlled welding with an unsymmetrical plate

- I-butt joint with an uneven gap. A 180 × 40 × 1.5 mm specimen was assembled without a gap at the starting point and a 0.6 mm gap at the end point. The results are shown in Fig. 14.41 where *a* is the variation of welding current, *b* is the isotherm width and *c* is the appearance of the weld bead.

14.8 Summary

1) The welding temperature field can be measured in real time by the colorimetric method developed by the author. The measurable temperature range can be extended to 800–1400°C by three exposures; the measurement duation was less than 0.5 s.
2) The measuring method can be used to check or modify the mathmatical model for numerical simulation of the welding temperature field and thus promote its application in practice.
3) It was proved by practical measurements that the bi-elliptical Gaussian distributed heat source is the theoretical model closest to the actual welding arc.
4) Important parameters, for example the parameters of the isotherm and the parameters of the thermal cycle, can be extracted from the

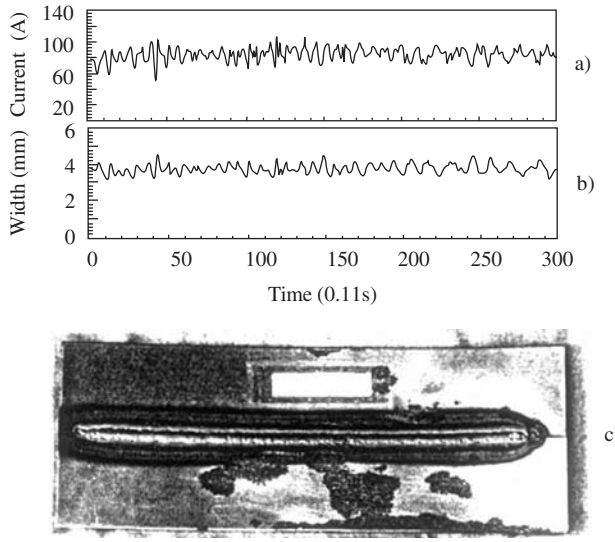

14.40 Closed-loop controlled welding of an I-butt joint without a gap

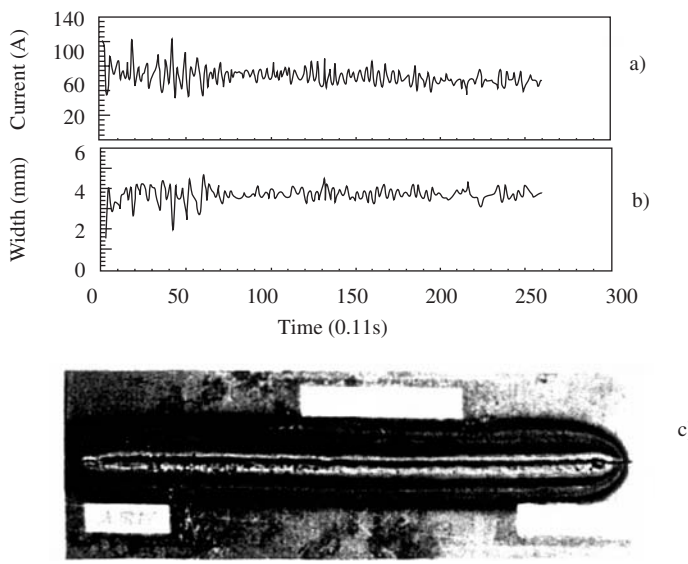

14.41 I-butt joint with uneven gap

measured temperature-field data. These parameters are important for the analysis of welding metallurgy in real time.

5) On the basis of the two-dimensional temperature field obtained by measurement, a mathematical model for a three-dimensional temperature field can be established. Practical numerical-simulation results demonstrated good agreement with the measured data.
6) A closed-loop control system was developed on the basis of the real-time temperature-field measuring system. Practical experiments proved that the system worked satisfactorily. The isotherm width or the penetration can be controlled well in the presence of various interference factors. The system has been applied in practice with successful results.

PART V

Automatic path programming of robot

15

Vision systems and automatic path programming

15.1 Recognition of the groove path

Robots have been applied extensively in industry. There are unmanned workshops in Japan and many robots in these factories are used for welding. The advantages of robots are obvious: high productivity, continuous working, lower manufacturing cost, and suitability for bad working environments such as the deep sea, outer space, and radioactive areas.

Although there are some kinds of sensors such as positional and tactile-force sensors that have a sensing ability, robots mainly provide playback. Their advantages are operational simplicity and repeatability. However, there also are problems:

- Teaching has to be done on-site so that reasonable parameters will be obtained according to the environment and the work piece.
- In welding production, the dimensions of the individual pieces and the assembled and welded workpiece are not consistent. In particular, the welding process introduces distortion. Varying dimensions affect the quality of welds.
- For accurate seam tracking and welding (play back), a suitable number of teaching points must be used, which can be time consuming particularly for single-piece manufacturing.
- Teaching is difficult or even impossible in extreme environments.

Therefore research on developing an adaptable robot is important. There are two approaches to this problem.

The first approach is to use dialogue among the human, robot and computer components so that the robot can be taught, operated and monitored by remote control. This is a system of human intelligence plus robot control. The key problems of this system are the signal transmission among the components and the accuracy of estimating path parameters. Therefore it has limitations.

The second approach is to develop local autonomous functioning of the robot and use man-machine interaction. In other words, the goal of this approach is to develop a machine having cognitive ability. It should have autonomous cognition of the weld groove and path programming, and real-time rectifying of any deviation, possibly by local, human – computer dialogue and manual intervention. This approach is the developing direction of intelligent welding robots. Figure 15.1 is a schematic diagram showing a large spherical tank. Because the volume is large, the plate is thick and the tank was constructed on site. The dimensional accuracy of the assembly cannot be guaranteed. Moreover, the plates must be preheated to 100–150°C for welding. Up to now, the assembly and welding of most tanks were performed manually. This is labour intensive and requires scaffolding. Obviously, a normal welding robot cannot be used. Therefore, the author anticipated developing a robot that is intelligent, has a visual sensor and can automatically program its path on site.[363,364] The author and his colleagues conducted trials in this direction. The results are introduced in this Chapter. Some work by Q. Chen, J. M. Jing and N. Chen also is described [359-362] in Section 15.1.1 to Section 15.1.5.

15.1.1 Review of the technology on path programming

In order to achieve path programming, a visual system normally is used, which includes the following three aspects:

- Two-dimensional (2D) image recognition
- Construction of three-dimensional (3D) information from two-dimensional images
- Weld-path programming.

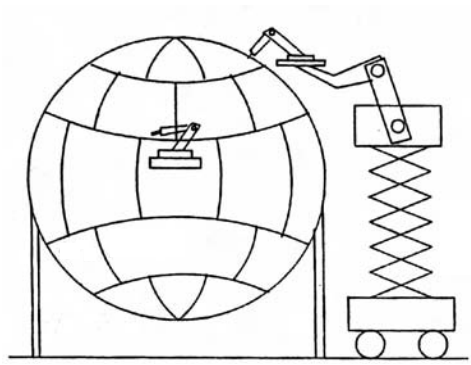

15.1 Anticipated welding method for large spherical tanks

The visual system discussed here is mainly for welding. Although a lot of work has been done on the visual system, the studies of 3D vision, 2D image recognition under arc light and algorithms for constructing 3D co-ordinates are not yet complete. In this section, typical investigations of conventional image recognition and 3D visual technology are described.

(i) *Image recognition*. Traditional image recognition is mainly a module-matching method and the recognition algorithm is based on border detection and image segmentation. A lot of excellent work has been done on this. However, the position of a welding seam is not fixed and there is interference from surface rust, etc. Simple module-matching is not suitable for image recognition during welding. The interference border and the object border might be confused in the case of border detection and filter operation, and thus mistakes could result. Therefore, up to the present time, no effective algorithm has been developed that has a strong anti-interference ability and that can recognise the object by detection of its border. In order to improve recognition accuracy and speed, illumination conditions have been improved recently for suppressing the interference and simplifying border detection. For example, visual systems with back lighting or structural lighting have been applied in welding technology. However, there are special requirements for the lighting source power and light coherence. The equipment is expensive, the field of view is small, and path programming is not possible. Developing an algorithm so that the weld-groove position can be recognized among various interferences under normal environmental light has the highest priority for research on developing a visual system for welding robots. This effort is at only the starting stage in this respect.

(ii) *Status of research on a 3D visual-system algorithm*. The key problem for developing a 3D visual-system algorithm is the matching of characteristic points. This is difficult even in non-welding applications. Normally there are two approaches.

- The first approach is the subjective-triangle method (structural-light method). The structural light can not only suppress interference but also simplify the problem of matching the characteristic points by extracting the stripe of the structural light from only the flat, more or less smooth surface. The biggest problem is the small viewing field and the requirement for suitable surface conditions.
- The second approach is the 3D visual method. This method is based on the 3D detection method used by human eyes. The basic principle is distance measurement by triangulation and calculation of distance by the visual difference between two separated images. The key problem for this method is still the problem of matching the characteristic points. Due to this difficulty, 3D vision remains in the research state. The normal way this method is used is to make a mark on the object or select a

special geometric characteristic as the characteristic point, thereby simplifying the aligning of matching points and increasing the aligning speed and reliability.

In recent years, with the development of optics and pattern-recognition technology, restoring shape by movement, veins, restoring depth by focusing, and the interference-frequency and diffraction methods are notable techniques for 3D vision. However, due to high cost or limitations of facilities, it is not suitable for 3D vision by an arc-welding robot.

The key problem for 3D vision by an arc-welding robot is developing the correspondence or matching of elements. Because the problem of matching characteristic points has not been solved, there is no commonly used and mature 3D vision.

(iii) *Automatic welding-path programming*. Because an intelligent 3D vision system is required for automatic path programming, at the moment no such 3D vision system is available. Therefore, the problem remains unsolved. In the following text, weld-groove recognition using a 3D construction method developed by Q. Chen on the basis of line-point matching and weld-path automatic programming are introduced.

15.1.2 Recognition using a 2D image

The recognition of a weld groove or detection of a groove edge is the basic problem for developing a 3D co-ordinate algorithm and automating path programming.

(i) *Pattern of the weld groove in a 2D image*. Comparing various interference sources such as rust, stain, scrapes and oxide films using a 2D image, the groove edge is smooth and continuous while the other interference sources are curved edges with discontinuities. Also, in a local small window, the groove edge can be considered as a straight line while the normal line of the edge of an interference source is directed in all direction without any rules; the curvature at various points of the edge is large. For a conventional V-groove, the image pattern can be established as shown in Fig. 15.2.

(ii) *Histogram statistical method*. In order to save time, an image of 100 × 100 or 100 × 20 pixels, which includes the groove edge, is taken for processing from the whole 512 × 512 image: see Fig. 15.3. The algorithm for recognition is performed by C-language. It consists of several program blocks, as shown in Fig. 15.4.

- Smoothing and edge-operator convolution. Various interferences are eliminated first by smoothing. An edge operator (Sober operator) is then used to calculate the grey-level gradient for detection of the border (see Fig. 15.5).

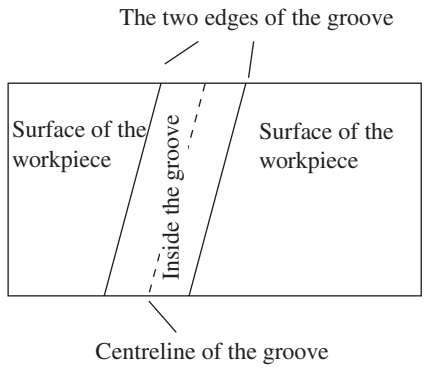

15.2 Recognition pattern of a weld groove in a 2D image

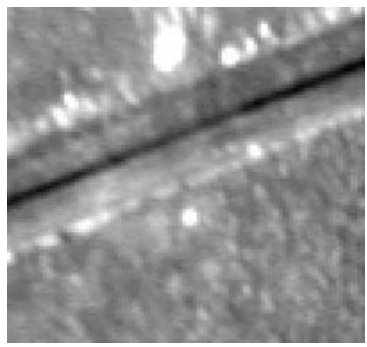

15.3 Actual image of a weld groove

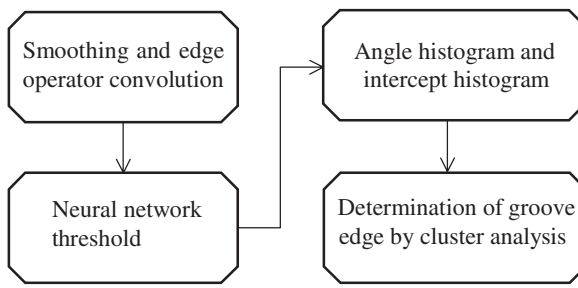

15.4 Flowchart for recognition of a groove by histogram statistics

- Adaptive threshold filtering using a neural network. A back-propagation neural network is used for this purpose. The structure of the network is shown in Fig. 15.6. The input was determined by the histogram statistics of the gradient field. The inclined part of the right side

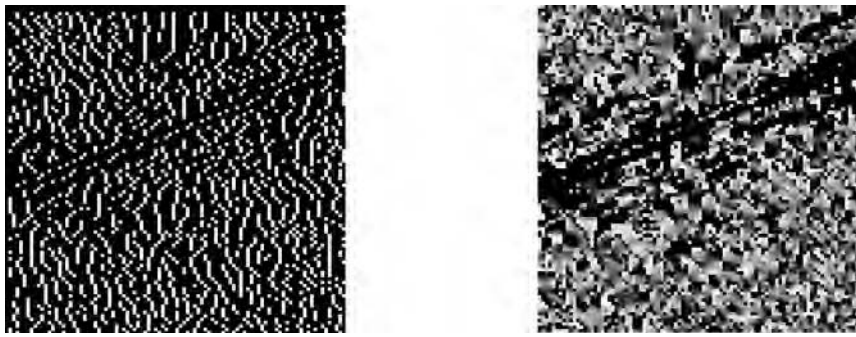

a) Gradient of grey level b) Gradient direction

15.5 Gradient and gradient direction obtained by edge operator

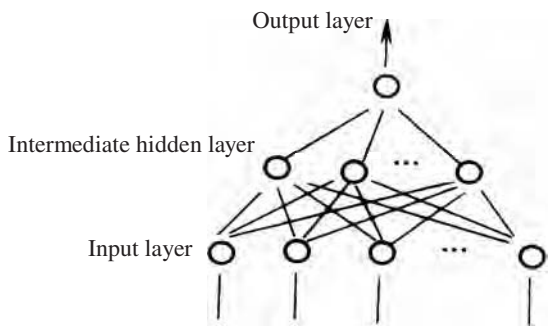

15.6 Structure of BP neural network

was divided into 11 segments (see Fig. 15.7). The ordinates of these dividing points were the input. The output of the neural network TH1 was used as the threshold. The gradient field was then filtered by this threshold. The pixels, which have the gradient G < TH1 were omitted (see Fig. 15.8).

- Histogram filtering. The intercept on the co-ordinates of the edge line, corresponding to each remaining pixel after the threshold treatment, can be found by its edge angle and its location in the window. After these operations are completed, there are two characteristic values for each pixel, namely, an edge-inclined angle φ and an edge-line intercept *b*. The histogram statistics then can be calculated for the edge angle and edge intercept (on the X-axis or Y-axis; this is not noted further in the following text).

  From the 2D image pattern, only the points on the groove edges are needed. On the angle histogram, the point is located at the peak value;

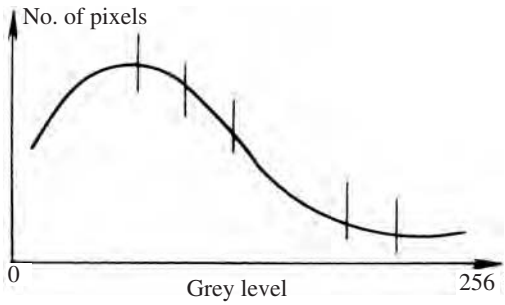

15.7 Sampling the data for neural imput

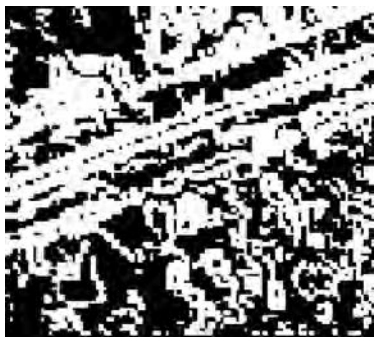

15.8 Image after sieving by threshold filtering

on the intercept histogram the point is located at one of two peak values. Based on this inference logic an 'AND' operation is used with two histograms. The pixels that are in the vicinity of the peak value of both histograms are retained (see Fig. 15.9).

- Determination of the groove-edge location by cluster analysis. After using the operations mentioned above, the location of the groove edge can be found accurately using Hough cluster analysis (see Fig. 15.10).

(iii) *Result of groove-image recognition*. The algorithm described above recognizes the 2D weld-groove image taken under mild environmental conditions. For the experiments, a CCD camera was located 400 mm above the groove, which was a V-groove, I-butt joint or a lap joint. The edge of the I-butt joint was roughened using an abrasive cloth. This preparation was used as the norm. If the error in recognising the edge point was within 2 pixels of the real edge, it was considered to be a correct recognition. If the location error from the real edge was 3–4 pixels, the result was considered unreliable. The results are illustrated in Table 15.1.

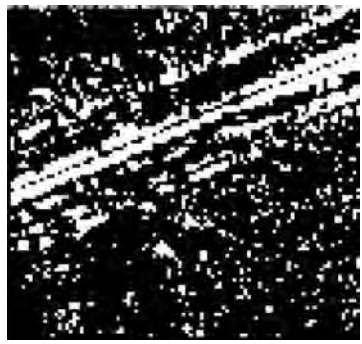

15.9 Image after histogram statistical filtering

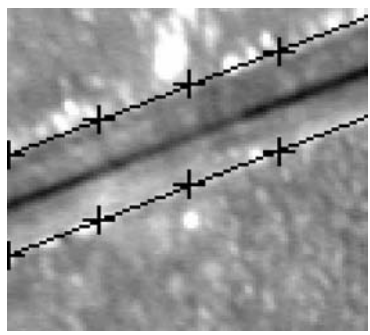

15.10 Final result obtained by cluster analysis

Table 15.1 Accuracy of recognition

Groove type	No.of pixels recognised	Correct pixels	Unreliable pixels**	Correctness (%)
V – Groove* (without tack)	140	135	5	96.4
V – Groove* (with tack)	83	76	7	91.6
I – Groove	67	61	6	91.0
Lap joint (unmachined)	56	45	11	80.4
Lap joint (machined)	42	38	4	90.5

*Centreline of V-groove is taken as standard. **Unreliable and incorrect pixels are included

15.1.3 Classical algorithm and neural network algorithm of 3D co-ordinates

In the classical algorithm, information from two 2D images should be matched to construct 3D information. Because the condition for matching is very rigorous, this method is not applicable. Although marks can be made on the weldment work piece as characteristic points, the accuracy of the actual experimental results is poor. In the following three sub-sections, two algorithms are briefly introduced:

(i) *Classical characteristic point-matching method*. In a binocular visual system, let $(i^{(1)}, j^{(1)})$ and $(i^{(2)}, j^{(2)})$ be the co-ordinates in the 2D image of the point P. Then, for the two CCDs, there are two matrices

$$\begin{cases} c_{h1}^{(1)} = a_{11}^{(1)}x + a_{12}^{(1)}y + a_{13}^{(1)}z + a_{14}^{(1)} \\ c_{h2}^{(1)} = a_{21}^{(1)}x + a_{22}^{(1)}y + a_{23}^{(1)}z + a_{24}^{(1)} \\ c_{h4}^{(1)} = a_{41}^{(1)}x + a_{42}^{(1)}y + a_{43}^{(1)}z + a_{44}^{(1)} \end{cases} \quad [15.1]$$

$$\begin{cases} c_{h1}^{(2)} = a_{11}^{(2)}x + a_{12}^{(2)}y + a_{13}^{(2)}z + a_{14}^{(2)} \\ c_{h2}^{(2)} = a_{21}^{(2)}x + a_{22}^{(2)}y + a_{23}^{(2)}z + a_{24}^{(2)} \\ c_{h4}^{(2)} = a_{41}^{(2)}x + a_{42}^{(2)}y + a_{43}^{(2)}z + a_{44}^{(2)} \end{cases} \quad [15.2]$$

where the superscript is the number of the CCD and the values $\{a\}$ are the parameters of the prospective transformation matrix.

According to the relationship of prospective transformation, four equations incorporating x, y, z, $(i^{(1)}, j^{(1)})$, and $(i^{(2)}, j^{(2)})$ can be derived as follows.

$$\begin{cases} a_{11}^{(1)}x + a_{12}^{(1)}y + a_{13}^{(1)}z + a_{14}^{(1)} - a_{41}^{(1)}i^{(1)}x - a_{42}^{(1)}i^{(1)}y - a_{43}^{(1)}i^{(1)}z - a_{44}^{(1)}i^{(1)} = 0 \\ a_{21}^{(1)}x + a_{22}^{(1)}y + a_{23}^{(1)}z + a_{24}^{(1)} - a_{41}^{(1)}j^{(1)}x - a_{42}^{(1)}j^{(1)}y - a_{43}^{(1)}j^{(1)}z - a_{44}^{(1)}j^{(1)} = 0 \end{cases} \quad [15.3]$$

$$\begin{cases} a_{11}^{(2)}x + a_{12}^{(2)}y + a_{13}^{(2)}z + a_{14}^{(2)} - a_{41}^{(2)}i^{(2)}x - a_{42}^{(2)}i^{(2)}y - a_{43}^{(2)}i^{(2)}z - a_{44}^{(2)}i^{(2)} = 0 \\ a_{21}^{(2)}x + a_{22}^{(2)}y + a_{23}^{(2)}z + a_{24}^{(2)} - a_{41}^{(2)}j^{(2)}x - a_{42}^{(2)}j^{(2)}y - a_{43}^{(2)}j^{(2)}z - a_{44}^{(2)}j^{(2)} = 0 \end{cases} \quad [15.4]$$

It is not difficult to prove that there is a unique solution x, y, z that can be derived from the simultaneous Equations [15.3] and [15.4] if the points in space are not on the connecting line of the principal points of the lens. The derivation can be obtained on the basis of three arbitrary functions of Equations. [15.3] and [15.4] or by the method of least squares applied to four equations. It can be expressed in matrix form as

$$\begin{bmatrix} a_{11}^{(1)} - a_{41}^{(1)}i^{(1)} & a_{12}^{(1)} - a_{42}^{(1)}i^{(1)} & a_{13}^{(1)} - a_{43}^{(1)}i^{(1)} \\ a_{21}^{(1)} - a_{41}^{(1)}j^{(1)} & a_{22}^{(1)} - a_{42}^{(1)}j^{(1)} & a_{23}^{(1)} - a_{43}^{(1)}j^{(1)} \\ a_{11}^{(2)} - a_{41}^{(2)}i^{(2)} & a_{12}^{(2)} - a_{42}^{(2)}i^{(2)} & a_{13}^{(2)} - a_{43}^{(2)}i^{(2)} \\ a_{21}^{(2)} - a_{41}^{(2)}j^{(2)} & a_{22}^{(2)} - a_{42}^{(2)}j^{(2)} & a_{23}^{(2)} - a_{43}^{(2)}j^{(2)} \end{bmatrix} \begin{bmatrix} x \\ y \\ z \end{bmatrix} = \begin{bmatrix} a_{44}^{(1)}i^{(1)} - a_{14}^{(1)} \\ a_{44}^{(1)}j^{(1)} - a_{24}^{(1)} \\ a_{44}^{(2)}i^{(2)} - a_{14}^{(2)} \\ a_{44}^{(2)}j^{(2)} - a_{14}^{(2)} \end{bmatrix} \quad [15.5]$$

When the co-ordinates of the two images are known for a space point, its 3D co-ordinate x, y, z, can be found using Eq. [15.5]. This is called the characteristic point-matching method. In the practical application of this method, defining the co-ordinates for a certain space point in two images is difficult and the frequency of mistakes is high. This is a big problem for this method.

(ii) *Use of a characteristic object*. Normally, there are no characteristic points on the weld groove. Although there are rust deposits, scrapes, stains and oxide films, their shapes are not typical and distinct. Tack welds are useful but some grooves do not have them. Therefore, placing a standard geometric piece in the groove to serve as a characteristic body was considered. The shape of the body can be simple, for example, a cylinder; its centre of gravity can be used as the characteristic point.

The accuracy of the characteristic-point method depends on the accuracy of detecting the characteristic point. There are the following problems:

- Recognising the geometric shape is time-consuming and the reliability of describing its position is poor. A non-symmetrical edge or a single edge often is detected. Matching the position of its centre of gravity is unreliable. Table 15.2 shows the results of matching the characteristic points of 40 images.
- For straight grooves, two characteristic cylinders are needed but for curved grooves, the number of characteristic cylinders required is uncertain.
- It is difficult to differentiate tack welds from characteristic bodies. Two procedures are needed for this method, i.e. inserting and removing the characteristic bodies. This is impossible when welding in harsh environments.

In conclusion, using characteristic bodies for the characteristic point-matching method is unreliable; its accuracy is poor. This is why this method is difficult to use.

(iii) *Artificial Neural Network (ANN) Algorithm*. From the point of view of function mapping, the algorithm for transforming 2D images to 3D

Table 15.2 Error of characteristic-point recognition and accuracy of 3D co-ordinates

CCD 1 recognition error		CCD 2 recognition error		Error of 3D co-ordinate		
i (pixels)	j (pixels)	i (pixels)	j (pixels)	x (mm)	y (mm)	z (mm)
23	19	20	21	13	11	24

images is the mapping of 2D to 3D. The ANN also has the function of 3D mapping. Theoretically, an arbitrary three-layer BP network can provide nonlinear mapping. Q. Chen explored this algorithm for producing 3D co-ordinates from binocular images using ANN.[359]

The input parameters were the straight-line function's coefficients on the CCD2 image and the co-ordinates of the points on the CCD1 image. Thus, the input parameters are 5-dimensional vectors. For convenience of description, the structure of the network is depicted as follows:

'Input point number – point number of the first hidden layer – point number of the Nth hidden layer – output point number'.

Regarding the algorithm of the ANN, the determination of the input parameters and their pretreatment, reference to other literature is advised. The following text introduces the 3D results obtained by BP ANN where K is the slope of the straight line.

In the present method, no characteristic point is necessary but there are shortcomings in its accuracy. The results show that:

(i) The accuracy of the results is better when the singular solution of line-point matching is used. This means that mapping from 2D to 3D by ANN is different from the mapping using a transformation function.

(ii) There is a strong correlation between the parameter of the input samples and the 3D co-ordinates. The accuracy for x and y is good for all auto-correlated and hetero-correlated ANN higher than second order. However, the z co-ordinate is very sensitive to the structure and order of the ANN. The highest accuracy can be obtained using a third-order hetero-correlated BP ANN (14-3-1). The 3D maximum error was ±4 mm for $|K| \geq 1$. The maximum error of the x,y co-ordinate also was ±4 mm (Table 15.3) for $|K| < 1$. However, the accuracy of the z co-ordinate was poorer (Table 15.4).

These tables show that the error is still large. Applying this method is not practical yet.

15.1.4 Line-point matching method

In response to the special features of welding grooves, a new algorithm for finding the groove in 3D, called the line-point matching method, was proposed by Q. Chen, and J. M. Jing for an arc-welding robot vision system.

(i) *Algorithm based on welding-groove features*. From the geometrical viewpoint, the weld groove can be described by a line or short broken lines for curved grooves. The algorithm is based on this concept.

Theorem: Suppose that the focus points of two CCDs are F_1 and F_2, the image surfaces are S_1 and S_2, and P is a point on the straight line L' in space. The image of L' on surface S_2 is L, and P_1 and P_2 are the images of P on S_1 and S_2, respectively. If L and P_1 are known, then the necessary

Table 15.3 $|K| \geq 1$ Training of samples and detection results (80 training samples 130 detections)

Structure of ANN	Co-ordinate	Results of training						Results of detection				
		Number of samples whose error was in the following range				Maximum error	Number of training $\times 10^3$	Number of samples whose error was in the following range				Maximum error
		>4	(3,4]	(2,3]	(1,2]			>4	(3,4]	(2,3]	(1,2]	
5-3-1	*x*	0	2	16	12	3.44	140	1	33	54	69	5.14
BP NN	*y*	0	3	10	10	3.32	20	0	28	54	65	3.77
	z	10	2	5	10	8.79	180	110	5	27	40	23.06
5-8-1	*x*	1	6	13	13	4.89	140	16	17	55	58	5.64
BP NN	*y*	0	1	3	13	3.09	3	2	38	16	49	5.90
	z	17	7	12	7	12.45	180	92	39	46	28	14.69
5-6-4-1	*x*	3	7	1	17	4.31	140	18	32	30	91	5.13
BP NN	*y*	5	7	0	19	4.43	3	9	11	6	100	4.79
	z	21	1	5	12	14.88	180	93	12	18	31	15.97
5-3-1	*x*	2	1	4	10	5.67	80	57	19	39	41	7.49
Bi-parallel forward	*y*	5	1	4	6	6.97	20	59	32	15	30	8.33
BP NN	*z*	13	3	3	5	12.72	180	101	9	18	27	14.28
5-3-1	*x*	1	2	6	6	6.14	140	45	29	54	37	6.72
Even drooping method	*y*	6	5	5	7	7.39	40	36	36	26	45	8.65
BP NN	*z*	7	5	2	6	13.46	140	80	11	20	40	16.27
5-3-1	*x*	0	2	5	5	3.76	35	1	25	47	49	4.47
PID + BP	*y*	0	1	3	11	3.73	5	0	5	45	38	3.68
NN	*z*	13	2	4	6	12.71	140	99	21	31	23	13.15
14-3-1	*x*	0	4	7	15	3.25	140	0	41	39	92	3.36
High-order BP	*y*	0	0	1	4	2.17	30	0	0	2	20	2.89
NN	*z*	0	0	5	10	2.98	80	0	15	43	65	3.74
Line-point matching	*x*	0	0	0	1	1.06		0	0	5	31	2.29
method*	*y*	0	0	0	2	1.20		0	0	0	54	1.44
	z	0	1	4	5	3.37		3	6	16	82	4.59

* The line-point matching method is described in subsequent sections; 30 calibrated samples were used for it and there were 1804 detection samples

Table 15.4 |K| < 1 Training of samples and detection results (80 training samples 220 detections)

Structure of ANN	Co-ordinate	Results of training						Results of detection				
		Number of samples whose error was in the following range				Maximum error	Number of training $\times 10^3$	Number of samples whose error was in the following range				Maximum error
		>4	(3,4]	(2,3]	(1,2]			>4	(3,4]	(2,3]	(1,2]	
5-3-1	*x*	1	4	8	10	4.77	10	6	12	46	40	5.14
BP NN	*y*	0	1	2	15	3.01	10	0	2	8	42	3.12
	z	23	3	3	4	11.32	30	103	4	5	8	16.58
5-8-1	*x*	3	4	7	9	5.30	10	12	19	38	37	5.60
BP NN	*y*	0	0	5	16	2.81	10	0	1	14	44	3.87
	z	24	3	1	6	11.64	20	104	4	3	10	16.19
5-6-4-1	*x*	1	4	7	14	5.01	10	3	21	30	58	5.25
BP NN	*y*	0	2	7	17	3.03	10	0	2	15	78	3.95
	z	21	3	4	5	11.40	20	101	4	8	16	16.88
5-3-1	*x*	3	4	7	10	5.04	10	32	28	27	24	7.52
Bi-parallel forward	*y*	12	3	6	12	6.25	10	36	13	12	37	8.80
BP NN	*z*	35	1	0	1	11.20	20	83	8	6	27	13.43
5-3-1	*x*	2	2	4	5	4.15	30	17	13	23	27	6.15
Even drooping method	*y*	6	5	7	4	6.42	30	19	22	24	24	7.67
BP NN	*z*	14	3	7	4	14.26	30	57	7	15	17	16.30
5-3-1	*x*	1	3	3	13	4.19	40	3	13	21	37	4.87
PID + BP	*y*	0	1	10	11	3.04	10	1	3	33	47	4.11
NN	*z*	4	3	5	5	11.55	40	31	10	18	29	16.07
14-3-1	*x*	1	2	9	7	4.15	20	7	20	29	25	4.18
High order BP	*y*	0	1	3	10	3.26	10	0	3	11	35	3.60
	z	16	2	1	2	10.42	80	57	11	25	21	15.10
Line-point	*x*	0	0	0	1	1.06		140	14	35	64	1855.3
matching method*	*y*	0	0	0	2	1.20		77	20	36	65	1142.4
	z	0	1	4	5	3.37		197	29	44	99	4101.2

* Line-point matching method: the number of calibrated samples was 30, the detection number was 707

and sufficient condition for the uniqueness of a space point p is that the connecting line F_1F_2 and L are not on a plane: see Fig. 15.11 (the proof is omitted).

This theorem suggests a new algorithm for finding the 3D co-ordinate of a point, which avoids the difficulty of characteristic point matching. The 3D co-ordinate of a point is found using a point P_1 on one image and a straight line L on the second image, i.e. the matching of a point and a line. The algorithm converts the recognition of a characteristic point to the recognition of the groove edge. The labour to accomplish this is less. It is called the 'straight line-point matching method'.

(ii) *Line-point matching using a homogeneous matrix*. Because the two elements being matched do not depend on which image is taken, suppose that a point on CCD1 and a line on CCD2 are taken. The standard straight-line function can be written as

$$S \cdot i^{(2)} + T \cdot j^{(2)} + R = 0 \qquad [15.6]$$

where S, T and R are the coefficients of the straight-line function; the superscript is the number of the CCD. Any point $(i^{(2)}, j^{(2)})$ on the straight line must satisfy Eq. [15.6].

Based on the perspective projection principle, substituting the co-ordinate of the image point into Eq. [15.6] gives

$$S \cdot \frac{a_{11}^{(2)}x + a_{12}^{(2)}y + a_{13}^{(2)}z + a_{14}^{(2)}}{a_{41}^{(2)}x + a_{42}^{(2)}y + a_{43}^{(2)}z + a_{44}^{(2)}} + T \cdot \frac{a_{21}^{(2)}x + a_{22}^{(2)}y + a_{23}^{(2)}z + a_{24}^{(2)}}{a_{41}^{(2)}x + a_{42}^{(2)}y + a_{43}^{(2)}z + a_{44}^{(2)}} + R = 0 \qquad [15.7]$$

After derivation, it becomes

$$\begin{aligned} &S \cdot a_{11}^{(2)} + T \cdot a_{21}^{(2)} + R \cdot a_{41}^{(2)}x + \left(S \cdot a_{12}^{(2)} + T \cdot a_{22}^{(2)} + R \cdot a_{42}^{(2)}\right)y \\ &+ \left(S \cdot a_{13}^{(2)} + T \cdot a_{23}^{(2)} + R \cdot a_{43}^{(2)}\right)z + \left(S \cdot a_{14}^{(2)} + T \cdot a_{24}^{(2)} + R \cdot a_{44}^{(2)}\right) = 0, \end{aligned} \qquad [15.8]$$

That is a function of x, y and z. Taking an image point $(i^{(1)}, j^{(1)})$ on CCD1, the following equation can be established:

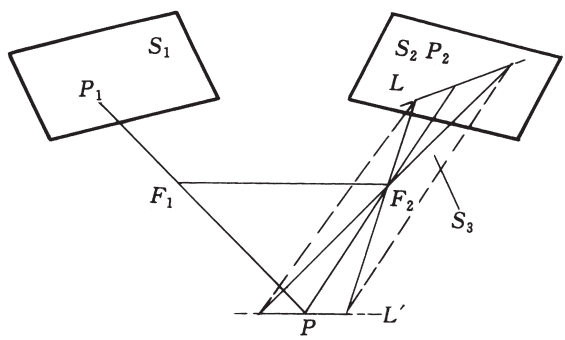

15.11 Determination of point *P* in space by line-point matching

$$a_{11}^{(1)}x + a_{12}^{(1)}y + a_{13}^{(1)}z + a_{14}^{(1)} - a_{41}^{(1)}i^{(1)}x - a_{42}^{(1)}i^{(1)}y - a_{43}^{(1)}i^{(1)}z - a_{44}^{(1)}i^{(1)} = 0$$

$$a_{21}^{(1)}x + a_{22}^{(1)}y + a_{23}^{(1)}z + a_{24}^{(1)} - a_{41}^{(1)}j^{(1)}x - a_{42}^{(1)}j^{(1)}y - a_{43}^{(1)}j^{(1)}z - a_{44}^{(1)}j^{(1)} = 0 \quad [15.9]$$

Solving Equations [15.8] and [15.9] simultaneously, the matrix equation can be expressed as follows:

$$\begin{bmatrix} a_{11}^{(1)} - a_{41}^{(1)}i^{(1)} & a_{12}^{(1)} - a_{42}^{(1)}i^{(1)} & a_{13}^{(1)} - a_{43}^{(1)}i^{(1)} \\ a_{21}^{(1)} - a_{41}^{(1)}j^{(1)} & a_{22}^{(1)} - a_{42}^{(1)}j^{(1)} & a_{23}^{(1)} - a_{43}^{(1)}j^{(1)} \\ S \cdot a_{11}^{(2)} + T \cdot a_{21}^{(2)} + R \cdot a_{41}^{(2)} & S \cdot a2_{12}^{(2)} + T \cdot a_{22}^{(2)} + R \cdot a_{42}^{(2)} & S \cdot a_{13}^{(2)} + T \cdot a_{23}^{(2)} + R \cdot a_{43}^{(2)} \end{bmatrix} \begin{bmatrix} x \\ y \\ z \end{bmatrix}$$

$$= \begin{bmatrix} a_{44}^{(1)}i^{(1)} - a_{14}^{(1)} \\ a_{44}^{(1)}j^{(1)} - a_{24}^{(1)} \\ -S \cdot a_{14}^{(2)} - T \cdot a_{24}^{(2)} - \boldsymbol{R} \cdot a_{44}^{(2)} \end{bmatrix} \quad [15.10]$$

After calibration of the vision system and recognition of the groove on the image, the coefficients of the Equations [15.10] are known and the x, y, z values can be found.

(iii) *Theorem and criterion for a singularity in the line-point matching method.* In the previous section, the algorithm of the line-point matching method was described. It was not mentioned that in this method there is a singularity problem. The theorem and criterion of the singularity are discussed as follows.

According to the theorem described in Section 15.1.4, the condition for good line-point matching is that the image line is on a different plane from the two focus-connecting lines. When the image straight line is on the same plane as the focus line, the 3D co-ordinate cannot be uniquely determined; the matching method is singular.

It has been pointed out that to judge whether the singularity happens depends on the relative positions of the image straight line and the focus-connecting line. Two criteria are given below (the proof was omitted).

Criterion 1: In the case where the focus-connecting line intersects the image surface and the image line passes through the intersecting point, then there is a singularity.

Criterion 2: If the optical axes of the two CCDs are parallel, the focus-connecting line forms with the I-axis of one image surface at an angle of ζ and the straight line on the image also forms with I at an angle ζ. Then the straight line on the image and F_1F_2 are coplanar and there is a singularity.

For convenience of comparison, simulation experiments were conducted on standard specimens. The structure of the vision system was: the distance between the CCDs was 150 mm, the height of the CCDs was 400 mm, the inclination angle of the optical axis of each CCD < 10° and the revolving angle of the CCD was 0°.

The accuracy of the algorithm is defined as the error of the calculated co-ordinates with the actual co-ordinates, which can be expressed as

$$\Delta d = \sqrt{(\Delta x)^2 + (\Delta y)^2 + (\Delta z)^2}$$

The singularity was evaluated by the condition number $\text{Cond}(M)_\infty$ of the coefficient matrix of Eq. [15.10].

The maximum error of the calibrated vision system was 1.3 mm. Experimental results demonstrated that the line-point matching method was well-behaved. When the condition number of the coefficient matrix was small, its accuracy was about ±1.5 mm. If there was a singularity, the error was large. The results of the well-behaved calculations are shown in Table 15.5.

The statistical results of the well-behaved and singular categories are shown in Table 15.6.

(iv) *Measures for avoiding a singularity*. The likelihood of a singularity is determined substantially by the location of the CCD. The focus-connecting line is determined by the structure of the vision system. The singularity could be turned into a well-behaved category if the focus-connecting line could be automatically staggered when the singularity tended to develop. To achieve this, two measures were taken, the first using three CCDs to form a triple-eyed vision system, and the second using a binocular vision system on a turntable.

Any two CCDs of the triple-eyed vision system can be used as a binocular vision system. Therefore, it corresponds to three binocular vision systems. If any binocular vision system has a singularity, then another pair of CCDs can be turned on. The three focus-connecting lines cannot be coplanar with a straight line in space simultaneously.

15.1.5 Results of path programming

Figure 15.12 shows the projection of a curved-space groove (consisting of two arcs) on the *xy* plane and *yz* plane, obtained by the line-point matching method. The solid line shows the programmed path and the dotted line is the actual location of the arc-shaped groove. The results show that the programmed path and the actual path coincide. Some errors are distributed, mainly in the depth dimension.

Errors of the path programme by the two methods were compared. In the first method, an exact formula was defined for the groove edge and the minimum distance of each of the recognised points to the exact curve was taken as the accuracy criterion. In the second method, the recognised points were used to find a curve-fitting formula. Then, the accuracy was determined; the curve-fitting formula facilitated the determination. For the curve shown in Fig. 15.12, the maximum error was 2.21 mm and the average error was 1.33 mm according to the first method. The maximum error was 1.78 mm and the average error was 0.93 mm for the second method. The

Table 15.5 Results obtained by line-point matching method (well-behaved category)

Co-ordinate on CCD 1 of the space point P		Straight-line function on CCD 2 image $AI + BJ + C = 0$			Actual 3D co-ordinate of space point P (x, y, z)			3D co-ordinate obtained by line-point matching			Error			Deviation	Condition number of coefficient matrix
i	j	A	B	C	x	y	z	x'	y'	z'	Δx	Δy	Δz	Δd	
92	58	−75.64	−100.0	16955.13	40	20	−10	40.077	19.861	−9.274	0.077	−0.139	0.726	0.74	198.2
6	119	−75.64	−100.0	16955.13	20	30	−10	20.049	30.011	−10.368	0.049	0.011	−0.368	0.37	178.0
181	115	76.81	−100.0	−2101.45	60	30	−18	59.763	29.909	−18.636	−0.237	−0.091	−0.636	0.68	156.8
433	243	56.04	−100.0	495.36	120	50	−18	119.901	49.927	−18.983	−0.099	−0.073	−0.983	0.99	227.6
134	59	51.28	−100.0	15810.26	50	20	−10	49.990	19.903	−9.542	−0.010	−0.097	0.458	0.47	229.1
6	119	51.28	−100.0	15810.26	20	30	−10	20.044	30.024	−10.478	0.044	0.024	−0.478	0.48	203.0
181	180	100.0	−93.04	−16217.4	60	40	−18	59.899	40.026	−17.483	−0.101	0.026	0.517	0.53	129.5
51	243	100.0	8.00	−9200.0	30	50	−18	29.973	49.974	−18.085	−0.027	−0.026	−0.085	0.09	74.3
135	246	100.0	−41.67	−5475.0	50	50	−10	50.038	49.960	−10.828	0.038	−0.040	−0.828	0.83	75.2
176	185	100.0	−64.17	−7687.50	60	40	−10	59.937	40.112	−9.608	−0.063	0.112	0.392	0.41	80.7
92	58	100.0	45.22	−15891.30	40	20	−10	40.026	19.935	−9.786	0.026	−0.065	0.214	0.23	10.03
95	179	100.0	1.43	−13282.61	40	40	−18	39.973	40.012	−17.696	−0.027	0.012	0.304	0.31	80.7
92	58	100.0	−24.35	−10673.91	40	20	−10	39.986	19.994	−10.192	−0.014	−0.006	−0.192	0.19	82.5
51	243	100.0	30.29	−14771.43	30	50	−18	29.974	49.974	−18.081	−0.026	−0.026	−0.081	0.09	7.08
95	243	100.0	7.39	−13053.98	40	50	−18	39.988	49.941	−17.747	−0.012	−0.059	0.253	0.26	74.3
135	246	100.0	−20.0	−11000.0	50	50	−10	50.055	49.952	−10.694	0.055	−0.048	−0.694	0.70	70.9
50	57	100.0	11.30	−9447.83	30	20	−10	30.138	20.035	−10.499	0.138	0.035	−0.499	0.52	92.2
139	243	100.0	−59.09	−368.18	50	50	−18	50.056	49.942	−17.952	0.056	−0.058	0.048	0.09	79.7
181	243	100.0	−81.36	1301.69	60	50	−18	59.951	49.957	−18.365	−0.049	−0.043	−0.365	0.37	109.1
140	309	100.0	−42.68	−1599.16	50	60	−18	50.127	60.197	−19.078	0.127	0.197	−1.078	1.10	75.2
140	373	100.0	−33.44	−2291.72	50	70	−18	50.076	70.161	−19.371	0.076	0.161	−1.371	1.38	72.6

Table 15.6 Statistics of the results obtained by the line-point matching method (two categories)

Number of samples according to the slope of line in image	Maximum error	Distribution of errors			
		>4	(3,4]	(2,3]	(1,2]
Well-behaved 846	1.41	0	0	0	5
Singularity sample 513	967.2	123	11	34	117

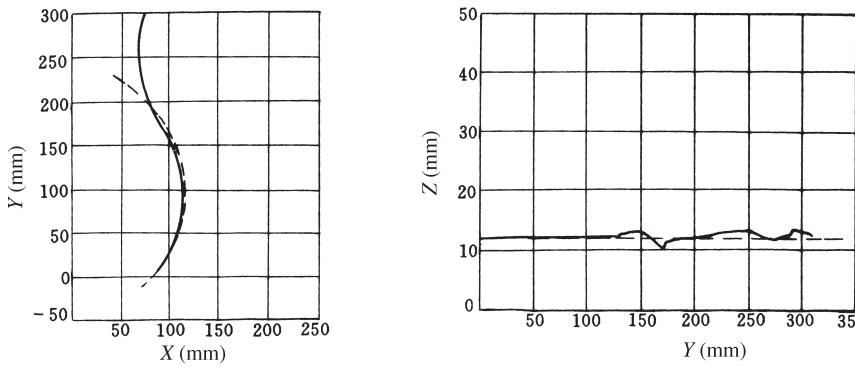

a) Projection on the *xy* plane

b) Projection on the *yz* plane

15.12 Projections of the programmed path on the *xy* and *yz* planes

error statistics in the path programming of 20 curves or straight lines are shown in Table 15.7.

15.2 A robot with automatic path programming

In order to demonstrate the usefulness of automatic path programming of a robot, T. P. Leung, in co-operation with the author, developed a robot with a 3D vision system that could provide path programming. Although the scope and field of view were small, its successful operation proved the possibility of the concept and served as an example.[349,365]

15.2.1 Design of a robot

In this section, the design and fabrication of a servo-controlled robot having $5\frac{1}{2}$ axes of freedom is described. Similar to all medium-sized industrial robots on the market, the first-stage 3-axis movements were driven by DC servomotors so that a larger torque-weight ratio, lower noise and faster dynamic response could be obtained. A stepping motor drove the opera-

Table 15.7 Statistics of path programming errors

Groove shape	By fitting formula (mm)		By exact formula (mm)	
	Max.error	Average error	Max.error	Average error
Straight	1.92	0.96	1.83	1.12
Curved	2.31	1.24	2.78	1.47

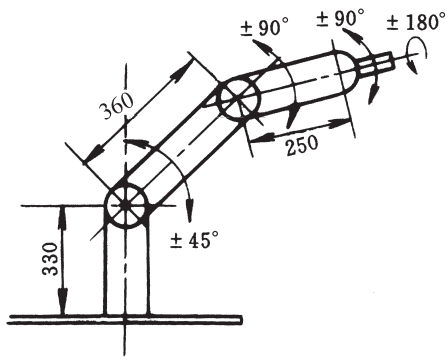

15.13 Side view of the robot

tion of the wrist because it was lighter and less expensive in this application, where high dynamic response was not required.

The controller was computer based. All of the software, mechanical structures, interfaces and signal processing were designed in the laboratory. The software included manual data input, a teaching program, and digital control of the servo-motors, stepping motor and the manual control. The software was developed based on a Motorola microprocessor.

15.2.1.1 Mechanical structure

The robot consisted of three parts (see Figures 15.13 and 15.14): an arm (three axes of freedom), a wrist (two axes of freedom) and a hand or end effecter. The robot could be bolted on a platform of a carriage.

The heavier parts, such as the three-phase transformer, servo amplifier, etc. could be mounted under the platform of the carriage so that the structure was light and stable. The five axes of freedom and their limits were

(i) Turning ±135° around the robot centre.
(ii) Upper arm swing on a vertical plane by ±45°.
(iii) Lower arm swing on a vertical plane by ±90°.

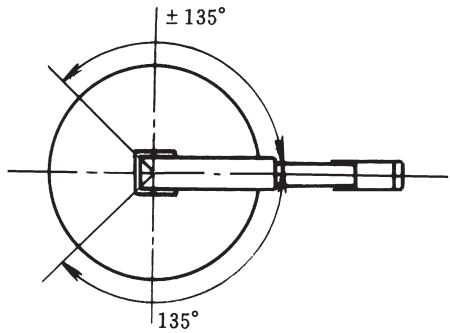

15.14 Vertical view of the robot

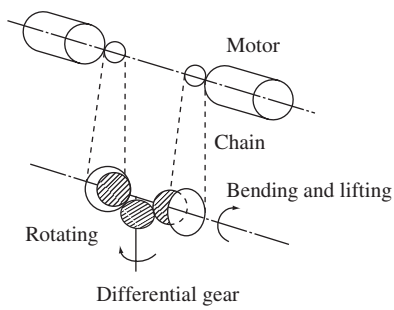

15.15 Wrist mechanism

(iv) End effector bending and lifting for ±90°.
(v) Rotation of the end effector for ±180°.

The robot consisted of two rotating joints and was fixed on a turntable base. Therefore, there were three axes of freedom for co-ordinate determination. The upper arm was connected to the lower arm by a toggle and the lower arm was connected to the foundation by a shoulder joint.

The end effector was linked to the main body of the robot by a wrist. Two axes of freedom were provided by the wrist using a three-link device. The structure of the wrist is shown in Fig. 15.15. It could perform bending, lifting and turning. The wrist mechanism consisted of a pair of chain wheels, a stepping motor and a differential gear. The hand turned if the two stepping motors rotated in opposite directions but at the same speed. Two actions were performed if the motors rotated at different speeds, regardless of the direction they rotated. In order to reduce the torque needed for the joint, the stepping motors were mounted under the joint as near as possible. The end effector was a two-finger hand (Fig. 15.16). It was operated by com-

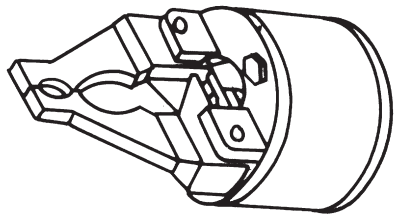

15.16 Two-finger hand

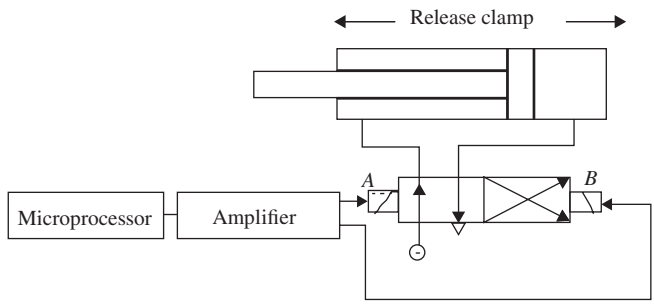

15.17 Control of valve by microprocessor

pressed air and could lift 2 kg. The hand consisted of a cylinder having a 12 mm stroke and a clamping mechanism. The compressed air was controlled by valves at each end of the cylinder. When the magnetic coil A was connected to a 12 V source, the clamp released. If coil B was energised, the clamp gripped (see Fig. 15.17).

15.2.1.2 Control system and trajectory interpolation

The controller of the machine was a single-board MC68010 Motorola microcomputer with a Model 6800 CPU. A 4-3-4 spline function was used for the interpolating function to find all of the points on the curve. Then, the Cartesian co-ordinates of all points and the angle of the joint were calculated. Commands were sent by the controller to drive the DC servomotors.

15.2.1.3 Transformation of co-ordinates

(i) *Geometric method*. In the present design, the angle of the joints was derived using Cartesian co-ordinates. For convenience in practical applications, the Cartesian co-ordinates of the end-effector are used. The user

needs to furnish the lifting angle, the rotating angle and the Cartesian co-ordinates of the arm.[366]

Traditional geometrical formulae were applied. The joint angle was derived using the given joint length and the arm size with the sine and cosine laws.

(ii) *Comparison of different co-ordinate transformations*. Among all of the available transformation methods, a homogeneous transformation can introduce a singularity and the number of calculations is large.[367] Two vector methods can avoid a singularity but are suitable only for changing direction. None of these three methods can give the physical explanation of the solution. Analytical geometry, however, can give a clear physical meaning. In using it, the mechanical structure is the key problem. If the mechanism is complicated, e.g. eight axes of freedom including rigid and soft joints, the three former methods are better.

15.2.1.4 Control of trajectory

In order to control the trajectory, calculating the displacement from one point to the next is necessary. Several of the displacement modes are discussed below.

(i) *Joint interpolation method*. This is probably the basic interpolation method.[368] In this method, each joint moves in a co-ordinated manner from one point to another. The joints accelerate at first and then maintain a constant speed until they decelerate to the end point. Although this method passes each point, its path is not controlled; therefore errors often occur.

(ii) *Straight-line interpolation method*. In this method, the joint moves so that the work piece moves along a straight line. Thus the trajectory of the work piece is controlled.[369] But when the direction changes, the work piece must stop to avoid an instantaneous change of acceleration. Such a stop is not acceptable for spraying lacquer and welding.

To avoid such a stop, the trajectory should be rounded. To avoid instantaneous acceleration, the work piece does not pass ideal points. The curvature at each point depends on the ideal acceleration; the higher the acceleration becomes, the smaller the curvature becomes and the better the curve is fitted.

(iii) *Spline function*. The application of a spline function as the interpolation function can avoid the shortcomings of the two methods described above. There are spline functions for different applications.[370,371] Several of these are discussed below.

- *x*-spline. In 1978, Chenshaw and Negus explored the *x*-spline, which was developed by Bechforooz.[370] It was an extension of the cubic spline. It

allows a discontinuity of the second-order derivative at a point. Therefore, the acceleration at every interval does not remain continuous. However, the *x*-spline has the advantage that once two of three points are known, then the trajectory of a local joint can be determined. Therefore, it is not necessary to solve all points on the trajectory before the robot starts. The trajectory can be calculated on line.

- Fourth-order spline function. This function has continuity of location, velocity and acceleration. Similar to the *x*-spline, the trajectory of the local joint can be determined by two of three points on the trajectory. Therefore, the trajectory can be calculated on-line.
- 4-3-4 spline function. According to the literature,[372] a single trajectory can be divided into three intervals, namely starting interval, central interval and end interval.

The central interval does not include the start interval or the end interval. In this interval the boundary condition is that the location, velocity and acceleration are continuous at its ends. Therefore, a third-order function can be used. For the starting interval, the initial velocity and initial acceleration are zero and, for the end interval, the ending velocity and ending acceleration are zero. Therefore, a fourth-order function should be used. All spline functions should be calculated simultaneously. This can be done only off-line.

Among the three kinds of spline functions described above, the shortcoming of the *x*-spline is that there is an abrupt change of acceleration. Although the fourth-order spline function can be calculated on line, the error is large. If the on-line calculation is not considered, then the 4-3-4 spline has the fewest shortcomings. This kind of spline function was used in the present design. The matrix coefficients were strictly diagonal and non-reduced and the non-inferior solution could be obtained by the Gauss elimination method. Therefore, it can be used directly and completed using a 16-bit computer.

The 4-3-4 spline function guarantees the optimum (shortest) trajectory and the anticipated location, velocity and acceleration. In the 4-3-4 spline function, a fourth-order function was used for the interpolation function in the starting and ending stages.

$$\theta(t) = A_1 + A_2 t + A_3 t^2 + A_4 t^3 + A_t t^4 \qquad [15.11]$$

In the central stage, a third-order function was used as the interpolation function

$$\theta(t) = B_1 + B_2 t + B_3 t^2 + B_4 t^3 \qquad [15.12]$$

where $\theta(t)$ = angle of the joint at moment t and A_i, B_j = are the coefficients of the spline function.

The coefficients for the spline function can be found from the boundary conditions, which are that the velocity and initial acceleration at the starting point and the ending point are zero, and that the location, velocity and acceleration in the central interval are continuous.

15.2.1.5 Control system

The three main axes of the robot were driven by servomotors and were closed-loop controlled. The wrist was controlled by a stepping motor and was open-loop controlled. The end effecter settings (on, off) were controlled by a compressed-air cylinder and magnetic valves.

Figure 15.18 shows the block diagram of the control system. A pair of gears, the ratio of which was 246:29, transmitted and amplified the turning angle of the body to a 10-turn potential meter, which provided output signals via a 12-bit A/D converter to the computer. The arm and shoulder joints were connected to an encoder having 1000 pulses per turn. With the aid of an electronic circuit, the resolution was up to 4000 pulses per turn. The pulse counter, which provided 12-bit data to the computer, was self-designed and fabricated.

The anticipated value (or the reference) of the location can be obtained using the 4-3-4-spline function. The computer output three signals after the reference values were compared with the feedback signal, and transmitted them to the servo-amplifier via a D/A converter. Each of the amplifiers was connected to a DC servomotor. For each servomotor there was a tachometer-generator, which was used to generate the velocity negative

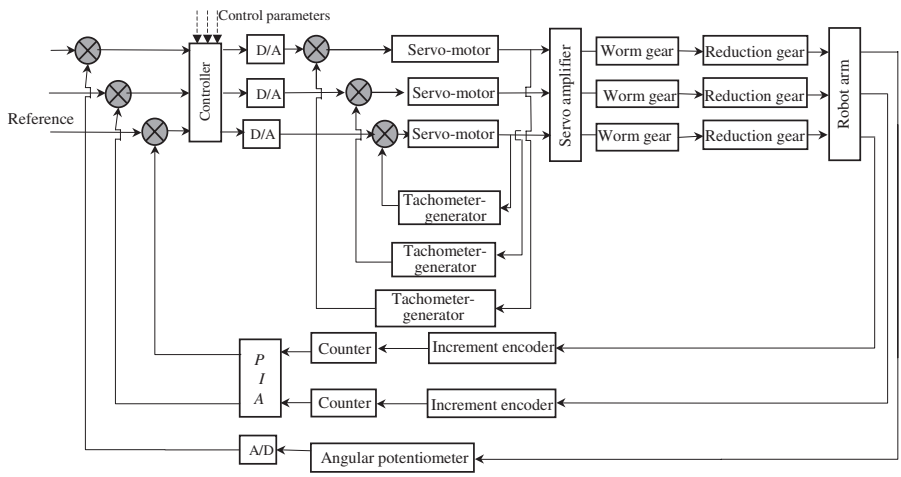

15.18 Block diagram of the robot-control system

feed-back signal. The servomotors drove the joints via a worm gear and a reduction gearbox.

Two control method, namely, *P* and *PI* digital closed-loop control, were used for the drive system. The integral element was used to eliminate errors while lifting and bending.

All three joints should operate according to the 3D reference value so that the robot would move according to a definite curve.

Figure 15.19 shows the open-loop control system of the wrist. The reference values of its lift-bending angle, turning angle, lift-bending velocity and turning speed were input to the microcomputer using a keyboard. The computer converted the signals into pulse numbers and pulse frequencies to control the two stepping motors. Because the angular movement of the stepping motor was stable, no reduction mechanism or control program were used.

15.2.1.6 Velocity of movement

Because there was no instrument for accurately measuring the 3D trajectory, the movement of each joint was repeated and recorded. The velocity of the hand was calculated from these data. Figures 15.20, 15.21 and 15.22 show the movements measured for each joint. From these data, the velocity of the hand was found to be less them 1 m/s, which was in the allowable normal range.

15.2.2 Vision system

Before designing the hardware and software of the vision system, determining the imaging method and the method for locating its position were necessary. The camera should be able to locate itself automatically, quickly and accurately, without human intervention. There are four methods for

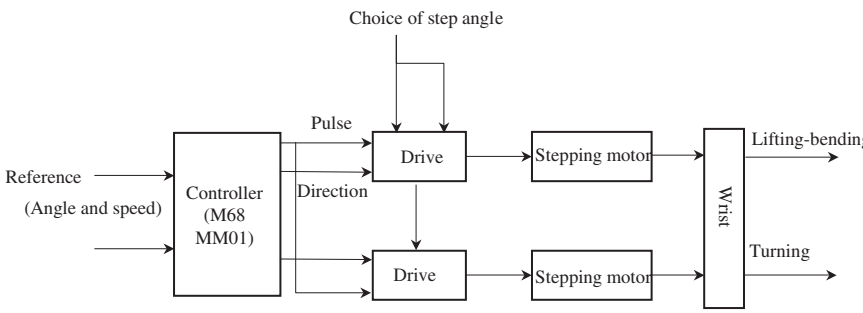

15.19 Open-loop control of wrist

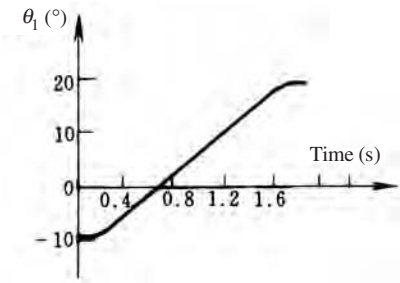

15.20 Turning of column −10° to 20°

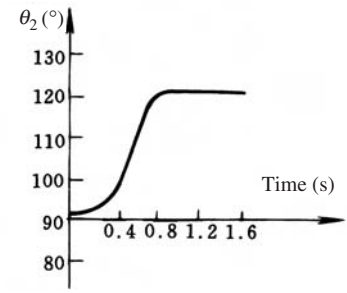

15.21 Turning of shoulder joint 90° to 120°

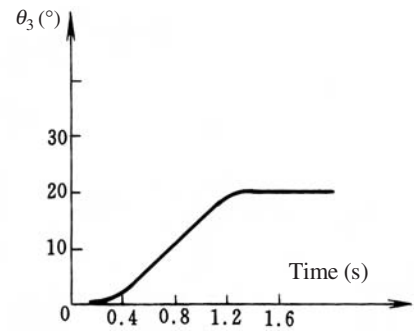

15.22 Turning of wrist joint 0° to 20°

identifying location. The first is the non-shallow full-scale optimizing method.[373] It is accurate but needs non-shallow searching. This searching is not independent and also is not effective. The second is the two-plane method.[374] Its advantage is its high efficiency, but an empirical formula is needed for the transformation between the object and the image. The third

is the geometric method.[375] In this method, knowing the focus length is necessary and the calculation is complicated. The fourth method, developed by Yakimovski and Cunningham,[376] which was used in the present design, was based on 3D measurement from a stereo pair of TV cameras. The transformation matrix was calculated using linear equations; the linearity was true if there was no distortion of the image by the lens. Errors in this method resulted mainly from the linear dependence of the unknown parameters solved by the linear equations. In the present case, the field of view was not large. The distance between the object and the camera was short so the error that resulted was small and acceptable. The other sources of error were the accuracy of repeatability of the robot, the 3D point and the predetermined centre point of the work piece. Normally, to determine a space point, a half line in the 3D space on which the point is located is taken. Because two cameras were used, the intersection of these two lines was used to determine the space point.[376] In practice, the two rays may not intersect at a point. Then, as a remedial measure, the middle point of the shortest line between these two rays is used to locate the space point. This is the original point of the measuring method.

The hardware and software used for the system are described below.

15.2.2.1 Hardware

Vision system. The software program was designed using C language on the IRID256 vision system (see Fig. 15.23). In the IRID256 vision system, the computer uses the UNIX operating system. The system consisted of a computer, camera-interface module, video-digitalisation module, image buffer,

15.23 IRIO256 vision system

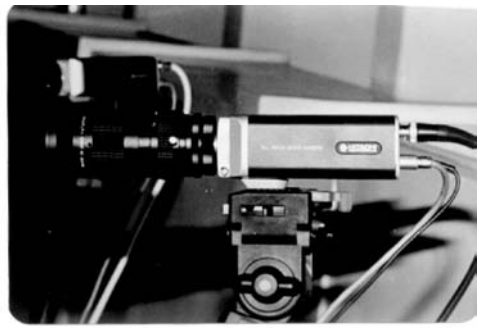

15.24 Hitachi KP-120U camera

image processor, etc. It can process 256 × 256 pixels with 256 grey levels. There is a software package called the 'Image core program package' that includes 100 standard vision programs such as image display, extraction of characteristic objects, strengthening of the characteristic objects and image segmentation.

Camera. Two Hitachi KP-120U CCD cameras were used (Fig. 15.24). Their resolution was 240 × 256 pixels. There was a lens that could be used for focusing, zooming and controlling exposure.

15.2.2.2 Software

Two software packages were needed for the vision system. One program was developed for the IRID256 system and the other was developed for the robot. C-language was used for both programs.

(i) *Image-recognition program*. The program consisted of two parts, namely, calibration of the camera, and recognition of the weld groove and control of the welding process. These two programs were called the '3D vision' program. The function of calibration was to determine the co-ordinates of the robot and its relation with the parameters of the camera. The details of this will be discussed in Section 15.2.3.

The flow chart for recognition of the weld groove is shown in Fig. 15.25.

(ii) *Trajectory of the weld groove and the robot program.* When the relationship between the camera and robot co-ordinates was determined, the camera could be used to observe the 3D space lines. According to the 2D images obtained by the two cameras, the 3D co-ordinates of any space point could be obtained. Then, the parameters for the joints of the robot can be calculated using the quaternion criterion. Finally, the 3D co-ordinates and the joint locations were fed to the location register.

During welding, the work piece was positioned 1.3 m from the camera. After filtering and line grouping, the lines and their intersecting points were

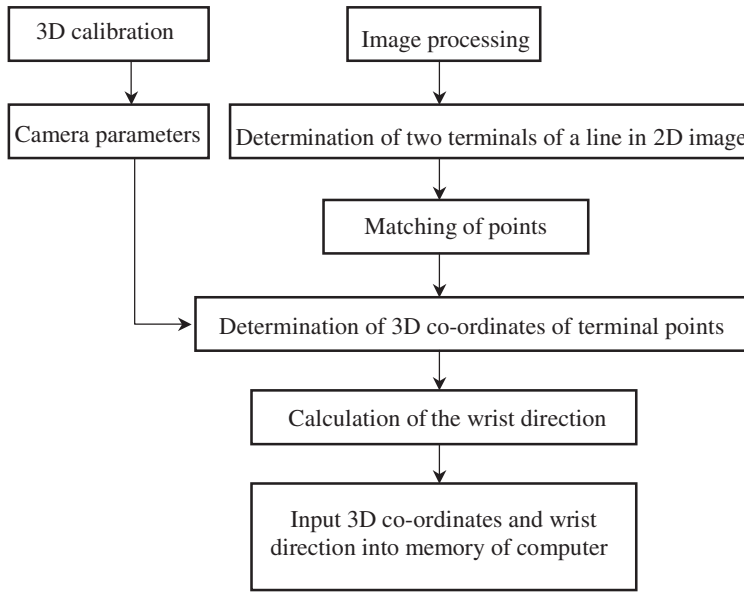

15.25 Flow chart for the vision program

obtained. The data after the 3D co-ordinate transformation, V-groove co-ordinate calculation, and quaternion calculation, were transmitted to the IBM AT computer via a subprogram called MITE. This program transmitted the data into the VME single-board computer via an RS232C port to control the robot. The recognition of the weld trajectory will be introduced in Section 15.2.4.

15.2.3 Calibration of the camera co-ordinates

15.2.3.1 Introduction

The camera was calibrated to determine its inner geometric parameters, its inherent optical characteristics and the relationship with external co-ordinates.

The extraction of 3D co-ordinates from 2D images was an important capability, for example, for the measurement of component dimensions, assembly of the mechanical and electronic parts, and welding-path analysis. Calibration provided the method to obtain the 3D point in space from the images projected by the point to the two cameras.

The model, algorithm and calibration procedure are described first. Then the data measured in practice are provided.

15.2.3.2 Model of the camera

The CCD of the camera consisted of 240 × 256 optically sensitive pixels. The pixels were indicated by (I, J), where $0 \le I \le 239$ and $0 \le J \le 255$. The aim of establishing the model was to find the algorithm by which the camera parameters could be obtained. Thus, the pixel (I, J) could be correlated to the corresponding ray $C + \lambda \cdot R(I, J)$, see Fig. 15.26, where C are the 3 D co-ordinates of focus, λ is the distance from C to the space point P, and $R(I, J)$ is the unit vector in the direction from C to P.

Suppose that the optical system is linear, which can be obtained using a high-quality lens and linear sensor, then the 3D model of the vision system can be illustrated as shown in Fig. 15.27.

In Fig. 15.27, the projected image of the real point P in space on the first camera is $T_1 = (I_1, J_1)$. C_1 and C_2 are vectors of the two focus points, which are measured on the basis of external co-ordinates. Therefore $P - C$ is a vector from the focus point to P. $A_1(A_2)$ are unit vectors that point in the direction of the optical axis of the first camera (or the second). The unit vectors H' and V' are two vectors; H' is parallel to the camera image horizontal line and V' is parallel to the camera-image vertical line. A, H' and V' are three orthogonal vectors.

The co-ordinates of the points on image (I, J) also can be expressed as $(I' + I_0, J' + J_0)$ where (I_0, J_0) is the centre of the image (see R_1, R_2 in Fig. 15.27). (I', J') are the deviation from the image centre. In the following derivation, the properties of the scalar product of vector X, Y, Z and the scalar C are often used. (X, Y) represents the scalar product of vectors X and Y. The properties are

$$C \cdot (X, Y) = (C \cdot X, Y) = (X, C \cdot Y) \quad [15.13]$$

$$(X, Y) + (X, Z) = (X, Y + Z) \quad [15.14]$$

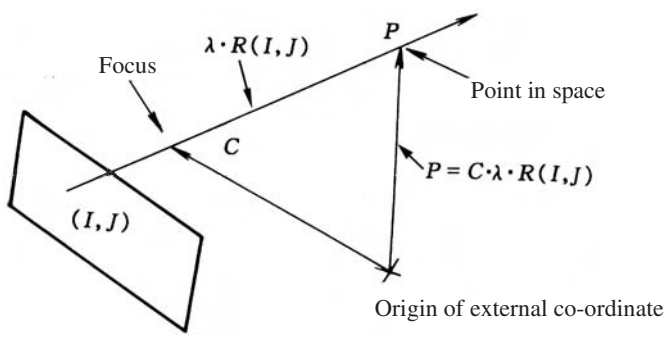

15.26 Image point (*I, J*) and real point *P*

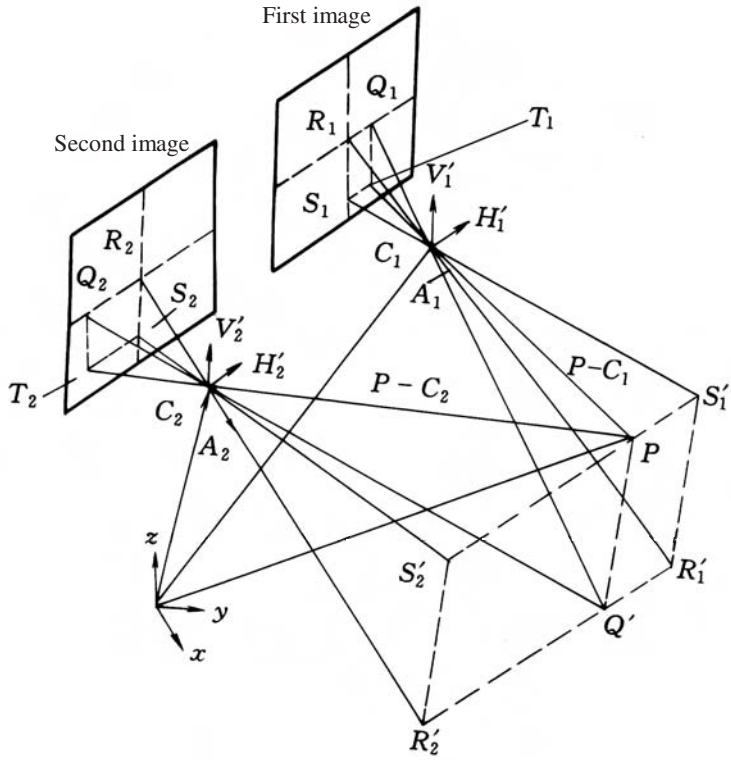

15.27 Model of vision system *P*-point in space

In the following text, (A, B) represents the scalar product, $(A \times B)$ is the vector product and $(C \cdot Y)$ is the product of the scalar and the vector; the other representations are analogues of this.

In the following text, the relationships of 2D co-ordinates (I, J) and 3D vectors C, A, H', V' and P were derived, based on the geometry given by Fig. 15.27.

$$-\frac{\ell(R_1Q_1)}{\ell(R_1C_1)} = \frac{\ell(R_1'Q')}{\ell(R_1'C_1)} \qquad [15.15]$$

where $\ell(R_1Q_1)$ is the length of R_1Q_1.

Because $\ell(R_1Q_1) = \ell(S_1T_1)$ and $\ell(R_1'Q') = \ell(S_1'P)$, Eq. [15.15] becomes

$$\frac{\ell(S_1T_1)}{\ell(R_1C_1)} = \frac{\ell(S_1'P)}{\ell(R_1'C_1)} \qquad [15.16]$$

where S_1T_1 is the horizontal deviation I'_1 from the image centre to T_1.

The length R_1C_1 is the focus length f_1. Because R_1C_1 and A_1 are in the same direction, A_1 is a unit vector. Therefore, the length $R_1'C_1$ can be

expressed as $(P - C_1, H_1')$. Similarly, because $S_1'P$ is parallel to H_1', the length $S_1'P$ is therefore $(P - C_1, H_1')$. Then Eq. [15.16] can be rewritten as

$$\frac{I_1'}{f_1} = \frac{(P - C_1, H_1')}{(P - C_1, A_1)}$$

or

$$I_1' = \frac{f_1 \cdot (P - C_1, H_1')}{(P - C_1, A_1)}$$

From Eq. [15.13] one obtains

$$I' = \frac{(P - C_1, f_1 \cdot H_1')}{(P - C_1, A_1)}$$

Because $I_1 = I_1' + I_0$ one can obtain $I_1 = \dfrac{(P - C_1, f_1 \cdot H_1')}{(P - C_1, A_1)} + I_0$ [15.17]

According to the scalar-product property, Eq. [15.17] can be converted to

$$I_1 = \frac{(P - C_1, f_1 \cdot H_1') + I_0 \cdot (P - C_1, A_1)}{(P - C_1, A_1)}$$

From Eq. [15.13]

$$I_1 = \frac{(P - C_1, f_1 \cdot H_1') + (P - C_1, I_0 \cdot A_1)}{(P - C_1, A_1)}$$

By Eq. [15.14] the following is shown

$$I_1 = \frac{(P - C_1) + (f_1 \cdot H_1' + I_0 \cdot A_1)}{(P - C_1, A_1)} \quad [15.18]$$

From the following relationship, i.e.

$$\frac{\ell(R_1S_1)}{\ell(R_1C_1)} = \frac{\ell(R_1'S_1')}{\ell(R_1'C_1')}$$

the result similar to Eq. [15.18] can be obtained as

$$J_1 = \frac{(P - C_1) + (f_1 \cdot V_1' + J_0 \cdot A_1)}{(P - C_1, A_1)} \quad [15.19]$$

Let $H_1 = f_1 \cdot H_1' + I_0 A_1$ and $V_1 = f_1 \cdot V_1' + I_0 A_1$
Equations [15.18] and [15.19] can then be rewritten as

$$I_1 = \frac{(P - C_1, H_1)}{(P - C_1, A_1)} \quad [15.20]$$

$$J_1 = \frac{(P - C_1, V_1)}{(P - C_1, A_1)} \quad [15.21]$$

Thus H_1 has two components, $f_1 \cdot H_1'$ and $I_0 \cdot A_1$. The term $f_1 \cdot H_1'$ is parallel to the image horizontal line; its length equals the focus length of the first camera. $I_0 \cdot A_1$ is parallel to A_1 and I_0 is the image centre; therefore its length equals one half of the number of pixel's of the image of each line.

Similarly, the two components of V_1 are, first, the length of f_1 parallel to the vertical line of the image component and, second, the length of J_0 parallel to the A_1 component. For the second camera, H_2 and V_2 correspond to H_1 and V_1. Therefore the following equations can be written:

$$I_2 = \frac{(P - C_2, H_2)}{(P - C_2, A_2)} \qquad [15.22]$$

$$J_2 = \frac{(P - C_2, V_2)}{(P - C_2, A_2)} \qquad [15.23]$$

15.2.3.3 Calibration algorithm

The aim of calibration was to determine C, A, H and V. Each of the two cameras was calibrated separately.

For calibration, n space points (the co-ordinates of which are known) are needed to project to both cameras. Their images $(i, j) \ldots, (i_m, j_m)$ were recorded and stored in the memory of the computer. For this purpose, a special body was made on which a fiducial mark was drawn as a characteristic point. The robot hand grasped the body and moved it to n specific points. The space co-ordinates of the points P_m could be obtained directly from the robot control board. The characteristic point could be found automatically by the robot. The images of these points $(i, j) \ldots, (i_m, j_m)$ were then taken from the camera. Substituting P_m, i_m and j_m into Equations [15.20], [15.21], [15.22] and [15.23], C, A, H and V can be solved.

(i) *Establishment of equations*. Substituting P_m, i_m and j_m into Equations [15.20] and [15.22] gives

$$i_m = \frac{(P_m - C, H)}{(P_m - C, A)} \qquad [15.24]$$

or

$$i_m \cdot (P_m - C, A) = (P_m - C, H)$$

or

$$i_m \cdot (P_m - C, A) - (P_m - C, H) = 0$$

According to the scalar product property given by Eq. [15.13], the equation above becomes

$$(P_m - C, i_m \cdot A) - (P_m - C, H) = 0$$

According to Eq. [15.14], the following is obtained:

$$(P_m, i_m \cdot A) - (C, i_m \cdot A) - (P_m, H) + (C, H) = 0 \qquad [15.25]$$

Let

$$P_m = \begin{bmatrix} P_{m1} \\ P_{m2} \\ P_{m3} \end{bmatrix} \quad C_i = \begin{bmatrix} C_{i1} \\ C_{i2} \\ C_{i3} \end{bmatrix} \quad A_i = \begin{bmatrix} A_{i1} \\ A_{i2} \\ A_{i3} \end{bmatrix} \quad H_i = \begin{bmatrix} H_{i1} \\ H_{i2} \\ H_{i3} \end{bmatrix},$$

represent the (x, y, z) components of P_m,C, A, H (where i indicates camera 1 or 2) and let

$$C_H = (C, H) \text{ and } C_A = (C, A)$$

Then the following homogeneous equation can be established:

$$\begin{aligned}(P_{m1} \cdot i_m)A_{i1} + (P_{m2} \cdot i_m)A_{i2} + (P_{m3} \cdot i_m)A_{i3} - P_{m1} \cdot H_{i1} \\ - P_{m2} \cdot H_{i2} - P_{m3} \cdot H_{i3} - i_m \cdot C_{iA} + C_{iH} = 0\end{aligned} \qquad [15.26]$$

Similarly, from Equations [15.21] and [15.23] the following is obtained.

$$\begin{aligned}(P_{m1} \cdot j_m)A_{i1} + (P_{m2} \cdot j_m)A_{i2} + (P_{m3} \cdot j_m)A_{i3} - P_{m1} \cdot V_{i1} \\ - P_{m2} \cdot V_{i2} - P_{m3} \cdot V_{i3} - j_m \cdot C_{iA} + C_{iV} = 0\end{aligned} \qquad [15.27]$$

where $m = 1, \ldots\ldots, n \quad n \geq 6$

In order to simplify the formula, one camera is taken as an example and the note 'i' is not indicated. There are 12 unknowns in Eq. [15.27], namely, A_1, A_2, A_3, H_1, H_2, H_3 and V_1, V_2, V_3, C_A, C_H, C_V. These parameters can be solved by sampling n observations. The symbol n means n groups of corresponding 3D and 2D data. Because there are 12 unknowns for each camera, 2 equations are needed for each camera in every observation. Therefore n should be equal to or greater than 6. Equations [15.26] and [15.27] can be written in matrix form as

$$\begin{bmatrix} P_{11}i_1 & P_{12}i_1 & P_{13}i_1 & -P_{11} & -P_{12} & -P_{13} & 0 & 0 & 0 & -i_1 & 1 & 0 \\ P_{11}j_1 & P_{12}j_1 & P_{13}j_1 & 0 & 0 & 0 & -P_{11} & -P_{12} & -P_{13} & -j_1 & 0 & 1 \\ \bullet & & & & & & & & & & & \bullet \\ \bullet & & & & & & & & & & & \bullet \\ \bullet & & & & & & & & & & & \bullet \\ \bullet & & & & & & & & & & & \bullet \\ \bullet & & & & & & & & & & & \bullet \\ \bullet & & & & & & & & & & & \bullet \\ \bullet & & & & & & & & & & & \bullet \\ \bullet & & & & & & & & & & & \bullet \\ P_{n1}i_n & P_{n2}i_n & P_{n3}i_n & -P_{n1} & -P_{n2} & -P_{n3} & 0 & 0 & 0 & -i_n & 1 & 0 \\ P_{n1}j_n & P_{n2}j_n & P_{n3}j_n & 0 & 0 & 0 & -P_{n1} & -P_{n2} & -P_{n3} & -j_n & 0 & 1 \end{bmatrix} * \begin{bmatrix} A_1 \\ A_2 \\ A_3 \\ H_1 \\ H_2 \\ H_3 \\ V_1 \\ V_2 \\ V_3 \\ C_A \\ C_H \\ C_V \end{bmatrix} = \begin{bmatrix} 0 \\ \bullet \\ \bullet \\ \bullet \\ \bullet \\ \bullet \\ \bullet \\ \bullet \\ \bullet \\ \bullet \\ \bullet \\ \bullet \end{bmatrix}$$

For an invalid solution, let $A_1 = 1$ (suppose $A_1 \neq 0$) and rewrite the matrix equation above as follows.

$$\underbrace{\begin{bmatrix} P_{12}i_1 & P_{13}i_1 & -P_{11} & -P_{12} & -P_{13} & 0 & 0 & 0 & -i_1 & 1 & 0 \\ P_{12}j_1 & P_{13}j_1 & 0 & 0 & 0 & -P_{11} & -P_{12} & -P_{13} & -j_1 & 0 & 1 \\ \bullet & & & & & & & & & & \\ \bullet & & & & & & & & & & \\ \bullet & & & & & & & & & & \\ \bullet & & & & & & & & & & \\ \bullet & & & & & & & & & & \\ \bullet & & & & & & & & & & \\ \bullet & & & & & & & & & & \\ P_{n2}i_n & P_{n3}i_n & -P_{n1} & -P_{n2} & -P_{n3} & 0 & 0 & 0 & -i_n & 1 & 0 \\ P_{n2}j_n & P_{n3}j_n & 0 & 0 & 0 & -P_{n1} & -P_{n2} & -P_{n3} & -j_n & 0 & 1 \end{bmatrix}}_{[D]} \underbrace{\begin{bmatrix} A_2 \\ A_3 \\ H_1 \\ H_2 \\ H_3 \\ V_1 \\ V_2 \\ V_3 \\ C_A \\ C_H \\ C_V \end{bmatrix}}_{[X]} = \underbrace{\begin{bmatrix} -P_{11}i_1 \\ -P_{11}j_1 \\ \bullet \\ \bullet \\ \bullet \\ \bullet \\ \bullet \\ \bullet \\ \bullet \\ -P_{n1}i_n \\ -P_{n1}j_n \end{bmatrix}}_{[B]}$$

Thus, the number of equations is more than the number of unknowns in the observations ($n \geq 6$). Using the symbols for matrices, the equation above can be written as $[D][X] = [B]$. The solution for the camera parameters can be solved by multi-linear regression analysis, i.e.

$$[D]^T[D][X] = [D]^T[B]$$

where $[D]$ is a $2n \times 11$ matrix, $[X]$ and $[D]^T[B]$ are 11×1 matrices, and $[D]^T[D]$ is an 11×11 matrix. Using a Gaussian elimination, the unknowns can be obtained.

Then, let vector $A = [A_1A_2A_3]^T = 1$. Now, all other parameters can be described in terms of A. Finally, $C = [C_1C_2C_3]^T$ can be calculated by the following equations:

$$C_A = (C, A) \quad \text{or} \quad C_A = C_1A_1 + C_2A_2 + C_3A_3$$

$$C_H = (C, H) \quad \text{or} \quad C_H = C_1H_1 + C_2H_2 + C_3H_3$$

$$C_V = (C, V) \quad \text{or} \quad C_V = C_1V_1 + C_2V_2 + C_3V_3$$

(ii) *Co-ordinates of the characteristic point*. The 2D co-ordinates on the image and the 3D co-ordinates in space for each observation must be known for calibration. Figure 15.28 shows the body where the characteristic point was located at the centre of gravity of the square.

The centre point of the gripper (TCP), that is the characteristic point, was determined by the characteristic vector pointed at by TCPϕ (the gripper centre provided by the robot). The location of the TCP was preset on the robot controller. After setting the TCP location, the 3D co-ordinates of the characteristic points were determined and transmitted to the vision system.

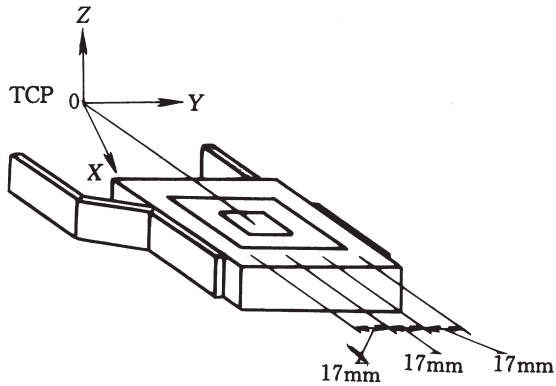

15.28 Characteristic point for calibration

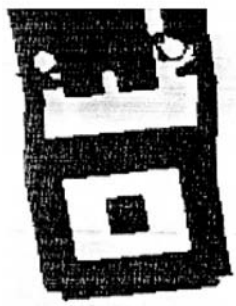

15.29 Image from the first camera

Figures 15.29 and 15.30 are the images after digital filtering of the characteristic point on the gripper.

In the meantime, the 2D co-ordinates of the characteristic point can be obtained using an algorithm for image recognition. First, the object on the gripper was moved to face the camera. Then, the computer (D256) recorded this image and converted it into a digital image as shown in Figures 15.29 and 15.30. The grey level of the image was 0–255. In order to find the characteristic point, the inner square was separated using the following procedure:

a. The computer scanned from the upper-left pixel ($i = 0, j = 0$). Initially, i was fixed and j varied from 0–255. Then i was increased until $i = 240$. The transition point between white and black was determined.
b. The ratio of white length to black length was determined. Taking Fig. 15.31 as an example, let (i_1, j_1), (i_2, j_2) and (i_3, j_3) be the transition points; then the ratio is

15.30 Image from the second camera

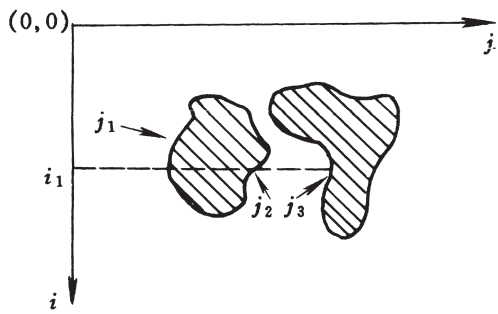

15.31 Length ratio of black and white lines

$$\text{Length ratio} = \frac{j_3 - j_2}{j_2 - j_1}$$

c. If the ratio was between 0.88~1.12 and $(j_3 - j_2) \geq 20$ pixels, then scanning continued at $(i_1 + 5, j_2 - 5)$. If the white-to-black transition appeared (Fig. 15.32), and the length ratio for j_4, j_5, j_6 was kept at 0.88~1.12, then the characteristic object was considered to have been found. The condition that $(j_3 - j_2) \geq 20$ was established to avoid being unable to recognise the object. The orientation of the object had no significant influence because the length ratio would not be changed once the object could be seen. Because the light intensity could vary over some range, the range of 0.88~1.12 therefore was selected. The square cannot be recognised under the following conditions, shown in Fig. 15.33. In Example (i), only one line satisfies the length-ratio criterion. In Example (ii), the length-ratio criterion cannot be satisfied because parts of the square are not on the image. In Example (iii),

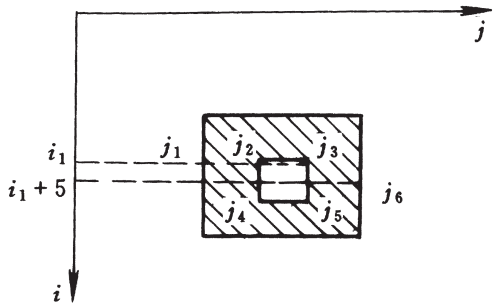

15.32 Black and white transition on the characteristic object

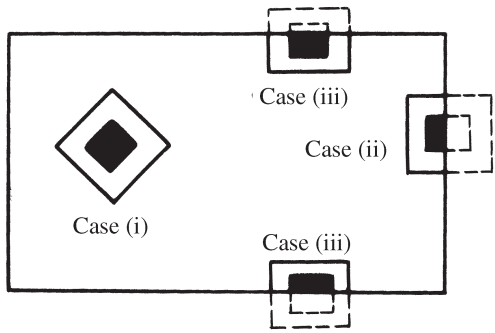

15.33 Examples of undetectable characteristic points

although the length-ratio criterion is satisfied, part of the inner square is not in the image.

d. The inner square was extracted using the following procedure:
   - A certain grey level was applied to the square, for example a level of 128.
   - All of the pixels having a grey level of 255 were removed, which meant substituting 0 for 255.

   Then only the image of square would remain in the image. The characteristic point could then be extracted easily, using the standard vision program.

15.2.3.4 Determining space points using two images

The parameters obtained by calibration of the camera were used to find the function representing space points. The image (I_1, J_1) of point P in the first camera should satisfy Equations [15.20] and [15.21]. The co-ordinates of P were derived using these equations as follows:

On the basis of Eq. [15.25] and Eq. [15.14], Equations [15.20] and [15.21], i.e.

$$I_1 = \frac{(P - C_1, H_1)}{(P - C_1, A_1)} \quad \text{and} \quad J_1 = \frac{(P - C_1, V_1)}{(P - C_1, A_1)}$$

can be converted into

$$(P - C_1, H_1 - I_1 \cdot A_1) = 0 \quad \text{and} \quad (P - C_1, V_1 - J_1 \cdot A_1) = 0.$$

Therefore $P - C_1$ and $(H_1 - I_1 \cdot A_1)$, $(V_1 - J_1 \cdot A_1)$ are orthogonal and the following equations can be obtained:

$$(P - C_1) // (V_1 - J_1 \cdot A_1) \times (H_1 - I_1 \cdot A_1)$$

or

$$P = C_1 + \lambda \cdot R_1(I_1, J_1) \quad \lambda > 0 \tag{15.28}$$

where

$$R_1(I_1, J_1) // (V_1 - J_1 \cdot A_1) \times (H_1 - I_1 \cdot A_1)$$

Because $R_1(I_1, J_1)$ is a unit vector, when the co-ordinates on image (I_1, J_1) are known for a space point P, P must be on the line L_1 in space, which can be expressed as

$$L_1 = C_1 + \lambda \cdot R_1(I_1, J_1) \quad 0 < \lambda < +\infty$$

Projection of any point from this line to the second camera can be found from Equations [15.22] and [15.23]. Suppose that projections of two points from this line on camera 2 are $T_n(I_n, J_n)$ and $T_f(I_f, J_f)$. $T_n(I_n, J_n)$ is the point located nearer to camera 1 and $T_f(I_f, J_f)$ is a point located farther from camera 1. Then, the projection of point P on the second camera will be a point on the line connecting $T_n(I_n, J_n)$ and $T_f(I_f, J_f)$. The location of this point can be found manually by computer scanning or it can be found automatically using an algorithm. Once this point (I_2, J_2) is found, the 3D co-ordinate of P can be calculated. (I_2, J_2) defines a straight line in space.

$$L_2 = C_2 + \lambda \cdot R_2(I_2, J_2)$$

The methods for defining L_1 and L_2 were the same (see Fig. 15.34). Theoretically, P should be located on both L_1 and L_2. Due to digital error resulting from calibration, these two lines may not intersect. In order to find the point P, first find P_1 on line L_1, whose distance to L_2 is shortest. Then find P_2 on line L_2, whose distance to L_1 is shortest. Then, the middle point of line P_1P_2 is considered to be the point in space that was sought. The distance from any point X to the straight line $C + \lambda \cdot R$ is

$$\sqrt{\|X - C\|^2 - (X - C, R)^2}$$

Let P_1 be a point on $L_1 = (C_1 + \lambda \cdot R_1)$ and suppose that the distance from P_1 to L_2 is minimum when $\lambda = \lambda_1$. Then, the square of the distance is

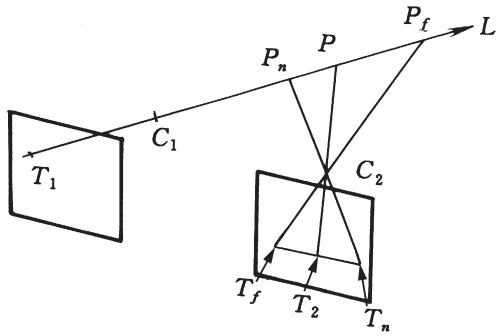

15.34 The image of point *P* on the second camera

$$\|P_1 - C_2\|^2 - (P_1 - C_2, R_2)^2$$

or
$$\|C_1 + \lambda_1 \cdot R_1 - C_2\|^2 - (C_1 + \lambda_1 \cdot R_1 - C_2, R_2)^2$$

Differentiate the equation by λ_1 and let it equal zero. This gives

$$(2 \cdot R_1, C_1 + \lambda_1 \cdot R_1 - C_2) - 2 \cdot (R_1, R_2) \cdot (C_1 + \lambda_1 \cdot R_1 - C_2, R_2) = 0$$

The following is found from Eq. [15.13]:

$$(R_1, C_1 - C_2 + \lambda_1 R_1) = (R_1, R_2) \cdot (C_1 - C_2, R_2) + \lambda_1 \cdot (R_1, R_2) \cdot (R_1, R_2),$$

or
$$(R_1, C_1 - C_2) + \lambda_1 (R_1, R_1) = (C_1 - C_2, (R_1, R_2) \cdot R_2) + \lambda_1 \cdot (R_1, R_2)^2$$

or
$$\lambda_1 \cdot \left(1 - (R_1, R_2)^2\right) = (C_1 - C_2, (R_1, R_2) \cdot R_2)(C_1 - C_2, R_1)$$

From Eq. [15.14]

$$\lambda_1 = \frac{(C_1 - C_2, (R_1, R_2) \cdot R_2 - R_1)}{1 - (R_1, R_2)^2} \qquad [15.29]$$

A similar derivation gives

$$\lambda_2 = \frac{(C_2 - C_1, (R_1, R_2) \cdot (R_1 - R_2)}{1 - (R_1, R_2)^2} \qquad [15.30]$$

After substituting λ_1 and λ_2 into the equation,

$$P_1 = C_1 + \lambda_1 \cdot R_1(I_1, J_1) \qquad [15.31]$$

$$P_2 = C_2 + \lambda_2 \cdot R_2(I_2, J_2) \qquad [15.32]$$

Thus P_1 and P_2 can be found.

The point P in space can be obtained by averaging the values of P_1 and P_2.

In 3D space, P is the middle point of the connecting line P_1P_2. Therefore the 3D co-ordinates of a space point are found from the images of the point in two cameras and co-ordination of the two images.

15.2.3.5 Calibration procedure

As described in Section 15.2.3.1, six or more observations should be performed and 10 are preferred to reduce error. More observations can be used to evaluate the accuracy of the calibration. The steps were as follows:

(i) Clamp the characteristic object in the gripper of the robot.
(ii) Connect the robot, vision system and camera to their power sources.
(iii) Set the camera in an appropriate location, adjust the aperture, zoom in or out from the object and set the focus length.
(iv) Touch '3D vision' on the keyboard to start the calibration program.
(v) Move the object using the control box to a location where it is visible to both cameras. Push key F_1 or F_2 so that image 1 or image 2 can be seen. The moving scope should be in the required working space. The 3D co-ordinates are stored in the robot for calibration.
(vi) Touch the number on the keyboard for the desired number of observations.
(vii) Execute the program according to Step 5. Push 'Return' so that the computer takes the images.
(viii) Repeat Step (vii) until the desired number of observations is completed.
(ix) Touch the number on the keyboard for the desired number of observations, which are used for calibration.

The parameters then will be stored on the hard disk. Figure 15.35 shows the flow chart for the calibration.

15.2.3.6 Calibration results and evaluation of accuracy

Table 15.8 lists the 3D and 2D co-ordinates of the characteristic points. i_1, j_1 and i_2, j_2 represent the 2D co-ordinates of the point in camera 1 and camera 2, respectively. Twenty observations (the 3D co-ordinates are known) were performed. Among them, 10 were used for calibration of the camera parameters. When the camera parameters C, A, H and V are known, the 2D co-ordinates (i_c, j_c) of the 20 points can be calculated. The difference between the calculated 2D co-ordinates and the 2D co-ordinates observed on the image then can be expressed as

$$i_c - i_m = \frac{(P_m - C, H)}{(P_m - C, A)} - i_m$$

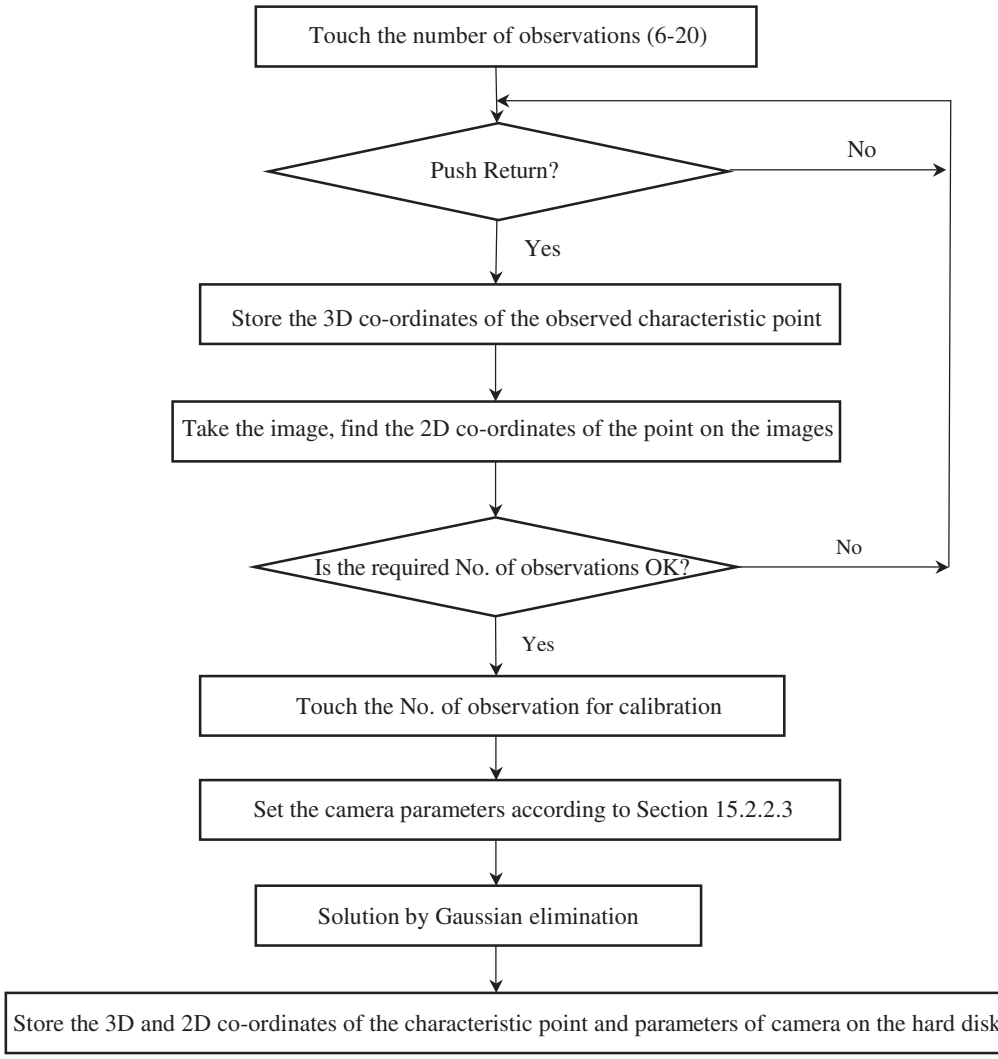

15.35 Flow chart for calibration

Similarly the difference in j is

$$j_c - j_m = \frac{(P_m - C, V)}{(P_m - C, A)} - j_m$$

where P_m are the 3D co-ordinates of the detected point in space
i_m, j_m are the 2D co-ordinates in the image of the detected point

Table 15.8 3D co-ordinates in space and 2D co-ordinates in the image of 20 points

Point No.	3D co-ordinate			Camera 1		Camera 2	
	x (mm)	y (mm)	z (mm)	i_{1m} (Pixel)	j_{1m} (Pixel)	i_{2m} (Pixel)	j_{2m} (Pixel)
1	829.7	–24.6	763.6	117	96	135	107
2	771.4	–46.9	806.2	52	38	63	94
3	789.1	0.4	802.6	67	101	81	152
4	793.7	23.5	749.8	69	133	85	177
5	790.7	47.3	826.3	65	149	78	223
6	837.7	72.4	754.6	113	215	132	215
7	877.2	48.9	780.4	170	184	187	205
8	892.7	11.0	803.6	200	132	216	175
9	890.9	–58.4	786.9	202	56	222	82
10	825.4	–24.5	783.5	115	86	131	116
11	857.9	–9.9	791.4	155	106	172	141
12	835.7	–6.6	775.7	124	113	141	135
13	857.5	14.4	786.5	151	137	167	167
14	865.9	–23.7	750.1	159	108	179	105
15	835.5	–23.7	750.2	123	103	142	102
16	835.5	10.9	797.3	126	125	141	166
17	876.9	–18.4	808.5	184	92	200	140
18	876.5	0.3	830.1	185	105	199	175
19	783.7	–39.3	799.2	66	53	79	102
20	829.7	–24.6	763.6	117	96	135	107

The error in the 2D image was found to be ±0.26 pixel. Because the error of the vision system itself was ±1 pixel, the total error was ±1.26 pixels.

Because the camera parameters C, A, H and V were known, the 3D co-ordinates of P_m could be calculated from the 2D co-ordinates i_m,j_m by backward reasoning. The maximum error of the 3D co-ordinates was ±1.0 mm. By comparing the calculated 3D co-ordinates with the actual co-ordinates of P_m, it was found that the maximum error of the 3D co-ordinates was ±1.0 mm.

15.2.4 Interface between the vision system and the welding robot

15.2.4.1 Robotic welding

In actual applications, all welding robots are of the arm type, which can flexibly move the welding point to the work piece. Robotic welding has the following advantages compared to manual welding:

- Ability to weld in all positions
- Good weld appearance and quality
- Possibility for using real-time control when an automatic seam-tracking system is incorporated
- Possibility for working in extreme conditions (for example, at high-temperatures).

The key problem in promoting intelligent control of welding robots is the automatic seam tracking. There are two categories of seam tracking systems:

(i) A non-vision type of automatic seam tracking. The sensor for this category is based on the principle of sound, magnetism, capacitance, etc. As described in Chapters 7, 8 and 9, an arc sensor is one of the most promising sensors for seam tracking.
(ii) A vision type of automatic seam tracking. The most popular vision sensor is a scanning laser or other structured light. A camera takes a 2D image and the groove centreline is obtained from the image by data processing. This category of sensor is mature and already commercialised, but it is used mainly for small work pieces. It has not been used for large structures welded at a field site.

15.2.4.2 Vision system and automatic welding

The present study was aimed at welding large structures. It attempts to apply the methods described in Sections 15.2.1, 15.2.2 and 15.2.3 to weld-groove recognition and control of robotic welding.

(i) *Weld-groove recognition*. When the parameters of the vision model are determined, the straight line or curve in space can be recognised. However, in an actual welding environment, two problems are encountered. The first is noise received by the camera from different sources and the second is that the object is not a simple line or curve but is a V–groove. In Section 15.1, weld-groove recognition was discussed in detail. A special groove-recognition method and its software were developed for the present system.

The program consisted of the following parts:

- Calculate the second-order derivative of the grey level (Laplace operator) to find the edge of the groove
- Locate the lines from the continuity of pixels
- Identify the lines using: a) length of line and b) the arrangement and continuity of pixels in each line.

The following is an example in which a line does not exist:

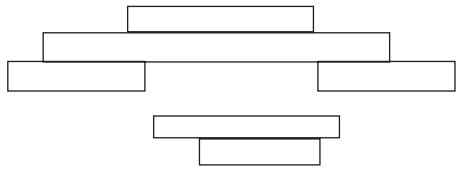

The following is an example in which a line does exist:

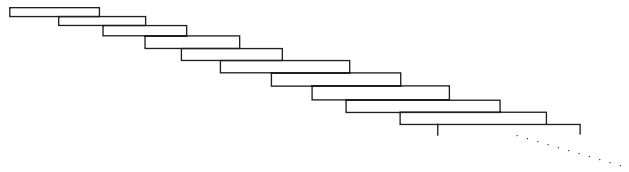

In addition, slope also is a factor that aids recognition. Slope should be used carefully because two lines having different slopes can be incorrectly identified as one line. As an example, the slopes of *ac* and *ad* are nearly the same but the slopes of *ac* and *af* have a larger difference. Therefore, the former are on one line whereas the latter are not on one line.

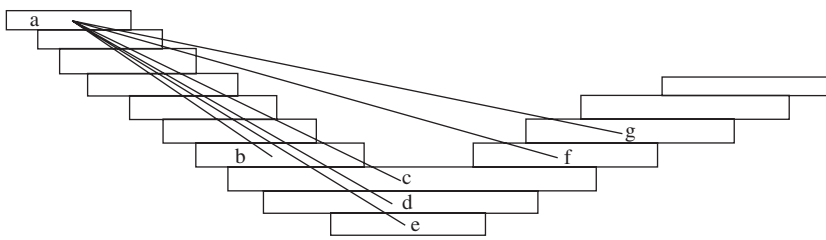

The other way of filtering noise is by monitoring the number of pixels that are continuous. Those lines that do not have many continuous pixels are omitted.

After performing all of the procedures described above, the formula of the line is found by the least-squares method.

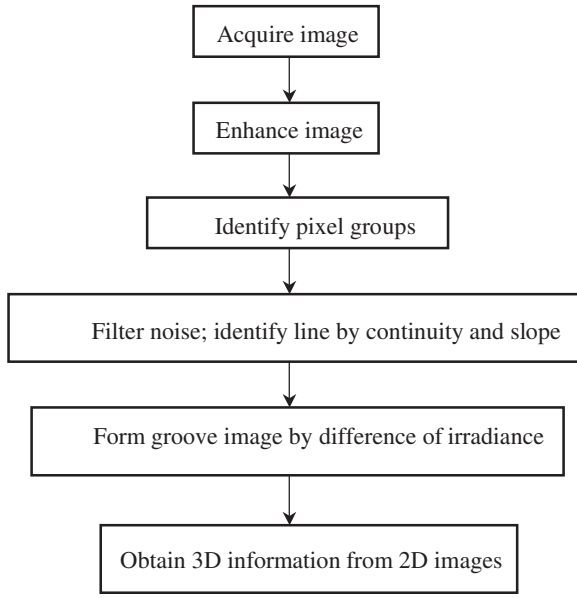

15.36 Flow chart for groove recognition

The irradiance values at the two surfaces of the edge are different, the grey levels are different, the first-order derivative is constant at the edge on both sides but the second-order derivative at the edge is zero.[377]

To eliminate the noise on the image caused by scratches or gouges, a program was written in which a recognised line was taken to compare with the line of a scratch. If the slopes were not close to each other, the scratch line was disregarded.

Once the edge was recognised, the weld groove could be identified with the input data such as width and groove type. In the case of a curved weld, the 3D points and the curve can be constructed from the 2D camera images. Figure 15.36 is the flow chart for groove recognition. Figure 15.37 is the workpiece displayed on the monitor.

(ii) *Signal output from the vision system*. After identifying the weld groove, the IRI D256 vision system stored the data in a database. Because the D256 could not be connected directly to the single-board Motorola VME110 computer, an IBM AT microcomputer was used for an interface. First, the data obtained by the IRI D256 was sent to the IBM AT using the Modems program MITE. The data were converted into an S–record form file and then transmitted to the VME110 single-board computer, see Fig. 15.38.

A high-level language was used for programming the IBM AT computer and the program MITE was used as the intermediary for data transfer.

15.37 Workpiece displayed on monitor

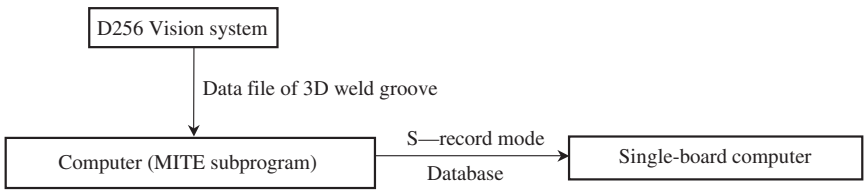

15.38 Data transfer and intermediary

15.2.4.3 MIG welding system

A MIG welding system consists of a power source and a wire feeder. A control box designed for operation of the robot provided the following functions:

- Transfer of the 'start' signal from the robot to the welding system.
- Transfer of the welding system 'ready' to the robot.
- Check the shielding gas.

For safety, two switches were included on the control board, namely, 'Start' and 'Urgent stop'. In addition, there was an automatic 'Urgent stop' control. The welding path was divided into 14 intervals; 15 points were input into the robot. Following a specified interval after a problem arose, the robot would stop.

15.2.5 Practical welding

15.2.5.1 Welding with an ASEA robot

For welding a large structure in the field, an ASEA IRB6/2 robot was used for further experimentation. The data were input to the robot from the D256 vision system as shown in Fig. 15.39. The specimens were 20 cm × 20 cm × 12 mm thick and 20 cm × 10 cm × 12 mm thick, with V–grooves. Welding was performed successfully. The average welding speed was 18 cm/min for improved bead formation. The speed during the starting period was 27 cm/min and the speed during the end period was 14 cm/min for filling the crater.

Because the V–groove depth was large, multi-pass welding was used. After each pass, the torch was shifted laterally and raised a specified distance before the next pass was started, as shown in Fig. 15.40.

According to Section 15.2.3.6, the accuracy of the vision system was ±1.0 mm, and the accuracy of the ASEA robot was ±0.5 mm. The accuracy of the torch position was about ±1.5 mm when the torch was moved along

15.39 ASEA robot and vision system

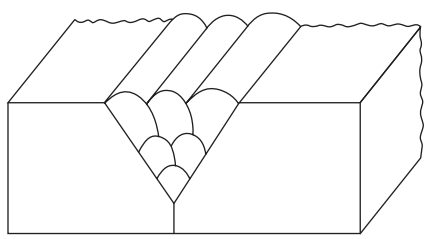

15.40 Multi-pass weld

the weld groove before actual welding. After welding, the positional accuracy of the weld bead was satisfactory. Figure 15.41 demonstrates the welding process performed by the ASEA robot.

15.2.5.2 Welding with a custom-built robot

After the successful experiments on the ASEA robot, a custom-built robot (self-made) was used for further experiments. Figure 15.42 shows the exterior of the custom-built robot. Figure 15.43 shows the welding process in progress and Fig. 15.44 shows the weld made by the robot. Because the

15.41 Welding carried out by ASEA robot

15.42 Exterior of the custom-built robot

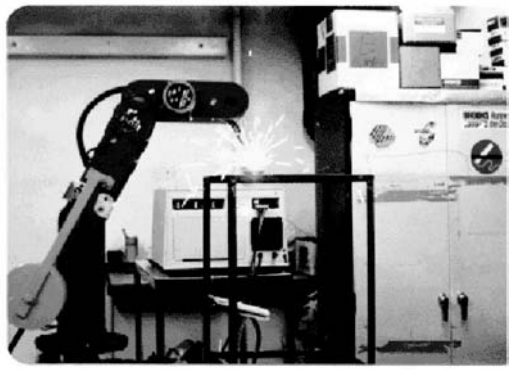

15.43 Custom-built robot during welding

15.44 Appearance of a multi-pass weld

accuracy of the custom-built robot was less than ±1.0 mm, the total error was around ±2.0 mm, which was acceptable for a thick-plate weld.

15.2.5.3 Method for improving accuracy

Weld-path error can be reduced or eliminated using the following measures:

- The accuracy of a CCD camera depends on the density of pixels on the optically-sensitive surface. If a CCD allowing 1024 × 1024 pixels were to be used instead of 240 × 256 pixels, the accuracy would be improved greatly.
- The accuracy of the custom-built robot can be improved.

- The accuracy increases as the area of the viewing field is reduced. In the present case, the viewing field was 20 cm × 20 cm and the distance of the camera from the work piece was 1.3 m. (The accuracy would be even worse if the distance and the size of the viewing field were increased.)

15.2.6 Summary

- The mechanical structure, control system and the trajectory-control system of the custom-built robot were good. The repeatable positioning accuracy was ±2.0 mm and the weight that could be grasped was 2 kg. This robot was satisfactory for the present study.
- The hardware and software developed by the authors for the 3D vision system were satisfactory. The accuracy of the 3D co-ordinates obtained from 2D images was about ±1.0 mm. Because the two rays considered in the present algorithm did not always intersect, the authors proposed using the middle point of the shortest line between these two rays as the intersection point in the 3D space. Experiments proved the correctness of this concept.
- By combining the robot and vision system, automatic weld-path programming was achieved. This work served as an example that illustrated an approach to arc-welding automation.

References

1 Pan, J.L., 'Welding arc control system', 4th Int. Symp. of JWS, Fundamental and Practical Approaches to the Reliability of Welded Structure, (1982), Vol. I, pp. 23–28
2 Pan, J.L., 'Welding arc control system', Chinese J. of Mech. Eng., (1983), No. 1 pp. 1–8 (Chinese)
3 Ou, Z.M., 'Control of MIG welding arc', Doctor's Dissertation, Tsinghua University, (1984) (Chinese)
4 Yu, Y.C., 'Fundamentals of automatic control', Publishing House of National Defence Industries, Beijing, (1985) (Chinese)
5 Katsuhiko Ogata, 'Modern control engineering', Prentice Hall, Englewood Cliffs, NJ, USA (1970)
6 Huang, S.S., 'Dynamic characteristics of arc welding rectifier', Electric Welding Machine, (1986), No. 2 (Chinese)
7 Nikitin, V.P., 'Fundamental theory of arc welding transformer and generator', Publishing House of Academy of Sciences, USSR, Moscow, (1956) (Russian)
8 Rabinowich, E.Y., 'Arc welding machine', National Science and Technology Publishing House, Machine Building Literature, Moscow, (1958) (Russian)
9 P.R. China Speciality Standard, 'Arc welding rectifier', ZBJ 64003-87 (1987) (Chinese)
10 Zheng, Y.T. and Huang, S.S., 'Arc welding power source', China Machine Press, (1989), Beijing, pp. 35–40, (Chinese)
11 Lu, G.Z. *et al*., 'Approach to dynamic properties of SCR manual arc welding machine', Trans. of the China Welding Institution, (1988), No. 2 (Chinese)
12 Lu, G.Z. *et al*., 'A view to China standard about dynamic characteristics of DC arc welding machine', Welding Correspondence, (1985), No. 1 (Chinese)
13 Lu, G.Z. *et al*., 'Study on the relationship between the spattering and characteristics of power source using basic electrode', Welding, (1985), No. 2 (Chinese)
14 Carrier, A. and Girard, V., 'Dynamic behavior of rotating DC arc welding generator', IIW Doc II-244-62
15 Huang, S.S., 'Arc welding power source', China Machine Press, Beijing (1980) (Chinese)
16 Weman, K. and Skarpengl, B., 'Method for analysis of dynamic characteristics of a welding power source' IIW-Commission XII F (1969)
17 Chendu Electric Welding Machine Research Institute, 'Manual arc welding rectifier', Welding, (1973), No. 4 (Chinese)

18 Zhuzhou Electric Welding Machine Factory, 'Discussion on the dynamic characteristics index of arc welding rectifier', (1978) (Chinese)
19 Sasdic, A., 'New rules for assessing the dynamic characteristics of direct current power source for manual arc welding', Welding and Cutting, (1982), 11, E196–198
20 Dorn, L. and Ripple, P., 'Process analysis for metal-arc welding assessing the static and dynamic behaviour of welding generator sets for manual arc welding', Welding and Cutting, (1983), 7, E113–115
21 Ando, K. and Hasegawa, M., 'Welding arc phenomena', China Machine Press, Beijing, (1985) (Translated from Japanese) (Chinese)
22 Kolasa, A., Matsunawa, A. and Arata, Y., 'Experimental study on dynamic properties of power sources for MIG/MAG welding', Transactions of JWRI, Vol. 14, No. 2, (1985), pp. 2–12
23 Xue, J.R., 'A view to the recent detection method of dynamic properties of manual arc welding machine', Welding Technique, (1989), No. 2 (Chinese)
24 Lebede, V.K., Zaruba, I.I. and Lauzhadis, A.I., 'On technological (welding) properties of power sources for arc welding', IIW Doc XIIF-216-80
25 Wang, H.T. *et al*., 'Experimental study on dynamic properties of CO_2 semi-automatic welding power source NBC-400', Electric Welding Machine, (1985), 5 (Chinese)
26 Su, B.S. *et al*., 'Study on dynamic properties of SCR manual arc welding machine', Trans. of the China Welding Institution, (1989), 9 (Chinese)
27 Tong, S.B., 'Fundamentals of analogue electronics', People's Education Publishing House, Beijing, (1980) (Chinese)
28 Hu, S.S., 'Principle of automatic control', Vol. 1, Publishing House of National Defence Industries, Beijing, (1984), 6, (Chinese)
29 Qi, B.J., 'Study on dynamic behaviour of arc welding process and its control', Doctor's Dissertation of Tsinghua University, (1990) (Chinese)
30 Ando, K., Yamamoto, H. *et al*., 'Dip type metal transfer in welding', Journal of JWS, 30, 711 (1961) (Japanese)
31 Potaevski, A.G., 'Gas shielded welding with consumable electrode', Machine Building Press, Moscow, (1974) (Russian)
32 Stadlmann, W., 'Ein Beitrag zur prozessfuhrung beim lichtbogen-schweissen', Doctor's Dissertation of Hannover University, (1976) (German)
33 Rehfeldt, D., 'Verfahren und analysiereinrichtung zur untersuchungder Schweissspannungsschwankungen bei elektroschweissverfahren', Doktor's Dissertation of Hannover University, (1969) (German)
34 Amin, M., 'Synergic pulse MIG welding', Metal Construction, (1981), No. 6
35 Ueguri, S. *et al*., European Patent Application No. 811 05288.5 (1981), Publication No. 0043589
36 Pan, J. *et al*., 'Closed loop controlled pulsed MIG welding', Schweissen und Schneiden, (1985), No. 4
37 Pan, J.L. *et al*., 'Influence of dynamic properties of welding machine to short-circuit metal transfer', Welding, (1979), No. 4 (Chinese)
38 Li, H.Q. and Xiao, G.M., 'Study on SCR non-linear MMA arc welding power source', Gansu University of Technology, (1984), (Chinese)
39 Yu, S.Z., 'CMC-80 Microcomputer-controlled automatic welding of ultra-thin stainless steel', Trans. of the China Welding Institution, (1984) (Chinese)

40 Li, D.Q., Yu, S.S. and Yang, Z.H., 'Study on arc length automatic regulation of AC DC tungsten electrode welding', Trans. of the China Welding Institution, (1983), No. 4 (Chinese)
41 Technical Report of 211 Factory, 'Monitoring technique of welding process by indutrial video', Beijing, (1983) (Chinese)
42 Qi, Z.Y. and Yan, X.M., 'Magnetic characteristics and control of TIG arc in narrow gap', Electric Welding Machine (1981), 1 (Chinese)
43 Zhang, X.Z. and Huang, S.H., 'Calculation of thermal process and its application for pulse welding of thin plate', Proc. National Welding Conf., (1982), CMES WI Doc. H-XII-87-82 (Chinese)
44 Zhang, C.J., 'Overcoming convex bead formation for automatic TIG overhead welding by improving pulse waveform', Welding, (1984), No. 7 (Chinese)
45 He, D.F., Yao, S. *et al.*, 'Penetration-control of pulse plasma welding by double closed loop control', Electric Welding Machine, (1983), No. 5 (Chinese)
46 Liu, M.Q., Wu, H.K. *et al.*, 'Automatic feedback control of plasma welding of drill rod by photo-electronic device', Welding (1980), 10 (Chinese)
47 He, D.F., Zhu, X.B., Yao, S. *et al.*, 'Penetration control system of plasma welding using micro-processor', Plasma Science and Technol., (1984), No. 1 (Chinese)
48 Huang, C.D., Hu, B.X., Tao, A.L. *et al.*, 'Microcomputer control system for plasma welding of boiler S-shape tube by sound signal', Trans. of the China Welding Institution, (1983) (Chinese)
49 Chi, Y.K., Yin, D.X. and Gao, Y.Z., 'Closed loop control for pulse plasma welding penetration', Trans. of the China Welding Institution, (1980), No. 1 (Chinese)
50 Zhao, J.K., Shang, X.H. and Shen, T.Y., 'Study on dynamic characteristics of CO_2 welding power source', Electric Welding Machine, (1980), No. 1 (Chinese)
51 Xu, X.G., Zhu, Q., Yu, M. *et al.*, 'Influence of welding power source parameters to spattering for thick wire CO_2 welding', Welding Correspondence, (1984), No. 1, (Chinese)
52 Song, T.H. and Huo, W.G., 'Study of welding in high pressure CO_2 atmosphere', Welding, (1983), No. 11, (Chinese)
53 Zhai, H.H., Li, C.G. *et al.*, 'Application of multi-segmental output characteristics controller of power source and new type of wire feed soft tube in industries', Welding, (1983), No. 7 (Chinese)
54 Welding Research Institute of 394 Factory of Weapon Manufacturing Ministry, 'Transistorised multi-function power source for gas shielded welding NJGD-500', (1984) (Chinese)
55 Yamamoto, H., 'Recent development of CO_2 MAG welding', Welding Technique, 29(7), (1981) (Japanese)
56 Ji, G.S., Zheng, S.Q. and Zhang, Q.F., 'Study on current waveform and technogical properties of pulsed short-circuit transfer', Technical report of Chengdu Electric Welding Machine Research Inst., Sept. (1987) (Chinese)
57 Wang, Q.L., Yin, S.Y. and Jiang, W.Y., 'New control method of CO_2 short-circuit metal transfer', Welding Correspondence, (1983), No. 4 (Chinese)
58 Qian, J.Y., Zhu, Y.R., Chen, G.S. *et al.*, 'Control of droplet transfer in CO_2-rich welding by pulsed current waveform', North-West Univ. of Technol., Tech. Report, (1981) (Chinese)
59 Matsuda, F., Ushio, M., Iionaga, K. and Yokoo, T., 'Pulsed CO_2 arc welding', IIW Doc 212-586-84

60 Essers, W.G. and Buelens, J.J.C., 'Pulsed wire feed GMA welding using a capstan and a GHP-feed system', IIW Doc XII-C-073-83
61 Ji, Y.G. *et al*., 'New type pulsed wire feed CO_2 welding machine', Proc. of Conf. on application of automatic welding and gas-shielded welding', Internat. Welding Conf., Hangzhou, Sept. (1984) (Chinese)
62 Zhengzhou Mechanical Engineering Research Institute, 'Characteristics of half-cycle pulsed wire feed CO_2 welding', (1980) (Chinese)
63 Zhengzhou Mechanical Engineering Research Institute, 'Technological features and welding parameters of half-cycle pulsed wire feed CO_2 short-circuit welding', (1980) (Chinese)
64 Wang, Q.L. *et al*., 'Control of short-circuit transfer in CO_2 welding by both current waveform and wire feed rate', CMES WI Doc H-XII-001-83 (Chinese)
65 Lin, J.C., Zhao, G.H. and Song, Q.L., 'Effect of sharp-angle magnetic field on CO_2 welding arc and metal transfer', Welding, (1983), No. 11 (Chinese)
66 Matsunawa, A. and Nishiguchi, K., 'Arc characteristics in high-pressure argon atmospheres', Internat. Conf., London, (1979) 5
67 Yamaguchi, T. *et al*., 'Pulsed MIG/MAG welding', Electric Welding Machine, (1983) (Chinese)
68 Lu, B., 'Mathematic model of welding arc', Electric Welding Machine, (1983), No. 5 (Chinese)
69 Wang, Y.S. and Jia, C.S., 'Characteristics of electrode melting and metal transfer of mixed-gas shielded arc welding', CMES WI Doc.H-XII-38-83 (Chinese)
70 Wang, C.L., Yen, S.Y. and Zhang, J.H. *et al*., 'Effects of the luminous region shape on metal transfer mode in MIG welding', 4JWS-I-1
71 Ma, J.L. and Apps, R.L., 'MIG transfer discovery of importance to industry', Welding and Metal Fabrication, September (1982)
72 Ma, J.L. and Apps, R.L., 'New MIG process results from metal transfer mode control', Welding and Metal Fabrication, May (1983)
73 Ma, J.L. and Apps, R.L., 'Analyzing metal transfer during MIG welding', Welding and Metal Fabrication, April (1983)
74 Ukai, J. *et al*., 'Characteristics of pulsed MAG welding using transistorised power source', Electric Welding Machine, (1982) (Translated from Japanese) (Chinese)
75 Lewevjing, W., 'Optimum control of metal transfer in pulsed MIG/MAG welding', Welding Abroad, (1977), No. 4 (Translated from Russian) (Chinese)
76 Maruo, H. and Hirata, Y., 'Effects of welding current waveform on metal transfer and bead formation', The 4th Int. Symp. of JWS, (1982)
77 Lucas, W., Weldl, F., Nasser, A. and Hutt, G.A., 'Process stability in MIG welding', IIW Doc 212-586-84
78 Wang, Q.L., Yin, S.Y. and Qian, Y.Y., 'Control of arc form in pulsed MIG/MAG welding and its significance', Trans. of the China Welding Institution, (1980), No. 1 (Chinese)
79 Wang, Q.L., Yin, S.Y. and Zhang, J.H., 'Study on rational metal transfer form in pulsed MIG/MAG welding', Trans. of the China Welding Institution, (1980), No. 3 (Chinese)
80 Jiang, Y.S. and Fu, B.Z., 'Effect of pulsed current waveform on MIG welding of Al-alloy with small current', CMES WI H-XIIa-028-81 (Chinese)
81 Maruo, H. and Hirata, Y., 'Study on pulsed MIG welding', SG212-585-84

82 Tomsic, M.J., Barhorst, S.E. and Cary, H.B., 'Welding of aluminum with variable polarity power', IIW Doc XII-839-84
83 Kiyohara, M. *et al*., 'On the stabilization for MIG welding of aluminum', IIW Doc XII-C-66-75
84 Fu, X.S., Li, C.X. and Chen, B. *et al*., 'Study on arc stability of MIG welding of Al', CMES WI H-XIIa-012-8 (Chinese)
85 Jiang, H.Z., 'Arc welding and electro-slag welding', China Machine Press, Beijing, pp. 174–176, (1990) (Chinese)
86 Li, H.Q., Li, A.L. and Xiao, G.M., 'Development of constant wire-feed rate constant current MIG welding power source and technological experiments', Trans. of the China Welding Institution, Vol. 5, No. 1, pp. 17–27 (1984) (Chinese)
87 Osaka Transformer Co., 'Transistorised welding power source TR-800', (1980)
88 Nishiguchi, K., 'Power sources used for gas shield arc welding, especially MIG/MAG processes', IIW Doc XII-F-185-77
89 Qu, Z.M., 'QHT-80 transistorised welding power source and control of the arc', Master's Dissertation of Tsinghua University, (1980) (Chinese)
90 Araya, T. and Endo, Y., 'Influence of power sources on the droplet transfer', IIW Doc XII-C-024-81
91 Keyser, D., 'New types of power sources for arc welding', IIW Doc XII-F-204-79
92 Huang, S.S., 'Discussion on electronic welding power source', (1), (2), (3), (4), Electric Welding Machine (1987) No. 2, 3, 4 and 5 (Chinese)
93 Budai, P. and Torstensson, B., 'A power source for advanced welding', Svetsaren (Sweden), (1986), No. 2
94 Rehfeldt, D. and Friedman-Jesnitzer, F., 'New electronic power sources', IIW Doc 212-433-78
95 Needham, J.C., 'A rational approach to arc welding power supplies', IIW Doc XII-F-190-78
96 Weman, K., 'The influence of modern solid-state technology on the development of welding power sources', Svetsaren, No. 1, (1984), inside front cover, plus pp. 1–5
97 Lopes, A.A., Cruz, J.M., Freitas, J.A. *et al*., 'Electronic arc welding power source for DC/AC/AC + DC: PULSARC III', IIW Doc XII-C-082-84
98 Chengdu Electric Welding Machine Research Institute, 'Development of transistorised welding power source', Electric Welding Machine, (1981), No. 5 (Chinese)
99 Huang, Q.Y., 'Analysis of MIG welding power source characteristics with chopped pulse current', Electric Welding Machine, (1981), No. 2 (Chinese)
100 Huang, S.S., 'Status of development and application of pulsed arc welding power source', Welding Correspondence, (1980), 1 (Chinese)
101 Zhao, J.R. *et al*., 'Development of switch mode transistorised arc welding power source', Electric Welding Machine, (1981), (Chinese)
102 Wu, Z.H., 'Study on multi-use variable frequency Ar-shielded arc welding machine', Electric Welding Machine, (1981) (Chinese)
103 Shanghai Jiaotong University, 'SCR-controlled Ar-shielded pulsed arc welding machines with mountain-like current waveform', Electric Welding Machine, (1980), No. 2 (Chinese)
104 Huang, S.S. *et al*., 'Transistor-welding-transverter and its loss of energy', IIW Doc 212

105 Daggett, E.H., 'New development in pulsed spray welding', Welding Journal, (1970)10
106 Paton, B.E., Sheiko, P.P. and Pashulya, M.P., 'Automatic control of metal transfer in pulsed arc welding', Automatic Welding (USSR), (1971), No. 9 (Russian)
107 Zhu, Z.X., 'Effect of waveform on the metal transfer of pulsed Ar-shielded metallic arc welding', Metal Science and Technology, (1983) No. 3 (Chinese)
108 Morigaki, O., Hoshi, R. *et al*., 'Automatic gas metal arc welding process with pulsating welding current', IIW Doc XII-B-215-77
109 Needham, J.C., 'Pulsed MIG welding with analogue transistor power supply', Proc. of Second Int. Symp. of JWS, Aug. (1975)
110 Pan, J.L. *et al*., 'New control method of welding arc', Trans. of the China Welding Institution, (1980), No. 4 (Chinese)
111 Chen, W.H., Huang, J.R. and Dong, W.I., 'All position automatic narrow gap double frequency MAG welding of thick wall tube controlled by transistorised power source', Trans. of the China Welding Institution, (1983) No. 8 (Chinese)
112 Nomura, H. and Sugitani, Y., 'Investigation on dynamic characteristics in low-frequency pulsed MIG welding', IIW Doc XII-F-189-78
113 Ukita, I., Ohshima, K., Abe, M., Kubota, T. and Okada, A., 'Effect of power source characteristics on the stability of welding arc', Journal of JWS, Vol. 49, No. 11 (1980) (Japanese)
114 Needham, J.C., 'Self-adjusting welding arcs; drift in power source output and electrode feed rate', British Welding Journal, 2, 506, (1955)
115 Ohshima, K., Abe, M. and Kubota, T., 'Stability of forced droplet transfer under periodically alternated non-linear output characteristics', Journal of JWS, Vol. 51, No. 2 (1982) (Japanese)
116 Ohshima, K., Abe, M., Kubota, T. and Okada, A., 'Improvement of arc stability and control under non-linear output characteristics of power source', Journal of JWS, Vol. 50, No. 10 (1981) (Japanese)
117 Ohshima, K., Abe, M. and Kubota, T., 'Welding method of forced droplet transfer by non-linear output characteristics of power source', Journal of JWS, Vol. 50, No. 8 (1981) (Japanese)
118 Ohshima, K., Abe, M. and Kubota, T., 'Effect of power source characteristic on stability of pulsed current transfer-sampled-data control of pulsed arc', 4JWS-I-3
119 Zhang, L.D., 'Study on melting rate of MIG welding', Journal of Tsinghua Univ., (1982), No. 3 (Chinese)
120 Zhang, R.H. *et al*., 'MIG welding with pulsed wire feed', Proc. of the Int. Conf. on Quality and Reliability in Welding', Hangzhuo, China, Vol. 4, D-19, (1984)
121 Pan, J.L. *et al*., 'Method of controlling the output characteristic of a welding power source, apparatus for arc welding and electrical circuit to be used for such apparatus', United States Patent 4, 628, 181, Dec. 9, (1986)
122 Smith, C.J., 'Advance in welding process', Third Int. Conf., Harrogate, England, 7–9 May, (1974), pp. 27–277
123 Lucas, W. and Naseer-Ahmed, 'Control of weld penetration in TIG welding: a review of factors affecting weld pool behaviour and of techniques to improve process control', Cambridge, England, The Welding Institute, (1985-02)
124 Suga, Y., Takennaka, D., Hibikiya, Y. and Ogawa, K., 'Automatic control of penetration by monitoring reverse-side shape of molten pool in all position welding

of fixed pipes', Proc. Int. Offshore and Polar Engineering Conf., ISSN 1098-6189, Jan. 2001, Vol. 4, pp. 286–291
125 Jackson, C.E. and Shrubsall, A.E., 'Control of penetration and melting rate ratio with welding technique', Journal of AWS, 32, 172-s (1953)
126 Zhang, Y.W., 'Infrared Optics Engineering', (1982), Shanghai Scientific & Technical Publishers, (Chinese)
127 Pan, J.L. *et al*., 'Control of welding power source output characteristics, welding machine and circuit', China Patent, No. 85 100037 (1985)
128 Liu, W.H. *et al*., 'Study on high dynamic wire feed system', Technical Report of Tsinghua Univ., (1986), (Chinese)
129 Eichhorn, F., 'Metal transfer in pulsed CO_2 arc welding of steel', Schweissen und Schneiden, (1974), No. 6 (German)
130 Chen, Q., 'QH-ARC CO_2 welding', Master's Dissertation of Tsinghua Univ., (1985) (Chinese)
131 Jiang, H.Z., 'Welding method and machine', Vol. 1, China Machine Press (1982) 3 (Chinese)
132 Lavlishev, V.Y., 'Mechanism of metal spattering in long arc of CO_2 welding', Automatic Welding 1978, No. 6 (Russian)
133 Pan, J.L., Qi, B.J. *et al*., 'Study on dynamic properties of welding power source', Proc. of the 6th National Welding Conf., pp. 169–173, (1990), (Chinese)
134 Bless, S.J., 'Drop transfer in short-circuit welding', J. of Physics D, (1974), 3
135 Defize, L.F., 'Metal transfer in gas-shielded welding arcs', Proc. of Int. Conf. on Welding Arc Physics, (1962)
136 Cooksey, C.G., 'Metal transfer in gas-shielded arc welding', Proc. of Int. Conf. on Welding Arc Physics, (1962)
137 Smith, A.A., 'Characteristics of the short-circuiting CO_2 shielded arc', Proc. of Int. Conf. on Welding Arc Physics, (1962)
138 Popokov, A.M., 'Development of automatic regulation and optimising of CO_2 welding parameters', Welding Production, (1978), No. 4 (Russian)
139 Zhao, J.K., 'Study on dynamic properties of CO_2 welding power source', Electric Welding Machine, (1980), No. 1 (Chinese)
140 Zhang, X.Z. *et al*., 'Gas-shielded arc welding', China Electric Power Industries Press, Beijing, (1982) (Chinese)
141 Ji, Y.G., 'New type of pulse wire feeding CO_2 welding machine', Proc. of Int. Welding Conf., Hongzhou, Sept. (1984), (Chinese)
142 Wang, Q.L. *et al*., 'New control method of short-circuit CO_2 welding', Research Report of Harbin University of Technology, No. 225, (1982), 10 (Chinese)
143 Reynolds, J., 'A new process for thin gauge aluminum', Welding Journal, July (1980)
144 Zhai, H.H. *et al*., 'Application of multi-characteristics controller and new wire feed tube in welding machine', Welding, (1983), No. 7 (Chinese)
145 Jiao, X.D., 'AC pulse MIG welding', Doctor's Dissertation of Tsinghua Univ., (1994) (Chinese)
146 Weber, J., 'Special report – 1985 Essen Welding Fair', Welding Journal, (1986), No. 1
147 Weber, J., 'The 1986 AWS Welding Show – A special report', Welding Journal, (1986), No. 7

148 Jiao, X.D., Pan, J.L. and Zhang, H., 'Study on alternated AC/DCRP MIG welding', China Mechanical Engineering, (1996), No. 7, pp. 88–89 (Chinese)
149 Jiao, X.D., Pan, J.L. and Zhang, H., 'Measurement of power loss on frequency conversion transistors of welding power source', Electric Welding Machine, (1995), 1, pp. 1–3 (Chinese)
150 Jiao, X.D., Pan, J.L. and Zhang, H., 'Study on control system of AC MIG welding', Electric Welding Machine, (1994) 2, pp. 9–11 (Chinese)
151 Jiao, X.D., Pan, J.L. and Zhang, H., 'Development of square wave AC MIG welding power source using FET as frequency converter', Electric Welding Machine, (1993), No. 2, pp. 11–15 (Chinese)
152 Ueguri, S. *et al*., 'Study of metal transfer in pulsed GMA welding', Welding Journal, Vol. 64, No. 8, pp. 242–250s, Aug. (1985)
153 Ecer, G.M., 'Magnetic deflection of the pulsed current welding arc', Welding Journal, June (1980)
154 Jennings, C.H. and White, A.B., 'Magnetic arc blow', J. of American Welding Soc., 20, 427-s. (1941)
155 Norman, E.W.L., 'Magnetic arc blow', Metal Construction, July (1984)
156 Perry, R.J., 'Effects associated with arc blow', Welding Journal, Sept. (1970)
157 Dagget, E.H., 'New development in pulsed spray welding', Welding Journal, Oct. (1970)
158 Abdelrahman, M., 'Feedback linearization control of current and arc length in GMAW system', Proc. of the 1998 American Control Conference, Vol. 3, 1757–61, Philadelphia, PA, USA, 24–26 June (1998)
159 Li, Y., 'Study on control system of pulse MIG welding power source', Doctor's Dissertation of Tsinghua University, (1988,9) (Chinese)
160 George, E., 'The effect of high-frequency pulsing of a welding arc', IEEE Trans. of Industrial Application, Sept./Oct. (1985)
161 Lucas, W. and Murch, M.G., 'Arc re-ignition characteristics when welding with sine-wave and square-wave power supplies', IEE Proceedings B (Electric power applications) (UK), Nov. (1987)
162 Liu, S.C., 'Theoretical analysis and design of AC to AC square-wave power source controlled by SCR', Electric Welding Machine, (1983), No. 6 (Chinese)
163 Huang, S.S., 'Electronic controlled welding power source', China Machine Press (1994), (Chinese)
164 Hou, M., 'Study on 50 Hz square wave AC welding power source', Electric Welding Machine, (1983) 2 (Chinese)
165 Zhang, J.H. *et al*., 'Development and technological experiment of square-wave AC power source', Trans. of the China Welding Institution, (1985) 3 (Chinese)
166 Zhang, Y. *et al*., 'Application of single-chip computer 8089 in the double bridge inverter type arc welding power source', Proc. of the 7th National Welding Conf. (1993) (Chinese)
167 Zhang, Y. *et al*., 'Study on double bridge square-wave AC welding power source using SCR-MOSFET', Proc. of the 7th National Welding Conf. (1993) (Chinese)
168 Geng, Z. *et al*., 'Welding power source for TIG welding of Al-alloy with alternated polarities', Proc. of the 7th National Welding Conf. (1993) (Chinese)
169 Zhang, J.H. *et al*., 'New development of AC welding power source', Electric Welding Machine, (1981) No. 1 (Chinese)

170 Stol, I., 'Advances in narrow groove welding', Conf. Proceedings, 'Trends in Welding Research in the USA', New Orleans, La., 16–18 Nov. 1981, Sponsored by the Joining Div. of American Soc. for Metals
171 Sun, H.G., 'Discussion on the phase changing process of AC square wave power source', Electric Welding Machine, (1984), No. 3 (Chinese)
172 Nagasaka, M. *et al.*, 'Progress of inverter type welding machine', Welding Technique, (1987) 2 (Japanese)
173 Mita, T. *et al.*, 'Application of TIG welding with inverter machine', Welding Technique, (1989) 2 (Japanese)
174 Hou, S.Z. *et al.*, 'Arc blow in the welding of 9% Ni steel and its prevention', Trans. of the China Welding Institution, (1985) 3 (Chinese)
175 Yang, S.Q. *et al.*, 'Study on AC plasma welding of Al with straight polarity', Metal Sci. and Technol., June (1985), (Chinese)
176 Zhang, J.H. *et al.*, 'Study on the principle of inverter type square wave power source', Metal Sci. and Technol., Dec. (1984) (Chinese)
177 Zhang, J.H. *et al.*, 'Study on the microcomputer-controlled 50 Hz square wave AC (DC) power source', Metal Sci. and Technol., March (1998) (Chinese)
178 Yamamoto, H., 'Progress of arc welding machine and automation arising from inverter type power source', Journal of JWS (1984) No. 4 (Japanese)
179 Maruyama, T. *et al.*, 'Sensor for penetration control of thin Al (AL350) plate in pulse MIG machine', Welding of Light Metals, (1992) No. 5 (Japanese)
180 Maruyama, T., 'Characteristics of GMA welding power source controlled by polarity ratio', Technical Report of Kobe Steel, (1989) No. 4 (Japanese)
181 Kuwayama, N., 'High-efficiency welding method based on alternating MIG/CO_2 welding process (SMAC method)', Welding Technique, Jan. (1982) (Japanese)
182 Tsusima, S., 'Development of large current AC-MIG welding process', Collection of papers of JWS (1992) No. 1 (Japanese)
183 Tsusima, S., 'Development of re-ignition apparatus for large current AC-MIG welding process', Collection of papers of JWS, (1992) No. 1 (Japanese)
184 Tsusima, S., 'Effect of oxygen on the toughness of Ti-B weld metal in AC-MIG welding', Collection of papers of JWS, (1992) No. 2 (Japanese)
185 Gross, J.H., 'The status of welding technology in the United States', Welding Research Abroad 29, (11) (1987)
186 Wu, Y.F., *et al.*, 'Disparity of welding technology between China and developed countries, proposals for developing welding technology in China', Symp. on Futurities of Mechanical Hot Working Technology, Sponsored by China NSF, (1988) 5 (Chinese)
187 Reeve, R.C., 'How far can welding automation go?', Welding Design and Fabrication Abroad 29, (11) (1987)
188 Cook, G.E., 'Feedback and adaptive control in automated arc welding systems', Metal Construction, Vol. 13, No. 9, pp. 551–556, Sept. (1981)
189 Cohen, C., 'Robots to gain eyes for seam welding', Electronics, 53, 11, (1980)
190 Nakamura, T., 'Current status of robotic welding in Japan', Conference Proceedings, 'Automation and Robotisation in Welding and Allied Processes', Sept. (1985)
191 Schraft, R.D., 'State of the art report on the application of industrial robots in the FRG with special respect to welding', Conf. Proceedings, 'Automation and Robotisation in Welding and Allied Processes', Sept. (1985)

192 Weston, J., 'Automation and robotisation in welding – the UK scene', Conf. Proceedings, 'Automation and Robotisation in Welding and Allied Processes', Sept. (1985)
193 Kisselevski, F., 'System of technological adaptation for industrial welding robots', Conf. Proceedings, 'Automation and Robotisation in Welding and Allied Processes', Sept. (1985)
194 Pilarczyk, J., 'Robotisation in welding in Poland', Conf. Proceedings, 'Automation and Robotisation in Welding and Allied Processes', Sept. (1985)
195 'Welding Technology: Japan 83', Metal Construction, 15, 9, (1983)
196 Sugitani, Y. *et al*., 'Intelligent arc welding robot with simultaneous control of penetration depth and bead height', NKK Report, Dec. (1988)
197 Thomas, A., 'Emphasis on automation in ESAB planning', Metal Construction, 20, 5, (1988)
198 Elliott, S., 'Hobart move into advanced welding system', Metal Construction, 16 (2) (1984)
199 Drews, P. *et al*., 'Development of parameter control for automated gas shielded arc welding processes', IIW Doc XII-1052-88
200 Bada, N. *et al*., 'Development of intelligent machine for MAG welding in all positions', IIW Doc XII-1055-88
201 Drews, P. *et al*., 'Automatic welding system', IIW Doc XII-945-86
202 Masumoto, I., 'Recent achievements of arc welding technology with respect to automation', IIW Doc XII-1057-88
203 Welding Division of Tsinghua University, 'Summary report on study of seam tracking system with infrared sensor', Document of Appraisal Committee of the 6th 5-year's Reseach Project Evaluation, (1986) (Chinese)
204 Chen, D.H. *et al*., 'Exploration of welding process control by computer image technique', Trans. of the China Welding Institution, Vol. 6, No. 1, (1985) (Chinese)
205 Nomura, H., 'Back bead width control in one-side SAW using flux copper backing', Trans. of the JWS, Vol. 18, No. 2, pp. 108–115, Oct. (1987)
206 Spynu, G.A., 'Problems of development and application of industrial robots for arc welding', Conf. Proceedings, 'Development in Mechanized, Automated and Robotic Welding', Nov. (1980)
207 Liden, G., 'Sensors for seam tracking and adaptive control', IIW Doc XII-1077-88
208 Fan, Q.R., 'Arc welding sensor and its system (1)', Welding Technique, (1987) 1 (Chinese)
209 Jiang, H.Z., 'Welding Process and Machine', Vol. 1, pp. 142–147, China Machine Press, (1981), (Chinese)
210 Osaka Transformer Co., 'User Manual of WG2100 Super Tracker', (1984)
211 Wada, K., 'Development of automatic welding system for heavy-wall steel structure', IIW Doc XII-1068-88
212 Widfeldt, M., 'The situation concerning robotics and welding automation in Sweden', IIW Doc XII-993-86
213 Tsuda, E. *et al*., 'Sensing methods for automatic welding', Fabrication, July, (1977)
214 Li, S.H. *et al*., 'Study on the suppression of interference due to tack weld in seam tracking system', Trans. of the China Welding Institution, Vol. 5, No. 3, (1984) (Chinese)

215 Goldberg, F., 'Inductive seam-tracking and high sensing systems for arc welding methods and thermal cutting', Conf. Proceedings, 'Development in Mechanized Automated and Robotic Welding', Nov. (1980)
216 Jing, S.L., 'Apparatus for welding automatic seam tracking', J. of Xian Jiaotong Univ., Vol. 14, No. 2, (1980) (Chinese)
217 Pan, J.L. *et al.*, 'Two-directional seam tracking system using the edge of groove as reference', Trans. of the China Welding Institution, Vol. 5, No. 2, (1984) (Chinese)
218 Yin, S.Y. *et al.*, 'Study of high-precision seam tracking system using laser as sensor and single-chip computer control.', Welding, (1989) 3 (Chinese)
219 Liu, Z.S. *et al.*, 'Study on seam tracking system using laser sensor for spiral pipe welding', Trans. of the China Welding Institution, Vol. 9, No. 4, (1988) (Chinese)
220 Wu, M.S. *et al.*, 'Modulated infrared sensor for welding automatic seam tracking', Report on Commission XII of China Welding Institution (1988) (Chinese)
221 Liden, G., 'Sensors in automatic arc welding', IIW Doc XII-887-85
222 Drews, P., 'A new optical method of measurement for seam tracking sensor in arc welding', IIW Doc XII-902-85
223 Appels, J.A.C., 'Application and economic aspects for a 3-dimensional He-Ne laser sensor', IIW Doc XII-1062-8
224 Omen, G.L., 'A real-time optical profile sensor for robot arc welding', Robotic Welding, pp. 117–128, IFS (Publications) Ltd., UK (1987)
225 Chen, W.Z. *et al.*, 'Application of image-processing technique in on-line detection of narrow gap MIG/MAG welding', Trans. of the China Welding Institution, Vol. 9, No. 4, (1988) (Chinese)
226 Pan, J.L. *et al.*, 'Detection of weld groove edge by photo-electronic sensor', China Patent ZL 93 2 13847.0 (1994) (Chinese)
227 Stenke, V., 'Allowable wire position tolerances in fully mechanized MAG welding', IIW Doc XII-1077-88
228 Nomura, H. *et al.*, 'Automatic control of arc welding by arc sensor system', NKK Technical Report, Overseas No. 47 (1986)
229 Nomura, H. *et al.*, 'Automatic real-time bead height control with arc sensor in TIG welding', IIW Doc XII-884-85
230 Eichhorn, F., 'GMA welding of filler passes with a new type of arc controlled seam tracking system', Proc. of 1st Int. Conf. 'Advanced Welding Systems', London, 19–21 Nov. 1985. pp. 181–190
231 Nishada, Y. *et al.*, 'Fully automatic control of vertical CO_2 welding', National Technical Report, 23 (2), (1988)
232 Eichhorn, F., 'State of technology of sensorless, process-orientated seam-tracking system for arc welding processes', IIW Doc XII-C-087-84
233 Sato, S. *et al.*, 'Development of narrow-gap GMAW welding processes with waved wire', IIW Doc XII-B-7-81
234 Kimura, S. *et al.*, 'The twist arc welding process', Conf. Proceedings, 'Advances in Welding Processes', May (1987)
235 Ditschun, A., 'The development and application of synchronized, twin-arc frequency modulated pulsed GMAW/MIG welding system', IIW Doc XII-1067-88
236 NKK Technical Report, 'All positional TIG welding equipment', Overseas No. 47 (1986)

237 Matsuda, F. and Ushio, M. *et al*, 'Narrow-gap welding (NGW), the state of the art in Japan', Book published by Japan Welding Society, Tokyo 101 Japan, (1986)
238 Nomura, H., 'Narrow-gap welding process with high speed rotating arc', IIW Doc. XII-C-033-82
239 Nomura, H., 'Development of automatic fillet welding process with high-speed rotating arc', IIW Doc XII-939-86
240 Sugitani, Y., 'Development of multi-electrode automatic fillet welding equipment with high-speed rotating arc', Proc. of 2nd Int. Conf., 'Recent Trends in Welding Science and Technology', Gatlinburg, TN, 14–18 May 1989
241 Nomura, H., 'Development of pulsed MAG arc welding robot with adaptive control by arc sensor system', Conf. Proceedings, 'Computer Technology in Welding', June (1986), London
242 Nomura, H., 'Automatic real-time bead height control with arc sensor', Trans. of JWS, Vol. 18, No. 2, Oct. (1987)
243 Pan, J.L., 'New type of seam tracking system', Chinese Journal of Mech. Eng., (1980), No. 1, pp. 1–14 (Chinese)
244 Fei, Y.N., 'Fundamental theory of arc sensor and seam tracking system', Doctor's Dissertation of Tsinghua Univ., (1990) (Chinese)
245 Liao, B.J., 'Multi-freedom intelligent arc welding machine using arc sensor', Doctor's Dissertation of Tsinghua Univ., (1993) (Chinese)
246 Pan, J.L., 'Rotating arc torch based an hollow shaft motor', China Patent No. 922 444 765, (1992) (Chinese)
247 Pan, J.L. and Fei, Y.N., 'Mathematic Model of Arc Sensor', Proc. of 6th National Welding Conf., Vol. 6, (1990), pp. 106–110 (Chinese)
248 Futman, T.E. *et al*., 'Introduction to linear control system', China Machine Press, (1979) (Chinese)
249 Amson, J.C., 'An analysis of the gas-shielded consumable electrode metal arc welding system', Report A1/47/64, British Welding Research Association, (1964) London
250 Cary, H.B., 'Modern welding technology', Prentice-Hall, Englewood Cliffs, NJ, USA (1979)
251 Wu, S.D. and Pan, J.L., 'Automatic seam tracking for CO_2 welding arc sensor', Proc. of the 8th National Welding Conf., Vol. III, (1997), pp. 161–163 (Chinese)
252 Lesnewich, A., 'Control of melting rate and metal transfer in gas-shielded metal AC welding, Part 1, Control of electrode melting rate', Welding Journal, 37(8), (1985)
253 Halmy, E., 'Wire melting rate, droplet temperature and effective anode melting potential', Conf. Proceedings, 'Arc Physics and Weld Pool Behaviour', London, (1979)
254 Liu, W.H., 'Development and application of high dynamic wire feeding system', Electric Welding Machine, (1987) 4 (Chinese)
255 Yan, P.Q. *et al*., 'Fundamentals of measuring and detection technology for mechanical engineering', Proc. of the National Measuring and Detection Technology Conf., organized by Higher Education Institutions, (1984) (Chinese)
256 Wei, W.L. *et al*., 'Analysis of detected signals', Precision Instrument Department of Tsinghua Univ., Teaching material (1985) Beijing (Chinese)

257 Yan, P.Q. *et al*., 'Detection and analysis of dynamic behaviour of mechanical system', Teaching material of Tsinghua Univ., (1984), Beijing (Chinese)
258 Wei, W.L. *et al*., 'Analysis of random signals and power spectrum estimation', Teaching material of Tsinghua Univ., (1984), Beijing, (Chinese)
259 Budai, P., 'A uniform method to describe and measure the static and dynamic characteristics of a welding power source', IIW Doc XII, (1987)
260 Wu, S.D., 'Signal processing of arc sensor for automatic seam tracking', Doctor's Dissertation of Tsinghua Univ., (1997) 2 Beijing (Chinese)
261 Li, Q.Y. *et al*., 'Numerical Analysis', Publishing House of Central China Univ. of Sci. and Technol., (1988) 5 (Chinese)
262 Chen, Y.H. *et al*., 'Principle of signal processing', Publishing House of Sichuan Univ., (1989) (Chinese)
263 Arimoto, T., 'Signal and image digit processing', (Translated by Li, S.L.), Electronics Industries Press, Beijing, (1988) (Chinese)
264 Yanolavski, 'Processing of digital image', (Translated from the Russian by Shi, Y.Q.), Electronics Industries Press, Beijing (1990) (Chinese)
265 Lu, S.T. *et al*., 'The C programming language and engineering program library', Electronics Industries Press, (1992) (Chinese)
266 Li, S.L. *et al*., 'Pulse Modulation and Digit Transmission System', People's Post and Telecommunication Press, Beijing, (1988) (Chinese)
267 Fang, C.Z. and Xiao, D.Q., 'Process Recognition', Publishing House of Tsinghua Univ., (1988), 2, (Chinese)
268 Zhao, S.J. *et al*., 'Statistical analysis of signals: theoretical detection estimation, filtering theory and application', Publishing House of North West Telecommunication Engineering Univ., (1986), 4 (Chinese)
269 Beck, 'Signal processing, demodulation and noise', (Translated book from English by Zhang, Z.M.), People's Post and Telecommunication Press, (1985), 8 (Chinese)
270 Huang, D.L., 'Fundamentals of statistical analysis of signals', Publishing House of Central China Univ. of Technology, (1986), 7 (Chinese)
271 Li, S.Z. *et al*., 'Discrete signal processing in time domain', Publishing House of National Defence Univ. of Sci. and Technol., (1994) (Chinese)
272 Wang, H.Y., 'Treatise on digital signal processing', National Defence Industries Press, (1995) (Chinese)
273 Lu, Y.S. *et al*., 'Introduction to random signal processing', Publishing House of Tianjin Univ., (1988) (Chinese)
274 Li, K. *et al*., 'Recognition method based on vein keeping unchanged during revolution of mathematic morphology', Signal Processing, Vol. 8, No. 1, pp. 18–23 (1992) (Chinese)
275 Zhu, Y.S. *et al*., 'Adaptive separation of mixed periodic signals', Signal Processing, Vol. 8, No. 4, Dec. (1992) (Chinese)
276 He, Z.J., 'Principle and application of averaging method of signal in time domain', Signal Processing, Vol. 2, No. 4, Dec. (1986) (Chinese)
277 Hu, D.K., 'Nonlinear filtering by increment restriction', Signal Processing, Vol. 1, No. 3, Sept. (1985) (Chinese)
278 Tang, S.C. *et al*., 'Characteristics detection of deep image using descrete orthogonal polynomials', Signal Processing, Vol. 7, No. 4, Dec. (1991) (Chinese)
279 Huang, X.T., 'Two-dimensional digital signal processing (O): transformation

and mean value filtering', Science Publishers, (1985), 10 (Translated by Hu, G.R.) (Chinese)
280 Zheng, J.L. *et al*., 'Signal and system', Vol. 1, Vol. 2, Higher Education Press, (1993) 11 (Chinese)
281 Wu, S.D. and Pan, J.L., 'Waveform characteristics of arc sensor in short-circuit transfer arc', Proc. of the 8th National Welding Conf., Vol. 3, (1997), pp. 164–166 (Chinese)
282 Cai, G.L., 'Electro-magnetic iron', Shanghai Scientific and Technical Publishers, (1965) (Chinese)
283 User's manual for software of development system of single-chip computer TP 98/96, Beijing Univ. of Technol., (1992) (Chinese)
284 User's manual for multi-function CPU board of TP STD 8805 Intel 8098, Beijing Univ. of Technol., (1992) (Chinese)
285 Fang, J.C., 'Principle and application of single-chip computer 8098 of MCS 96 series', Tianjin Scientific and Technical Publishers, (1990) 12 (Chinese)
286 Chen, E.Q., 'Interface technique of microcomputer and single-chip computer and its application', Publishing House of Chengdu Telecommunication Engineering Univ., (1989) 6 (Chinese)
287 Wang, X.L. *et al*., 'Design of A/D, D/A interface and data acquisition system of microcomputer', Tsinghua Univ. Press, (1984) 8 (Chinese)
288 Zhang, F.Y. *et al*., 'Principle and application of IBM PC microcomputer', Publishing House of Nanjing Univ., (1984) Nov. (Chinese)
289 Sun, H.F., 'Principle and application of single-chip computer MCS 51/96', Publishing House of Beijing Univ. of Aeronautics, (1988) 2 (Chinese)
290 Qian, L., 'Solving the inverse transformation of robotic kinematics by fuzzy logic', Information of Robotics, (1992) 5 (Chinese)
291 Pedrycz, W., 'Fuzzy control and fuzzy system', Research Studies Press, Taunton, Somerset, England, (1989)
292 Zadeh, L.A., 'Fuzzy set, language variable and fuzzy logic', Science Publishers, (1982) 5 (Translated by Chen, G.Q.) (Chinese)
293 Lou, S.B. *et al*., 'Theory and application of fuzzy switch and automat', Shanghai Scientific and Technical Publishers, (1984) 3 (Chinese)
294 Zhou, Y.Q. *et al*., 'Intelligent robotic system', Publishing House of Tsinghua Univ., (1989) (Chinese)
295 Su, Y., 'Welding temperature field colorimetric measuring system', Doctor's Dissertation of Tsinghua Univ., (1993) (Chinese)
296 Zhang, H., 'Real time measurement of welding temperature field and its application', Doctor's Dissertation of Tsinghua Univ., (1997) (Chinese)
297 Rykalin, N.N., 'The calculation of thermal processes in welding', Machine Building Press (1958) (Russian)
298 Adams, C.M., 'Cooling rate peak temperature in fusion welding', Welding Journal, Vol. 37, (1958)
299 Kou, S., 'Welding thin plates of aluminum alloys – a quantitative heat-flow analysis', Welding Journal, (1982), 61(6), pp. 175–191
300 Chen, C. *et al*., 'Finite element analysis and calculation of non-linear heat conduction in welding', Trans. of the China Welding Institution, (1983), 4(3), pp. 139–148 (Chinese)
301 Zhu, L.Z., 'Principle and application of high-temperature measurement', Science Publishers, (1991) (Chinese)

302 Cheng, G.S., 'Detection technique of welding process', North West Industries Press, (1988) (Chinese)
303 You, F.E. *et al*., 'Study on temperature field measurement by radiation', J. of Harbin Univ. of Technol., (1990), No. 4 (Chinese)
304 Chen, D.H. *et al*., 'Study on temperature field measurement by microcomputer', J. of Harbin Univ. of Technol., (1980) No. 4 (Chinese)
305 Pan, J.L. *et al*., 'Sensor for measuring welding temperature field', China Patent ZL 93 2 13847.0 (1993) (Chinese)
306 Li, Y.A. *et al*., 'Study on detection of dynamic arc welding temperature field', J. of Beijing Univ. of Technol., (1983) No. 4, pp. 13–20 (Chinese)
307 Hu, Z.H. *et al*., 'Real time detection of weld bead width', J. of Beijing Univ. of Technol., (1983) No. 4, pp. 43–48 (Chinese)
308 Begin, G. and Boillot, J.P., 'Proc. of 3rd ICRVSC (Int. Conf. on Robot Vision and Sensory Control)', pp. 649–658, (1983)
309 Chin, B.A., Madsen, N.H. and Goodling, J.S., 'Infrared thermography for sensing the arc welding processes', Welding Journal, 62, pp. 227–234, (1983)
310 Chin, B.A., Madsen, N.H. and Goodling, J.S., 'Infrared themography shows promise for sensors in robotics welding', Robotic Today, 5, pp. 85–87, (1983)
311 Nagarajan, S., Groom, K.N. and Chin, B.A., 'Infrared for seam tracking in gas tungsten arc welding processes', Proc. of 2nd Int. Conf., Gatlinburg, TN, 14–18 May 1989, Recent Trends in Welding Science and Technology, pp. 951–955 (1989)
312 Smith, C.J., 'Self-adaptive control of penetration in tungsten inert gas weld', Advances in Welding Processes, Weld. Inst., (1974), pp. 272–282
313 Vroman, A.R. *et al*., 'Feedback control of GTA welding using puddle-width measurement', Welding Journal, (1978), Sept., pp. 742-s–746-s
314 Zhao, J.R., 'Diagnoses of high-frequency TIG welding arc by microcomputer image method', Trans. of the China Welding Institution, (1987) No. 4 (Chinese)
315 Hu, Z.H. *et al*., 'Infrared image technique for welding process and temperature field measurement', Proc. of Automation Inst. of Mechanical Engineering Industries, (1981) (Chinese)
316 Hu, Z.H. *et al*., 'Investigation in the real time sensing of welding width', Proc. of Int. Welding Conf., Sept. (1984), Hang Zhou, China
317 Inoue, K., 'Image processing for in-line detection of welding process', (Report I), Trans. of JWRI, Vol. 8, No. 2, pp. 169–174, (1979)
318 Nomura, H., 'Behaviour of molten pool in submerged arc welding', Nippon Kokan Technical Report, (1979), (82), p. 92
319 Nomura, H., 'Behaviour of molten pool in submerged arc welding', Journal of JWS, (1982), 51(9), p. 43
320 Kozono, K., 'Relation between surface temperature and reverse-side bead width in TIG welding of thin mild steel plate', Journal of JWS, (1982), 51(3), p. 52
321 Boillot, J.P., 'Adaptive welding by fiber optic thermographic sensing: an analysis of thermal and instrumental considerations', Welding Journal, (1985), Vol. 64, No. 7, pp. 209s–217s
322 Kozono, Y., 'Relation between surface temperature and reverse-side bead width

in a low-frequency pulsed TIG welding of stainless steel plate', Journal of JWS, (1983), 52(1), p. 45
323 Kozono, Y., 'Relation between surface temperature and reverse-side bead width in girth TIG welding for stainless steel tube quantity', Journal of JWS, (1986), 4(2), p. 53
324 Chen, Q., 'Study on penetration control of MIG welding', Doctor's Dissertation of Tsinghua Univ., (1988) (Chinese)
325 Pan, J.L., 'Sensor for real time, measurement of dynamic temperature field', China Patent ZL 96 2 11738.2, (1996) (Chinese)
326 Yang, C.H. *et al.*, 'Laser and infrared technique handbook', National Defence Industries Press, (1990) (Chinese)
327 Zhang, M.P. *et al.*, 'Night vision system', Publishing House of Beijing Univ. of Sci. and Technol., (1993) 10 (Chinese)
328 Chen, H., 'Infrared physics', National Defence Industries Press, (1985) 10 (Chinese)
329 Liu, X.D., 'Fundamentals for infrared system design', Publishing House of Central China Univ. of Technol., Wuhan, (1985) 10, (Chinese)
330 Wang, Q.Y. *et al.*, 'Applied technique of CCD', Publishing House of Tianjin Univ., Tianjin, (1993) 3, (Chinese)
331 Zhang, Y.S., 'Selection of wavelength for colorimetric temperature measurement by radiation', Trans. of Infrared and mm-Length Wave, (1993) 8, Vol. 12, No. 4, pp. 324–328 (Chinese)
332 Zhang, H. *et al.*, 'Selection of wavelength for temperature field measurement by ICCD image', Trans. of Infrared and mm-Length Wave, (1996) 12, Vol. 15 (6), pp. 433–430 (Chinese)
333 Yang, J.G. *et al.*, 'Optimisation of parameters for double-color colorimetric temperature measurement'. Metrology Transactions, (1991) (10), Vol. 12, No. 4, pp. 275–279 (Chinese)
334 Sha, Z.X., 'Characteristics and selection of camera lens', China Photography Press, Beijing, (1989) 6 (Chinese)
335 Tian, F.A. *et al.*, 'Principle of temperature measuring instrument by radiation and its inspection', China Metrology Press, Beijing, (1990) 3 (Chinese)
336 Zhang, H., Pan, J.L. *et al.*, 'Real time measurement of temperature field by ICCD, 1. Principle and method of temperature field division', Science in China, (1997), (10), Vol. 27 (5) (Chinese)
337 Zhang, H. and Pan, J.L., 'Real time measurement of temperature field by ICCP, 2. Principle and method for optimisation design of wavelength', Science in China, (1997), (12), Vol. 27 (6) (Chinese)
338 Zhang, H. and Pan, J.L., 'Effect of various factors on the measurement of temperature by image colorimetric method', Science in China, (1998), (2) Vol. 28 (1), (Chinese)
339 Zhang, H., Pan, J.L. *et al.*, 'Real time measurement of temperature field and closed-loop control of the isotherm', Science in China, (1998) (6) (Chinese)
340 Zhang, H., Pan, J.L. *et al.*, 'Real-time measurement of temperature field with ICCD as sensor, 1. Principle and method for division of temperature range', Science in China, (Series E), June (1998), Vol. 41 (3)
341 Zhang, H., Pan, J.L. *et al.*, 'Real time measurement of temperature field with

ICCD as Sensor, 2. Principle and method for optimum design of wave length', Science in China (series E), October (1998), Vol. 41 (5)
342 Zhang, H. and Pan, J.L., 'Real time measurement of temperature field by image colorimetric method', Chinese J. of Mech. Engineering, (1998), (4), Vol. 34 (2) (Chinese)
343 Zhang, H. and Pan, J.L., 'Real time detection and sensing system based on two-colour ICCD thermal images', Instrument Transactions, (1998) Vol. 19 (1) (Chinese)
344 Zhang, H. and Pan, J.L., 'Calibration of temperature field measuring system based on two-colour ICCD images', Chinese J. of Mech. Engineering, (1998) (8), Vol. 9 (8) (Chinese)
345 Zhang, H. and Pan, J.L., 'Microcomputer processing technique of temperature field obtained by real time colorimetric measurement', J. of Tsinghua Univ. (Science Edition), (1997) (11), Vol. 37, 11 (Chinese)
346 Zhang, H. *et al.*, 'A new structure of coupler between single-mode optical-fiber and thin-film wave-guide', SPIE (1996) (10), Vol. 2893, pp. 518–522 (Chinese)
347 Pan, J.L., Zhang, H. and Liao, B.J., 'Real time temperature field measurement based on ICCD image colorimetric method', Abstract of China Academic Periodicals, (1997) (4), pp. 501 (Chinese)
348 Pan, J.L., 'Control of arc welding process', Proc. of the 8th National Welding Conf., Vol. 1 (1997) (Chinese)
349 Pan, J.L., 'Manufacturing science (hot working)', Report on Developing Strategy of Nature Sciences, Forum organized by China National Science Foundation, Scientific Publishers, (1995) (Chinese)
350 Zhang, H., Pan, J.L. *et al.*, 'A new method for measuring temperature field by two-colour calibration and one-colour measurement', SPIE Vol. 3558, (1998) 9, pp. 498–504
351 Zhang, H., Pan, J.L. *et al.*, 'Closed-loop control of penetration by real time measurement of welding temperature field', Proc. of TIWC'98 (Taiwan) Int. Welding Conf., (1998) 9, pp. 79–84
352 Zhang, H. and Pan, J.L., 'Application of microcomputer in the temperature field. Measurement by two-colour image colorimetric method', Proc. of Conf. on Application of Microcomputer in Welding Technology, Taiyuan, (1966) 10, pp. 252–261 (Chinese)
353 Zhang, W.Y., 'Heat transfer in welding', China Machine Press, Beijing, (1989) 10 (Chinese)
354 Wang, J.B. *et al.*, 'Microcomputer control of process', Publishing House of Tsinghua Univ., Beijing, (1988), 2 (Chinese)
355 Yang, Y.K. *et al.*, 'Improvement method of PID optimum parameter design', Automation and Instrument of Chemical Engineering, Vol. 15 (No. 5), pp. 13–17 (Chinese)
356 Eagar, T.W. *et al.*, 'Temperature fields produced by travelling distributed heat sources', Welding Journal (1983) (Dec.), pp. 346s–355s
357 Pan, J.L. and Zhang, H., 'Real time measurement of temperature field with CCD as sensor', Proc. of TIWC'98 (Taiwan) Int. Welding Conf., (1998) (9)
358 Wu, C.S., 'Numerical analysis of heat transfer in welding', China Machine Press, Beijing, (1989), 10, (Chinese)

359 Jin, J.M., 'Study on automatic path programming of welding robot', Doctor's Dissertation of Tsinghua Univ., (1996) (Chinese)
360 Jin, J.M., 'Weld groove recognition based on histogram statistical method', J. of Tsinghua University Graduates, (1995) (Chinese)
361 Chen, Q., 'Image processing method for automatic seam tracking of multi-path weld', Futurity of Mechanical Science and Technology, Forum of Young Mechanical Scientists Sponsored by China NSF, (1993), China Machine Press (Chinese)
362 Chen, Q. *et al.*, 'An adaptive thresholding for weld seam image recognition in real time', China Welding, Vol. 4 (2), Nov, (1995)
363 Pan, J.L. *et al.*, 'Direction of automation of welding structure production in China', National Symp. on Futurity of Mechanical Hot Working Technology, (1988), 5 (Chinese)
364 Pan, J.L. *et al.*, 'Future direction of welding structure production', SIMAP'88, Trans. of JWRI Vol. 17, No. 1. (1988) (Osaka)
365 Liang, T.P., 'Study on welding robot and its vision system', Doctor's Dissertation of Tsinghua Univ., (1990) (Chinese)
366 Paul, R.P., Shiman, B. and Mayer, G.E., 'Kinematic control equations for simple manipulators', IEEE Trans. on Systems, Man and Cybernetics, Vol. SMC-11, No. 6, June (1981), pp. 449–455
367 Paul, R.P., 'Manipulator cartesian path control', IEEE Trans. on Systems, Man and Cybernetics, Vol. SMC-9, Nov. (1979), pp. 702–711
368 Paul, R.P., 'Modelling trajectory calculation and servoing of a computer controller manipulater', Stanford Artificial Intelligence Laboratory Memo 177, (1982) Stanford University, USA
369 Sugimoto, K., 'Trajectory interpolation of a robot hand', Bulletin of the JSME, Vol. 26, No. 213, March (1983)
370 Ahlberg, J.H., Nilson, E.N. and Walsh, J.L., 'The theory of splines and their applications', Academic Press, New York (1967)
371 Lin, C.S. and Chang, P.R., 'Joint trajectories of mechanical manipulators for cartesian path approximation', IEEE Trans. on System, Man and Cybernetics, Vol. SMC-13, No. 6, Nov./Dec. (1983), pp. 1094–1102
372 Edwall, C.W., Ho, C.Y. and Pottinger, H.J., 'Trajectory generation and control of a robot arm using spline function', Robots VI Conf. Proceedings, March 2–4, (1982), Detroit, Michigan
373 Faig, W., 'Calibration of close-range photogrammetry systems: mathematical formulation', Photogrammetric Eng. Remote Sensing, Vol. 41, pp. 1479–1486 (1975)
374 Martins, H.A., Birk, J.R. and Kelley, R.B., 'Camera models based on data from two calibration planes', Computer Graphics Image Processing, Vol. 17, pp. 173–180, (1981)
375 Fischler, M. and Bolles, R., 'Random sample sensors: a paradigm for model fitting applications to image analysis and automated cartography', Proc. Image Understanding Workshop, April (1980), pp. 71–77
376 Yakimovsky, Y. and Cunningham, R., 'A system for extracting three-dimensional measurements from a stereo pair of TV cameras', Computer Graphics Image Processing, Vol. 7, pp. 195–210, (1978)
377 Fu, K.S. *et al.*, 'Robotics: control, sensing, vision and intelligence', McGraw Hill Int. Ed., (1987)

378 McDonald, C. and Anthony, C., 'Robotic technology, theory, design & application', A Reston Book, Prentice Hall, Englewood Cliffs, New Jersey, (1988)
379 Pan, J.L., 'Control of arc welding process', Papers on Science and Technology of China, Vol. 3, pp. 3187–3196, Science and Technology Document Publishers, Beijing, (1998) (Chinese)
380 Pan, J.L., 'Advance in arc sensing system for automatic seam tracking', Proc. of Taiwan Int. Welding Conf., TIWC98, Sept. (1998)
381 Qi, B.J. and Pan, J.L., 'Measurement of dynamic properties of arc welding power source in frequency domain', Trans. of the China Welding Institution, (1996) 12, Vol. 17, No. 4, pp. 243–248, (Chinese)
382 Pan, J.L. *et al.*, 'Welding Handbook', Vol. 1, Welding Institution of the Chinese Mech. Engineering Soc., China Machine Press (1992) (Chinese)
383 Pan, J.L. *et al.*, 'Eine neue Methode der steuerung des Schweisslichtbogens', Schweissen und Scheiden, 33 (1981), Heft. 10, pp. 523–527

Index